



Analytical method development for synthesized conjugated metabolites of *trans*-resveratrol, and application to pharmacokinetic studies

Otito F. Iwuchukwu¹, Satish Sharan¹, Daniel J. Canney, Swati Nagar*

Department of Pharmaceutical Sciences, Temple University School of Pharmacy, Philadelphia, PA 19140, USA

ARTICLE INFO

Article history:

Received 21 September 2011
Received in revised form 6 December 2011
Accepted 7 December 2011
Available online 16 December 2011

Keywords:

Resveratrol
Metabolites
Sulfates
Glucuronides
LC–MS/MS
Pharmacokinetics

ABSTRACT

Trans-3,5,4'-trihydroxystilbene (*trans*-resveratrol, RES) exhibits very low bioavailability due to extensive conjugative metabolism. Whether RES metabolites exhibit pharmacologic activity is of great interest. The present study aimed at synthesis of monoconjugates of RES – the 3- and 4' monosulfates (R3S and R4'S), and the 3- and 4' monoglucuronides (R3G and R4'G). Synthesis, purification, and yield are described. Synthesized metabolites were utilized to develop a sensitive LC–MSⁿ assay for direct quantitation of all analytes. The assay was validated for intra- and inter-day precision and accuracy. Synthesis of RES conjugates and development and validation of a sensitive bioanalytical assay were applied to pharmacokinetic evaluation of RES and its circulating monoconjugates in C57BL mice. The study is a first report of direct quantitation of RES monosulfates and monoglucuronides. These results will aid in characterizing the disposition of RES and its major or active metabolites *in vivo*.

© 2011 Elsevier B.V. All rights reserved.

1. Introduction

Trans-3,5,4'-trihydroxystilbene (*trans*-resveratrol, RES) is a dietary phytochemical thought to have beneficial health effects *via* pleiotropic mechanisms [1,2]. One major hurdle to its development is its extremely low oral bioavailability due to metabolism [3,4]. RES is known to be efficiently and almost completely converted in humans to its glucuronidated and sulfated metabolites. Human studies indicate that systemic exposure of RES is predominantly in the form of its conjugated metabolites [5,6]. This has led to the hypothesis that the conjugates of RES might themselves be active, and therefore need to be evaluated.

While a few studies have attempted evaluation of RES conjugates *in vitro* [7], it is critical to evaluate the *in vivo* disposition of

these metabolites. The pharmacokinetics (PK) of metabolites are expected to be different from those of the parent. Thus, knowledge of systemic levels of metabolites is necessary in order to correlate metabolite exposure to any observed pharmacologic activity.

As stated above, one hypothesis is that conjugated metabolites of RES are themselves active. However, the possibility of inactive metabolites also exists. Conjugation of RES is a complex process. Sulfation and glucuronidation are reversible processes and reversible metabolism can result in these metabolites acting as 'depots' for the active parent. Further, these conjugates are good candidates for enterohepatic recirculation. Recirculation of RES metabolites has indeed been suggested in preclinical studies [8]. The pharmacokinetics and pharmacodynamics of RES and its metabolites is therefore complicated by extensive first-pass metabolism, reversible conjugation, and enterohepatic recirculation.

The comprehensive study of RES and its metabolites *in vivo* requires two critical tools: (i) synthesis of adequate amounts of pure RES metabolites for *in vivo* dosing experiments, and (ii) a validated bioanalytical assay with low detection capability in order to quantitate low circulating levels of RES and its metabolites. The present work aimed at developing these two tools. Synthetic methods were developed for four monoconjugates of RES: the 3- and 4'-monosulfates (R3S and R4'S respectively), and the 3- and 4'-monoglucuronides (R3G and R4'G respectively). Our synthetic methods allowed us to produce adequate levels of pure metabolites that had application in subsequent bioanalytical assay development as standards, as well as *in vivo* PK studies. It should be noted

Abbreviations: APAP, acetaminophen; CS, calibration standards; IA, intra-arterial administration; IS, internal standard; LC–MS/MS, liquid chromatography with tandem mass spectrometry; LOQ, limit of quantitation; MRM, multiple reaction monitoring; NaOMe, sodium methoxide; PK, pharmacokinetics; QC, quality control; RES, *trans*-3,5,4'-trihydroxystilbene, *trans*-resveratrol; R3G, *trans*-resveratrol-3-O-glucuronide; R4'G, *trans*-resveratrol-4'-O-glucuronide; R3S, *trans*-resveratrol-3-sulfate; R4'S, *trans*-resveratrol-4'-sulfate; SO₃·Py, sulfur trioxide pyridine complex; THF, tetrahydrofuran.

* Corresponding author at: Temple University School of Pharmacy, 3307 N Broad Street, Philadelphia, PA 19140, USA. Tel.: +1 215 707 9110; fax: +1 215 707 3678.

E-mail addresses: otitof@temple.edu (O.F. Iwuchukwu),

satish.sharan@temple.edu (S. Sharan), daniel.canney@temple.edu (D.J. Canney), swati.nagar@temple.edu (S. Nagar).

¹ These authors contributed equally to this work.

that while these monoconjugates have recently become commercially available, their cost is prohibitive to conducting *in vivo* studies in replicates necessary for statistical power. We developed and validated an LC–MSⁿ assay for the quantitation of RES and each of its monoconjugates at low concentrations. While methods have been reported for the quantitation of RES and qualitative identification of its metabolites [9], to our knowledge direct quantitation of RES metabolites has not been conducted to date. RES metabolites have previously been evaluated by hydrolysis and against a RES standard curve. Finally, we applied our synthetic metabolite standards and validated bioanalytical assay to a pharmacokinetic analysis of RES and its metabolites in a mouse model.

2. Materials and methods

2.1. Materials

Resveratrol (*trans*-resveratrol, purity >99%; RES), chlorosulfonic acid, anhydrous pyridine, sulfur trioxide pyridine complex, sodium carbonate, acetobromo- α -D-glucuronic acid methyl ester, sodium methoxide, acetic acid, tetrahydrofuran (THF) and methanol were purchased from Sigma-Aldrich (St. Louis, MO). R3S, R3G and R4'G for initial calibration were purchased from Toronto Research Chemicals (North York, Canada). Ammonium acetate was purchased from ThermoFisher Scientific (Pittsburgh, PA). HPLC grade methanol was purchased from Mallinckrodt Baker (Phillipsburg, NJ). All chemicals used to prepare buffers and other reagents were of analytical grade and were used as such.

2.2. Synthesis of RES glucuronides

Initial attempts to synthesize RES glucuronides using a glycosyl donor in the presence of silver carbonate (as reported by Wang

et al. [10]) proved unsuccessful. The synthesis was accomplished by a direct substitution reaction between RES monosodium salt and a suitably protected glycosyl donor (acetobromo- α -D-glucuronic acid methyl ester). The acetyl protecting groups on the glycosyl moiety ensured formation of the desired β -D-glucuronide products. Briefly, RES (100 mg, 1 eq.) was dissolved in dry MeOH (3.5 ml) at room temperature, sodium methoxide (24 mg in 1.5 ml dry MeOH; 1 eq.) was added dropwise and the solution was stirred. After 1.5 h, a solution of acetobromo- α -D-glucuronic acid methyl ester (176 mg, 1 eq.) in dry MeOH (1 ml) was added slowly and the reaction was stirred for 4 h. Dry diethyl ether (30 ml) was added and the mixture was centrifuged and the organic phase was collected and evaporated to dryness. The residue was redissolved in a solution of THF and 1 M NaOH (1:1 ratio) and set to stir. After 6 h, the reaction was quenched with a 1% acetic acid in MeOH solution. The solvent was evaporated and the crude solid separated by semi-preparative chromatography to afford the desired monoglucuronides. Fig. 1 depicts this reaction scheme.

2.3. Synthesis of RES sulfates

RES sulfation was carried out with two different procedures as described below.

- RES was treated with 1 equivalent (eq.) of sulfur trioxide-pyridine complex in excess pyridine using controlled temperature conditions (35–45 °C) [11,12].
- RES was treated with 10 eq. of chlorosulfonic acid in excess pyridine at –16 °C [13]. Details of the two methods are provided below. This is the first report on the use of chlorosulfonic acid for the synthesis of resveratrol sulfates.

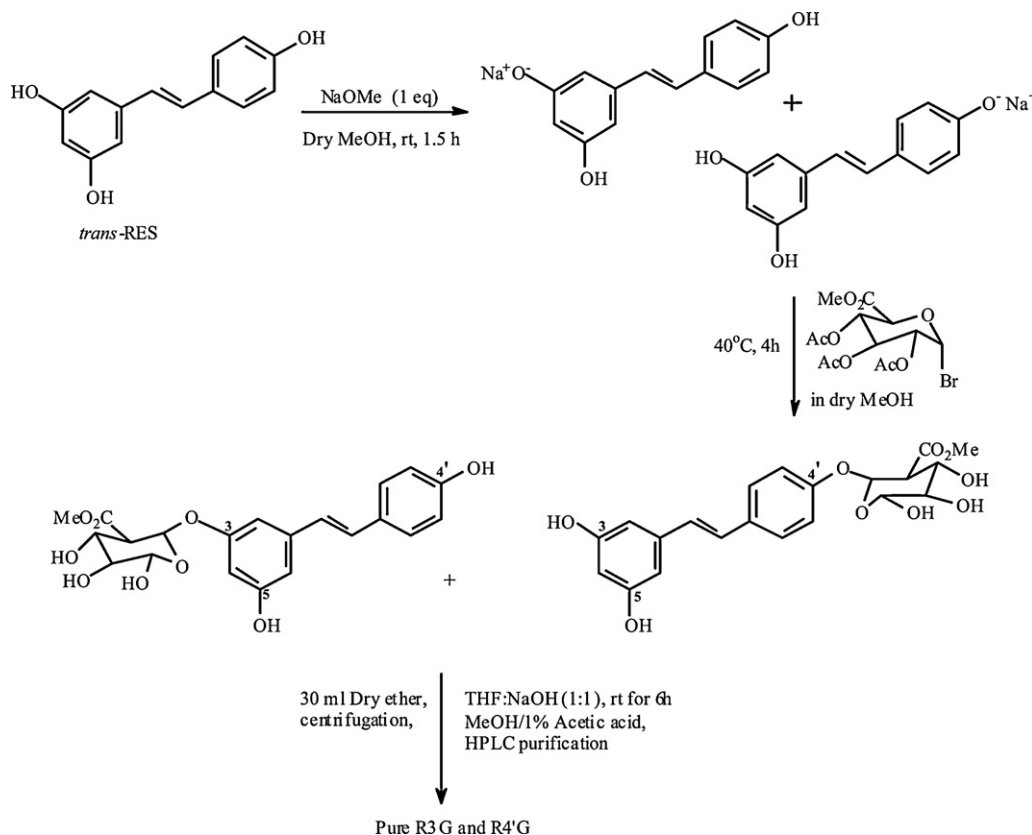


Fig. 1. Reaction scheme for RES glucuronidation using the glycosyl donor – acetobromo- α -D-glucuronic acid methyl ester.

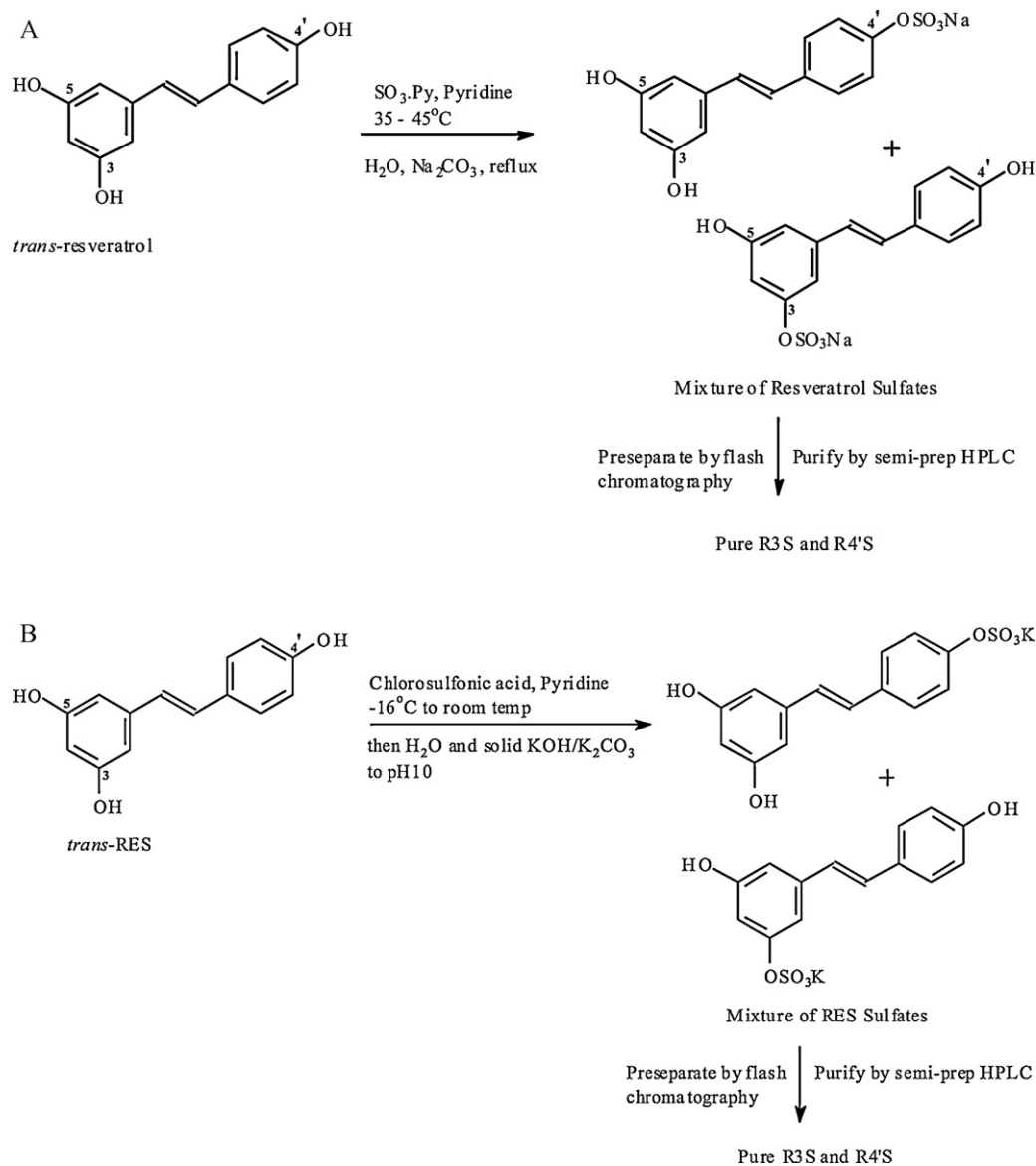


Fig. 2. Reaction schemes for RES sulfation with (a) sulfur trioxide pyridine complex and (b) chlorosulfonic acid.

2.3.1. Reaction with sulfur trioxide pyridine complex

To a stirred solution of RES (100 mg, 1 eq.) in dry pyridine at 35°C was added the SO₃·Py complex (70 mg, 1 eq.) dissolved in anhydrous pyridine and the solution was set to stir for 6–12 h. The reaction was quenched with an equal volume of water and the excess solvent was evaporated. The residue was then loaded onto a 30 g RediSep Rf Gold® High Performance HP C18 Combiflash chromatography column (Teledyne Isco, Lincoln, NE) for pre-separation of the sulfates from the parent RES. A gradient separation over 9 min was run using a water:acetonitrile mobile phase. The fractions containing a mixture of monosulfates were combined and concentrated. Final separation and purification were carried out by semi-preparative chromatography to afford the monosulfates, R3S and R4'S. The reaction scheme is depicted in Fig. 2.

2.3.2. Reaction with chlorosulfonic acid

To a chilled (–16°C) solution of RES (100 mg, 1 eq.) in dry pyridine was added chlorosulfonic acid (0.3 ml, 10 eq.) with stirring. The mixture was allowed to warm to room temperature and after 12 h the reaction was stopped and the pyridine was evaporated under reduced pressure. The residue was dissolved in water, solid KOH

or K₂CO₃ was added (to raise pH to 10) before loading onto the Combiflash column. Pre-separation and final purification was done as stated for the reaction with SO₃·Py to provide the target mono sulfates in approximately 45% yield.

2.4. Semi-preparative HPLC purification of RES conjugates

The HPLC system (HP 1100 series; Agilent Technologies, Santa Clara, CA) consisted of a solvent delivery quaternary pump, an autosampler, a diode array detector with UV detection set at 303 nm and a Phenomenex Hyperclone ODS column (250 mm × 10 mm I.D., 5 μ particle size; Phenomenex, Torrance, CA) at a flow rate of 2.5 ml/min. A modification of the gradient method reported by Murias and co-workers [14] was used to elute the target compounds according to their lipophilicities in the following order – R4'G, R3G, R4'S, and R3S. All RES conjugates were separated and collected under the following conditions: starting with a mixture of 90% aqueous ammonium acetate (solvent A) and 10% methanol (solvent B), the organic phase was linearly increased to 20% within 10 min, further increased to 35% B within 22 min and a final increase to 60% B at 25 min, where it remained constant until 30 min.

Subsequently, the percentage of methanol (B) was decreased to 10% within 2 min, and the column was equilibrated for a further 8 min before application of the next sample. HPLC retention times for RES conjugates were 15, 18, 23.4 and 24.8 min for R4'G, R3G, R4'S and R3S respectively.

Peaks corresponding to the respective RES metabolites were collected individually from each chromatographic run and pooled. The pooled fractions were then evaporated under reduced pressure and dried under vacuum. The metabolites synthesized herein were shown to be of 98% or greater purity as determined by HPLC analysis using two mobile phases (ammonium acetate/methanol gradient mobile phase detailed above, and an independent experiment with an acetonitrile/water gradient). Portions of the purified compounds were used for NMR spectroscopic measurements (see Section 2.6 below). NMR spectra of the metabolites were consistent with this high level of purity.

2.5. Identification of RES conjugates by LC-MS/MS

LC-MS analysis was performed using an Agilent HP 1200 series HPLC coupled to a 6100 series single quadrupole electrospray mass spectrometer (Agilent Tech, Santa Clara, CA) operating in both negative and positive ESI modes. UV spectra were recorded from 250 to 350 nm on the photodiode array detector. Negative and positive ion electrospray mass spectra were obtained with the electrospray capillary set at 3 kV. The flow rate of the nitrogen drying gas was 12.0 l/min at a temperature of 350 °C. Mass spectra were recorded over the range of m/z 100–1000. Alternatively, selected ion monitoring was used for greater sensitivity by recording signals for ions of m/z 307 for the sulfates and 403 for the glucuronides. Identification was done on an Agilent Zorbax SB-C18 column (30 mm \times 2.1 mm ID, 3.5 μ particle size) using a water:acetonitrile (with 0.1%, v/v formic acid) mobile phase set at a gradient of 5–100% B over 4 min and a flow rate of 1 ml/min.

2.6. NMR spectroscopic characterization

¹H, 2D-COSY, ¹³C (DEPT-135) experiments (where appropriate) were performed on a Bruker Avance III 400 MHz spectrometer (Bruker, USA). Samples were dissolved in appropriate deuterated solvents (DMSO or methanol) and all measurements were made at room temperature (298 K). Evaluation of the experiments was carried out using Bruker's automated software, TopSpin 2.1. Spectroscopic data for the metabolites reported herein were identical to those previously reported by others [15–17].

2.7. LC-MS assay development for analysis of RES and metabolites

2.7.1. Preparation of stock solutions, calibration standards (CS) and quality control (QC) samples

Stock solutions of RES, R4'G, R3G, R4'S, R3S and APAP (IS) were prepared separately in DMSO. CS samples were prepared by spiking stock standard working solution into heparinized mouse plasma to give eight CS in the concentration range of 2.46–2460 ng/ml for R3S, 3.57–3570 ng/ml for R3S and 10–10,000 ng/ml for R4'G, R3G and RES. Similar to calibration standards, QC samples were prepared in replicates ($n = 3$ and $n = 5$ for the inter-day and intra-day validation respectively) at five concentration levels representing the entire range of concentrations (10, 20, 50, 1000 and 10,000 ng/ml for RES, R4'G, and R3G; 3.57, 7.15, 17.9, 357 and 3570 ng/ml for R4'S and 2.46, 4.93, 12.3, 246 and 2460 ng/ml for R3S).

2.7.2. Sample preparation

RES, R4'G, R3G, R4'S, and R3S were isolated from plasma with protein precipitation. To 10 μ l of plasma sample, 2.5 μ l of 15%

ascorbic acid was added and vortexed for 1 min. Then 30 μ l of methanol containing 78 ng/ml APAP (internal standard) was added and again vortexed for 1 min and centrifuged at 15,000 rpm for 15 min at room temperature. Supernatant (10 μ l) was injected into the liquid chromatography tandem mass spectrometry system.

2.7.3. LC-MS/MS conditions

The LC-MS/MS assay was carried out on an Agilent series 1100 high-performance liquid chromatography system equipped with a binary pump, autosampler and degasser coupled to an API 4000 triple-quadrupole tandem mass spectrometer from ABSciex with ESI source operated in the negative ion mode. Analyst software version 1.4.2 (ABSciex) was used for instrument control, data acquisition and data processing for both chromatography and mass spectrometry. The chromatographic separation system consisted of a guard column (Zorbax SB-C18, 5 μ m, 4.6 mm \times 12.5 mm; Agilent Technologies), an analytical column (Zorbax SB-C18, 5 μ m, 4.6 mm \times 150 mm; Agilent Technologies) and a gradient mobile phase of A: 5 mM ammonium acetate and B: methanol. The elution started with 90% A at 0 min to 80% at 2 min, 65% at 10 min, 40% at 12 min to 17 min and 90% at 19 min. Flow rate of the mobile phase was 1 ml/min and the flow from the column was split 1:3 into a ABSciex API4000 triple quadrupole mass spectrometer equipped with a Turbo ionspray source operating at 450 °C. The column temperature was maintained at 35 °C. The ESI instrument settings were optimized for the analysis and the appropriate MRM transitions and MS/MS parameters were determined for individual compounds by direct infusion into the mass spectrometer. Nitrogen was used as the curtain, collision and ion source gas.

2.8. Assay validation

The method was validated according to published recommendations for bioanalytical method validation [18]. Calibration curves were constructed from the peak area ratios of each analyte to internal standard versus plasma concentrations with linear least squares regression calculation and a weighting factor of $1/X^2$. Solvent (methanol) and blank were run after every two samples. Intra-day accuracy and precision were determined by analyzing five replicates of QC samples. Inter-day accuracy and precision were evaluated on five separate days. Precision was expressed as the relative standard deviation of the determined concentrations. Accuracy was calculated with the following equation: Accuracy = [(mean measured concentration – nominal concentration)/nominal concentration] \times 100. Recovery of metabolites was investigated by analyzing five individual plasma samples at low, medium and high concentrations. These concentrations were: 20, 1000, and 10,000 ng/ml for R3G and R4'G; 4.93, 246, and 2460 ng/ml for R3S; and 7.15, 357, and 3570 ng/ml for R4'S. The recovery was determined by comparing analyte: IS peak area ratio upon extraction from spiked plasma to analyte: IS peak area ratio in pre-prepared plasma matrix.

2.9. Application of synthesis and bioanalytical method: pharmacokinetics of RES and quantitation of its metabolites in vivo

Male C57BL/6 mice weighing between 20 and 25 g were supplied by Jackson Labs and maintained in the American Association for the Accreditation of Laboratory Animal Care-accredited University Laboratory Animal Resources of Temple University. All animal studies were approved by the Institutional Animal Care and Use Committee.

A carotid artery cannula was surgically implanted into the right carotid artery of each mouse, and animals were allowed to recover overnight. Carotid artery cannula was used for systemic

Table 1
Yields and spectroscopic data for RES mono-sulfates and glucuronides.

Compound (Mol. Wt.)	Theoretical yield	Actual yield (%)	¹ H NMR	LC-MS (<i>m/z</i> , RT, % purity)
R4'S (308)	135 mg	23 mg (17%)	(MeOH- <i>d</i> ₄ , DQF COSY): δ = 6.2 (t, <i>J</i> = 2.1 Hz, H-4), 6.5 (d, <i>J</i> = 2.1 Hz, H-2,6), 6.95 (d, <i>J</i> = 16.3 Hz, <i>trans</i> -vinyl), 7.04 (d, <i>J</i> = 16.3 Hz, <i>trans</i> -vinyl), 7.29 (d, <i>J</i> = 8.7 Hz, H-3',5'), 7.50 (<i>J</i> = 8.7 Hz, H-2',6')	307 [M-H] ⁺ , 1.77 min, 99%
R3S (308)	135 mg	37 mg (27%)	(MeOH- <i>d</i> ₄ , DQF COSY): δ = 6.66 (t, <i>J</i> = 2.1 Hz, H-4), 6.74 (t, H-6), 6.76 (d, <i>J</i> = 8.6 Hz, H-3',5'), 6.85 (d, <i>J</i> = 16.2 Hz, <i>trans</i> -vinyl), 6.97 (t, H-2), 7.05 (d, <i>J</i> = 16.2 Hz, <i>trans</i> -vinyl), 7.37 (d, <i>J</i> = 8.6 Hz, H-2',6')	307 [M-H] ⁺ , 1.98 min, 98%
R4'G ^a (404)	176 mg	20 mg (11%)	(MeOH- <i>d</i> ₄ , DQF COSY): δ = 3.52 (m, 3H, 3 × H, H2''-H4''), 3.78 (m, 1H, H5''), 4.93 (s, 1H, H1''), 6.16 (t, <i>J</i> = 2.1 Hz, H-4), 6.46 (d, <i>J</i> = 2.1 Hz, H-2,6), 6.85 (d, <i>J</i> = 16.3 Hz, <i>trans</i> -vinyl), 6.96 (d, <i>J</i> = 16.3 Hz, <i>trans</i> -vinyl), 7.11 (d, <i>J</i> = 8.7 Hz, H-3',5'), 7.43 (<i>J</i> = 8.7 Hz, H-2',6')	403 [M-H] ⁺ , 1.78 min, 99%
R3G ^a (404)	176 mg	34 mg (19%)	(MeOH- <i>d</i> ₄ , DQF COSY): δ = 3.43 (m, 3H, 3 × H, H2''-H4''), 3.68 (m, 1H, H5''), 4.82 (s, 1H, H1''), 6.40 (t, <i>J</i> = 2.1 Hz, H-4), 6.52 (d, <i>J</i> = 2.1 Hz, H-2,6), 6.67 (d, <i>J</i> = 8.7 Hz, H-3',5'), 6.75 (d, <i>J</i> = 16.3 Hz, <i>trans</i> -vinyl), 6.91 (d, <i>J</i> = 16.3 Hz, <i>trans</i> -vinyl), 7.28 (<i>J</i> = 8.7 Hz, H-2',6')	403 [M-H] ⁺ , 1.95 min, 99%

Quantity of starting material (RES) was 100 mg (0.44 mM).

^a Numbering for glucuronic acid proton assignment.

drug administration and blood sampling. Heparin-saline (20 μl, 50 IU/ml) was used to flush the cannula after systemic administration or blood sampling. RES solubilized in 20% 2-hydroxypropyl-β-cyclodextrin in saline was administered intra-arterially (I.A.) at a dose of 60 mg/kg. The I.A. route was selected in order to achieve 100% systemic bioavailability. The dose was selected in order to achieve measurable concentrations of all RES conjugates including quantitatively minor metabolites. Blood (20 μl) was serially sampled at 2.5, 5, 10, 15, 45, 90, 180, 300, 420 and 600 min. Blood samples were centrifuged at 14,000 rpm for 2 min, the harvested plasma was collected and stored at -80 °C until LCMS/MS analysis. PK data analysis was performed with the software package WinNonlin Version 5.2 (Pharsight, Mountain View, CA). Pharmacokinetics of RES and metabolites were analyzed by standard non-compartmental methods that yielded individual animal estimates of total clearance, volume of distribution, elimination half-life, area under the RES plasma concentration-time curves from time 0 to 10 h (AUC₀₋₁₀) and 0 to infinity (AUC_{0-inf}), and metabolite plasma concentration-time curves from time 0 to 10 h (metabolite AUC₀₋₁₀) and 0 to infinity (metabolite AUC_{0-inf}).

3. Results

3.1. Synthesis of RES glucuronides and sulfates

The synthesis of the glucuronides was accomplished using a modification of the procedure reported by Vitaglione and co-workers [15]. The route used to prepare R3G and R4'G is shown in Fig. 1. RES mono-sulfates were prepared using modifications to two precedented procedures [11–13,19]. Fig. 2A depicts the use of SO₃-Py complex while Fig. 2B involves the use of chlorosulfonic acid. Yields and spectroscopic data for RES mono-sulfates and glucuronides are listed in Table 1.

3.2. LC-MS/MS assay for quantitation of RES and its metabolites

ESI operated in negative ion mode was used for the LC-MS/MS analysis to provide optimum sensitivity and selectivity. The optimized tandem mass spectrometry conditions are summarized in Table 2. The following precursor-product ion transitions were observed: *m/z* 227 → 185 for RES, *m/z* 150 → 107 for acetaminophen (APAP, internal standard IS), 403 → 113 for R4'G and R3G and 307 → 227 for R4'S and R3S with a dwell time of 400 ms for each ion transition. The daughter ion for sulfated metabolites (227) corresponds to the RES moiety and the daughter ion for glucuronidated metabolites (113) corresponds to the glucuronide moiety fragment [20]. The retention time was ~5 min for APAP,

Table 2

Optimized ESI-MS/MS operating, MRM and MS/MS parameters for RES, R4'G, R3G, R4'S, R3S and APAP (IS).

Operating parameters	Setting			
Collision gas (psi)	6			
Curtain gas (psi)	40			
Ion source gas 1 (psi)	55			
Ion source gas 2 (psi)	55			
Ion spray voltage (V)	-4500			
Temperature (°C)	450			
EP (V)	-10			
Run duration (min)	19			
	RES	R4'G/R3G	R4'S/R3S	APAP(IS)
Precursor ion (<i>m/z</i>)	227	403	307	150
Product ion (<i>m/z</i>)	185	113	227	107
Dwell time (ms)	400	400	400	400
DP (V)	-70	-65	-40	-40
CE (V)	-26	-24	-32	-24
CXP (V)	-11	-5	-5	-5

~5.9 min for R4'G, ~7.3 min for R3G, ~9.2 min for R4'S, ~10.2 min for R3S and ~14.2 min for RES. A representative chromatogram is presented in Fig. 3.

In this study, the calculated peak area ratios of RES, R4'G, R3G, R4'S and R3S to APAP versus the nominal concentration of the analyte displayed a good linear relationship with coefficients

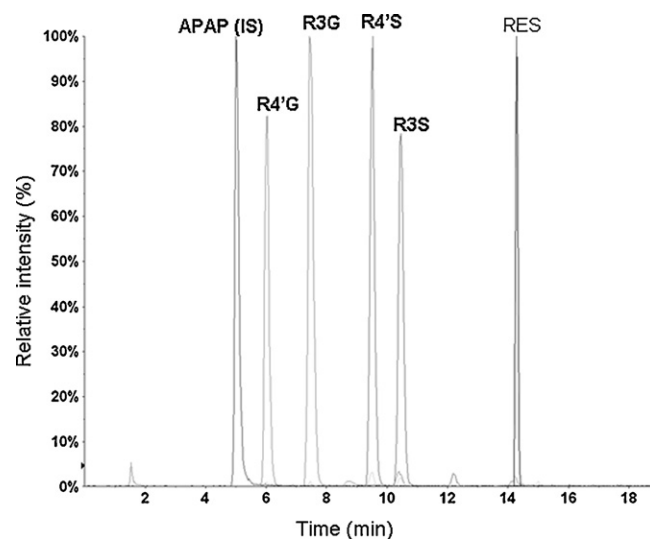


Fig. 3. Representative chromatograms of RES, APAP (IS), R4'G, R3G, R4'S and R3S.

Table 3
Intra-day ($n=5$) and inter-day ($n=5$) precision and accuracy for RES, R4'G, R3G, R4'S and R3S in mouse plasma.

Analytes	Nominal concentration (ng/ml)	Intra-day ($n=5$)			Interday ($n=5$)		
		Measured concentration \pm SD (ng/ml)	Precision (%)	Accuracy (%)	Measured concentration \pm SD (ng/ml)	Precision (%)	Accuracy (%)
RES	10 ^a	9.34 \pm 0.93	10	-6.64	9.83 \pm 0.89	9.02	-1.7
	20	19.66 \pm 1.81	9.2	-1.7	20.80 \pm 1.70	8.16	3.99
	50	54.82 \pm 1.92	3.52	9.16	50.70 \pm 4.18	8.24	1.41
	1000	1017.6 \pm 81.99	8.06	1.76	1020.32 \pm 59.84	5.86	2.03
	10,000	10,218 \pm 501.12	4.9	2.18	10,038.27 \pm 780.66	7.78	0.38
R4'G	10 ^a	9.01 \pm 0.91	10.07	-9.88	9.69 \pm 0.83	8.52	-3.09
	20	18.68 \pm 1.23	6.59	-6.6	19.64 \pm 1.25	6.34	-1.82
	50	48.96 \pm 2.11	4.32	-2.08	47.73 \pm 3.00	6.28	-4.55
	1000	1053.20 \pm 33.78	3.21	5.32	1058.11 \pm 23.5	2.22	5.81
	10,000	10,254 \pm 422	4.12	2.54	10,202.8 \pm 471.46	4.62	2.03
R3G	10 ^a	9 \pm 0.35	3.83	-9.96	9.64 \pm 0.56	5.84	-3.58
	20	17.64 \pm 0.42	2.39	-11.8	19.09 \pm 1.21	6.33	-4.56
	50	47 \pm 1.96	4.16	-6	46.49 \pm 1.91	4.12	-7.03
	1000	1047.60 \pm 44.03	4.2	4.76	1075.65 \pm 27.76	2.58	7.57
	10,000	10,366 \pm 426.36	4.11	3.66	10,351.20 \pm 429.35	4.15	3.51
R4'S	3.57 ^a	3.55 \pm 0.32	8.89	-0.5	3.73 \pm 0.25	6.82	4.46
	7.15	7 \pm 0.71	10.19	-2.07	7.12 \pm 0.41	5.70	-0.41
	17.9	17.76 \pm 0.75	4.24	-0.78	17.63 \pm 1.35	7.68	-1.5
	357	359.40 \pm 12.18	3.39	0.67	378.68 \pm 11.89	3.14	6.07
	3570	3708 \pm 164.07	4.42	3.87	3826.93 \pm 114.03	2.98	7.2
R3S	2.46 ^a	2.30 \pm 0.25	10.88	-6.5	2.42 \pm 0.14	5.97	-1.63
	4.93	5.03 \pm 0.44	8.78	1.95	4.83 \pm 0.28	5.88	-2
	12.3	12.38 \pm 0.40	3.25	0.65	11.79 \pm 0.82	6.98	-4.15
	246	255.40 \pm 8.02	3.14	3.82	259.01 \pm 3.62	1.4	5.29
	2460	2740 \pm 140.36	5.12	11.38	2610 \pm 162.48	6.23	6.1

^a Concentrations determined to be LOQ.

of determination ≥ 0.99 over a concentration range of 10–10,000 ng/ml for RES, R4'G, R3G, 3.57–3570 ng/ml for R4'S and 2.46–2460 ng/ml for R3S using a weighting factor of $1/X^2$. The limits of quantitation (LOQs) were established at the lowest points of the standard curves, i.e. 3.57 ng/ml for R4'S, 2.46 ng/ml for R3S and 10 ng/ml for R4'G, R3G and RES. The results of intra-day and inter-day accuracy and precision are presented in Table 3. The intra- and inter-day precision for all the analytes was less than 15%. The recovery of R3G and R4'G at low (20 ng/ml), medium (100 ng/ml) and high (10,000 ng/ml) concentrations was 79.58, 91 and 90.98% for R3G and 89.93, 86.15 and 94.83% for R4'G respectively. Recovery of R3S at low (4.93 ng/ml), medium (246 ng/ml) and high (2460 ng/ml) concentration was 105.13, 99.21 and 96.11% respectively. R4'S recovery at low (7.15 ng/ml), medium (357 ng/ml) and high (3570 ng/ml) concentration was 97.31, 108.71 and 103.61% respectively. The results indicate that the recovery, precision and accuracy of this method were adequate for bioanalytical purposes.

3.3. Application to pharmacokinetic studies

The mean plasma concentration–time profiles of RES and its metabolites are shown in Fig. 4, with pharmacokinetic parameter and metric estimates listed in Table 4. RES exhibited a high steady-state volume of distribution and an elimination half life of 110 min. At the end of 10 h, R3G was quantitatively the most abundant metabolite, followed by R3S. Both R4'S and R4'G were quantitatively minor metabolites. The mean systemic clearance of RES was high (251.14 ml/min/kg) when compared with hepatic blood flow in the mouse (90 ml/min/kg) [21,22].

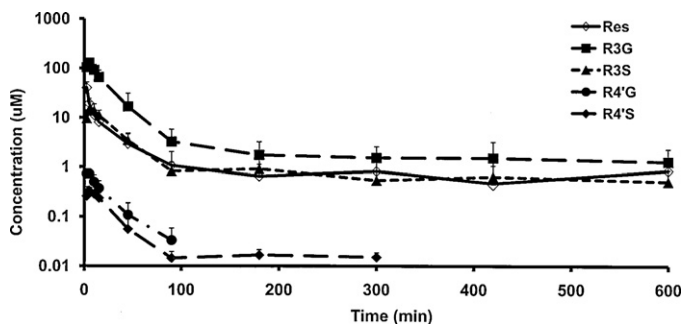


Fig. 4. Plasma concentration–time profile of RES and its monoconjugated metabolites. RES and metabolite concentrations in plasma were determined in C57BL/6J mice ($n=6$) receiving 60 mg/kg RES as an IA short infusion (10 s). Data are represented as mean \pm SD, $n=6$.

Table 4
Noncompartmental analysis of RES and its metabolites upon a single 60 mg/kg IA RES dose.

PK parameter/metric (units)	Estimate \pm SD, $n=6$
AUC ₀₋₁₀ (min μ M)	1065.93 \pm 394.89
AUC _{0-inf} (min μ M)	1206.87 \pm 475.51
Cl (ml/min/kg)	251.14 \pm 109.08
V _{ss} (l/kg)	38.35 \pm 13.56
t _{1/2} (min)	109.75 \pm 22.90
R3GAUC ₀₋₁₀ (min μ M)	3891.47 \pm 1179.42
R3GAUC _{0-inf} (min μ M)	4191.01 \pm 1297.29
R3SAUC ₀₋₁₀ (min μ M)	823.80 \pm 214.63
R3SAUC _{0-inf} (min μ M)	1023.86 \pm 352.44
R4'GAUC ₀₋₁₀ (min μ M)	17.49 \pm 7.30
R4'GAUC _{0-inf} (min μ M)	18.78 \pm 7.61
R4'SAUC ₀₋₁₀ (min μ M)	11.27 \pm 3.75
R4'SAUC _{0-inf} (min μ M)	12.17 \pm 4.39

4. Discussion and conclusions

4.1. Synthesis of RES metabolites

For RES glucuronidation, facile synthesis of the 3 and 4' glucuronide products was achieved with the use of 1 eq of acetobromo glucuronic acid methyl ester. This method is a modification of the procedure reported by Vitaglione and co-workers [15]. This one pot reaction involves the use of NaOMe in methanol which serves as the protonating agent for RES and the deprotecting agent for the acetyl groups.

The majority of reports on the chemical synthesis of RES sulfates [17,23–25] use a modification of the sulfation procedure reported by Kawai et al. (1 eq. $\text{SO}_3 \cdot \text{Py}$ complex at 60 °C) [11]. An exception is the work by Hoshino and co-workers [27]. Kawai et al. stated that carrying out the reaction at room temperature yielded more monosulfated products and heating to 60 °C ensured disulfation. In our hands, RES sulfation at 60 °C yielded predominantly disulfated products (a finding confirmed by others [11,12]) while at room temperature no measurable sulfates were isolated. However, when the temperature was carefully maintained at 35 °C, RES monosulfates were obtained but with lower yields. Thus, the sulfation of RES using the $\text{SO}_3 \cdot \text{Py}$ complex was found to be highly temperature dependent. Hoshino et al. [26] attempted to avoid the challenge of disulfate formation by selectively protecting the hydroxyl groups. This method was not used here due to the multiple steps involved in the approach and the modest increase in yields reported.

The synthesis of RES monosulfates reported herein was carried out using $\text{SO}_3 \cdot \text{Py}$ complex at 35 °C. Removal of unreacted RES was accomplished by pretreating the reaction mixture with a reverse phase Combiflash (RediSep™ Gold) column. The recovered RES was dried and used for future reactions thus improving reaction efficiency. Fractions containing the sulfates were pooled, concentrated and loaded directly onto a semi-prep column where an effective separation of the 3 and 4' regio-isomers was achieved (evaporation of fractions to dryness was found to result in solvolysis, presumably due to the presence of sulfuric acid – the reaction byproduct).

Another sulfating agent reported for polyphenol sulfation is chlorosulfonic acid which has been used successfully for sulfating daidzein and other isoflavonoids such as quercetin, genistein and equol [13,19]. The use of 10 eq. of chlorosulfonic acid (more than 10 eq. increased the non-selectivity) in excess pyridine at –16 °C afforded the desired monosulfates of RES with less disulfate formation than the $\text{SO}_3 \cdot \text{Py}$ complex method. With respect to the separation and purification, the same measures applied for the work up of the $\text{SO}_3 \cdot \text{Py}$ complex reaction were utilized to obtain the final purified sulfated products. Both the $\text{SO}_3 \cdot \text{Py}$ complex reaction and the reaction involving chlorosulfonic acid afford the monosulfates in approximately 45% yield. However, sulfation using the $\text{SO}_3 \cdot \text{Py}$ complex was preferred due to the milder nature of the sulfating agent and the reduced reaction time.

4.2. Development and validation of LC–MSⁿ method

There are reports of synthetic RES metabolites used as qualitative standards, but no study to date has directly quantitated these metabolites [6,27,28]. Studies to date have utilized a RES standard curve to quantitate its conjugates after their hydrolysis. Hydrolysis of conjugated metabolites to convert them to parent RES adds uncertainty to their quantitation due to experimental issues such as incomplete deconjugation, degradation, and error introduced due to additional sample preparation steps. Thus, quantitation of RES conjugates directly against their synthetic standards is a vast improvement. Table 3 shows the validation of our assay for the parent as well as all monoconjugate analytes. The LC method reported here was modified from a previously published method [14]. Our

modified method had a shorter run time (19 min versus 30 min), and included an internal standard (APAP). The sensitivity of the present assay is greatly increased (2.46 ng/ml for R3S) as compared to the earlier method (100 ng/ml for R3S). This improved sensitivity is critical to evaluation of low levels of metabolites formed *in vivo*. The most important distinction in our assay is the resolution of R3S and R4'S metabolites, and quantitation of each metabolite against its synthetic standard. Given the purported activity of R4'S in cell-based assays [7], it is especially important to analyze this metabolite and understand its *in vivo* disposition. Finally, the direct quantitation of RES glucuronides has not been previously reported. The present method offers a major advantage over previous methods in being a highly sensitive and specific assay for concomitant determination of RES and all 4 of its monoconjugated metabolites.

4.3. Application to PK studies

RES pharmacokinetics have previously been reported in rats, pigs, and humans [6,8,9,27,29,30]. Aspects of its disposition such as absorption, metabolism, and distribution have been evaluated in mouse models [31,32]. Similar to disposition in rats, RES was highly metabolized to R3G in the present study with mice [9]. The systemic clearance of RES in the present study (251 ml/min/kg) was of a similar magnitude as that reported in rats (195 ml/min/kg by Marier et al., 183 ml/min/kg by Kapetanovic et al.) [8,27]. Previous studies in rodents did not report any RES 4' conjugates. Quantitation of R4'G and R4'S in the present study was enabled by the synthesis of standards as well as development of a sensitive bioanalytical assay. Our results indicate the utility of our synthesis and bioanalytical methods in comprehensive PK evaluation of RES, to resolve issues such as its metabolism, enterohepatic recirculation, formation and disposition kinetics of potentially active metabolites, and reversible metabolism of potentially 'depot' conjugates. Studies are currently underway in our laboratories to evaluate the PK of not only RES but also its pre-formed synthetic sulfates and glucuronides.

5. Conclusion

All four monoconjugates of RES – R3S, R4'S, R3G, and R4'G – have been successfully synthesized, purified, and characterized. These metabolites were utilized as synthetic standards to develop and validate a highly sensitive LC–MSⁿ assay for concomitant quantitation of RES and all its monoconjugates. Together, synthetic metabolites and validation of a bioanalytical method were applied to characterize the plasma PK of RES in mice. Future studies will include characterization of biological activity of RES metabolites, as well as the pharmacokinetics of these pre-formed metabolites. An understanding of RES disposition will allow better RES regimen design for increased efficacy, as well as design of analogs with improved PK characteristics such as increased bioavailability.

Acknowledgments

The work was partially supported by Award number R03CA133943 from the National Cancer Institute to SN and DJC. The content is solely the responsibility of the authors and does not necessarily represent the official views of the NIH or NCI. The authors are grateful also for support supplied by Temple University Graduate School (OFI) and to the School of Pharmacy (SS).

Appendix A. Supplementary data

Supplementary data associated with this article can be found, in the online version, at doi:10.1016/j.jpba.2011.12.006.

References

- [1] B.B. Aggarwal, S. Shishodia (Eds.), *Resveratrol in Health and Disease*, CRC Press, Taylor and Francis Group, Boca Raton FL, 2006.
- [2] J.A. Baur, D.A. Sinclair, Therapeutic potential of resveratrol: the in vivo evidence, *Nat. Rev. Drug Discov.* 5 (2006) 493–506.
- [3] T. Walle, F. Hsieh, M.H. DeLegge, J.E. Oatis, U.K. Walle Jr., High absorption but very low bioavailability of oral resveratrol in humans, *Drug Metab. Dispos.* 32 (2004) 1377–1382.
- [4] A.A.E. Bertelli, Pharmacokinetics and metabolism of resveratrol, in: B.B. Aggarwal, S. Shishodia (Eds.), *Resveratrol in Health and Disease*, CRC Press, Boca Raton, FL, 2006.
- [5] L. Almeida, M. Vaz-da-Silva, A. Falcao, E. Soares, R. Costa, A.I. Loureiro, C. Fernandes-Lopes, J.F. Rocha, T. Nunes, L. Wright, P. Soares-da-Silva, Pharmacokinetic and safety profile of trans-resveratrol in a rising multiple-dose study in healthy volunteers, *Mol. Nutr. Food Res.* 53 (2009) S7–S15.
- [6] D.J. Boocock, G.E. Faust, K.R. Patel, A.M. Schinas, V.A. Brown, M.P. Ducharme, T.D. Booth, J.A. Crowell, M. Perloff, A.J. Gescher, W.P. Steward, D.E. Brenner, Phase I dose escalation pharmacokinetic study in healthy volunteers of resveratrol, a potential cancer chemopreventive agent, *Cancer Epidemiol. Biomarkers Prev.* 16 (2007) 1246–1252.
- [7] B. Calamini, K. Ratia, M.G. Malkowski, M. Cuendet, J.M. Pezzuto, B.D. Santariero, A.D. Mesecar, Pleiotropic mechanisms facilitated by resveratrol and its metabolites, *Biochem. J.* 429 (2010) 273–282.
- [8] J.F. Marier, P. Vachon, A. Gritsas, J. Zhang, J.P. Moreau, M.P. Ducharme, Metabolism and disposition of resveratrol in rats: extent of absorption, glucuronidation, and enterohepatic recirculation evidenced by a linked-rat model, *J. Pharmacol. Exp. Ther.* 302 (2002) 369–373.
- [9] M.E. Juan, M. Maijo, J.M. Planas, Quantification of trans-resveratrol and its metabolites in rat plasma and tissues by HPLC, *J. Pharm. Biomed. Anal.* 51 (2010) 391–398.
- [10] L.X. Wang, A. Heredia, H. Song, Z. Zhang, B. Yu, C. Davis, R. Redfield, Resveratrol glucuronides as the metabolites of resveratrol in humans: characterization, synthesis, and anti-HIV activity, *J. Pharm. Sci.* 93 (2004) 2448–2457.
- [11] N. Kawai, Y. Fujibayashi, S. Kuwabara, K.-i. Takao, Y. Ijuin, S. Kobayashi, Synthesis of a potential key intermediate of akaterpin, specific inhibitor of PI-PLC, *Tetrahedron* 56 (2000) 6467–6478.
- [12] N. Kawai, K.-i. Takao, S. Kobayashi, Synthetic study of akaterpin: determination of the relative stereochemistry of the upper decalin moiety with disulfated hydroquinone, *Tetrahedron Lett.* 40 (1999) 4193–4196.
- [13] B. Fairley, N.P. Botting, A. Cassidy, The synthesis of daidzein sulfates, *Tetrahedron* 59 (2003) 5407–5410.
- [14] M. Murias, M. Miksits, S. Aust, M. Spatzenegger, T. Thalhammer, T. Szekeres, W. Jaeger, Metabolism of resveratrol in breast cancer cell lines: impact of sulfotransferase 1A1 expression on cell growth inhibition, *Cancer Lett.* 261 (2008) 172–182.
- [15] P. Vitaglione, S. Sforza, G. Galaverna, C. Ghidini, N. Caporaso, P.P. Vescovi, V. Fogliano, R. Marchelli, Bioavailability of trans-resveratrol from red wine in humans, *Mol. Nutr. Food Res.* 49 (2005) 495–504.
- [16] E. Wenzel, T. Soldo, H. Erbersdobler, V. Somoza, Bioactivity and metabolism of trans-resveratrol orally administered to Wistar rats, *Mol. Nutr. Food Res.* 49 (2005) 482–494.
- [17] C. Yu, Y.G. Shin, A. Chow, Y. Li, J.W. Kosmeder, Y.S. Lee, W.H. Hirschelman, J.M. Pezzuto, R.G. Mehta, R.B. van Breemen, Human, rat, and mouse metabolism of resveratrol, *Pharm. Res.* 19 (2002) 1907–1914.
- [18] V.P. Shah, K.K. Midha, J.W. Findlay, H.M. Hill, J.D. Hulse, I.J. McGilveray, G. McKay, K.J. Miller, R.N. Patnaik, M.L. Powell, A. Tonelli, C.T. Viswanathan, A. Yacobi, Bioanalytical method validation – a revisit with a decade of progress, *Pharm. Res.* 17 (2000) 1551–1557.
- [19] O. Soidinsalo, K. Wähälä, Synthesis of phytoestrogenic isoflavonoid disulfates, *Steroids* 69 (2004) 613–616.
- [20] D. Wang, T. Hang, C. Wu, W. Liu, Identification of the major metabolites of resveratrol in rat urine by HPLC–MS/MS, *J. Chromatogr. B: Analyt. Technol. Biomed. Life Sci.* 829 (2005) 97–106.
- [21] H. Boxenbaum, Interspecies variation in liver weight, hepatic blood flow, and antipyrine intrinsic clearance: extrapolation of data to benzodiazepines and phenytoin, *J. Pharmacokin. Biopharm.* 8 (1980) 165–176.
- [22] B. Davies, T. Morris, Physiological parameters in laboratory animals and humans, *Pharm. Res.* 10 (1993) 1093–1095.
- [23] J.D. Kenealey, L. Subramanian, P. van Ginkel, S. Darjatmoko, M. Lindstrom, V. Somoza, S. Ghosh, Z. Song, R. Hsung, G.S. Kwon, K. Eliceiri, D. Albert, A. Polans, Resveratrol metabolites do not elicit early pro-apoptotic mechanisms in neuroblastoma cells, *J. Agric. Food Chem.* 59 (2011) 4979–4986.
- [24] M. Miksits, K. Wlcek, M. Svoboda, O. Kunert, E. Haslinger, T. Thalhammer, T. Szekeres, W. Jaeger, Antitumor activity of resveratrol and its sulfated metabolites against human breast cancer cells, *Planta Med.* 75 (2009) 1227–1230.
- [25] E. Wenzel, V. Somoza, Metabolism and bioavailability of trans-resveratrol, *Mol. Nutr. Food Res.* 49 (2005) 472–481.
- [26] J. Hoshino, E.J. Park, T.P. Kondratyuk, L. Marler, J.M. Pezzuto, R.B. van Breemen, S. Mo, Y. Li, M. Cushman, Selective synthesis and biological evaluation of sulfate-conjugated resveratrol metabolites, *J. Med. Chem.* 53 (2010) 5033–5043.
- [27] I.M. Kapetanovic, M. Muzzio, Z. Huang, T.N. Thompson, D.L. McCormick, Pharmacokinetics, oral bioavailability, and metabolic profile of resveratrol and its dimethylether analog, pterostilbene, in rats, *Cancer Chemother. Pharmacol.* 68 (2010) 593–601.
- [28] V.A. Brown, K.R. Patel, M. Viskaduraki, J.A. Crowell, M. Perloff, T.D. Booth, G. Vasilinin, A. Sen, A.M. Schinas, G. Piccirilli, K. Brown, W.P. Steward, A.J. Gescher, D.E. Brenner, Repeat dose study of the cancer chemopreventive agent resveratrol in healthy volunteers: safety, pharmacokinetics, and effect on the insulin-like growth factor axis, *Cancer Res.* 70 (2010) 9003–9011.
- [29] T. Nunes, L. Almeida, J.F. Rocha, A. Falcao, C. Fernandes-Lopes, A.I. Loureiro, L. Wright, M. Vaz-da-Silva, P. Soares-da-Silva, Pharmacokinetics of trans-resveratrol following repeated administration in healthy elderly and young subjects, *J. Clin. Pharmacol.* 49 (2009) 1477–1482.
- [30] M. Azorin-Ortuno, M.J. Yanez-Gascon, F.J. Pallares, F. Vallejo, M. Larrosa, M.T. Garcia-Conesa, F. Tomas-Barberan, J.C. Espin, Pharmacokinetic study of trans-resveratrol in adult pigs, *J. Agric. Food Chem.* (2010).
- [31] X. Vitrac, A. Desmouliere, B. Brouillaud, S. Krisa, G. Deffieux, N. Barthe, J. Rosenbaum, J.M. Merillon, Distribution of [¹⁴C]-trans-resveratrol, a cancer chemopreventive polyphenol, in mouse tissues after oral administration, *Life Sci.* 72 (2003) 2219–2233.
- [32] I. Alfaras, M. Perez, M.E. Juan, G. Merino, J.G. Prieto, J.M. Planas, A.I. Alvarez, Involvement of breast cancer resistance protein (BCRP1/ABCG2) in the bioavailability and tissue distribution of trans-resveratrol in knockout mice, *J. Agric. Food Chem.* 58 (2010) 4523–4528.



A rapid LC–MS/MS method for the quantitation of a series of benzonaphthyridine derivatives: Application to *in vivo* pharmacokinetic and lipophilicity studies in drug development

Pradeep B. Lukka^{a,b}, James W. Paxton^b, Graham J. Atwell^a, Philip Kestell^a, Bruce C. Baguley^{a,*}

^a Auckland Cancer Society Research Centre, Faculty of Medical and Health Sciences, The University of Auckland, Private Bag 92019, Auckland, New Zealand

^b Department of Pharmacology & Clinical Pharmacology, Faculty of Medical and Health Sciences, The University of Auckland, Private Bag 92019, Auckland, New Zealand

ARTICLE INFO

Article history:

Received 6 October 2011
Received in revised form 19 January 2012
Accepted 19 January 2012
Available online 28 January 2012

Keywords:

Lipophilicity
Antitumour
Benzonaphthyridine
LC–MS/MS
Topoisomerase poison
SN 28049

ABSTRACT

Drug lipophilicity is a vital physicochemical parameter that influences drug absorption, distribution, metabolism, excretion and toxicology. A comparative study of a homologous series based on a pharmaceutically active drug represents a powerful approach to the study of the effects of drug lipophilicity. We have developed a rapid and sensitive LC–MS/MS method suitable for such a homologous series and applied it to a series of DNA binding benzonaphthyridine-based antitumour drugs of differing lipophilicity. The method used a gradient elution with a run time of 7 min for simultaneous quantitation of five analogues in a pooled sample. Method validation was carried out in plasma (human and mouse) and mouse tissues (brain, heart, kidney, liver and lung). It had a limit of quantitation of 0.001 $\mu\text{mol/L}$ and was linear (0.001–0.3 $\mu\text{mol/L}$) in all matrices with acceptable intra- and inter-assay precision and accuracy. This method allowed the pharmacokinetic parameters of these compounds in mice to be related to their lipophilicity as determined by their partition coefficient ($\text{Log } D$). Both the plasma CL ($r=0.95$; $P=2 \times 10^{-7}$) and V_{ss} ($r=0.95$; $P=2 \times 10^{-7}$) exhibited a significant positive correlation with $\text{Log } D$ values after intravenous bolus administration to mice. Consequently the plasma mean residence time for each of these five analogues decreased with increasing lipophilicity. There was also a significant positive correlation ($r=0.91$; $P=2 \times 10^{-7}$) between $\text{Log } D$ values and the brain to plasma AUC ratio indicating the importance of lipophilicity in the distribution of these compounds into the brain tissue.

© 2012 Elsevier B.V. All rights reserved.

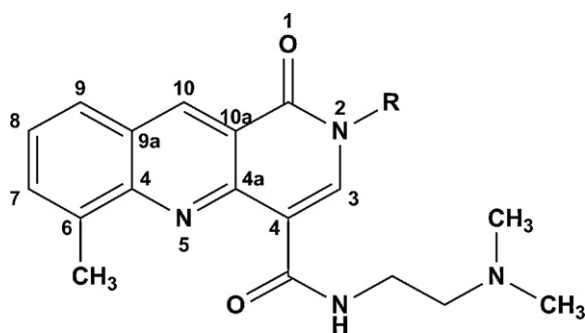
1. Introduction

Drug lipophilicity and its importance in determining pharmacological responses was known for over a century starting with the early studies by Richet [1]. Introduction of sophisticated quantitative structure–activity relationships (SARs) by Hansch [2,3] led to an increase in the prominence of lipophilicity in various classes of drugs. Furthermore, a review by Lipinski in 1997 [4] suggested that the desired lipophilicity values for drug candidates are universal to a degree, specifically highlighting the desirability of $\text{Log } D$ values < 5 . While a comprehensive review on the subject of lipophilicity is beyond the scope of this article, several publications review this topic of lipophilicity and its role in ADMET (absorption, distribution, metabolism, elimination and toxicology) in detail [5,6].

N-[2-(dimethylamino)ethyl]-2,6-dimethyl-1-oxo-1,2-dihydrobenzo[b]-1,6-naphthyridine-4-carboxamide (SN 28049) is a DNA intercalating topoisomerase II poison being tested for its anticancer activity. The latter (methyl analogue) along with hydrogen, ethyl, n-propyl, and n-butyl substitutions at the N-2 position of the benzonaphthyridine ring structure (Fig. 1) were synthesised and utilised as a homologous series to study the effects of lipophilicity (as determined by their partition coefficient ($\text{Log } D$)) on their pharmacokinetics. SN 28049 exhibited curative antitumour activity in a Colon-38 murine tumour model and was greatly superior to the standard topoisomerase II poisons such as etoposide and doxorubicin as demonstrated by Deady et al. [7]. A previous study by Lukka et al. [8] suggested that pharmacokinetics may play a major role in its superior antitumour properties. We have previously reported an ion-trap LC–MS method [9] for the quantitation of SN 28049 and its application to a pharmacokinetic study in mice. The limit of quantitation (LOQ) of the latter method (0.062 $\mu\text{mol/L}$) was acceptable, but the sensitivity was insufficient to measure the concentrations beyond 12 h post administration. In addition, no analytical method was available for the other four analogues to be investigated. This study demonstrates the development and

* Corresponding author at: Auckland Cancer Society Research Centre, Faculty of Medical and Health Sciences, The University of Auckland, Private Bag 92019, Auckland, New Zealand. Tel.: +64 99236142; fax: +64 93737502.

E-mail address: b.baguley@auckland.ac.nz (B.C. Baguley).



R = -H, Hydrogen; SN 28101
-CH₃, Methyl; SN 28049
-C₂H₅, Ethyl; SN 28668
-C₃H₇, Propyl; SN 32116
-C₄H₉, Butyl; SN 28048
-C₃D₇, deuterated IS; SN 32444

Fig. 1. Chemical structure of benzonaphthyridine with substitutions at N-2 position.

validation of a more sensitive (LOQ, 0.001 $\mu\text{mol/L}$), relatively rapid (7 min per pooled sample containing all five analogues) method utilising an Agilent® 6410 triple quadrupole mass spectrometer (QqQ) (Agilent® Technologies, USA) coupled to an Agilent® 1200 Rapid Resolution LC (Agilent® Technologies, USA) to simultaneously and quantitatively five benzonaphthyridine derivatives in human and mouse plasma and mouse tissues.

2. Experimental

2.1. Materials and methods

The series of benzonaphthyridine analogues with substitutions at the N-2 position is shown in Fig. 1. SN 28101 (hydrogen) (free base, 99% pure by LC; MW, 324); SN 28049 (methyl) (free base, 99% pure by LC; MW, 338); SN 28668 (ethyl) (free base, 99% pure by LC; MW, 352); SN 32116 (propyl) (free base, 99% pure by LC; MW, 366); SN 28048 (butyl) (free base, 99% pure by LC; MW, 380) and the deuterated internal standard (IS) SN 32444 (free base, 98% pure by LC; MW, 374) were synthesized in the Auckland Cancer Society Research Centre using previously published methods [7]. Unless stated, all other chemicals were commercially available and of analytical grade. Water used in all experiments was purified by filtering through ion exchange columns and a 0.22 μm filter (Milli-Q Purification System, Millipore Corporation, Bedford, USA).

2.1.1. Mice

C57 Bl/6 female mice (20–25 g; 8–12 weeks old) were housed under constant temperature, humidity and lighting (12 h light per day). All experiments which included blood collection in mice from the ocular sinus under isoflurane anaesthesia were approved by The University of Auckland Animal Ethics Committee, and conformed to the Guidelines for the Welfare of Animals in Experimental Neoplasia, as set out by the United Kingdom Co-ordinating Committee on Cancer Research.

2.1.2. Drug formulation and administration

All analogues were dissolved in phosphate buffered saline (PBS) and administered to mice at 25 $\mu\text{mol/kg}$ (a volume of 10 $\mu\text{L/g}$). Intravenous (i.v.) bolus injection was via the tail vein using a

1 cm^3/mL Tuberculin syringe (Terumo, Laguna, Philippines) with a 27 gauge needle. Intraperitoneal (i.p.) administration was carried out by injecting the drug into the peritoneal cavity using a 1 cm^3/mL Tuberculin syringe with a 26 gauge needle.

2.1.3. Preparation of mouse plasma and tissue homogenates

Mouse plasma was prepared from the blood of anaesthetised C57 Bl/6 mice and stored at -80°C . To prevent coagulation, blood was collected in BD Vacutainer® (BD Biosciences, Franklin Lakes, NJ, USA) tubes coated with K₂ EDTA, and plasma was separated by centrifugation at 6000 $\times g$ for 10 min. Tissues (brain, heart, kidney, liver, and lung) were collected after cervical dislocation of the anaesthetized mice. Collected tissues were washed with 1 mL PBS to remove blood contamination, briefly dried, transferred to 2 mL nunc CryoTubes® (Thermo Scientific, Rochester, NY, USA) and stored at -80°C . Frozen tissues were thawed at room temperature (25°C) and transferred into glass tubes, weighed and homogenized in PBS (4-volumes) using a tissue homogenizer (S/N TH-71, Omni TH homogenizer, Gainesville, VA, USA) operated at 24,000 rpm.

2.2. Instrumentation

2.2.1. Liquid chromatograph–mass spectrometer

The LC–MS/MS system was an Agilent® 1200 Rapid Resolution HPLC and Agilent® 6410 triple quadrupole mass spectrometer equipped with a multimode ionisation source (Agilent® Technologies, USA). Chromatographic separation was achieved on an Agilent® Zorbax® SB-C18 (50 mm \times 2.1 mm, 5 μm) column with a 0.2 μm in-line filter and was maintained at 35°C . The mobile phase consisted of 80% acetonitrile with 0.01% formic acid (mobile phase A) and water containing 0.01% formic acid (mobile phase B) with fast gradient elution at a flow rate of 0.5 mL/min and run time of 7 min. The following gradient was applied: 0 min, 90% B; 1 min, 90% B; 2.5 min, 10% B; 5 min, 10% B; 6 min, 90% B; 7 min, 90% B. The column was equilibrated for 1 min between injections. The eluent flow was led into the MS/MS starting 0.5 min after injection by switching the MS inlet valve. The sample volume injected was 25 μL and the autosampler was set at 4°C . The mass spectrometer was run in positive ion ESI-APCI combined mode using multiple reaction monitoring (MRM) to monitor the mass transitions. The retention times for the analogues were as follows: hydrogen, 3.04 min; methyl, 3.60 min; ethyl, 3.81 min; propyl, 4.05 min; butyl, 4.36 min; d₇ IS, 4.05 min. The mass resolution was set at 0.7 μ FWHM (unit mass resolution) for both quadrupoles. Other parameters of the mass spectrometer were: collision energy 15 V; fragmentor voltage 130 V; gas flow 5.5 L/min; gas temperature 350°C ; vaporizer temperature 225°C ; nebulizer 55 psi; capillary 3000 V, corona current positive 3 μA ; charging voltage 1500 V. Data were acquired and analysed with Agilent® MassHunter® software.

2.3. Stock solutions, calibrants and quality controls

Stock solutions (1 mmol/L) of all 5 benzonaphthyridine analogues were prepared individually in acetonitrile. Subsequent dilutions of individual analogues using a pooled approach resulted in a final concentration range of 0.001, 0.005, 0.01, 0.025, 0.05, 0.1, 0.3 $\mu\text{mol/L}$ for the calibration curve for all 5 analogues in plasma and tissue homogenates. Freshly prepared working solutions of all 5 analogues from an independently weighed 1 mmol/L stock were used to prepare quality control (QC) samples. Appropriate volumes were then added to freshly thawed particle-free human plasma, mouse plasma and mouse tissue homogenates to give concentrations of 0.001, 0.025 and 0.3 $\mu\text{mol/L}$ (5 mL of each concentration). Aliquots (200 μL) of each QC samples were stored at -80°C immediately after the preparation. During each subsequent analytical run, one set (triplicate) of each QC concentration was included

(scattered in between the calibrants and the unknown samples) and processed with the calibrants and *in vivo* study samples.

2.4. Sample preparation

Aliquots (25 μ L) of plasma or tissue homogenates (either calibrants, quality controls) were precipitated with 3-volumes (75 μ L) acetonitrile:methanol (3:1) mixture containing deuterated (d_7) internal standard (IS) (0.05 μ mol/L). For analysis of samples from the *in vivo* study, 25 μ L samples of each analogue were pooled and precipitated with 3-volumes of the acetonitrile:methanol (3:1) mixture containing deuterated (d_7) internal standard (IS) (0.05 μ mol/L). Samples were vortexed for 30 s, followed by centrifugation at $13,000 \times g$ (5 min, 4 °C). A 50 μ L aliquot of each supernatant was then diluted in 50 μ L of mobile phase B and injected into the LC–MS/MS (25 μ L injection volume). Blank samples were prepared from plasma (human and mouse) and tissue homogenates using the same extraction procedure.

2.5. Validation procedures

Analytical specificity was tested by inspection of chromatograms of extracted drug-free plasma and tissue homogenate samples for interfering peaks. Extraction recoveries were assessed by comparing peak areas of each analyte and IS from extracted plasma QC samples, to standards prepared in blank matrix extract. All recovery studies were performed at three different concentrations and in triplicate. To determine intra-day reproducibility 5–6 replicates of the QC samples were analysed, including the LOQ. Inter-day precision was calculated from QC samples analysed on three or more different days. At each concentration, precision was calculated as the relative standard deviation (RSD) and accuracy as the percentage of the true value. Acceptable precision was defined by a RSD within 15% and accuracy within 85–115%. The LOQ was defined to be the lowest concentration that could be measured with the minimum acceptable accuracy (within 80–120% of the true value) and precision (RSD within 20%). Matrix effects on each analyte were assessed in triplicate by spiking the analytes in different batches of extracted (with 3-volumes of acetonitrile:methanol (3:1)) plasma (mouse and human) and mouse tissue homogenates. Each analytical run consisted of a single calibration curve, triplicate QC samples at three concentrations, one reagent blank, one plasma/tissue blank and one zero-level (blank matrix sample with d_7 IS) standard. The stability of all 5 analogues was measured in duplicate at room temperature over 24 h in plasma and tissue homogenates. At each time point, plasma/tissue samples containing all 5 analogues were removed, and then extracted as described above. In addition, the stability of all 5 analogues in plasma and tissue homogenates was assessed at three different concentrations in triplicate when left on ice or on the benchtop for 0–24 h. Similarly, stability during storage in the autosampler was determined at three different concentrations in triplicate over 24 h at 4 °C. Three freeze–thaw cycles at –80 °C were used to test the stability of all 5 analogues in plasma. Long-term plasma stability was assessed at –80 °C over 1 year. For short-term/bench-top, long-term and freeze–thaw stability, mean concentrations of triplicate samples were compared to the initial values.

2.6. Pharmacokinetic evaluation

C57 Bl/6 female mice used for the *i.v.* pharmacokinetic studies. Mice ($n=3$ per time point) were administered 25 μ mol/kg of each analogue. Blood samples were collected at various time points (0.08, 0.5, 1, 2, 4, 8, 12 and 24 h). For the tissue distribution study, C57 Bl/6 female mice ($n=3$ per time point) were administered with each of the analogues intraperitoneally. Blood and tissue

samples (brain, heart, liver, lung, and kidney) were collected at similar timepoints to the *i.v.* study. Non-compartmental pharmacokinetic parameters were calculated using WinNonlin[®] version 5.3. Values for area under the plasma concentration–time profile curve (AUC) were calculated using the log trapezoidal rule with extrapolation of the terminal slope to infinity by log-linear regression. The terms C_{\max} and T_{\max} represent the maximum concentration achieved and the time to maximum concentration respectively, and were determined from the concentration–time profiles. The model-independent pharmacokinetic parameters, clearance (CL), volume of distribution at steady state (V_{ss}), and mean residence time (MRT) were calculated by the following equations: $CL = \text{dose}/\text{AUC}$; $V_{ss} = \text{dose} \times \text{AUMC}/(\text{AUC})^2$; and $\text{MRT} = \text{AUMC}/\text{AUC}$, where AUMC represents the total area under the first moment of the concentration–time curve, computed in a similar fashion to that used for AUC. Correlation (represented by ‘ r ’) analysis was performed by Spearman rank order method and P values less than 5×10^{-2} were considered significant.

3. Results and discussion

3.1. Validation of the assay

3.1.1. Specificity

The product ion fragments of all the 5 analogues and the IS were monitored using MRM following extraction from the matrices. No interference was observed from the endogenous components of the matrices. A blank chromatogram (Fig. 2a) and extracted MRM traces for all mass transitions at the LOQ are shown in Fig. 2b. Additionally, precursor ions arising from possible metabolites (N-demethylation, hydroxymethylation, and N-mono demethylation) were verified for each analogue, and no interference from transitions was observed.

3.1.2. Linearity

The calibration curve was assessed based on a plot of the ratio of peak areas for each analogue/IS. A linear fit model with no weighting best described the concentration–response relationship. The assay was found to be linear for all the analogues over the concentration range of 0.001–0.3 μ mol/L in all the matrices tested ($r^2 > 0.991$). Plasma and tissue samples with concentrations $> 0.3 \mu$ mol/L were diluted accordingly and are unvalidated results. Accuracy and precision data obtained from the calibration curves of plasma and tissues matrices prepared on six different occasions over the concentration range were within the acceptable range (precision, $< 7.0\%$ and accuracy, 93.8–106.2% of nominal values).

3.1.3. Fragmentation patterns

SN 28101 (hydrogen) ionizes in the positive ionization mode, gaining a proton and entering the metastable state of $[M+H]^+$ and can be seen in the spectrum as m/z 325. The latter can then be fragmented and characterized in MS2 mode ($[M+H]^+ - C_2H_7N$) to give a MS2 ion at m/z 280. The other analogues in this series (methyl, ethyl, propyl, and butyl) and the d_7 also fragment in the similar fashion producing product ions as follows: methyl, 339–294; ethyl, 353–308; propyl, 367–322; butyl, 381–366; d_7 IS, 374–329. The structure of these fragments were simulated and established with the help of ACD/MS fragmenter (version 12, ACD Labs, Toronto, Ontario, Canada). The fragmentation pattern and the mass spectra are shown in Fig. 3.

3.1.4. Recovery and matrix effects

The extraction recovery was determined by comparing peak areas of standards prepared in Milli-Q water

containing 0.01% formic acid to those extracted from spiked plasma and tissue homogenates. Authentic standards, spiked plasma and tissue homogenates were prepared in triplicate in the same manner over three concentrations 0.001, 0.025 and 0.3 $\mu\text{mol/L}$. The absolute recoveries for all analogues (0.001–0.3 $\mu\text{mol/L}$) were $>82.0 \pm 1.5\%$ and the IS (0.05 $\mu\text{mol/L}$) $>87.1 \pm 2.5\%$, respectively. Matrix effects tested by spiking the analytes in extracted plasma and tissue homogenates and comparing them by standards prepared in Milli-Q water containing

0.01% formic acid indicated a lack of ion suppression by matrix components.

3.1.5. LOQ

The lower limit of quantitation in plasma and tissue matrices analysed by LC–MS/MS was found to be 0.001 $\mu\text{mol/L}$. Concentrations below the LOQ were detected with unacceptable accuracy and precision (i.e., RSD $> 20\%$, accuracy $< 80\%$ and $> 120\%$ of the nominal values).

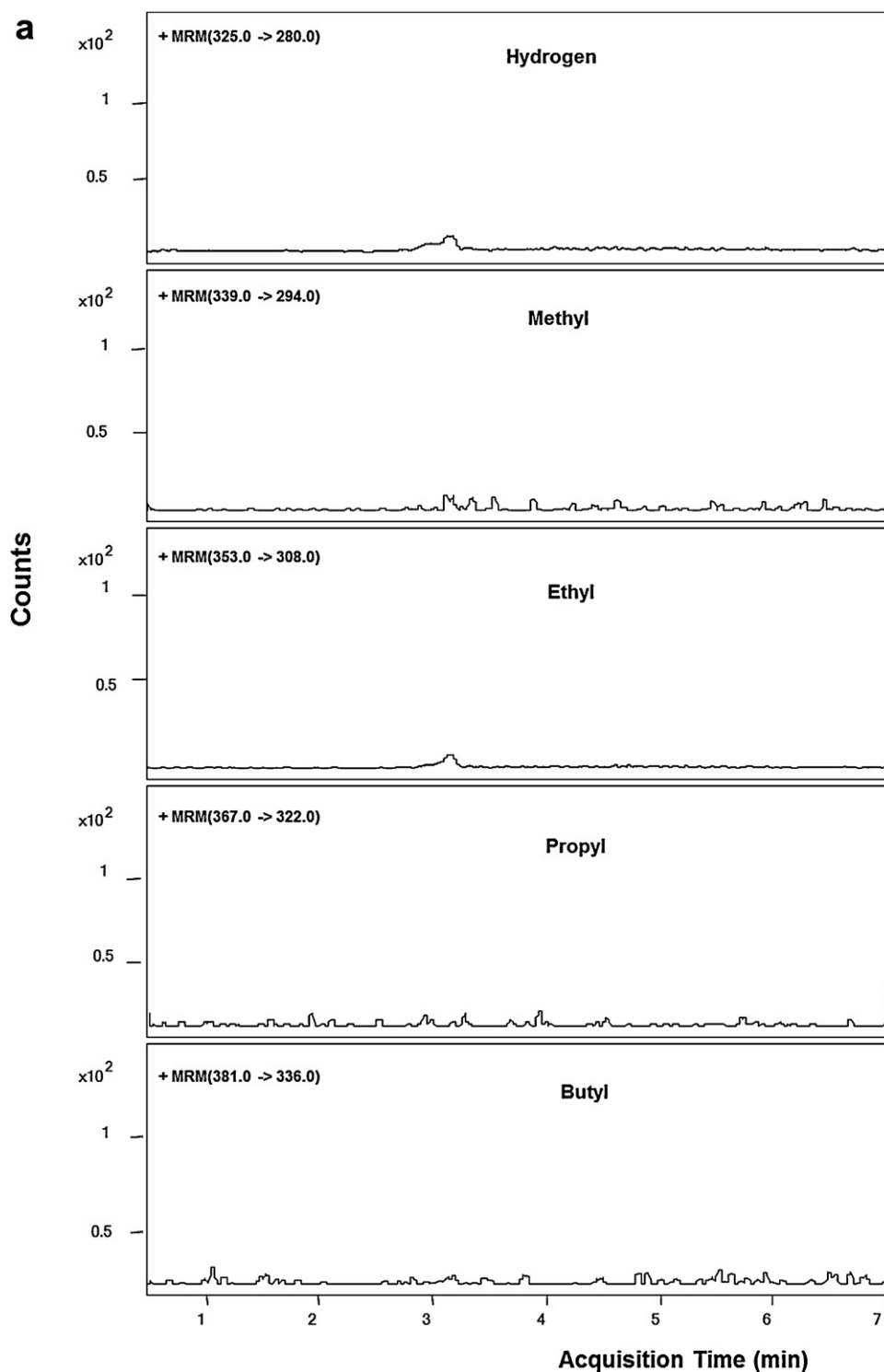


Fig. 2. (a) Blank and (b) MRM traces of 5 benzophenanthridine analogues (hydrogen–butyl) at the LOQ. The d_7 internal standard is co-eluted with the propyl analogue and has a retention time on 4.05 min.

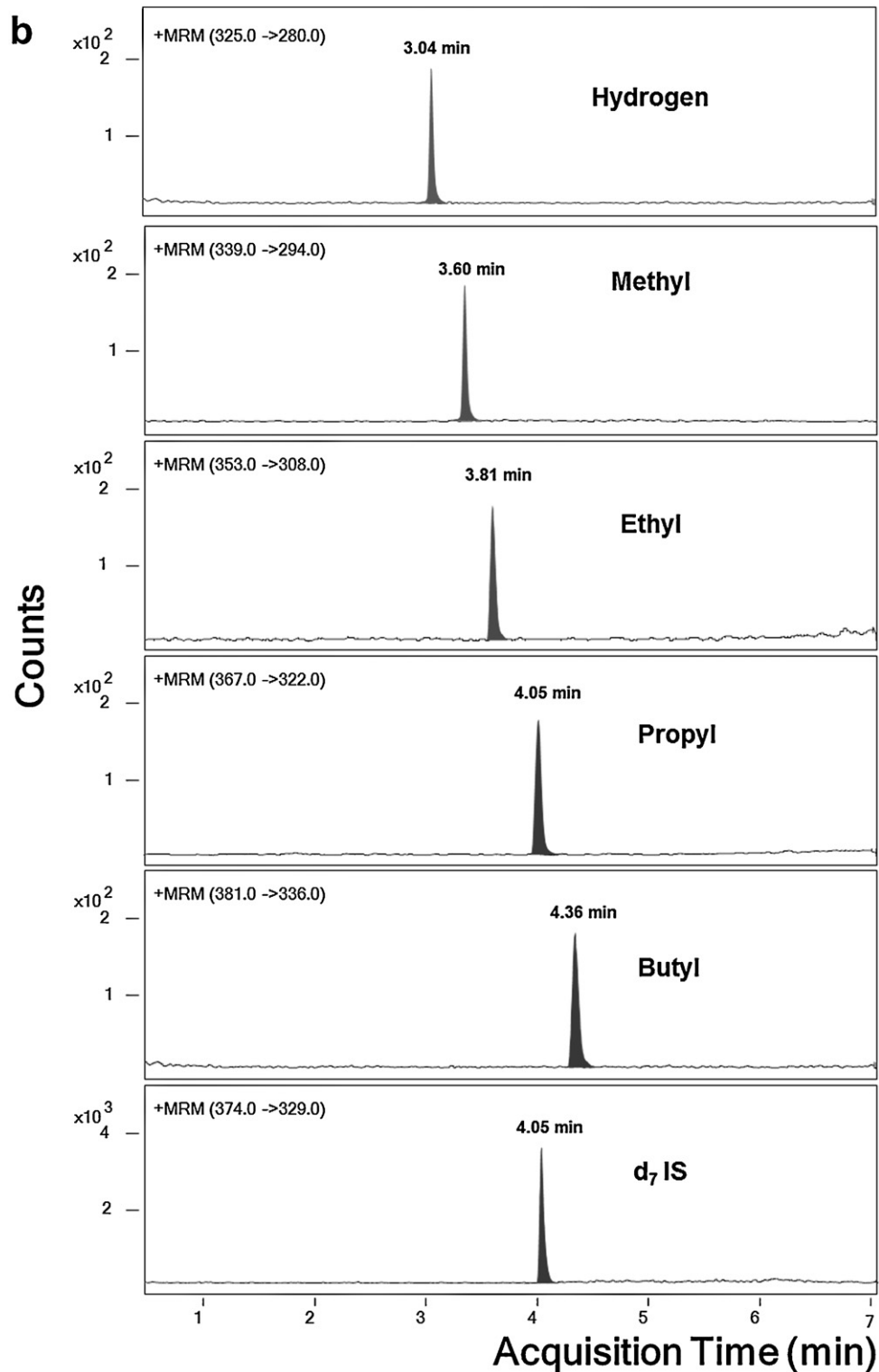


Fig. 2. (continued)

3.1.6. Precision and accuracy

The intra-assay precision was determined by calculating the RSD of 8 repeat measurements at three different concentrations (0.001, 0.025 and 0.3 $\mu\text{mol/L}$) of all analogues in plasma and tissue homogenates on 1 day and was found to be <7.1% for all concentrations. The intra-assay accuracy was determined by comparing the means of the measured concentrations to their true concentrations on the same day. The intra-assay accuracy was

also acceptable over the three concentrations, varying between $92.1 \pm 5.5\%$ and $102.1 \pm 3.8\%$ of the true values.

The inter-assay precision was determined by replicate measurements performed on ten different occasions over 1-year for three concentrations in plasma and tissue homogenates. The inter-assay precision was less than 6.5%. The inter-assay accuracy was calculated over 10 different occasions and was between $92.1 \pm 5.5\%$ and $102.1 \pm 5.5\%$ of the nominal values.

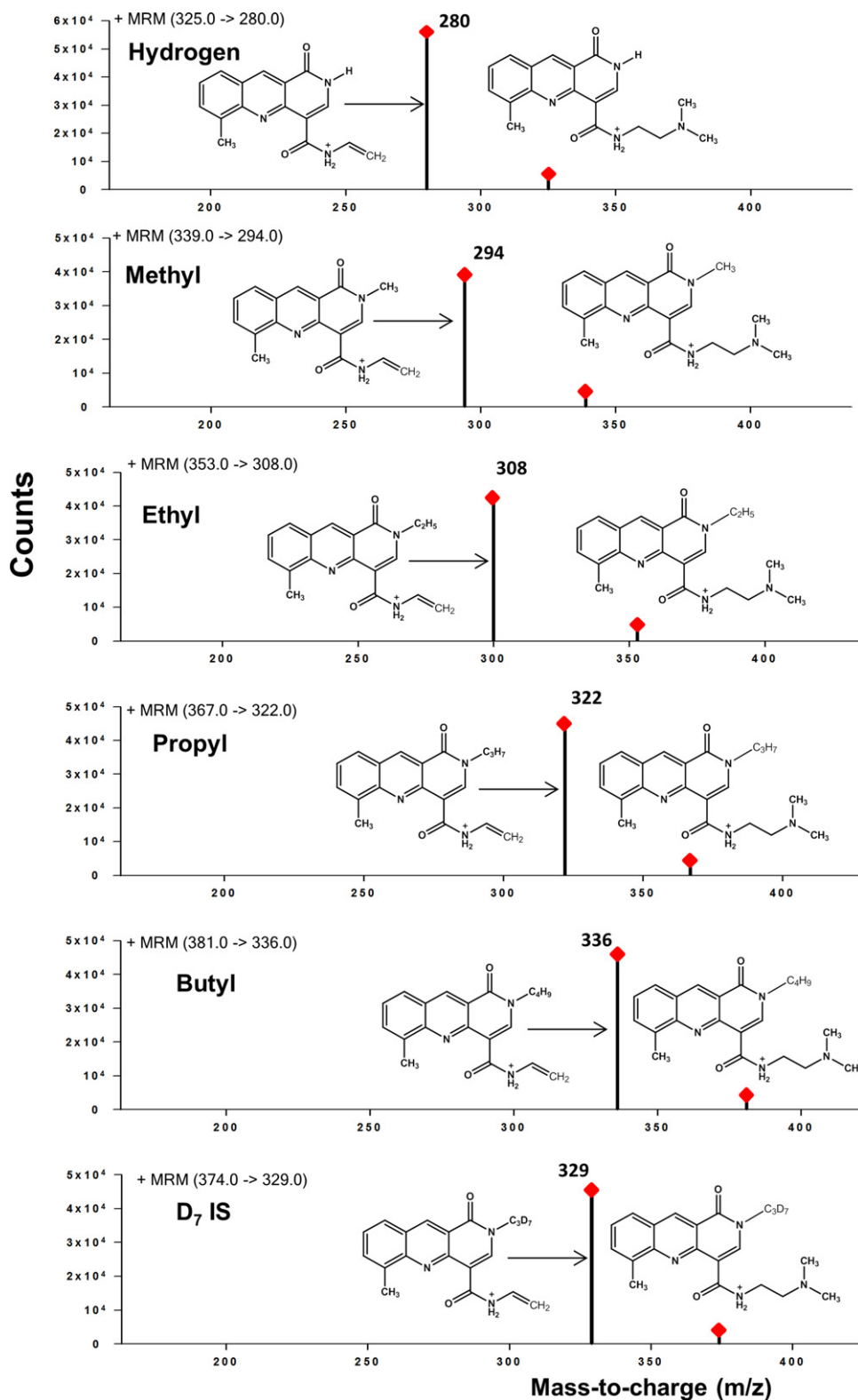


Fig. 3. Fragmentation spectra and simulated structures of the fragments of the benzonaphthyridine analogues (hydrogen–butyl) and the d_7 internal standard.

3.1.7. Stability

3.1.7.1. Freeze–thaw stability. All analogues in plasma and tissue homogenates were tested for stability by subjecting to multiple freeze–thaw cycles over 48 h. Three concentrations (0.001, 0.025 and 0.3 $\mu\text{mol/L}$) were prepared in human plasma and frozen at -80°C . These samples were then thawed and frozen three times at

24, 36, and 48 h after preparation. Samples were analysed in triplicate after the third freeze–thaw cycle and concentrations were determined from the calibration curve. The mean accuracies were in the range of $96.0 \pm 0.3\%$ to $103.1 \pm 4.1\%$ of the nominal values for all the analogues, indicating acceptable stability over 3 freeze–thaw cycles.

Table 1

Pharmacokinetic parameters calculated using non-compartmental analysis from concentration–time profiles of plasma after i.v. administration of benzonaphthyridine analogues (hydrogen–butyl; 25 $\mu\text{mol/kg}$) in C57 Bl/6 female mice ($n=3$ per time point). Values are means \pm s.e.

Analogue	AUC ($\mu\text{mol h/L}$)	C_{max} ($\mu\text{mol/L}$)	$T_{1/2}$ (h)	Mean residence time (h)	CL (L/h/kg)	V_{ss} (L/kg)
Hydrogen	5.7 \pm 0.1	1.2 \pm 0.02	4.2 \pm 0.1	5.6 \pm 0.2	4.2 \pm 0.1	22.0 \pm 0.9
Methyl	3.3 \pm 0.2	0.9 \pm 0.04	4.8 \pm 0.3	5.3 \pm 0.2	7.5 \pm 0.2	37.0 \pm 1.2
Ethyl	2.3 \pm 0.03	0.7 \pm 0.02	4.3 \pm 0.02	4.4 \pm 0.02	10.6 \pm 0.2	47.3 \pm 2.0
Propyl	0.9 \pm 0.1	0.4 \pm 0.01	2.5 \pm 0.1	3.2 \pm 0.1	29.7 \pm 0.8	108.8 \pm 8.1
Butyl	0.7 \pm 0.02	0.3 \pm 0.03	2.0 \pm 0.01	2.5 \pm 0.1	32.6 \pm 0.9	172.7 \pm 3.7

3.1.7.2. Long term storage stability. All analogues were stable in plasma and tissue homogenates over the 1-year validation period when stored at -80°C . QC samples prepared during the intra-assay analysis were stored for 1-year and subsequently analysed. The results showed an acceptable precision $<6.2\%$ and an accuracy of $102.1 \pm 5.5\%$.

3.1.7.3. Stock solution stability. Stock solutions were prepared in acetonitrile over a concentration range of 0.02–6.0 $\mu\text{mol/L}$ which were then diluted 20-fold in water containing 0.01% formic acid leading to a concentration range of 0.001–0.3 $\mu\text{mol/L}$. The stability of these solutions was then tested at room temperature as well as 4°C for 24 h. These solutions were found to be stable at room temperature ($97.4 \pm 0.2\%$ to $102.4 \pm 0.4\%$) as well as 4°C ($95.1 \pm 0.6\%$ to $104.4 \pm 0.2\%$).

3.1.7.4. Bench top stability. The analogue mix was spiked into plasma and tissue homogenates at three concentrations (0.001, 0.025 and 0.3 $\mu\text{mol/L}$) and left at room temperature. Triplicate aliquots of each concentration were analysed at 0, 12, and 24 h and found to be in the range of $94.5 \pm 3.1\%$ to $103.2 \pm 1.7\%$ and was acceptable.

3.1.7.5. Post preparative stability. Post preparative stability of the analogue mix was determined by processing the quality control samples in plasma and tissue homogenates (0.001, 0.025 and 0.3 $\mu\text{mol/L}$) in triplicate and were held in the autosampler (4°C) for 24 h. These samples were then analysed at 0, 12, and 24 h. All samples demonstrated accuracies in the range of $93.2 \pm 0.7\%$ to $102.1 \pm 1.3\%$.

3.2. LogD values

Partition coefficients (LogD) of this benzonaphthyridine series were determined by a low-volume octanol/PBS (pH 7.4) shake-flask method [10] and were determined as: 1.25 ± 0.003 (hydrogen); 1.82 ± 0.005 (methyl); 2.24 ± 0.08 (ethyl); 2.56 ± 0.03 (propyl); and 2.91 ± 0.03 (butyl).

3.3. Pharmacokinetic application

Plasma concentration–time profiles following i.v. administration of all 5 analogues are shown in Fig. 4. Pharmacokinetic parameters from non-compartment analysis of the plasma concentration–time data are reported in Table 1. It was found that the least lipophilic hydrogen analogue produced the highest AUC of all the compounds and that this parameter decreased with increasing lipophilicity across this homologous series. This result was statistically significant with plasma AUC decreasing linearly with increasing LogD of each compound ($r=-0.95$; $P=2 \times 10^{-7}$). Similarly there was a significant positive correlation with both plasma CL ($r=0.95$; $P=2 \times 10^{-7}$) and V_{ss} ($r=0.95$; $P=2 \times 10^{-7}$) with LogD values. Consequently the plasma mean residence time for each of these five analogues decreased with increasing lipophilicity ($r=-0.93$; $P=2 \times 10^{-7}$). Tissue concentrations of all five compounds were considerable greater than the

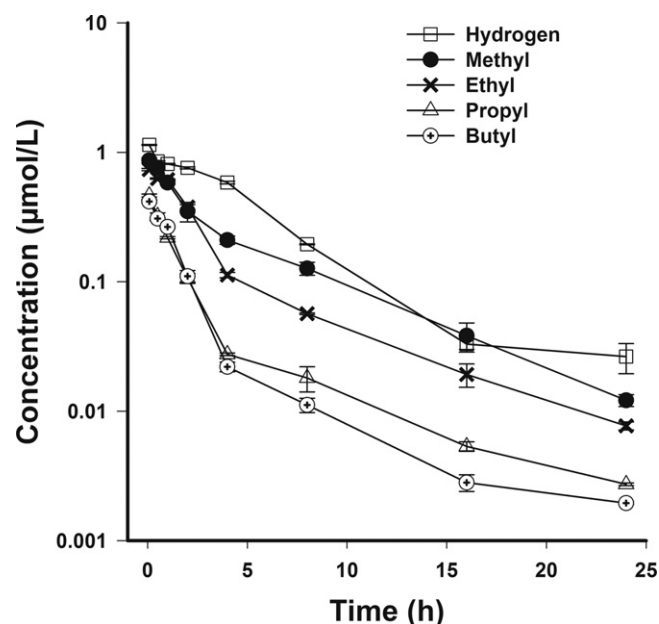


Fig. 4. Plasma pharmacokinetic (concentration–time) profiles of benzonaphthyridine analogues (hydrogen–butyl) following i.v. administration ($25 \mu\text{mol/kg}$) in healthy C57 Bl/6 mice ($n=3$ per time point). Values are represented as mean \pm s.e.

Table 2

Brain to plasma AUC ratios after i.p. administration of benzonaphthyridine analogues (hydrogen–butyl; $25 \mu\text{mol/kg}$) in C57 Bl/6 female mice ($n=3$ per time point). Values are means \pm s.e.

Analogue	Brain to plasma AUC ratio
Hydrogen	0.6 \pm 0.1
Methyl	1.6 \pm 0.2
Ethyl	2.1 \pm 0.2
Propyl	3.5 \pm 0.3
Butyl	4.4 \pm 0.6

corresponding plasma concentrations. A significant positive correlation ($r=0.91$; $P=2 \times 10^{-7}$) was also observed between LogD values and the brain to plasma AUC ratio (Table 2).

4. Conclusion

A relatively rapid and sensitive LC–MS/MS method was developed which allowed the simultaneous measurement of five benzonaphthyridine analogues down to a concentration of 0.001 $\mu\text{mol/L}$ in plasma and mouse tissues with acceptable precision and accuracy with a run time of 7 min. The method utilised the superior performance of the QqQ mass spectrometer in terms of selectivity and sensitivity to make sample pooling practicable. This feature is a more sophisticated development of our previously reported methodology for one of the analogues, SN 28049, using an ion-trap LC–MS [9].

All five analogues were measured simultaneously for up to 24 h in a 25 μL mouse plasma sample after these compounds were

administered individually by i.v. injection at a therapeutic dose. The plasma pharmacokinetic parameters of this homologous series indicated that quite small changes in lipophilicity ($\text{Log } D$, 1.25–2.91) had a significant impact on CL and V_{ss} , with the most lipophilic compound having an 8-fold increase in CL and V_{ss} compared to the least lipophilic analogue. These results are consistent with the literature where high lipophilicity is associated with a higher V_{ss} (due to increased tissue distribution) and a higher plasma clearance (due to increased access and binding to the phase I and II metabolic enzymes) [11–13]. Not unexpectedly, lipophilicity appeared to play a crucial role in determining the penetration of these compounds through blood brain barrier, with the most lipophilic analogue (the butyl derivative) exhibiting the greatest brain to plasma ratio. From the plasma concentration–time curves, one might have predicted that the hydrogen analogue (the least lipophilic) would have the greatest antitumour activity due to its greatest plasma AUC and longest mean residence time in this mouse model. However, although the hydrogen analogue demonstrated growth delays, it gave no significant cure rate in the Colon-38 murine tumour model [7,14]; while the substitution of a methyl group at the N-2 position resulted in cures. This study indicates the limited utility of plasma pharmacokinetic parameters to select and optimize anti-cancer therapy due to the lack of translation of parameters obtained from plasma as surrogates for tumour exposure. It would appear that the measurement of concentrations in the tumour tissue may be more appropriate and may likely correlate better with the *in vivo* antitumour activity.

Altogether, this sensitive validated method may further aid in more detailed mouse pharmacokinetic and tissue distribution studies required at the preclinical drug development stage.

Acknowledgements

This study was supported by the Auckland Cancer Society and Auckland Uniservices Ltd., New Zealand.

References

- [1] C. Richet, On the relationship between the toxicity and the physical properties of substances, *Compt. Rend. Seances Soc. Biol.* 9 (1893) 775–776.
- [2] C. Hansch, Quantitative approach to biochemical structure–activity relationships, *Acc. Chem. Res.* 2 (1969) 232–239.
- [3] R.P. Verma, C. Hansch, Investigation of DNA-binding properties of organic molecules using quantitative structure–activity relationship (QSAR) models, *J. Pharm. Sci.* 97 (2008) 88–110.
- [4] C.A. Lipinski, F. Lombardo, B.W. Dominy, P.J. Feeney, Experimental and computational approaches to estimate solubility and permeability in drug discovery and development settings, *Adv. Drug Deliv. Rev.* 23 (1997) 3–25.
- [5] M.J. Waring, Lipophilicity in drug discovery, *Expert Opin. Drug Discov.* 5 (2010) 235–248.
- [6] D.A. Smith, B.C. Jones, D.K. Walker, Design of drugs involving the concepts and theories of drug metabolism and pharmacokinetics, *Med. Res. Rev.* 16 (1996) 243–266.
- [7] L.W. Deady, T. Rodemann, L. Zhuang, B.C. Baguley, W.A. Denny, Synthesis and cytotoxic activity of carboxamide derivatives of benzo[b][1,6]naphthyridines, *J. Med. Chem.* 46 (2003) 1049–1054.
- [8] P.B. Lukka, J.W. Paxton, P. Kestell, B.C. Baguley, Pharmacokinetics and distribution of SN 28049, a novel DNA binding anticancer agent, in mice, *Cancer Chemother. Pharmacol.* 65 (2010) 1145–1152.
- [9] P.B. Lukka, P. Kestell, J.W. Paxton, B.C. Baguley, Development and validation of a liquid chromatography–mass spectrometry (LC–MS) assay for the determination of the anti-cancer agent N-[2-(dimethylamino)ethyl]-2,6-dimethyl-1-oxo-1,2-dihydrobenzo[b]-1,6-naphthyridine-4-carboxamide (SN 28049), *J. Chromatogr. B: Anal. Technol. Biomed. Life Sci.* 875 (2008) 368–372.
- [10] B.G. Siim, K.O. Hicks, S.M. Pullen, P.L. van Zijl, W.A. Denny, W.R. Wilson, Comparison of aromatic and tertiary amine N-oxides of acridine DNA intercalators as bioreductive drugs: cytotoxicity, DNA binding, cellular uptake, and metabolism, *Biochem. Pharmacol.* 60 (2000) 969–978.
- [11] D. Smith, Discovery and ADMET: where are we now, *Curr. Top. Med. Chem.* 11 (2011) 467–481.
- [12] R. Scott Obach, Predicting clearance in humans from *in vitro* data, *Curr. Top. Med. Chem.* 11 (2011) 334–339.
- [13] M.V. Varma, B. Feng, R.S. Obach, M.D. Troutman, J. Chupka, H.R. Miller, A. El-Kattan, Physicochemical determinants of human renal clearance, *J. Med. Chem.* 52 (2009) 4844–4852.
- [14] L.W. Deady, M.L. Rogers, L. Zhuang, B.C. Baguley, W.A. Denny, Synthesis and cytotoxic activity of carboxamide derivatives of benzo[b][1,6]naphthyridin-(5H)ones, *Bioorg. Med. Chem.* 13 (2005) 1341–1355.



Development of a method for the determination of 4-(Methylnitrosamino)-1-(3-pyridyl)-1-butanol in urine of nonsmokers and smokers using liquid chromatography/tandem mass spectrometry

Hou Hongwei^{a,*}, Zhang Xiaotao^{a,b}, Tian Yongfeng^a, Tang Gangling^a, Liu Yulan^b, Hu Qingyuan^{a,*}

^a China National Tobacco Quality Supervision & Test Center, No. 2 Fengyang Street, Zhengzhou High & New Technology Industries Development Zone, Zhengzhou 450001, People's Republic of China

^b School of Grain and Food, Henan University of Technology, Zhengzhou 450001, People's Republic of China

ARTICLE INFO

Article history:

Received 21 September 2011

Received in revised form 4 January 2012

Accepted 20 January 2012

Available online 30 January 2012

Keywords:

NNAL

Urine

LC–MS/MS

MIP

Biomarker

ABSTRACT

4-(Methylnitrosamino)-1-(3-pyridyl)-1-butanol (NNAL) is an efficient biomarker of tobacco-specific carcinogen 4-(Methylnitrosamino)-1-(3-pyridyl)-1-butanone (NNK). The ability to monitor biomarker concentrations is very important in understanding potential cancer risk. An analytical method using molecularly imprinted polymer (MIP) column coupled with liquid chromatography/tandem mass spectrometry (LC–MS/MS) for the determination of total NNAL in human urine was developed and validated. The combination of MIP column extraction and LC–MS/MS can provide a high sensitive and relatively simple analytical method. The limit of detection (LOD) was 0.30 pg/ml and analysis time was 6 min. The method has been applied to urine samples of 36 nonsmokers and 207 smokers. NNAL was found to be significantly higher in the urine of smokers compared with nonsmokers. Compared with smokers with blended cigarettes, Chinese virginia cigarettes smokers had low urinary NNAL levels. There was a direct association between the 24-h mouth-level exposure of carcinogen NNK from cigarette smoking and the concentration of NNAL in the urine of smokers. However, there was not a positive correlation between urinary total NNAL levels in 24 h and tar. Total urinary NNAL is a valuable biomarker for monitoring exposure to carcinogenic NNK in smokers and in nonsmokers. A prediction model of cigarette smoke NNK and urinary average NNAL levels in 24 h was established ($y = 2.8987x - 245.38$, $r^2 = 0.9952$, $n = 204$).

© 2012 Elsevier B.V. All rights reserved.

1. Introduction

Tobacco smoking is currently responsible for approximately 30% of cancer deaths in developed countries, and for an increasing proportion of the cancer deaths in developing countries. Furthermore, smoking causes more deaths from vascular, respiratory, and other diseases than it does from cancer [1]. 4-(Methylnitrosamino)-1-(3-pyridyl)-1-butanone (NNK), a tobacco-specific nitrosamine found only in tobacco products and the tar smoke, causes lung cancer [2], adenocarcinoma [3], and liver cancer at the highest dose level ($P < 0.05$) in all laboratory animal species tested [4]. In humans, NNK is almost entirely reduced to 4-(Methylnitrosamino)-1-(3-pyridyl)-1-butanol (NNAL), which is also carcinogenic and excreted in urine [3] (Fig. 1). Higher urine NNAL was also related to greater dyspnea, poorer physical health status, and more restricted activity [5]. The urine NNAL-to-creatinine ratio (per interquartile increment) was associated

with greater chronic obstructive pulmonary disease severity. Study indicated there was a direct association between the NNK of 24-h mouth-level exposure from cigarette smoking and the NNAL concentration of its primary metabolite in the urine of smokers [6].

An important method to determine individual and collective risk from exposure to tobacco products is evaluation of tobacco carcinogen biomarkers [7,8]. Urinary metabolites have arose as highly practical biomarkers for determining uptake of specific carcinogens and toxicants in tobacco smoke and are likely to have more utility in predicting tobacco associated harm than machine measurements of smoke constituents. But the urine matrix was very complex, where the presence of many potentially interfering substances in concentrations far greater than those of the NNAL set demands for high selectivity and low limit of quantification (LOQ) for unequivocal identification and quantification. The analytical procedures for urinary NNAL are challenging indeed. Recently, liquid chromatography/tandem mass spectrometry (LC–MS/MS) have been developed for the analysis of urinary NNAL [9,10,11,12,13,14,15]. In order to get good analyte recoveries and improve method's accuracy and precision, complex sample cleanup is often required including liquid–liquid or solid-phase extraction (SPE). However, traditional liquid–liquid extraction need relatively large solvent

* Corresponding authors. Tel.: +86 371 67672727/67672601; fax: +86 371 67672625.

E-mail addresses: houhw@ztri.com.cn (H. Hou), huqy@ztri.com.cn (Q. Hu).

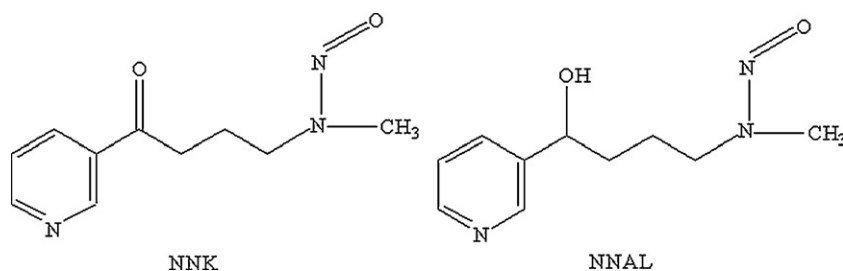


Fig. 1. Chemical structure of NNK and NNAL.

consumption, and the process is complex. SPE has many advantages compared to traditional liquid–liquid extraction methods. Bhat [13] described the use of LC–MS combined with a novel sample cleanup method using SPE on a WCX column developed specifically for extracting NNAL from urine samples. The method made it possible to analyze free NNAL in only 0.25 ml urine. But the pre-preparation was very complex, it involved derivatization, liquid–liquid extraction and SPE. Recently, molecularly imprinted polymer (MIP) column was applied to prepare for SPE of urinary NNAL. Xia [11] described the use of LC/APCI-MS/MS combined with a novel sample cleanup method using SPE for extracting NNAL from urine samples. However, the matrix suppression effect was strong. In 2009, Shah [9] improved the assay, by changing the liquid chromatography conditions, the response for this method was enhanced approximately 25-fold through avoidance of ionization suppression, and the lower LOQ for the assay was 20 pg/ml. The combination of MIP column extraction and LC/ESI-MS/MS can provide a sensitive and relatively simple analytical method.

In this present study, a method for the determination of total NNAL in human urine by extraction on a MIP column and LC/ESI-MS/MS was developed and validated. Higher sensitivity and good recovery were achieved. The limit of detection (LOD) was 0.30 pg/ml and analysis time was 6 min. The validated method was applied to quantify urinary NNAL levels of 207 smokers and 36 non-smokers, then the relationship between the urinary concentrations of total NNAL and Chinese virginia cigarette smoke analytes of NNK and tar were assessed.

2. Experimental

2.1. Chemical

Ammonium acetate, acetic acid, methanol and acetonitrile were obtained from TEDIA Company Inc. (Fairfield, OH, USA). Dichloromethane and hexane were purchased from J.T. Baker Chemical Products Co. Ltd. (Philipsburg, MO, USA). All solvents were high performance liquid chromatography (HPLC)-grade. β -Glucuronidase (type IX-A, *Escherichia coli*) was obtained from Sigma–Aldrich (Taufkirchen, Germany). Potassium dihydrogen phosphate and heptane were purchased from CNW Technologies GmbH (Dusseldorf, Germany). NNK, NNAL, NNAL- d_3 and NNK- d_4 were purchased from Toronto Research Chemical (North York, Ontario, Canada).

2.2. Urine sample preparation

The sample preparation was processed and optimized with a TSNA MIP cartridge (50 mg, 10 ml, Supelco, Taufkirchen, Germany) according to a previous published method [9] after slight modification. 5 ml of 50 mM phosphate buffer (pH 6.3; 50 mM) was added to 5 ml of urine. Adjusting pH to 6.3, then 20 μ l methanol containing 100 ng/ml of NNAL- d_3 and 100 μ l β -glucuronidase in phosphate buffer (pH 7.2, 100 units/ μ l) were added to mixture. The mixture

was incubated overnight (24 h) at 37 °C in the dark. The cartridge was preconditioned with 1 ml dichloromethane, 1 ml methanol and 1 ml water, and then washed with 2 ml water, 1 ml heptane, 1 ml hexane and eluted with 3 ml dichloromethane/methanol (9:1). The extract was reduced to dryness in a SpeedVac evaporator (Thermo-Fisher, Dreieich, Germany) and redissolved in 100 μ l 0.1% acetic acid in water.

2.3. Instrument and analytical conditions

All samples were analyzed using Agilent 1200 rapid resolution liquid chromatograph from Agilent Technologies (Wilmington, NC, USA) coupled with an API 5500 triple quadrupole mass spectrometer equipped with a TurbolonSpray™ source from Applied Biosystems (Foster City, CA, USA). An Agilent Zorbax Eclipse XDB-C18 column 2.1 mm \times 150 mm, 3.5 μ m from Agilent Technologies (Wilmington, NC, USA) was used for LC separation. LC conditions were as follows: column temperature, 50 °C; mobile phase, solvent A (0.1% acetic acid in water) and 50% solvent B (0.1% acetic acid in methanol); flow-rate, 0.2 ml/min; the injected volume, 5 μ l. A linear gradient condition was used as follows (time, solvent A:solvent B): 0–3 min, 50:50–10:90; 4–5 min, 0:100; 5.5–6 min, 50:50. ESI-MS conditions were as follows: nebulizer gas, N_2 (50 psi); ionspray voltage, 5000 V; the turbo ion spray temperature, 450 °C; declustering potential, 35 V; entrance potential, 8 V; collision energy and collision cell exit potential, 10 V; the dwell time, 100 ms; ionization mode, positive ion. NNAL and NNAL- d_3 were assayed by quantifying the multiple reaction monitoring (MRM) transition of $[M+H]^+$ ion of NNAL at m/z 210.2 \rightarrow 180.2 and NNAL- d_3 at 213.0 \rightarrow 183.0.

2.4. Calibration

The method was calibrated by spiking a nonsmoker pooled urine with 3, 20, 100, 200, 400, 1000 pg/ml NNAL. Method validation was performed with an injection volume of 5 μ l. The background peak area ratio in unspiked urine was zero for NNAL. Each calibrator was analyzed twice. The means of the analyte/internal standard ratio was used for calculation of the regression function. The regression curves were forced through the origin.

2.5. Method validation

The method was validated according to the U.S. Food and Drug Administration (FDA) guidelines for bioanalytical methods [16]. Recovery rates were determined by comparing the analyte concentrations at the low, middle and high level, measured when nonsmoker urine extract was spiked after sample work-up and before the LC–MS/MS measurements (reference, 100%), and when the nonsmoker urine was spiked at the beginning of the sample work-up procedure. As a criterion, the accuracy at a average concentration level tested in these six matrices should be in the range of 85–115%. Intra-day precision was determined by evaluating three analyte concentration levels in authentic human urine samples,

to which only NNAL was spiked in appropriate concentrations. For intra-day precision, each sample was analyzed five times. For inter-day precision, samples were analyzed once on six different days within 2 weeks. Acceptance criteria for precision was $\pm 15\%$ and $\pm 20\%$ at levels up to three times the LOQ. Accuracies at low, medium, and high concentrations were determined with human urine samples spiked at low, medium and high levels. Each level was analyzed five times. Acceptance criteria were rates of 85–115% (80–120% at levels up to $3 \times$ LOQ) as well as coefficient of variations (CV) of $\pm 15\%$ ($\pm 20\% < 3 \times$ LOQ). LOD and LOQ were estimated with the signal/noise method using the integrated function of the Analyst software. Signal/noise ratios of 3:1 and 10:1 were applied for estimating the LOD and LOQ, respectively. Matrix effects were determined by calculating the peak area ratios of the analytes at low and high concentrations when spiked to worked-up urine extracts (with the background areas subtracted) and the same amounts of analytes in solvent (methanol). Stability under post-sample preparation conditions was determined by storing the extracts 13–20 day at -20°C and subsequently for 24 h at room temperature. Carry-over effects in the chromatographic system were tested by injecting urine extracts with high analyte concentrations five times, followed by blank (methanol) injection. This was repeated 3 times.

2.6. Urine samples

The studies were approved by Zhengzhou University Ethics Committee. 243 healthy volunteers were recruited into the study: 207 smokers and 36 nonsmokers. Three commercial brands of cigarettes were used for this study, yielding nominally 8, 10 and 13 mg tar under International Organization for Standardization (ISO) smoking regime thereby spanning the full range of tar yields legally available in China at the time of the study. The smokers belonged to three groups, smoking Chinese cigarettes with 8 mg ($n = 63$), 10 mg ($n = 70$), and 13 mg ($n = 74$) tar and 15 cigarettes per day, determined according to the ISO standard smoking regime. The selection per group was at random. For all subjects 24 h urine samples were obtained at baseline from ongoing studies (Urinary biomarkers related to smoke exposure) in Institute of Clinical Pharmacology of Zhengzhou University. Informed consent and/or assent were obtained from each of the subjects.

2.7. Data analysis

All chromatographic peaks were reviewed, and any integration corrections were made manually, when necessary. Calibration curves were prepared using a linear regression with $1/x$ weighting. All standard and sample concentrations were determined using internal standard areas versus analyte areas. Data analysis was performed using Origin 8.0 and Microsoft Office Excel 2003.

3. Results and discussion

3.1. Method performance

Loss of NO (m/z 30) is the predominant mass transition, which is used as quantifier for all analytes and internal standards (Fig. 2A). Typical chromatogram of the mass of transition for NNAL and the corresponding deuterated internal standards for a urine sample of a smoker were shown in Fig. 2B and C. The method performance data was shown in Table 1. The peak area ratio of NNAL to internal standard in human urine was linear as a function of concentration over the range 3–1000.0 pg/ml. Excellent linearity was obtained with correlation coefficient values ($r = 0.9990$), and the corresponding equation was $y = 0.0492x + 0.0281$. The LOD and LOQ for NNAL were 0.30 and 0.99 pg/ml.

Accuracies determined in 5 different urine matrices were between 88.00 and 112.00% and thus regarded as acceptable. Precision (both intra- and inter-day) of the method was found to be acceptable (CV < 10%). Recovery rates of the whole analytical procedure at low, medium and high levels were 88.00–113.00% for NNAL. The lowest recovery rates were usually observed at the lowest concentration. Slightly positive matrix effect of 20% was observed for the NNAL. NNAL was found to be stable in urine under short-term (24 h, 20°C), RSDs of low level and high level were 2.30% and 1.90%, respectively. NNAL was found to be stable in urine under long-term storage conditions (6 months, -20°C), RSDs of low level and high level were 3.03% and 4.09%, respectively. This was accordant with previous studies [14,17]. Three freeze/thaw cycles did not lead to measurable losses of the analytes. No carry-over effects during LC–MS/MS analysis were observed for NNAL. 15% of the total samples were chosen to reanalysis, and the differentia was less than 20%, which is acceptable.

3.2. NNK in cigarette smoke

Three commercial brands of cigarettes were used for this study, yielding nominally 8, 10 and 13 mg tar under ISO smoking regime. The ISO smoking regime was as follows: Each cigarette was smoked at 1 puff/60 s, 2 s puff during, 35 ml puff volume. However, the Canadian intense smoking regime was as follows: Each cigarette was smoked at 1 puff/30 s, 2 s puff during, 55 ml puff volume and 100% filter ventilation blocked. Five cigarettes were smoked per port for ISO smoking regime and three cigarettes were smoked per port for Canadian intense smoking regime. All samples were smoked to a butt mark of 3 mm past the tipping paper overwrap. Their corresponding NNK yields were determined by LC–MS/MS adapting a previously published method [18]. The corresponding total NNK yields of 15 cigarettes was 51.45, 71.70 and 53.40 ng under ISO smoking regime daily and 103.50, 141.50 and 95.50 ng under Canadian intense smoking regime.

3.3. NNAL in human urine

The method was applied to 36 nonsmokers and 207 smokers (63 smokers with 8 mg tar yields, 70 smokers with 10 mg tar yields and 74 smokers with 13 mg tar yields). The concentration of total NNAL in nonsmokers 24 h urine ranged from 0 to 174.30 ng/24 h with a mean of 36.93 ng/24 h, the concentration of urinary total NNAL in smokers with 8 mg tar yields was 0–375.16 ng/24 h with a mean of 121.66 ng/24 h, that in smokers with 10 mg tar yields was 13.25–473.36 ng/24 h with a mean of 137.07 ng/24 h, and that in smokers with 13 mg tar yields was 16.65–317.25 ng/24 h with a mean of 119.36 ng/24 h (Fig. 3). Cigarette smoking primarily increased the urinary excretion of NNAL.

Urinary creatinine concentrations for the subjects were determined by LC–MS/MS adapting a previously published method [19] and showed in Fig. 4, the NNAL values were corrected for urine flow after five outliers being removed from raw data. The available data included 34 nonsmokers and 204 smokers (62 smokers with 8 mg tar yields, 69 smokers with 10 mg tar yields and 73 smokers with 13 mg tar yields). A similar trend was observed when the NNAL values were expressed as $\mu\text{g}/\text{mol}$ creatinine (Fig. 5). The concentration of urinary NNAL in nonsmokers was 0–17.29 $\mu\text{g}/\text{mol}$ with a mean of 3.19 $\mu\text{g}/\text{mol}$, the concentration of urinary NNAL in smokers with low tar yields was 1.10–58.10 $\mu\text{g}/\text{mol}$ with a mean of 12.25 $\mu\text{g}/\text{mol}$, that in smokers with middle tar yields was 1.28–60.22 $\mu\text{g}/\text{mol}$ with a mean of 12.74 $\mu\text{g}/\text{mol}$, and that in smokers with high tar yields was 0.97–49.13 $\mu\text{g}/\text{mol}$ with a mean of 11.83 $\mu\text{g}/\text{mol}$. One-way ANOVA showed that all smokers had significantly higher mean urinary NNAL concentrations, more than 3 times, than the nonsmokers (nonsmokers versus smokers with 8 mg tar

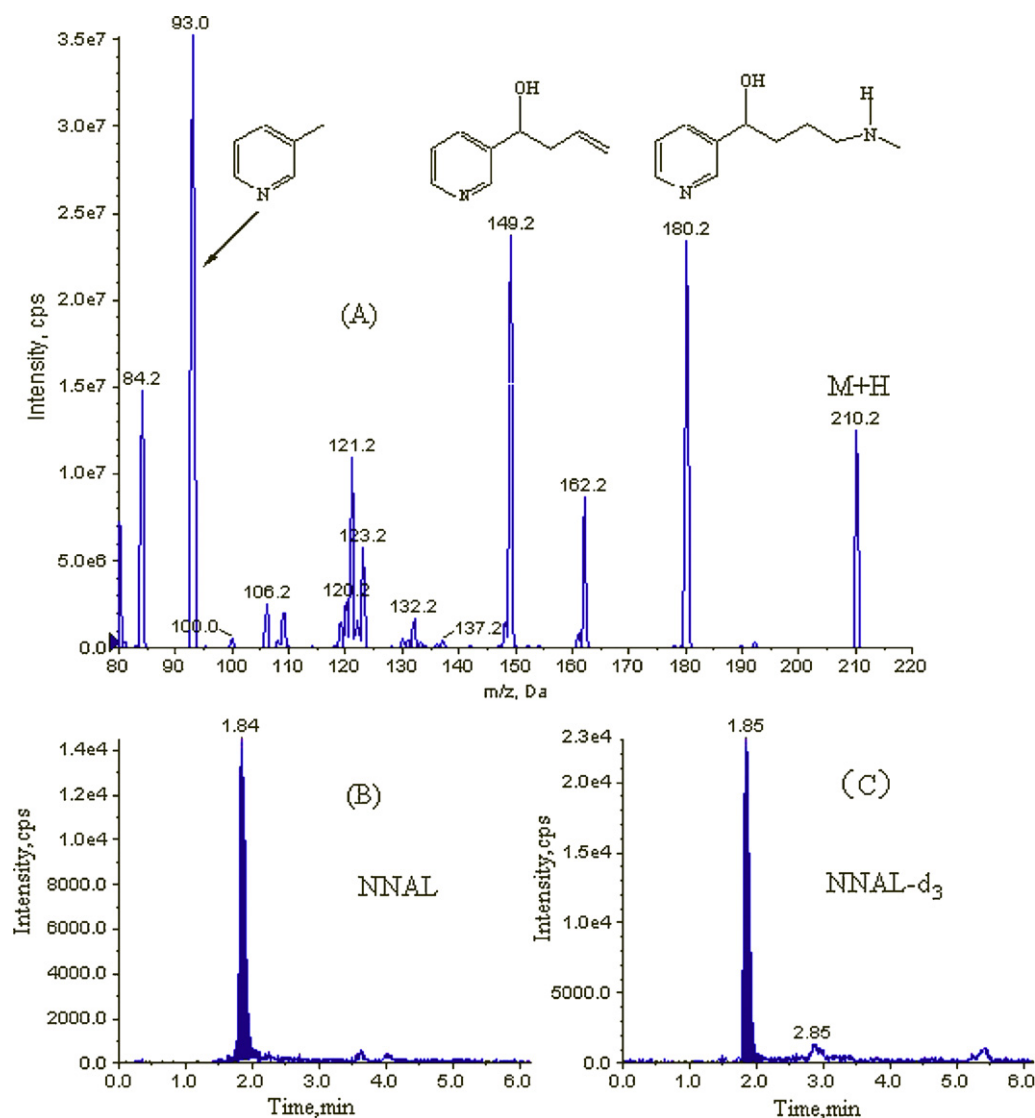


Fig. 2. Product-ion mass spectra of NNAL (A), chromatograms of the ion transitions for NNAL (B) and its respective deuterated internal standards (C) in a urine sample of a smoker.

cigarette/smokers with 10 mg tar cigarette/smokers with 13 mg tar cigarette, $P < 0.001$ in all cases).

Urinary total NNAL is an efficient biomarker to detect tobacco smoke exposure [20]. To the best of our knowledge, this is the first study to evaluate the associations between differing levels of tar/NNK yield Chinese virginia cigarettes and urinary total NNAL. In the present data, the urinary average NNAL level of nonsmokers was 37.38 ng/24 h. It was higher than that in the Kavvadias' study (16.06 ng/24 h). The reason for this may be exposure of second-hand smoke or environment tobacco smoke, and the long half-life of total NNAL was 10–18 days [20]. In addition, the urinary average NNAL levels of smokers with 10 mg tar cigarettes was 133.53 ng/24 h, which was lower than that in the Kavvadias' study (287.70 ng/24 h). The reason may be inherent differences

in the cigarettes used in both studies. In the Kavvadias' study, blended style cigarette was used, which has high level of smoke NNK. Whereas Chinese virginia cigarette was used in this study. Its concentration of smoke NNK was much lower than the former.

A further comparison was made between the concentration of urinary NNAL in smokers and tar yields. In this study, the concentration of urinary NNAL in smokers had an approximately 3-fold higher than that in nonsmokers in our study; further, the levels of urinary total NNAL increased incrementally with cigarette smoke NNK, however the levels of urinary total NNAL did not increase with tar yields. This is different with previous studies [6,21,22]. In their studies, they found that smokers have lower NNAL levels in their urine when they have lower mouth level exposure to TSNA in mainstream smoke from their usual cigarette. It is important to

Table 1
Performance data of the analytical method for NNAL in urine.

	Spiked amount (pg)	Conc. (pg)	Recovery $N=5$ (%)	Intra-day precision $N=5$ (%)	Inter-day precision $N=5$ (%)	Accuracy Intra-day ($N=5$)
NNAL	20.00	20.40	102.00	4.80	1.50	99.30
	100.00	93.00	93.00	0.70	3.80	92.20
	400.00	430.80	107.70	4.50	1.10	96.10

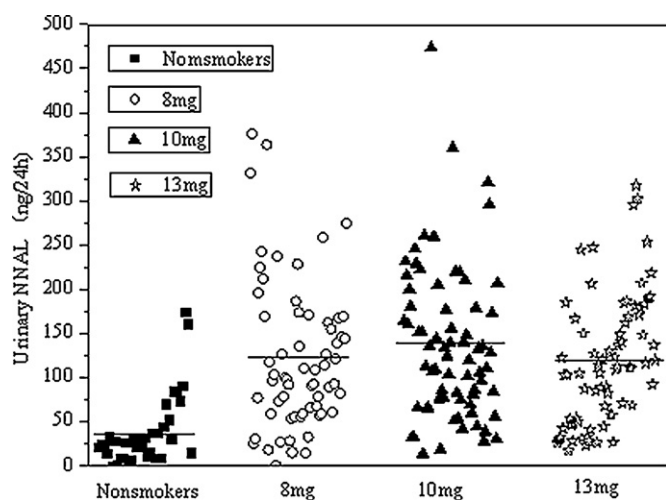


Fig. 3. The concentration of urinary NNAL with different tar yields. Horizontal lines show the means.

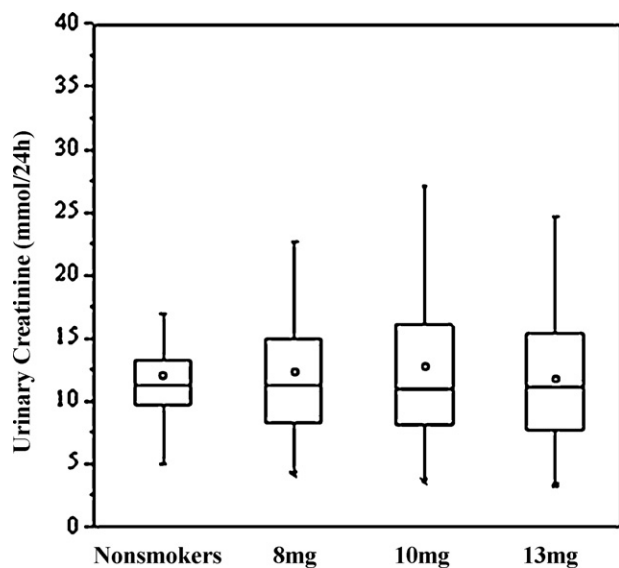


Fig. 4. The concentration of urinary creatinine of subjects.

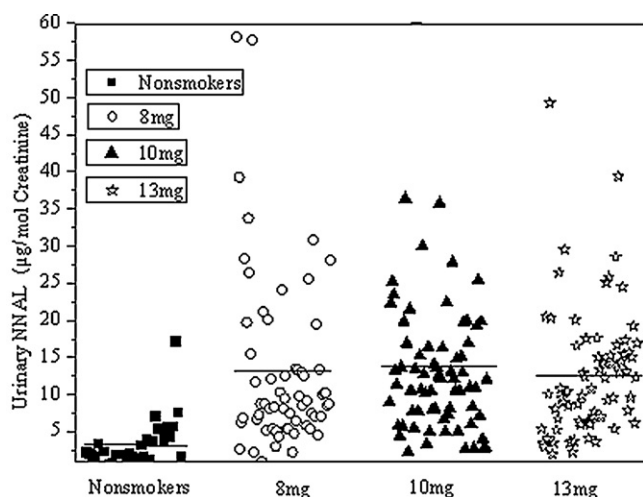


Fig. 5. Urinary NNAL for nonsmokers and smokers: NNAL µg/mol creatinine. Horizontal lines show the means.

note that the cigarettes used in both study were different. Cigarette ingredients of blended cigarettes and Chinese virginia cigarettes are not the same. The main component of blended cigarettes is burley tobacco. And the formula of blended cigarettes and Chinese virginia cigarettes are distinct. In addition, smoking behavior of smokers was different.

The relationship between cigarette smoke NNK and urinary average NNAL levels in 24 h urine was established. Under ISO condition, the equation was $y = 1.2976x - 101.79$, and the correlation coefficient r^2 was 0.9682 ($n = 204$). However, NNK emission was greatly influenced by smoking behaviors [23], smokers tend to take higher puff volumes and lower duration, with much shorter inter-puff intervals than ISO smoking regime. The emission generated under ISO smoking regime cannot fully represented the actual measures of human exposure [24]. Smoking behavior of smokers was closer to Canadian intense smoking conditions. A prediction model of cigarette smoke NNK and urinary average NNAL levels in 24 h was established. The equation was $y = 2.8987x - 245.38$ with a good correlation coefficient: $r^2 = 0.9952$, $n = 204$.

4. Conclusions

In conclusion, an analytical method using MIP coupled with LC-MS/MS for the determination of total NNAL in human urine has been developed and applied to urine samples of 36 nonsmokers and 207 smokers. The main advantage compared to other methods is its improved sensitivity and short analysis time. NNAL was found to be significantly higher in the urine of smokers compared with nonsmokers. Compared smokers with blended cigarettes, who smoked Chinese virginia cigarette had low urinary NNAL levels. There was a direct association between the 24-h mouth-level exposure of carcinogen NNK from cigarette smoking and the concentration of NNAL in the urine of smokers. However, there was not a positive correlation between urinary total NNAL levels in 24 h and tar. Total urinary NNAL is a valuable biomarker for monitoring exposure to carcinogenic NNK in smokers and in nonsmokers. A prediction model of cigarette smoke NNK and urinary average NNAL levels in 24 h was established.

Acknowledgments

This work was supported by the National Natural Science Foundation of China. The authors wish to thank vice-profession Gao Na from Institute of Clinical Pharmacology (School of medical, Zhengzhou University, China) for providing 24 h urine samples of smokers and blank urine samples of nonsmokers.

Appendix A. Supplementary data

Supplementary data associated with this article can be found, in the online version, at [doi:10.1016/j.jpba.2012.01.028](https://doi.org/10.1016/j.jpba.2012.01.028).

References

- [1] P. Vineis, M. Alavanja, P. Buffler, E. Fontham, S. Franceschi, Y.T. Gao, P.C. Gupta, A. Hackshaw, E. Matos, J. Samet, F. Sitas, J. Smith, L. Stayner, K. Straif, M.J. Thun, H.E. Wichmann, A.H. Wu, D. Zaridze, R. Peto, R. Doll, Tobacco and cancer: recent epidemiological evidence, *J. Natl. Cancer Inst.* 96 (2004), doi:10.1093/jnci/djh1014.
- [2] J.M. Yuan, W.P. Koh, S.E. Murphy, Y.H. Fan, R.W. Wang, S.G. Carmella, S.M. Han, K. Wickham, Y.T. Gao, M.C. Yu, S.S. Hecht, Urinary levels of tobacco-specific nitrosamine metabolites in Relation to lung cancer development in two prospective cohorts of cigarette smokers, *Cancer Res.* 69 (2009) 2990–2995.
- [3] S.S. Hecht, Biochemistry, biology, and carcinogenicity of tobacco-specific N-nitrosamines, *Chem. Res. Toxicol.* 11 (1998) 559–603.
- [4] D. Hoffmann, A. Rivenson, S. Amin, S.S. Hecht, Dose-response study of the carcinogenicity of tobacco-specific N-nitrosamines in F344 rats, *J. Cancer Res. Clin. Oncol.* 108 (1984) 81–86.
- [5] M.D. Eisner, P. Jacob, N.L. Benowitz, J. Balmes, P.D. Blanc, Longer term exposure to secondhand smoke and health outcomes in COPD: impact of urine

- 4-(methylnitrosamino)-1-(3-pyridyl)-1-butanol, *Nicotine Tob. Res.* 11 (2009) 945–953.
- [6] D.L. Ashley, R.J. O'Connor, J.T. Bernert, C.H. Watson, G.M. Polzin, R.B. Jain, D. Hammond, D.K. Hatsukami, G.A. Giovino, K.M. Cummings, A. McNeill, L. Shahab, B. King, G.T. Fong, L.Q. Zhang, Y. Xia, X.Z. Yan, J.M. McCraw, Effect of differing levels of tobacco-specific nitrosamines in cigarette smoke on the levels of biomarkers in smokers, *Cancer Epidemiol. Biomarkers Prev.* 19 (2010) 1389–1398.
- [7] D.K. Hatsukami, N.L. Benowitz, S.I. Rennard, C. Oncken, S.S. Hecht, Biomarkers to assess the utility of potential reduced exposure tobacco products, *Nicotine Tob. Res.* 8 (2006) 600–622.
- [8] S.S. Hecht, Human urinary carcinogen metabolites: biomarkers for investigating tobacco and cancer, *Carcinogenesis* 23 (2002) 907–922.
- [9] K.A. Shah, M.S. Halquist, H. Thomas Karnes, A modified method for the determination of tobacco specific nitrosamine 4-(methylnitrosamino)-1-(3-pyridyl)-1-butanol in human urine by solid phase extraction using a molecularly imprinted polymer and liquid chromatography tandem mass spectrometry, *J. Chromatogr. B: Anal. Technol. Biomed. Life Sci.* 877 (2009) 1575–1582.
- [10] Y. Xia, J.T. Bernert, Quantitation of the tobacco-specific nitrosamine 4-(methylnitrosamino)-1-(3-pyridyl)-1-butanol (NNAL) in urine by LC tandem mass spectrometry, *Epidemiology* 19 (2008) S230.
- [11] Y. Xia, J.E. McGuffey, S. Bhattacharyya, B. Sellergren, E. Yilmaz, L.Q. Wang, J.T. Bernert, Analysis of the tobacco-specific nitrosamine 4-(methylnitrosamino)-1-(3-pyridyl)-1-butanol in urine by extraction on a molecularly imprinted polymer column and liquid chromatography/atmospheric pressure ionization tandem mass spectrometry, *Anal. Chem.* 77 (2005) 7639–7645.
- [12] Y.Y. Yang, H.G. Nie, C.C. Li, Y. Bai, N. Li, J. Liao, H.W. Liu, On-line concentration and determination of tobacco-specific N-nitrosamines by cation-selective exhaustive injection-sweeping-micellar electrokinetic chromatography, *Talanta* 82 (2010) 1797–1801.
- [13] S.H. Bhat, S.L. Gelhaus, C. Mesaros, A. Vachani, I.A. Blair, A new liquid chromatography/mass spectrometry method for 4-(methylnitrosamino)-1-(3-pyridyl)-1-butanol (NNAL) in urine, *Rapid Commun. Mass Spectrom.* 25 (2011) 115–121.
- [14] K.A. Shah, M.C. Peoples, M.S. Halquist, S.C. Rutan, H. Thomas Karnes, Microfluidic direct injection method for analysis of urinary 4-(methylnitrosamino)-1-(3-pyridyl)-1-butanol (NNAL) using molecularly imprinted polymers coupled on-line with LC-MS/MS, *J. Pharm. Biomed. Anal.* 54 (2011) 368–378.
- [15] P. Jacob, C. Havel, D.H. Lee, L.S. Yu, M.D. Eisner, N.L. Benowitz, Subpicogram per milliliter determination of the tobacco-specific carcinogen metabolite 4-(methylnitrosamino)-1-(3-pyridyl)-1-butanol in human urine using liquid chromatography–tandem mass spectrometry, *Anal. Chem.* 80 (2008) 8115–8121.
- [16] Food and Drug Administration (FDA), Guidance for Industry–Bioanalytical Method Validation. <http://www.fda.gov/downloads/Drugs/GuidanceComplianceRegulatoryInformation/Guidances/UCM070107.pdf> (accessed 17.04.09).
- [17] D. Kavvadias, G. Scherer, M. Urban, F. Cheung, G. Errington, J. Shepperd, M. McEwan, Simultaneous determination of four tobacco-specific N-nitrosamines (TSNA) in human urine, *J. Chromatogr. B: Anal. Technol. Biomed. Life Sci.* 877 (2009) 1185–1192.
- [18] W. Xiong, H.W. Hou, X.Y. Jiang, G.L. Tang, Q.Y. Hu, Simultaneous determination of four tobacco-specific N-nitrosamines in mainstream smoke for Chinese virginia cigarettes by liquid chromatography–tandem mass spectrometry and validation under ISO and Canadian intense machine smoking regimes, *Anal. Chim. Acta* 674 (2010) 71–78.
- [19] H.W. Hou, W. Xiong, D.K. Song, G.L. Tang, Q.Y. Hu, LC-MS-MS measurements of urinary creatinine and the application of creatinine normalization techniques on cotinine in smokers urine, *J. Automated Methods Manag. Chem.*, submitted for publication.
- [20] M.L. Goniewicz, C.M. Havel, M.W. Peng, P. Jacob, D. Dempsey, L. Yu, W. Zielinska-Danch, B. Koszowski, J. Czogala, A. Sobczak, N.L. Benowitz, Elimination kinetics of the tobacco-specific biomarker and lung carcinogen 4-(methylnitrosamino)-1-(3-pyridyl)-1-butanol, *Cancer Epidemiol. Biomarkers Prev.* 18 (2009) 3421–3425.
- [21] C.J. Shepperd, A.C. Eldridge, G. Errington, M. Dixon, A study to evaluate the effect on mouth level exposure and biomarkers of exposure estimates of cigarette smoke exposure following a forced switch to a lower ISO tar yield cigarette, *Regul. Toxicol. Pharmacol.* (2011), doi:10.1016/j.yrtph.2011.1005.1011.
- [22] P. Mendes, Q.W. Liang, K. Frost-Pineda, S. Munjal, R.A. Walk, H.J. Roethig, The relationship between smoking machine derived tar yields and biomarkers of exposure in adult cigarette smokers in the US, *Regul. Toxicol. Pharmacol.* 55 (2009) 17–27.
- [23] T. Adam, J. McAughy, C. Mocker, C. McGrath, R. Zimmermann, Influence of filter ventilation on the chemical composition of cigarette mainstream smoke, *Anal. Chim. Acta* 657 (2010) 36–44.
- [24] S.W. Purkis, V. Troude, G. Duputié, C. Tessier, Limitations in the characterisation of cigarette products using different machine smoking regimes, *Regul. Toxicol. Pharmacol.* 58 (2010) 501–515.



Methods to measure the binding of therapeutic monoclonal antibodies to the human Fc receptor FcγRIII (CD16) using real time kinetic analysis and flow cytometry

Alice Harrison, Zhe Liu, Schona Makweche, Kevin Maskell, Hong Qi, Geoff Hale*

Millipore BioPharma Services, 91 Milton Park, Abingdon, Oxfordshire OX14 4RY, UK

ARTICLE INFO

Article history:

Received 21 September 2011
Received in revised form 3 January 2012
Accepted 20 January 2012
Available online 30 January 2012

Keywords:

FcγRIII
CD16
Surface plasmon resonance
Flow cytometry
Therapeutic antibody

ABSTRACT

Two different methods have been developed to measure the binding of therapeutic antibodies to the low affinity human Fc receptor FcγRIII (CD16). The first measures binding of antibody to recombinant soluble receptor by surface plasmon resonance and the second uses flow cytometry to measure antibody binding to cells which express the receptor. Both methods have been formatted as parallel line assays and show high levels of accuracy, precision and linearity, making them suitable for comparability, potency and stability assays. They are both readily able to detect structural differences such as glycosylation, which affect Fc receptor binding. The same approaches can be used to measure the binding of any antibody to any Fc receptor. These assays show greater internal precision and long-term reproducibility than traditional cell-based assays such as antibody-dependent cell-mediated cytotoxicity. A combinational approach with a target binding might be appropriate for routine drug batch release as these assays are likely to be significantly more sensitive to small changes in drug structure or activity.

© 2012 Elsevier B.V. All rights reserved.

1. Introduction

Monoclonal antibodies comprise the largest category of biotech-produced drugs in development. The physiologic properties which make them so useful, namely multivalent binding to unique target antigens and multifunctional interactions with natural effector systems, provide special challenges to the analytical scientist. Reproducible and precise assays for measuring drug potency are the cornerstone of quality control of manufactured products. Developing a suitable method to quantify the complete physiological activity of an antibody is usually not feasible.

In this article, the therapeutic antibody alemtuzumab (Campath®) is used to illustrate how a complex cell-based assay can be broken down into simpler steps which are amenable to precise measurements of molecular interactions. Increasing

precision of analysis leads to a better ability to determine lot to lot variability in the manufactured product and allows the assessment of drug stability and the impact of process changes.

Alemtuzumab was the first humanised therapeutic antibody [1]. It is a human IgG1 which recognises the lymphocyte antigen CD52 and is remarkably effective at killing cells both by complement-mediated cytotoxicity (CMC) and antibody-dependent cell-mediated cytotoxicity (ADCC). In 2001, alemtuzumab was approved for the treatment of patients with chronic lymphocytic leukaemia who had failed prior chemotherapy. Early batch release assays measured its CMC activity [2]. However, ADCC is thought to be the more important mechanism of tumour clearance and it is known that this can be markedly affected by changes in glycosylation that might not affect CMC in the same way. ADCC assays were considered difficult to standardise due to the requirement for a consistent source of human effector cells. With the availability of suitable cell lines or commercial sources of cryopreserved peripheral blood mononuclear cells (PBMC) this has become more practicable but the variability inherent in the method still limits its routine application for drug batch release.

An alternative procedure for quantifying the activity of the Fc domain is to measure the functional interactions of the antibody with recombinant human Fc receptors. The most important receptor for ADCC is believed to be CD16 (FcγRIII). CD16 exists in two isoforms, CD16A (a heterodimeric transmembrane protein) on lymphocytes and CD16B (GPI-anchored) on neutrophils. There are also different alleles at amino acid position 158 with 158Val showing

Abbreviations: ADCC, antibody-dependent cell-mediated cytotoxicity; BSA, bovine serum albumin; CFSE, carboxyfluorescein diacetate succinimidyl ester; CMC, complement-mediated cytotoxicity; CV, coefficient of variation; FBS, foetal bovine serum; GPI, glycosylphosphatidylinositol; HBS-EP, Hepes-buffered saline containing EDTA and surfactant P20; IMDM, Iscove's modified Dulbecco's medium; MFI, median fluorescence intensity; PBMC, peripheral blood mononuclear cells; PBS, phosphate buffered saline; PI, propidium iodide; PL, parameter logistic; SPR, surface plasmon resonance.

* Correspondence to: Managing Director, Millipore BioPharma Services, 91 Milton Park, Abingdon, Oxon, OX14 4RY. Tel.: +44 0 1235 444100.

higher affinity for IgG than 158Phe. Both alleles occur with similar frequency but donors homozygous for 158Val show higher levels of ADCC. Hitherto, CD16A was difficult to express in transfected cells but Armour et al. [3] have constructed hybrid molecules consisting of the extracellular domain of CD16A-158Val or CD16A-158Phe and the transmembrane (lipid-anchored) domain of CD16B. CHO cells which express these receptors are ideal for analysis of IgG binding.

It is known that the precise structure of the N-linked carbohydrate on the Fc domain significantly affects binding to CD16 and ADCC [4]. It is also established for rituximab that the affinity of CD16–antibody interaction correlates well with the extent of target cell death mediated by ADCC [5]. Although the same correlation has not yet been shown for alemtuzumab, experiments in CD52 transgenic mice provided evidence for the importance of CD16 by showing that ADCC mediated by NK cells and/or neutrophils was responsible for lymphocyte depletion in vivo [6]. Therefore, an assay which measures the interaction of therapeutic antibodies with CD16 provides a sensitive and functionally relevant indicator of the consistency and quality of the antibody in this regard. It is also useful as a stability-indicating test since the interaction between IgG Fc and CD16 is normally of low affinity, but is likely to be enhanced by antibody aggregation, which is an important type of deterioration that might be seen under certain storage conditions.

This paper describes two complementary methodologies which can be used to accurately measure IgG–FcR interactions and are amenable to validation as drug batch release assays.

Glycoengineered forms of alemtuzumab have been prepared from cells transfected with glycosyltransferases to enable secretion of antibody with an increased proportion of bisecting N-acetylgalactosamine and a reduced proportion of fucose in the Fc-linked carbohydrate [7,8]. These variations of glycosylated alemtuzumab are used as models to illustrate the correlation between FcR binding and functional ADCC.

2. Materials and methods

2.1. Antibodies and cells

Glyco-engineered alemtuzumab (Glyco1 and Glyco2), chimeric, aglycosylated CD3 (otelixizumab or ChAglyCD3) [9] and Wien133 cells (which expresses a high level of CD52 antigen) were generously provided by Prof Herman Waldmann, University of Oxford, Oxford, UK. The cell line A4, created by transfecting Chinese Hamster Ovary (CHO) cells with a gene encoding the high affinity allele (CD16A-V158) for human IgG Fc [3] was obtained from Dr Mike Clark, University of Cambridge, Cambridge, UK, who also provided helpful advice on the initial assay development. Cryopreserved human peripheral blood mononuclear cells (PBMC) were obtained from CTL-Europe GmbH, Bonn, Germany.

2.2. ADCC assay

Wien133 target cells were labelled with CFSE [10] and resuspended in culture medium (IMDM containing 10% FBS, 100 U/ml penicillin and 100 µg/ml streptomycin). Serial dilutions of test samples (50 µL) were added to a round bottom microplate and 50 µL of the target cells (5×10^5 cell/mL) were added and incubated for 30 min at 37 °C, 5% CO₂. Effector cells (50 µL PBMC at $1-3 \times 10^7$ cells/mL) were added and the plate was incubated for a further 4 h. 50 µL of PBS containing 2 mM EDTA, 10 µg/ml propidium iodide and 6000 latex beads/mL was added and the samples were promptly analysed by flow cytometry on a Beckman Coulter FC500. The unstained latex beads were added so that the number of viable target cells (CFSE+, PI⁻) could be normalised to eliminate any variability between samples due to changes in the flow rate

or sample volume. It was not possible to count dead target cells (CFSE+, PI⁺) reliably because many of them appeared to disintegrate. Use of serum in the culture medium raised the possibility that complement-mediated cytotoxicity could contribute to the killing. However, any such effect was likely to be minimal since the concentration of alemtuzumab required for CMC (half maximal at 500–700 ng/mL) [2] is substantially higher than required for ADCC (half maximal at less than 20 ng/mL).

2.3. Measurement of protein concentrations

Concentrations of antibody stock solutions were measured by absorbance at 280 nm using a Nanodrop 1000 (Thermo-Fisher, Loughborough, UK) taking the extinction coefficient (E1%) of alemtuzumab to be 13.2 (based on its protein sequence) and assuming the same coefficient for other samples.

2.4. SPR assay – Biacore

Monoclonal anti-His₄ antibody (Qiagen Crawley, UK, cat no 34670) was coupled to a Biacore CM5 chip (Biacore, Uppsala, Sweden) by standard amine chemistry according to the manufacturer's instructions. His-tagged recombinant human CD16A (R&D Systems Abingdon, UK, cat no 4325-FC) at 1 µg/mL was injected for 2 min at 5 µL/min to be captured by the anti-His antibody. Independent serial dilutions of the test samples were prepared in triplicate in a microplate. Each sample was injected for 5 min at 5 µL/min over two flow cells; one control and one which had been exposed to the CD16A. The difference in binding responses was measured at the end of injection. After each sample, the chip was regenerated by injection of 20 µL of 10 mM glycine pH 3.0 and re-charged with CD16A. All experiments were carried out in HBS-EP buffer (Biacore) at a constant temperature of 25.0 °C using Biacore 2000 and Biacore 3000 instruments. BIAcontrol software (Versions 3.2 and 4.1 respectively) was used for data collection and BIAevaluation software (Version 4.1) was used for export of data.

2.5. SPR assay – ProteOn

Essentially identical experimental conditions were used for SPR experiments conducted on the ProteOn XPR36 instrument (Bio-Rad, kindly made available by Anton van der Merwe, University of Oxford, Oxford, UK). However, this instrument has 36 binding spots (comparable to four flow cells in the Biacore) and so a degree of parallel processing was possible. Anti-His₄ was coupled to all six spots of channels 1, 2, 3, 5, 6 of a ProteOn GLM chip according to the manufacturer's instructions. Channel 4 was sham-coupled as a reference. His-tagged recombinant human CD16A at 1 µg/mL was injected over channel 1 for 2 min at 25 µL/min to be captured by the anti-His antibody. Independent serial dilutions of the test samples were prepared in triplicate in a microplate. Each sample was injected for 5 min at 25 µL/min over six spots; one which had been exposed to the CD16A, four controls and one reference. Six samples were processed in parallel. The difference in binding responses between the specific and the reference was measured at the end of injection. After each sample, the chip was regenerated by injection of 25 µL of 10 mM glycine pH 3.0 and re-charged with CD16A. All experiments were carried out in HBS-EP buffer at a constant temperature of 25.0 °C. ProteOn Manager software (Version 2.1.0.38) was used for data collection and export.

2.6. Flow cytometry assay

Independent serial dilutions of the test samples (final volume 50 µL) were prepared in triplicate in a microplate. A4 cells were

suspended in assay buffer (PBS containing 0.1% BSA and 0.05% sodium azide) to give a concentration of 6×10^5 cells/mL. 50 μ L of cell suspension was added to each well of the microplate. The plate was incubated for 30 min at 25 °C and then washed four times with assay buffer by centrifugation. The cells were resuspended in detection reagent, FITC-conjugated goat F(ab')₂ anti-human kappa light chain (AbD Serotec, Kidlington, UK cat no STAR101FB), diluted 1 in 25 with assay buffer. The plate was incubated and washed three times as previously. Finally the cells were resuspended in 100 μ L assay buffer and 50 μ L of 3% formaldehyde was added. The cells were analysed using a FC500 flow cytometer (Beckman Coulter, UK). Cells were gated by forward and side scatter and the median fluorescence intensity (MFI) was recorded.

2.7. Statistical analysis

Curve fitting using weighted four and five parameter logistic models (4PL, 5PL) and parallel line analysis was carried out using StatLIA version 3.2 [11]. The chi-squared statistic was used as a measure of parallelism at a probability $p=0.05$. Weighting parameters for Biacore and flow experiments were experimentally determined using all the available data from reference and test samples of alemtuzumab. Default weighting parameters were used for ProteOn experiments due to the comparatively small dataset.

3. Results and discussion

3.1. ADCC assay

Samples of alemtuzumab and its glyco-engineered variants Glyco1 and Glyco2 were analysed by ADCC using human PBMC as effectors and Wien133 cells as targets at a ratio of approx 40:1. The results are shown in Figs. 1 and 2. As expected, the glyco-engineered antibodies were more potent in this assay and gave half maximal cell killing at a concentration of 7.4 ng/mL whereas 17.9 ng/mL of alemtuzumab was required to obtain half-maximal killing. However, the variability of this assay was relatively high with CVs of the individual replicates in the range 0.2–18.6% (mean 5.4%). Between

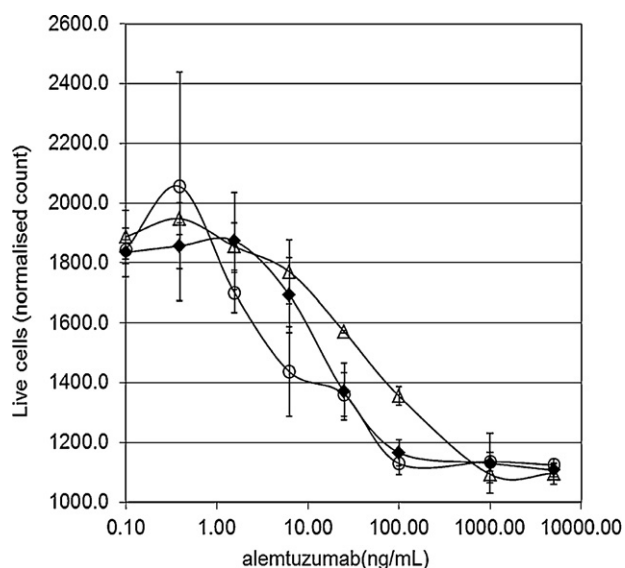


Fig. 1. Antibody-dependent cell-mediated cytotoxicity of Wien133 cells by human PBMC in the presence of alemtuzumab. The starting concentration of the test samples was adjusted to simulate different potency. The data are plotted as if the test samples had the same concentration as the reference sample so that potency differences show as a relative shift in the dose response curves. Error bars show the standard deviation of the triplicate measurements. ♦ Reference (100%) △ 50% ○ 100%.

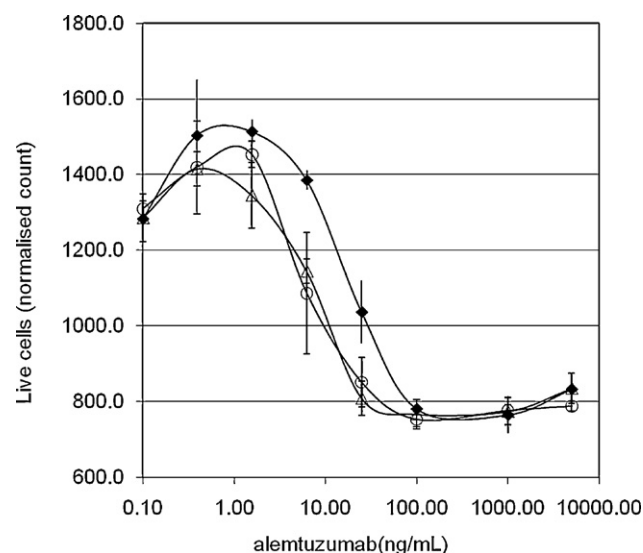


Fig. 2. Antibody-dependent cell-mediated cytotoxicity of Wien133 cells by human PBMC in the presence of different glycoforms of alemtuzumab. Error bars show the standard deviation of the triplicate measurements. ♦ Wild-type alemtuzumab △ Glyco1 ○ Glyco2.

2217 and 4655 events (live target cells) were acquired for each sample, giving a theoretical mean CV (based on Poisson distribution) of 1.8%. The relatively high level of assay variability and the apparent “hook effect” observed at the ends of the dose response made it difficult to model by conventional 4PL or 5PL equations with a sufficient degree of accuracy to detect deviations from parallelism. It is likely that the ADCC assay method might be improved with further work. Perhaps a suitable human cell line could be used as a source of effectors and a homogeneous readout of cell lysis could reduce the tendency for assay drift and stochastic errors inherent in the sequential analysis of cells by flow cytometry. Nevertheless, it is unlikely that a cell based assay can attain the same degree of accuracy and precision as a ligand binding assay.

3.2. SPR assay – Biacore

The binding of alemtuzumab to recombinant CD16A was measured by SPR in three separate experiments, each using a different pair of flow cells. In each experiment three test samples were compared to a reference sample. The test samples and reference samples were all prepared from a single batch of alemtuzumab but the concentrations of the test samples were adjusted to simulate drug samples of differing nominal potencies: 50%, 70%, 80%, 100%, 120%, 130% and 150% of the reference sample. (Nominal potency is the concentration at which the drug sample was prepared relative to the reference; measured potency is the concentration which is measured relative to the reference.) Each sample was analysed in triplicate. An example of the binding curves is shown in Fig. 3a. Analysis using a 4PL model gave poor fit probabilities by the χ^2 test ($p < 0.03$) therefore this model was deemed to be unsuitable. In contrast, analysis using a 5PL model with experimentally determined weighting factors gave good fit probabilities and all test sample curves were deemed to be parallel to the reference sample curve ($p > 0.05$). The correlation between measured and nominal potencies is shown in Fig. 4a. The assay showed good linearity with a correlation coefficient (R^2) of 0.993 and all measured potencies were within 9% of the nominal values (range 91.4–100.6%).

A negative control antibody, ChAglyCD3, engineered to eliminate binding to CD16A, showed no response in this assay (Fig. 5). However, the glycoengineered antibodies Glyco1 and Glyco2 showed significantly enhanced CD16A binding compared to wild

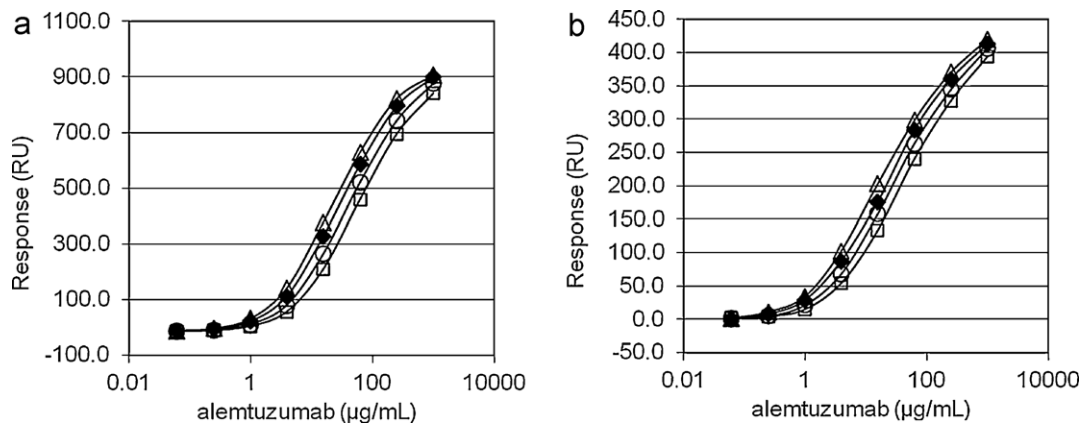


Fig. 3. Binding of alemtuzumab to human CD16A measured by SPR. The starting concentration of the test samples was adjusted to simulate samples of different potency. The standard deviations of the triplicate measurements were smaller than the plotted symbols. ♦ Reference (100%) △ 130% ○ 70% □ 50%. (a) Analysed on Biacore instrument. (b) Analysed on ProteOn instrument.

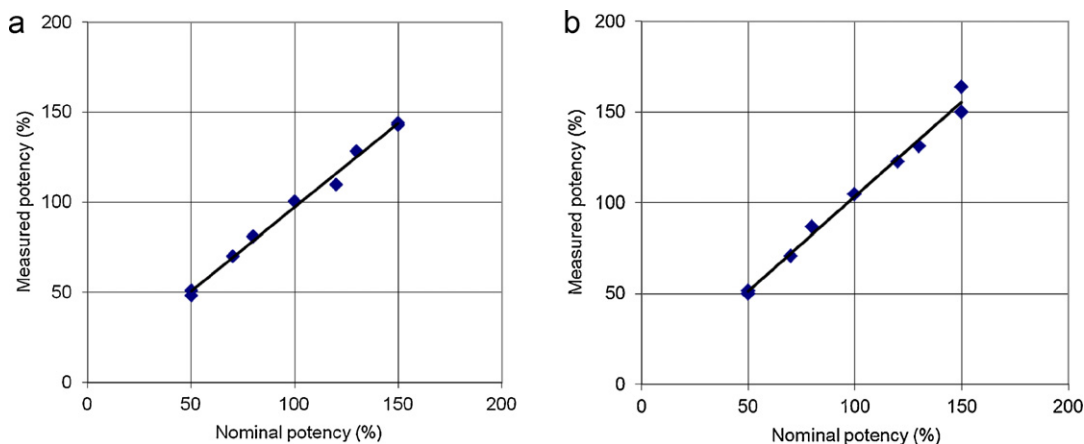


Fig. 4. Binding of alemtuzumab to human CD16A measured by SPR. Relationship between measured and nominal potency. (a) Analysed on Biacore instrument. (b) Analysed on ProteOn instrument.

type alemtuzumab with relative potencies of 300.5% and 410.8% respectively. In contrast to the dilutions of alemtuzumab, the glycoengineered samples showed small deviations from strict parallelism ($p = 0.017$ and 0.038 respectively) which is not unexpected when there are structural differences between samples.

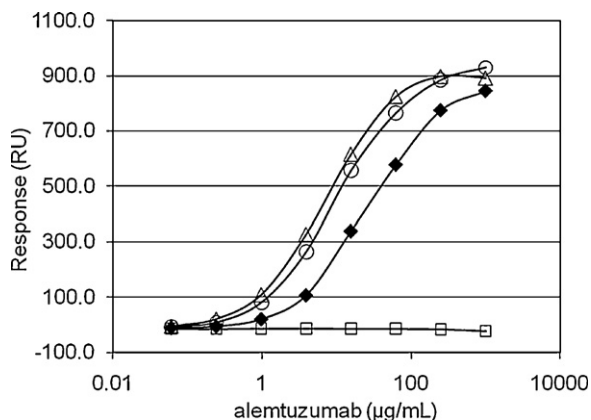


Fig. 5. Binding of glycoengineered and control antibodies to human CD16A measured by SPR. The starting concentration of the test samples was adjusted to simulate samples of different potency. The standard deviations of the triplicate measurements were smaller than the plotted symbols. ♦ Reference (100%) △ Glyco2 ○ Glyco1 □ ChAglyCD3.

3.3. SPR assay – ProteOn

The binding of alemtuzumab to recombinant CD16A was repeated using the ProteOn instrument. An example of the binding curves is shown in Fig. 3b. Both 4PL and 5PL models gave good fits and all test sample curves were deemed to be parallel to the reference sample curve ($p > 0.05$). The correlation between measured and nominal potencies (using 5PL model) is shown in Fig. 4b. The assay showed good linearity with a correlation coefficient (R^2) of 0.990 and all measured potencies were within 9% of the nominal values (range 93.8–108.3%).

3.4. Flow cytometry assay

The binding of alemtuzumab to cell-surface CD16A was measured by flow cytometry in two separate experiments, each consisting of two microplates with the same design as used for the SPR experiments. An example of the binding curves is shown in Fig. 6. The data were analysed using 4PL and 5PL models using experimentally determined weighting factors. Both models gave acceptable fits and all test samples were deemed parallel to the reference sample curve ($p > 0.05$). The relative potencies calculated using both models were almost indistinguishable. The correlation between measured and nominal potencies (using 5PL model) is shown in Fig. 7. The assay showed good linearity with a correlation coefficient (R^2) of 0.988 and all measured potencies were within 8% of the nominal values (range 97.4–107.4%). CHO cells which

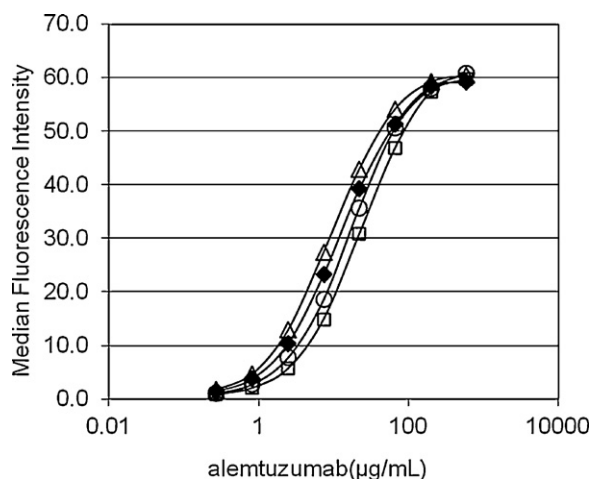


Fig. 6. Binding of alemtuzumab to human CD16A measured by flow cytometry. The starting concentration of the test samples was adjusted to simulate samples of different potency. The standard deviations of the triplicate measurements were smaller than the plotted symbols. ♦ Reference (100%) △ 130% ○ 70% □ 50%.

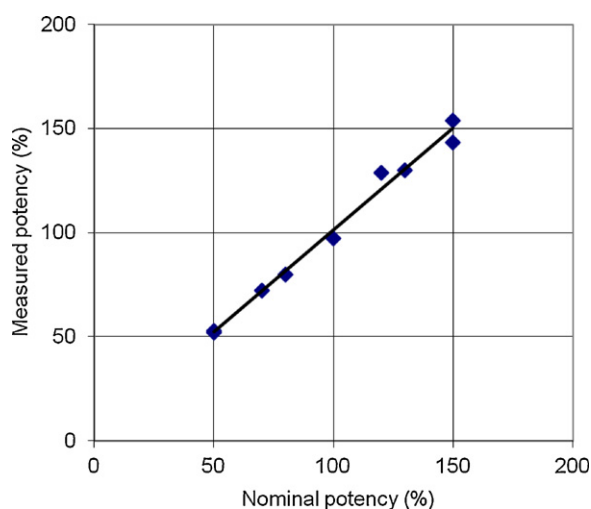


Fig. 7. Binding of alemtuzumab to human CD16A measured by flow cytometry. Relationship between measured and nominal potency.

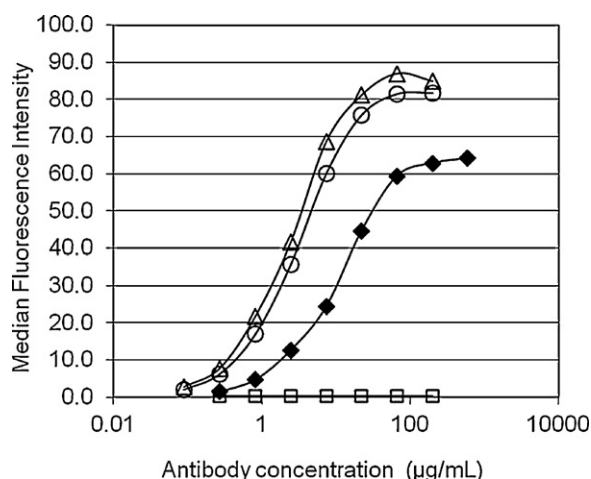


Fig. 8. Binding of glycoengineered and control antibodies to human CD16A measured by flow cytometry. The starting concentration of the test samples was adjusted to simulate samples of different potency. The standard deviations of the triplicate measurements were smaller than the plotted symbols. ♦ Reference (100%) △ Glyco2 ○ Glyco1 □ ChAglyCD3.

expressed CD16A-158Phe bound alemtuzumab with low affinity, giving responses substantially lower than the CD16A-158Val cells (A4) (data not shown). The glycoengineered antibodies and control antibody were also compared to the reference antibody. The results are shown in Fig. 8. The control antibody ChAglyCD3 gave no measurable response. Both Glyco1 and Glyco2 gave response curves which were distinctly non-parallel to the reference ($p < 0.0001$) as they reached a higher plateau of binding. It was therefore not possible to calculate true relative potencies by the parallel line method.

4. Conclusion

Accurate and precise measurement of potency is critical for control of drug quality. It is desirable that the analytical method should reflect, as closely as practicable, the biological activity of the drug. However appropriate bioassays, whether in vivo, or cell-based, can be cumbersome and lack essential reproducibility required for reliable comparisons over the lifetime of a drug product. This dilemma is exemplified by monoclonal antibodies for tumour therapy, such as alemtuzumab. In this case, ADCC using tumour cells as targets and fresh human PBMC as effectors, is a good model of the presumed physiological mode of action. However, the long term reliability of such an assay is questionable due to the potential for variability in the donor or effector cells as well as the complexity of the procedure.

In contrast, the cell-based assay for binding to CD16 showed excellent accuracy, precision and linearity. The precision of replicate measurements makes the method sensitive to small differences in drug structure (such as glycosylation) which would make the binding curves non-parallel.

Equally good results were obtained with the SPR assays and the assay was independent of platform, since the results from Biacore and ProteOn were very similar. Either the SPR or the flow method is suitable for accurate determination of the Fc binding properties of a therapeutic antibody. The throughput of the cell based assay was potentially higher as several microplates could be processed in one day, whereas the Biacore instrument could only process one microplate in 24 h. In practice, the choice between them is likely to be determined by issues such as the availability of reagents and equipment.

These methods are equally suitable for drug comparability, stability or lot release assays. Measurement of FcR binding alone is not a complete substitute for the analysis of physiological activity by ADCC. However, analogous methods can be developed for accurate and precise measurement of the binding of antibody to antigen, either by SPR or by flow cytometry, and the combination of the methods may well provide an acceptable substitute for the laborious and much less precise measurement of activity by ADCC.

References

- [1] L. Riechmann, M. Clark, H. Waldmann, G. Winter, Reshaping human antibodies for therapy, *Nature* 332 (1988) 323–327.
- [2] J. Phillips, A. Drumm, P. Harrison, P. Bird, K. Bhamra, E. Berrie, G. Hale, Manufacture and quality control of CAMPATH-1 antibodies for clinical trials, *Cytotherapy* 3 (2001) 233–242.
- [3] K.L. Armour, C.S. Smith, M.R. Clark, Expression of human FcγRIIIa as a GPI-linked molecule on CHO cells to enable measurement of human IgG binding, *J. Immunol. Methods* 354 (2010) 20–33.
- [4] R.M. Lively, C. Hale, S. Boyce, M.J. Keen, J. Phillips, Glycosylation and biological activity of CAMPATH-1H expressed in different cell lines and grown under different culture conditions, *Glycobiology* 5 (1995) 813–822.
- [5] E. Hatjiharissi, L. Xu, D.D. Santos, Z.R. Hunter, B.T. Ciccarelli, S. Verselis, M. Modica, Y. Cao, R.J. Manning, X. Leleu, E.A. Dimmock, A. Kortsaris, C. Mitsiades, K.C. Anderson, E.A. Fox, S.P. Treon, Increased natural killer cell expression of CD16 augmented binding and ADCC activity to rituximab among individuals expressing the FcγRIIIa-158V/V and V/V polymorphism, *Blood* 110 (2007) 2561–2564.

- [6] P. Hu, M.J. Turner, J. Shields, M.S. Gale, E. Hutto, B.L. Roberts, W.M. Siders, J.M. Kaplan, Investigation of the mechanism of action of alemtuzumab in a human CD52 transgenic mouse model, *Immunology* 128 (2009) 260–270.
- [7] P. Umana, J. Jean-Mairet, R. Moudry, H. Amstutz, J.E. Bailey, Engineered glycoforms of an antineuroblastoma IgG1 with optimized antibody dependent cellular cytotoxic activity, *Nat. Biotechnol.* 17 (1999) 1276–2180.
- [8] M.J.S. Dyer, S. Moser, P. Brünker, P. Bird, N. Almond, U. Puentener, L.M.W. Wheat, E. Bolam, E. Berrie, R. Grau, E. Buckby, B. Kennedy, R. Stebbings, G. Hale, P. Umana, Enhanced potency of glycoengineered anti-cd52 monoclonal antibodies, *Blood (ASH Annual Meeting Abstracts)* 106 (2005), Abstract 2958.
- [9] B. Keymeulen, E. Vandemeulebroucke, A.G. Ziegler, C. Mathieu, L. Kaufman, G. Hale, F. Gorus, M. Goldman, M. Walter, S. Candon, L. Schandene, L. Crenier, C. De Block, J.-M. Seigneurin, P. De Pauw, D. Pierard, I. Weets, P. Rebello, P. Bird, E. Berrie, M. Frewin, H. Waldmann, J.-F. Bach, D. Pipeleers, L. Chatenoud, Insulin needs after CD3-antibody therapy in new-onset type I diabetes, *N. Engl. J. Med.* 352 (2005) 2598–2608.
- [10] M. Bracher, H.J. Gould, B.J. Sutton, D. Dombrowicz, S.N. Karagiannis, Three-colour cytometric method to measure antibody-dependent tumour cell killing by cytotoxicity and phagocytosis, *J. Immunol. Methods* 323 (2007) 160–171.
- [11] P.G. Gottschalk, J.R. Dunn, Measuring parallelism, linearity, and relative potency in bioassay and immunoassay data, *J. Biopharm. Sci.* 15 (2005) 437–463.



Identification of major compounds in rat bile after oral administration of total triterpenoids of *Ganoderma lucidum* by high-performance liquid chromatography with electrospray ionization tandem mass spectrometry

Xiao-Yu Guo^a, Jian Han^a, Min Ye^a, Xiao-Chi Ma^b, Xuan Shen^a, Bin-Bin Xue^a, Qing-Ming Che^{a,*}

^a Department of Natural Medicines, School of Pharmaceutical Sciences, Peking University, Beijing 100191, China

^b School of Pharmacy, Dalian Medical University, Dalian 116044, China

ARTICLE INFO

Article history:

Received 30 September 2011

Received in revised form

30 December 2011

Accepted 20 January 2012

Available online 30 January 2012

Keywords:

Ganoderma lucidum

Triterpenoids

Metabolites

HPLC–DAD–ESI–MSⁿ

LC–ESI–IT–TOF/MS

ABSTRACT

Triterpenoids are the main bioactive components of *Ganoderma lucidum*, a famous traditional Chinese medicine. After oral administration of total triterpenoids of *G. lucidum* (TTGL), the rat bile was analyzed by high-performance liquid chromatography coupled with diode array detection and electrospray ion trap tandem mass spectrometry (HPLC–DAD–ESI–MSⁿ) and liquid chromatography coupled with electrospray ionization hybrid ion trap and time-of-flight mass spectrometry (LC–ESI–IT–TOF/MS). From rat bile and TTGL samples, a total of 31 triterpenoids, including seven new compounds, were identified or tentatively characterized based on their fragmentation behaviors. Among them, 22 triterpenoids were identified from TTGL and 29 triterpenoids were detected from rat bile after oral administration of TTGL. The results indicated that the majority of triterpenoids detected in TTGL extract could be excreted through rat bile. It is the first report on excretion of total triterpenoids of *G. lucidum* in rat bile.

© 2012 Elsevier B.V. All rights reserved.

1. Introduction

Ganoderma lucidum (Leyss. ex Fr.) Karst, so-called Lingzhi in China, is a well-known medicinal fungus in traditional Chinese medicine. It was used for health-improvement and anti-aging purposes in China and other Asian regions for over 2000 years. *G. lucidum* is involved in clinical treatment of a wide range of diseases, such as chronic bronchitis, asthma, cardiovascular diseases, neurasthenia, chronic viral hepatitis, male sexual dysfunction, chemotherapy-induced toxicity, antitumor, etc. [1,2]. Triterpenoids and polysaccharide are two main types of components in *G. lucidum* and play important roles in its pharmacological effects. Up to now, more than 135 triterpenoids have been isolated from fruiting bodies, spores and mycelia [1,3], some of which are accounted for anticancer [4,5], anti-HIV-1 [6,7], anti-inflammatory [8], antioxidative [9] and immunoregulatory [10], anti-androgenic [11], neurotrophic [12] and cytotoxic [13] properties. Additionally, total triterpenoids isolated from *G. lucidum* showed powerful protective effects against liver damage in our previous study [14]. Therefore, the triterpenoids in *G. lucidum* were proved for potential medicinal values and have been regarded as important marker

components in quality evaluation of *G. lucidum* and related species [15] and differentiation between species under *Ganoderma* genus [16]. However, studies on metabolism of triterpenoids in *G. lucidum* *in vivo* were rare. We have previously reported the identification of ganoderic acids in rat plasma after oral administration of total triterpenoids of *G. lucidum* [17]. Other researches mainly focused on the determination of major triterpenoids in rat plasma and urine after oral administration of *G. lucidum* extraction [18,19] and pharmacokinetics of the single triterpenoids, ganoderic acid A, ganoderic acid T and ganoderiol F [20–22] in rat plasma.

In this study, the rat bile after oral administration of total triterpenoids of *G. lucidum* (TTGL) was analyzed by HPLC–DAD–ESI–MSⁿ and LC–ESI–IT–TOF/MS. Major triterpenoids in rat bile were identified or tentatively characterized on the basis of mass fragmentation pathways of triterpenoids in *G. lucidum* reported in literature [23,24] and confirmed in our experiments. This study will help us to understand the excretion of major triterpenoids of *G. lucidum* in bile after oral administration of TTGL to rats.

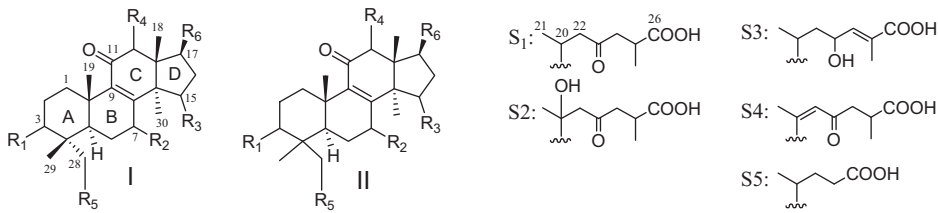
2. Materials and methods

2.1. Reagents and chemicals

Ganoderic acids C2 (**13**), C6 (**16**), G (**18**), B (**20**), A (**25**), E (**30**) and 7β, 12β-dihydroxy-3, 11, 15, 23-tetraoxo-lanost-8-en-26-oic acid

* Corresponding author. Tel.: +86 10 82802468; fax: +86 10 82802468.

E-mail address: cheqingming2008@sina.com (Q.-M. Che).



The figure shows two main triterpenoid skeletons, I and II, with various substituents labeled R₁ through R₆. To the right, five side chains are defined: S1 (21,22,26-trihydroxyheptanoic acid), S2 (21,22,26-trihydroxyheptanoic acid with a methyl group at C21), S3 (21,22,26-trihydroxyheptanoic acid with a methyl group at C22), S4 (21,22,26-trihydroxyheptanoic acid with a methyl group at C22 and a hydroxyl group at C21), and S5 (21,22,26-trihydroxyheptanoic acid with a methyl group at C21).

No.	Compound name	Type	R ₁	R ₂	R ₃	R ₄	R ₅	R ₆	MW
1	ganoderic acid C2 3- <i>O</i> -glucuronide	I	β-O-GlcA	β-OH	α-OH	H	H	S1	694
2	3,7,15-trihydroxy-4-(hydroxymethyl)-11,23-dioxo-lanost-8-en-26-oic acid	II	OH	OH	OH	H	OH	S1	534
3	ganoderic acid C2 7- <i>O</i> -glucuronide	I	β-OH	β-O-GlcA	α-OH	H	H	S1	694
4	lucidenic acid C	I	β-OH	β-OH	=O	β-OH	H	S5	476
5	lucidenic acid H	I	β-OH	β-OH	=O	H	OH	S5	476
6	12-hydroxyganoderic acid C2	I	β-OH	β-OH	α-OH	OH	H	S1	534
7	ganoderic acid C2 15- <i>O</i> -glucuronide	I	β-OH	β-OH	α-O-GlcA	H	H	S1	694
8	3,7,12-trihydroxy-4-(hydroxymethyl)-11,15,23-trioxo-lanost-8-en-26-oic acid	II	OH	OH	=O	OH	OH	S1	548
9	7,12,15-trihydroxy-4,4,14-trimethyl-3,11-dioxo-chole-8-en-24-oic acid	I	=O	OH	OH	OH	H	S5	476
10	ganoderic acid η	I	β-OH	β-OH	=O	β-OH	H	S3	532
11	3,12,15-trihydroxy-11,23-dioxo-lanost-8-en-26-oic acid	I	OH	H	OH	OH	H	S1	518
12	3,7,15-trihydroxy-4,4,14-trimethyl-11-oxo-chole-8-en-24-oic acid	I	OH	OH	OH	H	H	S5	462
13	ganoderic acid C2	I	β-OH	β-OH	α-OH	H	H	S1	518
14	ganoderic acid L	I	β-OH	β-OH	α-OH	H	H	S2	534
15	lucidenic acid N	I	β-OH	β-OH	=O	H	H	S5	460
16	ganoderic acid C6	I	β-OH	=O	=O	β-OH	H	S1	530
17	3β-hydroxy-4,4,14-trimethyl-7,11,15-trioxo-chole-8-en-24-oic acid	I	β-OH	=O	=O	H	H	S5	458
18	ganoderic acid G	I	β-OH	β-OH	=O	β-OH	H	S1	532
19	ganoderenic acid B	I	β-OH	β-OH	=O	H	H	S4	514
20	ganoderic acid B	I	β-OH	β-OH	=O	H	H	S1	516
21	ganoderic acid AM1	I	β-OH	=O	=O	H	H	S1	514
22	ganoderic acid K	I	β-OH	β-OH	=O	β-OAc	H	S1	574
23	7,15-dihydroxy-4,4,14-trimethyl-3,11-dioxo-chole-8-en-24-oic acid	I	=O	OH	OH	H	H	S5	460
24	ganoderic acid H	I	β-OH	=O	=O	β-OAc	H	S1	572
25	ganoderic acid A	I	=O	β-OH	α-OH	H	H	S1	516
26	ganolucidic acid A	I	=O	H	α-OH	H	H	S1	500
27	7β,12β-dihydroxy-3,11,15,23-tetraoxo-lanost-8-en-26-oic acid	I	=O	β-OH	=O	β-OH	H	S1	530
28	lucidenic acid A	I	=O	β-OH	=O	H	H	S5	458
29	ganoderic acid D	I	=O	β-OH	=O	H	H	S1	514
30	ganoderic acid E	I	=O	=O	=O	H	H	S1	512
31	12-acetoxylanoderic acid F	I	=O	=O	=O	β-OAc	H	S1	570

Fig. 1. Possible chemical structures of triterpenoids identified from rat bile after oral administration of TTGL and TTGL.

(27) (see their structures in Fig. 1) were isolated by the authors from *G. lucidum* and identified by comparing their spectral data (UV, IR, MS and NMR) with those reported before [25–29]. The purities of them were over 95% by HPLC analysis. Acetonitrile, methanol (Fisher Scientific, Fairlawn, NJ, USA) and formic acid (J.T. Baker, Philipsburg, NJ, USA) were of HPLC grade. De-ionized water was prepared by a Milli-Q system (Millipore, Bedford, MA, USA). Chloroform, dichloromethane, ethyl acetate, ether, 95% ethanol, hydrochloric acid (HCl) and sodium hydrogen carbonate (NaHCO₃) were of analytical reagent grade and purchased from Beijing Chemical Corp. (Beijing, China). Phenomenex Strata C18-E solid-phase

extraction cartridge (200 mg/3 ml, 55 μm, 70 Å) was purchased from Phenomenex (Torrance, CA, USA).

2.2. Preparation of total triterpenoids of *G. lucidum*

G. lucidum was purchased from Guangxi province (China) in 2006 and identified by Professor Shaoqing Cai (Peking University, Beijing, China). Crude powder of *G. lucidum* (1.5 kg) was extracted with 95% ethanol (10.51 × 4) under reflux for four times, 1.5 h for each time. The extract was concentrated in vacuum to afford a dark-brown residue which was extracted with chloroform by

Table 1The compounds identified from rat bile after oral administration of TTGL and TTGL by HPLC-DAD–ESI-MSⁿ and LC–ESI-IT-TOF/MS.

No.	Rt (min)	Identification	UV λ_{\max} (nm)	Formula	[M–H] [–] (m/z)			Fragment ions (m/z)	Detected resource	
					Measured	Predicted	Difference (ppm)		1	2
1 ^a	7.91	Ganoderic acid C2 3-O-glucuronide	249	C ₃₆ H ₅₄ O ₁₃	693.3494	693.3492	0.29	675.3422, 657.3169, 631.3447, 613.3325, 517.3261, 499.3065, 437.2947, 303.1975, 302.1853, 301.1839, 287.1594	+	–
2 ^a	8.96	3,7,15-Trihydroxy-4-(hydroxymethyl)-11,23-dioxo-lanost-8-en-26-oic acid	254	C ₃₀ H ₄₆ O ₈	533.3129	533.3120	1.69	515.2990, 497.2912, 453.2980, 423.2594, 319.1909, 318.1853, 317.1740, 303.1608, 195.1037	+	–
3 ^a	9.03	Ganoderic acid C2 7-O-glucuronide	250	C ₃₆ H ₅₄ O ₁₃	693.3503	693.3492	1.59	517.3180, 499.3009, 481.2920, 437.3009, 302.1953, 301.1741, 287.1858	+	–
4	11.83	Lucidenic acid C	254	C ₂₇ H ₄₀ O ₇	475.2707	475.2701	1.26	457.2565, 445.2062, 439.2470, 427.2505, 413.2560, 409.2458, 401.2345, 319.1887, 305.1792, 303.1915, 275.1646, 265.1477	+	+
5	12.68	Lucidenic acid H	254	C ₂₇ H ₄₀ O ₇	475.2697	457.2701	–0.84	457.2611, 445.2239, 439.2478, 427.2617, 413.2727, 401.2339, 319.1924, 305.1741, 303.1603, 275.1617, 265.1428, 235.1342	+	+
6	12.95	12-Hydroxyganoderic acid C2	255	C ₃₀ H ₄₆ O ₈	533.3166	533.3120	–0.75	515.3010, 497.2874, 485.2887, 467.2832, 453.3009, 449.2685, 423.2774, 405.2770, 319.1882, 318.1816, 317.1742, 303.1597, 289.1785, 195.1041	+	+
7 ^a	13.23	Ganoderic acid C2 15-O-glucuronide	254	C ₃₆ H ₅₄ O ₁₃	693.3479	693.3492	–1.87	675.3268, 517.3115, 499.2968, 455.3323, 437.3100, 303.2080, 302.1948, 301.1772, 249.1436	+	–
8 ^a	13.48	3,7,12-Trihydroxy-4-(hydroxymethyl)-11,15,23-trioxo-lanost-8-en-26-oic acid	253	C ₃₀ H ₄₄ O ₉	547.2894	547.2913	–3.47	529.1799, 511.2792, 485.2897, 470.2637, 467.2786, 335.1866, 319.1867, 317.1738, 281.1406, 263.1286, 205.1246	+	–
9 ^a	13.69	7,12,15-Trihydroxy-4,4,14-trimethyl-3,11-dioxo-chol-8-en-24-oic acid	248	C ₂₇ H ₄₀ O ₇	475.2688	475.2701	–2.74	445.2571, 439.2526, 409.2429, 315.1615, 301.1423, 299.1558	+	–
10	14.91	Ganoderic acid η	255	C ₃₀ H ₄₄ O ₈	531.2949	531.2963	–2.64	513.2853, 469.2917, 451.2869, 439.2526, 421.2437, 319.1863, 303.1585, 301.1812, 265.1433	+	+
11 ^a	17.01	3,12,15-Trihydroxy-11,23-dioxo-lanost-8-en-26-oic acid	258	C ₃₀ H ₄₆ O ₇	517.3161	517.3171	–1.93	499.3056, 455.3177, 425.3053, 305.2116, 303.1967, 285.1864, 255.1776	+	+
12	17.83	3,7,15-Trihydroxy-4,4,14-trimethyl-11-oxo-chol-8-en-24-oic acid	252	C ₂₇ H ₄₂ O ₆	461.2886	461.2909	–4.99	443.2746, 425.2728, 417.2988, 399.2851, 303.1954, 302.1889, 301.1776, 287.1632, 269.0989, 217.0779	+	+
13 ^b	18.84	Ganoderic acid C2	256	C ₃₀ H ₄₆ O ₇	517.3152	517.3171	–3.67	499.3063, 481.2958, 455.3177, 437.3030, 407.2592, 304.1990, 303.1956, 302.1845, 301.1783, 287.1625, 195.1043, 179.1132	+	+
14	19.59	Ganoderic acid L	257	C ₃₀ H ₄₆ O ₈	533.3105	533.3120	–2.80	515.2994, 497.2959, 453.2920, 304.1990, 303.1940, 288.1697, 193.0859	+	–
15	20.60	Lucidenic acid N	256	C ₂₇ H ₄₀ O ₆	459.2746	459.2752	–1.31	441.2659, 423.2520, 397.2714, 379.2645, 303.1968, 259.1696, 249.1496	+	+
16 ^b	20.68	Ganoderic acid C6	256	C ₃₀ H ₄₂ O ₈	529.2802	529.2807	–0.94	511.2670, 493.2590, 481.2164, 467.2788, 449.2645, 437.2364, 317.1724, 303.1524, 301.1744	+	+
17	21.16	3 β -Hydroxy-4,4,14-trimethyl-7,11,15-trioxo-chol-8-en-24-oic acid	253	C ₂₇ H ₃₈ O ₆	457.2600	457.2596	0.87	439.2474, 413.2681, 397.2389, 385.2368, 353.245, 249.1483	+	+

Table 1 (Continued)

No.	Rt (min)	Identification	UV λ_{\max} (nm)	Formula	[M–H] [−] (m/z)			Fragment ions (m/z)	Detected resource	
					Measured	Predicated	Difference (ppm)		1	2
18 ^b	21.63	Ganoderic acid G	254	C ₃₀ H ₄₄ O ₈	531.2955	531.2963	−1.51	513.2840, 469.2975, 454.2723, 451.2850, 436.2631, 319.1901, 303.1971, 265.1428, 249.1506	+	+
19	22.03	Ganoderenic acid B	249	C ₃₀ H ₄₂ O ₇	513.2861	513.2858	0.58	495.2729, 480.2434, 451.2809, 436.2578, 433.2777, 331.1891, 303.1959, 287.1949, 285.1869, 263.1648, 249.1494, 191.1113	+	+
20 ^b	22.82	Ganoderic acid B	253	C ₃₀ H ₄₄ O ₇	515.3008	515.3014	−1.16	497.2907, 453.3002, 438.2734, 435.2941, 420.2643, 409.3122, 304.1972, 303.1953, 302.1855, 287.1664, 263.1661, 249.1494, 195.1410	+	+
21	23.14	Ganoderic acid AM1	263	C ₃₀ H ₄₂ O ₇	513.2850	513.2858	−1.56	495.2744, 451.2838, 436.2611, 302.1861, 249.1467	–	+
22	23.79	Ganoderic acid K	254	C ₃₂ H ₄₆ O ₉	573.3065	573.3069	−0.70	555.2950, 511.3031, 469.2900, 451.2840, 303.1948, 302.1874, 301.1795, 265.1418	+	+
23	24.37	7,15-Dihydroxy-4,4,14-trimethyl-3,11-dioxo-cholestan-24-oic acid	248	C ₂₇ H ₄₀ O ₆	459.2746	459.2752	−1.31	441.2641, 423.2498, 397.2694, 301.1765, 300.1701, 299.1625, 285.1475	+	+
24	24.93	Ganoderic acid H	254	C ₃₂ H ₄₄ O ₉	571.2895	571.2913	−3.15	553.2819, 511.2693, 509.2884, 467.2796, 437.2342, 423.2855, 317.1729, 303.1594, 302.1813, 301.1783	+	+
25 ^b	25.28	Ganoderic acid A	253	C ₃₀ H ₄₄ O ₇	515.3013	515.3014	−0.19	497.2895, 479.2811, 453.3008, 435.2889, 405.2412, 302.1810, 301.1774, 300.1717, 299.1627, 285.1478, 195.1036	+	+
26 ^b	25.87	Ganolucidic acid A	245	C ₃₀ H ₄₄ O ₆	499.3051	499.3065	−2.80	481.2949, 437.3038, 419.3017, 287.1988, 285.1857, 269.1610	+	+
27 ^b	27.22	7 β ,12 β -Dihydroxy-3,11,15,23-tetraoxo-lanost-8-en-26-oic acid	244	C ₃₀ H ₄₂ O ₈	529.2795	529.2807	−2.27	511.2710, 467.2790, 452.2550, 449.2662, 434.2450, 317.1727, 301.1713, 299.1620, 285.1474, 263.1295, 249.1501	+	+
28	27.34	Lucidenic acid A	244	C ₂₇ H ₃₈ O ₆	457.2598	457.2596	0.44	439.2445, 421.2404, 395.2570, 301.1756, 287.1633, 285.1839, 261.1484, 257.1544, 247.1324, 193.1228	+	+
29	28.72	Ganoderic acid D	253	C ₃₀ H ₄₂ O ₇	513.2856	513.2858	−0.39	495.2747, 451.2848, 433.2716, 421.2243, 415.2602, 301.1786, 285.1491, 283.1680, 247.1347, 193.1305	+	+
30 ^b	29.90	Ganoderic acid E	254	C ₃₀ H ₄₀ O ₇	511.2686	511.2701	−2.93	493.2533, 449.2710, 434.2365, 300.1765, 247.1338	–	+
31	31.63	12-Acetoxyganoderic acid F	250	C ₃₂ H ₄₂ O ₉	569.2764	569.2756	1.41	551.2637, 509.2523, 479.2083, 465.2608, 435.2216, 299.1611	+	+

^a Reported for the first time.

^b Confirmed by comparing with authentic compounds: 1, rat bile after oral administration of TTGL; 2, TTGL; +, detected; –, not detected.

ultrasonic extraction method. The chloroform extract was concentrated to 500 ml and extracted with the same volume of saturated aqueous solution of NaHCO₃ for four times. The NaHCO₃ aqueous solution was acidified with HCl (6 M) to pH 3–4 and filtered. The obtained precipitate was dissolved in chloroform and then was evaporated in vacuum to yield the powder of total triterpenoids (200 g). The TTGL extract was mainly composed of ganoderic acids C2, C6, G, B, A, E and 7 β , 12 β -dihydroxy-3, 11, 15, 23-tetraoxo-lanost-8-en-26-oic acid, which were confirmed by comparing their HPLC-DAD and ESI-MSⁿ data with those of the authentic compounds. The TTGL extract was dissolved in 80% aqueous acetonitrile solution (v/v) and filtered through a 0.22 μ m membrane filter unit to obtain a TTGL sample (3.2 mg/ml) for LC–MS analyses.

2.3. Animals experiment

Animal experiments adhered to the National Institutes of Health Guide for the Care and Use of Laboratory Animals (Institute of Laboratory Animal Resources, 1996) and were approved by the Institutional Animal Care and Use Committee of Peking University. Six male Sprague–Dawley rats (180–200 g) were purchased from the Department of Laboratory Animal Science of Peking University Healthy Science Center and kept in an environmentally controlled room at 22–24 °C and 55–60% humidity for three days. The rats were fasted for 12 h with free access to water prior to the experiments. They were anesthetized with ether, and then fixed on wooden plates. An abdominal incision was made and common bile duct was cannulated with PE-10 tubing for collection of bile

samples, and closed by suture. Control bile was collected before treatment. When the treatment rat regained consciousness, a TTGL extract suspended in 2 ml of 6% carboxymethyl cellulose sodium (CMC-Na) aqueous solution at the dose of 800 mg/kg body weight was administered by oral gavage, and bile was collected at 0–2, 2–4, 4–8 and 8–12 h after oral administration. Approximately 2 ml of bile sample was continuously collected from each interval and stored at -20°C until sample preparation and analysis. During the experiment, the rats were fixed on wooden plates and allowed for free access to water.

2.4. Rat bile sample preparation

A solid-phase extraction (SPE) method was used for sample pretreatment. Before applied to bile sample, a SPE cartridge was treated with 2 ml of water, 2 ml of methanol and 2 ml of water, successively. A 0.5 ml of bile sample was vortexed, loaded, and allowed to flow through the SPE cartridge with gravity. The SPE cartridge was washed with 2 ml of water and 3 ml of methanol, successively. The methanol eluate was collected and evaporated to about 1 ml under a stream of N_2 at room temperature. The concentrated sample was filtered through a $0.22\ \mu\text{m}$ membrane filter unit before analysis.

2.5. HPLC-DAD-ESI-MSⁿ analysis

HPLC-DAD-ESI-MSⁿ analysis was performed on an Agilent 1100 series HPLC system (Agilent Technologies, Waldbronn, Germany) coupled with a Finnigan LCQ Advantage ion trap mass spectrometer (ThermoFinnigan, San Jose, CA, USA) via an electrospray ionization (ESI) interface. The HPLC system was equipped with a quaternary pump, a diode-array detector (DAD), an autosampler and a column compartment. The chromatographic separation was achieved on a Phenomenex Gemini 5 μm C18 110A column (250 mm \times 4.6 mm i.d., 5 μm , Phenomenex, Torrance, CA, USA) with a Phenomenex SecurityGuard guard cartridge (C18, 4 mm \times 2 mm i.d., Phenomenex, Torrance, CA, USA) at 30°C and a flow rate of 1 ml/min. A linear gradient elution of solvent acetonitrile (A) and water containing 0.2% formic acid (B, v/v) was applied with the following program: 0–8 min, 28–29% A; 8–25 min, 29–45% A; 25–35 min, 45% A; 35–40 min, 45–50% A. The spectral data was collected from 200 to 400 nm, and a representative chromatogram was recorded at 254 nm. The injection volume of all the tested samples was 10 μl . The HPLC effluent was directed into the mass spectrometer from 5 min to 40 min for each sample. The eluent flow was roughly split as 5:1 before entering the ESI ion source. Ultrahigh-purity helium (He) was used as the collision gas and high purity nitrogen (N_2) as the nebulizing gas. The optimized parameters in negative mode were as follows: source voltage, 4.5 kV; sheath gas (N_2), 50 arbitrary units; auxiliary gas (N_2), 10 units; capillary temperature, 350°C ; capillary voltage, -15V ; tube lens offset voltage, -60V . The spectra were recorded in the range m/z 200–1100 for full scan MS analysis. The isolation width of precursor ions was 3.0 Da. The data-dependent acquisition was used so that the most abundant ions in each scan could be selected and subjected to tandem mass spectrometry (MSⁿ, $n = 2-4$) analyses. The collision energy for MSⁿ experiments was 40%. The HPLC-DAD-ESI-MSⁿ system was controlled by XcaliburTM 1.4 software.

2.6. LC-ESI-IT-TOF/MS analysis

To confirm the elemental composition of fragment ions with high-accurate mass, an LC-ESI-IT-TOF/MS experiment was performed on a Shimadzu LCMS-IT-TOF instrument equipped with a Shimadzu Prominence HPLC system (Shimadzu, Kyoto, Japan). The HPLC system consisted of a CBM-20A controller, two LC-20AD

binary pumps, an SPD-M20A diode array detector, an SIL-20AC autosampler, a CTO-20A column oven and a DGU-20A5 degasser. The HPLC conditions were the same as those for HPLC-DAD-ESI-MSⁿ analysis except that the autosampler tray temperature was set at 15°C . The LCMS-IT-TOF instrument was equipped with an ESI source. The HPLC effluent was directed into the mass spectrometer from 3 min to 40 min for each sample. The eluent flow was roughly split as 5:1 before entering the ESI source. The optimized MS conditions were as follows: negative ion mode; electrospray voltage, -3.5 kV ; detector voltage, 1.7 kV ; curved desolvation line (CDL) temperature, 200°C ; heat block temperature, 200°C ; nebulizing gas (N_2), 1.5 l/min; drying gas (N_2) pressure, 100 kPa; scan range, m/z 100–1000 for MS¹, 100–800 for MS² and 100–800 for MS³. The ultrahigh purity argon was used as the collision gas for collision-induced dissociation (CID) experiments, and the collision energy was set at 50% for MS² and MS³; TOF region pressure, $1.4 \times 10^{-4}\text{ Pa}$; ion trap pressure, $1.8 \times 10^{-2}\text{ Pa}$; ion accumulated time, 30 ms; precursor ion selected width, 3.0 Da. The MSⁿ data were collected in an automatic mode and the software could automatically select precursor ions for MSⁿ analysis according to criteria settings. Accurate mass determination was corrected by calibration using the sodium trifluoroacetate clusters as reference. The data acquisition and analysis were performed by LCMS Solution Version 3 software (Shimadzu, Kyoto, Japan). The formula predictor function of LCMS Solution was used to predict chemical formulas.

3. Results and discussion

3.1. Sample preparation

In this study, solid-phase extraction (SPE) and liquid-liquid extraction (LLE) methods were compared in order to purify triterpenoids and eliminate the endogenous substance from rat bile samples. In LLE method, dichloromethane, dichloromethane-ethyl acetate (9:1, 1:1, v/v) and ethyl acetate (4 ml) were used to extract rat bile samples (0.5 ml). In SPE experiment, the Phenomenex Strata C18-E solid-phase extraction cartridge (200 mg/3 ml, 55 μm , 70 A) was chosen. The rat bile samples (0.5 ml) were loaded to SPE cartridges, and firstly eluted with H_2O and 10% methanol (v/v), respectively. In terms of the second eluent, 3, 4 and 5 ml of methanol were compared. All the extracts and eluates were dried under N_2 at room temperature and dissolved in 0.5 μl of 80% aqueous acetonitrile solution (v/v). The injection volume was 10 μl for HPLC analyses. For SPE method, a few triterpenoids in rat bile sample could be eluted by 10% methanol and the volumes of methanol had no significant influence on elution of major constituents in rat bile. Although the extraction efficiency of major triterpenoids in rat bile for LLE and SPE methods had no significant difference (Fig. 1S and Table 1S), the elimination effect on endogenous substances for SPE method was obvious by HPLC-DAD analyses. Therefore, SPE was finally selected to prepare rat bile samples and 2 ml of H_2O and 3 ml of methanol were used as the first and second eluents, successively.

3.2. Mass spectrometric analyses of authentic triterpenoids

In HPLC-DAD-ESI-MSⁿ experiment, major characteristic fragmentation pathways of triterpenoids in *G. lucidum* were neutral losses of H_2O and CO_2 as well as significant fragment ions of a, b, c and d resulted from the cleavages of C- and D-rings, respectively (Fig. 4), which are in accordance with the literature [23]. Ganoderic acids C2 and A which possessed the structures of 7, 15-dihydroxy groups could give the most prominent ions of $[\text{M}-\text{H}]^-$ in their full scan mass spectra. In corresponding MS² spectra, the neutral loss of H_2O could generate the most prominent ions of $[\text{M}-\text{H}-\text{H}_2\text{O}]^-$ and

a group of b , $b-1$, $b-2$ and $b-H-CH_3$ ions due to D-ring cleavage. The sequential losses of H_2O and CO_2 from ions of $[M-H-H_2O]^-$ produced the most prominent ions of $[M-H-H_2O-H_2O-CO_2]^-$ in further MS^3 spectra. Ganoderic acids G, B and 7β , 12β -dihydroxy-3, 11, 15, 23-tetraoxo-lanost-8-en-26-oic acid, as the 7-hydroxy-15-oxo derivatives, gave the most prominent ions of $[M-H-H_2O]^-$ in their full scan mass spectra, which generated the most prominent ions of $[M-H-H_2O-CO_2]^-$ and dominant ions as well as a group of b , $b+2-H_2O$ and $b-H_2O$ ions. In MS^3 spectra of $[M-H-H_2O-CO_2]^-$ ions, C-ring cleavage generated the most prominent ions. Ganoderic acid E possessed the structure of 7, 15-dioxo groups and gave the most prominent ion of $[M-H]^-$. In corresponding MS^2 spectra, the neutral losses of H_2O and CO_2 generated the most prominent ion of $[M-H-H_2O-CO_2]^-$ as well as minor ions of $b+1$ and $a+2$. The 12-hydroxy-7, 15-dioxo derivative, ganoderic acid C6 gave the prominent ion of $[M-H-H_2O]^-$, which generated the most prominent ion of $[M-H-H_2O-CO_2]^-$ and a group of b , $b+2-H-CH_3$ and $b+2-H_2O$ ions due to D-ring cleavage in MS^2 spectrum. Furthermore, accurate masses of major fragment ions of authentic triterpenoids were obtained by LC-ESI-IT-TOF/MS analysis, which proved their proposed fragmentation pathways and contributed to structural identification of the triterpenoids in rat bile. The formulas, observed and predicted masses, and mass errors of fragment ions in LC-ESI-IT-TOF/MS spectra of representative authentic compounds are shown in Table 2S.

3.3. Identification of triterpenoids from rat bile

By comparing the UV spectra and chromatograms of rat bile sample after oral administration of TTGL with those of the blank, mixed authentic compounds and TTGL samples, a total of 31 compounds were identified or tentatively characterized from all the tested samples. The chromatographic and mass spectrometric data of all the compounds are shown in Tables 1 and 3S, and their structures are shown in Fig. 1. The total ion chromatograms (TICs) of the tested samples and extracted ion chromatograms (EICs) of major triterpenoids in rat bile are shown in Figs. 2 and 3, respectively. All compounds (1–31) displayed a characteristic maximum absorption at 244–258 nm in UV spectra due to the $\Delta^{8,9}$ and 11-oxo groups of triterpenoids in *G. lucidum*. Among them, 7 compounds (13, 16, 18, 20, 25, 30 and 27) were unambiguously identified as ganoderic acids C2, C6, G, B, A, E and 7β , 12β -dihydroxy-3, 11, 15, 23-tetraoxo-lanost-8-en-26-oic acid based on the direct comparisons of their retention times, UV spectra and mass spectra with those of the authentic compounds. Furthermore, 24 compounds were tentatively characterized according to the mass spectrum fragmentation pathways of triterpenoids in *G. lucidum* reported in the literature [23,24] and acquired in our experiment. Most of the detected compounds were ganoderic acids and lucidenic acids (Fig. 4).

3.3.1. Identification of 7, 15-dihydroxy derivatives of ganoderic acids

The LC-IT-TOF/MS spectra of compounds 1, 3 and 7 showed $[M-H]^-$ ions at 693.3494, 693.3503 and 693.3479, respectively, which were calculated as $C_{36}H_{54}O_{13}$ by the Formula Predictor software. As shown in Table 3S, the neutral losses of 176 Da from their ions at m/z 693 $[M-H]^-$ produced abundant $[M-H-GlcA]^-$ ions at m/z 517 (Fig. 2S(A) and (C)) and other major fragment ions were very similar with those of ganoderic acid C2 (13), suggesting they were monoglucuronides of ganoderic acid C2 and the glucuronic acid moiety could be in conjunction with 3-, 7- or 15-OH, respectively. The glucuronic acid moiety in the structure of ganoderic acid C2 15-O-glucuronide could be form stronger intramolecular hydrogen bonds with 25-COOH and 7-OH than hydrogen bonds formed between glucuronic acid moiety

and 15-OH in the structure of ganoderic acid C2 7-O-glucuronide, which would lower the polarities of them than that of ganoderic acid C2 3-O-glucuronide and extend their retention times on reversed-phase chromatography. Therefore, compounds 1, 3 and 7 were tentatively characterized as ganoderic acid C2 3-O-glucuronide, ganoderic acid C2 7-O-glucuronide and ganoderic acid C2 15-O-glucuronide, respectively, which are reported for the first time.

Compounds 2, 6 and 14 gave the same $[M-H]^-$ ions at m/z 533, which produced the most prominent fragment ions at m/z 515 ($[M-H-H_2O]^-$) in their MS^2 spectra, suggesting the presence of an extra hydroxyl group in their structures than in the structure of ganoderic acid C2 (13). In MS^3 spectrum of compound 6, the neutral loss of 30 Da (CH_2O) from ions at m/z 515 and 497 yielded the dominant fragment ions at m/z 485 and 467 (Table 3S), respectively, indicating the presence of a hydroxyl group on C-12 [23]. The characteristic fragment ions of compound 6 were also detected in LC-IT-TOF/MS spectrum at m/z 485.2887 and 467.2832 (Table 1). Thus, compound 6 was identified as 12-hydroxyganoderic acid C2 [23]. Compound 2 produced similar fragment ions with those of compound 6 except the absence of ions at m/z 485 and 467 (Fig. 2S(B)), suggesting compound 2 lacked 12-OH. In its LC-IT-TOF/MS spectrum, the characteristic product ion at m/z 195.1037 ($d-H-H_2O$) (Table 1) indicated compound 2 possessed the same side chain as that of ganoderic acid C2 (13) (Table 2S). According to structural characteristics of triterpenoids in *G. lucidum* [3], compound 2 was proposed as 3, 7, 15-trihydroxy-4-(hydroxymethyl)-11, 23-dioxo-lanost-8-en-26-oic acid, which is a new compound. The proposed fragmentation pathways of compound 2 are shown in Fig. 5. Compound 14 showed fragment signals at m/z 304 ($b+1$), 303 (b) and 301 ($b-2$) in MS^3 spectrum, suggesting that it possessed the same structure of A-, B- and C-rings as that of ganoderic acid C2 (13). The LC-IT-TOF/MS spectrum showed characteristic fragment ion at m/z 193.0859 ($d-H-H_2O-H_2O$) (Table 1), indicating compound 14 possessed an extra hydroxyl group at the side chain on C-17. Therefore, compound 14 was inferred as 20-hydroxyganoderic acid C2, i.e. ganoderic acid L [30].

3.3.2. Identification of 7-hydroxy-15-oxo derivatives of ganoderic acids

Compound 8 and ganoderic acid G (18) gave the similar ESI- MS^n spectra except that the major fragment ions of compound 8 were 16 Da higher than those of ganoderic acid G (18) (Table 1). Particularly, in MS^3 spectrum of compound 8 (Fig. 2S(E)), the fragment ion at m/z 281 (a) indicated that an extra hydroxyl group existed on its A-, B-, or C-rings in comparison with ganoderic acid G (18). On the basis of literature [31], the extra hydroxyl group could be on C-28 or C-29. Thus, compound 8 was tentatively characterized as 3, 7, 12-trihydroxy-4-(hydroxymethyl)-11, 15, 23-trioxo-lanost-8-en-26-oic acid, which is reported for the first time. The proposed fragmentation pathways of compound 8 are shown in Fig. 6.

Compound 10, an isomers of ganoderic acid G (18), showed very similar ESI- MS^n spectra to those of ganoderic acid G (18) (Table 1). However, the retention time of compound 10 in reversed-phase chromatography was even shorter than that of ganoderic acid C2 (13). So we inferred that compound 10 and ganoderic acid G (18) only possessed different side chains on C-17. According to its HPLC behavior and MS^n data in the literature [32,16], compound 10 was inferred as ganoderic acid η .

Compound 22 gave its $[M-H-H_2O]^-$ ion at m/z 555 in full scan mass spectrum, which produced the most prominent ion at m/z 469 due to the neutral losses of CO_2 and CH_2CO . The MS^3 and MS^4 spectra of compound 22 showed similar signals to those of ganoderic acid G (18) (Table 3S). Thus, compound 22 was identified as ganoderic acid K [23], a 12-acetylated derivative of ganoderic acid G.

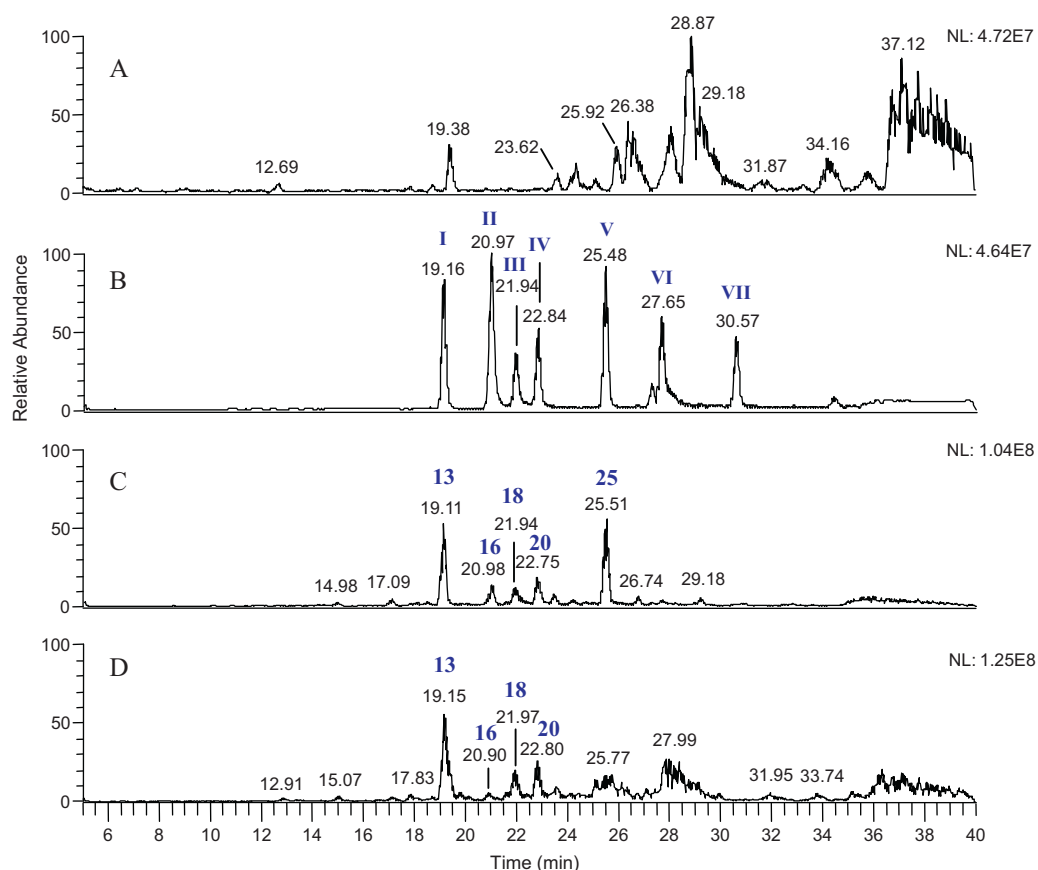


Fig. 2. Representative total ion chromatograms of blank bile (A), mixed authentic compounds (B), TTGL (C) and rat bile after oral administration of TTGL (D) by LC-DAD–ESI-MSⁿ: I, ganoderic acid C2; II, ganoderic acid C6; III, ganoderic acid G; IV, ganoderic acid B; V, ganoderic acid A; VI, 7 β , 12 β -dihydroxy-3, 11, 15, 23-tetraoxo-lanost-8-en-26-oic acid; VII, ganoderic acid E.

The major fragment ions of compound **29** were only 2 Da lower than those of ganoderic acid B (**20**) (Table 1). It indicated the C-3 of compound **29** was oxidized to be a carbonyl group. Thus, compound **29** was identified as ganoderic acid D [23].

3.3.3. Identification of other ganoderic acids

As shown in Table 1, the major fragment ions of compound **21** were only 2 Da higher than those of ganoderic acid E (**30**).

According to the ESI-MSⁿ data in the literature [23], compound **21** was identified as ganoderic acid AM1. Compound **24** showed the [M–H–H₂O][–] at *m/z* 553 in full scan mass spectrum and its corresponding MS² spectrum showed two dominant ion at *m/z* 511 ([M–H–H₂O–CH₂CO][–]) and 467 ([M–H–H₂O–CO₂–CH₂CO][–]) (Table 3S). The further MS³ spectrum of *m/z* 467 was the same with those of ganoderic acid C6 (**16**) (Table 3S). Thus, compound **24** was identified as ganoderic acid H, a 12-acetylated

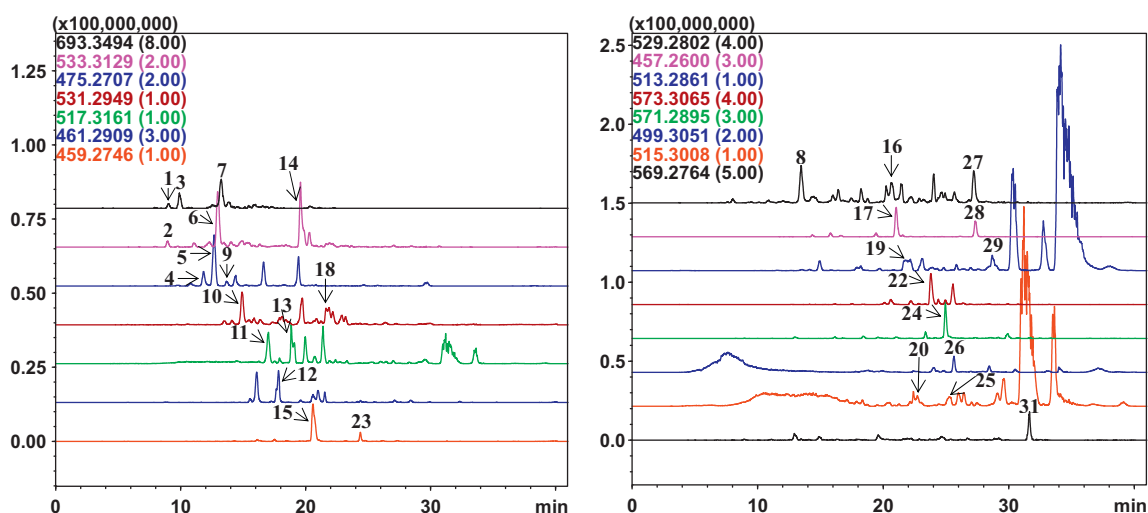


Fig. 3. Extracted ion chromatograms of triterpenoids in rat bile after oral administration of TTGL by LC-ESI-IT-TOF/MS.

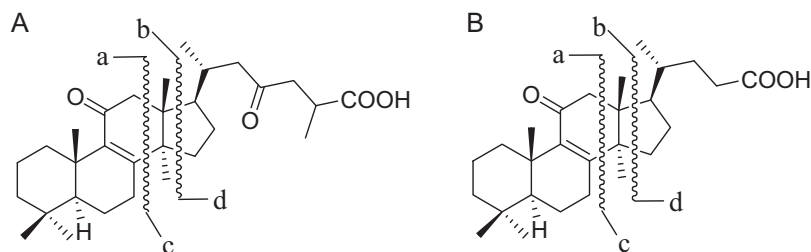


Fig. 4. Characteristic fragmentation pathways of ganoderic acids (A) and lucidenic acids (B).

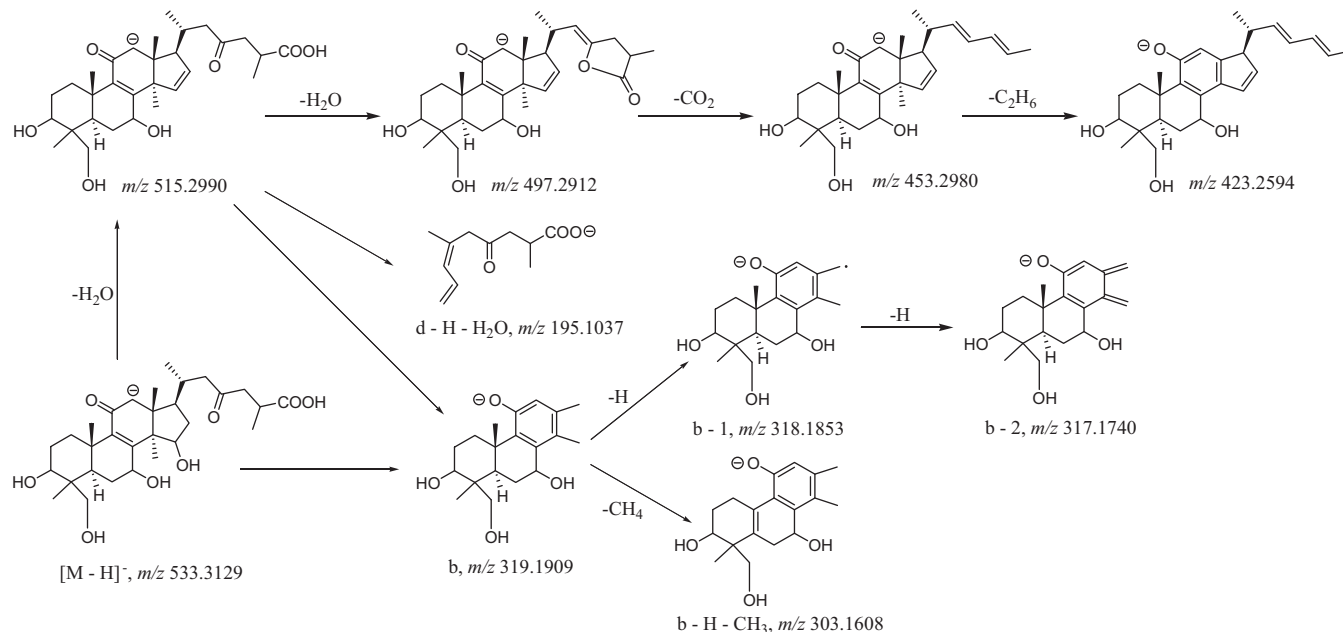


Fig. 5. Proposed fragmentation pathways of 3, 7, 15-trihydroxy-4-(hydroxymethyl)-11, 23-dioxo-lanost-8-en-26-oic acid (compound 2).

derivative of ganoderic acid C6 [23]. Compound **31** showed the [M-H-H₂O]⁻ at m/z 551 in full scan mass spectrum and its fragment ions in ESI-MSⁿ spectra were only 2 Da higher than those of compound **24** (Table 3S), suggesting that C-3 of compound **31** was oxidized to be a carboxyl group. Therefore, compound **31** was identified as 12-acetoxyganoderic acid F [23].

3.3.4. Identification of lucidenic acids

Compounds **4**, **5**, **9**, **12**, **15**, **17**, **23** and **28** possessed 27 carbon atoms in their elemental compositions calculated by the Formula Predictor software. Most of them gave the dominant ions of [M-H]⁻ in their full scan mass spectra, which produced prominent ions of [M-H-H₂O]⁻ and [M-H-H₂O-H₂O]⁻ in MS² and MS³ spectra in HPLC-ESI-MSⁿ analyses (compound **5** see Fig. 2S(D)), respectively.

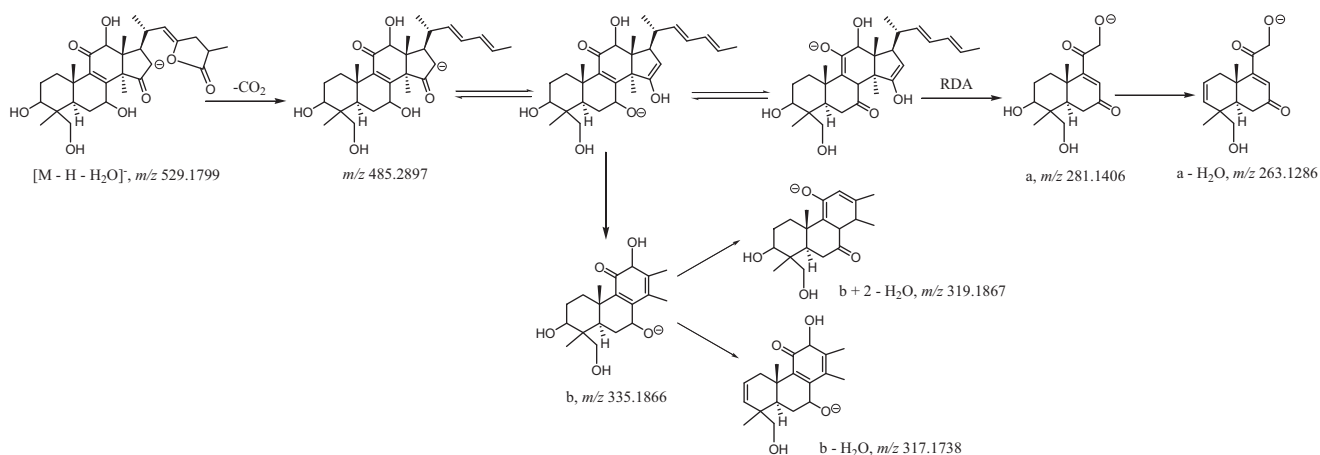


Fig. 6. Proposed fragmentation pathways of 3, 7, 12-trihydroxy-4-(hydroxymethyl)-11, 15, 23-trioxo-lanost-8-en-26-oic acid (compound 8).

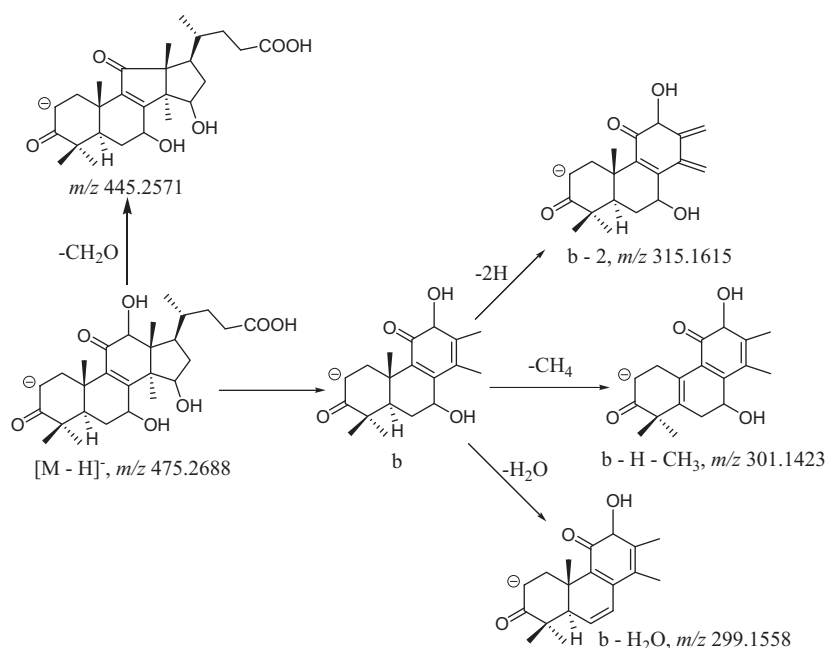


Fig. 7. Proposed fragmentation pathways of 7, 12, 15-trihydroxy-4, 4, 14-trimethyl-3, 11-dioxo-chol-8-en-24-oic acid (compound 9).

These fragmentation characteristics were attributed to the structures of lucidenic acids [23].

Compounds 4 and 5 gave the $[M-H]^-$ ions at m/z 475 in their full scan mass spectra. As shown in Table 3S, their characteristic fragment ions at m/z 319 (b), 303 ($b-H-CH_3$) and 265 (a) suggested they possessed the structures of 7-hydroxy-15-oxo groups and the amount of hydroxyl groups on A-, B- and C-rings were the same with those of ganoderic acid G (18). Furthermore, an extra fragment ion at m/z 235.1342 ($a-CH_2O$) (Table 1) was detected in LC-IT-TOF/MS spectrum of compound 5, which indicated a hydroxymethyl group could be on its A- or B-ring. According to the literature, compounds 4 and 5 were tentatively characterized as lucidenic acid C [33] and lucidenic acid H [34], respectively. Compound 9, an isomer of compounds 4 and 5, showed dominant fragment ions at m/z 445.2571 ($[M-H-CH_2O]^-$) and 301.1423

($b-H-CH_3$) in LC-IT-TOF/MS spectrum (Table 1), which possessed the similar characteristic fragmentation pathways (Fig. 7) to those of compound 6, a 7, 12, 15-trihydroxy derivative. Thus, compound 9 was inferred as 7, 12, 15-trihydroxy-4, 4, 14-trimethyl-3, 11-dioxo-chol-8-en-24-oic acid, a new compound.

Fragmentation behaviors of compounds 15, 17, 23 and 28 in HPLC-DAD-ESI-MSⁿ spectra were highly consistent with the previous report [23]. Therefore, compounds 15, 17, 23 and 28 were identified as lucidenic acid N, 3 β -hydroxy-4, 4, 14-trimethyl-7, 11, 15-trioxo-chol-8-en-24-oic acid, 7, 15-dihydroxy-4, 4, 14-trimethyl-3, 11-dioxo-chol-8-en-24-oic acid and lucidenic acid A, respectively, which were confirmed by their accurate masses in LC-IT-TOF/MS analyses (Table 1). The major fragment ions of compound 12 were only 2 Da higher than those of compound 15 (Table 1), suggesting that the C-15 of compound 12 might be substituted

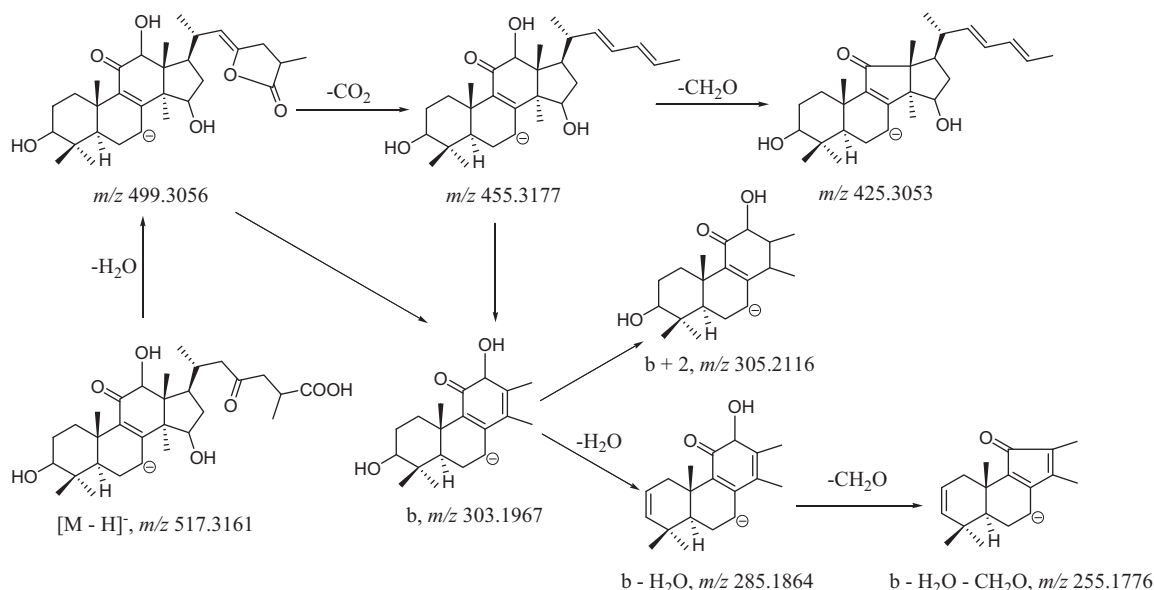


Fig. 8. Proposed fragmentation pathways of 3, 12, 15-trihydroxy-11, 23-dioxo-lanost-8-en-26-oic acid (compound 11).

with a hydroxyl group. Thus, compound **12** was identified as 3, 7, 15-trihydroxy-4, 4, 14-trimethyl-11-oxo-chole-8-en-24-oic acid [34].

3.3.5. Identification of other triterpenoids in rat bile

As shown in Table 3S, ESI-MSⁿ data of compound **26** was very similar to those of ganolucidic acid A in the literature [23]. The characteristic fragment ions at *m/z* 287.1988 (b+2), 285.1857 (b) and 269 (b–H–CH₃) in LC–IT–TOF/MS spectrum (Table 1) indicated that D-cleavage was its major fragmentation pathway. Thus, compound **26** was identified as ganolucidic acid A. Compound **11** was calculated as C₃₀H₄₆O₇ (*m/z* 517.3161) in LC–IT–TOF/MS analysis and an isomer of ganoderic acid C2 (**13**). The major fragment ions of compound **11** in LC–IT–TOF/MS spectrum (Table 1) were 18 Da higher than those of compound **26** except the presence of the characteristic fragment ions at *m/z* 425.3053 ([M–H–H₂O–CO₂–CH₂O][–]) and 255.1776 (b–H₂O–CH₂O), which indicated the existence of 12-OH in the structure of compound **11** (Fig. 8). Therefore, compound **11** was tentatively characterized as 3, 12, 15-trihydroxy-11, 23-dioxolanost-8-en-26-oic acid belonging to ganolucidic acids and is a new compound. Compound **19** gave [M–H–H₂O][–] at *m/z* 495, which was only 2 Da lower than that of ganoderic acid B (**20**). However, they possessed the same characteristic ions at *m/z* 303 (b), 287 (b+2–H₂O) and 249 (a) in ESI-MSⁿ spectra (Table 3S), suggesting they possessed the same A-, B- and C-rings. Therefore, we inferred that they possessed different side chains on C-17. According to the reported data, compound **19** were identified as ganoderic acid B [23].

3.4. Excretion of total triterpenoids of *G. lucidum* in rat bile

Among the 31 compounds, 29 compounds were detected and identified or tentatively characterized during the interval of 0–12 h in rat bile after oral administration of TTGL and 22 compounds were detected in TTGL extract. The majority of triterpenoids detected in TTGL extract could be excreted through rat bile. Seven compounds (**1–3**, **7–9** and **14**) were only detected in rat bile and might be the metabolites of triterpenoids in *G. lucidum*. Compounds **1**, **3** and **7**, as the monoglucuronide of ganoderic acid C2, might be phase II metabolites. The high-polarity triterpenoids in rat bile were more abundant than those in TTGL extract, which facilitated the excretion of triterpenoids in *G. lucidum* through bile.

4. Conclusions

By HPLC–DAD–ESI–MSⁿ and LC–ESI–IT–TOF/MS, a total of 31 triterpenoids were identified or tentatively characterized from rat bile after oral administration of TTGL and TTGL extract. The majority of triterpenoids detected in TTGL extract could be excreted through bile in the interval of 0–12 h after oral administration of TTGL to rats. Some of the triterpenoids in *G. lucidum* might be transformed to glucuronidated and hydroxylated metabolites in rats, which should be confirmed by further studies on the metabolites of single triterpenoids of *G. lucidum* in rats. It is the first report on excretion of total triterpenoids of *G. lucidum* in rat bile. Both methods and results of this study could be valuable for further metabolic and pharmacokinetic study of triterpenoids in *G. lucidum* in rats and humans.

Acknowledgements

This research was financially supported by the program of National Natural Science Foundation of China (No. 30701078). Authors thank Professor Shaoqing Cai (Peking University, Beijing, China) for the identification of *G. lucidum*. Thanks are also extended

to Xue Qiao (Peking University, Beijing, China) for HPLC–DAD–ESI–MSⁿ experiments and Dr. Jun Li for LC–IT–TOF/MS experiments.

Appendix A. Supplementary data

Supplementary data associated with this article can be found in the online version, at doi:10.1016/j.jpba.2012.01.030.

References

- [1] Z.B. Chen, Modern Research of *Ganoderma lucidum*, 2nd ed., Beijing Medical University Press, Beijing, 2001, pp. 219–304.
- [2] S.P. Wasser, Reishi or Ling Zhi (*Ganoderma lucidum*), Encyclopedia of Dietary Supplements, 604 pp., doi:10.1081/E-EDS-120022119.
- [3] J.L. Gao, Z.L. Yu, S.P. Li, Y.T. Wang, Research advance on triterpenoids of *Ganoderma lucidum*, Edible Fungi China 24 (2004) 6–11.
- [4] A. Thyagarajan, A. Jedinak, H. Nguyen, C. Terry, L.A. Baldrige, J.H. Jiang, D. Sliva, Triterpenes from *Ganoderma lucidum* induce autophagy in colon cancer through the inhibition of p38 mitogen-activated kinase (p38 MAPK), Nutr. Cancer 62 (2010) 630–640.
- [5] L.M.H. Trajkovic, S.A. Mijatovic, D.D. Maksimovic-Ivanic, I.D. Stojanovic, M.B. Momcilovic, S.J. Tufegdžic, V.M. Maksimovic, Z.S. Marjanovic, S.D. Stosic-Grujicic, Anticancer properties of *Ganoderma lucidum* methanol extracts in vitro and in vivo, Nutr. Cancer 61 (2009) 696–707.
- [6] B.S. Min, N. Nakamura, H. Miyashiro, K.W. Bae, M. Hattori, Triterpenes from the spores of *Ganoderma lucidum* and their inhibitory activity against HIV-1 protease, Chem. Pharm. Bull. 46 (1998) 1607–1612.
- [7] S. El-Mekkawy, M.R. Meselhy, N. Nakamura, Y. Tezuka, M. Hattori, N. Kakiuchi, K. Shimotohno, T. Kawahata, T. Otake, Anti-HIV-1 and anti-HIV-1-protease substances from *Ganoderma lucidum*, Phytochemistry 49 (1998) 1651–1657.
- [8] S. Dudhgaonkar, A. Thyagarajan, D. Sliva, Suppression of the inflammatory response by triterpenes isolated from the mushroom *Ganoderma lucidum*, Int. Immunopharmacol. 9 (2009) 1272–1280.
- [9] M. Zhu, Q. Chang, L.K. Wong, F.S. Chong, R.C. Li, Triterpene antioxidants from *Ganoderma lucidum*, Phytother. Res. 13 (1999) 529–531.
- [10] B.S. Min, J.J. Gao, M. Hattori, H.K. Lee, Y.H. Kim, Anticancer activity of triterpenoids from the spores of *Ganoderma lucidum*, Planta Med. 67 (2001) 811–814.
- [11] J. Liu, K. Shimizu, F. Konishi, K. Noda, S. Kumamoto, K. Kurashiki, R. Kondo, Anti-androgenic activities of the triterpenoids fraction of *Ganoderma lucidum*, Food Chem. 100 (2007) 1691–1696.
- [12] X.Q. Zhang, F.C. Ip, D.M. Zhang, L.X. Chen, W. Zhang, Y.L. Li, N.Y. Ip, W.C. Ye, Triterpenoids with neurotrophic activity from *Ganoderma lucidum*, Nat. Prod. Res. 25 (2011) 1607–1613.
- [13] C.R. Cheng, Q.X. Yue, Z.Y. Wu, X.Y. Song, S.J. Tao, Cytotoxic triterpenoids from *Ganoderma lucidum*, Phytochemistry 71 (2010) 1579–1585.
- [14] M.Y. Wang, Q. Liu, Q.M. Che, Z.B. Lin, Effects of triterpenoids from *Ganoderma lucidum* (Leyss. ex Fr.) Karst on three different experimental liver injury models in mice, Acta Pharm. Sin. 35 (2000) 326–329.
- [15] X.M. Wang, M. Yang, S.H. Guan, R.X. Liu, J.M. Xia, K.S. Bi, D.A. Guo, Quantitative determination of six major triterpenoids in *Ganoderma lucidum* and related species by high performance liquid chromatography, J. Pharm. Biomed. 41 (2006) 838–844.
- [16] C.M. Fu, G.H. Lu, O.J. Schmitz, Z.W. Li, K.S.Y. Leung, Improved chromatographic fingerprints for facile differentiation of two *Ganoderma* spp., Biomed. Chromatogr. 23 (2009) 280–288.
- [17] B.B. Xue, X.Y. Guo, Q.M. Che, Determination of ganoderic acids in rat plasma after oral administration of total triterpenoids from *Ganoderma lucidum*, J. Chin. Pharm. Sci. 17 (2008) 236–240.
- [18] X.M. Wang, R.X. Liu, J.H. Sun, S.H. Guan, M. Yang, K.S. Bi, D.A. Guo, HPLC method for the determination and pharmacokinetic studies of four triterpenoids in rat plasma after oral administration of *Ganoderma lucidum* extract, Biomed. Chromatogr. 21 (2007) 389–396.
- [19] X.M. Wang, S.H. Guan, R.X. Liu, J.H. Sun, Y. Liang, M. Yang, W. Wang, K.S. Bi, D.A. Guo, HPLC determination of four triterpenoids in rat urine after oral administration of total triterpenoids from *Ganoderma lucidum*, J. Pharm. Biomed. 43 (2007) 1185–1190.
- [20] J.J. Gao, B.S. Min, T. Akao, M.R. Meselhy, N. Nakamura, M. Hattori, Enzyme immunoassay for the quantitative determination of ganoderic acid A from *Ganoderma lucidum*, J. Tradit. Med. 18 (2001) 154–160.
- [21] X. Chen, S.L. Tao, F. Gao, Y.B. Li, J.J. Zhong, Quantitative determination of ganoderic acid T in rat plasma by a sensitive RP–HPLC method and its application in pharmacokinetic studies, J. Chin. Pharm. Sci. 19 (2010) 209–213.
- [22] Q. Zhang, F. Zuo, N. Nakamura, C.M. Ma, M. Hattori, Metabolism and pharmacokinetics in rats of ganoderic acid F, a highly cytotoxic and antitumor triterpene from *Ganoderma lucidum*, J. Nat. Med. 63 (2009) 304–310.
- [23] M. Yang, X.M. Wang, S.H. Guan, J.M. Xia, J.H. Sun, H. Guo, D.A. Guo, Analysis of triterpenoids in *Ganoderma lucidum* using liquid chromatography coupled with electrospray ionization mass spectrometry, J. Am. Soc. Mass Spectrom. 18 (2007) 927–939.
- [24] C.R. Cheng, M. Yang, Z.Y. Wu, Y. Wang, F. Zeng, W.Y. Wu, S.H. Guan, D.A. Guo, Fragmentation pathways of oxygenated tetracyclic triterpenoids and their application in the qualitative analysis of *Ganoderma lucidum* by

- multistage tandem mass spectrometry, *Rapid Commun. Mass Spectrom.* 25 (2011) 1323–1335.
- [25] X.Q. Zhang, Z.Q. Yin, W.C. Ye, S.X. Zhao, Chemical constituents from fruiting bodies of *Ganoderma lucidum*, *Chin. Tradit. Herb. Drugs* 36 (2005) 1601–1603.
- [26] T. Kikuchi, S. Kanomi, Y. Murai, S. Kadota, K. Tsubono, Z.I. Ogita, Constituents of the fungus *Ganoderma lucidum* (Fr.) Karst. II. Structures of ganoderic acids F, G, and H, lucidenic acids D2 and E2, and related compounds, *Chem. Pharm. Bull.* 34 (1986) 4018–4029.
- [27] Q.H. Pu, H. Chen, R.Y. Chen, Chemical constituents of *Ganoderma tsugae*, *Chin. Tradit. Herb. Drugs* 36 (2005) 502–504.
- [28] H. Kohda, W. Tokumoto, K. Sakamoto, M. Fujii, Y. Hirai, K. Yamasaki, Y. Komoda, H. Nakamura, S. Ishihara, M. Uchida, The biologically active constituents of *Ganoderma lucidum* (Fr.) Karst. Histamine release-inhibitory triterpenes, *Chem. Pharm. Bull.* 33 (1985) 1367–1374.
- [29] T. Kikuchi, S. Kanomi, S. Kadota, Y. Murai, K. Tsubono, Z.I. Ogita, Constituents of the fungus *Ganoderma lucidum* (Fr.) Karst. I. Structures of ganoderic acids C2, E, I, and K, lucidenic acids F and related compounds, *Chem. Pharm. Bull.* 34 (1986) 3695–3712.
- [30] T. Nishitoba, H. Sato, S. Sakamura, New terpenoids, ganolucidic acid D, ganoderic acid L, lucidone C and lucidenic acid G, from the fungus *Ganoderma lucidum*, *Agric. Biol. Chem.* 50 (1986) 809–811.
- [31] T. Nishitoba, H. Sato, S. Sakamura, New terpenoids, ganoderic acid J and ganolucidic acid C, from the fungus *Ganoderma lucidum*, *Agric. Biol. Chem.* 49 (1985) 3637–3638.
- [32] J.J. Gao, N. Nakamura, B.S. Min, A. Hirakawa, F. Zuo, M. Hattori, Quantitative determination of bitter principles in specimens of *Ganoderma lucidum* using high-performance liquid chromatography and its application to the evaluation of ganoderma products, *Chem. Pharm. Bull.* 52 (2004) 688–695.
- [33] T. Nishitoba, H. Sato, T. Kasai, H. Kawagishi, S. Sakamura, New bitter C₂₇ and C₃₀ terpenoids from the fungus *Ganoderma lucidum* (Reishi), *Agric. Biol. Chem.* 48 (1984) 2905–2907.
- [34] T. Nishitoba, H. Sato, S. Sakamura, Triterpenoids from the fungus *Ganoderma lucidum*, *Phytochemistry* 26 (1987) 1777–1784.



Interaction of antioxidant flavonoids with calf thymus DNA analyzed by spectroscopic and electrochemical methods

Ashwini H. Hegde, S.N. Prashanth, J. Seetharamappa*

Department of Chemistry, Karnatak University, Dharwad 580003, India

ARTICLE INFO

Article history:

Received 31 October 2011

Received in revised form 24 January 2012

Accepted 24 January 2012

Available online 2 February 2012

Keywords:

DNA double helix

Intercalation

Flavonoid

Spectroscopic methods

ABSTRACT

Mechanism of interaction of bioactive flavonoids, hesperitin (HES) and naringenin (NAR) with calf thymus deoxyribonucleic acid (DNA) was studied employing UV absorption, fluorescence, circular dichroism, melting temperature, fluorescence anisotropy and differential pulse voltammetric methods. The observed fluorescence quenching of DNA-ethidium bromide system by the flavonoid indicated the intercalative mode of binding between the flavonoid and DNA. Stern–Volmer plots have revealed the presence of static quenching mechanism. Binding and thermodynamic characteristics of interaction were evaluated. Melting temperature of DNA was found to be increased up to 5 °C in the presence of the flavonoid indicating the stabilization of DNA double helix upon binding. CD and fluorescence anisotropic results have revealed the conformational changes in DNA upon binding to the flavonoid. The observed positive shift in peak potential and decreased peak current of the flavonoid in the presence of DNA further supported the intercalative mode of binding.

© 2012 Elsevier B.V. All rights reserved.

1. Introduction

In vitro study of the interaction of many naturally occurring compounds with DNA adducts is an active area of research in chemistry and biology which leads to the understanding of drug–DNA interaction and the consequent design of new efficient drugs targeted to DNA [1,2]. Due to the central role of DNA in replication and transcription, DNA has been a major target for antibiotic, anti-cancer and antiviral drugs. Drugs bind to DNA in different ways. These include intercalation between adjacent base pairs, intrusion into the minor groove and major groove, and electrostatic interaction. Intercalation and minor-groove binding are the predominant DNA-binding modes of small ligands [3] while electrostatic interactions between the cationic species and negatively charged DNA phosphate backbone usually occur along the exterior of the helix.

The food diet comprising of micronutrients such as vitamins, carotenoids and flavonoids is essential for maintenance of human health. Flavonoids are easily found in citrus fruits, apples, olive oil, grapes, tea, red wine and other fruits and vegetables. The dietary flavonoids are gaining attention as potential protectors against a variety of human diseases, in particular age related diseases such as cardiovascular disease and cancer [4,5]. A large number of mechanisms of their actions have been attributed to the diverse functions of the flavonoids including antioxidant properties.

Among fruits, citrus varieties are important sources of polyphenolic compounds, which could be responsible for the health-promoting effects. The selected HES and NAR are the flavonones that belong to flavonoid class of compounds, found in citrus fruits. The structures of HES and NAR are shown in Fig. 1a and b.

Most of the ligand–nucleic acid binding studies are based on the quenching or enhancement of fluorescence of various flavonoids upon binding to nucleic acids [6–8]. These studies have revealed that the flavonoids could bind to DNA by groove binding or intercalation. Many chemical reagents of small molecular size have been used as sensitive probes of DNA when the ligands are non-fluorescent. For example, ethidium bromide (EB), a cationic, conjugated planar molecule (Fig. 1c) interacts strongly and specifically with double helical DNA was employed as a probe due to its striking fluorescence enhancement upon intercalation with DNA [9,10].

In the present study, we have investigated the interaction of two flavonoids (HES and NAR) with DNA using spectrophotometric, circular dichroism and voltammetric techniques. The spectroscopic methods are relatively sensitive compared to an electroanalytical technique like voltammetric method. It is not possible to study the thermodynamic parameters, number of binding ligands and conformational changes in DNA (upon binding to a ligand) by voltammetric methods. Further, the ligand is expected to be electroactive for voltammetric studies. Electrochemistry coupled with spectroscopy techniques could provide a relatively easy way to obtain useful insights into the molecular mechanism of drug–DNA

* Corresponding author. Tel.: +91 836 2215286/27; fax: +91 836 2747884.
E-mail address: jseetharam@yahoo.com (J. Seetharamappa).

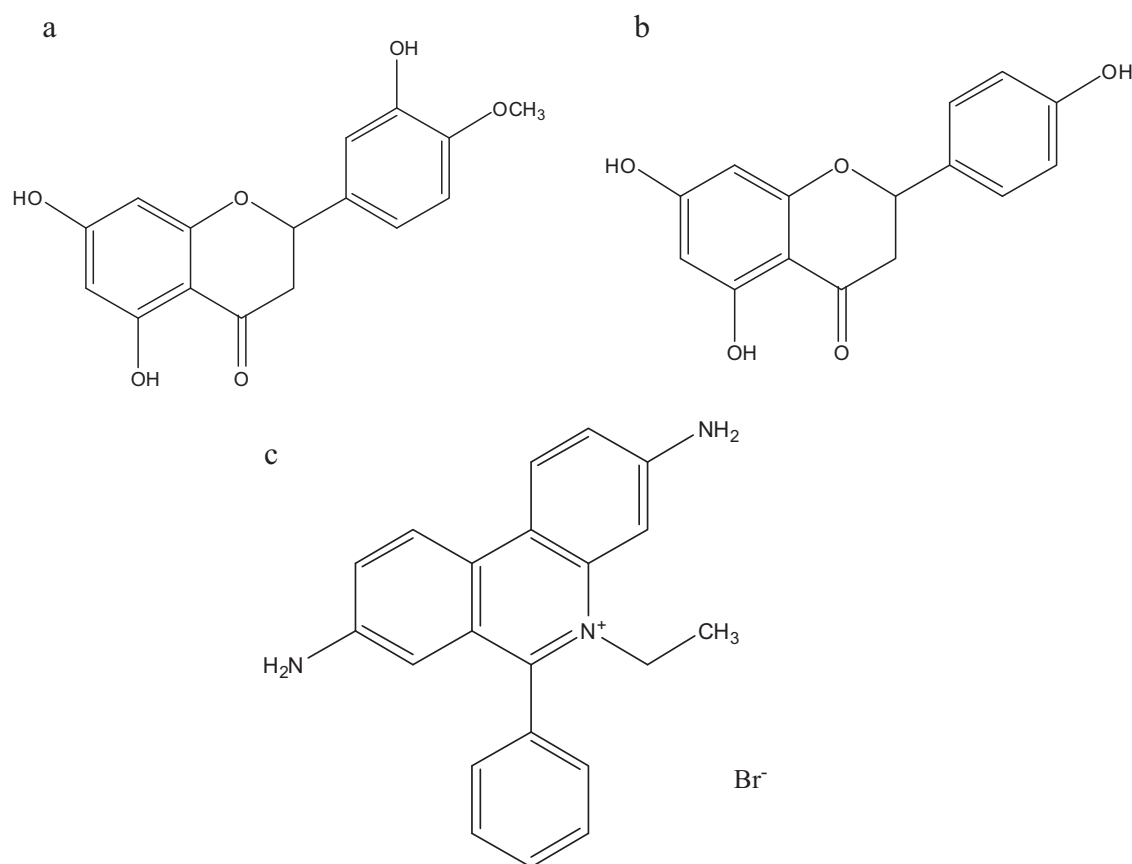


Fig. 1. Structures of hesperitin (a), naringenin (b) and ethidium bromide (c).

interaction, which could be an important step in the development of a new anticancer drug. Further, binding modes of the flavonoid to DNA can be used as model for DNA binding of anticancer drugs. The present paper attempts to understand the mechanism of binding of two flavonoids with DNA by employing spectroscopic and electro-analytical techniques.

2. Materials and methods

2.1. Chemicals and reagents

Calf thymus DNA, EB and flavonoids were purchased from Sigma–Aldrich, India and used without further purification. Stock solutions of DNA and EB were prepared by dissolving the appropriate amounts of DNA and EB in phosphate buffer of pH 7.4 and Millipore water, respectively while those of flavonoids (each of 250 μM) were prepared in 10% DMSO. Both DNA and flavonoid solutions were stored at 4 °C. The concentration of DNA was determined spectrophotometrically using the extinction coefficient value of 6600 $\text{L mol}^{-1} \text{cm}^{-1}$ at 260 nm. The solution of DNA was found to be free from protein as evident from its absorbance ratio value in the range of 1.8–1.9 for A_{260}/A_{280} [11]. All measurements were carried out at the physiological pH of 7.4 using 0.1 M phosphate buffer.

2.2. Instrumentation

Absorbance values were recorded on a double beam CARY 50-BIO UV–vis spectrophotometer (Varian, Australia) equipped with a 150 W Xenon lamp and a slit width of 5 nm. Fluorescence measurements were performed on a spectrofluorimeter Model F-7000 (Hitachi, Japan) equipped with a 150 W Xenon lamp and a slit width of 5 nm. The CD measurements were made on a

JASCO-810 spectropolarimeter (Tokyo, Japan) using a 0.1 cm cell at 0.2 nm intervals, with 3 scans averaged for each CD spectrum in the range of 220–340 nm. Electrochemical studies were performed using CHI-1103a electrochemical Analyzer (CH Instruments Ltd. Co., USA, version 9.03) with electrode system consisting of a glassy carbon electrode (3 mm diameter) as the working electrode, a platinum wire as a counter electrode and an Ag/AgCl (3 M KCl) as reference electrode.

2.3. Absorption and fluorescence measurements

Absorption spectra of DNA were recorded in the absence and presence of increasing concentrations of HES/NAR in the range of 200–400 nm. Emission spectra were recorded in the range of 530–730 nm upon excitation at 525 nm by maintaining the concentration of DNA-EB constant and varying that of the flavonoid.

2.4. DNA melting studies

DNA melting experiments were carried out by monitoring the fluorescence intensities of the sample at various temperatures in the absence and presence of the flavonoid. The temperature of the sample was maintained with a thermocouple attached to the sample holder. The temperature was varied from 20 to 90 °C. The melting temperature (T_m) of DNA was determined as the transition midpoint.

2.5. Anisotropy measurements

Anisotropy measurements were carried out at 25 °C. The slit width of the instrument was changed to 20 nm for the emission

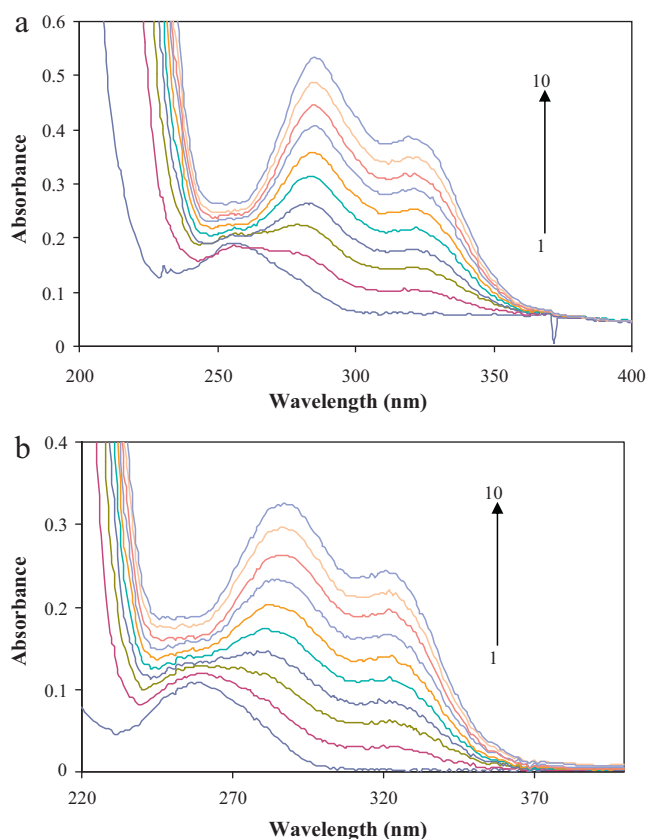


Fig. 2. (a) UV-vis spectra of DNA, $1.7 \times 10^{-5} \text{ mol L}^{-1}$ (1) with increasing concentrations of HES, 2.5 (2), 5 (3), 7.5 (4), 10 (5), 12.5 (6), 15 (7), 17.5 (8), 20 (9) and 22.5 μM (10). (b) UV-vis spectra of DNA, $1.7 \times 10^{-5} \text{ mol L}^{-1}$ (1) with increasing concentrations of NAR, 2.5 (2), 5 (3), 7.5 (4), 10 (5), 12.5 (6), 15 (7), 17.5 (8), 20 (9) and 22.5 μM (10).

of the flavonoid. The concentration of flavonoid was kept constant and that of DNA was varied.

2.6. Circular dichroism

The CD spectra of buffer were used and were automatically subtracted from the CD spectra of the samples as baselines. CD band intensities were expressed in terms of mean residue ellipticity (MRE) in $\text{deg cm}^2 \text{ dmol}^{-1}$.

2.7. Differential pulse voltammetry (DPV)

Differential pulse voltammograms of HES/NAR (fixed concentration) were recorded in the presence of increasing concentrations of DNA in phosphate buffer of pH 7.4. After each addition of DNA to HES/NAR, an interaction time of 15 min was maintained and voltammogram was recorded.

3. Results and discussion

3.1. UV-vis absorption studies of the binding of flavonoid to DNA-EB system

Absorption spectroscopy is the most useful technique to understand the interaction of flavonoid with DNA. As evident from Fig. 2a and b, the absorbance values of DNA increased (at 260 nm) upon the addition of flavonoid. This indicated that the flavonoid might have intercalated between the two strands of DNA thereby increasing the absorption of DNA due to the unwinding of DNA double helical

Table 1

The binding constants (K) of the flavonoids with DNA-EB at a range of temperatures.

Flavonoid	Temperature (K)	K_{SV} (L mol^{-1})	$^a R^2$	K (L mol^{-1})
HES	290	11.856×10^3	0.9943	9.93×10^3
	300	11.727×10^3	0.9898	3.99×10^3
	310	11.268×10^3	0.9922	3.07×10^3
NAR	290	17.009×10^3	0.9967	4.63×10^3
	300	15.950×10^3	0.9934	4.19×10^3
	310	15.226×10^3	0.9974	3.82×10^3

^a R^2 = correlation coefficient.

structure to a little extent. Due to this slight unwinding of DNA, the aromatic bases get more exposed to UV radiation and resulted in increased intensity of absorption [12]. Further, the absorption maximum of DNA at 260 nm exhibited red shift (up to 285 nm) indicating the intercalative mode of binding.

3.2. Binding properties of EB with DNA

The fluorescence intensity of EB (excited at 525 nm) is weak; however, enhanced fluorescence intensity was observed upon the addition of DNA to it (Fig. not shown). The experimental results and the earlier reports confirmed that the EB intercalated into the base pairs of DNA double helix and the complex formed was stabilized by the stacking interaction between EB and DNA bases [13].

3.3. Binding characteristics of flavonoids with DNA in the presence of EB

It is known that the enhanced fluorescence of EB upon the addition of DNA could be quenched, at least partly, by the addition of a second molecule [14]. The extent of fluorescence quenching of EB bound to DNA was utilized to determine the extent of binding between the second molecule and DNA.

In order to find the interaction mode between the flavonoid and DNA, we have carried out fluorescence quenching experiments of DNA-EB system by selected flavonoids and the binding constant of flavonoid–DNA in the presence of EB was calculated using the fluorescence data.

On the addition of HES/NAR to DNA-EB system, the shape of the fluorescence peak did not change, but its fluorescence intensity decreased regularly with successive addition of the flavonoid (Fig. 3a and b). The quenching of fluorescence intensity of DNA-EB by the flavonoid was analysed using the Stern–Volmer equation [15] shown below:

$$\frac{F_0}{F} = 1 + K_{SV}[Q] \quad (1)$$

where F_0 and F are the fluorescence intensities in the absence and presence of the quencher, respectively $[Q]$, is the concentration of the quencher and K_{SV} is the Stern–Volmer quenching constant. It was found that the K_{SV} values decreased with increase in temperature thereby indicating the presence of static quenching [16]. The corresponding K_{SV} values are listed in Table 1.

To understand the mode of binding of flavonoid to DNA, the fluorescence quenching of EB–single stranded DNA (ssDNA) and EB–double stranded DNA (dsDNA) by flavonoid was studied. The ssDNA was obtained by heating the dsDNA in a boiling water bath for 30 min and immediately cooling in an ice-water bath for 10 min. The corresponding binding constant values of flavonoid–dsDNA/ssDNA are shown in Table 2. From these results, it is evident that the binding constant of flavonoid–dsDNA is much greater than that of flavonoid–ssDNA. This indicated the greater ability of binding of flavonoid to dsDNA compared to that with ssDNA. This is possible since helical structure of dsDNA facilitated the intercalation.

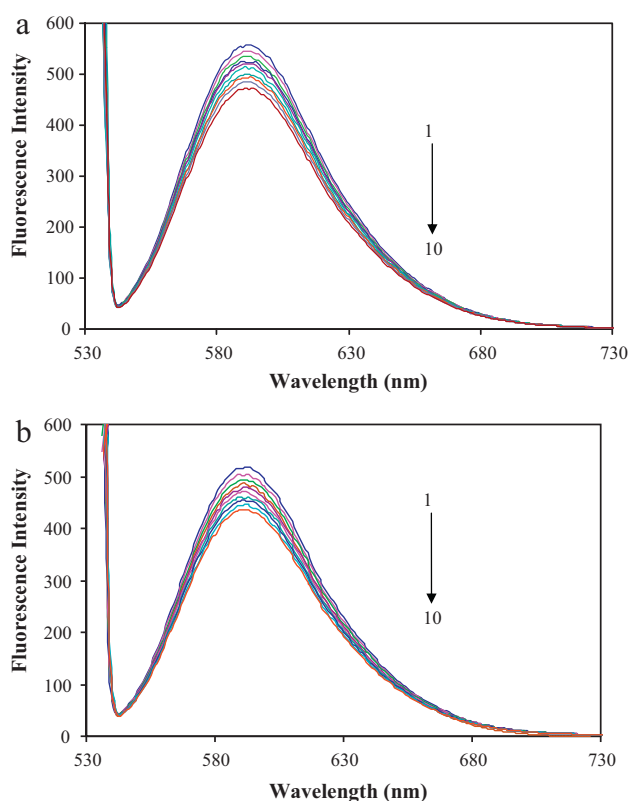


Fig. 3. (a) Fluorescence quenching spectra of EB-DNA ($C_{EB} = 2.5 \mu\text{M}$, $C_{DNA} = 1.7 \times 10^{-5} \text{mol L}^{-1}$) upon addition of increasing amount of HES (1) 0, (2) 2.5, (3) 5, (4) 7.5, (5) 10, (6) 12.5, (7) 15, (8) 17.5, (9) 20 and (10) 22.5 μM . (b) Fluorescence quenching spectra of EB-DNA ($C_{EB} = 2.5 \mu\text{M}$, $C_{DNA} = 1.7 \times 10^{-5} \text{mol L}^{-1}$) upon addition of increasing amount of NAR (1) 0, (2) 2.5, (3) 5, (4) 7.5, (5) 10, (6) 12.5, (7) 15, (8) 17.5, (9) 20 and (10) 22.5 μM .

3.4. Binding and thermodynamic characteristics of interactions

Various types of non-covalent interactions that can play a role in the binding of a ligand to a biomolecule include hydrogen bonds, van der Waals forces, electrostatic and hydrophobic interactions. Generally, the complex of intercalation is stabilized by van der Waals forces while the complex of minor groove binding is stabilized mainly by hydrophobic interactions.

The binding constant, K can be calculated using the following equation:

$$\frac{\log(F_0 - F)}{F} = \log K + n \log [Q] \quad (2)$$

The values of K were obtained by plotting the values of $\log(F_0 - F)/F$ versus $\log [Q]$ (Fig. not shown) and the corresponding values are given in Table 1.

The values of change in enthalpy and change in entropy were calculated using the equation shown below:

$$\log K = \frac{-\Delta H^0}{2.303RT} + \frac{\Delta S^0}{2.303R} \quad (3)$$

Table 2

Comparison of flavonoids binding to dsDNA and ssDNA.

Flavonoid	dsDNA K (L mol^{-1})	ssDNA K (L mol^{-1})
HES	4.19×10^3	9.7×10^2
NAR	3.99×10^3	8.4×10^2

Utilizing the values of ΔH^0 and ΔS^0 , the value of free energy change, the values of ΔG^0 were evaluated from the following equation:

$$\Delta G^0 = \Delta H^0 - T\Delta S^0 \quad (4)$$

The corresponding values of ΔG^0 , ΔH^0 and ΔS^0 are listed in Table 3. These results showed that the van der Waals and hydrogen bond played a major role. As per the thermodynamic data, the formation of flavonoid–DNA complex is enthalpy favored while it is entropy disfavored. The complex formation results in a more ordered state, possibly due to the freezing of the motional freedom of both HES/NAR and DNA molecules. Therefore, the negative ΔS^0 value confirmed the intercalative mode of binding of HES/NAR to DNA [17].

3.5. Effects of metal ions

DNA is a negatively charged polyanion attracting counter ions, positively charged ions as well as basic residues of proteins. The presence of small counter ions affect the binding of the drug, since the counter ions can screen and shield the negative backbone surface allowing non electrolytes as well as positively charged ligands to interact more strongly with the DNA target. Hence, the effect of some cations on the binding of the flavonoid to DNA was studied and the corresponding binding constant values were calculated (Table 4). It was evident that the binding constant of DNA-EB-HES/NAR was not significantly affected by the selected metal ions and hence, we could not draw any conclusions.

3.6. Melting studies

DNA denaturation, also called DNA melting, is the process by which dsDNA unwinds and separates into ssDNA through the breaking of hydrogen bonding between the bases. When solutions of DNA are exposed to extremes of pH or heat, the double helical structure of DNA undergoes a transition into a randomly single-stranded form at the melting temperature (T_m). The intercalation of small molecules into the double helix is known to increase the DNA melting temperature, at which the double helix denatures into ssDNA owing to the increased stability of the helix in the presence of an intercalator [18]. The intercalative mode of binding can increase T_m by about 5–8 °C, but the non-intercalative binding causes no obvious increase in T_m [19]. The values of T_m of DNA-EB, HES-DNA-EB and NAR-DNA-EB were determined by fluorescence method. For this, the fluorescence intensity of DNA-EB, HES-DNA-EB and NAR-DNA-EB were noted down in the temperature range of 20–90 °C. From the plot of $F_{20} \circ C/F$ versus temperature, the value of T_m was obtained (Fig. 4a and b). The T_m value of DNA was found to be increased by 5 °C (from 75 °C to 80 °C) upon binding to the flavonoid thereby confirming the intercalative mode of binding.

3.7. Anisotropy

Fluorescence anisotropy assays the rotational diffusion of a molecule from the decorrelation of polarization in fluorescence. The anisotropy value is expected to be very low in fluid solution where the fluorophore can freely rotate, and high for rigid environment. Anisotropic studies are ideal for studying the drug–DNA interaction as the complex formed is larger and tumbles more slowly than the unbound DNA. When the flavonoid intercalates into the helix, its rotational motion would be restricted and, hence the fluorescence from the bound flavonoid would be polarized. In the absence of DNA, the fluorescence of flavonoid was weakly polarized due to the rapid tumbling motion of the flavonoid in aqueous medium. However, when flavonoid bound to DNA containing alternative base sequences, the fluorescence would be significantly

Table 3
Thermodynamic parameters of binding of flavonoids to DNA.

Flavonoid	Temperature (K)	ΔG^0 (KJ mol ⁻¹)	ΔH^0 (KJ mol ⁻¹)	ΔS^0 (J mol ⁻¹ K ⁻¹)
HES	290	-15.27	-34.41	-66.93
	300	-14.61		
	310	-13.95		
NAR	290	-16.5	-44.05	-95.36
	300	-15.5		
	310	-14.6		

Table 4
Effect of metal ions on flavonoids-DNA binding.

Flavonoid	Binding constant K (L mol ⁻¹)				
	Without	Cu ²⁺	Co ²⁺	Ni ²⁺	K ⁺
HES	4.19×10^3	4.32×10^3	4.35×10^3	4.30×10^3	4.58×10^3
NAR	3.99×10^3	3.94×10^3	4.04×10^3	3.70×10^3	3.96×10^3

polarized. Generally, mere binding to the phosphate backbone or to the DNA grooves do not enhance fluorescence polarization [20] of the flavonoid. The significant increase in fluorescence polarization [anisotropy of HES increased from 0.0139 to 0.0224 while that of NAR increased from 0.0161 to 0.0262 upon the addition of DNA (Fig. 5a and b)], noticed in the present study was attributed to the binding of the flavonoid to DNA. This is consistent with the view that the flavonoid molecules were firmly incorporated in motionally constrained site(s) of the DNA double helix, thus suggesting the intercalative mode of binding.

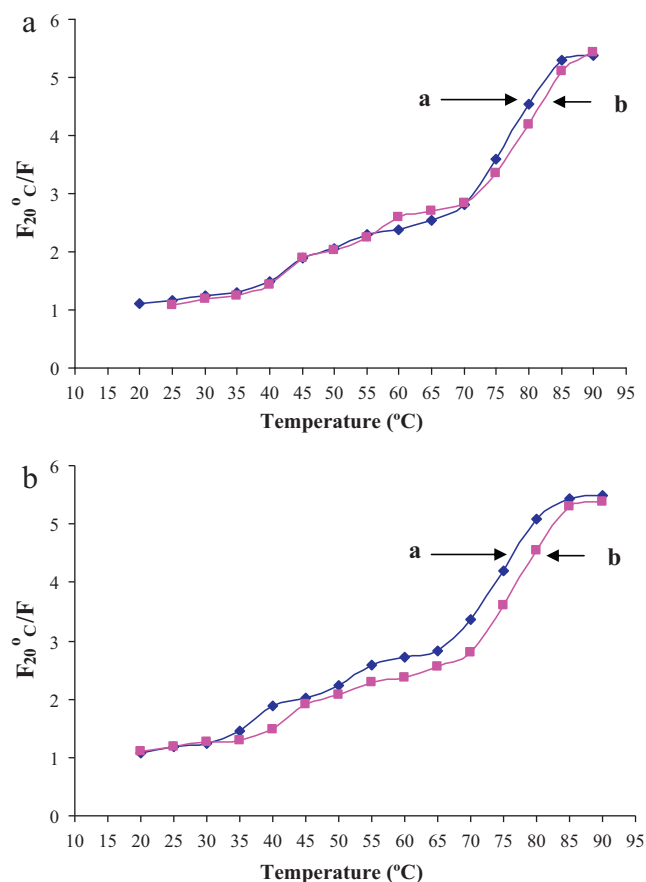


Fig. 4. (a) Melting curves of DNA-EB in the (a) absence and (b) presence of HES ($C_{DNA} = 1.7 \times 10^{-5}$ mol L⁻¹, C_{EB} and $C_{HES} = 2.5$ μ M). (b) Melting curves of DNA-EB in the (a) absence and (b) presence of NAR ($C_{DNA} = 1.7 \times 10^{-5}$ mol L⁻¹, C_{EB} and $C_{NAR} = 2.5$ μ M).

3.8. Circular dichroism

Circular dichroism (CD) is a powerful and reliable tool to understand the conformational changes in a biomacromolecule upon interaction. It is known that the intercalation of linear or flat aromatic molecules into double-stranded DNA induce large chirality changes and consequently significant effects on their CD spectra [21]. The CD spectrum of free DNA shows a negative band at 247 nm due to helicity, and a positive band at 279 nm due to the base stacking, which is the characteristic of DNA in the right-hand B form [22].

In the present study, the negative band at 247 nm decreased while the positive band at 279 nm increased with the addition of increased concentrations of the flavonoid to DNA (Fig. 6a and b). This indicated the possibility of B \rightarrow A conformational transition of

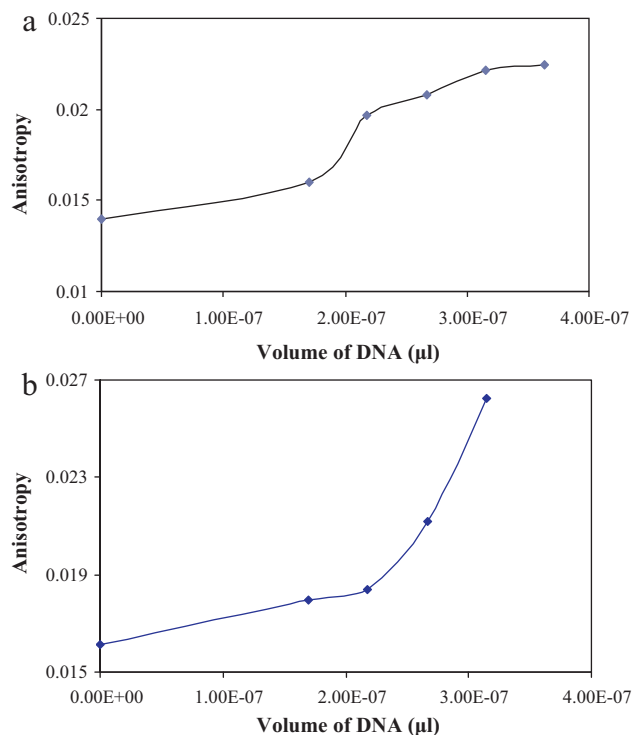


Fig. 5. (a) Change in fluorescence anisotropy of HES ($C_{HES} = 2.5$ μ M) upon the addition of DNA (0, 1.7, 2.18, 2.67, 3.15 and 3.64×10^{-5} mol L⁻¹). (b) Change in fluorescence anisotropy of NAR ($C_{NAR} = 2.5$ μ M) upon the addition of DNA (0, 1.7, 2.18, 2.67, 3.15 and 3.64×10^{-5} mol L⁻¹).

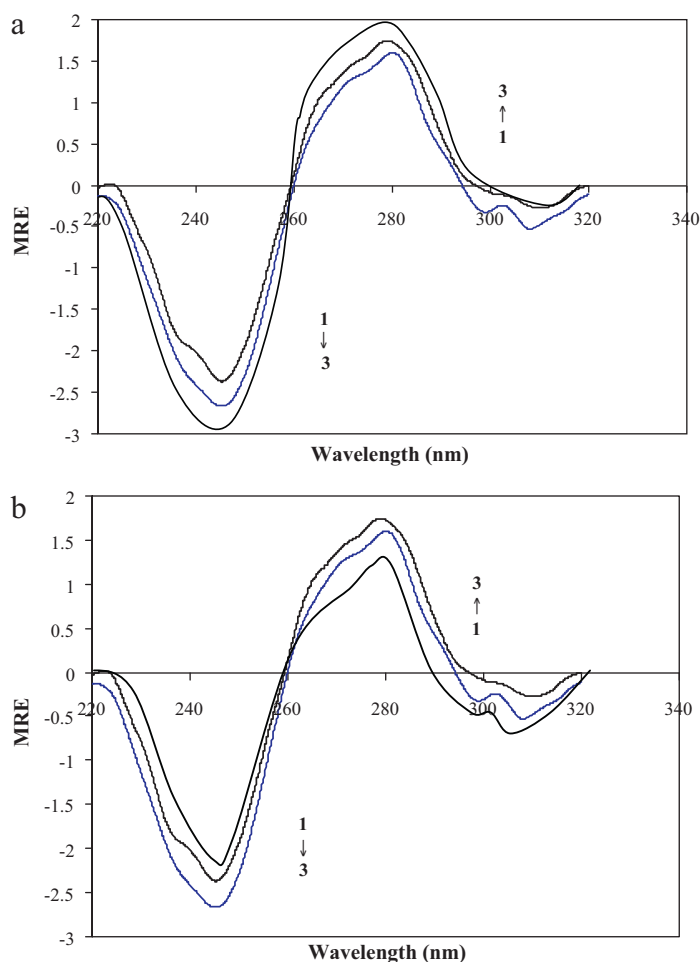


Fig. 6. (a) CD Spectra of DNA, $C_{\text{DNA}} = 1.7 \times 10^{-5} \text{ mol L}^{-1}$ (a) and DNA in presence of 5 (b) and 10 μM (c) of HES. (b) CD Spectra of DNA, $C_{\text{DNA}} = 1.7 \times 10^{-5} \text{ mol L}^{-1}$ (a) and DNA in presence of 5 (b) and 10 μM (c) of NAR.

DNA [23] upon interaction with the flavonoid. In this way, CD studies support the conformational changes in DNA upon interaction with the flavonoid.

3.9. Voltammetric studies

The differential pulse voltammograms of HES and NAR in the presence of different amounts of DNA were recorded in phosphate buffer of pH 7.4 and are shown in Fig. 7a and b, respectively. The voltammograms of HES and NAR showed a prominent oxidation peak at 0.488 V and 0.744 V, respectively. These peaks were found to be shifted towards positive potentials (to 0.500 V and 0.764 V for HES and NAR, respectively) in the presence of DNA. Further, decreased peak current was observed upon successive addition of DNA to the flavonoid. Such observation might be attributed to one of the following two factors: (i) the non conducting DNA could block the electron transfer from the flavonoid or (ii) the DNA–flavonoid complex formed was electrochemically inactive. If the electron transfer was blocked, then the current should decrease (relative to that of the clean electrode) but no peak shift would be expected [24]. The observed shift in the peak potential and decreased peak current was attributed to the formation of DNA–flavonoid complex through intercalative mode of binding [25]. Thus, the electrochemical studies complimented the spectroscopic results to propose the intercalative mode of binding between the flavonoid and DNA.

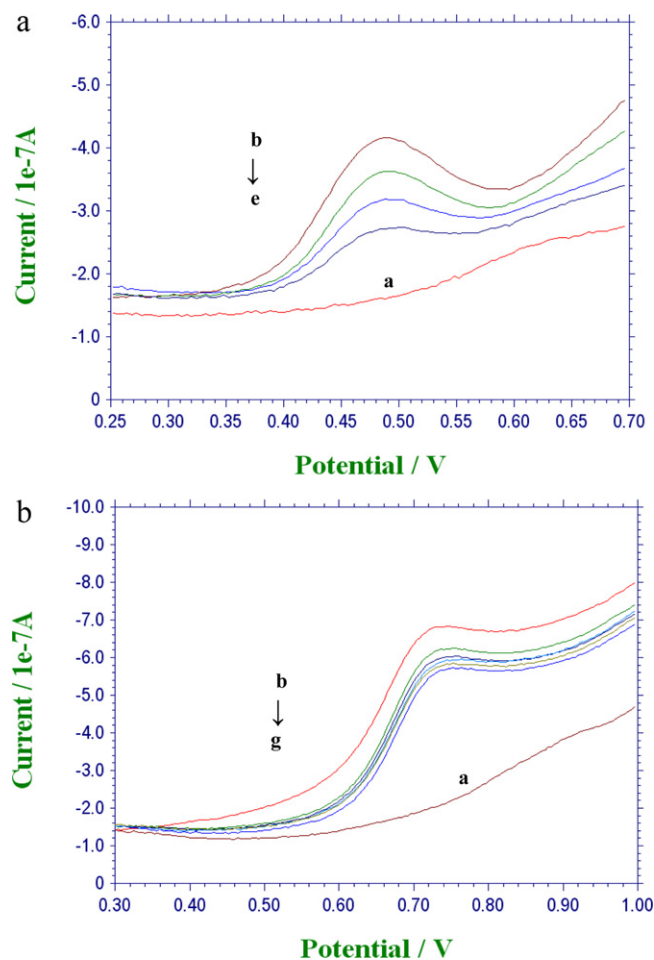


Fig. 7. (a) Differential pulse voltammograms of 2.5 μM HES in the absence (b) and presence of 1.7 (c), 2.18 (d), $2.67 \times 10^{-5} \text{ mol L}^{-1}$ DNA (e) and only DNA, $C_{\text{DNA}} = 1.7 \times 10^{-5} \text{ mol L}^{-1}$ (a) in phosphate buffer of pH 7.4. (b) Differential pulse voltammograms of 2.5 μM NAR in the absence (b) and presence of 1.7 (c), 2.18 (d), 2.67 (e), 3.15×10^{-5} (f), 3.64 mol L^{-1} DNA (g) and only DNA, $C_{\text{DNA}} = 1.7 \times 10^{-5} \text{ mol L}^{-1}$ (a) in phosphate buffer of pH 7.4.

4. Conclusions

The spectroscopic results indicate that the EB could be proposed as a probe for understanding the mechanism of interaction between the flavonoid and DNA. Based on spectroscopic and electrochemical data, intercalative mode of binding was proposed between the flavonoid and DNA.

Acknowledgements

We are grateful to the Council of Scientific and Industrial Research, New Delhi, for financial assistance (grant no. 01(2279)/08/EMR-II dated 20-11-2008). The author (A.H. Hegde) thanks the UGC, New Delhi for the award of meritorious Fellowships in Science. Thanks are also due to the authorities of the Karnatak University, Dharwad, for providing the necessary facilities.

References

- [1] T. Fiebig, C. Wan, S.O. Kelley, J.K. Barton, A.H. Zewail, Femtosecond dynamics of the DNA intercalator ethidium and electron transfer with mononucleotides in water, *Proc. Natl. Acad. Sci. U.S.A.* 96 (1999) 1187–1192.
- [2] X. Qu, C. Wan, H.C. Becker, D. Zhong, A.H. Zewail, The anticancer drug–DNA complex: femtosecond primary dynamics for anthracycline antibiotics function, *Proc. Natl. Acad. Sci. U.S.A.* 98 (2001) 14212–14217.

- [3] S. Neidle, C.M. Nunn, Crystal structures of nucleic acids and their drug complexes, *Nat. Prod. Rep.* 5 (1998) 1–15.
- [4] R. Ziegler, Vegetables, fruits and carotenoids and the risk of cancer, *Am. J. Clin. Nutr.* 53 (1991) 251S–259S.
- [5] J. Seetharamappa, M. Noboru, G.P. Mamatha, N.H. James, *Top Heterocycl. Chem. Chapter: Bioactive Mechanism of Interaction between Anthocyanins and Macromolecules like DNA and proteins*, Springer-Verlag, Berlin, Heidelberg, 2008, pp. 49–65.
- [6] W.R. Solimani, Quercetin and DNA in solution: analysis of the dynamics of their interaction with a linear dichroism study, *Int. J. Biol. Macromol.* 18 (1996) 287–295.
- [7] Y. Sun, S. Bi, D. Song, C. Qiao, D. Mu, H. Zhang, Study on the interaction mechanism between DNA and the main active components in *Scutellaria baicalensis* Georgi, *Sens. Actuators B* 129 (2008) 799–810.
- [8] S. Bi, C. Qiao, D. Song, Y. Tian, D. Gao, Y. Sun, H. Zhang, Study of interactions of flavonoids with DNA using acridine orange as a fluorescence probe, *Sens. Actuators B* 119 (2006) 199–208.
- [9] M.J. Waring, Complex formation between ethidium bromide and nucleic acids, *J. Mol. Biol.* 13 (1965) 269–282.
- [10] J.B. Le Pecq, C. Paoletti, A fluorescent complex between ethidium bromide and nucleic acids: physical–chemical characterization, *J. Mol. Biol.* 27 (1967) 87–106.
- [11] Z.Y. Chen, J. Liu, D. Luo, *Biochemistry Experiments*, Chinese University of Science and Technology Press, Hefei, 1994, p. 111.
- [12] S. Charak, D.K. Jangir, G. Tyagi, R. Mehrotra, Interaction studies of Epirubicin with DNA using spectroscopic techniques, *J. Mol. Struct.* 1000 (2011) 150–154.
- [13] J. Olmsted III, D.R. Kearns, Mechanism of ethidium bromide fluorescence enhancement on binding to nucleic acids, *Biochemistry* 16 (1977) 3647–3654.
- [14] B.C. Baguley, M. LeBret, Quenching of DNA–ethidium fluorescence by amsacrine and other antitumor agents: a possible electron-transfer effect, *Biochemistry* 23 (1984) 937–943.
- [15] J.R. Lakowicz, G. Weber, Quenching of fluorescence by oxygen. A probe for structural fluctuations in macromolecules, *Biochemistry* 12 (1973) 4161–4170.
- [16] G. Zhang, P. Fu, L. Wang, M. Hu, Molecular spectroscopic studies of farrerol interaction with calf thymus DNA, *J. Agric. Food Chem.* 59 (2011) 8944–8952.
- [17] S. Kashanian, S. Askari, F. Ahmadi, K. Omidfar, S. Ghobadi, F.A. Tarighat, In vitro study of DNA interaction with clodinafop-propargyl herbicide, *DNA Cell Biol.* 27 (2008) 581–586.
- [18] D.J. Patel, Nuclear magnetic resonance studies of drug–nucleic acid interactions at the synthetic DNA level in solution, *Acc. Chem. Res.* 12 (1979) 118–125.
- [19] C.V. Kumar, R.S. Turner, E.H. Asuncion, Groove binding of a styrylcyanine dye to the DNA double helix: the salt effect, *J. Photochem. Photobiol. A: Chem.* 74 (1993) 231–238.
- [20] C.K. Kumar, E.H. Asuncion, DNA binding studies and site selective fluorescence sensitization of an anthryl probe, *J. Am. Ceram. Soc.* 115 (1993) 8547–8553.
- [21] G.D. Fasman, *Circular Dichroism and Conformational Analysis of Biomolecules*, Plenum Press, New York, 1996, p. 413.
- [22] A. Rich, A. Nordheim, A.H.J. Wang, The chemistry and biology of left-handed Z-DNA, *Annu. Rev. Biochem.* 53 (1984) 791–843.
- [23] Y.Y. Yang, Z.C. Zhang, H. Sheng, F.Y. Liu, X.H. Qian, Q. Xu, Zhang, Studies on the binding geometry of intercalation of 4-(2-diethylamino-ethylamino)-8-oxo-8H-acenaphtho [1,2-b] pyrrole-9-carbonitrile to DNA by molecular spectra, *Chem. J. Chin. Univ.* 28 (2007) 453–457.
- [24] Y. Wang, Y. Ni, S. Kokot, Voltammetric behaviour of complexation of salbutamol with calf thymus DNA and its analytical application, *Anal. Biochem.* 419 (2011) 76–80.
- [25] M.T. Carter, M. Rodriguez, A.J. Bard, Voltammetric studies of the interaction of metal chelates with DNA. 2. Tris-chelated complexes of cobalt (III) and iron (II) with 1,10-phenanthroline and 2,2'-bipyridine, *J. Am. Chem. Soc.* 111 (1989) 8901–8911.



Determination of a novel TAZ modulator, 2-butyl-5-methyl-6-(pyridine-3-yl)-3-[2'-(1H-tetrazole-5-yl)-biphenyl-4-ylmethyl]-3H imidazo[4,5-b]pyridine (TM-25659) in rat plasma by liquid chromatography–tandem mass spectrometry

Sung Heum Choi^a, Kyeong-Ryoon Lee^a, Jae-Chun Woo^a, Nak Jeong Kim^b, Dong Cheul Moon^c, Eun Sook Hwang^d, Sung-Hoon Ahn^a, Myung Ae Bae^a, Min-Sun Kim^{a,*}

^a Drug Discovery Platform Technology Team, Medicinal Science Division, Korea Research Institute of Chemical Technology, Daejeon 305-600, South Korea

^b Center for Metabolic Syndrome Therapeutics, Medicinal Science Division, Korea Research Institute of Chemical Technology, Daejeon 305-600, South Korea

^c College of Pharmacy, Chungbuk National University, Cheongju, South Korea

^d College of Pharmacy and Division of Life and Pharmaceutical Sciences and Center for Cell Signaling and Drug Discovery Research, Ewha Womans University, Seoul 120-750, South Korea

ARTICLE INFO

Article history:

Received 20 October 2011

Received in revised form 2 January 2012

Accepted 28 January 2012

Available online 7 February 2012

Keywords:

TM-25659

Method validation

Pharmacokinetics

LC–MS/MS

Rat plasma

ABSTRACT

TM-25659 compound, a novel TAZ modulator, is developed for the control of bone loss and obesity. TAZ is known to bind to a variety of transcription factors to control cell differentiation and organ development. A selective and sensitive method was developed for the determination of TM-25659 concentrations in rat plasma. The drug was measured by liquid chromatography–tandem mass spectrometry after liquid–liquid extraction with ethyl acetate. TM-25659 and the internal standard imipramine were separated on a Hypersil GOLD C18 column with a mixture of acetonitrile–ammonium formate (10 mM) (90:10, v/v) as the mobile phase. The ions m/z 501.2 → 207.2 for TM-25659 and m/z 281.0 → 86.0 for imipramine in multiple reaction monitoring mode were used for the quantitation. The calibration range was 0.1–100 μg/ml with a correlation coefficient greater than 0.99. The lower limit of quantitation of TM-25659 in rat plasma was 0.1 μg/ml. The percent recoveries of TM-25659 and imipramine were 98.6% and 95.7% from rat plasma, respectively. The intra- and inter-batch precisions were 3.17–15.95% and the relative error was 0.38–10.82%. The developed assay was successfully applied to a pharmacokinetic study of TM-25659 administered intravenously (10 mg/kg) to rats.

© 2012 Elsevier B.V. All rights reserved.

1. Introduction

Transcriptional coactivator with PDZ-binding motif (TAZ) was originally identified as a 14-3-3 – interacting protein, also called WW-domain-containing transcription co-regulator-1 (WWTR1) [1,2]. TAZ is a key modulator for mesenchymal stem cell differentiation into osteoblasts and adipocytes through its regulation of lineage-specific master transcription factors such as core-binding factor-1 (Cbfa1)/runt-related transcription factor-2 (Runx2) and PPAR γ (peroxisome proliferator-activated receptor- γ) [3–7]. It is involved in the control of cell cycle progression, cell differentiation, and apoptosis through interactions with phosphorylated signaling molecules [8,9]. TM-25659, 2-butyl-5-methyl-6-(pyridine-3-yl)-3-[2'-(1H-tetrazole-5-yl)-biphenyl-4-ylmethyl]-3H imidazo[4,5-b]pyridine], a newly

synthesized small molecule, enhanced TAZ expression in the nucleus. The TAZ-dependent modulatory activity of TM-25659 in adipocyte and osteoblast differentiation was evidenced by loss of the anti-adipogenic and osteogenic activity of TM-25659 in TAZ-deficient cells. [10]. Thus, TM-25659 may play beneficial roles in the control of obesity and bone loss through activation of TAZ.

Liquid chromatography coupled with tandem mass spectrometry (LC–MS/MS) provides unique capabilities for preclinical biopharmaceutical and clinical pharmacology studies [11–13]. This method is applicable to a wide range of compounds of pharmaceutical interest with sensitivity, selectivity, speed of analysis, and cost-effectiveness [14,12]. Multiple reaction monitoring (MRM) enables the detection of a specific precursor ion that is programmed to select certain ions chosen by the operator. The precursor ion is fragmented by certain collision energy and it is possible to detect a specific product ion following fragmentation [15,16].

The aim of this study was to develop a LC–MS/MS method for the determination of TM-25659 in rat plasma after simple liquid–liquid extraction (LLE). The method was validated for accuracy, precision,

* Corresponding author. Tel.: +82 42 860 7170.

E-mail addresses: mksime777@gmail.com, smkim9677@naver.com (M.-S. Kim).

selectivity, sensitivity, reproducibility, and stability. This is the first method for the biological quantitation of TM-25659 and its application for a preliminary pharmacokinetic study.

2. Experimental

2.1. Chemicals

TM-25659 was synthesized by the Medicinal Science Division at the Korea Research Institute of Chemical Technology (Daejeon, Korea). Imipramine was purchased from Sigma–Aldrich (St. Louis, MO, USA). Organic solvents of HPLC grade (ethyl acetate, methanol, acetonitrile) were acquired from Burdick & Jackson Inc. (Muskegon, MI, USA). Distilled water was obtained from a Milli-Q system (Millipore, Bedford, MA, USA). All other chemicals and solvents were of the highest analytical grade available.

2.2. Calibration standard and quality control samples

Stock solution of TM-25659 (1 mg/ml) was prepared in methanol. Working standard solutions at the desired concentration for preparing a calibration curve and quality control (QC) samples were made by serial dilution with methanol:water (50:50, v/v). An internal standard (IS) working solution (1 µg/ml) was diluted from the stock IS solution of imipramine (1 mg/ml) with methanol:water (50:50, v/v). All solutions were stored at -20°C when not in use.

A calibration curve for TM-25659 was prepared by spiking the working standard solution equivalent to levels of 0.1, 0.3, 5, 40, 80, and 100 µg/ml in blank plasma. QC samples were also prepared for TM-25659 concentrations of 0.3, 5, and 80 µg/ml in rat plasma. They were prepared from independent weightings of the analytes.

2.3. Instrumentation and chromatographic conditions

Sample analyses were carried out with a 1200 series HPLC system (Agilent, Santa Clara, CA, USA) coupled to an API 4000 Q trap Mass Spectrometer (Applied Biosystems, Foster City, CA, USA) equipped with a turbo-electrospray interface in positive ionization mode for the LC–MS/MS analysis. The spectrometer was used in MRM mode. The optimized instrument conditions were as follows: source temperature, 400°C ; curtain gas, 20 psi; nebulizing (GS1), 50 psi; heating (GS2), 50 psi; collision energy (CE), 37 V for TM-25659 and 25 V for imipramine. The most abundant product ions of the compounds were at m/z 207.2 from the parent m/z 501.2 of TM-25659, and m/z 86.0 from the m/z 281.0 of the IS. Analyst software (ver. 1.4; Applied Biosystems) was used for instrument control and data collection.

The LC chromatograph was equipped with a Hypersil GOLD C18 column (50 mm \times 2.1 mm i.d., 3 µm; Thermo, Waltham, MA, USA). The mobile phase consisted of acetonitrile–ammonium formate (10 mM; 90:10, v/v), and was filtered and degassed before use. The flow rate was set at 0.3 ml/min for sample analysis. The method used isocratic elution with a total run time of 2 min. The temperatures of the autosampler and column oven were 4°C and 30°C , respectively.

2.4. Sample preparation

A volume of 30 µl of rat plasma was aliquoted in a 1.5 ml microfuge tube. Then 20 µl of the IS solution of imipramine at 1 µg/ml was added to an individual sample tube and vortex mixed for 1 min. Then 1 ml of cold ethyl acetate was added to each sample. After vortexing for another 10 min, the extract was centrifuged (13,000 rpm, 5 min, 4°C). Next, the organic phase was transferred to another tube and evaporated to dryness under nitrogen gas at room temperature. The residue was dissolved in 1 ml mobile phase

and vortexed for 1 min. Finally, 5 µl of the supernatant was injected onto the analytical column.

2.5. Validation

The analytical method for TM-25659 was validated with regard to selectivity, linearity, accuracy, and precision. For the presence of analytical interferences, the selectivity of the method was investigated by analyzing the extract from six different sources. Calibration curves were constructed by linear regression of the peak area ratios (y) of TM-25659 to the IS versus the concentration (x) in µg/ml. The lower limit of detection was calculated as three-times the signal-to-noise ratio. The lower limit of quantitation (LLOQ) was defined as the lowest concentration that could be accurately quantitated above the noise level with acceptable precision (within 20%). Precision and accuracy of the method were evaluated by analyses of QCs at three levels in five replicates. The intra- and inter-assay reproducibilities were investigated by analyzing the spiked samples at four different concentrations (0.1, 0.3, 5 and 80 µg/ml) in a single day and for 5 days, respectively. The percentage of deviation of the mean from calculated concentrations was expressed as the relative error (RE). Precision was expressed as the relative standard deviation (RSD). All results were within the ranges of precision (%) and accuracy (%) specified by US Food and Drug Administration (FDA) guidelines [17].

2.6. Matrix effect and recovery

The matrix effect, recovery, and process efficiency for TM-25659 were assessed by analyzing three sets of standards at three concentrations (0.3, 5 and 80 µg/ml). To determine the matrix effect, those of the analyte-spiked post-extraction matrix (set 2) were compared with reference standards (set 3). The recovery was determined by comparing the peak areas of analyte spiked before extraction (set 1) with set 2. The process efficiency was calculated by comparing the peak area of set 3 with that of set 1. Each sample set was analyzed five times.

2.7. Stability

The stability of TM-25659 was assessed by analyzing three QC levels in five replicates under different conditions. The stock solution stability was estimated at -20°C for 3 weeks. The study of TM-25659 stability in rat plasma included short- and long-term tests. The short-term stability included (a) freeze–thaw cycle stability, (b) exposure of samples to room temperature for 1 day, (c) exposure to 4°C for 1 day, (d) exposure to -20°C for 1 day, (e) exposure to -80°C for 1 day, (f) exposure in the mobile phase at 4°C for 1 day and 1 week after preparation, and (g) exposure in the mobile phase at room temperature for 1 day after preparation. Long-term stability included (a) exposure of samples to -80°C for 30 days and (b) exposure to -20°C for 30 days.

2.8. Pharmacokinetic study

Three male Sprague–Dawley rats, aged 8 weeks and weighing 212.9 ± 6.6 g, were used for the pharmacokinetic disposition study. Animals were kept in plastic cages with free access to standard rat diet and water. The room was maintained at a temperature of $23 \pm 3^{\circ}\text{C}$, relative humidity of $50 \pm 10\%$, and an approximately 12/12 h light/dark cycle.

The intravenous dose solutions (10 mg/kg) were prepared in PEG 400:distilled water:dimethyl sulfoxide at a ratio of 40:55:5. Blood (about 0.2 ml) was collected at pre-dose, 0.033, 0.167, 0.5, 1, 2, 4, and 8 h after intravenous administration. Blood samples were centrifuged immediately and stored at -80°C until analysis.

A non-compartmental method using the nonlinear least-squares regression program WinNonlin (Pharsight, Mountain View, CA, USA) was used to calculate the pharmacokinetic parameters. The area under the plasma concentration–time curve from time zero to the last measured concentration ($AUC_{0 \rightarrow \text{last}}$) and to infinite time ($AUC_{0 \rightarrow \infty}$) by adding extrapolated area were estimated. The terminal elimination half-life ($t_{1/2}$), total body clearance (CL), volume of distribution at steady state (V_{ss}), and mean residence time (MRT) for TM-25659 were determined by individual plasma concentration–time profiles.

3. Results and discussion

3.1. Mass spectra and chromatography

The MRM mode produces very specific and sensitive responses for the selected analytes. TM-25659 has mass spectrometric response either in the positive ionization or in the negative ionization mode, although signal intensity in positive mode is higher than that in the negative mode. TM-25659 and the IS were investigated for the abundant precursor ions $[M+H]^+$ at m/z 501.2 and 281.0, respectively. The precursor ions of the analyte and IS were formed using declustering potentials of 111 and 75 V, respectively. The quantitation of analytes was performed using MRM mode for high selectivity and sensitivity of acquisition data. To confirm the correct identification and to prevent false positives, two or more different ions were selected for each analyte, and the peak area ratio of two selected ions (quantitative ion and confirmative ion) was compared with that of the standard compound. Fig. 1 shows the chemical structure and product ion mass spectra of TM-25659 and the IS (imipramine). The predominant ion at m/z 207.2 was chosen for the quantitation, and that at m/z 267.2 was used as the confirmative ion for TM-25659. Imipramine was fragmented to produce intense product ion signals at m/z 281.0 \rightarrow 86.0. The optimal values

of the collision energy were 37 and 25 eV for TM-25659 and the IS, respectively.

The chromatographic separation was performed on a Hypersil GOLD C18 column offering excellent peak shape, efficient separation, desired linearity and reproducibility for TM-25659 and IS in plasma matrix.

The optimization of the mobile phase was based on peak selectivity and retention time. Increasing the ratio of organic solvent, the peak shapes of TM-25659 and the IS were sharp, but the retention time decreased. Therefore, a mixture of acetonitrile–ammonium formate (10 mM) (90:10, v/v) was adopted as the isocratic mobile phase. TM-25659 and the IS were retained on the column with good peak shape at the retention times of 0.59 and 1.44 min, respectively. Fig. 2 shows the typical peak shapes and retention times of MRM chromatograms.

3.2. Sample preparation

For the extraction, LLE was chosen because of its efficiency, specificity, and low cost. Ethyl acetate, methylene chloride, and methyl-*t*-butyl ether (MTBE) were tested as the LLE solvents to extract TM-25659 from spiked plasma. Methylene chloride and MTBE exhibited relatively low extraction efficiency (recoveries 63% and 14%, respectively). Ethyl acetate is the most effective solvent for the recovery of spiked TM-25659 (recovery 91%). Although the relatively polar solvent is able to extract polar impurities, no interference peaks and a stable baseline appeared in MRM mode.

The extraction time required no more than 10 min and 1 ml of solvent was enough to efficiently extract TM-25659 from a 30 μ l plasma sample.

3.3. Validation and matrix effect

Typical MRM chromatograms of six different lots of rat plasma, double blank plasma, blank plasma, and the LLOQ samples are

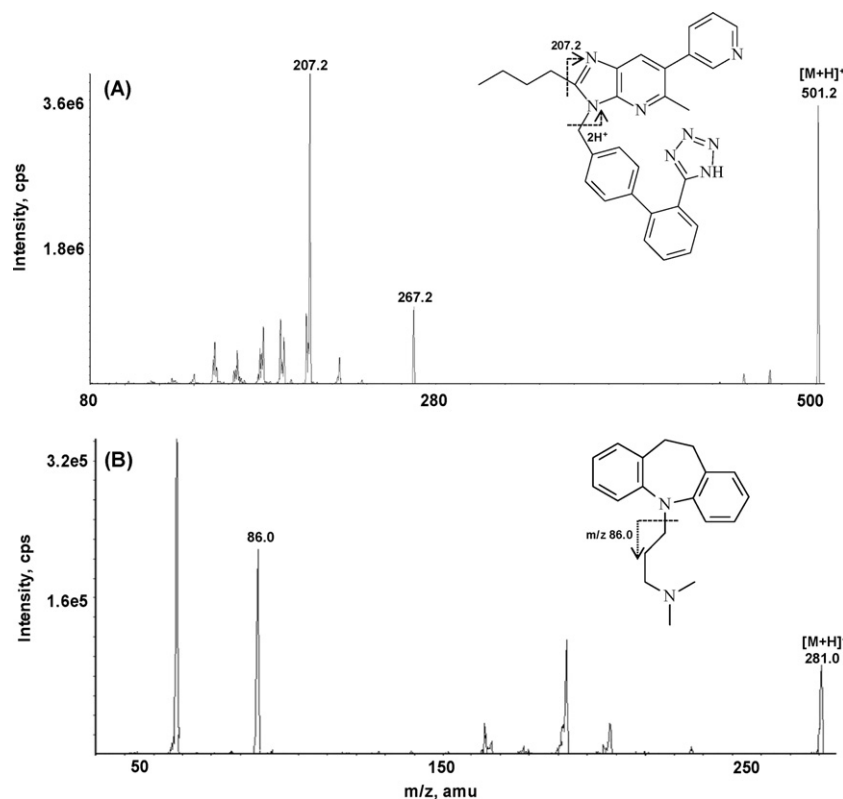


Fig. 1. The structures and product-ion scan spectra of (A) TM-25659 and (B) imipramine (IS).

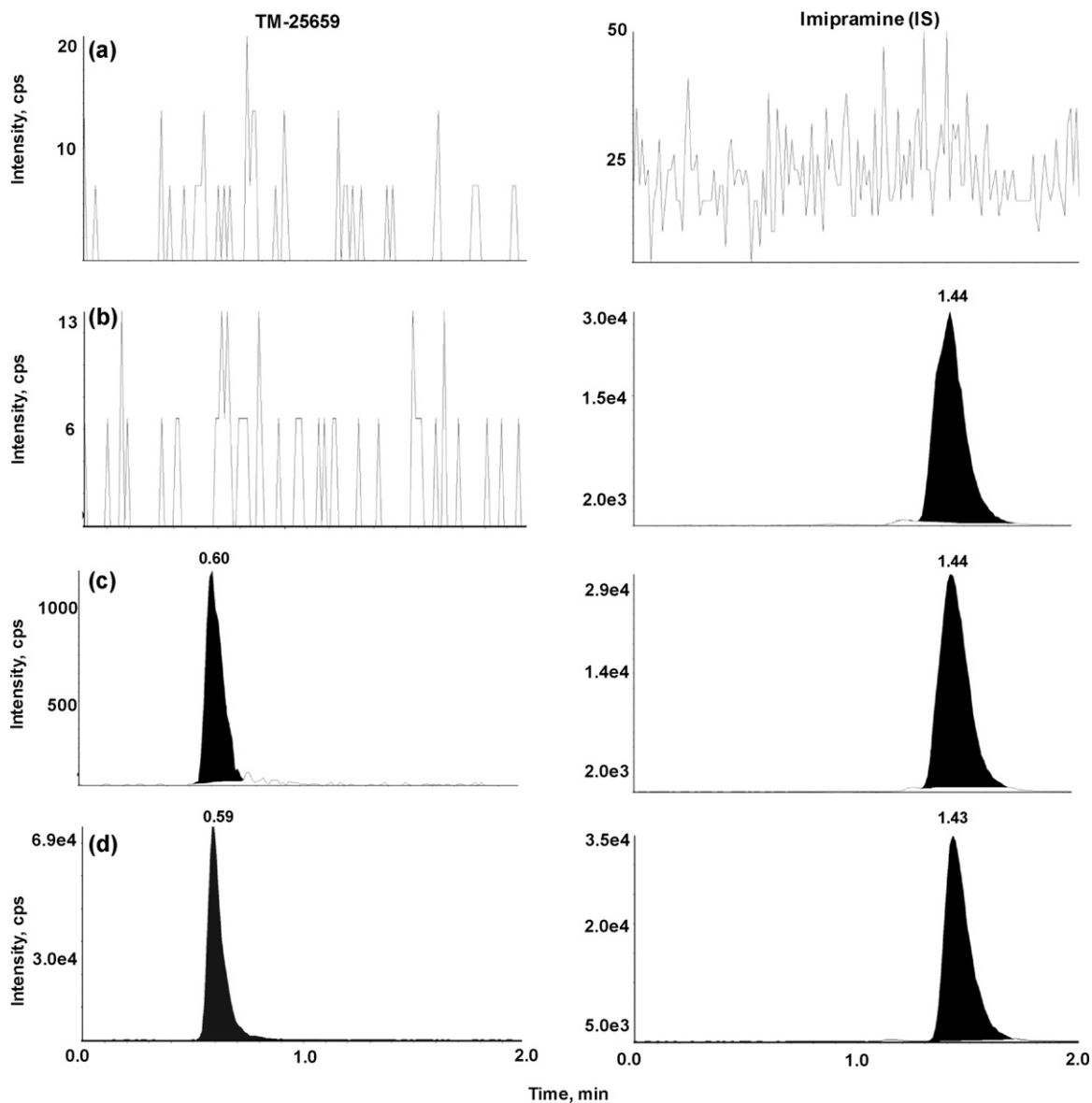


Fig. 2. Representative MRM chromatograms of (a) double blank rat plasma, (b) blank rat plasma spiked with the IS, (c) blank rat plasma spiked with 0.1 µg/ml (LLOQ) of TM-25659 and the IS, (d) a plasma sample obtained 1 h after intravenous administration of TM-25659 at 10 mg/kg to rats.

shown in Fig. 2. No significant endogenous peaks were observed that directly interfered at the retention times of the analyte or IS.

The calibration curve for TM-25659 was generated by a linear least squares regression analysis of the TM-25659/IS peak area ratio versus the amount of spiked TM-25659 in the range of 0.1–100 µg/ml. The weighted regression (i.e., 1/x) was used for quantification of the analytes. The coefficient of determination (R^2)

for the mean standard curve of five different lots of plasma was 0.99, indicating excellent linearity. The intra- and inter-assay reproducibilities of the assay were investigated in terms of accuracy and precision. As shown in Table 1, the intraday accuracy ranged from 0.38 to 5.62% (defined as RE), with RSD values ranging from 3.17 to 6.03%, and the inter-day accuracy ranged from 3.85 to 10.82%, with RSD values ranging from 8.17 to 15.95%, indicating excellent accuracy.

Table 1
Reproducibility and accuracy for TM-25659 in rat plasma (n = 5).

Theoretical concentration (µg/ml)	Intra-day			Inter-day		
	Concentration found (µg/ml)	RSD ^a (%)	RE ^b (%)	Concentration found (µg/ml)	RSD (%)	RE (%)
0.1	0.11	6.03	5.62	0.11	15.95	10.82
0.3	0.29	3.73	1.95	0.27	8.17	9.21
5	5.18	3.97	3.63	4.81	13.15	3.85
80	80.31	3.17	0.38	85.95	14.04	7.44

^a RSD (%) = standard deviation of the concentration/mean concentration × 100.

^b RE (%) = (calculated concentration – theoretical concentration)/theoretical concentration × 100.

Table 2
Recovery, matrix effect and process efficiency ($n=5$).

	Concentration ($\mu\text{g/ml}$)	Matrix effect ^a (%)	Recovery ^b (%)	Process efficiency ^c (%)
TM-25659	0.3	74.1	99.5	72.2
	5	79.8	98.9	78.5
	80	77.9	97.5	76.3
	Mean	77.3	98.6	75.7
IS (Imipramine)	1	94.6	95.7	90.6

^a Matrix effect expressed as the ratio of the mean peak area of an analyte added post-extraction (set 2) to the mean peak area of the same analyte standards (set 3) multiplied by 100.

^b Recovery calculated as the ratio of the mean peak area of an analyte added before extraction (set 1) to the mean peak area of an analyte spiked post-extraction (set 2) multiplied by 100.

^c Process efficiency calculated as the ratio of the mean peak area of an analyte added before extraction (set 1) to the mean peak area of the same analyte standards (set 3) multiplied by 100.

The matrix effects are considered attributable to co-eluting, reducing, or enhancing the ion intensity of the analytes. The mean matrix effects at TM-25659 concentrations of 0.3, 5, and 80 $\mu\text{g/ml}$ were 74.1, 79.8, and 77.9%, respectively; the mean percentage recoveries at the three concentrations were 99.5, 98.9, and 97.5%, respectively (Table 2). These results indicate the presence of some matrix effect in terms of the TM-25659/imipramine response ratio, but the LLOQ signal intensity was sufficient. To evaluate the process efficiency, the standards spiked before extraction were compared with standards injected directly in the mobile phase. It is determined by a combination of matrix effects and analyte recovery from the matrix by sample extraction. The process efficiency of TM-25659 was 72.2–78.5%. The sensitivity of this method was high enough to analyze samples during the pharmacokinetic study.

3.4. Stability

The stability of TM-25659 was investigated in QC plasma samples under a variety of conditions used for sample handling and processed samples. The stock solution of TM-25659 in methanol (1 mg/ml) was confirmed to be stable for 3 weeks at -20°C ; TM-25659 was stable, ranging from 90.0 to 98.8%.

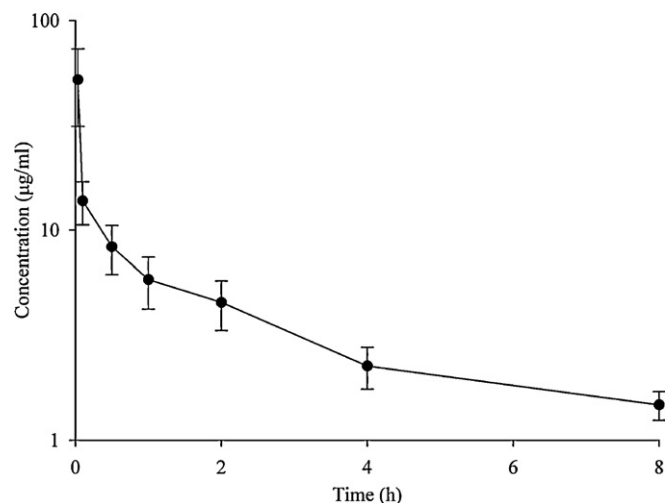
Table 3 summarizes the short-term and long-term stability of TM-25659 in plasma. There was no significant change when fresh plasma were kept at -20°C and -80°C for the short and long term, respectively, in QC samples (0.3, 5 and 80 $\mu\text{g/ml}$). Three freeze–thaw cycles and post-preparative stability had little effect on the quantitation. However, the concentration of TM-25659 at room temperature and 4°C for 1 day decreased. The stability of TM-25659 at room temperature for 1 day was 81.4, 70.0, and 73.6%,

Table 3
Stability of TM-25659 in rat plasma ($n=5$).

Condition tested	QCL (0.3 $\mu\text{g/ml}$)			QCM (5 $\mu\text{g/ml}$)			QCH (80 $\mu\text{g/ml}$)		
	Mean	RSD ^a (%)	RE ^b (%)	Mean	RSD (%)	RE (%)	Mean	RSD (%)	RE (%)
Short-term stability									
Control samples (freshly prepared)	–	10.0	–	–	1.2	–	–	7.6	–
Freeze–thaw (-80°C , 3 cycle)	0.28	1.6	–7.5	4.98	0.6	–0.3	80.53	1.8	0.6
Bench (room temperature, 1 day)	0.24	0.2	–18.6	3.50	0.8	–30.0	58.81	1.9	–26.4
Refrigerator (4°C , 1 day)	0.25	0.9	–17.5	3.68	0.3	–26.3	69.25	1.5	–13.4
Freezer (-20°C , 1 day)	0.27	0.6	–9.8	4.40	0.5	–12.0	78.34	1.5	–2.0
Freezer (-80°C , 1 day)	0.33	0.8	9.8	4.70	0.2	–6.0	80.12	0.8	0.1
Post-preparative stability (4°C , 1 day)	0.30	1.0	–0.8	5.00	0.3	–0.0	83.38	1.4	4.2
Post-preparative stability (4°C , 1 week)	0.31	0.9	4.6	5.39	1.8	7.7	80.09	2.1	0.1
Post-preparative stability (room temperature, 1 day)	0.33	0.9	9.9	4.79	0.9	–4.2	73.72	1.1	–7.8
Long-term stability									
Freezer (-80°C , 30 days)	0.32	0.8	7.3	4.88	1.2	–2.4	71.08	1.5	–11.1
Freezer (-20°C , 30 days)	0.24	2.6	–19.6	4.80	0.8	–3.9	69.04	2.8	–13.6

^a RSD (%) = standard deviation of the concentration/mean concentration \times 100.

^b RE (%) = (calculated concentration – theoretical concentration)/theoretical concentration \times 100.

**Fig. 3.** Mean plasma concentration–time plot of TM-25659 after intravenous administration of TM-25659 at 10 mg/kg to rats (mean \pm standard deviation, $n=3$ rats).

respectively, and 82.5, 73.7, and 86.6% at 4°C for 1 day. Therefore, careful sample storage conditions are required above -20°C .

3.5. Application to clinical testing

The method has been successfully applied to analyze plasma samples obtained from male rats that received intravenous TM-25659 at a dose of 10 mg/kg. Fig. 3 illustrates the mean plasma concentration profiles of TM-25659 in rats. The concentration of TM-25659 was readily measurable in plasma samples collected up

to 8 h post-dose. The terminal half-life and AUC_{∞} values of TM-25659 were 3.51 ± 0.62 h and 39.80 ± 3.75 $\mu\text{g h/ml}$, respectively. The $AUC_{0 \rightarrow \text{last}}/AUC_{0 \rightarrow \infty}$ ratio was higher than 75% for all subjects (mean values, $81.02 \pm 5.53\%$). The CL, V_{ss} , and MRT were 0.25 ± 0.02 l/h/kg, 1.09 ± 0.21 l/kg, and 2.20 ± 0.06 h, respectively.

4. Conclusions

A sensitive and selective LC–MS/MS method was developed and validated for determining TM-25659 in rat plasma. Plasma samples were treated with LLE followed by LC–MS/MS analysis. The present assay was demonstrated in terms of selectivity, linearity, accuracy, precision, and stability. The R^2 was greater than 0.99, and the recovery of QC samples was 98.6%. The intraday and interday accuracy was $\leq 15.95\%$ RSD and precision was less than 10.82% RE. In the stability test, some losses of TM-25659 were observed under room temperature and 4 °C, so the samples should be kept below –20 °C. The method was successfully applied to a pharmacokinetic study of TM-25659 in rats. The successful application of this method to a pharmacokinetic study supports its applications in future preclinical studies on TM-25659.

Acknowledgement

This research was supported by the Ministry of Knowledge Economy (Grant NO. 2011-10033279).

References

- [1] Z. Strakova, J. Reed, I. Ihnatovych, Human transcriptional coactivator with PDZ-binding motif (TAZ) is downregulated during decidualization, *Biol. Reprod.* 82 (2010) 1112–1118.
- [2] A. Mitani, T. Nagase, K. Fukuchi, H. Aburatani, R. Makita, H. Kurihara, Transcriptional coactivator with PDZ-binding motif is essential for normal alveolarization in mice, *Am. J. Respir. Crit. Care Med.* 180 (2009) 326–338.
- [3] J.H. Hong, E.S. Hwang, M.T. McManus, A. Amsterdam, Y. Tian, R. Kalmukova, E. Mueller, T. Benjamin, B.M. Spiegelman, P.A. Sharp, N. Hopkins, M.B. Yaffe, TAZ, a transcriptional modulator of mesenchymal stem cell differentiation, *Science* 309 (2005) 1074–1078.
- [4] M. Murakami, M. Nakagawa, E.N. Olson, O. Nakagawa, A WW domain protein TAZ is a critical coactivator for TBX5, a transcription factor implicated in Holt–Oram syndrome, *Proc. Natl. Acad. Sci. U.S.A.* 102 (2005) 18034–18039.
- [5] K.S. Park, J.A. Whitsett, T.D. Palma, J.H. Hong, M.B. Yaffe, M. Zannini, TAZ interacts with TTF-1 and regulates expression of surfactant protein-C, *J. Biol. Chem.* 279 (2004) 17384–17390.
- [6] M.T. Bedford, D. Sarbassova, J. Xu, P. Leder, M.B. Yaffe, A novel Pro-Arg motif recognized by WW domains, *J. Biol. Chem.* 279 (2000) 10359–10369.
- [7] F. Kanai, P.A. Marignani, D. Sarbassova, R. Yagi, R.A. Hall, M. Donowitz, A. Hisaminato, T. Fujiwara, Y. Ito, L.C. Cantley, M.B. Yaffe, TAZ: a novel transcriptional co-activator regulated by interactions with 14-3-3 and PDZ domain proteins, *EMBO J.* 19 (2000) 6778–6791.
- [8] F. Hu, R.R. Subramanian, S.C. Masters, 14-3-3 proteins: structure, function, and regulation, *Annu. Rev. Pharmacol. Toxicol.* 40 (2000) 617–647.
- [9] J.H. Hong, M.B. Yaffe, TAZ, a b-catenin-like molecule that regulates mesenchymal stem cell differentiation, *Cell Cycle* 5 (2006) 176–179.
- [10] E.J. Jang, H. Jeong, J. Kang, N.J. Kim, M.S. Kim, S.H. Choi, S.E. Yoo, J.H. Hong, M.A. Bae, E.S. Hwang, Identification of TM-25659, a novel TAZ modulator that enhances osteogenic differentiation and suppresses adipogenic differentiation, *Br. J. Pharmacol.* DOI: 10.1111/j. 1476-5381.2011.01664.x.
- [11] N.R. Srinivas, Applicability of bioanalysis of multiple analytes in drug discovery and development: review of select case studies including assay development considerations, *Biomed. Chromatogr.* 20 (2006) 383–414.
- [12] G. Hopfgartner, E. Bourgoigne, Quantitative high-throughput analysis of drugs in biological matrices by mass spectrometry, *Mass Spectrom. Rev.* 22 (2003) 195–214.
- [13] S. Devanshu, M. Rahul, G. Annu, S. Kishan, N. Anroop, Quantitative bioanalysis by LC–MS/MS: a review, *J. Pharm. Biomed. Anal.* 7 (2010) 1–9.
- [14] T.A. Gillespie, B.E. Winger, Mass spectrometry for small molecule pharmaceutical product development: a review, *Mass Spectrom. Rev.* 30 (2011) 479–490.
- [15] R.W. Kondrat, G.A. McClusky, R.G. Cooks, Multiple reaction monitoring in mass spectrometry/mass spectrometry for direct analysis of complex mixtures, *Anal. Chem.* 50 (1978) 2017–2021.
- [16] N.S. Lee, E.H. Kerns, LC/MS applications in drug, *Mass Spectrom. Rev.* 18 (1999) 187–279.
- [17] Guidance for Industry, Bioanalytical Method Validation, US Department of Health and Human Services, Food and Drug Administration, Center for Drug Evaluation and Research (CDER), 2001.



Solid-state characterization of tacrine hydrochloride

Milena Sorrenti^{a,*}, Laura Catenacci^a, Giovanna Bruni^b, Barbara Luppi^c,
Federica Bigucci^c, Giampiero Bettinetti^a

^a Department of Drug Sciences, University of Pavia, V.le Taramelli, 12, 27100 Pavia, Italy

^b Department of Chemistry, University of Pavia, V.le Taramelli, 14, 27100 Pavia, Italy

^c Department of Pharmaceutical Science, University of Bologna, Via S. Donato, 19/2, 40127 Bologna, Italy

ARTICLE INFO

Article history:

Received 20 September 2011

Received in revised form

15 December 2011

Accepted 16 December 2011

Available online 25 January 2012

Keywords:

Tacrine monohydrochloride

Differential scanning calorimetry

Simultaneous thermogravimetric analysis

X ray powder diffractometry

Fourier transform infrared spectroscopy

ABSTRACT

The present study deals with the physicochemical characterization of solid forms of tacrine monohydrochloride (TCR), a centrally active reversible acetylcholinesterase inhibitor for treating the symptoms of mild to moderate Alzheimer's disease, obtained by recrystallization of hot saturated solutions from different solvents. Recrystallization of the commercially available hydrate, TCR·H₂O, from water, hydroalcoholic solutions with ethanol, n-propanol, methanol and isopropanol (1:1, v/v) and isopropanol/water (8:2, v/v) afforded a new dihydrate phase TCR·2H₂O form I. The TCR samples obtained by desolvation of TCR·H₂O and TCR·2H₂O show temperature and melting enthalpy values very similar, thus confirming the existence of a unique anhydrous crystalline phase.

Exposure of anhydrous TCR powder samples under different atmospheric conditions at room temperature, resulted in rehydration to TCR·H₂O at 32% relative humidity (RH), whereas at 100% RH a new solid form of TCR·2H₂O (TCR·2H₂O form II), i.e. a polymorph of the dihydrate isolated by recrystallization, was obtained.

Differential scanning calorimetry (DSC), simultaneous thermogravimetric analysis (TGA/DSC), and thermo optical analysis (TOA) with support from X-ray powder diffractometry (PXRD) and Fourier transform infrared spectroscopy (FT-IR), were used for the characterization of the isolated solid forms of TCR and monitoring the water uptake of anhydrous TCR.

© 2011 Elsevier B.V. All rights reserved.

1. Introduction

Characterization of the solid state of active pharmaceutical ingredients is one of the most important steps in drug development due to its implications in physical and physicochemical properties such as density, chemical stability, melting point, solubility, etc. that may significantly affect the performance of drug products. In this respect, the occurrence of polymorphism (i.e., crystalline forms with the same chemical composition but different arrangements and/or conformations of molecules in the crystal lattice), solvatomorphism (i.e., crystalline forms in which solvent molecules are included in the structure in stoichiometric or non-stoichiometric amounts) and amorphism (i.e., disordered arrangements of molecules in solids with no crystal structure) are to be considered for selecting the most suitable solid form of a drug to be transformed into a drug product [1–5]. In particular, incorporation of solvent molecules into a solid form influences the intermolecular interaction in the crystal structure with a

consequent modification of the thermodynamic activity and therefore the physicochemical and pharmaceutical properties. A drug solvate with a non-toxic organic solvent may exhibit a significantly higher solubility in aqueous media than the stable anhydrous form or an existing hydrate. So the isolation and solid-state characterization of hydrates or solvates has to be considered during preformulation studies as a possible strategy to enhance the dissolution rate and bioavailability of poorly water soluble drug [6].

Another aspect to be considered is the hydration or dehydration phenomena that can occur, sometimes unexpectedly, during the manufacturing processes or storage conditions of the final products as a consequence of drug exposition to different temperature and/or relative humidity (RH) conditions [7–10]. Upon dehydration crystal hydrates can transform either into a crystalline anhydrous form or a different hydrate form, retaining more or less their original crystal structure, or into an amorphous phase losing their original crystallinity. Since the formation of new hydrated solid phases may have a same impact on the bioavailability, toxicity and stability, as true polymorphism, the manufacture and characterization of hydrates is a part of the study of the physical properties of drug substances according to the International Conference on Harmonization (ICH) guidelines [11,12].

* Corresponding author. Tel.: +39 382 987372; fax: +39 382 422975.

E-mail address: milena.sorrenti@unipv.it (M. Sorrenti).

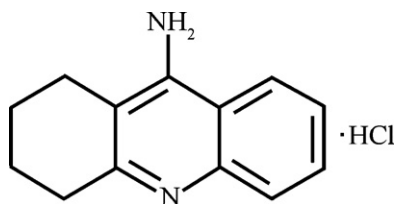


Fig. 1. Chemical structure of TCR-H₂O.

The centrally active reversible acetylcholinesterase inhibitor tacrine (1,2,3,4-tetrahydro-9-aminoacridine monohydrochloride, hereafter abbreviated as TCR) (Fig. 1) was the first drug approved by the United States Food and Drug Administration (FDA) in 1993 for treating the symptoms of mild to moderate Alzheimer's disease, the most common form of dementia [13]. The main rationale for use of TCR stems from the recognition that Alzheimer leads to degeneration of neurons, with a predilection for certain neuronal subgroups that are especially affected, i.e. neurons that release acetylcholine.

The official form listed in the USP 34 [14] is a monohydrate C₁₃H₁₄N₂·HCl·H₂O, MW 252.74 (TCR-H₂O), a pale yellow crystalline powder (mp 283–284 °C) readily soluble in water. Despite the favorable aqueous solubility, peroral administration of TCR-H₂O is associated with low bioavailability (i.e., 17%) [15]. Hence the search for alternative routes of TCR delivery such as transdermal [16,17] or, more recently, the nasal route deserves attention for a rapid drug delivery to the central nervous system [18,19].

This paper is aimed at isolating new solid forms of TCR, which is only known to exist as TCR-H₂O from previous reports [20,21].

The solid forms were prepared by recrystallization of commercial hydrate TCR from hot saturated solutions in different solvents since drug polymorphs and/or solvates can often be discovered just by changing the solvent system or the recrystallization conditions [4].

Moreover, because different solid forms of a drug can be isolated by rehydration of the desolvation products under controlled experimental conditions, the solvent adsorption of anhydrous TCR powder samples by exposure under different RH conditions at room temperature (RT) was investigated.

Differential scanning calorimetry (DSC), simultaneous thermogravimetric analysis (TGA/DSC), and thermo optical analysis (TOA) with support from X-ray powder diffractometry (PXRD) and Fourier transform infrared spectroscopy (FT-IR), were used for the characterization of the isolated solid forms of TCR.

2. Materials and methods

2.1. Materials

TCR-H₂O (1,2,3,4-tetrahydro-9-acridinamine monohydrochloride monohydrate) was purchased from Sigma Aldrich (Milan, Italy). All other materials and solvents used were of analytical reagent grade.

2.2. Sample preparation

Samples were prepared by recrystallization of commercial TCR-H₂O from solutions in the solvents and at the concentrations indicated in Table 1 at the respective boiling points. The solutions were filtered and allowed to recrystallize by spontaneously cooling to RT. The resulting crystals were filtered and dried in a desiccator containing P₂O₅. The solid-state forms of the crystals and the stoichiometry of the solvates were assessed by DSC and TGA/DSC (see below).

Commercial TCR-H₂O was sieved collecting the <250 μm granulometric fraction and dried in oven at 150 °C for 2 h to obtained

Table 1
TCR samples isolated by recrystallization from the tested solutions.

Solvent	mL per 1 g _{TCR}	Sample
Water	15	TCR·2H ₂ O form I
Ethanol	11	TCR·H ₂ O
Ethanol/water 1:1 (v/v)	6	TCR·2H ₂ O form I
Ethanol/water 8:2 (v/v)	5	TCR·H ₂ O
Methanol	4	TCR·H ₂ O
Methanol/water 1:1 (v/v)	10	TCR·2H ₂ O form I
Methanol/water 8:2 (v/v)	8	TCR·H ₂ O
Isopropanol	29	TCR·H ₂ O
Isopropanol/water 1:1 (v/v)	14	TCR·2H ₂ O form I
Isopropanol/water 8:2 (v/v)	9	TCR·2H ₂ O form I
n-Propanol	22	TCR·H ₂ O
n-Propanol/water 1:1 (v/v)	12	TCR·2H ₂ O form I
n-Propanol/water 8:2 (v/v)	11	TCR·H ₂ O

TCR anhydrous form. 1 g of each TCR anhydrous samples were uniformly distributed in a Petri dish and placed for variable period of time at RT (~22 °C) in a desiccator in which the RH of 32% was controlled by saturated solution of CaCl₂ [22]. Another desiccator contained a saturated water solution was used to generated RH of 100%.

Samples (10–15 mg) were taken out at appropriate intervals and checked for the solid phase composition by DSC and TGA/DSC (see below).

2.3. Methods

2.3.1. Differential scanning calorimetry (DSC)

Temperature and enthalpy values were measured with a Mettler STAR^e system (Mettler Toledo, Novate Milanese, MI, Italy) equipped with a DSC821^e Module and an Intracooler device for subambient temperature analysis (Julabo FT 900) on 2–3 mg (Mettler M3 Microbalance) samples in sealed aluminium pans with pierced lid ($\beta = 10 \text{ K min}^{-1}$, nitrogen air atmosphere (flux 50 mL min⁻¹), 30–350 °C temperature range). The instrument was preventively calibrated with Indium as standard reference. Measurements were carried out at least in triplicate.

2.3.2. Simultaneous thermogravimetric analysis (TGA/DSC)

Mass losses were recorded with a Mettler STAR^e system (Mettler Toledo, Novate Milanese, MI, Italy) TGA with simultaneous DSC (TGA/DSC1) on 3–5 mg samples in alumina crucibles with lid ($\beta = 10 \text{ K min}^{-1}$, nitrogen air atmosphere (flux 60 mL min⁻¹), 30–350 °C temperature range). The instrument was preventively calibrated with Indium as standard reference. Measurements were carried out at least in triplicate.

2.3.3. Thermo optical analysis (TOA)

Microscopic observation of the sample morphology and thermal events on heating ($\beta = 10 \text{ K min}^{-1}$, 30–300 °C temperature range) was performed under a Reichert (Arnsberg, Germany) polarized light microscope equipped with a Mettler FP82HT/FP80 system (Mettler Toledo, Novate Milanese, MI, Italy). Images were taken at different time intervals during heating with a MOTICAM 2000 video camera.

2.3.4. Powder X-ray diffractometry (PXRD)

PXRD patterns (CuK α , voltage of 40 kV and current of 30 mA) were collected with a Bruker D5005 powder diffractometer (Siemens, Germany) equipped with a θ - θ vertical goniometer and a position sensitive detector (PSD, Braun). The spectra have been recorded in the step scan mode (step: 0.015°, counting time: 0.5 s) in the angular range 5° < 2 θ < 30° at room temperature.

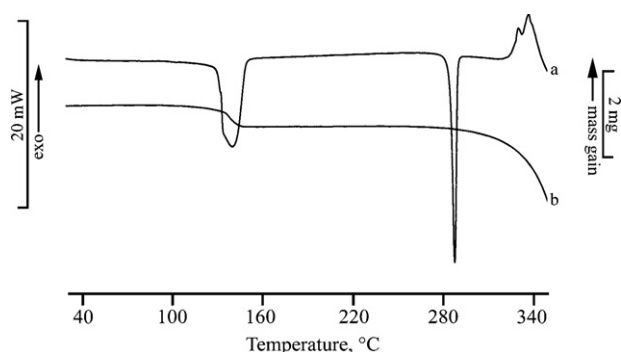


Fig. 2. DSC (curve a) and TGA (curve b) of commercial TCR·H₂O.

2.3.5. Fourier transform infrared spectroscopy (FT-IR)

Mid-IR (650–4000 cm⁻¹) spectra were recorded on powder samples using a Spectrum One Perkin-Elmer FT-IR spectrophotometer (resolution 4 cm⁻¹) (Perkin Elmer, Wellesley, MA, USA) equipped with a MIRacle™ ATR device (Pike Technologies, Madison, WI, USA).

2.3.6. Karl Fischer titrimetry (KFT)

The water content of the samples was determined with a Mettler DL40GP Memo titrator apparatus. Samples (60–70 mg) were quickly transferred to the titration vessel containing anhydrous methanol and titrated using Hydranal Composite 5 (Riedel-de Haen).

3. Results and discussion

DSC profile (Fig. 2, curve a) of the commercial product shows a couple of endothermic effects with a peak maximum temperature at $138 \pm 2^\circ\text{C}$ ($T_{\text{onset,des}} = 133 \pm 2^\circ\text{C}$, $\Delta H_{\text{des}} = 193 \pm 8 \text{ J g}^{-1}$) and $285.7 \pm 0.9^\circ\text{C}$ ($T_{\text{onset,m}} = 284.4 \pm 0.2^\circ\text{C}$, $\Delta H_{\text{m}} = 117 \pm 2 \text{ J g}^{-1}$) due to dehydration and melting of the anhydrous form, respectively. The exothermic effect at around 320°C was attributable to sample decomposition. TGA/DSC analysis of this sample (Fig. 2, curve b) revealed a weight loss of $6.6 \pm 0.4\%$ over the $110\text{--}170^\circ\text{C}$ temperature range, in agreement with the theoretical value for the TCR·H₂O (7.1%). The total weight loss beginning just after melting temperature in DSC confirmed thermal decomposition of the melted TCR.

Thermoanalytical characterization of the TCR samples recrystallized from different saturated solutions is illustrated in Fig. 3 (DSC curves up, and TGA curves down). The sample obtained from ethanol (Fig. 3, curve b) showed the same profiles as the TCR·H₂O, as well as the samples obtained by recrystallization from n-propanol (curve d) and ethanol:water 8:2 (v/v), methanol, methanol:water 8:2 (v/v), isopropanol and n-propanol:water 8:2 (v/v) (curves not shown). DSC curve of the sample isolated by recrystallization of commercial TCR·H₂O from water (Fig. 3, curve a) showed a two-step dehydration profile, with two distinct endothermic effects attributable to water losses with a peak maximum temperature at $84 \pm 1^\circ\text{C}$ ($T_{\text{onset,des,1}} = 79 \pm 1^\circ\text{C}$, $\Delta H_{\text{des,1}} = 120 \pm 4 \text{ J g}^{-1}$) and $152 \pm 2^\circ\text{C}$ ($T_{\text{onset,des,2}} = 141 \pm 5^\circ\text{C}$, $\Delta H_{\text{des,2}} = 193 \pm 9 \text{ J g}^{-1}$), respectively. The anhydrous dehydration product which melts at $285.1 \pm 0.4^\circ\text{C}$ ($T_{\text{onset,m}} = 282.3 \pm 0.9^\circ\text{C}$, $\Delta H_{\text{m}} = 107 \pm 4 \text{ J g}^{-1}$) was the same as that obtained by commercial TCR (see Fig. 2). TGA curve shows weight losses of $7.4 \pm 0.9\%$ and $5.5 \pm 0.6\%$, respectively, over the same temperature range of the endothermic effects in DSC, in reasonable agreement with the theoretical value for the loss of two water molecules for TCR molecule (TCR·2H₂O form I) (13.3%) (Fig. 3, curve a'). The same thermal profile was recorded for samples obtained by recrystallization from equivolumetric hydroalcoholic solutions with ethanol, n-propanol (Fig. 3, curves c, c' and e, e'),

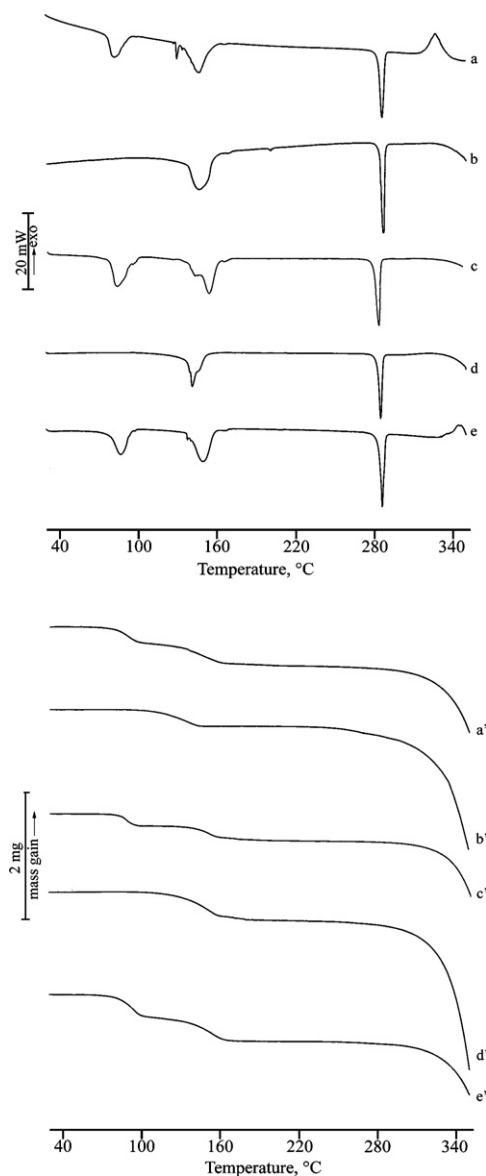


Fig. 3. DSC (up) and TGA (down) curves of commercial TCR recrystallized from water (a, a'), ethanol (b, b'), ethanol/water 1:1 (v/v) (c, c'), n-propanol (d, d'), n-propanol/water 1:1 (v/v) (e, e').

as well as, methanol, isopropanol and isopropanol/water 8:2 (v/v) (curves not shown).

The TGA curves of the samples obtained by recrystallization from ethanol and n-propanol (Fig. 3, curves b' and d') revealed the same weight loss of $7.2 \pm 0.4\%$, thus confirming the monohydrate nature of the isolated crystals.

The thermogravimetric and calorimetric data of all solid forms isolated by recrystallization from different solutions are collected in Table 2. Experimental data show that all the samples, mono or dihydrate, after dehydration converted into an anhydrous TCR solid form with similar calorimetric data, suggesting that, in these experimental conditions, was not possible to isolate new TCR forms.

The total percent mass loss recorded for each sample isolated in TGA analysis was in agreement with KFT data (see Table 2) confirming the solvent nature and the stoichiometry of the TCR hydrates.

The percent of mass loss measured over the TGA/DSC dehydration step ($\Delta m_s\%$) was related to the enthalpy change calculated

Table 2
Calorimetric data (up) and thermogravimetric data and water content by KFT (down) for samples obtained by recrystallization from different solvent solutions (standard deviations in parentheses).

Sample	Desolvation, step 1			Desolvation, step 2			Melting		
	T_{onset} (°C)	T_{peak} (°C)	ΔH_{des} (J g ⁻¹)	T_{onset} (°C)	T_{peak} (°C)	ΔH_{des} (J g ⁻¹)	T_{onset} (°C)	T_{peak} (°C)	ΔH_{m} (J g ⁻¹)
TCR recrystallized by									
Water	80(1)	84(1)	120(5)	141(5)	152(2)	193(9)	282(1)	285(1)	107(4)
Ethanol				140(1)	149(1)	157(8)	285(1)	287(1)	120(1)
Ethanol/water 1:1 (v/v)	73(7)	80(6)	154(8)	141(3)	150(4)	184(7)	282(2)	285(2)	107(7)
Ethanol/water 8:2 (v/v)				134(5)	149(2)	180(3)	283(2)	285(1)	112(5)
Methanol				139(7)	154(2)	159(9)	285(1)	288(1)	119(2)
Methanol/water 1:1 (v/v)	80(4)	85(6)	154(9)	147(9)	154(8)	184(9)	283(1)	286(1)	108(1)
Methanol/water 8:2 (v/v)				134(1)	143(2)	120(9)	284(1)	287(1)	116(1)
Isopropanol				140(4)	150(4)	150(9)	284(1)	286(1)	117(3)
Isopropanol/water 1:1 (v/v)	80(3)	85(1)	155(3)	140(3)	151(1)	182(7)	282(3)	287(1)	110(3)
Isopropanol/water 8:2 (v/v)	79(3)	86(5)	154(8)	141(2)	150(3)	181(9)	283(1)	285(1)	107(6)
n-Propanol				138(1)	145(6)	175(9)	283(1)	285(1)	116(1)
n-Propanol/water 1:1 (v/v)	73(8)	82(7)	133(9)	140(2)	150(2)	181(9)	283(1)	285(1)	107(6)
n-Propanol/water 8:2 (v/v)				142(4)	153(4)	165(4)	283(1)	285(1)	112(9)

Sample	Desolvation, step 1		Desolvation, step 2		Water content (%)	
	Mass loss (%)		Mass loss (%)		TGA	KFT
TCR recrystallized by						
Water	7.4(9)		5.5(6)		11.9(8)	14.7(3)
Ethanol			7.2(4)		7.2(4)	7.5(2)
Ethanol/water 1:1 (v/v)	6.9(9)		6.1(7)		13.0(9)	12.8(4)
Ethanol/water 8:2 (v/v)			7.1(6)		7.1(6)	6.9(2)
Methanol			7.1(4)		7.1(4)	7.1(2)
Methanol/water 1:1 (v/v)	7.6(6)		5.2(8)		12.8(8)	13.2(3)
Methanol/water 8:2 (v/v)			7.4(7)		7.4(7)	7.1(2)
Isopropanol			6.9(1)		6.9(1)	7.0(3)
Isopropanol/water 1:1 (v/v)	6.8(5)		6.1(4)		12.9(4)	13.4(5)
Isopropanol/water 8:2 (v/v)	7.6(9)		5.8(9)		13.4(9)	15.2(3)
n-Propanol			6.9(5)		6.9(5)	6.7(3)
n-Propanol/water 1:1 (v/v)	6.5(7)		6.0(9)		12.5(9)	13.4(4)
n-Propanol/water 8:2 (v/v)			6.8(1)		6.8(1)	6.9(1)

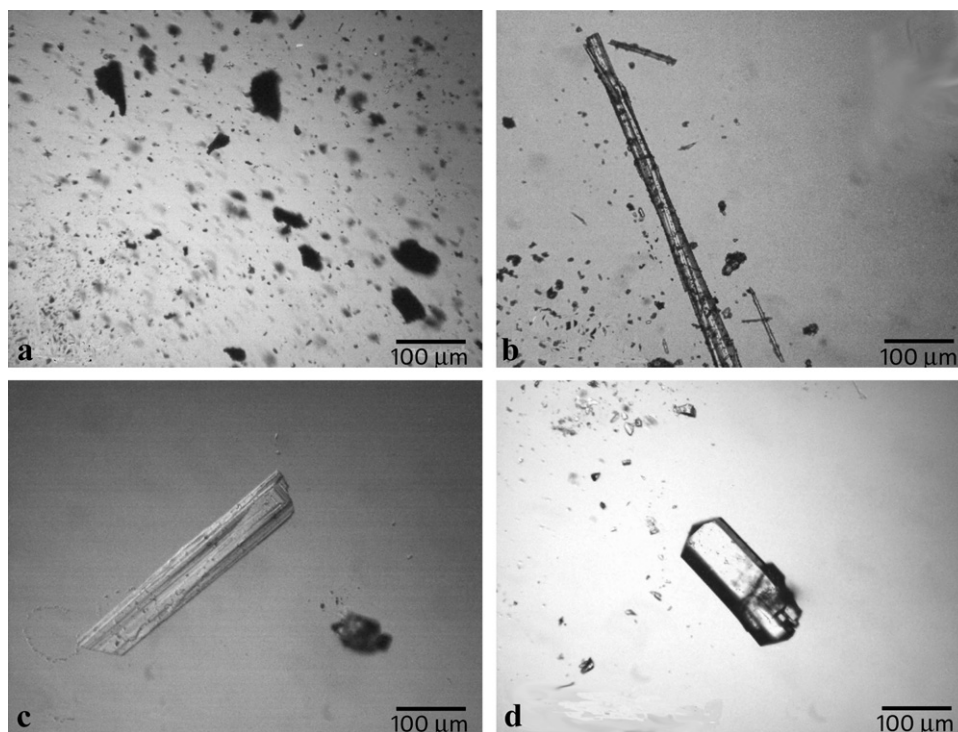


Fig. 4. Photomicrographs of commercial product (a) and crystals obtained by recrystallization of TCR from water (b), ethanol (c) and n-propanol (d).

over the corresponding DSC desolvation endotherm ($\Delta H_{S,exp}$, in $J g^{-1}$) as in Eq. (1):

$$\Delta H_S = \left[\frac{\Delta H_{S,exp} \times 100}{\Delta m_S\%} \right] M_S \quad (1)$$

where ΔH_S (in $J mol^{-1}$) is the heat of vaporization of the TCR bound solvent and M_S the molecular weight of water.

On comparison of the ΔH_S values collected in Table 3 with the heat of vaporization for the pure solvent (tabulated as a function of temperature [22]), an approximate evaluation of the water binding strength in the hydrate TCR crystals was possible.

In the monohydrate sample the heat of vaporization calculated was practically coincident with the heat of vaporization of pure water at 140 °C, although the higher onset temperature value indicated a stronger interaction of water molecule within the TRC host.

In the dihydrate crystals of TCR-2H₂O form I, instead, the presence of weakly bound solvent for the first water molecule was evident both from the lower desolvation onset temperature, as well as from the ΔH_S value, that indicated an about 23% lower interaction with the TCR host compared to heat of vaporization of pure water at 80 °C. For the second step of desolvation, the onset temperature was comparable to that of monohydrate but a heat of vaporization about 65% higher than that of pure solvent at 140 °C, indicated a stronger interaction for this second water molecule within the TCR host. Similar results are obtained for TCR-2H₂O form II (see the following discussion).

In Fig. 4 the photomicrographs of very small crystals of the commercial product (a) compared to TCR crystals obtained by recrystallization from water (b), ethanol (c) and n-propanol (d) are shown. These samples revealed larger dimensions and different morphologies, respectively, acicular, parallelepipedon and prismatic.

Photomicrographs of sample morphology modifications observed on heating TCR-H₂O (a) and TCR-2H₂O form I (b) immersed in silicon oil, are shown in Fig. 5.

The evolution of TCR hydrate microcrystals upon heating under ambient atmosphere from room temperature to 300 °C showed that the overall shape of the initial particle was preserved in both samples just before melting.

The observation of TCR-H₂O crystal showed the occurrence of solvent escape in the range of 150–160 °C followed by the melting of the anhydrous form until decomposition at 290 °C.

In the TCR-2H₂O form I crystal the first step of desolvation at 90 °C appeared as a browning of the crystal, whereas in the second step the solvent escape was evident as a bubbles flux at about 150 °C. The shape and the colour of the crystal were maintained just before melting with decomposition at 300 °C.

The distinct solid phases of the two crystalline hydrate forms of TCR with different stoichiometry were also confirmed by their PXRD patterns (Fig. 6). In particular, the PXRD pattern of TCR-H₂O obtained by recrystallization from ethanol (pattern b) matched the computer-generated pattern data from single-crystal X-ray analysis [20,21], as reference for TCR-H₂O crystalline phase (pattern a).

On the other hand the distinct PXRD pattern recorded for crystals obtained by recrystallization of commercial product from water (pattern c) give evidence for different structural arrangements in the hydrate phase as TCR-2H₂O form I.

By exposure of the anhydrous form of TCR (Fig. 7, curves a, a') to about 32% RH at RT, it was possible to demonstrate the gradual hydration of the anhydrous solid phase up to the complete transformation into the monohydrate form. The presence of the endothermal effect in the DSC curve corresponding to a mass loss in the TGA curve, was evident just after ten days of exposure (curves b, b') and went to completion after two months (curves d, d') with the

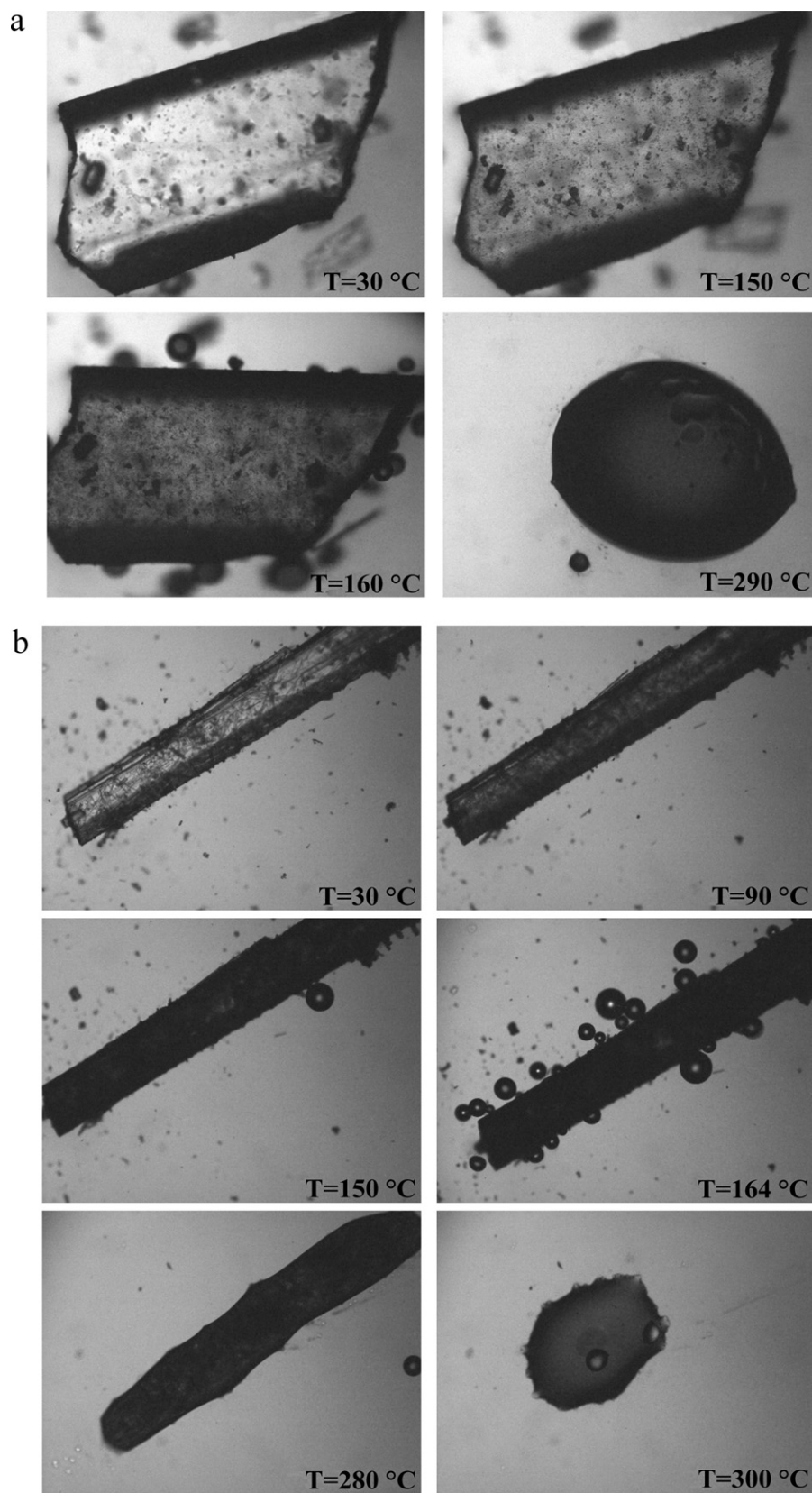


Fig. 5. Photomicrographs of TCR recrystallized from ethanol (a) and water (b) at various temperatures recorded by TOA.

Table 3
Thermogravimetric and Calorimetric data for TCR hydrates (standard deviations in parentheses).

Sample	Desolvation onset temperature T_{onset} (°C)	Desolvation enthalpy change $\Delta H_{\text{S,exp}}$ (J g^{-1})	Percent mass loss $\Delta m_{\text{S}}\%$	Heat of vaporization of the bound solvent ΔH_{S} (kJ mol^{-1})	Heat of vaporization of the pure solvent ΔH_{PS} (kJ mol^{-1}) ^a
TCR·H ₂ O	140(0)	156(8)	6.9(1)	39(4)	38.6
TCR·2H ₂ O	80(2)	120(4)	7.4(9)	32(3)	41.6
Form I	Step 2 141(5)	193(9)	5.5(6)	64(9)	38.6
TCR·2H ₂ O	Step 1 87(1)	152(9)	8.8(8)	31(3)	41.6
Form II	Step 2 134(1)	165(9)	4.2(4)	71(6)	38.6

^aHeat of vaporization of water tabulated as a function of temperature, 80 °C and 140 °C, respectively.

total transformation of anhydrous TCR into TCR·H₂O. The monohydrate nature of the sample powder was confirmed by PXRD (Fig. 8) where the pattern of the completely re-equilibrated sample (pattern c) was different from that of the initial anhydrous form (pattern a), but comparable to that of the monohydrate form obtained by recrystallization (see Fig. 6, pattern b). In the sample exposed to humidity for just twenty days, the rehydration of the powder was not completed and actually in the PXRD pattern some characteristic diffraction peaks of both the anhydrous and monohydrate forms were present (Fig. 8, pattern b).

Anhydrous TCR exposed to 100% RH absorbed higher water amounts, as can be seen by the two endothermic effects in DSC curves corresponding to distinct desolvation steps in TGA curves (Fig. 9).

Although the total mass loss of the sample after exposition for 40 days at 100% RH (Fig. 9, curves e and e') corresponded to that of the TCR·2H₂O form I obtained by recrystallization, the single effects attributable to dehydration ($T_{\text{onset,des,1}} = 87 \pm 1$ °C, $T_{\text{peak,des,1}} = 92 \pm 2$ °C, $\Delta H_{\text{des,1}} = 152 \pm 9 \text{ J g}^{-1}$, $\Delta m_{\text{des,1}} = 8.8 \pm 0.8\%$),

and $T_{\text{onset,des,2}} = 134 \pm 1$ °C, $T_{\text{peak,des,2}} = 143 \pm 4$ °C, $\Delta H_{\text{des,2}} = 165 \pm 9 \text{ J g}^{-1}$, $\Delta m_{\text{des,2}} = 4.2 \pm 0.4\%$) were different, and a possible isolation of a new dihydrate form (TCR·2H₂O form II) can be deduced.

This hypothesis was confirmed by PXRD. In Fig. 10 are reported the pattern recorded on the completely rehydrated sample (pattern b), which was different for diffraction peak positions from that of the anhydrous form (pattern a) such as from that of the TCR·2H₂O

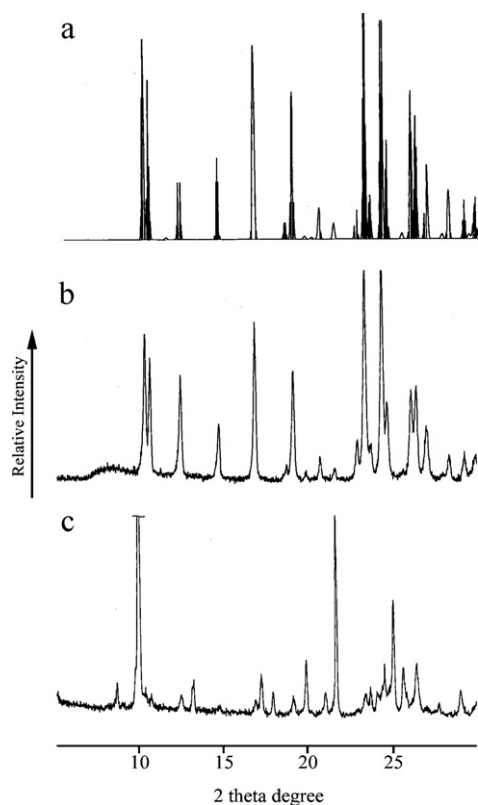


Fig. 6. Computer generated (a) and experimental PXRD patterns for TCR·H₂O (b) and experimental PXRD pattern for TCR·2H₂O form I (c).

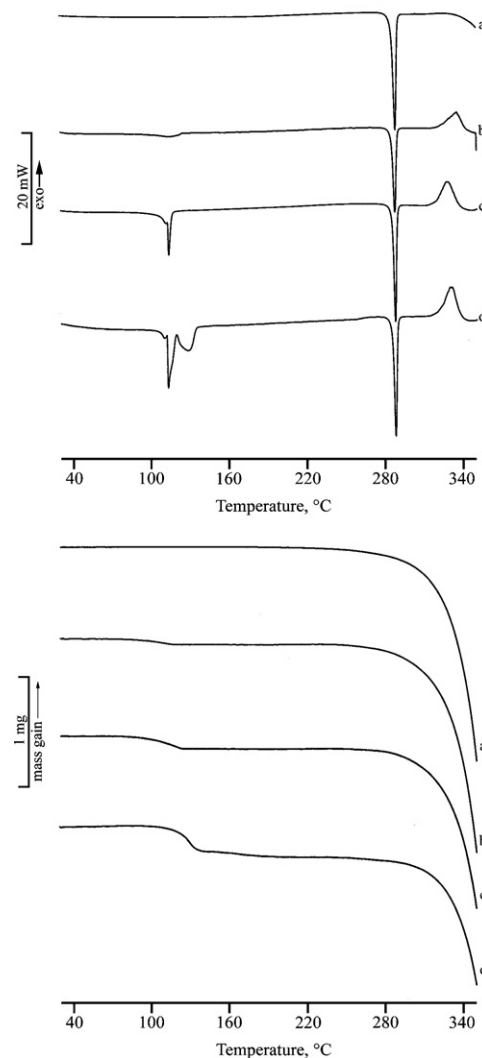


Fig. 7. DSC (top) and corresponding TGA (down) curves of TCR anhydrous form exposed to 32% RH at RT after times $t = 0$ (a, a'), $t = 10$ days (b, b'), $t = 20$ days (c, c') and $t = 60$ days (d, d').

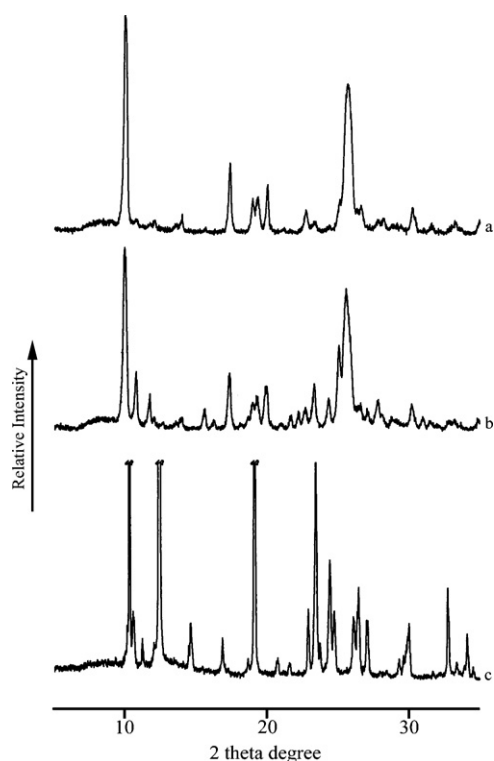


Fig. 8. PXRD patterns of TCR anhydrous form (a) and exposed to 32% RH at RT after times $t = 20$ days (b) and $t = 60$ days (c).

form I (Fig. 6, pattern c) confirming the existence of the new dihydrate phase.

The differences in the structure of the two dihydrate forms are evident also in FT-IR spectra that permit to be distinguished the new phase TCR·2H₂O form II from the TCR·2H₂O form I. In Fig. 11 are compared the FT-IR spectra of the commercial product (spectrum a), TCR·H₂O obtained by recrystallization from methanol (spectrum b), TCR·2H₂O form I (spectrum c) and TCR·2H₂O form II (spectrum d). The stretching bands in the N–H and O–H absorption region at 3400–2900 cm⁻¹ are very similar for the commercial and

Table 4
Transformation of the anhydrous TCR at different RH.

RH (32%)	Sampling time	Gain in weight (%)	
	6 d ^a	0.10	
	8 d	0.65	
	10 d	0.83	
	13 d	1.06	
	20 d	2.60	
	26 d	3.24	
	35 d	4.93	
	40 d	5.47	
	60 d	6.27	
	90 d	6.25	
RH (%)	Sampling time	Gain in weight (%)	
100		Step 1	Step 2
	0.5 h ^b	6.67	–
	1 h	2.74	5.41
	4 h	3.84	5.06
	24 h	6.51	6.44
	7 d	7.46	6.46
	20 d	8.28	3.71
	40 d	9.41	3.08
	90 d	9.45	3.32

^a d, days.

^b h, hours.

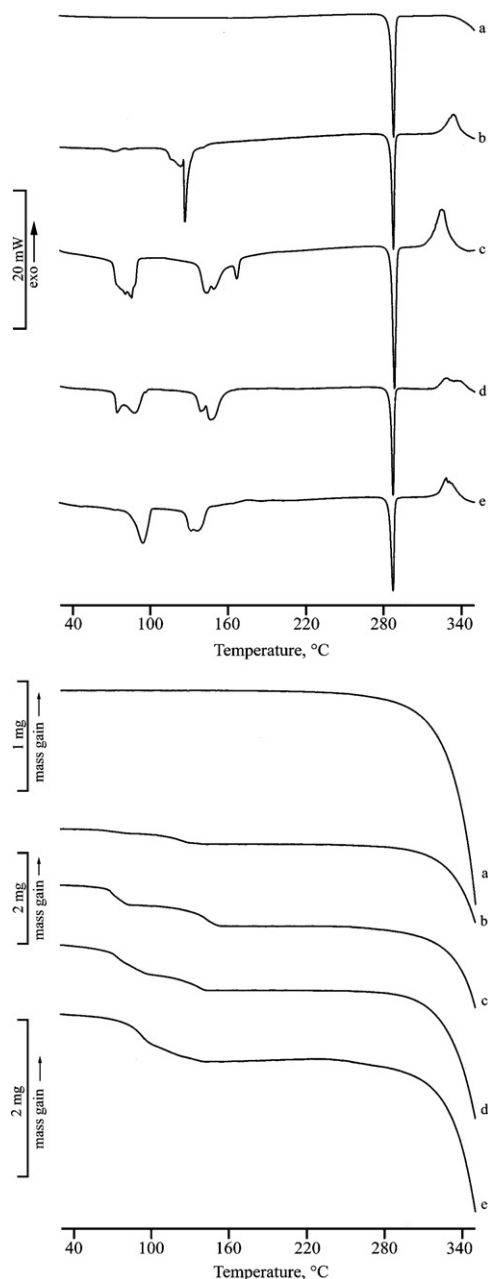


Fig. 9. DSC (top) and corresponding TGA (down) curves of TCR anhydrous form exposed to 100% RH at RT after times $t = 0$ (a, a'), $t = 1$ h (b, b'), $t = 24$ h (c, c'), $t = 20$ days (d, d') and $t = 40$ days (e, e').

monohydrate samples but different from those of the dihydrate forms. Shifts of the bands at 3151–3186 cm⁻¹ and 2946–2957 cm⁻¹ in the TCR·2H₂O form I and in the TCR·2H₂O form II spectra, respectively, can be related to different arrangements of the water molecules in the dihydrate structures.

The transformation of the anhydrous TCR into the various hydrate forms is schematically summarized in Table 4. For every RH conditions are reported the progressive percent mass gain until the equilibrium was reached. After six months in atmosphere conditions the equilibrated samples had already the same water content (by TGA analyses) confirming their solid state stability.

Unfortunately, until now, in our experimental conditions was not possible to isolate crystals of TCR·2H₂O suitable to single X-ray analysis to solve the structures.

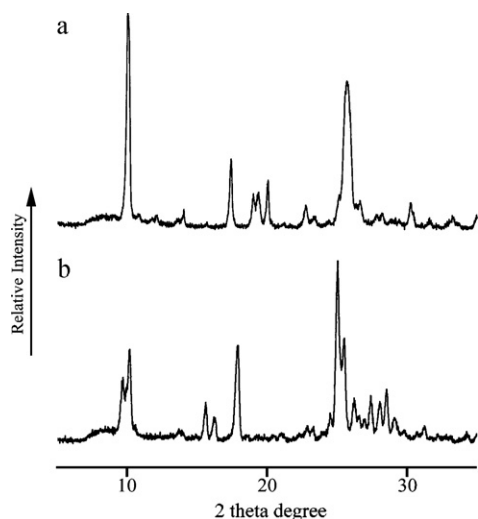


Fig. 10. PXRD patterns of TCR anhydrous form (a) and after exposition to 100% RH at RT for 40 days (TCR·2H₂O form II) (b).

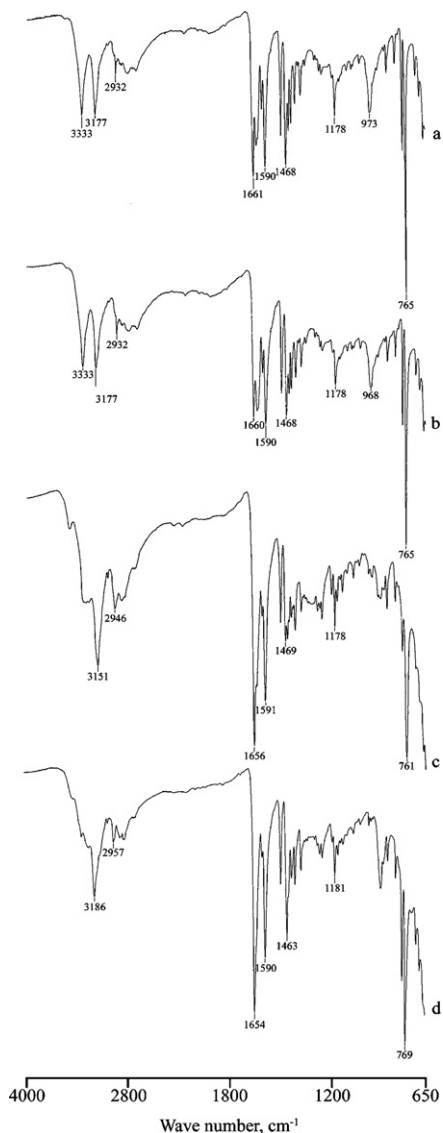


Fig. 11. FT-IR spectra for commercial TCR (a), TCR·H₂O (b), TCR·2H₂O form I (c) and TCR·2H₂O form II (d).

4. Conclusions

TCR recrystallized by different solvents (i.e. ethanol, n-propanol, methanol, isopropanol and isopropanol:water 8:2 (v/v)) was isolated as the same commercially available monohydrate crystal form (TCR·H₂O). A new hydrate phase with two molecules of solvent for one molecule of TCR (TCR·2H₂O form I) was obtained by recrystallization of TCR from water, hydroalcoholic solutions with ethanol, n-propanol, methanol and isopropanol (1:1, v/v) and isopropanol:water 8:2 (v/v). Desolvation studies of all samples, mono and dihydrates, demonstrated the absence of polymorphism for desolvated TCR, thus confirming the existence of a unique anhydrous solid phase.

A polymorphic form of dihydrate TCR (TCR·2H₂O form II) was isolated by exposure of anhydrous TCR at 100% RH at RT.

This kind of studies is relevant from the viewpoint of drug formulation design because the anhydrous form stability under ambient conditions has implications at both technological and biopharmaceutical levels, due to the less favorable dissolution rate and bioavailability of hydrate with respect to the corresponding anhydrous form.

References

- [1] R. Hilfiker, F. Blatter, M. Von Raumer, Relevance of solid-state properties for pharmaceutical products, in: R. Hilfiker (Ed.), *Polymorphism in the Pharmaceutical Industry*, Wiley-VCH, Germany, 2006, pp. 1–19.
- [2] H.G. Brittain, *Polymorphism and solvatomorphism* 2009, *J. Pharm. Sci.* 100 (2011) 1260–1279.
- [3] J. Lu, S. Rohani, *Polymorphism and crystallization of the active pharmaceutical ingredients (APIs)*, *Curr. Med. Chem.* 16 (2009) 884–905.
- [4] J. Aaltonen, M. Allesø, S. Mirza, V. Koradia, K.C. Gordon, J. Rantanen, *Solid form screening – a review*, *Eur. J. Pharm. Biopharm.* 71 (2009) 23–37.
- [5] N. Chieng, T. Rades, J. Aaltonen, *An overview of recent studies on the analysis of pharmaceutical polymorphs*, *J. Pharm. Biomed. Anal.* 55 (2011) 618–644.
- [6] U.J. Griesser, *The importance of solvates*, in: R. Hilfiker (Ed.), *Polymorphism in the Pharmaceutical Industry*, Wiley-VCH, Germany, 2006, pp. 211–233.
- [7] D. Giron, C. Goldbronn, M. Mutz, S. Pfeffer, P. Piechon, P. Schwab, *Solid-state characterizations of pharmaceutical hydrates*, *J. Therm. Anal. Calorim.* 68 (2002) 453–465.
- [8] S. Nordhoff, J. Ulrich, *Solvent-induced phase transformation of hydrates*, *J. Therm. Anal. Calorim.* 57 (1999) 181–192.
- [9] M.R. Caira, G. Bettinetti, M. Sorrenti, L. Catenacci, *Relationships between structural and thermal properties of anhydrous and solvated crystalline forms of bromidoprim*, *J. Pharm. Sci.* 96 (2007) 996–1007.
- [10] G. Bettinetti, M.R. Caira, M. Sorrenti, L. Catenacci, M. Ghirardi, L. Fábán, *Thermal studies of solvent exchange in isostructural solvates of a tetraoxoprim-sulfametrole complex*, *J. Therm. Anal. Calorim.* 77 (2004) 695–708.
- [11] *International Conference on Harmonization (ICH) Guideline Q6A, Test procedures and acceptance criteria for new drug substances and new drug products: chemical substances*, vol. 65, Federal Register: December 29, 2000.
- [12] D. Giron, M. Mutz, S. Garnier, *Solid-state of pharmaceutical compounds. Impact of the ICH Q6 guideline on industrial development*, *J. Therm. Anal. Calorim.* 77 (2004) 709–747.
- [13] W.K. Summers, *Tacrine and Alzheimer's treatments*, *J. Alzheimers Dis.* 9 (2006) 439–445.
- [14] *The United States Pharmacopeia Monographs*, 34th ed., National Formulary 29, 2011.
- [15] K.L. Davis, P. Powchik, *Tacrine*, *Lancet* 345 (1995) 625–630.
- [16] G. Sathyan, W.A. Ritschel, A.S. Hussain, *Transdermal delivery of tacrine: identification of suitable delivery vehicle*, *Int. J. Pharm.* 114 (1995) 75–83.
- [17] T. Kankkunen, R. Sulkava, M. Vuorio, K. Kontturi, J. Hirvonen, *Transdermal iontophoresis of tacrine in vivo*, *Pharm. Res.* 19 (2002) 705–708.
- [18] V.V. Jogani, P.J. Shah, P. Mishra, A.K. Mishra, A.R. Misra, *Nose-to-brain delivery of tacrine*, *J. Pharm. Pharmacol.* 59 (2007) 1199–1205.
- [19] B. Luppi, F. Bigucci, G. Corace, A. Delucca, T. Cerchiara, M. Sorrenti, L. Catenacci, A.M. Di Pietra, V. Zecchi, *Albumin nanoparticles carrying cyclodextrins for nasal delivery of the anti-Alzheimer drug tacrine*, *Eur. J. Pharm. Sci.* 44 (2011) 559–565.
- [20] D.E. Zacharias, J.P. Glusker, *9-Amino-1,2,3,4-tetrahydroacridine hydrochloride monohydrate (THA-HCl)*, *Acta Crystallogr. C* 44 (1988) 1656–1658.
- [21] G. Bandoli, A. Dolmella, S. Gatto, M. Nicolini, *Solid-state structures and conformational studies of four 1,2,3,3-tetrahydroacridine Alzheimer's disease therapeutics*, *J. Chem. Crystallogr.* 24 (1994) 301–310.
- [22] *Handbook of Chemistry and Physics*, D.R. Lide, Editor in Chief, 84th ed., CRC Press, 2003–2004, section 6.



Separation and identification of degradation products in eprinomectin formulation using LC, LTQ FT-MS, H/D exchange, and NMR

Atul Awasthi^a, Majid Razzak^b, Raida Al-Kassas^a, David R. Greenwood^c, Joanne Harvey^d, Sanjay Garg^{a,*}

^a School of Pharmacy, The University of Auckland, Private Bag 92019, Auckland, New Zealand

^b Ancare Scientific Ltd, Auckland, PO Box 36240, Northcote, Auckland 0748, New Zealand

^c School of Biological Sciences, The University of Auckland, Private Bag 92019, Auckland, New Zealand

^d School of Chemical and Physical Sciences, Victoria University of Wellington, PO Box 600, Wellington, New Zealand

ARTICLE INFO

Article history:

Received 15 October 2011

Received in revised form

26 December 2011

Accepted 26 December 2011

Available online 28 January 2012

Keywords:

Eprinomectin degradation products

High resolution FT-MS and MSⁿ

H/D exchange

NMR

Geometric and structural isomers

ABSTRACT

The aim of this study was to evaluate the suitability of the compendial active pharmaceutical ingredient (API) method for the analysis of finished products and characterization of degradation products in eprinomectin (EPM) samples. Heat stressed sample tests revealed a limitation of the API method in distinguishing an impurity merging with the principal analyte peak. A new selective, specific and sensitive method was therefore developed for the determination of EPM in formulations that separates its degradation products currently undetectable with the official method. The determination was carried out by reversed-phase HPLC using an isocratic solvent elution. The method was validated and found to be precise, accurate and specific; the detector response was linear over 50–150 µg/ml (EPM) and 0.1–3 µg/ml (degradation product) range of concentrations.

Two major degradation products detected with the new method were isolated from sample matrices and characterized using LC-PDA, high resolution FT-ICR MS, NMR and hydrogen/deuterium exchange (HX-MS) studies. FTMS analysis showed accurate mass of molecular ion peaks for EPM and its two degradation products at m/z 914.52505 (mass error ≤ 1 ppm) with almost identical fragmentation patterns. Given the isomeric nature of the compounds, all three were further evaluated by ¹H, ¹³C, 1D NOESY and 2D (COSY) NMR experiments. The interpretation of experimental data positively identified Unknown 1 as the 2-epimer of EPM and Unknown 2 as the structural isomer Δ 2,3-EPM containing a conjugated enoate. The new HPLC method and identification exercise is useful for analysis of EPM and its degradation products.

© 2012 Elsevier B.V. All rights reserved.

1. Introduction

Eprinomectin (EPM) [(4R)-4-(acetylamino)-4-deoxy-avermectin B1] belongs to a group of compounds known as the avermectins (AVMs), and is commercially available as a mixture of two closely related homologues (see Fig. 1), EPM B1_a (>90%; M.W.: 914.13) with EPM B1_b (<10%; M.W.: 900.10) [1,2]. It is currently licensed for the treatment of a broad spectrum of endo- and ectoparasites of cattle such as gastrointestinal roundworms, lungworms, lice, grubs and mange mites [3] and has a zero slaughter withdrawal and milk discard [4,5].

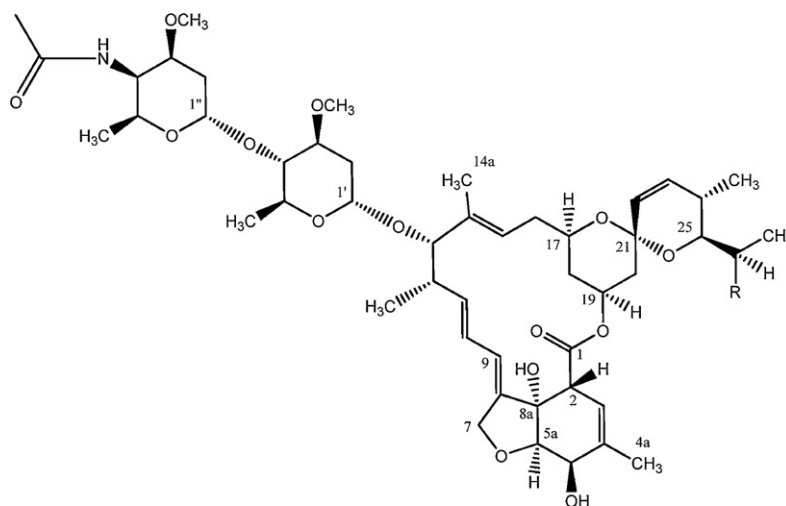
The avermectins have a 16-membered macrocyclic ring and contain a spiroketal group, a benzofuran ring and a modified disaccharide attached via a glycosidic linkage [6]. EPM is obtained by chemical modification of abamectin (ABM) [7,8].

There are a number of reports published on the High Performance Liquid Chromatography (HPLC) analysis of EPM in environmental, food, milk and other matrices using different extraction and detection methods. A comprehensive methodology review by Danaher on macrocyclic lactones (ML) outlines details of commonly used techniques for analysis of the AVMs, including EPM [9]. In general, EPM is detected by reverse phase chromatography using an ODS column. However, none of the published work was carried out to determine the degradation products (DPs) of EPM in pharmaceutical preparations.

As EPM is an active pharmaceutical ingredient (API), a United States Pharmacopeia (USP) method is available for its assay and analysis of related substances [2]. But it is known that API methods are not necessarily suitable for the analysis of finished products due to the interactions of excipients and vehicles with the drug molecules themselves. Hence, there was a need to evaluate the suitability of the API pharmacopeial EPM method for the finished product, and if deemed unsuitable, then to develop and validate an alternative/supplementary method for the EPM assay and DPs in finished products. Since no EPM impurity reference standards

* Corresponding author. Tel.: +64 9 923 2836; fax: +64 9 367 7192.

E-mail address: s.garg@auckland.ac.nz (S. Garg).



R = CH₂CH₃ : C₅₀H₇₅NO₁₄ (component B1_a), Mol. wt. 914.13,
 R = CH₃ : C₄₉H₇₃NO₁₄ (component B1_b), Mol. wt. 900.10.

Fig. 1. Chemical structure and molecular formula of EPM (B1_a & B1_b).

are available, the major DPs require further identification and characterization using HPLC, mass spectrometry (MS) and nuclear magnetic resonance (NMR) spectroscopy techniques.

Several MS methods for confirmation of AVM drugs, including EPM, in biological and environmental samples have been published. Ballard et al. have used LC–MS/MS method to confirm EPM marker residues in biological samples [10]. The Danaher review discussed detection systems for the determination of AVMs and their residues with a particular emphasis on new developments in screening technologies [9,11]. Despite an increase in analytical papers using LC–MS/MS for the determination of AVMs in environmental and food samples, there has been a general lack of detailed published reports targeting high end approaches such as high resolution FT-ICR MS accurate mass determination, multistage mass fragmentation and mechanistic pathway analysis, H/D exchange [12,13] and use of *in silico* approaches for EPM analysis and quantitation.

Overall, there are no specific reports detailing analysis of EPM and its DPs in finished products using LC and high resolution MS. Therefore, the aim of the present work is to evaluate the USP HPLC method against a newly developed method for the separation and characterization of EPM and its major DPs in formulations. Furthermore, this study also aims to identify and characterize DPs using LC, FT-MS, HX-MS, and NMR techniques. Structure elucidation using comparative studies of MS data and the establishment of degradation pathway/mechanism of decomposition highlighted by the determinative method, are proposed.

2. Materials and methods

2.1. Chemicals

EPM (Zhejiang Hisun Pharmaceutical Co. Ltd., Taizhou, China) was kindly given by Ancare Scientific Ltd (Auckland, New Zealand). The base catalyzed DPs of EPM were generated and purified in-house. HPLC grade methanol (MeOH) and acetonitrile (ACN) were purchased from Merck (Darmstadt, Germany). Deuterated chloroform (CDCl₃) with 0.03%, v/v TMS (D, 99.8%) was supplied by Cambridge Isotope Laboratories Inc. (Andover, MA, USA). All other analytical reagent grade chemicals were purchased from Ajax Fine Chem (Auckland, New Zealand). Ultrapure water (H₂O) was

obtained from a Purelab Ultra water system (ELGA LabWater, High Wycombe, Bucks, UK).

2.2. Apparatus and equipment

2.2.1. HPLC set-up

HPLC analysis of samples were performed using a LC20 series HPLC system (Shimadzu Inc., Kyoto, Japan), equipped with an DGU-20A5 on-line degasser, LC-20AT low-pressure quaternary pump, SIL-20AC auto-injector, CTO-20AC thermostated column compartment and SPD-20A UV–Vis detector. For data acquisition and processing, LCsolutions (v 6.7) software was used. Photodiode array (PDA) experiments and method validation were performed on an Ultimate 3000 Liquid Chromatographic system (Dionex Corporation, Idstein, Germany) equipped with an on-line degasser, gradient pump, auto-injector, thermostated column compartment and PDA detector (all Ultimate 3000 modules). For data acquisition and processing, Chromeleon (v 6.8) software was used.

2.2.2. Mass spectrometry (MS)

Commercial EPM as well as synthesized DPs were dissolved in diluent (H₂O:MeOH:ACN 25:25:50, v/v/v) at concentrations of 1 µg/ml, and analyzed by positive ion electrospray ionization (ESI), on a high resolution LTQ FT-ICR mass spectrometer (Thermo Scientific, San Jose, CA, USA) with a detection accuracy ≤ 2 ppm [14]. Samples were introduced into the mass spectrometer by means of a syringe, infused at a flow rate of 3 µl/min. The source voltage was set to 3.80 kV, to maintain a source current of ~4.60 µA, the sheath gas and auxiliary gas flow rates were set to 10 and 2 units respectively, the capillary temperature was 275 °C and the tube lens voltage was set to 90 V. Collision-induced dissociation (CID) using He was set at a value of 35% collision energy for fragmentation of analytes. Instrument control and data collection were handled by Xcalibur (v 2.0.7 SP1) software. The system was calibrated prior to analysis of the test samples. *In silico* evaluation of MS data was carried out on HiChem Mass Frontier™ (v 5.1), and ACD/MS Manager™ (v 12).

2.2.3. H/D-exchange experiments

The exchange of labile hydrogen atoms of EPM and DPs by deuterium atoms was carried out by preparing a 100 µg/ml solution in chloroform, and then incubation of 100× diluted solution with

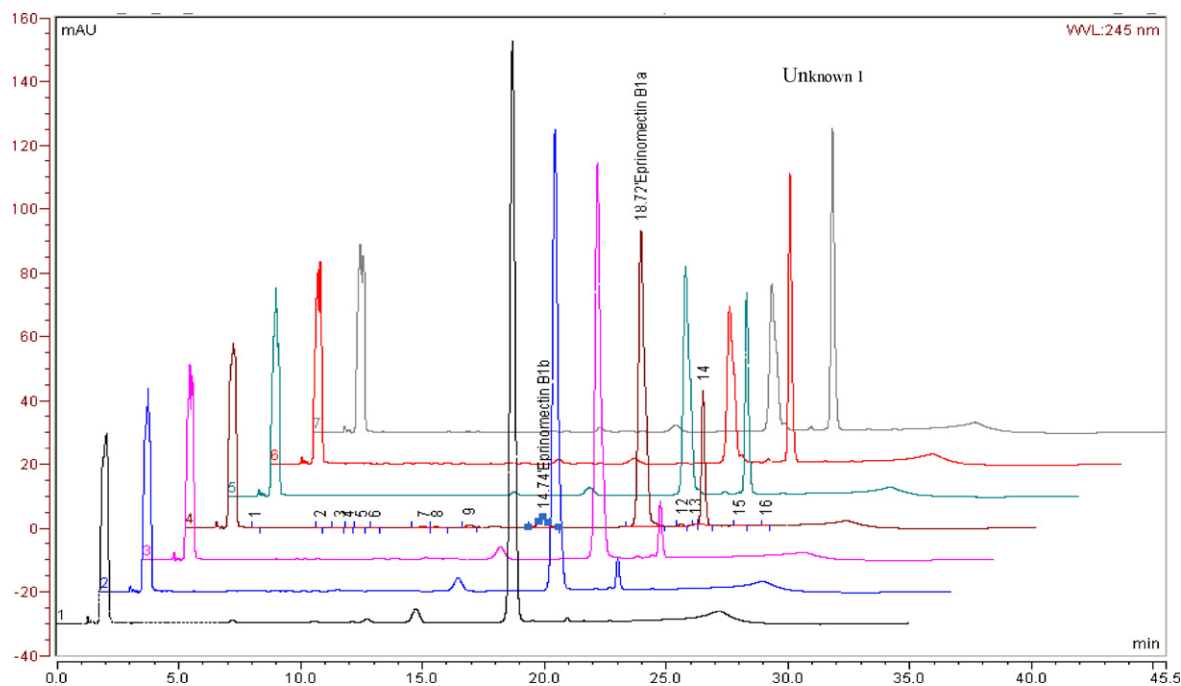


Fig. 2. EPM heat-stress study sample chromatogram using the USP method: (1) day-0, (2) day-5, (3) day-10, (4) day-20, (5) day-30, (6) day-40, and (7) day-50.

deuterating agent (10 ml of methanol and deuterium oxide 9:1, v/v with 5 mM ammonium acetate, pH 7.2) for 15 min at room temperature. The resulting solution was quickly cooled in a dry ice/ethanol bath, and then the reaction was quenched by addition of 100 μ l formic acid with further cooling for 5 min. The final samples were immediately infused directly into the ESI FT-MS system.

2.2.4. NMR spectroscopy

The ^1H , ^{13}C , 1D NOESY and 2D experiments (^1H - ^1H COSY) were carried out on 1 mg/ml solutions of EPM and DPs in CDCl_3 , on an Avance III 400 NMR spectrometer (Bruker BioSpin GmbH, Rheinstetten, Germany) using ICON-NMR real-time software. The

evaluation of data was carried out with Bruker-Topspin (v 2.1) and MestReNova (v 6.2.1-7569) Software.

2.2.5. Isolation and purification of degradation products

Isolation of DPs from finished products was carried out on a semi-preparative flash chromatographic system connected with an UV monitor, and an external pump (Ecom Ltd, Prague, Czech Republic). The pure compounds were recovered *in vacuo*, using a rotary evaporator system.

2.2.6. Other equipment

During the development and validation process, samples were heat stressed at 70 °C in a fully calibrated Therмотec 2000 oven

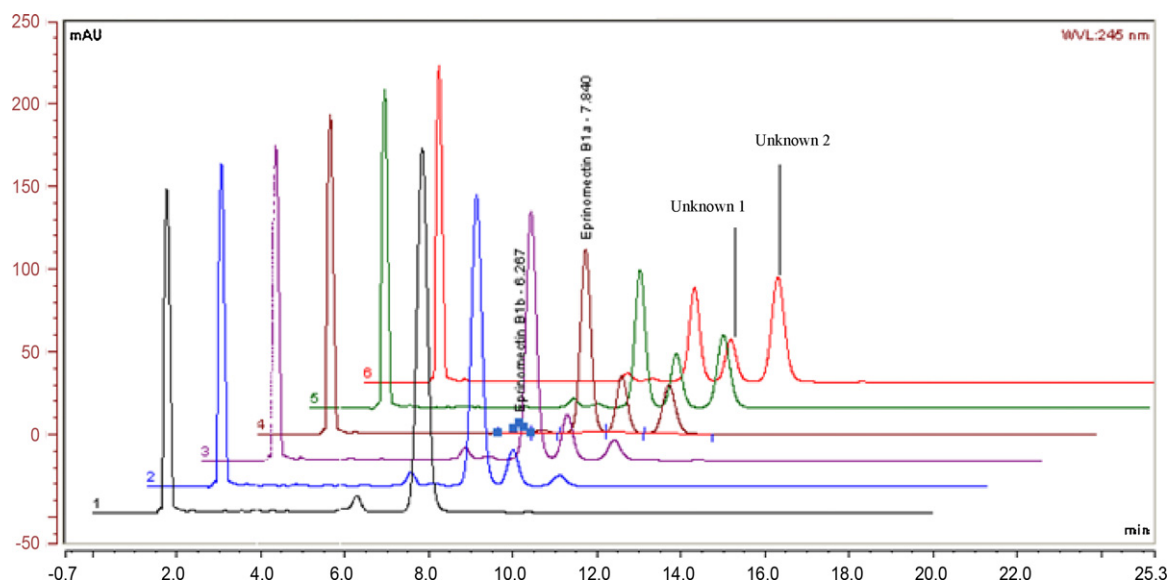


Fig. 3. EPM heat-stress study sample chromatogram (new method): (1) day-0, (2) day-5, (3) day-10, (4) day-20, (5) day-30, (6) day-40, and (7) day-50.

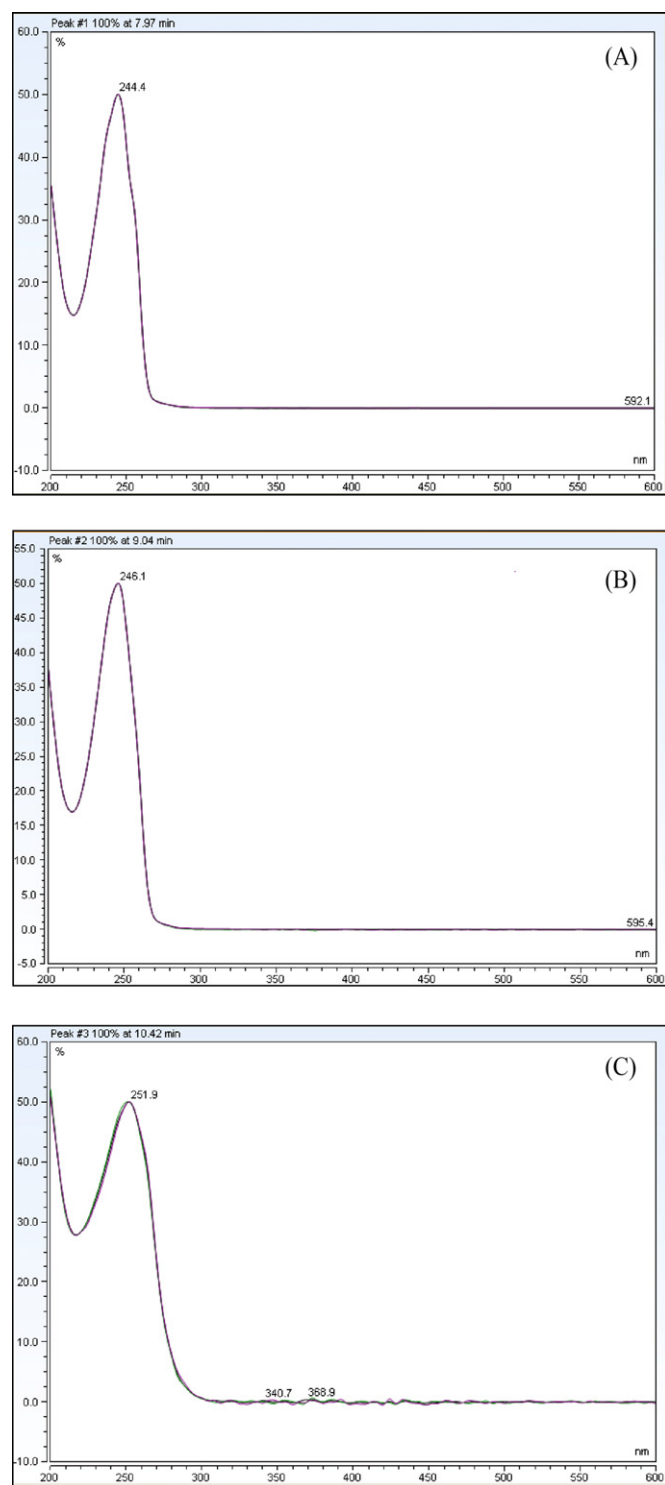


Fig. 4. UV spectrum and λ_{\max} values for (A) EPM B1_a, (B) Unknown 1, and (C) Unknown 2.

(Contherm Scientific Ltd, Petone, New Zealand). The pH of solutions was measured by a Cyberscan 510 pH meter (Eutech Instruments, Singapore).

2.3. HPLC methods

2.3.1. EPM USP HPLC method

The EPM assay and DP analysis of stress study samples were carried out using the specified reverse phase liquid

chromatography method [2]. Separation of compounds was achieved using a Zorbax C8, 250 mm \times 4.6 mm i.d., particle size 5 μ m, HPLC column (Agilent Technologies, Santa Clara, CA, USA). A mobile phase gradient consisting of solution A (0.1%, v/v perchloric acid solution), and solution B (100% ACN) was eluted at a flow rate of 1.5 ml/min through the column maintained at 40 °C. During the gradient programme, the composition of solution A and B was kept isocratic at 45%:55% for the first 15 min, followed by a linear change of solution B to 95% over 5 min, and then back to the original composition over the next 5 min. The system was equilibrated for another 5 min before the next injection was made. UV detection was performed at a wavelength of 245 nm.

Analytical standard and sample solutions were prepared in diluent (20% H₂O in MeOH) at a concentration of 100 μ g/ml of EPM; the injection volume was 20 μ l.

2.3.2. Alternate HPLC method

A new method was developed based on the ivermectin USP method [2] with further modifications to suit a fast and isocratic separation of EPM and its degradation peaks in stress study samples.

Chromatographic separations were achieved on a Prodigy ODS3, 150 mm \times 4.6 mm i.d., particle size 5 μ m, HPLC column (Phenomenex Inc., Torrance, CA, USA). An isocratic mobile phase consisting of H₂O/MeOH/ACN (27:25:48, v/v/v) at a flow rate of 1.5 ml/min was pumped through the column maintained at 40 °C monitoring the eluate at 245 nm. The standard and sample preparations were kept the same way as described in Section 2.3.1.

3. Results and discussion

3.1. USP method

EPM standard and test samples were prepared as described in Section 2.3.1. The chromatogram of reference standard solution showed adequately separated principal peaks EPM B1_a (RT 18.65 min) and EPM B1_b (RT 14.73 min). This method was then used for the analysis of EPM formulation samples under stress. The study involved heat stressing 1%, w/v EPM solutions in dimethylformamide (DMF) at 70 °C (detailed discussion of the stress study will be reported elsewhere). HPLC analysis performed at 0, 5, 10, 20, 30, 40 and 50 days showed an impurity at relative retention time (RRT) 1.10, continuously increasing with time. The principal analyte peak EPM B1_a in chromatograms from the initial study phase was clean, but after day 20 in the heat stress study, broadening became evident. From day 30 to day 50, broadening of the EPM B1_a peak in sample chromatograms becomes very obvious and consequently raised the question of the suitability of the USP method for finished product analysis. The representative chromatograms of various days are shown in Fig. 2.

3.2. Development of alternative HPLC method

The EPM reference standards and stress study solutions used for the USP method were again analyzed using the newly developed method to achieve a short run time using a reverse phase isocratic elution with adequate separation of principal peaks as well as potential DPs (see Section 2.3.2 for detailed chromatographic condition). The standard preparation showed distinctly separated principal peaks *i.e.* EPM B1_a (RT 7.9 min), and EPM B1_b (RT 6.0 min). Interestingly, a new DP peak emerged (in addition to one DP peak earlier seen with USP method) after the EPM B1_a peak in chromatograms, and was noticed growing from day 10 to day 50 stress study samples. These two major degradation peaks (Unknown 1 and Unknown 2) were adequately separated with acceptable resolution from adjacent peaks as shown in Fig. 3.

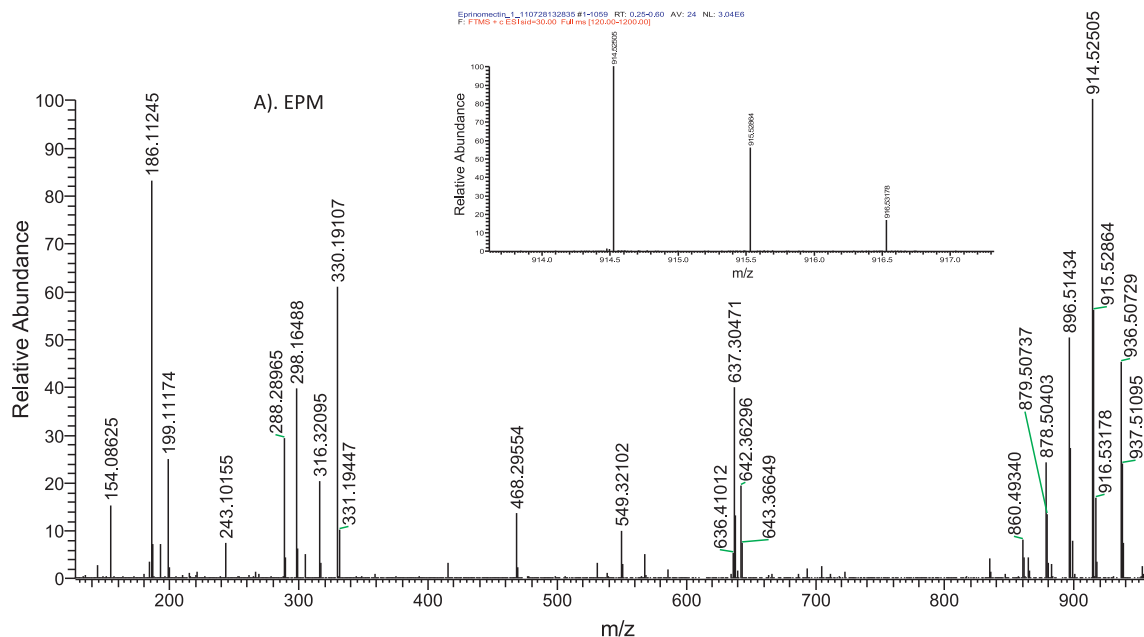
Using the new HPLC method therefore, EPM and DP peaks are well separated. The resolution factors for Unknown 1 and Unknown 2 were both >1 . The peaks were found to be pure and ultraviolet (UV) spectrum λ_{\max} values for EPM B1_a and Unknown 1 peaks were 245 ± 1 nm, whilst the Unknown 2 λ_{\max} was 252 ± 1 nm (see Fig. 4). EPM and Unknown 1 showed identical UV absorption, indicate this DP was merging with the principal peak when samples were analyzed using the USP method and HPLC purity analysis was unable to differentiate co-eluting compounds possessing similar spectra in the UV region. On other hand Unknown 2 exhibiting λ_{\max} 252 ± 1 nm with USP as well as new method, confirmed the detection of the same DP by both methods.

3.3. Method validation

3.3.1. Stability indicating assay method (SIAM) validation

The new HPLC assay method was fully validated with respect to linearity, method precision (intra-day, inter-day, and inter-mediate), accuracy, specificity and solution stability, using well established guidelines [15–18]. EPM solutions in the concentration range of 50–150 $\mu\text{g/ml}$ showed linear detector response with a correlation coefficient (r^2) value >0.99 . The % relative standard deviation (RSD) for intra- and inter-day precision established by analyzing six replicate preparations on the same day and next day, was less than 2%. The accuracy determined by spiking excipients

Eprinomectin_1_110728132835 #1-1059 RT: 0.25-0.60 AV: 24 NL: 3.04E6
F: FTMS + c ESI sid=30.00 Full ms [120.00-1200.00]



2epi_eprinomectin_1 #1-1713 RT: 0.17-0.77 AV: 41 NL: 1.28E7
F: FTMS + c ESI sid=30.00 Full ms [120.00-1200.00]

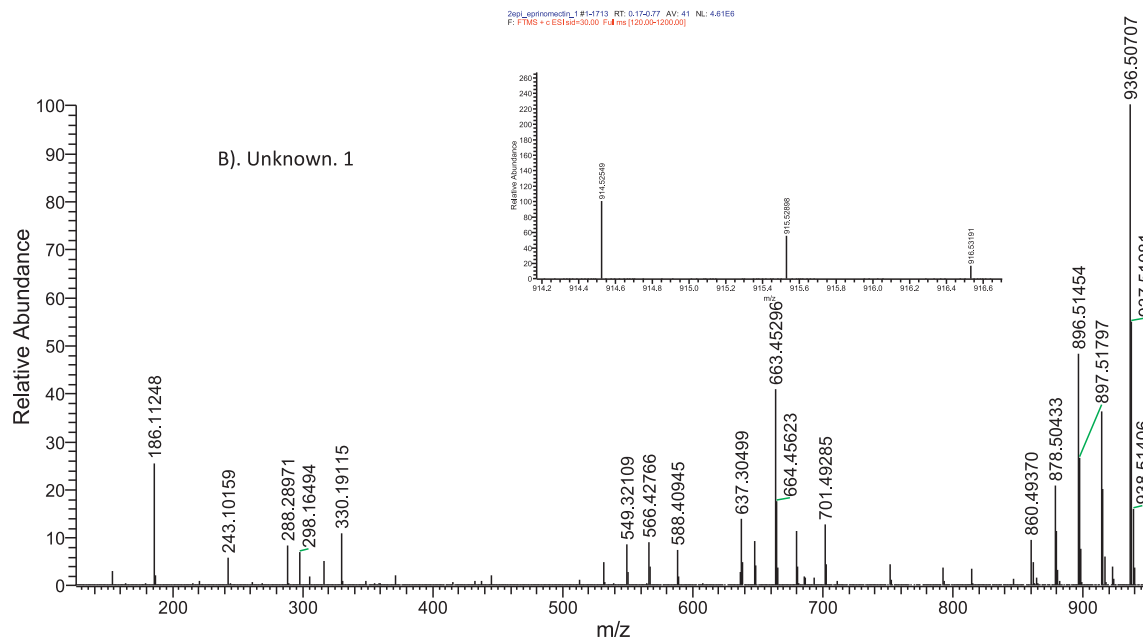


Fig. 5. FT-MS spectra of (A) EPM, (B) 2-*epi* isomer, and (C) $\Delta 2,3$ isomer (isotopic pattern of molecular ion peaks is shown in insets).

Delta23epinomectin_1 #1-1319 RT: 0.09-0.29 AV: 11 NL: 1.09E7
 F: FTMS + c ESI sid=30.00 Full ms [50.00-1200.00]

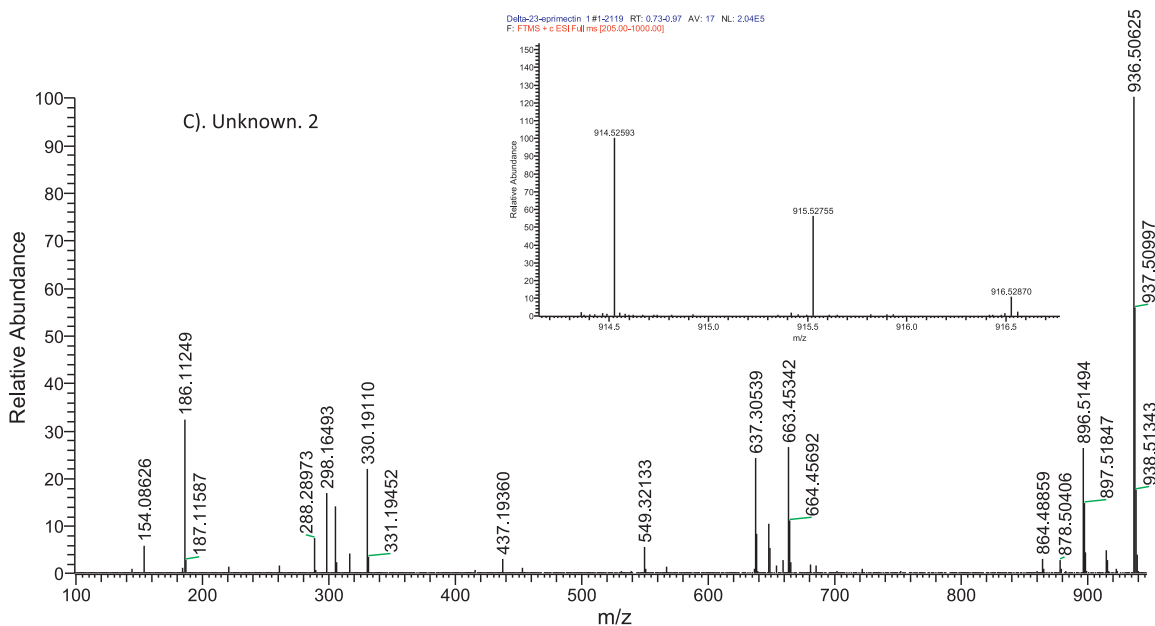


Fig. 5. (Continued).

with a known concentration of EPM in triplicate for each of three concentrations, showed all values within 98.0–102.0% of spiked concentration. Specificity study (stress study under acid, alkali, peroxide, light and thermal conditions) experiment showed peak purity values >0.99 for principal analytes and also points out sensitivity of EPM under alkaline conditions. The standard and sample solutions were stable for 24 h at room temperature. Overall, the method for EPM assay was found to be stability indicating.

3.4. Degradation products method validation

Impurity method validation was carried out using EPM and DP solutions prepared at impurity reporting and specification levels, using established guidelines [18,19]. The limit of quantitation (LOQ) of EPM and DP concentrations were found to be 0.1 µg/ml. The accuracy, linearity, and method precision experiments were designed considering impurity specification at <1% (identification threshold 1%) [19]. The linearity of detector response was achieved with 0.1–3 µg/ml of solution taking into consideration the EPM concentration in assay samples at 100 µg/ml. The method precision, accuracy, and stability of analytical solutions were also found to be satisfactory.

3.5. Isolation and purification of impurities

A stress study sample from day 50, showing >10% levels of DPs was used for their isolation and purification on a flash chromatographic system, using a glass column (700 mm × 25 mm) filled with silica gel (Devisil, 63 µm). A concentrated DCM aliquot was applied to the column and eluted with diethylether:dichloromethane:methanol (9:9:1, v/v/v). First, EPM and Unknown 2 eluted as a mixture, followed by Unknown 1. Similar observations were earlier reported for the isolation of DPs of other AVM analogues [20]. The mixture of EPM and Unknown 2 were further separated on a preparative thin layer chromatography (TLC) system using the same mobile phase, and pure samples were collected by scraping off relevant bands and dissolving the organic compounds from the silica using DCM. The recovered solvent

eluates were concentrated *in vacuo* using a rotary evaporator and the resulting chromatographically pure compounds were collected and stored refrigerated under nitrogen for further analysis.

3.6. Mass spectrometry characterization

In general, MS techniques have been reported for identification of drugs and impurities using accurate mass and fragmentation patterns [13,21,22]. Recent strategies in the analysis of AVMs have been based on liquid chromatography/mass spectrometric (LC/MS) assays in addition to conventional gas chromatographic/mass spectrometric (GC/MS) techniques that require time-consuming sample preparation protocols and results are prone to higher uncertainties in measurement. LC/MS/MS procedures described in the literature employ either triple-quadrupole or quadrupole ion trap analyzers, and the product ion mass spectra generated by collision-induced dissociation (CID) demonstrate significant differences regarding the presence or absence of fragment ions as well as product ion abundances. CID fragmentation of target analytes giving rise to major product ions has been proposed in the literature occasionally but was not further evaluated by systematic chemical or mass spectrometric experiments with higher resolution and accuracy. We have examined EPM and its DPs for comparison of accurate mass, isotopic patterns, fragmentation pathways, multistage mass fragmentation (MS^n), and H/D exchange studies using high resolution LTQ FT-MS. MS^n and H/D exchange data are also explored for the possibility of distinguishing between EPM and DPs which are supposed to be structural isomers.

MS data management programmes (HiChem MassFrontier™ and ACD/MS Manager™) were initially used to predict theoretical mass fragmentation pathways. The fragmentation patterns observed were then correlated with experimental fragment data.

Since ABM, a precursor of EPM, does not ionize well under electrospray (ESI) conditions [23], 10 mM ammonium acetate was added to the solvent mixture (MeOH:ACN:H₂O 27:48:25) to assist with sample ionization.

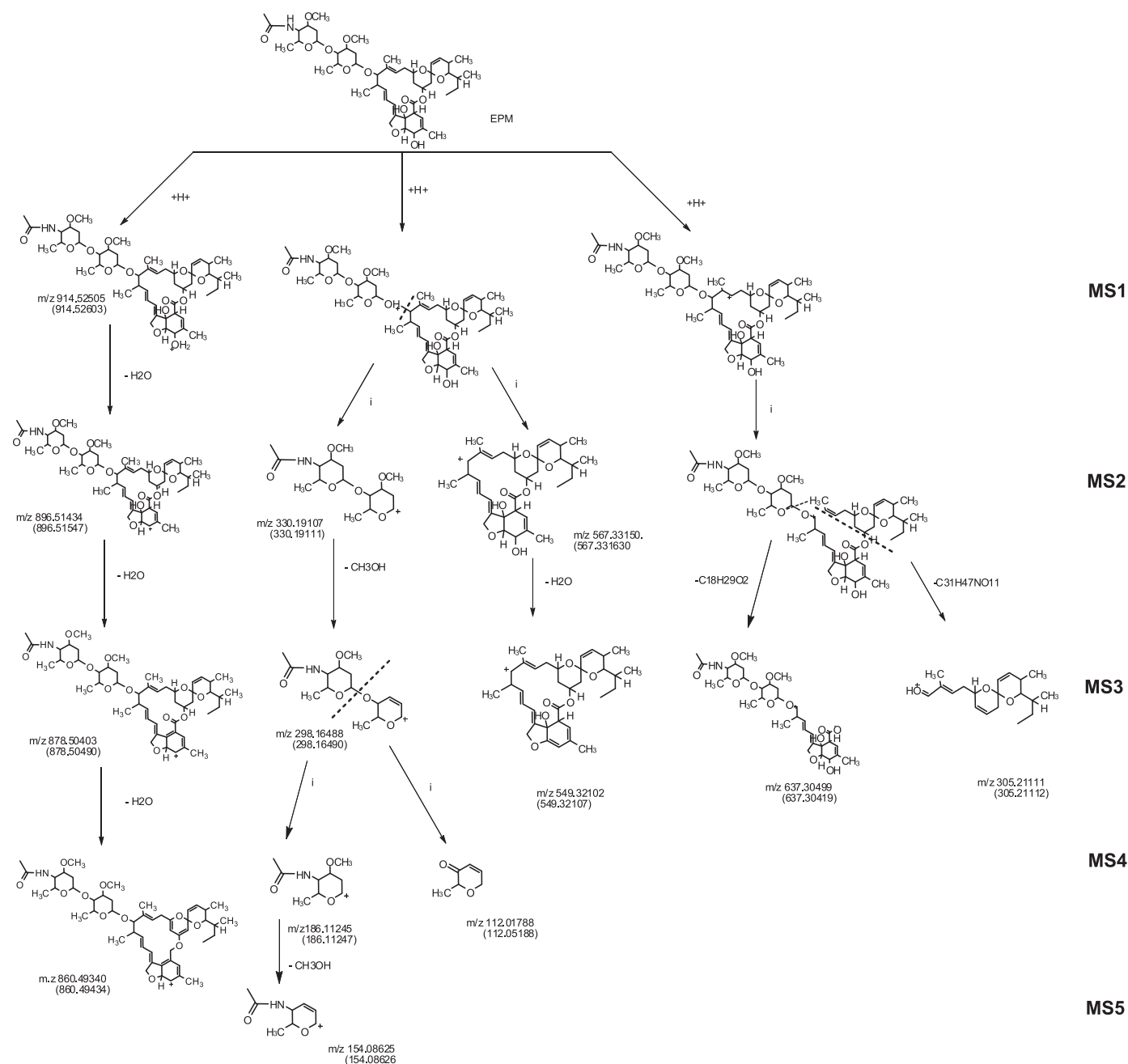


Fig. 6. Fragmentation pathways for molecular ion peak m/z 914.52.

The FT mass spectra and isotopic pattern for molecular ion peaks in Fig. 5 exhibits, that EPM presents a pseudomolecular ion at m/z 914.52505 and a more intense sodiated adduct peak $[M+Na]^+$ at m/z 936.50729. The common fragments observed for molecular ion peaks were m/z 896.51434, 878.50403, 860.49340, 637.30471, 549.32102, 468.29554, 330.19107, 298.16488, 186.11245, and 154.08625. As anticipated EPM DPs Unknown 1 and Unknown 2, both show an identical pseudomolecular ion adduct peak $[M+Na]^+$ m/z of 936.50 and pseudomolecular ion at m/z 914.52. Their fragmentation profiles were similar to EPM with the exception of a few additional ions (may be an adduct with solvents used in the synthesis). Furthermore, the isotopic pattern for the molecular ion peaks of all three compounds was determined, and experimental results show a good match to theoretical values for the assigned atomic compositions.

Comprehensive and elaborate MS fragmentation patterns of the EPM and its DPs were undertaken using CID at 30–35% collision energy to generate MSⁿ mass fragment data with concomitant HR-MS when ion intensity was sufficient (see Fig. 6). To elucidate the fragmentation scheme, accurate masses of the fragments were used to derive molecular formulae and assign elemental composition to the losses. MSⁿ studies clearly help to understand the origin and pathways of ions shown in mass spectra. The molecular ion at peak m/z 914.52504 undergoes fragmentation with three consecutive H₂O losses resulting the ions at m/z 896.51434 (MS2) followed by m/z 878.50430 (MS3), and m/z 860.49340 (MS4). On the other hand, cleavage of the glycosidic bond at C13 at the macrocyclic ring of the parent ion results in the formation of an aglycone ion at m/z 567.33150 (MS2) and a disaccharide amide ion at m/z 330.19107 (MS2). A water loss from the aglycone ion at C4–C5

Table 1
Proton assignment and chemical shift (δ) for eprinomectin, Unknown 1, and Unknown 2.

Assignments	Eprinomectin B1 _a	Unknown 1	Unknown 2	
2	—CH	3.30, m	3.21, obs. m	—
3	—CH	5.43, obs. m	5.70, m (obs)	6.15, d ($J=1.8$)
4	—CH	—	—	2.51 obs. m
4a	—CH ₃	1.87, app. t ($J=1.6$)	1.88, s	1.22, d ($J=7.2$)
5	—CH	4.29, app. t ($J=7.3$)	4.24, s (br)	3.59, dd ($J=9.3, 1.5$)
5	—OH	2.35, d ($J=8.2$)	—	—
5a	—CH	3.97, d ($J=6.2$)	4.31, d ($J=3.0$)	4.05, d ($J=2.2$)
7	—CH ₂	4.70, dd ($J=14.3, 2.3$) and 4.66, dd ($J=14.3, 2.5$)	4.60, dd ($J=12.9, 1.3$) and 4.13, dd ($J=12.9, 2.3$)	4.58, dd ($J=14.1, 2.1$) and 4.50, dd ($J=14.1, 2.2$)
8a	—OH	4.01, s	—	4.75, s (br)
9	—CH	5.87, app. dq ($J=10.7, 2.3$)	5.95, app. dt ($J=10.2, 1.9$)	6.16, m (obs)
10	—CH	5.75–5.71, complex m	5.68, dd ($J=15.2, 10.3$)	5.68, dd ($J=15.0, 10.6$)
11	—CH	5.75–5.71, complex m	5.72, dd ($J=15.2, 5.9$)	5.76, dd ($J=14.9, 9.5$)
12	—CH	2.52, m	2.46, m	2.46, m (obs)
12a	—CH ₃	1.16, d ($J=7.0$)	1.15, d ($J=6.4$)	1.15, d ($J=8.1$)
13	—CH	3.93, br. s	3.93, m	3.91, obs. m
14a	—CH ₃	1.49, br. s	1.47, s	1.45, s
15	—CH	4.98, m	4.93, m	4.94, d (br) ($J=9.9$)
16	—CH ₂	2.33–2.22 complex obs. m	2.31, obs. m and 2.23 obs. m	2.29, obs. m and 2.21, obs. m
17	—CH	3.87, obs. m	3.90, obs. m	3.91, obs. m
18	—CH ₂	1.77, m and 0.88, obs. m	1.83, m and 0.79, m	1.89, dd ($J=10.2, 2.1$) and 0.75, m
19	—CH	5.41, obs. m	5.50, m	5.37, obs. m
20	—CH ₂	2.01, obs. m and 1.48, obs. m	1.94, ddd ($J=12.1, 4.7, 1.5$) and 1.67, obs. m	1.98, dd ($J=12.0, 3.4$) and 1.64, obs. m
22	—CH	5.76, dd ($J=9.9, 1.7$)	5.78, dd ($J=9.9, 1.7$)	5.77, dd ($J=9.9, 1.5$)
23	—CH	5.55, partially obs. dd ($J=9.9, 2.6$)	5.58, dd ($J=9.8, 2.6$)	5.57, dd ($J=10.0, 2.5$)
24	—CH	2.27, obs. m	2.27, obs. m	2.27, obs. m
24a	—CH ₃	0.91, d ($J=7.2$)	0.92, obs. m	0.91, d ($J=6.7$)
25	—CH	3.48, dd ($J=9.9, 1.3$)	3.49, obs. m	3.48, obs. m
26	—CH	1.60, obs. m	1.62, obs. m	1.60, obs. m
26a	—CH ₃	0.92, d ($J=6.5$)	0.89, obs. m	0.89, d ($J=6.7$)
27	—CH ₂	1.50, obs. m	1.50, obs. m	1.47, obs. m
28	—CH ₃	0.94, t ($J=7.3$)	0.94, obs. m	0.93, obs. t ($J=7.0$)
1'	—CH	4.77, d ($J=3.2$)	4.76, d ($J=3.0$)	4.76, obs. m
2'	—CH ₂	2.23, obs. m and 1.56, obs. m	2.25, obs. m and 1.62, obs. m	2.23, obs. m and 1.56, obs. m
3'	—CH	3.62, ddd ($J=13.2, 8.8, 4.8$)	3.64, m	3.65, obs. m
4'	—CH	3.21, t ($J=9.0$)	3.21, obs. m	3.21, t ($J=9.0$)
5'	—CH	3.84, obs. m	3.83, dq ($J=9.4, 6.3$)	3.85, partially obs. dq ($J=9.4, 6.3$)
6'	—CH ₃	1.24, d ($J=6.2$)	1.24, d ($J=6.2$)	1.24, d ($J=6.9$)
1''	—CH	5.39, obs. m	5.40, m	5.39, d ($J=4.1$)
2''	—CH ₂	2.03, obs. m and 1.61, obs. m	2.05, obs. m and 1.62, obs. m	2.06, obs. m and 1.59, obs. m
3''	—CH	3.69, app. dt ($J=12.0, 4.5$)	3.68, m	3.70, partially obs. dt ($J=12.1, 4.4$)
4''	—CH	4.43, ddd ($J=9.8, 3.7, 1.0$)	4.44, dd ($J=10.0, 3.2$)	4.43, dd ($J=10.0, 3.2$)
5''	—CH	4.07, qd ($J=6.2, 1.0$)	4.07, qd ($J=6.5, 1.2$)	4.07, obs. m
6''	—CH ₃	1.13, d ($J=6.5$)	1.13, d ($J=6.4$)	1.13, d ($J=6.7$)
3'	—OCH ₃	3.44, s	3.48, s	3.48, s
3''	—OCH ₃	3.30, s	3.41, s	3.40, s
4''	CH ₃ COCH ₃	2.07, s	2.07, s	2.07, s
4'	—NH	5.57, br. d ($J=9.4$)	5.59, br. d ($J=10.0$)	5.59, d ($J=10.3$)

s, singlet; d, doublet; t, triplet; q, quartet; m, multiplet; app., apparent; br., broad; obs., obscure.

position further gives rise to a dehydrated aglycone ion at m/z 549.32102 (MS3), whilst disaccharide amide loses methanol to give the ion at m/z 298.16488 (MS3). Further lysis of the demethylated amide ion produces abundant ions at m/z 186.11245 (MS4), and m/z 112.01788 (MS4). The monosaccharide amide ion at m/z 186.11245 (MS4) further loses methanol to produce an ion at m/z 154.08625 (MS5). On other hand, allylic cleavage at C13–C14 position of the molecular ion peak in addition to C19–O cleavage, leads to the formation of ions at m/z 637.30499 and m/z 305.21111 separately.

3.7. HX-MS studies

An HX-MS (hydrogen/deuterium exchange) experiment involves the replacement of acidic protons with deuterons from heavy water (D₂O) [24]. Due to the back exchange problem associated with the commonly used online exchange method and access to pure compounds, herein hydrogen/deuterium exchange

was carried out by a chilling and quenching process as described in Section 2.2.3, and spectra were recorded by FT-MS. The ions possessing labile hydrogen underwent that exchange process. The pseudomolecular ion peak had an increase of 3 m/z units corresponding to 3 exchangeable hydrogens present at OH-5, OH-8a and NH. Sequential loss of water molecules is reflected in a decrease in exchangeable sites; therefore at m/z 878.50, only one hydrogen exchanged. The disaccharide amide ion (m/z 330.19) and monosaccharide amide ion (m/z 186.11) showed a single proton from the NH group undergoing exchange.

3.8. Use of MS data to distinguish structural isomer

One of the advantages of high resolution MS is its application towards study of structural isomers [25], whereas Madhusudan [26] has successfully tried to distinguish the diastereoisomers of monosaccharide using MS^{*n*} data, and used relative abundance and appearance/disappearance of isobaric peaks as a complementary

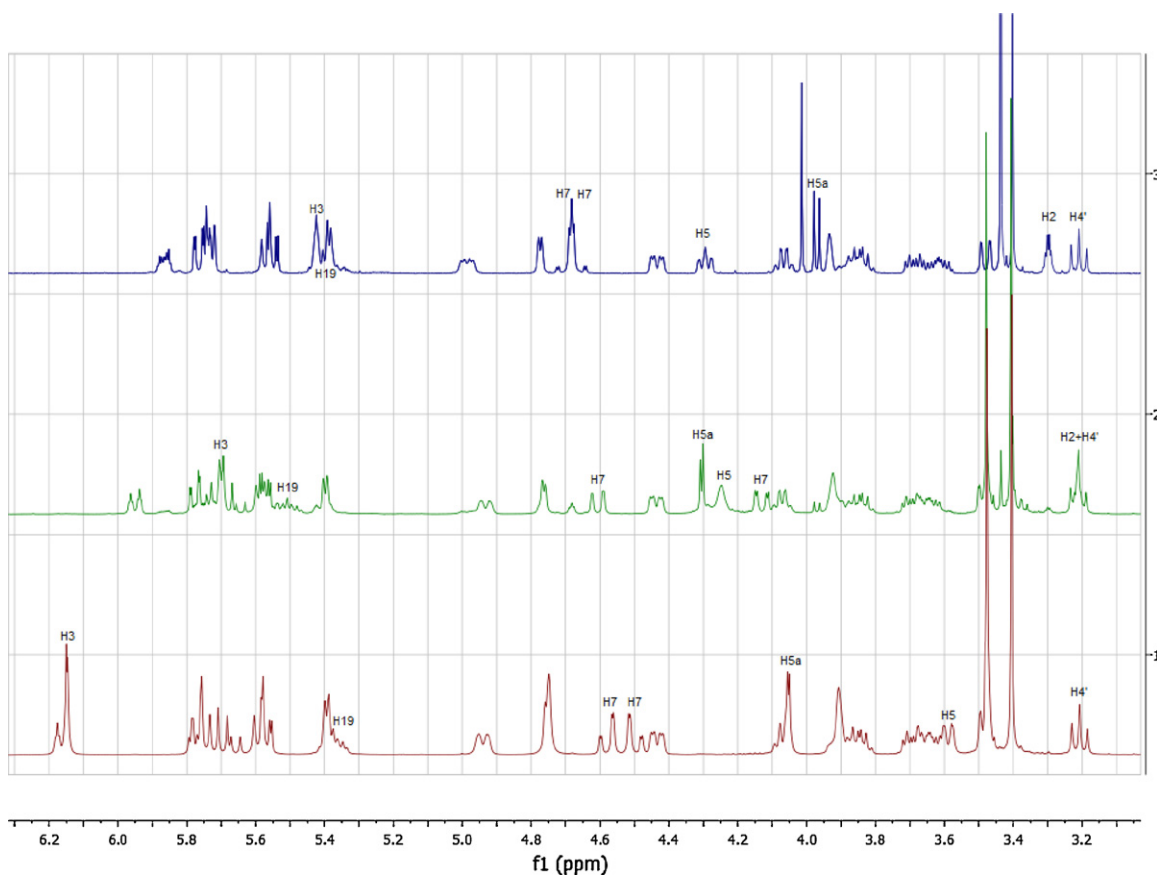


Fig. 7. Expansion of ^1H NMR spectra of (from top) (3) EPM (blue), (2) Unknown 1 (green) and (1) Unknown 2 (red), showing key differences in δ 3.1–6.3 ppm region. (For interpretation of the references to color in this figure legend, the reader is referred to the web version of the article.)

tool. ABM (a precursor for EPM) and IVM are known to produce stereo- and structural isomers under alkaline conditions [27,28]. Hence the two DPs of EPM formed under same conditions are postulated to be similar structural isomers. The isotopic pattern of molecular ion peaks for all three compounds was found to be similar; examination of the MS spectra of the $[\text{M}+\text{Na}]^+$ peak at m/z 936.50 clearly distinguishes all three molecules. The ratio, relative abundances and appearance of various ions confirm the presence of three individual chemical entities possessing similar mass, but a distinguishable chemical environment due to the unique orientation of the protons and position of saturation.

A close look at the isotopic pattern of key ions from the MS spectrum of m/z 937.50 $[\text{M}+\text{Na}+\text{D}]^+$ and m/z 936.50 $[\text{M}+\text{Na}]^+$ shows the differences as a fingerprint for EPM and its DPs, whereas isotopic ratio of leading ions in this spectra also shows a significant variation.

3.9. NMR studies

Proton NMR spectra for EPM, Unknown 1 and Unknown 2 were fully assigned (see Table 1) with the aid of COSY data and shown overlaid in Fig. 7. The chemical shifts for the C2 hydrogen in the former two compounds are similar (δ 3.30 and 3.21), as expected for stereoisomers, and that of Unknown 1 is in agreement with the avermectin 2-*epi* isomer (δ 3.22) [6]. There are substantial differences in the chemical shifts of several protons attached to the bicyclic system, which would be affected by the change in stereochemistry at C2, namely the C3, C5a, and C7 hydrogens. The chemical shifts of the two C7 hydrogens are different, indicating

that they are in different environments, as expected in a fused bicyclic system with chiral centres and seen in EPM itself. Furthermore, the chemical shifts of these hydrogens have moved upfield and their chemical shift difference is larger (δ 4.60 and 4.13) in comparison with EPM (δ 4.70 and 4.66). Similar shifts have been reported for the C7 hydrogens of the avermectin 2-*epimer* (δ 4.61 and 4.13) [6]. Chemical shift changes of the protons attached to C18, C19 and C20 in Unknown 1 compared to EPM together with almost constant values throughout the rest of the structure also indicate that a nearby region of the EPM structure is perturbed due to a degradation reaction consistent with 2-*epimerization*. Strong two-way NOE correlations between the signals at δ 3.21 (H2) and δ 4.24 (H5) for Unknown 1 are consistent with the proposed epimerization at C2, as H2 and H5 will be on the same face of the six membered ring in 2-*epi*-EPM. A weak correlation from H2 to H5a is also seen, again consistent with epimerization of C2. These facts, coupled with the facility of carbonyl α -centres to undergo epimerization, suggest Unknown 1 is 2-*epi*-EPM (represented by the structure shown in Fig. 8). The chemical shift changes that were observed are in very good agreement with the data reported for the base-catalyzed epimerization of other avermectin derivatives [20].

Analysis of the proton resonances of Unknown 2 with the aid of the $^1\text{H}/^1\text{H}$ COSY data showed further alteration of the bicyclic system. Most notably, H2 was absent and the chemical shift of H3 was significantly downfield from that in EPM or its 2-*epimer* (δ 6.15 vs 5.43 or 5.70, respectively), consistent with the deshielding of the β -position typically observed in conjugated enoates. Furthermore, correlation of H3 to a new signal (H4, δ 2.51) and

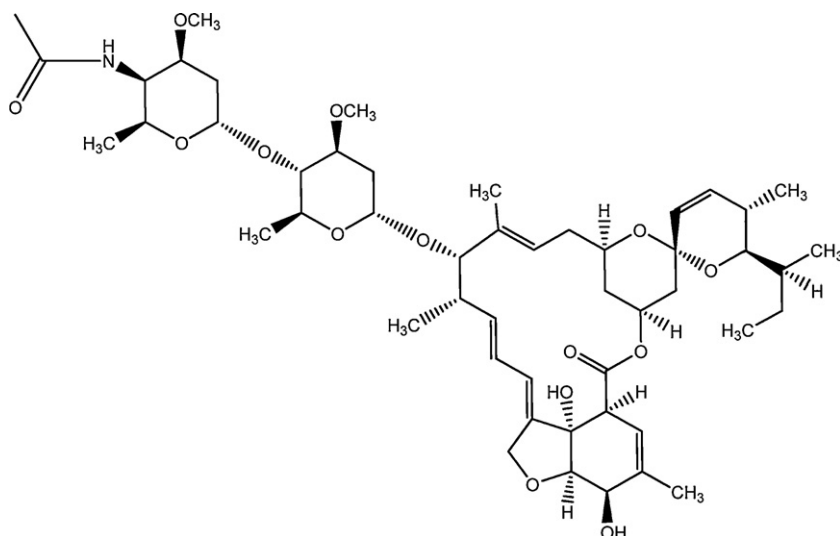


Fig. 8. Chemical structure and molecular formula of Unknown 1: 2-*epi*-EPM (B_{1a}).

the upfield shift of the attached (and no longer allylic) CH₃ (H_{4a}, from δ 1.87 in EPM to δ 1.22 in Unknown 2) and CH (H₅, from δ 4.29 in EPM to δ 3.59 in Unknown 2) corroborated the hypothesis of isomerism of the alkene into conjugation during the degradation process. The majority of other differences between the spectra of EPM and Unknown 2 were within the fused bicyclic system and close to C19, giving further evidence of Unknown 2 being Δ 2,3-EPM (represented by the structure shown in Fig. 9).

The carbon NMR data for EPM were found to correspond with earlier work [13]. Assisted by the ¹H/¹³C HSQC spectrum, assignment of the carbon resonances of EPM was carried out. Comparison of the EPM data with the carbon resonances of Unknown 1 and Unknown 2 indicated differences in structure, particularly around the lactone carbonyl. For example, whilst one carbonyl resonance remained constant in all three compounds (δ 170.8–170.9) and is thus presumably that of the amide, the other varied considerably between EPM, Unknown 1 and Unknown 2 (δ 173.9, 171.4 and 169.1, respectively) and is attributed to the lactone. Remarkable

similarities are seen in the ¹³C shifts of atoms distant from the lactone carbonyl for the three compounds (e.g. the three acetal signals at δ 98.8–98.9, δ 95.8–95.9 and δ 95.0–95.1), whereas local signals are affected markedly (e.g. C2, δ 45.9 in EPM, δ 51.1 in 2-*epi*-EPM and absent from the aliphatic methine region of the spectrum in Δ 2,3-EPM).

3.10. Mechanism of EPM degradation pathway to 2-*epi*-EPM and Δ 2,3-EPM

As discussed in Section 1, EPM is a synthetic acetylated amino derivative of ABM. The degradation chemistry of its precursor ABM (AVM B_{1a} and B_{1b}) and its close derivative ivermectin (22,23-dihydro AVM) is well established [27,28]. In alkaline conditions these compounds degrade to the 2-*epi* and Δ 2,3 isomers. The base-catalyzed mechanism of action for ABM is shown in Fig. 10, whereby 2-*epi* is formed by isomerization at the C-2 position of the parent compound, and then gradually transforms into the thermodynamically stable Δ 2,3-isomer.

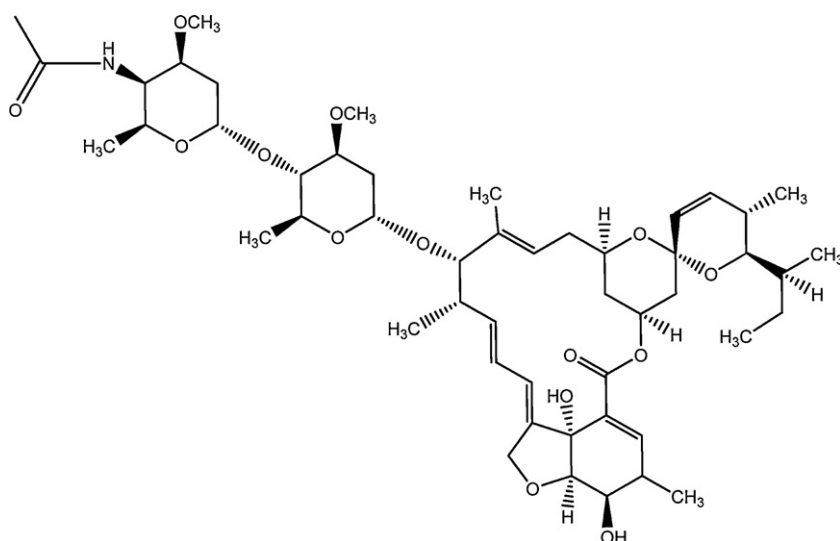


Fig. 9. Chemical structure and molecular formula of Unknown 2: Δ 2,3 EPM (B_{1a}).

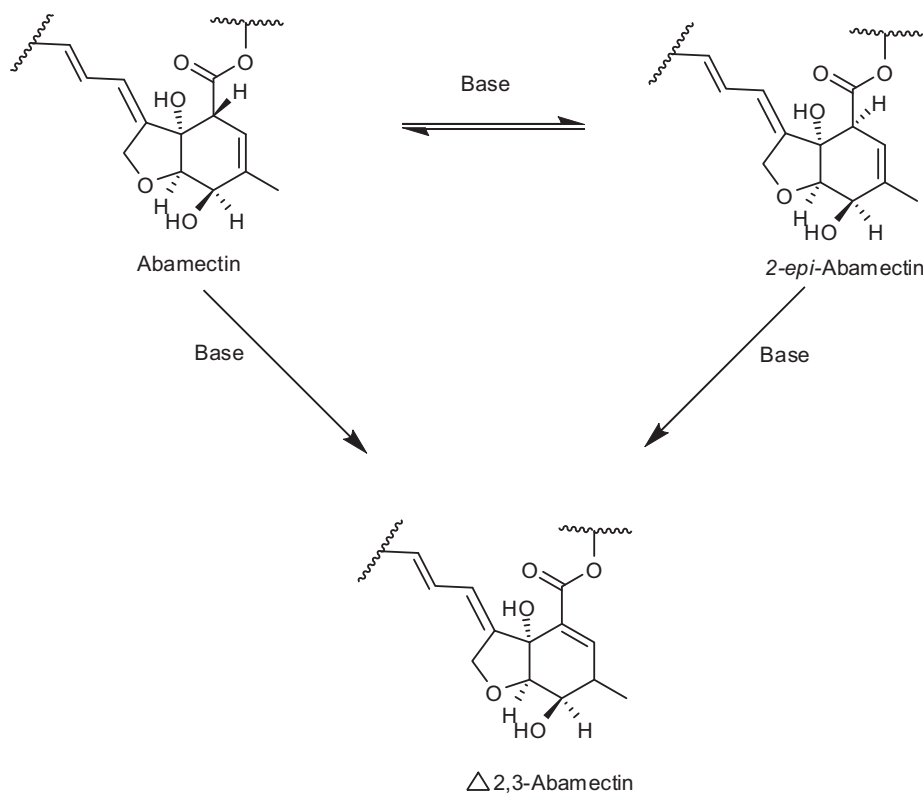


Fig. 10. Base-catalyzed isomerization of ABM [28].

It is postulated that degradation of EPM also followed the base catalyzed mechanism as shown by ABM (DMF used in formulation is apparently an alkaline solvent). Initially it degrades to the 2-*epi* isomer (Unknown 1) as the major and Δ 2,3 isomer (Unknown 2) as a minor DP. Gradually with time the Δ 2,3 species becomes the principal DP at the expense of the 2-*epimer* and EPM in sample.

4. Conclusion

From the above studies it is concluded that the current pharmacopeial method for API has deficiencies for analysis of EPM in finished products containing DPs. A new method has been developed, in which a significant DP (2-*epi*-EPM) earlier merging with the EPM peak obtained using USP method, is now fully separated. The data also showed that this DP merging was not elucidated by the established spectral and purity analysis, because the molecular weight and λ_{\max} of EPM and Unknown 1 are similar. The other major DP Unknown 2 is also positively identified as Δ 2,3 isomer of EPM. The method is fully validated and found to be stability indicating. The DPs are successfully isolated from sample matrix and positively identified using FT-MS, HX-MS and NMR studies. The new stability indicating HPLC method for EPM and DPs in formulations will support the clinical, residue and environmental analysis of matrices containing EPM and its DPs.

Acknowledgements

This research work was supported by Technology New Zealand (TechNZ). The authors would like to take this opportunity to thank Mr. Robert Holmes, and Ancare Scientific Ltd, New Zealand, for their continuous support. Also special thanks to Prof. Saranjit Singh (NIPER, India), for his guidance on characterization protocols.

References

- [1] J. Vercruyse, R.S. Rew (Eds.), *Macrocyclic Lactones in Antiparasitic Therapy*, CABI, Publishing, Wallingford, UK, 2002.
- [2] United States Pharmacopeia 33 NF-28, United States Pharmacopeial Convention Inc., Rockville, MD, USA, 2010.
- [3] W.L. Shoop, P. Demontigny, D.W. Fink, J.B. Williams, J.R. Egerton, H. Mrozik, Efficacy in sheep and pharmacokinetics in cattle that led to the selection of eprinomectin as a topical endectocide for cattle, *Int. J. Parasitol.* 26 (1996) 1227–1235.
- [4] M. Alvinerie, J.F. Sutra, P. Galtier, C. Mage, Pharmacokinetics of eprinomectin in plasma and milk following topical administration to lactating dairy cattle, *Res. Vet. Sci.* 67 (1999) 229–232.
- [5] G. Dusi, E. Faggionato, L. Bertocchi, S. Facchetti, M. Baiguera, Determination of avermectin and milbemycin residues in milk for human consumption using liquid chromatography with fluorescence detection, *Ind. Alim.* 40 (2001) 11–14.
- [6] W.H. Shoop, H. Mrozik, M.H. Fisher, Structure and activity of avermectins and milbemycins in animal health, *Vet. Parasitol.* 59 (1995) 139–156.
- [7] H.H. Mrozik, 4-Keto- and 4-amino-4-deoxy avermectin compounds and substituted amino derivatives thereof, United State Patent 4,427,663, 1984.
- [8] W.L. Shoop, Eprinomectin: a novel avermectin for use as a topical endectocide for cattle, *Int. J. Parasitol.* 26 (1996) 1237–1242.
- [9] M. Danaher, Review of methodology for the determination of macrocyclic lactone residues in biological matrices, *J. Chromatogr. B* 844 (2006) 175–203.
- [10] J.M. Ballard, L.D. Payne, R.S. Egan, T.A. Wehner, G.S. Rahn, S. Tom, Development and validation of an HPLC/MS/MS method for the confirmation of eprinomectin marker residue in bovine liver tissue, *J. Agric. Food Chem.* 45 (1997) 3507–3510.
- [11] R. Sheridan, L. Desjardins, Determination of abamectin, doramectin, emamectin, eprinomectin, ivermectin, and moxidectin in milk by liquid chromatography–electrospray tandem mass spectrometry, *J. AOAC Int.* 89 (2006) 1088–1094.
- [12] L. Konermann, J. Pan, Y. Liu, Hydrogen exchange mass spectrometry for studying protein structure and dynamics, *Chem. Soc. Rev.* 40 (2011) 1224–1234.
- [13] R.P. Shah, S. Singh, Identification and characterization of a photolytic degradation product of telmisartan using LC–MS/TOF, LC–MSⁿ, LC–NMR and on-line H/D exchange mass studies, *J. Pharm. Biomed. Anal.* 53 (2010) 755–761.
- [14] K.S. Wolfgang, P. Scott, H. Muenster, Accurate Mass Measurements using the Finnigan LTQ FT, Application Note 30045, Thermo Electron Corporation, 2004.
- [15] S.P. Boudreau, Method validation by phase of development: an acceptable analytical practice, *Pharm. Technol.* 28 (2004) 54–66.
- [16] S.K. Branch, Guidelines from the International Conference on Harmonisation (ICH), *J. Pharm. Biomed. Anal.* 38 (2005) 798–805.
- [17] International Conference on Harmonisation of Technical Requirements for Registration of Veterinary Medicinal Products, VICH GL-1: Validation of Analytical

- Procedures: Definition and Terminology, VICH Steering Committee, Brussels, Belgium, 1998.
- [18] International Conference on Harmonisation of Technical Requirements for Registration of Veterinary Medicinal Products, VICH GL-2: Validation of Analytical Procedures: Methodology, VICH Steering Committee, Brussels, Belgium, 1998.
- [19] International Conference on Harmonisation of Technical Requirements for Registration of Veterinary Medicinal Products, VICH GL-11: Impurities in New Veterinary Medicinal Products (revision), VICH Steering Committee, Brussels, Belgium, 2008.
- [20] A.J. Faulkner, Q. Wang, P. Demontigny, J.S. Murphy, Stability studies and high-performance liquid chromatographic procedures for L-648,548 and its major degradates in an animal health formulation, *J. Pharm. Biomed. Anal.* 15 (1997) 523–536.
- [21] D.K. Raijada, B. Prasad, A. Paudel, R.P. Shah, S. Singh, Characterization of degradation products of amorphous and polymorphic forms of clopidogrel bisulphate under solid state stress conditions, *J. Pharm. Biomed. Anal.* 52 (2010) 332–344.
- [22] R.N. Tiwari, C.G. Bonde, LC–MS/TOF and MSⁿ studies for the identification and characterization of degradation products of nelfinavir mesylate, *J. Pharm. Biomed. Anal.* 55 (2011) 435–445.
- [23] S. Grimalt, Ó.J. Pozo, J.M. Marín, J.V. Sancho, F. Hernández, Evaluation of different quantitative approaches for the determination of noneasily ionizable molecules by different atmospheric pressure interfaces used in liquid chromatography–tandem mass spectrometry: abamectin as case of study, *J. Am. Soc. Mass Spectrom.* 16 (2005) 1619–1630.
- [24] D.Q. Liu, L. Wu, M. Sun, P.A. MacGregor, On-line H/D exchange LC–MS strategy for structural elucidation of pharmaceutical impurities, *J. Pharm. Biomed. Anal.* 44 (2007) 320–329.
- [25] J.M. Dela Cruz, V.V. Lozovoy, M. Dantus, Isomeric identification by laser control mass spectrometry, *J. Mass Spectrom.* 42 (2007) 178–186.
- [26] K.P. Madhusudanan, Tandem mass spectra of ammonium adducts of monosaccharides: differentiation of diastereomers, *J. Mass Spectrom.* 41 (2006) 1096–1104.
- [27] D.W. Fink, in: F. Klaus (Ed.), *Ivermectin: Analytical Profiles of Drug Substances*, vol. 17, 1988, pp. 155–184.
- [28] J.V. Pivnichny, B.H. Arisen, F.A. Preiser, J.K. Shim, H. Mrozik, Base-catalyzed isomerization of avermectins, *J. Agric. Food Chem.* 36 (1988) 826–828.



Sulfamethoxazole:hydroxypropyl- β -cyclodextrin complex: preparation and characterization

Claudia Garnero, Virginia Aiassa, Marcela Longhi*

Departamento de Farmacia, Facultad de Ciencias Químicas, Universidad Nacional de Córdoba, Ciudad Universitaria, X5000HUA Córdoba, Argentina

ARTICLE INFO

Article history:

Received 16 September 2011

Received in revised form

30 December 2011

Accepted 9 January 2012

Available online 2 February 2012

Keywords:

Sulfamethoxazole

Hydroxypropyl- β -cyclodextrin

Aggregation

Conductivity

Solid-state analysis

ABSTRACT

A complex of sulfamethoxazole (SMX) and hydroxypropyl- β -cyclodextrin (HP- β -CD) was developed and characterized in order to investigate their interactions in aqueous solution and the solid state. The SMX solubility was significantly increased upon complexation with HP- β -CD, with the solubility isotherm being an A_N type due to the presence of aggregates and the stability constant calculated for a 1:1 complex being $302 \pm 3 \text{ M}^{-1}$. Fourier-transform infrared (FT-IR) spectroscopy and scanning electron microscopy (SEM) experiments were used to compare the freeze-dried system with a physical mixture, and demonstrated the complex formation in the solid state. The differential scanning calorimetry (DSC) and thermogravimetric analysis (TGA) showed that the thermal stability of SMX was enhanced in the presence of HP- β -CD.

© 2012 Elsevier B.V. All rights reserved.

1. Introduction

Cyclodextrins (CDs) are water-soluble cyclic oligosaccharides composed by 6 (α -CD), 7 (β -CD) or 8 (γ -CD) D-(+)-glucopyranose units arranged in a truncated cone-shaped structure [1]. Hydroxypropyl- β -cyclodextrin (HP- β -CD) (Fig. 1), derivative of β -CD, has attracted a growing interest due to its improved complexing ability, high solubility and low toxicity [2,3]. Different molecules can penetrate into the relatively hydrophobic cavity and form non-covalent inclusion complexes modifying their physical, chemical and biological properties [4,5]. CDs are used to improve the solubility and dissolution of poorly soluble drugs in water and provide a way to increase their stability and bioavailability. Recently it has been observed that non-inclusion complexes can also participate in the solubilization of poorly soluble drugs by CDs. In aqueous solutions, CDs and their complexes show a tendency to self-associate to form aggregates with solubilizing properties. Also, the formation of CD complexes can increase the tendency of CDs to form aggregates and can lead to the formation of micellar-type CD aggregates capable of solubilizing poorly soluble compounds [6–8].

Sulfonamides are synthetic agents used in human and veterinary therapy for the prevention and treatment of infections

[9]. However, their poor aqueous solubility has hindered their application in the therapy as pharmaceutical formulations. In previous studies, we demonstrated that the CD:sulfonamide complexes improved their solubility in water compared to that of the free drugs [10–12]. In addition, the sulfonamides exhibit interesting solid state properties, among which is the ability to exist in two or more polymorphic forms through the propensity for hydrogen bonding due to the presence of various hydrogen bond donors and acceptors [13]. Sulfamethoxazole (SMX) (Fig. 1) is a sulfonamide agent frequently used in human medicine to treat bronchitis and urinary tract infections. It is widely used in combination with trimethoprim, since this mixture possesses synergistic antibacterial effects [14]. SMX is sparingly soluble in water, and is known to exist in the three polymorphic forms, I, II and III (hemihydrates) [15].

Studies involving the complexation of SMX with β -CD have been reported [16–18]. The formation of a 1:1 complex with HP- β -CD at various pH values was able to improve the aqueous solubility of the drug in trimethoprim/sulfamethoxazole parenteral solutions but could not prevent its precipitation [19]. The chemical stability under oxidation stress of SMX in co-trimoxazole (a 5:1 combination of SMX with trimethoprim) aqueous buffer solutions was increased using HP- β -CD [20]. In addition, we previously developed a method for the simultaneous quantification of trimethoprim and SMX in mixtures using HP- β -CD solutions [21]. However, no reports about the characterization of the new systems SMX:HP- β -CD in solution or in solid state have been published.

* Corresponding author. Tel.: +54 351 4334127; fax: +54 351 4334127.

E-mail addresses: garneroc@fcq.unc.edu.ar (C. Garnero), aiassa@fcq.unc.edu.ar (V. Aiassa), mrlcor@fcq.unc.edu.ar (M. Longhi).

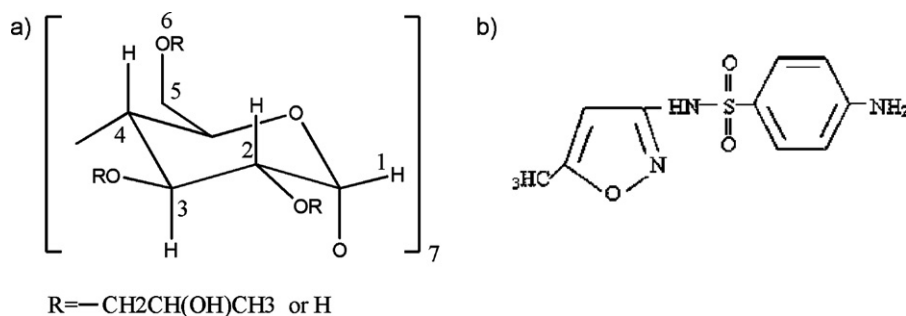


Fig. 1. Chemical structure of (a) HP- β -CD and (b) SMX.

Taking into account these previous studies, in the present work we prepared and characterized a complex between the commercial SMX active ingredient and HP- β -CD.

2. Materials and methods

2.1. Chemicals and reagents

All the experiments were performed with analytical grade chemicals and solvents. HP- β -CD, with a degree of substitution of 0.63, was kindly supplied by Ferromet agent of Roquette (France). Millipore Milli Q Water Purification System was used to generate the water used in these studies.

2.2. Phase solubility studies

The solubility measurements were performed according to the method of Higuchi and Connors [22] in aqueous solutions containing different concentrations of HP- β -CD, ranging from 14.3 mM to 143.2 mM.

2.3. Conductivity measurements

The conductance measurements were taken in HP- β -CD solutions, in the range 1.65–161.55 mg/ml, in the presence of a constant SMX concentration throughout the experiment. The critical concentration for the aggregate formation was determined by measuring the specific conductivity change as a function of concentration, using a Malvern Zetasizer 3000 (Malvern Instruments Inc., London, UK). All measurements were recorded at 25 °C, with the values shown being the mean of 20 conductance measurements.

2.4. Solid sample preparation

The preparation of a solid complex SMX:HP- β -CD with a 1:1 molar ratio was carried out using the freeze-dry method [23]. Physical mixtures were prepared by mixing the SMX and HP- β -CD powders or the corresponding freeze-dried components, with a 1:1 molar ratio uniformly in a mortar.

2.5. Fourier-transform infrared (FT-IR) spectroscopy

The FT-IR spectra (potassium bromide disks) were recorded on a Nicolet 5 SXC FT-IR Spectrophotometer (Madison, WI, USA).

2.6. Differential scanning calorimetry (DSC) and thermogravimetric analysis (TGA)

The DSC curves of the samples were produced using a DSC TA 2920, and the TGA curves were recorded on a TG TA 2920. The samples were placed in aluminum hermetic pans, with the

experiments being carried out under a nitrogen gas flow, at a heating rate of 10 °C/min, and over a temperature range of 25–400 °C.

2.7. Scanning electron microscopy (SEM)

Microscopic morphological structures of the solid samples were investigated and photographed using a scanning electron microscope LEO Model EVO 40XVP. To improve the conductivity, samples were gold-coated under vacuum employing a sputter coater PELCO Model 3.

3. Results and discussion

3.1. Phase solubility analysis

The phase solubility diagram of SMX and HP- β -CD, obtained by plotting the changes in guest solubility as a function of HP- β -CD concentration (Fig. 2) can be classified as an A_N type, with the negative deviation from linearity at higher concentrations. This curve may originate from both an alteration in the effective nature of the solvent in the presence of large concentrations of HP- β -CD and a self-association of HP- β -CD at higher concentrations [22,24].

The initial ascending portion of the diagram had a slope less than 1, which indicated that a soluble inclusion complex with a 1:1 molar ratio was formed at low HP- β -CD concentrations. The apparent stability constant (K_C) value of $302 \pm 3 \text{ M}^{-1}$ was estimated from the slope of the initial linear portion of the diagram and the

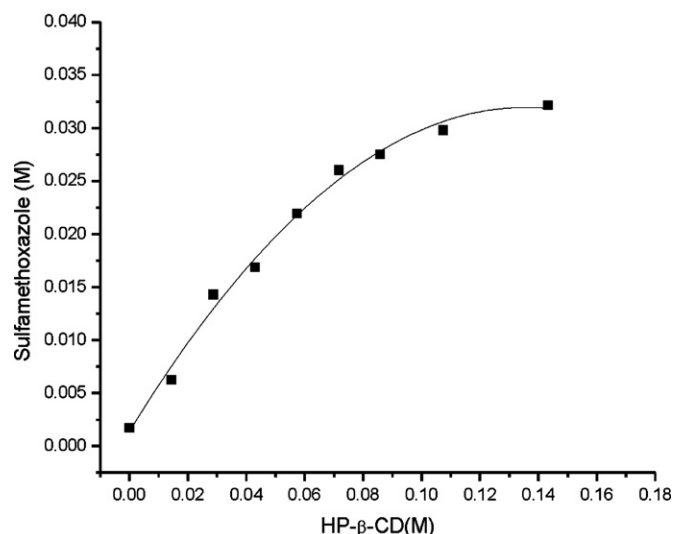


Fig. 2. Effect of HP- β -CD on the solubility of SMX in an aqueous solution at 25.0 °C.

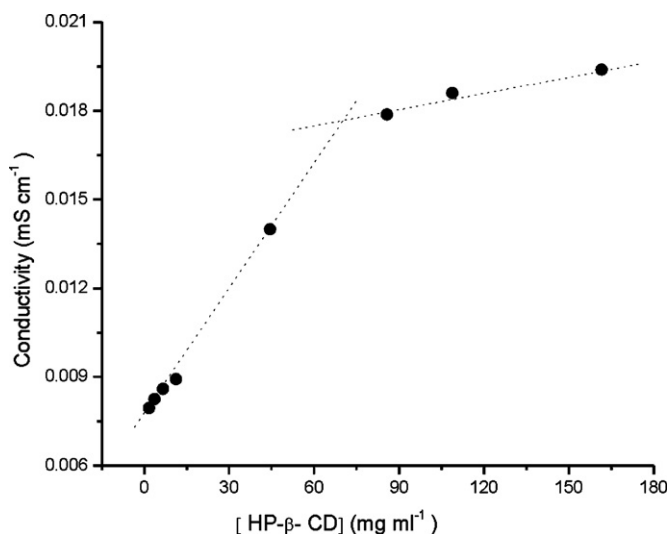


Fig. 3. Conductivity measurements as a function of HP- β -CD concentration for aqueous solutions of SMX:HP- β -CD at 25 °C.

solubility of SMX in water (S_0), according to the following equation:

$$K_c = \frac{\text{Slope}}{S_0(1 - \text{Slope})}$$

SMX (pK_a 5.6) mainly existed in its unionized form in aqueous solutions of pH 4.7, which was the reason why the interaction with HP- β -CD occurred efficiently, and consequently, an important increase in solubility was observed as a function of HP- β -CD concentration. The aqueous solubility of SMX in water was 0.4 mg/ml. This increased approximately 10.5 times (4.6 mg/ml) in 57.3 mM HP- β -CD solution, while 143.2 mM HP- β -CD caused a 20.2-fold rise in the drug solubility (8.7 mg/ml). Therefore, these results showed the large solubilizing effect of HP- β -CD. It seems that our results are in good agreement with those obtained previously by Loftsson et al. [25]. They have described the phase solubility studies of SMX with HP- β -CD and reporting K_c value of 370 M^{-1} .

3.2. Aggregation behavior of SMX:HP- β -CD complex

The formation of aggregates in aqueous solution and the critical concentration for the SMX:HP- β -CD complex was studied, by conductivity, to interpret the phase solubility diagrams observed. In Fig. 3, a plot of conductivity is shown as a function of the HP- β -CD concentration for aqueous solutions of SMX:HP- β -CD at 25 °C. The results revealed a significant increase in the conductance of the solutions caused by SMX:HP- β -CD system compared to pure HP- β -CD (with this latter value has already been determined in our previous work, [26]), demonstrating that the complex SMX:HP- β -CD was more effective as charge carrier than the free macromolecule in aqueous solution, because the conductivity of water is dependent on the concentration of the conducting species present. A break point on the slope of the plot demonstrates that at high concentrations of HP- β -CD was favored the formation of aggregates. The critical concentration, defined as the point corresponding to the maximum change in gradient of a physical property of solution against ligand concentration, was determined from the intersection point of the linear segments, corresponding to the monomeric and aggregate forms, and the best correlation coefficient was chosen. A value of was 70.99 mg/ml (about 50.8 mM) was determined, and its similarity with the value of 69.3 mg/ml reported for free HP- β -CD [26] suggests that the complex formation did not affect the balance of the intermolecular forces that

held the HP- β -CD molecules together in the aggregates. These experimental results indicated that the self-association between SMX:HP- β -CD complexes as well as that between free HP- β -CD molecules and the complexes may explain why the observed solubilization phenomena had a negative deviation from linearity at higher host concentrations (Fig. 2).

Taken together, the results suggest that the increase in the solubility of SMX, at low concentrations of HP- β -CD, was the result of the formation of an inclusion complex. However, at ligand concentrations above the critical concentration, water-soluble aggregates were formed, which possess the capacity to solubilize SMX by forming non-inclusion complexes [6].

3.3. Solid-state studies

The pure materials, the freeze-dried system SMX:HP- β -CD and the corresponding physical mixture were examined.

3.3.1. Fourier-transform infrared (FT-IR) spectroscopy

In order to identify the polymorph form of SMX in the commercial sample, the characteristic FT-IR bands in the region 3500–3100 cm^{-1} were examined. As shown in Fig. 4a, bands were found at 3467.3 and 3375.7 cm^{-1} (NH_2), 3300 cm^{-1} (NH) and 3143.7 cm^{-1} (CH), which are in agreement with the FT-IR spectrum corresponding to the SMX form I reported by Takasuka et al. [15]. Also, other bands were located at 1620.9 cm^{-1} (a combination of NH_2 and isoxazole ring CN), 1596.9 and 1504 cm^{-1} (phenyl ring C=C), 1473.4 and 1380.8 cm^{-1} (isoxazole ring), 1307.5 and 1145.8 cm^{-1} (SO_2), 926.2 cm^{-1} (SN), 884.3 cm^{-1} (isoxazole ring CH) and 829.4 cm^{-1} (benzene ring CH). SMX showed a large variation in the hydrogen-bond pattern between polymorphs, and the polymorphic conversion resulted in a change in the hydrogen-bond pattern of the amido proton. It is also noteworthy that Form I appeared to have the weakest hydrogen bonds [13,27].

The FT-IR spectrum of the freeze-dried system (Fig. 4b) did not reveal any new bands, although if SMX and HP- β -CD form a solid inclusion complex, the non-covalent interactions between them such as hydrophobic interactions, Van der Waals interactions and hydrogen bonds lower the energy of the included part of SMX, thereby reducing the intensity of the corresponding absorption bands. Based on these considerations, the differences between the spectra of SMX, freeze-dried system and the physical mixture were analyzed to obtain supporting evidence of complexation. We can see an absence of SMX bands in the region 3700–3000 cm^{-1} , demonstrating that the aniline NH_2 , and the sulphonamide NH and the CH of the isoxazole ring of the drug were involved in the interaction process. In addition, the band assigned to the combination of the NH_2 group and the CN isoxazole ring was broader and shifted to 1619.3 cm^{-1} with intensity reduction, indicating a host restriction of vibration within the cavity of the HP- β -CD. The isoxazole ring bands became broadened and shifted to lower frequencies of 1465.3 and 1376.2 cm^{-1} , respectively, with the bands assigned to SO_2 group being broader and shifted to higher frequencies of 1325.9 and 1154.9 cm^{-1} respectively, suggesting that the sulphonamide group of SMX interacts with the groups of the host during inclusion complexation. The characteristic band assigned to CH of the isoxazole ring disappeared, and the band of the aromatic protons was broader and shifted to a higher frequency of 838.6 cm^{-1} . According to these observations, there seemed to be formation of an inclusion complex between SMX and HP- β -CD in the solid state. In contrast, the FT-IR spectra of the physical mixture (Fig. 4c) there were no changes since they were derived from the superposition of the spectra of the single components, suggesting the absence of interactions.

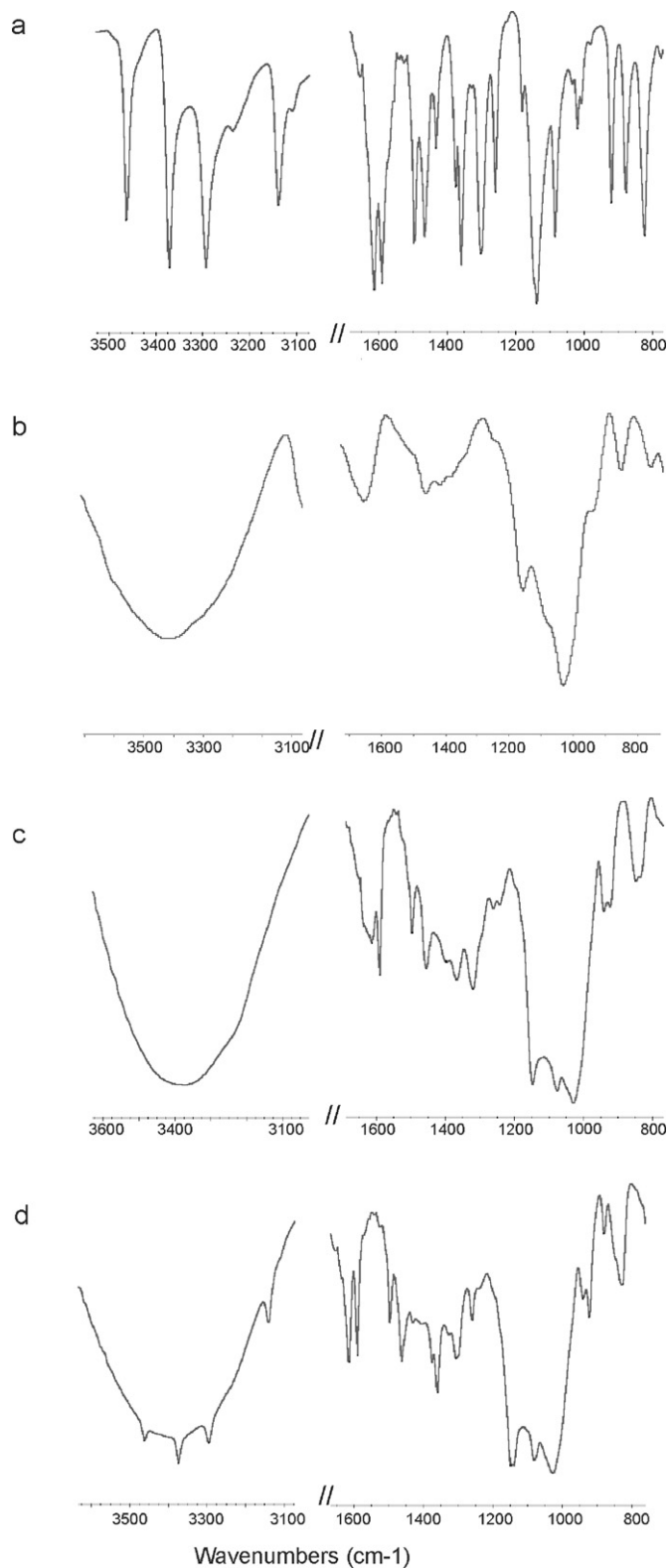


Fig. 4. FT-IR spectra of: (a) SMX, (b) HP- β -CD, (c) SMX:HP- β -CD freeze-dried, (d) SMX:HP- β -CD physical mixture.

3.3.2. Differential scanning calorimetry (DSC) and thermogravimetric analysis (TGA)

The DSC and TGA profiles in Fig. 5 SMX showed a sharp endothermic peak at 170.5 °C due to drug melting. The exothermic peak at 283.8 °C ascribed to the oxidation of evolved products [28] was

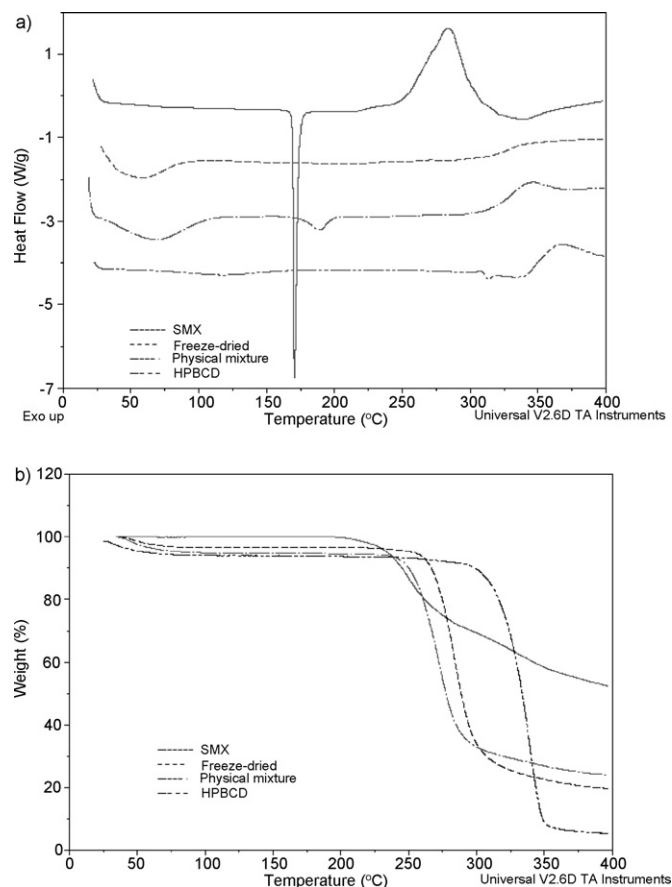


Fig. 5. (a) DSC curves of SMX (solid line), SMX:HP- β -CD freeze-dried (short dash) SMX:HP- β -CD physical mixture (dash dot line) and HP- β -CD (broken double dash line). (b) TGA curves of SMX (solid line), SMX:HP- β -CD freeze-dried (short dash) SMX:HP- β -CD physical mixture (dash dot line) and HP- β -CD (broken double dash line).

associated with a loss in the mass fraction of 30%, between 200 and 300 °C in the TGA curve. HP- β -CD exhibited a typical broad endothermic peak between 50 and 175 °C, which resulted from a dehydration process (6.5% mass loss) that corresponded to a loss of about 4.5 water molecules per HP- β -CD molecule. Also, at temperature higher than 300 °C, the CD decomposition began to appear.

The DSC curve of the binary freeze-dried system showed complete disappearance of the SMX melting peak, indicating molecular encapsulation of the drug inside the CD cavity. Interestingly, the TGA curve for the system showed that the dehydration stage contained only 3.3% of water compared to the 5.0% present in the physical mixture, which indicates that most of the water molecules in the HP- β -CD cavity were replaced by SMX during the inclusion process. In addition, in the physical mixture, the characteristic events observed for the individual curves of SMX and HP- β -CD were also found.

Finally, the TGA curves showed mass losses indicating the following order of thermal stability: freeze-dried system > physical mixture > SMX, with the drug being thermally stable up to 243, 234 and 200 °C, respectively. Furthermore, the mass loss observed for the freeze-dried system and physical mixture occurred through a fast process whereas the mass loss for SMX began as a slow process. The considerably higher temperature needed for degrading the freeze-dried system compared with the pure drug, suggests a substantial enhancement of the thermal stability of SMX in solid state through the formation of the inclusion complex.

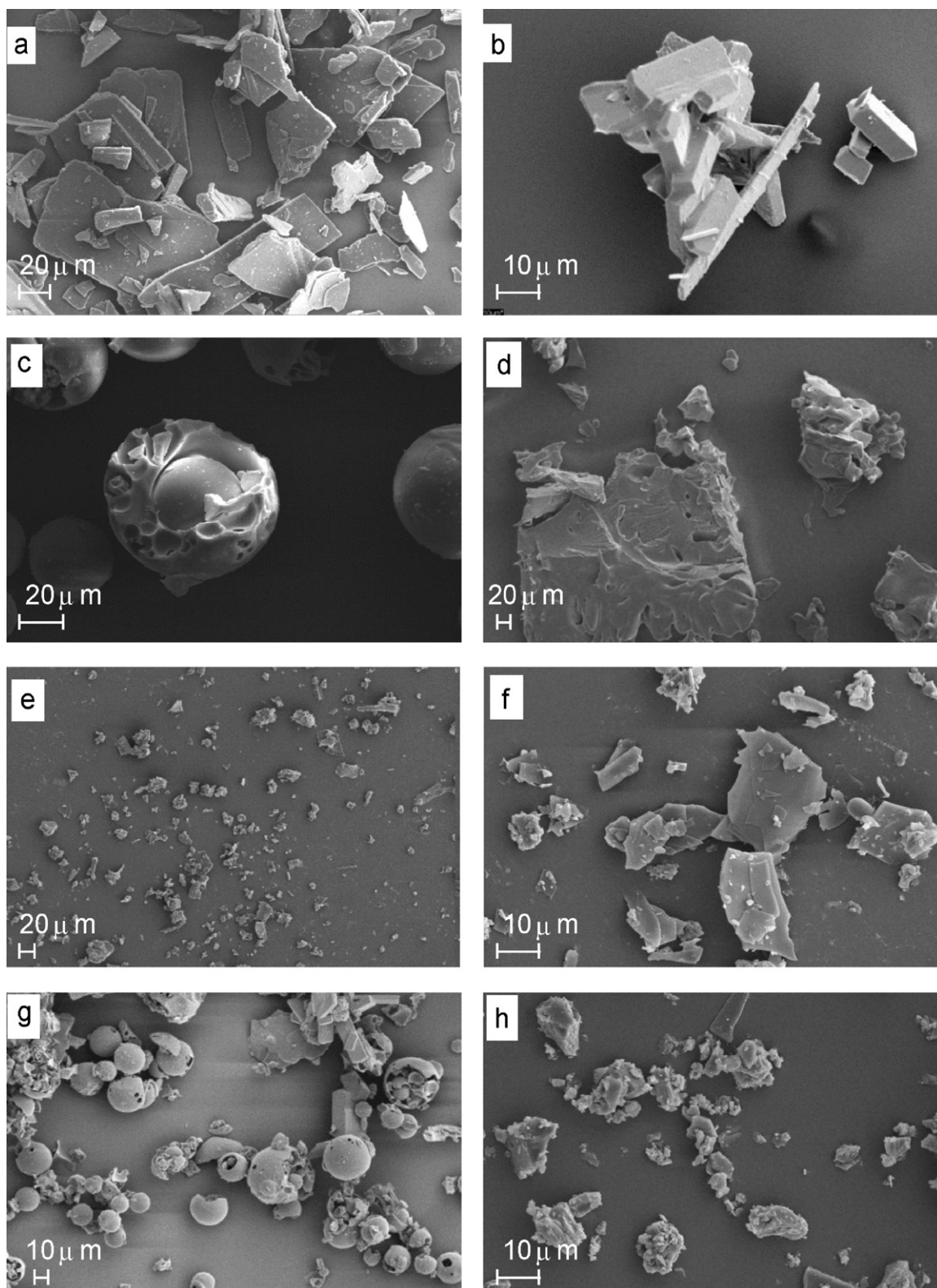


Fig. 6. Scanning electron microphotographs of: SMX (a) powder and (b) freeze-dried, HP- β -CD (c) powder and (d) freeze-dried; SMX:HP- β -CD freeze-dried (e and f); SMX:HP- β -CD physical mixture prepared with (g) pure powders and (h) freeze-dried components.

3.3.3. Scanning electron microscopy (SEM)

Supporting evidence for complexation of SMX with HP- β -CD was also obtained from SEM microphotographs (Fig. 6). Samples of SMX and HP- β -CD freeze-dried powders were included

in the assays to evaluate the effect of the lyophilization process on the morphology of the solids used to prepare the solid systems. SMX showed a plate like habit crystal, compact structures can be observed with irregular shapes and different sizes,

characterized by a smooth surface. Their morphology was not affected by the lyophilization process. On the other hand, the HP- β -CD microphotographs reveal hollow spherical particles with a broad size distribution (10–50 μm). In addition, large particles were detected containing smaller particles, which may be assumed to be an aggregation of HP- β -CD in the solid powder. However, the HP- β -CD freeze-dried appeared in the form of irregular particles in which the original morphology disappeared.

The images of the freeze-dried system showed a less crystalline structure. By image magnification, it was possible to visualize laminated structures of irregular size and shape, with smooth surfaces and a fragile aspect. By contrast, both physical mixtures, prepared with pure powders or freeze-dried components, showed the characteristic crystals of SMX mixed with particles of HP- β -CD, confirming the presence of crystalline drug and revealing the absence of interaction in the solid system.

Considering the drastic change in the shape of particles obtained by the freeze-dried method in which the original morphology of both components disappeared, together with their differences with the systems obtained by physical mixing, reveals a solid-state interaction and constitutes clear evidence of a new solid phase formation resulting from the molecular complexation of SMX in the cavity of HP- β -CD.

4. Conclusions

This study clearly evidence that the complexation with HP- β -CD is an effective strategy to increase the solubility of SMX form I. Furthermore, the results show that the ligand is capable of producing binary complexes in solution and solid state.

Acknowledgments

Financial support from Fondo para la Investigación Científica y Tecnológica (FONCYT) Préstamo BID 1728/OC-AR PICT 1376, the Consejo Nacional de Investigaciones Científicas y Técnicas (CONICET) and the Secretaría de Ciencia y Técnica de la Universidad Nacional de Córdoba (SECyT-UNC), are greatly acknowledged. We also thank Ferromet S.A. (agent of Roquette in Argentina) for their donation of hydroxypropyl- β -cyclodextrin. Finally, we would like to thank Dr. Paul Hobson, native speaker, for revision of the manuscript.

References

- [1] T. Loftsson, H. Fridriksdottir, B. Olafsdottir, O. Gudmundsson, Solubilization and stabilization of drugs through cyclodextrin complexation, *Acta Pharm. Nord.* 3 (1991) 215–217.
- [2] D. Duchene, D. Wouessidjewe, Physicochemical characteristics and pharmaceutical uses of cyclodextrin derivatives. Part II, *Pharm. Technol.* 14 (1990) 26–34.
- [3] T. Loftsson, M. Brewster, Pharmaceutical applications of cyclodextrins. 1. Drug solubilization and stabilization, *J. Pharm. Sci.* 85 (1996) 1017–1025.
- [4] T. Loftsson, Effects of cyclodextrins on the chemical stability of drugs in aqueous solutions, *Drug Stability* 1 (1995) 22–33.
- [5] R. Rajewski, V. Stella, Pharmaceutical applications of cyclodextrins. 2. In vivo drug delivery, *J. Pharm. Sci.* 85 (1996) 1142–1169.
- [6] T. Loftsson, M. Masson, H. Sigurdsson, Cyclodextrins and drug permeability through semi-permeable cellophane membranes, *Int. J. Pharm.* 232 (2002) 35–43.
- [7] T. Loftsson, M. Masson, M. Brewster, Self-association of cyclodextrins and cyclodextrin complexes, *J. Pharm. Sci.* 93 (2004) 1091–1099.
- [8] M. Messner, S.V. Kurkov, P. Jansook, T. Loftsson, Self-assembled cyclodextrin aggregates and nanoparticles, *Int. J. Pharm.* 387 (2010) 199–208.
- [9] A. Nieto, F. Borrull, R.M. Marce, E.J. Pocurull, Selective extraction of sulfonamides, macrolides and other pharmaceuticals from sewage sludge by pressurized liquid extraction, *J. Chromatogr. A* 1174 (2007) 125–131.
- [10] G. Granero, C. Garnero, M. Longhi, The effect of pH and triethanolamine on sulfisoxazole complexation with hydroxypropyl- β -cyclodextrin, *Eur. J. Pharm. Sci.* 20 (2003) 285–293.
- [11] G. Granero, M.S. Maitre, C. Garnero, M. Longhi, Synthesis, characterization and in vitro release studies of a new acetazolamide:HP- β -CD-TEA inclusion complex, *Eur. J. Med. Chem.* 43 (2008) 464–470.
- [12] A. Zoppi, M. Quevedo, A. Delrivo, M. Longhi, Complexation of sulfonamides with β -cyclodextrin studied by experimental and theoretical methods, *J. Pharm. Sci.* 99 (2010) 3166–3176.
- [13] D.A. Adson, D.J.W. Grant, Hydrogen bonding in sulphonamides, *J. Pharm. Sci.* 90 (2001) 2058–2077.
- [14] L. López Martínez, P.L. López de Alba, L.M. de León Rodríguez, M.L. Yezpe Murieta, Simultaneous determination of binary mixtures of trimethoprim and sulfamethoxazole or sulphamethoxypridazine by the bivariate calibration spectrophotometric method, *J. Pharm. Biomed. Anal.* 30 (2002) 77–85.
- [15] M. Takasuka, H. Nakai, IR and Raman spectral and X-ray structural studies of polymorphic forms of sulfamethoxazole, *Vib. Spectrosc.* 25 (2001) 197–204.
- [16] A. Muthu Prabhu, G. Venkatesh, N. Rajendiran, Spectral characteristics of sulfa drugs: effect of solvents, pH and β -cyclodextrin, *J. Solution Chem.* 39 (2010) 1061–1086.
- [17] Y.Q. Wu, D.X. Li, B.G. Li, J. Wang, Preparation of inclusion compound of β -cyclodextrin with sulfamethoxazole, *J. Univ. Shanghai Sci. Technol.* 29 (2007) 315–320.
- [18] N.M. Diez, A.M. De La Peña, M.C.M. García, D.B. Gil, F. Cañada Cañada, Fluorimetric determination of sulphaguanidine and sulphamethoxazole by host-guest complexation in β -cyclodextrin and partial least squares calibration, *J. Fluoresc.* 17 (2007) 309–318.
- [19] C. McDonald, Faridah, Solubilities of trimethoprim and sulfamethoxazole at various pH values and crystallization of trimethoprim from infusion fluids, *J. Parenter. Sci. Technol.* 45 (1991) 147–151.
- [20] M. Pourmohhtar, G.A. Jacobson, Enhanced stability of sulfamethoxazole and trimethoprim against oxidation using hydroxypropyl- β -cyclodextrin, *Pharmazie* 60 (2005) 837–839.
- [21] G. Granero, C. Garnero, M. Longhi, Second derivative spectrophotometric determination of trimethoprim and sulfamethoxazole in the presence of hydroxypropyl- β -cyclodextrin (HP- β -CD), *J. Pharm. Biomed. Anal.* 29 (2002) 51–59.
- [22] T. Higuchi, K.A. Connors, Phase-solubility techniques, in: C.N. Reilly (Ed.), in: *Advances in Analytical Chemistry and Instrumentation*, Wiley-Interscience, New York, 1965, pp. 117–212.
- [23] O. Funk, L. Schwabe, K. Fromming, Freeze-dried preparations of ketoprofen and heptakis-(2,6-o-dimethyl)- β -cyclodextrin, *Drug Dev. Ind. Pharm.* 20 (1994) 1957–1969.
- [24] M.E. Brewster, T.T. Loftsson, Cyclodextrins as pharmaceutical solubilizers, *Adv. Drug Deliv. Rev.* 59 (2007) 645–666.
- [25] T. Loftsson, T. Guomundsdottir, H. Fridriksdottir, The influence of water-soluble polymers and pH on hydroxypropyl- β -cyclodextrin complexation of drugs, *Drug Dev. Ind. Pharm.* 22 (1996) 401–405.
- [26] C. Garnero, A. Zoppi, D. Genovese, M. Longhi, Studies on trimethoprim:hydroxypropyl- β -cyclodextrin: aggregate and complex formation, *Carbohydr. Res.* 345 (2010) 2550–2556.
- [27] S.S. Yang, J.K. Guillory, Polymorphism in sulfonamides, *J. Pharm. Sci.* 61 (1972) 26–40.
- [28] N.S. Fernandes, M.A. da Silva Carvalho Filho, R.A. Mendes, M. Ionashiro, Thermal decomposition of some chemotherapeutic substances, *J. Braz. Chem. Soc.* 10 (1999) 459–462.



A comparative study of the use of powder X-ray diffraction, Raman and near infrared spectroscopy for quantification of binary polymorphic mixtures of piracetam

Denise M. Croker^{a,b,*}, Michelle C. Hennigan^{a,c,d}, Anthony Maher^{a,b}, Yun Hu^{a,c}, Alan G. Ryder^{a,d}, Benjamin K. Hodnett^{a,b}

^a Solid State Pharmaceutical Cluster, Ireland

^b Materials and Surface Science Institute, Department of Chemical and Environmental Sciences, University of Limerick, Ireland

^c School of Chemistry, National University of Ireland, Galway, Ireland

^d Nanoscale Biophotonics Laboratory, School of Chemistry, National University of Ireland, Galway, Ireland

ARTICLE INFO

Article history:

Received 20 October 2011

Received in revised form 9 January 2012

Accepted 11 January 2012

Available online 18 January 2012

Keywords:

Piracetam polymorphs

Quantitative analysis

Powder X-ray diffraction

Raman spectroscopy

Near-infrared spectroscopy

ABSTRACT

Diffraction and spectroscopic methods were evaluated for quantitative analysis of binary powder mixtures of FII(6.403) and FIII(6.525) piracetam. The two polymorphs of piracetam could be distinguished using powder X-ray diffraction (PXRD), Raman and near-infrared (NIR) spectroscopy. The results demonstrated that Raman and NIR spectroscopy are most suitable for quantitative analysis of this polymorphic mixture. When the spectra are treated with the combination of multiplicative scatter correction (MSC) and second derivative data pretreatments, the partial least squared (PLS) regression model gave a root mean square error of calibration (RMSEC) of 0.94 and 0.99%, respectively. FIII(6.525) demonstrated some preferred orientation in PXRD analysis, making PXRD the least preferred method of quantification.

© 2012 Elsevier B.V. All rights reserved.

1. Introduction

Polymorphism is a well recognized phenomenon whereby a pure chemical compound may exist in two or more structural orientations, each displaying different physical characteristics. Pseudo-polymorph—solvates and hydrates which have a molecule of solvent included in the crystal structure are also possible. As different polymorphs display individual physical properties, such as density, melting point and solubility, polymorph purity is vitally important to the manufacture of chemicals, in particular, pharmaceuticals. Production of an unwanted, or impure, polymorph will give a product that most likely will not satisfy the intended purpose, or processing characteristics, of the required polymorph. Identification and quantification of polymorphic forms has become a necessary requirement in the production of modern day pharmaceuticals [1,2].

A range of analytical techniques have proven suitable for the analysis and quantification of polymorphic mixtures. Powder X-ray diffraction (PXRD) [3–11], near-infrared spectroscopy (NIR) [12–16], attenuated total reflectance infrared (ATR-IR) spectroscopy [14], diffuse reflectance infrared spectroscopy (DRIFTS) [4,17], Raman spectroscopy [7,9,14,18–21] and, more recently, solid state ¹³C CP/MAS NMR spectroscopy [22] have been used to successfully quantify polymorphic mixtures with methods ranging from simple univariate correlations to more complicated multivariate chemometric approaches.

Piracetam (2-oxo-1-pyrrolidine acetamide) is a polymorphic drug compound (Fig. 1) with five reported polymorphs, of which two (FIV and FV) are obtained only under high pressure (>0.5 GPa) conditions [23]. The remaining polymorphs FI, FII and FIII, have been identified and structurally characterized under ambient conditions [24,25]. FI is highly unstable at ambient conditions and can be isolated only by heating FII or FIII to 400 K and then quenching to room temperature. It transforms back to FII in the solid state within a few hours, and, as such, is not of much practical relevance. FII is metastable, and FIII is the stable polymorph at ambient conditions, as determined by melting data [25]. A quantification model for polymorphic mixtures of FII and FIII piracetam is desired to investigate the solution mediated polymorphic transformation of

* Corresponding author at: Materials and Surface Science Institute, Department of Chemical and Environmental Sciences, University of Limerick, Ireland. Tel.: +353 61 234166; fax: +353 61 213529.

E-mail address: Denise.Croker@ul.ie (D.M. Croker).

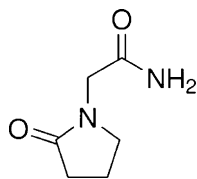


Fig. 1. Chemical structure of piracetam (2-oxo-1-pyrrolidine acetamide).

FII to FIII. To our knowledge, no efforts have been made in published literature to quantify mixtures of FII and FIII piracetam. Throughout the literature there is some confusion over the nomenclature of the different polymorphs. In this work the system used for identifying the polymorphs is simply the form number followed by the *a* lattice parameter reported for the particular polymorph in the Cambridge Crystallographic Data Centre (CCDC) in brackets, so that Form II and Form III will subsequently be referred to as FII(6.403) and FIII(6.525) respectively. The reference codes for piracetam FII(6.403) and FIII(6.525) in the CCDC are BISMEV and BISMEV01, respectively.

As polymorphs differ fundamentally in their crystal structure, powder X-ray diffraction (PXRD) has become the gold standard for polymorph analysis [2,26]. Quantification using PXRD is based on the principle that the intensity of diffraction peak for a component in a mixture is related to the concentration of that component in the mixture [27]. A number of different peak parameters on PXRD patterns can be used for this analysis: peak height intensity [4], a ratio of peak height intensity [6], and peak area [7–9] being the most common in univariate analysis. Pharmaceutical compounds present an issue for X-ray diffraction analysis in that these materials can tend to display a high degree of preferred orientation. This can lead to difficulty in obtaining good quality, representative, reproducible diffractograms. Campbell Roberts et al. completed a comprehensive quantitative study for binary mixtures of mannitol polymorphs, and investigated the effect of preferred orientation on the quantification [5]. For particle sizes below 125 μm , this effect was deemed negligible. However, grinding pharmaceutical products to achieve this small particle size is not always feasible, as grinding may induce some phase transformation.

In addition to PXRD methods, vibrational spectroscopy, such as NIR, MIR, and Raman spectroscopies, can be used for rapid characterization and quantification of polymorphs of pharmaceutical materials. NIR is associated with the overtones and combination modes of fundamental molecular vibrations that occur in the NIR to IR spectral region [28]. The coupling of NIR with chemometrics allows for interpretation of the resulting broad spectra and it is a technique widely used in pharmaceutical environments, in reaction monitoring, quality control and quantification of pharmaceutical materials [29,30]. For Raman spectroscopy the gross selection rule is that for a Raman active vibration to occur there must be a change in polarizability of the molecule during its molecular vibration [31]. As many active pharmaceutical ingredients (APIs) contain aromatic functional groups with symmetric vibrational modes, they are considered to be strong Raman scatterers. Raman spectroscopy requires little or no sample preparation, and allows for *in situ* analysis and high chemical specificity. However fluorescence of samples can obscure useful spectral information, although this may be overcome by use of NIR excitation and/or the application of various data pre-processing methods. Raman Spectroscopy has been utilized successfully for the quantification of polymorphic mixtures, tablets, capsules and for inline analysis of fluid bed drying processes [32–36].

The objective of this work is to develop and compare quantification models for binary mixtures of FII(6.403) and FIII(6.525) piracetam using PXRD, Raman, and NIR spectroscopy.

2. Materials and methods

2.1. Preparation of polymorphs

Piracetam was supplied by AXO Industry Ltd., Belgium, and complies with European Pharmacopoeia standards (CAS Number: 7491-74-9). Methanol was reagent grade. 10 g of the FIII(6.525) polymorph of piracetam was prepared by recrystallization from methanol [1]. The FII(6.403) polymorph was prepared by heating 5 g of FIII(6.403) crystals to 140 °C for 72 h, and storing under ambient conditions for 5 days [2]. Isolation of pure polymorphic forms was confirmed using PXRD, DSC, and ATR-FTIR spectroscopy (Supplementary Information).

2.2. Preparation of polymorphic standards

The pure forms were ground individually in an agate mortar with a pestle for 30 s each, and a 90–125 μm sieve fraction collected for standard preparation. The possibility of any phase change occurring during grinding was discounted by testing a control sample before and after grinding. 100 mg binary calibration mixtures containing 0, 1, 5, 10, 20, 30, 40, 50, 60, 70, 80, 90, 95, 99 and 100% of FII(6.403), with the remaining mass balance provided by FIII(6.525), were prepared by gentle mixing of weighed quantities of both polymorphs in an agate mortar with pestle. Validation mixtures containing 15, 50, 75 and 85% of FII(6.403) were prepared in the same way.

2.3. X-ray powder diffractometry

Diffractograms of the samples were obtained in reflectance mode using a Phillips PANalytical X'Pert MPD Pro instrument with a Cu K α source ($\lambda = 1.5418 \text{ \AA}$), nickel filter, fixed divergence slit of 1/2°, and accelerating voltage and anode current set as 40 kV and 35 mA, respectively. Data was recorded over the range 8–35° 2 θ , using a step size of 0.017° 2 θ , a count time of 33 s per step, a scan speed of 0.064° 2 θ /s, and a sample rotation of 4 rpm using PANalytical Data Collector, version 2.0.

The polymorph mixture was placed on a silicon crystal zero-background disc, which was mounted into a sample holder using a clip. The sample surface was smoothed with a glass slide. The samples were measured consecutively in triplicate. Sample preparation using pressed cellulose discs was also attempted, but this was found to result in amplified preferred orientation effects in the recorded diffractograms.

Reference PXRD patterns for the FII and FIII polymorph were generated with the CIF files BISMEV and BISMEV01, respectively, from the Cambridge Crystallographic Data Centre (CCDC), using Mercury 2.4.

2.4. Raman spectroscopy

Raman spectra were collected at room temperature using a RamanStation spectrometer (AVALON Instruments Ltd., Belfast, Northern Ireland; now PerkinElmer) equipped with 785 nm laser diode excitation, cooled (–77 °C) CCD detector, and a motorized XYZ sample stage. The samples were placed in aluminum crucibles (Thorn Scientific Services Ltd., UK) of 2 mm depth and 5 mm diameter and measured with a laser power of 79.9 mW at the sample (spot size ~200 μm). An exposure time of 2 s \times 10 acquisitions was used for each measurement and spectra were collected over a range of 250–3310 cm^{-1} with 4 cm^{-1} resolution. Each sample was analyzed on a 3 \times 3 grid with 0.5 mm spacing to reduce sub-sampling effects. An average spectrum was calculated from the 9 individual spectra.

2.5. NIR spectroscopy

NIR data were collected using a PerkinElmer Spectrum One spectrometer fitted with an NIR reflectance attachment. NIR spectra were collected with interleaved scans in the 10,000–4000 cm^{-1} range with a resolution of 8 cm^{-1} , using 32 co-added scans. Sample vials (SUN-Sri Ltd.) were shaken and repositioned between triplicate measurements of each sample.

2.6. Data analysis

X'Pert HighScore Plus software (PANalytical) was used to calculate peak height intensity and area, and correct the shifts along the 2θ axis for PXRD scans. The cubic spline data interpolation technique was then used to reconstruct the PXRD scans. Multivariate data analysis was carried out using The Unscrambler v9.8 software (Camo, Norway). To remove unimportant baseline (offset) interferences from samples or correct scatter effects and accentuate spectral signals of interest, various different pre-processing methods, including multiplicative scatter correction (MSC), standard normal variate (SNV), first and second derivative and their combinations were applied for Raman and NIR data. Savitzki-Golay first and second derivative calculations were performed with a window size of 15 points and a second order polynomial. Mean normalization was used for PXRD data. The PXRD and spectroscopic data were subjected to mean centering prior to partial least squares (PLS) analysis. The optimal number of PLS factors was determined by using a leave-one-out cross validation procedure. The performance of the model was evaluated by using the correlation coefficient (R^2) and root mean square error (RMSE) of the calibration (RMSEC), cross-validation (RMSECV) and prediction (RMSEP). RMSE was calculated using the following equation,

$$\text{RMSE} = \sqrt{\frac{\sum_{i=1}^n (y_i - \hat{y}_i)^2}{n}} \quad (1)$$

where \hat{y}_i , y_i and n represent the calculated value, the actual value and the number of samples.

3. Results and discussion

3.1. Characterization of piracetam polymorphs

Production of the pure FII(6.403) and FIII(6.525) polymorphs was confirmed with PXRD, DSC and FTIR analysis, as seen in Fig. 2 and Supplementary Information. The experimental PXRD patterns were compared to the theoretical patterns (Fig. 2) and no polymorph impurity was detected. Some preferred orientation was evident in the FIII(6.525) pattern. Transmission mode PXRD could have provided for superior diffraction results, but this capability was not available in this study. The FTIR spectra and DSC thermograms (Supplementary Information) were compared to those published by Pavlova [24] and Kuhnert-Brandstaetter et al. [25]. The endothermic peaks in the DSC thermograms indicated that the transformation to FI(6.747) at 114 and 120 °C in FII(6.403) and FIII(6.525), respectively and melting of FI(6.747) at 152 °C.

3.2. Powder X-ray diffraction analysis

Diffraction patterns for the pure polymorphs were examined to identify regions of sufficient selectivity for either polymorph to be used for quantification studies. A region with a well resolved diffraction peak, showing no overlap with the corresponding region for the alternative polymorph was desired. The (101) peak of FII(6.403) at 15.8° 2θ and the (014) peak of FIII(6.525) at 25.7° 2θ were selected, and the change in intensity of these peaks as

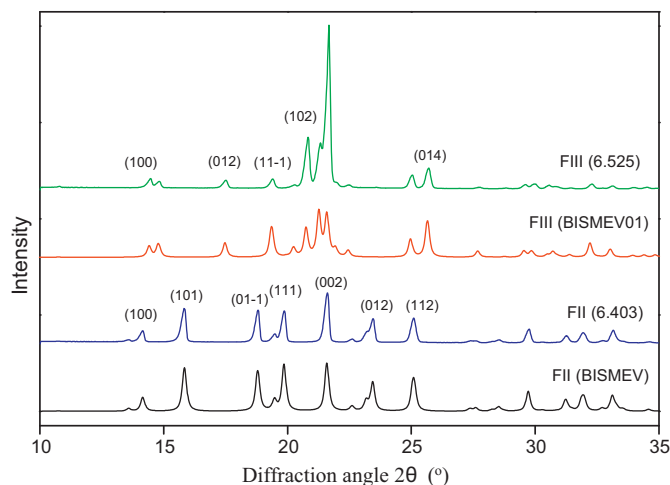


Fig. 2. Theoretical and experimental PXRD patterns of FII(6.403) and FIII(6.525) of piracetam.

a function of FII(6.403) content is shown in Fig. 3. Accordingly, a simple univariate quantification method was attempted using the PXRD data [37]. The PXRD patterns for calibration samples were analyzed quantitatively by calculating the percentage of FII(6.403) using peak height intensities and area (Eq. (2), $K=1$), and relating this to the measured percentage weight composition. The use of a response factor, K , to account for the difference in peak intensity, or area, observed for the (101) peak of FII and the (014) peak of FIII(6.525) in the diffraction pattern of pure FII(6.403) and FIII(6.525), respectively, was also assessed.

$$X_A = \frac{I_A}{I_A + (I_B + K)} \quad (2)$$

$$K = \frac{I_{Ao}}{I_{Bo}} \quad (3)$$

The peak intensity and area for PXRD data were calculated with the X'Pert HighScore Plus software, which uses a mathematical function designed to identify the peaks present in the experimental pattern and their exact position and area. The settings used for this procedure were a minimum peak significance of 1.00, minimum tip width of 0.01° 2θ , maximum tip width of 1.00° 2θ , and a peak base width of 2.00° 2θ . The univariate calibration correlations for FII calculated using peak intensity and peak area, without and with the response factor K , are presented in Fig. 4. While linear correlations were achieved, there was significant scatter around the lines resulting in poor correlation coefficients (Table 1). A slightly higher

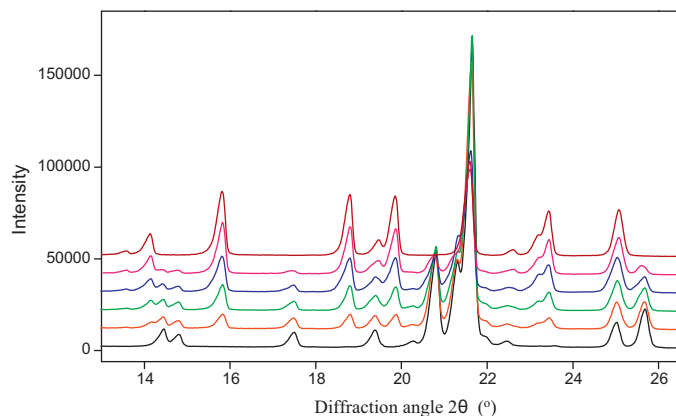


Fig. 3. PXRD patterns of different piracetam FII(6.403) and FIII(6.525) binary mixtures, and the content of FII from bottom to top is: 0, 20, 40, 60, 80, 100%.

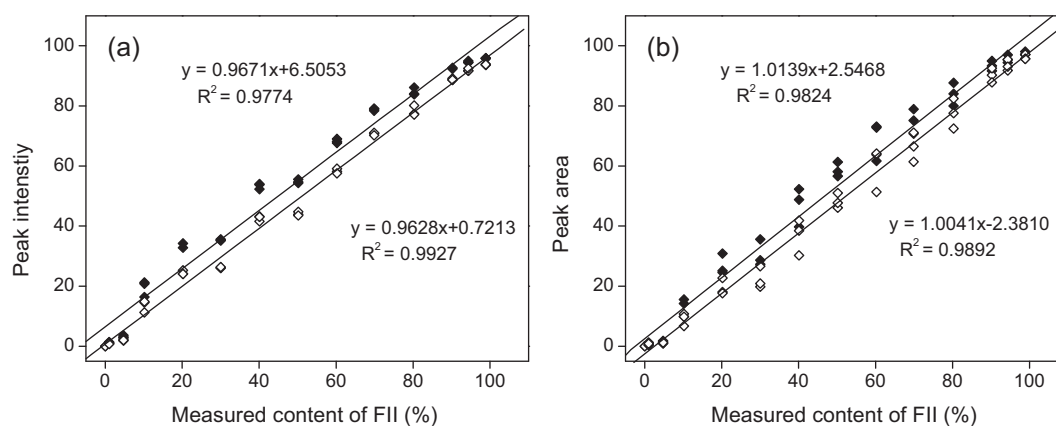


Fig. 4. Calibration curve for determination of the % (by mass) of FII(6.403) in mixtures of FII(6.403) and FIII(6.525) using the FII (0 1 0) and FIII (0 1 4) (a) peak height intensity, and (b) peak area as per Eq. (2). Calculations were made without (full symbol) and with (hollow symbol) a response factor, K (Eq. (3)).

Table 1

Performance of the regression models for quantifying FII(6.403) in binary mixtures using different analytical methods.

Methods	Pretreatments	R^2	PLS factors	RMSEC (%)	RMSECV (%)	RMSEP (%)
PXRD (peak intensity)	Without K	0.977		5.20		4.64
	With K (=1.54)	0.993		2.94		1.91
PXRD (peak area)	Without K	0.982		4.58		6.71
	With K (=1.52)	0.989		3.57		8.13
PXRD (PLS)	Mean normalization	0.997	1	2.07	2.17	1.81
Raman (PLS)	MSC and 2nd derivative	0.999	1	0.94	1.06	1.21
NIR (PLS)	MSC and 2nd derivative	0.999	1	0.99	1.11	0.64

linear correlation coefficient was achieved when a response factor K was used with the peak intensity data. The calibration model(s) was tested by using a set of validation standards, and the results are presented in Table 2.

The limit of detection (LOD) and limit of quantification (LOQ) for each correlation were calculated using Eqs. (3) and (4), the standard deviation (STD) of three measurements of a sample with 95% FIII and the slope (m) of the calibration plot for the peak intensity and peak area:

$$\text{LOD} = \frac{3 \times \text{STD}}{m} \quad (4)$$

$$\text{LOQ} = \frac{10 \times \text{STD}}{m} \quad (5)$$

Multivariate calibrations were performed on the 15.1–21.0 and 22.8–26.1° 2θ range excluding the reflection around 21.3° and 21.7° which exhibited extraordinary intensity variation with the concentration change of FII(6.403), as shown in Fig. 3. The PLS regression analysis used 45 PXRD scans from 15 calibration samples. The best calibration model (requiring only 1 PLS factor) was achieved for the quantification of FII(6.403) in the binary mixtures when PXRD patterns of calibration samples were subjected to mean normalization. The RMSEC, RMSECV and RMSEP values are presented in Table 1 and the results show a significant improvement over the univariate analysis using peak intensity or peak area. A good linear

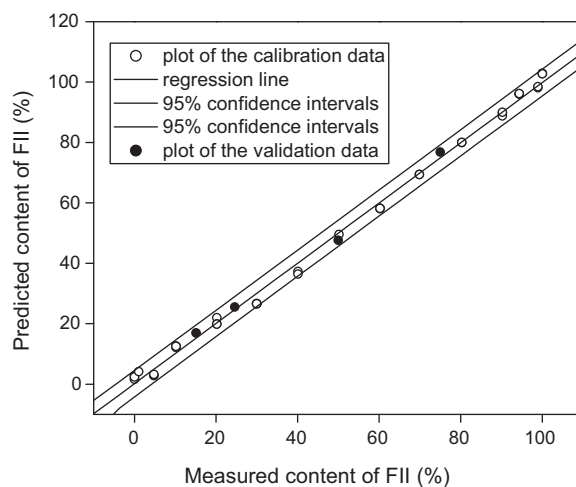


Fig. 5. Correlation curve of predicted vs. measured content of FII in FIII using PXRD by PLS analysis.

relationship was observed between the PLS predicted content of FII(6.403) against the measured content (Fig. 5) with R^2 of 0.997. LOD and LOQ for the multivariate method were estimated using the same sample, and similar results were obtained (Table 2).

Table 2

Comparison of the three techniques for the quantification of FII(6.403) in validation samples and calculated limits of detection (LOD) and quantification (LOQ).

Actual fraction of FII (%)	PXRD (peak intensity with $K = 1.54$)	PXRD (PLS)	Raman (PLS)	NIR (PLS)
15.12	18.02	16.95	14.53	14.59
24.58	25.74	25.57	25.10	24.79
49.95	52.01	47.69	51.26	49.14
74.95	74.20	76.86	76.59	74.13
LOD	0.88	0.75	1.48	0.84
LOQ	2.68	2.26	4.47	2.56

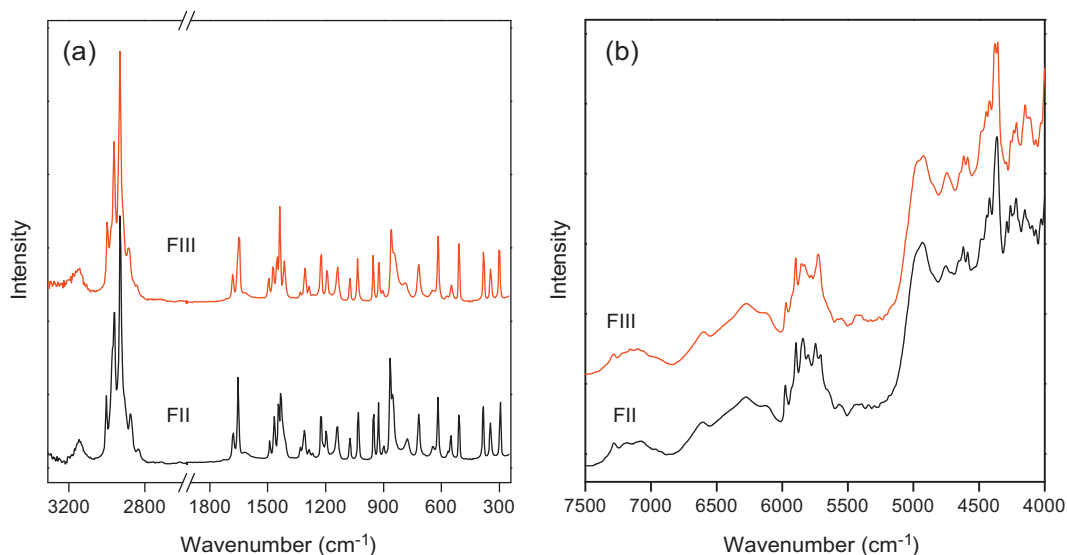


Fig. 6. (a) Raman and (b) NIR spectra of the piracetam batches FII and FIII used in this study.

3.3. Raman and NIR spectroscopic analysis

Raman spectroscopy has distinct advantages in the analysis of solid materials because of the minimal sample preparation required and the non-contact, non-destructive nature of the measurement. Different polymorphs of the same compound have different packing of molecules, and so the Raman spectra of the various polymorphs will be different due to subtle differences in molecular vibrations and rotations. Recently, the polymorphic form (FII(6.403) or FIII(6.525)) of piracetam produced from a cooling crystallization in ethanol was successfully monitored *in situ* by Raman spectroscopy [38]. Fig. 6a shows the Raman spectra (from 250 cm^{-1} to 3310 cm^{-1}) for the polymorphs FII and FIII of piracetam. The band at 3140 cm^{-1} is due to symmetric stretching vibrations of NH_2 while the 2750–2990 cm^{-1} bands can be assigned to the symmetric and anti symmetric stretching vibrations of the CH_2 groups. The 1680 and 1650 cm^{-1} bands are ascribed to the C=O stretching vibrations in the ring and acetamide, respectively. The remaining Raman band assignments can be found in the literature [39]. It is noted that there are some differences in the Raman spectra of these two polymorphs. For example, FII(6.403) has one characteristic amide peak at 1654 cm^{-1} , while in FIII(6.525) the band is split into two at 1658 and 1648 cm^{-1} . There is also a peak specific to FIII(6.525) at 1410 cm^{-1} and band shifts in the region 1530–1370 cm^{-1} . Furthermore, band shifts are also observed between of 890–750 cm^{-1} which are related to changes in the bond lengths and angles made by atoms adjacent to the carbonyl group.

Partial least squares (PLS) regression analysis was carried out using the whole and several selected spectral regions of interest (RoI). In addition, various pretreatment methods, including SNV, MSC, derivative and their combinations were used to reduce the effect of systematic variations, which are not related to the measured parameters. The results suggested the spectral region from 1730 to 1370 cm^{-1} was the most suitable for quantification and therefore selected for the model. The best PLS model was achieved for the quantification of FII(6.403) in these two binary mixtures when Raman data subjected to MSC and 2nd derivative treatment. MSC has been proved useful as it eliminated any light scattering from the powders and then subsequent use of the 2nd derivative on these pre-processed spectra gave more meaningful quantitative models with low RMSEC and RMSEP values of 0.94% and 1.12%, respectively. The plot of predicted vs. measured content of

FII(6.403) is presented in Fig. 7a and shows an R^2 value of 0.999 with high linearity.

NIR spectroscopy is also suitable for quantitative polymorph analysis and the method has been successfully applied to a wide variety of solid state characterizations [12–15,18,21]. The NIR spectra (Fig. 6b and Supplementary Information) of these two polymorphs show some differences in the 5870–5600 and 4314–4080 cm^{-1} spectral regions. For example, FII(6.403) has one peak at 5724 cm^{-1} , while FIII(6.525) has two peaks at 5748 and 5708 cm^{-1} . In addition, FII(6.403) has one peak at 4364 cm^{-1} , while FIII(6.525) has two peaks at 4380 and 4358 cm^{-1} . These two spectral RoIs were combined and used to construct PLS model. The optimal PLS model was generated after assessing the effects of several different pretreatments and combinations thereof. This optimal model was obtained by using a combination of MSC and 2nd derivative pretreatments, which gave a good linear relationship ($R^2 = 0.999$) between the predicted and measured FII(6.403) content (Fig. 7b). LOD and LOQ for the multivariate Raman and NIR based models were estimated from the mixtures containing 95% of FIII(6.525), and the results are listed in Table 2.

3.4. Comparison of the three techniques

The above results clearly show that accurate quantification of FII(6.403) in binary mixtures with FIII is possible by either PXRD or spectroscopic analysis, but the spectroscopic methods outperform PXRD. This is evident from the 95% confidence intervals (Figs. 5 and 7) where those of PXRD are much wider than for the Raman or NIR techniques. The RMSEC and RMSEP values for the Raman and NIR models are also significantly smaller than the PXRD model. To further compare the accuracy of these three techniques, a set of validation samples containing different amounts of FII(6.403) were analyzed (Table 2). For example, determination of the sample 15% FII(6.403), Raman and NIR proved to be the most accurate, followed by PXRD with PLS analysis, while PXRD with peak intensity was the least accurate. However as the FII(6.403) content increases the differences decrease, and, overall, NIR gives the most accurate predictions.

It is well known that sample homogeneity is very important in the quantification of solid powder mixtures. In this study, all the samples were sieved using a 90–125 μm sieve fraction and samples were rotated during the PXRD acquisition. Nine measurements (from a 3 × 3 grid with 0.5 mm spacing) were performed on each

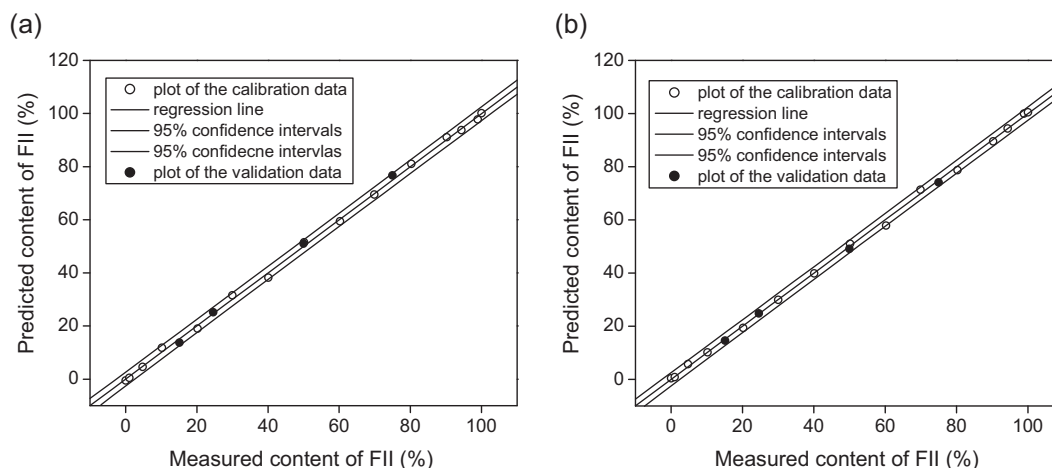


Fig. 7. Correlation curve of predicted vs. measured content of FII in FIII using (a) Raman and (b) NIR data by PLS analysis.

sample for the Raman measurements to reduce potential errors which could arise from the small sampling size. To clarify this, the relative standard deviation (RSD) values of quantitation of the 95% FIII sample obtained from the average spectrum and from individual spectra were 6.22% and 58.81%, respectively. The results clearly show that the increase in sampled volume using the 3×3 mapping reduces the errors associated with sub-sampling. NIR spectra were collected from glass sample vials and the spectra were recorded from a sample area which was 15 mm in diameter. Each sample was measured in triplicate to reduce sampling errors arising from local inhomogeneity [14].

4. Conclusion

Binary polymorphic mixtures of the nootropic drug piracetam have been prepared and analyzed quantitatively by PXRD, Raman and NIR spectroscopy, coupled with univariate and multivariate analysis. The spectroscopic techniques gave superior correlation and proved accurate in quantifying a validation data set. The FIII(6.525) polymorph of piracetam exhibits a degree of preferred orientation in XRD analysis, making quantification with this technique less accurate.

Acknowledgment

This research was made possible by the financial support of Science Foundation Ireland under Grant Number 07/SRC/B1158.

Appendix A. Supplementary data

Supplementary data associated with this article can be found, in the online version, at doi:10.1016/j.jpba.2012.01.013.

References

- [1] S. Byrn, R. Pfeiffer, M. Hoiberg, C. Ganey, G. Poochikian, Pharmaceutical solids: a strategic approach to regulatory considerations, *Pharm. Res.* 12 (1995) 945–954.
- [2] N. Chieng, T. Rades, J. Aaltonen, An overview of recent studies on the analysis of pharmaceutical polymorphs, *J. Pharm. Biomed. Anal.* 55 (2011) 618–644.
- [3] S. Agatonovic-Kustrin, V. Wu, T. Rades, D. Saville, I.G. Tucker, Powder diffractometric assay of two polymorphic forms of ranitidine hydrochloride, *Int. J. Pharm.* 184 (1999) 107–114.
- [4] D.E. Bugay, A.W. Newman, W.P. Findlay, Quantitation of cefepime-2HCl dihydrate in cefepime-2HCl monohydrate by diffuse reflectance IR and powder X-ray diffraction techniques, *J. Pharm. Biomed. Anal.* 15 (1996) 49–61.
- [5] S.N. Campbell Roberts, A.C. Williams, I.M. Grimsey, S.W. Booth, Quantitative analysis of mannitol polymorphs. X-ray powder diffractometry—exploring preferred orientation effects, *J. Pharm. Biomed. Anal.* 28 (2002) 1149–1159.
- [6] W. Dong, C. Gilmore, G. Barr, C. Dallman, N. Feeder, S. Terry, A quick method for the quantitative analysis of mixtures. 1. Powder X-ray diffraction, *Pharm. Technol.* 97 (2008) 2260–2276.
- [7] Z. Németh, G.C. Kis, G. Pokol, Á. Demeter, Quantitative determination of famotidine polymorphs: X-ray powder diffractometric and Raman spectrometric study, *J. Pharm. Biomed. Anal.* 49 (2009) 338–346.
- [8] R. Suryanarayanan, Determination of the relative amounts of anhydrous carbamazepine and carbamazepine dihydrate in a mixture by powder X-ray diffractometry, *Pharm. Res.* 6 (1989) 1017–1024.
- [9] F. Tian, F. Zhang, N. Sandler, K.C. Gordon, C.M. McGoverin, C.J. Strachan, D.J. Saville, T. Rades, Influence of sample characteristics on quantification of carbamazepine hydrate formation by X-ray powder diffraction and Raman spectroscopy, *Eur. J. Pharm. Biopharm.* 66 (2007) 466–474.
- [10] M. Tiwari, G. Chawla, A.K. Bansal, Quantification of olanzapine polymorphs using powder X-ray diffraction technique, *J. Pharm. Biomed. Anal.* 43 (2007) 865–872.
- [11] Y. Li, P. Shan Cow, R.B.H. Tan, Quantification of polymorphic impurity in an enantiotropic polymorph system using differential scanning calorimetry, X-ray powder diffraction and Raman spectroscopy, *Int. J. Pharm.* 415 (2011) 110–118.
- [12] C.M. McGoverin, L.C.H. Ho, J.A. Zeidler, C.J. Strachan, K.C. Gordon, T. Rades, Quantification of binary polymorphic mixtures of ranitidine hydrochloride using NIR spectroscopy, *Vib. Spectrosc.* 41 (2006) 225–231.
- [13] E. Ziémons, H. Bourichi, J. Mantanus, E. Rozet, P. Lebrun, E. Essassi, Y. Cherrah, A. Bouklouze, P. Hubert, Determination of binary polymorphic mixtures of fluconazole using near infrared spectroscopy and X-ray powder diffraction: a comparative study based on the pre-validation stage results, *J. Pharm. Biomed. Anal.* 55 (2011) 1208–1212.
- [14] Y. Hu, A. Erxleben, A.G. Ryder, P. McArdle, Quantitative analysis of sulfathiazole polymorphs in ternary mixtures by attenuated total reflectance infrared, near-infrared and Raman spectroscopy, *J. Pharm. Biomed. Anal.* 53 (2010) 412–420.
- [15] A.D. Patel, P.E. Luner, M.S. Kemper, Quantitative analysis of polymorphs in binary and multi-component powder mixtures by near-infrared reflectance spectroscopy, *Int. J. Pharm.* 206 (2000) 63–74.
- [16] Y. Xie, W. Tao, H. Morrison, R. Chiu, J. Jona, J. Fang, N. Cauchon, Quantitative determination of solid-state forms of a pharmaceutical development compound in drug substance and tablets, *Int. J. Pharm.* 362 (2008) 29–36.
- [17] K. Pöllänen, A. Häkkinen, M. Huhtanen, S.-P. Reinikainen, M. Karjalainen, J. Rantanen, M. Louhi-Kultanen, L. Nyström, DRIFT-IR for quantitative characterization of polymorphic composition of sulfathiazole, *Anal. Chim. Acta* 544 (2005) 108–117.
- [18] C.M. Deeley, R.A. Spragg, T.L. Threlfall, A comparison of Fourier transform infrared and near-infrared Fourier transform Raman spectroscopy for quantitative measurements: an application in polymorphism, *Spectrochim. Acta A: Mol. Spectrosc.* 47 (1991) 1217–1223.
- [19] M.J. Pelletier, Quantitative analysis using Raman spectrometry, *Appl. Spectrosc.* 57 (2003) 20A–42A.
- [20] N. Chieng, S. Rehder, D. Saville, T. Rades, J. Aaltonen, Quantitative solid-state analysis of three solid forms of ranitidine hydrochloride in ternary mixtures using Raman spectroscopy and X-ray powder diffraction, *J. Pharm. Biomed. Anal.* 49 (2009) 18–25.
- [21] A. Heinz, M. Savolainen, T. Rades, C.J. Strachan, Quantifying ternary mixtures of different solid-state forms of indomethacin by Raman and near-infrared spectroscopy, *Eur. J. Pharm. Sci.* 32 (2007) 182–192.
- [22] T. Virtanen, S.L. Maunu, Quantitation of a polymorphic mixture of an active pharmaceutical ingredient with solid state ^{13}C CP/MAS NMR spectroscopy, *Int. J. Pharm.* 394 (2010) 18–25.
- [23] F.P.A. Fabbiani, D.R. Allan, S. Parsons, C.R. Pulham, An exploration of the polymorphism of piracetam using high pressure, *CrystEngComm* 7 (2005) 79–186.
- [24] A. Pavlova, Polymorphisms of piracetam, *Pharmazie* 34 (1979) 449–450.

- [25] M. Kuhnert-Brandstaetter, A. Burger, R. Voellenkelee, Stability behaviour of piracetam polymorphs, *Sci. Pharm.* 62 (1994) 307–316.
- [26] G.A. Stephenson, R. Forbes, S.M. Reutzel-Edens, Characterization of the solid state: quantitative issues, *Adv. Drug Deliv. Rev.* 48 (2001) 67–90.
- [27] L. Alexander, H.P. Klug, Basic aspects of X-ray absorption in quantitative diffraction analysis of powder mixtures, *Anal. Chem.* 20 (1948) 886–889.
- [28] D.A. Burns, E.W. Ciurczak, *Handbook of Near-Infrared Analysis*, vol. 27, 2nd ed., 2001.
- [29] Y. Roggo, P. Chalus, L. Maurer, C. Lema-Martinez, A. Edmond, N. Jent, A review of near infrared spectroscopy and chemometrics in pharmaceutical technologies, *J. Pharm. Biomed. Anal.* 44 (2007) 683–700.
- [30] G. Reich, Near-infrared spectroscopy and imaging: Basic principles and pharmaceutical applications, *Adv. Drug Deliv. Rev.* 57 (2005) 1109–1143.
- [31] C.V. Raman, K.S. Krishnan, A new type of secondary radiation, *Nature* 121 (1928) 501–502.
- [32] C.J. Strachan, T. Rades, K.C. Gordon, J. Rantanen, Raman spectroscopy for quantitative analysis of pharmaceutical solids, *J. Pharm. Pharmacol.* 59 (2007) 179–192.
- [33] K. Kachrimanis, D.E. Braun, U.J. Griesser, Quantitative analysis of paracetamol polymorphs in powder mixtures by FT-Raman spectroscopy and PLS regression, *J. Pharm. Biomed. Anal.* 43 (2007) 407–412.
- [34] S. Mazurek, R. Szostak, Quantification of atorvastatin calcium in tablets by FT-Raman spectroscopy, *J. Pharm. Biomed. Anal.* 49 (2009) 168–172.
- [35] J. Johansson, A. Sparén, O. Svensson, S. Folestad, M. Claybourn, Quantitative transmission Raman spectroscopy of pharmaceutical tablets and capsules, *Appl. Spectrosc.* 61 (2007) 1211–1218.
- [36] G. Févotte, In situ Raman spectroscopy for in-line control of pharmaceutical crystallization and solids elaboration processes: a review, *Chem. Eng. Res. Des.* 85 (2007) 906–920.
- [37] B.D. Cullity, S.R. Stock, *Elements of X-ray Diffraction*, 3rd ed., Prentice Hall Inc., 2001.
- [38] M. Barrett, H. Hao, A. Maher, K. Hodnett, B. Glennon, D. Croker, In situ monitoring of supersaturation and polymorphic form of piracetam during batch cooling crystallization, *Org. Process Res. Dev.* 15 (2011) 681–687.
- [39] Y.D. Khamchukov, S.N. Shashkov, I.V. Lukomskii, Vibrational spectra of 2-oxopyrrolidineacetamide, *J. Appl. Spectrosc.* 53 (1990) 1281–1286.



Simultaneous quantification of L- α -phosphatidylcholine and cholesterol in liposomes using near infrared spectrometry and chemometry

Alina Porfire, Ioan Tomuta*, Lucia Tefas, Sorin E. Leucuta, Marcela Achim

Department of Pharmaceutical Technology and Biopharmaceutics, University of Medicine and Pharmacy "Iuliu Hatieganu", Cluj-Napoca, Romania

ARTICLE INFO

Article history:

Received 28 September 2011
Received in revised form 11 January 2012
Accepted 12 January 2012
Available online 31 January 2012

Keywords:

NIR spectroscopy
PLS
L- α -Phosphatidylcholine
Cholesterol
Liposomes

ABSTRACT

This paper describes the development and validation of a multivariate method based on transmittance NIR spectroscopy for simultaneous quantification of L- α -phosphatidylcholine (LPC) and cholesterol (CHO). Method development was based on a D-optimal experimental design consisting of 16 LPC–CHO mixtures. Calibration models were generated by partial least-squares (PLS) and principal component regression (PCR) method followed by leave-one-out cross-validation. Among the spectra pretreatment methods tested, Norris Gap first derivative was the best for both LPC and CHO quantification, combined with PLS multivariate method. The method was validated (trueness, precision, accuracy) for the concentration range 50–150% of the expected concentration in liposomes. This method was successfully applied for the characterization of liposomes prepared using the two excipients.

© 2012 Elsevier B.V. All rights reserved.

1. Introduction

Phosphatidylcholine (PC) is the principal component of egg lecithin, which represents the major structural component of cellular membranes. Lecithin is used in a variety of pharmaceutical products as dispersing, emulsifying and stabilizing agent, for its absorption-enhancing properties and as component of enteral and parenteral nutrition formulations [1]. Also, they are commonly used for the preparation of liposomes, vesicles consisting of one or more concentrically ordered assemblies of phospholipids bilayers. For liposomes preparation, egg phosphatidylcholine and phospholipids such as phosphatidylserine, synthetic dipalmitoyl-DL- α -phosphatidylcholine or phosphatidylinositol, are used in association with cholesterol (CHO) and positively or negatively charged amphiphiles such as stearylamine or phosphatidic acid [2].

Cholesterol, another important component of most natural membranes, is used in cosmetics and topical pharmaceutical formulations as an emulsifying agent [1]. CHO is incorporated in the lipid bilayer of liposomes to increase their stability by modulating the fluidity of the lipid bilayer, preventing crystallization of the phospholipids acyl chains and providing steric hindrance to their movement [3].

The characterization of liposomes usually is done through phospholipids content and the ratio between phospholipids and drug content of these carriers. However, phospholipids are difficult to be quantified by conventional and current techniques. Several colorimetric methods are usually applied for phosphate assay, but they can be used only after destruction of phospholipids to inorganic phosphate or after derivatization of the phospholipids with a chromophore and they are quite time consuming [4–6]. Besides colorimetric methods, high-performance liquid chromatography with evaporating light scattering detector or mass spectroscopy [7–9] and enzyme-based assays [10,11] could be implemented.

In this work we have developed a suitable analytical method for the quantification of LPC and CHO in the same sample, as a review of the literature showed that currently there are no methods available for this purpose. In the context of the above presented difficulties in phospholipids quantification, the near infrared spectroscopy (NIR) has been chosen as an alternative. NIR spectroscopy has numerous applications in the pharmaceutical field, including determination of physical parameters, polymorphs, moisture and chemical composition (active pharmaceutical ingredient and excipients) of pharmaceuticals [12]. Our group of research has recently developed a NIR–chemometric method for the quantification of meloxicam as active pharmaceutical ingredient and two excipients in tablets which is readily applicable to tablet testing [13]. The use of this technique in liposomes' characterization has first been described by Christensen et al. [14] who determined simultaneously the lipid (dimethyldioctadecylammonium bromide and trehalose-dibehenate) and lyoprotector in a liposomal vaccine adjuvant system.

* Corresponding author at: Department of Pharmaceutical Technology and Biopharmaceutics, Faculty of Pharmacy, 41 Victor Babes, 400012 Cluj-Napoca, Romania. Tel.: +40 264595770; fax: +40 264595770.

E-mail addresses: tomutaioan@yahoo.com, tomutaioan@umfcluj.ro (I. Tomuta).

Table 1
Composition of calibration set, according with a D-optimal experimental design.

Exp. name	X_1 ($\mu\text{g/ml}$)	X_2 ($\mu\text{g/ml}$)
N1	2000	200
N2	3000	200
N3	5000	200
N4	6000	200
N5	2000	300
N6	4000	300
N7	6000	400
N8	2000	500
N9	4000	500
N10	2000	600
N11	3000	600
N12	5000	600
N13	6000	600
N14	4000	400
N15	4000	400
N16	4000	400

X_1 , lecithin and X_2 , cholesterol.

This paper describes the development of NIR spectrophotometric–chemometric method reliable for simultaneous quantification of LPC and CHO, the validation of the method and finally its application in the characterization of LPC–CHO liposomes.

2. Materials and methods

2.1. Materials

L- α -Phosphatidylcholine (LPC, lecithin) ($\geq 50\%$, TLC) was from Sigma–Aldrich (Germany), and cholesterol (CHO) ($>98\%$) was provided by Avanti Polar Lipids (USA). All the other reagents (chloroform, ethanol, phosphates) were of analytic grade purity, commercially available.

2.2. Samples

2.2.1. Preparation of calibration samples

Stock solutions of LPC and CHO (with a concentration of 16 mg/ml and 1.6 mg/ml, respectively) were separately prepared by dissolving 800 mg LPC and 80 mg CHO in 50 ml of chloroform. Five standard solutions of LPC (2, 3, 4, 5 and 6 mg/ml) were prepared by dilution of the stock solution with appropriate volume of chloroform. Similarly, the CHO standard solutions (0.2, 0.3, 0.4, 0.5 and 0.6 mg/ml) were prepared by dilution of stock solution with appropriate volumes of chloroform. Finally, a training calibration set (Table 1) of 16 standard mixtures containing LPC and CHO in chloroform was prepared according with a D-optimal experimental design, developed in Modde 9.0 Software (Umetrics, Sweden). For that purpose, stock solutions of LPC and CHO were used and were appropriately diluted with chloroform to give reference mixtures with concentration values within the range 2–6 mg/ml for LPC, and 0.2–0.6 mg/ml for CHO.

2.2.2. Preparation of validation samples

The NIR method was validated in order to demonstrate that this analytical tool is suitable for its intended use. For validation purpose, 3 independent series (corresponding to 3 different days) were prepared at 3 concentration levels for both LPC (3, 4 and 5 mg/ml) and CHO (0.3, 0.4 and 0.5 mg/ml). For each concentration level 6 independent mixtures were prepared and analyzed (18 samples/day). The validation set was prepared using the same LPC and CHO stock solutions used for the preparation of calibration samples.

2.2.3. Preparation of liposomes

The liposomes were prepared using the “film method”. Briefly, PC (50 $\mu\text{M/ml}$) and cholesterol (5 $\mu\text{M/ml}$) were dissolved in 5 ml ethanol in a 300 ml round-bottomed flask. After complete dissolution, the solvent was evaporated under reduced pressure at 50 °C in a rotary evaporator, leading to the formation of a thin film of lipids on the surface of the flask. In order to completely remove the residual solvent, the film was maintained under a nitrogen gas flow for 1 h. Then the film of lipids was hydrated with 5 ml phosphate buffered saline (PBS, pH = 7.8) for 15 min at 37 °C. The liposomes’ dispersion was maintained overnight at 4 °C and then the liposomes were separated by centrifugation (30 min, 8000 $\times g$). Finally, the liposomes were diluted to 5 ml with the hydration buffer and stored at 4 °C until analysis.

2.3. Calibration and validation protocol

An experimental protocol was followed for the calibration and validation steps, in order to develop and validate the near infrared method. Calibration and validation samples were prepared and analyzed in 3 different days (3 series), using freshly prepared stock solutions of LPC and CHO. The usual targeted concentration in liposomes samples is 4 mg/ml for LPC and this has been considered as 100% LPC content. The standard mixtures in the calibration set were prepared on a concentration range of 50–150% of usual LPC content (50, 75, 100, 125 and 150%), according to D-optimal experimental design (Table 1). The validation has been conducted on independent samples: 75, 100 and 125% of usual LPC content, in 6 replicates for each concentration level. Similarly, the concentration of 0.4 mg/ml has been considered as 100% CHO content. The standard mixtures in the calibration set were prepared on a concentration range of 50–150% of usual CHO content (50, 75, 100, 125 and 150%), according to D-optimal experimental design (Table 1). The validation has been conducted on 6 independent samples in the range 75–125% of usual CHO content (75, 100 and 125%). All the calibration and validation samples were prepared in the laboratory.

2.4. NIR equipment and software

The NIR spectra were collected in the transmission mode, using a multipurpose analyzer (MPA) near infrared (NIR) spectrometer (Bruker Optics, Germany), with MPA-SC (Multi Purpose Analyzer-Sample Compartment) configuration specially designed for liquids analysis. The light transmitted through the sample is then measured using a sensitive indium gallium arsenide (InGaAs) detector placed immediately next to it.

Each spectrum was recorded using OPUS 6.5 software (Bruker Optics, Germany), over the range from 12500 to 4000 cm^{-1} , with a resolution of 8 cm^{-1} , in a 20 mm diameter vial. Each spectrum was the average of 32 scans. Chloroform was used as reference and its previously obtained spectrum was subtracted from samples’ spectrum.

2.5. Data processing

Spectra pre-processing methods were used in order to enhance the information searched for the study, to decrease the influence of the side information contained in the spectra and finally to construct the calibration methods. In this study, spectral pre-processing methods were applied comparatively, and they were smoothing (Smoothing – Moving Average, Smoothing – Savitsky Golay), derivatives (Norris Gap first derivative, Norris Gap second derivative) and deresolve.

The ability and efficiency of calibration were studied by estimating the standard variation of chemometric calibrations in the case

of the investigated samples. The root mean square error of cross validation (RMSECV) has also been calculated.

The Unscrambler X software package (CAMO Software AS, Norway) has been used for multivariate regressions, with no spectra pre-treatment as well as after applying pre-processing methods. This software permits models' validation by full cross-validation. In this procedure, iterative calibrations were performed by removing in turn each standard from the training set and then predicting the excluded sample with that calibration [15].

The regression methods were partial least squares (PLS) and principal component regression (PCR) analysis. In PLS methods, the regressions are computed with least squares algorithms, in order to establish a linear link between two matrices, the spectral data X and the reference values Y . The goal is to find out the variables in the X matrix that will best describe the Y matrix through linear combinations of wavelengths, called factors, in order to find the maximum covariance between the X and Y matrices [12]. In PCR method, the spectral data are treated first with principal component analysis (PCA), for the reduction of the number of variables (scores) and the representation of a multivariate table in a low dimensional space. The new variables are linear combinations of the original ones and can be interpreted like spectra. In the second step a multi-linear regression is performed on the scores as predictive variables, in order to establish a link between a reduced number of wavelengths and a property of the samples [2].

For validation purpose, the method developed using Unscrambler X software was then implemented in OPUS Quant software (Bruker Optics, Germany), because this software offers rapid analysis for a large amount of samples. The calculation of validation parameters (trueness, precision, accuracy) was realized using Microsoft Office Excel 2007 (Microsoft Corporation, USA).

2.6. Application of the method

The NIR-chemometric method was applied to determine the PC and CHO content in liposomes. In order to do that, liposomes samples were evaporated at 40 °C for 24 h and the resulted film was dissolved in 4 ml of chloroform. The yield of liposome preparation process was also calculated as the ratio between the final lipid concentration of liposomes and the initial lipid concentration used in the preparation process. For comparison, the yield of the preparation process was also calculated using the phospholipids content determined by the method of Steward-Marshall [6,16]. In this method, liposomes samples were mixed with chloroform (1.5 ml) and reagent (0.1 mol/l ammonium ferrioxalate, 1.5 ml) and shaken vigorously. After shaking, the samples were centrifuged and the absorbance of the organic phase was read at 490 nm. A calibration curve was performed with LPC in chloroform.

3. Results and discussions

The aim of our research was to develop an analytical method suitable for the quantification of both materials (PC and CHO) used in the preparation of liposomes by film hydration method. Although PC and CHO are widely used in the preparation of liposomes, no analytical method specifically designed for their simultaneous quantification has been described in the literature.

3.1. Spectra investigation

The NIR spectra for PC at 3 concentration ranges (2000 µg/ml, 4000 µg/ml and 6000 µg/ml) are presented in Fig. 1(a) and the NIR spectra for CHO at 3 concentration ranges (200 µg/ml, 400 µg/ml and 600 µg/ml) are shown in Fig. 1(b). Seen from Fig. 1(a and b), the intensive spectral peaks are mainly in

the region of 7000–4000 cm⁻¹. In addition, significant differences in the absorption bands of PC and CHO are found in the same region. As a result, for PC model development and future analysis the spectral regions 7000–6100 cm⁻¹, 5830–5450 cm⁻¹, 5212–4300 cm⁻¹, 4150–4000 cm⁻¹ have been selected. Similarly, for CHO model development and future analysis the spectral regions 7000–6100 cm⁻¹, 5830–5450 cm⁻¹, 5212–4300 cm⁻¹ have been selected. As highlighted in Fig. 1, the negative bands in the spectra were excluded from model development. These negative bands were the result of subtracting the chloroform absorption bands. Chloroform was used as solvent and absorbs NIR radiation only between 5970 and 5830 cm⁻¹, 5400 and 5240 cm⁻¹, 4300 and 4160 cm⁻¹, the NIR spectral regions excluded from model development.

3.2. Calibration of models

In this study, model development consisted in checking five different spectra pretreatments in combination with the whole spectra or different spectral regions containing strong bands of LPC and CHO. The spectral regions used in analysis were selected before applying any spectral pre-treatment method. Multivariate calibration using mathematical models was then applied to analyze the two excipients and the analysis was improved by evaluating two chemometric approaches based on PLS and PCR. After designing the calibration model, its predictive ability was tested with the samples used during its development.

The first step in model development was to investigate the most adequate pre-processing method. This investigation was mainly based upon the choice of the number of factors (principal components), and the calculation of RMSECV and R^2 .

The validation of the model was done using cross-validation method, leaving out one sample at a time, and the predicted concentrations were compared with the known concentrations of the compounds in each sample. The RMSECV was used as a diagnostic test for examining the errors in the predicted concentrations, as it indicates both precision and accuracy of predictions. It was calculated upon addition of each new factor to the PLS and PCR models. For each pre-processing method, the squared correlation coefficient, R^2 , between actual known concentration and predicted concentration was computed, in order to select the model with good predictive ability. The predictive ability of the chosen model was checked on independent samples during method validation step.

An appropriate choice of the number of factors is necessary for PCR and PLS calibration. The optimum number of factors was selected by following the criterion of Haaland and Thomas [17]. The selected model is that with the smallest number of factors such that RMSECV for that model is not significantly greater than RMSECV of the model with one or more additional factors.

The RMSECV and statistical parameters' values for simultaneous determination of PC and CHO, obtained by optimizing the calibration matrix of the absorption spectra for the PLS and PCR methods, without data pretreatment as well as after applying different spectra pre-processing methods are presented in Table 2. As seen in this table, satisfactory correlation coefficient values between actual and predicted concentrations are obtained for both LPC and CHO in the training set by PLS and PCR optimized models, indicating good predictive abilities of the models.

Concerning the results for LPC, the R^2 values for all proposed models were greater than 0.99, in both PLS and PCR algorithm. The lowest number of PCR factors was 3 for (f) model and the lowest number of PLS factors was also 3 for models (b), (c), (d) and (f). Considering the RMSECV and bias for those models, together with the R^2 values and the number of factors, the (d) model, Norris Gap

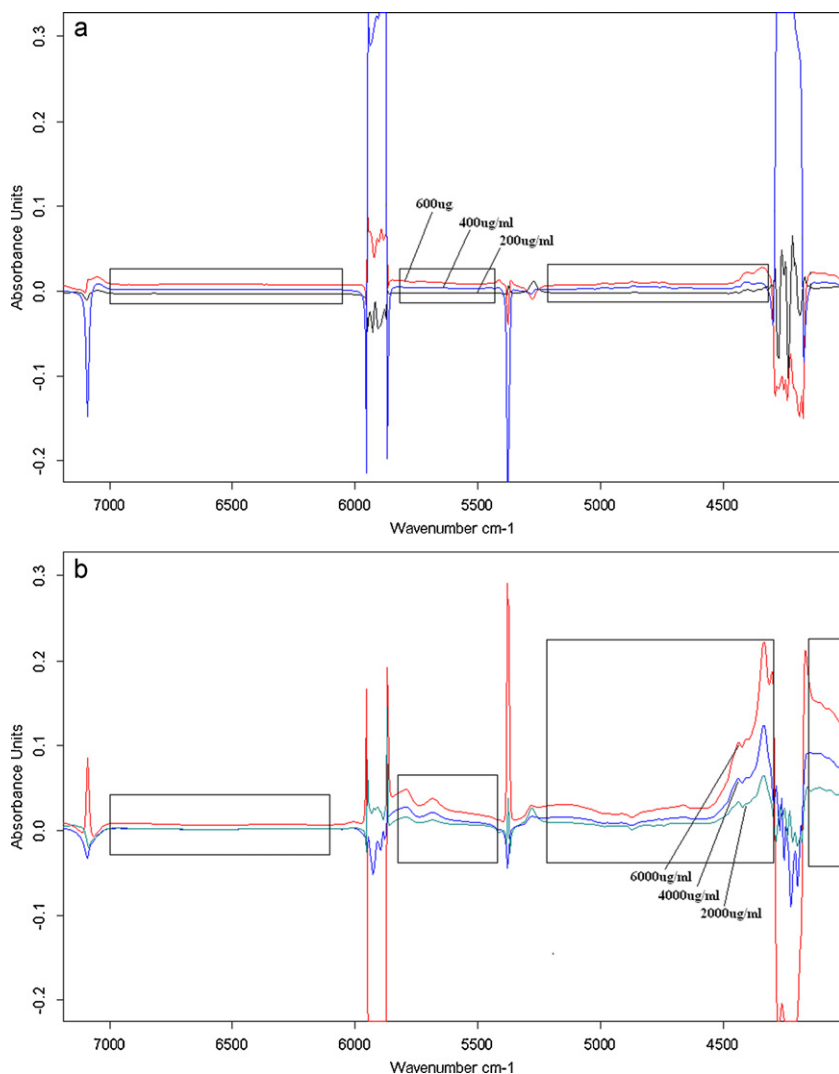


Fig. 1. NIR spectra of lecithin and cholesterol for: (a) PC (2000 µg/ml, 4000 µg/ml and 6000 µg/ml) and (b) CHO (200 µg/ml, 400 µg/ml and 600 µg/ml). The highlighted areas define the selected spectral ranges for the NIR model.

first derivative, has been chosen as the best fitted model for LPC quantification, using PLS algorithm.

In the case of CHO, only (c) model with PLS algorithm resulted in R^2 value greater than 0.99. For PCR regression, the best R^2 was obtained in Norris Gap first derivative model while for PLS

regression, the best R^2 was obtained in Smoothing – Savitsky Golay method. The lowest number of factors was 4 for (d) method in both PCR and PLS algorithms. Considering the number of factors, the R^2 and RMSECV values, Norris Gap first derivative has been chosen as the best model for CHO quantification, using PLS algorithm.

Table 2
Statistical parameters and number of principal components for LPC and CHO in the PLS and PCR method, without data pre-treatment as well as after different spectra pretreatments.

Pre-treatment	Model	No. of PC		RMSECV		R^2		Bias	
		LPC	CHO	LPC	CHO	LPC	CHO	LPC	CHO
(a)	PLS	4	7	108.50	27.28	0.998	0.987	-14.53	1.16
(b)	PLS	3	5	150.58	28.37	0.995	0.986	-2.22	1.93
(c)	PLS	3	7	142.07	23.20	0.996	0.990	5.55	-1.47
(d)	PLS	3	4	112.26	30.20	0.997	0.984	0.60	2.56
(e)	PLS	4	7	120.71	28.82	0.997	0.985	-6.06	-0.27
(f)	PLS	3	5	135.40	25.20	0.996	0.989	-0.31	-1.65
(a)	PCR	4	6	116.51	28.45	0.997	0.986	-2.79	0.55
(b)	PCR	4	6	116.51	28.23	0.997	0.986	-2.79	0.53
(c)	PCR	4	6	113.77	28.14	0.997	0.986	-2.76	0.49
(d)	PCR	4	4	111.96	25.69	0.997	0.989	-1.73	-0.84
(e)	PCR	5	6	129.50	38.86	0.996	0.973	-2.21	-1.39
(f)	PCR	3	6	159.77	27.68	0.994	0.986	-0.89	0.42

(a) No-treatment, (b) Smoothing – Moving Average, (c) Smoothing – Savitsky Golay, (d) Norris Gap first derivative, (e) Norris Gap second derivative and (f) Deresolve.

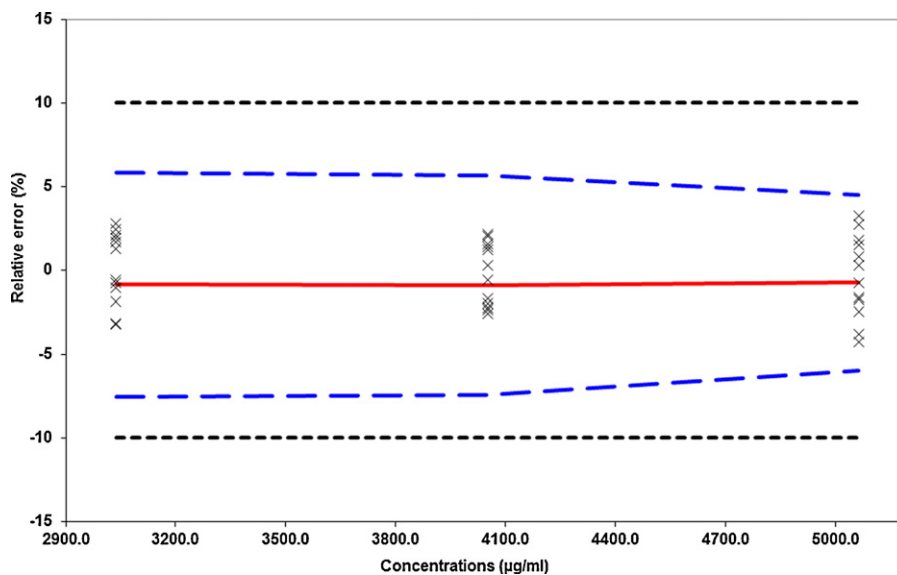


Fig. 2. Accuracy profile for LPC. The plain line is the relative bias, the dashed lines are the β -expectation tolerance limits ($\beta=95\%$) and the dotted curves are the acceptance limits ($\pm 10\%$).

Based on the results presented in Table 2, Norris Gap first derivative has been chosen as the best fitted model for LPC quantification, using PLS algorithm and the optimal number of factors was 3. For CHO quantification, according to the results shown in Table 2, the best fitted model was also Norris Gap first derivative with PLS algorithm but the optimal number of factors was 4.

3.3. Validation of model for LPC and CHO

In order to validate the model for quantitative evaluation of LPC and CHO, three sets of experiments have been performed. Each experiment consisted in the preparation and analysis of 16 calibration mixtures according to the experimental design, taken proportionately in the concentration range between 50 and 150% of the usual LPC and CHO content.

The NIR-chemometric model was developed taking into account all the samples of the three sets in the experimental design,

which were used for the determination of the concentrations of LPC and CHO, respectively, in the validation samples of each series.

The predicted values were obtained using the number of PLS factors (3 for LPC and 4 for CHO) chosen in the calibration of model. For LPC, all the developed methods have good linearity when using 3 factors and the correlation coefficients were good for both model calibration (0.9967) and model validation (0.9947). Similarly, in the case of CHO, a good linearity was obtained when using 4 factors and good correlation coefficients were calculated for both model calibration (0.9842) and model validation (0.9702).

3.4. Method validation

For method validation the methodology reported by Hubert et al. [18,19] was used. The following validation parameters were calculated: linearity, trueness, precision and accuracy.

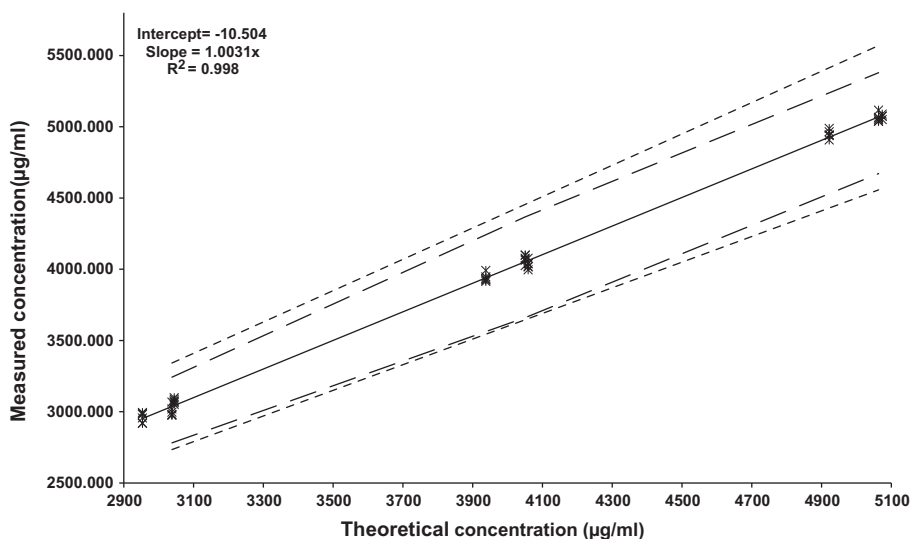


Fig. 3. Linear profile of NIR model for LPC. The dashed limits on the graph correspond to the accuracy profile and the dotted curves represent the acceptance limits at $\pm 10\%$ expressed in concentration unit. The continuous line is the identity line $y=x$.

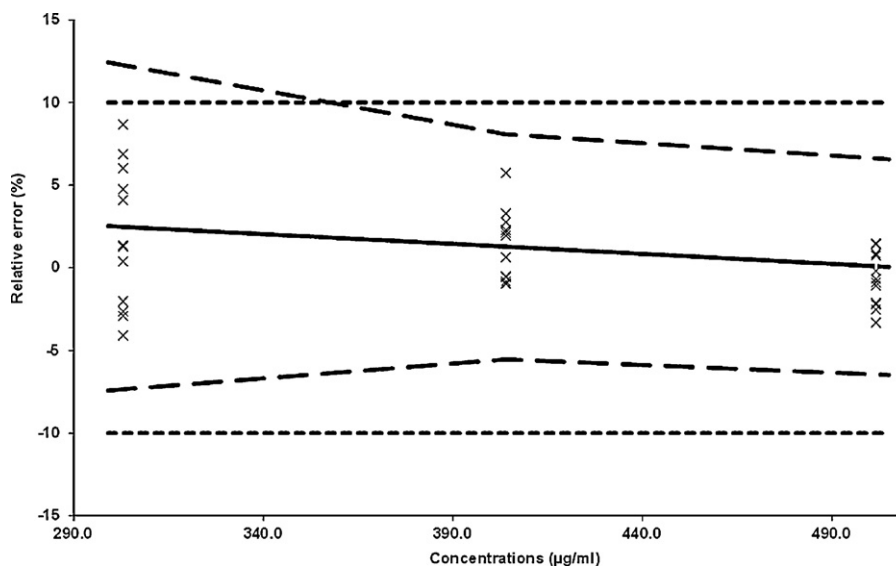


Fig. 4. Accuracy profile of cholesterol. The plain line is the relative bias, the dashed lines are the β -expectation tolerance limits ($\beta=95\%$) and the dotted curves are the acceptance limits ($\pm 10\%$).

3.4.1. Validation of NIR method for LPC

The model predictive performance was evaluated with accuracy profiles computed on the external validation results. This approach is using tolerance intervals as statistical methodology that allows predicting a region of concentration where each future result has a defined by analyst probability to fall [20]. The accuracy profile has the advantage of taking into account the total error, which is the sum of the trueness (systematic error) and precision (random error), and meets the ICH Q2 (R1) guideline requirements [18,19].

Fig. 2 shows the accuracy profile for LPC, based on the validation results obtained with Norris Gap first derivative model. The acceptance limits were set at $\pm 10\%$. The β -expectation tolerance limits should be included in the acceptance limits. As for LPC the β -expectation tolerance limits are fully included within the $\pm 10\%$ acceptance limits, it can be concluded that this method will provide results with adequate accuracy for LPC over the whole concentration range (3000–5000 $\mu\text{g/ml}$).

Table 3 shows the ICH Q2 (R1) validation criteria of the developed method for LPC. As seen in the accuracy profile and in Table 3, the relative bias has values between -0.75% and -0.9% for all the concentration levels in the validation set.

The precision of the method was evaluated by calculating two parameters: repeatability and intermediate precision at the three LPC concentration level in the validation protocol. Both parameters had satisfactory values for all LPC concentration levels. The best repeatability and intermediate precision values were obtained at the highest LPC concentration level, 5000 $\mu\text{g/ml}$, while the worst concentration level for repeatability and intermediate precision was 3000 $\mu\text{g/ml}$.

As shown in Fig. 2 and Table 3, the accuracy of the method for the entire LPC concentration domain is good, as the β -expectation

tolerance limits do not exceed the $\pm 10\%$ acceptance limits. Again, the best accuracy was obtained at LPC concentration level 5000 $\mu\text{g/ml}$.

The linear profile of the prediction model is shown in Fig. 3. The linear model was represented by plotting the calculated concentrations of the validation samples as a function of the introduced concentrations. As seen in the figure, the R^2 value is 0.998 and the slope is very close to 1, confirming the linearity of the model for LPC.

According to data presented in Figs. 2 and 3 and Table 3, the NIR-chemometric method has reproducibility and satisfactory accuracy profile and linearity profile. After analyzing the statistical parameters it can be concluded that the NIR-chemometric method is linear and sufficiently precise and accurate for the quantification of lecithin.

3.4.2. Validation of NIR method for CHO

The model predictive performance for CHO quantification was evaluated using accuracy profiles. The accuracy profile for CHO is shown in Fig. 4. As in the case of LPC, for CHO the acceptance limits were set at $\pm 10\%$. For CHO, the β -expectation tolerance limits are not fully included within the $\pm 10\%$ acceptance limits. Thus, the model is inaccurate for the quantification of CHO in the concentration range 300–400 $\mu\text{g/ml}$. It can be concluded that the lower limit of quantification (LLOQ) for CHO, defined as the lower concentration that can be accurately quantified by the analytical method, is 400 $\mu\text{g/ml}$.

Table 4 shows the ICH Q2 (R1) validation criteria of the developed method for CHO. As seen in the accuracy profile and in Table 4, the relative bias has values between 0.04% and 2.51% for all the concentration levels in the validation set.

Table 3
Validation results of NIR method for LPC quantification.

Concentration level ($\mu\text{g/ml}$)	Mean concentration ($\mu\text{g/ml}$)	Trueness		Precision		Accuracy	
		Relative bias (%)	Recovery (%)	Repeatability (RSD %)	Intermediate precision (RSD %)	Relative tolerance limits (%)	Tolerance limits ($\mu\text{g/ml}$)
3000	3012.0	-0.86	99.14	1.00	2.13	[-7.5, 5.8]	[2734.3, 3341.9]
4000	4014.3	-0.90	99.10	0.69	1.80	[-7.4, 5.6]	[3645.7, 4455.8]
5000	5025.6	-0.75	99.25	0.48	1.44	[-5.9, 4.5]	[4557.1, 5569.8]

Table 4
Validation results of NIR method for CHO quantification.

Concentration level ($\mu\text{g/ml}$)	Mean concentration ($\mu\text{g/ml}$)	Trueness		Precision		Accuracy	
		Relative bias (%)	Recovery (%)	Repeatability (RSD %)	Intermediate precision (RSD %)	Relative tolerance limits (%)	Tolerance limits ($\mu\text{g/ml}$)
300	310.6	2.51	102.51	2.05	2.86	[−7.4, 12.4]	[272.7, 333.3]
400	409.1	1.27	101.27	1.19	2.19	[−5.5, 8.1]	[363.2, 444.0]
500	501.8	0.04	100.04	1.22	1.86	[−6.5, 6.6]	[469.0, 534.5]

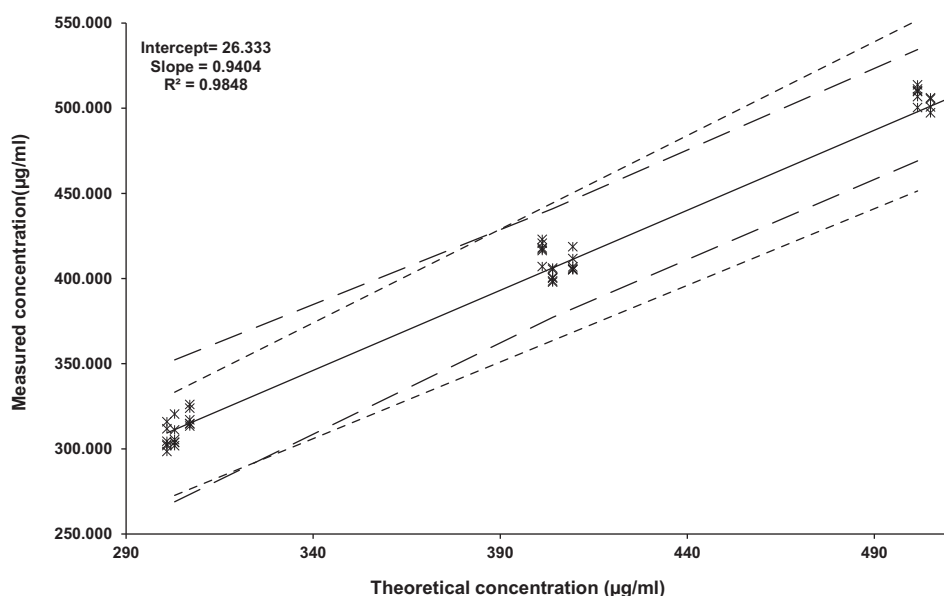


Fig. 5. Linear profile of NIR method for cholesterol. The dashed limits on the graph correspond to the accuracy profile and the dotted curves represent the acceptance limits at $\pm 10\%$ expressed in concentration unit. The continuous line is the identity line $y=x$.

In the same way as for LPC, the precision of the method was evaluated at the three concentration levels of CHO in the validation protocol. The best repeatability was obtained at the 400 $\mu\text{g/ml}$ concentration level, while the best intermediate precision was obtained at the highest concentration level. As expected, the worst results for precision were obtained at 300 $\mu\text{g/ml}$.

Concerning the accuracy of the method for CHO, the results shown in Table 4 confirm the fact that for 300 $\mu\text{g/ml}$ CHO the relative tolerance limits exceed the acceptance limits of $\pm 10\%$. Thus, the relative tolerance limits at the lowest CHO concentration were between -7.41 and 12.43% , and the best relative tolerance limits, between -6.48 and 6.56% were obtained at the highest CHO concentration level in the validation samples.

Fig. 5 shows the linear profile of the prediction model for CHO, plotted as the calculated concentration versus the introduced concentration in validation samples. The intercept, the slope and the R^2 values are also presented in Fig. 5. The linearity of the results obtained by the NIR method is demonstrated for the 400–500 $\mu\text{g/ml}$ concentration domain, since here the β -expectation tolerance limits are included in the absolute acceptance limits, while for the 300–400 $\mu\text{g/ml}$ concentration domain the β -expectation tolerance limits are exceeding the absolute acceptance limits.

According to data presented in Figs. 4 and 5 and Table 4, the NIR-chemometric method has reproducibility and satisfactory accuracy profile and linearity profile. After analyzing the statistical parameters it can be concluded that the NIR-chemometric method is linear and sufficiently precise and accurate for the quantification of cholesterol.

3.5. Application of the method

The described NIR method has been used for the quantification of LPC and CHO in liposomes. However, this method can be used to estimate the yield of the film hydration step in the preparation process of liposomes. For this purpose, different liposomes batches were prepared and analyzed in 3 different days, resulting in a total of nine batches. Thus, using data obtained from NIR analysis of liposomes samples, the yield of the preparation process was calculated to be close to $90.4 \pm 2.3\%$. This value is in the same order with that obtained by the method of Steward-Marshall ($96.3 \pm 5\%$). The NIR method has the advantage of taking into account both LPC and CHO concentration in the final liposomal dispersion, while the result in Steward-Marshall method is only based on LPC concentration.

4. Conclusions

The overall results of this study demonstrate that the content of LPC and CHO in liposomes can be simultaneously determined by NIR spectroscopy with an appropriate multivariate calibration method. Among the spectra treatment methods tested, Norris Gap first derivative was the best for both LPC and CHO quantification, combined with PLS multivariate method. For both analytes, PLS regression method was better than PCR regression method concerning the results obtained during model calibration. The calibration was done using a set of 16 PC-CHO mixtures, according to a D-optimal experimental design and afterwards method was validated by linearity, trueness, precision and accuracy.

In conclusion, NIR–chemometric spectrophotometrical method described in this study can be an interesting and appropriate tool for chemical characterization of liposomes prepared using LPC and CHO, due to the simplicity of the technique and adequate precision and accuracy for two principal components which can be present in the liposomal wall.

Acknowledgment

This work was supported by grants from The National University Research Council in Romania (PD.482, contract number 142/13.08.2010).

References

- [1] R.C. Rowe, P.J. Sheskey, S.C. Owen, Handbook of Pharmaceutical Excipients, 5th ed., Pharmaceutical Press, London, Chicago, 2006.
- [2] W. Ranade, Drug delivery systems. 1. Site-specific drug delivery using liposomes as carriers, *J. Clin. Pharmacol.* 29 (1989) 685–694.
- [3] A.S. Abreu, E.M. Castanheira, M.J. Ribeiro Peixoto Queiroz, P.M. Teixeira Ferreira, L.A. Vale-Silva, E. Pinto, Nanoliposomes for encapsulation and delivery of the potential antitumoral methyl 6-methoxy-3-(4-methoxyphenyl)-1H-indole-2-carboxylate, *Nanoscale Res. Lett.* 6 (2011), 482 (URL: <http://www.nanoscalereslett.com/content/6/1/482>).
- [4] G.R. Bartlett, Phosphorus assay in column chromatography, *J. Biol. Chem.* 234 (1959) 466–468.
- [5] C.J.F. Botcher, C.M. Van Gent, C. Pries, A rapid and sensitive sub-micro phosphorus determination, *Anal. Chim. Acta* 24 (1961) 203–204.
- [6] J.C. Steward-Marshall, Colorimetric determination of phospholipids with ammonium ferrioxalate, *Anal. Biochem.* 104 (1980) 10–14.
- [7] J.H. Felgner, Separation and quantitation of cationic liposome components by high performance liquid chromatography with evaporative light-scattering detection, *Pharm. Res.* 14 (1997) 1269–1271.
- [8] O. Meyer, O. Roch, D. Elmlinger, H.V.J. Kolbe, Direct lipid quantitation of cationic liposomes by reversed-phase HPLC in lipoplex preparation process, *Eur. J. Pharm. Biopharm.* 50 (2000) 353–356.
- [9] R. Singh, M. Ajagbe, S. Bhamidipati, Z. Ahmad, I. Ahmad, A rapid isocratic high performance liquid chromatography method for determination of cholesterol and 1,2-dioleoyl-sn-glycero-3-phosphocholine in liposome-based drug formulations, *J. Chromatogr. A* 1073 (2005) 347–353.
- [10] C.C. Allain, L.S. Poon, C.S. Chan, W. Richmond, P.C. Fu, Enzymatic determination of total serum cholesterol, *Clin. Chem.* 20 (1974) 470–475.
- [11] H. Shmeeda, S. Even-Chen, R. Honen, R. Cohen, C. Weintraub, Y. Barenholz, Enzymatic assays for quality control and pharmacokinetics of liposome formulations: comparison with nonenzymatic conventional methodologies, *Methods Enzymol.* 367 (2003) 272–292.
- [12] Y. Roggo, P. Chalus, L. Maurer, C. Lema-Martinez, A. Edmond, N. Jent, A review of near infrared spectroscopy and chemometrics in pharmaceutical technologies, *J. Pharm. Biomed. Anal.* 44 (2007) 683–700.
- [13] I. Tomuta, R. Iovanov, E. Bodoki, S.E. Leucuta, Quantification of meloxicam and excipients on intact tablets by near infrared spectrometry and chemometry, *Farmacia* 58 (2010) 559–571.
- [14] D. Christensen, M. Allesø, I. Rosenkrands, J. Rantanen, C. Foged, E.M. Agger, P. Andersen, H.M. Nielsen, NIR transmission spectroscopy for rapid determination of lipid and lyoprotector content in liposomal vaccine adjuvant system CAF01, *Eur. J. Pharm. Biopharm.* 70 (2008) 914–920.
- [15] A. Espinosa-Mansilla, F. Salinas, I. De Orbe Paya, Simultaneous determination of sulfadiazine, doxycycline, furaltadone and trimethoprim by partial least squares multivariate calibration, *Anal. Chim. Acta* 313 (1995) 103–112.
- [16] R. Sabate, R. Barnadas-Rodriguez, J. Callejas-Fernandez, R. Hidalgo-Alvarez, J. Estelrich, Preparation and characterization of extruded magnetoliposomes, *Int. J. Pharm.* 347 (2008) 156–162.
- [17] C.P. Meza, M.A. Santos, R.J. Romanach, Quantitation of drug content in a low dosage formulation by transmission near infrared spectroscopy, *AAPS Pharm-SciTech* 7 (2006), Article 29.
- [18] Ph. Hubert, J.J. Nguyen-Huu, B. Boulanger, E. Chapuzet, P. Chiap, N. Cohen, P.A. Compagnon, W. Dewé, M. Feinberg, M. Lallier, M. Laurentie, N. Mercier, G. Muzard, C. Nivet, L. Valat, Harmonization of strategies for the validation of quantitative analytical procedures: a SFSTP proposal-part I, *J. Pharm. Biomed. Anal.* 36 (2004) 579–586.
- [19] Ph. Hubert, J.J. Nguyen-Huu, B. Boulanger, E. Chapuzet, P. Chiap, N. Cohen, P.A. Compagnon, W. Dewé, M. Feinberg, M. Lallier, M. Laurentie, N. Mercier, G. Muzard, C. Nivet, L. Valat, E. Rozet, Harmonization of strategies for the validation of quantitative analytical procedures: a SFSTP proposal. Part II, *J. Pharm. Biomed. Anal.* 45 (2007) 70–81.
- [20] E. Ziemons, J. Mantanus, P. Lebrun, E. Rozet, B. Evrard, Ph. Hubert, Acetaminophen determination in low-dose pharmaceutical syrup by NIR spectroscopy, *J. Pharm. Biomed. Anal.* 53 (2010) 510–516.



Method development for pharmaceuticals: Some solutions for tuning selectivity in reversed phase and hydrophilic interaction liquid chromatography

Josephine Ruta^a, Julien Boccard^a, Deirdre Cabooter^b, Serge Rudaz^a, Gert Desmet^b, Jean-Luc Veuthey^a, Davy Guillarme^{a,*}

^a School of Pharmaceutical Sciences, University of Geneva, University of Lausanne, Boulevard d'Yvoy 20, 1211 Geneva 4, Switzerland

^b Vrije Universiteit Brussel, Department of Chemical Engineering, Pleinlaan 2, B-1050 Brussels, Belgium

ARTICLE INFO

Article history:

Received 7 December 2011
Received in revised form 18 January 2012
Accepted 19 January 2012
Available online 28 January 2012

Keywords:

UHPLC
HILIC
RPLC
Orthogonality
Column coupler

ABSTRACT

In LC method development, the choice of suitable experimental conditions is often challenging for the analyst because of the huge diversity of stationary phases, mobile phase pH and organic modifiers, that could significantly alter the selectivity.

The influence of these parameters on selectivity was experimentally tested in both RPLC and HILIC conditions for the analysis of 45 pharmaceutical compounds covering a wide range of physico-chemical properties. Principal component analysis (PCA) models were built to assess the resulting multivariate dataset. The complementarity between RPLC and HILIC was clearly demonstrated. The importance of mobile phase pH as one of the main experimental factors to be considered was confirmed.

The RPLC and HILIC methods were thus employed for the analysis of a drug cocktail containing two substrates and their numerous desmethylated metabolites. All the compounds were finally resolved in both modes, with a very distinct elution order. In addition, the possibility to combine columns of different selectivity was highlighted using a column coupler set-up and found to be extremely promising. The same type of experiments was also carried out for the impurity profiling of an antihistaminic drug. In this example, compounds of very distinct polarity were satisfactorily eluted in both RPLC and HILIC modes, using suitable conditions of pH and stationary phase.

In conclusion, this study demonstrates the complementary and interest of RPLC and HILIC in the case of pharmaceutical method development.

© 2012 Elsevier B.V. All rights reserved.

1. Introduction

In the pharmaceutical field, the analyst has to deal with ever more complex samples containing an increasing number of individual compounds that need to be separated. The purpose of liquid chromatography method development is thus to find suitable conditions allowing a sufficient resolution between individual constituents of the mixture. In LC, the choice of the experimental conditions is a major concern for the analyst because of the various parameters that influence the selectivity and their numerous combinations. Indeed, the LC separation mode, the stationary phase type, the organic modifier nature or pH have been proven to be the most relevant parameters for tuning selectivity [1–10] while temperature, gradient profile or buffer concentration appear to be less critical.

Concerning the choice of LC separation mode, several recent studies explored the orthogonality of chromatographic systems for an implementation in 2D-LC set-up [1,11]. The combination of hydrophilic interaction liquid chromatography (HILIC) and reversed phase liquid chromatography (RPLC) has demonstrated the highest degree of orthogonality for both low molecular weight analytes and peptides [12]. RPLC remains the method of choice for the separation of a wide range of compounds but in the case of polar compounds, the lack of retention is often an issue. On the other hand, HILIC, proposed by Alpert in 1990 [13], is characterized by a hydrophilic stationary phase and a mobile phase consisting of a mixture of water and usually more than 70% of aprotic organic solvent (generally acetonitrile) [14]. Consequently, the latter appears to be complementary to RPLC and provides reasonable retention and selectivity for polar compounds [15–20]. In addition, McCalley also demonstrated the use of HILIC as a valuable alternative to RPLC for the separation of ionisable compounds of diverse polarity [21,22]. One aim of the present work was to confirm the applicability of HILIC to a large panel of compounds with diverse polarity, in the case of “real” pharmaceutical applications.

* Corresponding author. Tel.: +41 22 379 34 63; fax: +41 22 379 68 08.
E-mail address: davy.guillarme@unige.ch (D. Guillarme).

In this study, 45 pharmaceutical compounds possessing different physico-chemical properties (pK_a , MW and lipophilicity) were chosen to evaluate the complementarity of various chromatographic conditions in RPLC and HILIC. In RPLC, four stationary phases, two organic modifiers and, three mobile phase pH were tested. In HILIC conditions, two different HILIC materials, two mobile phase pH and one organic modifier were tested. First, principal component analysis (PCA) was performed to evaluate the selectivity of the different chromatographic conditions and determine the most important parameter. Second, the most promising conditions for each mode were selected for future applications: (i) the analysis of a drug cocktail containing two substrates and their desmethylated metabolites and, (ii) an impurity profiling of an antihistaminic drug in both RPLC and HILIC.

2. Experimental

2.1. Chemical and reagents

Water was obtained from a Milli-Q Water Purification System from Millipore (Bedford, MA, USA). Acetonitrile and methanol were of HPLC gradient grade from Panreac Quimica (Barcelona, Spain). Ammonium hydroxide was from Sigma–Fluka (Buchs, Switzerland).

Methanol and acetonitrile (used in MS analysis) were of ULC-MS grade and purchased from Biosolve (Valkenswaard, Netherlands). Formic acid was from Merck (Darmstadt, Germany) and acetic acid from Sigma–Aldrich (Steinheim, Germany).

Formate buffer 10 mM (or 20 mM for HILIC analysis) was prepared with an adapted volume of formic acid and pH adjusted to 3.0 with ammonium hydroxide 28%. Acetate buffer 10 mM (or 20 mM for HILIC analysis) was prepared with an adapted volume of acetic acid and the pH adjusted to 4.5 and 6.0 with ammonium hydroxide 28%. Ammonium buffer 10 mM was prepared with an adapted volume of ammonium hydroxide 28% and the pH adjusted to 9.0 with formic acid.

2.1.1. Pharmaceutical compounds dataset

A dataset of 45 analytes was assessed. Amphetamine, methadone, 3,4-methylenedioxyamphetamine (MDMA) were supplied by Lipomed (Arlesheim, Switzerland). Maprotiline, chlorpromazine, levomepromazine, clotiapine, thioridazine, risperidone, fluphenazine, olanzapine, chlorprothixen, clozapine, trazodone, pipamperone, brotizolam, flupentixol and duloxetine were generously provided by E. Bachmann from the Department of Clinical Chemistry (Lausanne, Switzerland). Lidocaine, prilocaine, methylphenidate, ketamine, promethazine, cocaine, mandelic acid, baclofen, flurbiprofen, atropine, cetirizine, trimipramine, strychnine, pentobarbital, scopolamine, hyoscyamine, metolazone, betamethasone, clopamide and mefloquine were purchased from Sigma–Aldrich (Steinheim, Germany). Codeine, morphine, oxycodone, indapamide, acebutolol, ephedrine, warfarin were from Sigma–Fluka (Buchs, Switzerland). Two mixtures were prepared by an appropriate dilution of a 1 mg/ml stock solution of each compound prepared in pure MeOH. The first mixture contained amphetamine, prilocaine, methylphenidate, ketamine, maprotiline, promethazine, duloxetine, cocaine, methadone, chlorpromazine, levomepromazine, clotiapine, thioridazine, risperidone each at 2 $\mu\text{g}/\text{ml}$ and mandelic acid, ephedrine, baclofen, flurbiprofen, atropine, oxycodone, acebutolol, indapamide, cetirizine, betamethazone, fluphenazine each at 10 $\mu\text{g}/\text{ml}$. Mixture 2 contained 3,4-methylenedioxyamphetamine (MDMA), trimipramine, olanzapine, chlorprothixen, clozapine, strychnine, trazodone, brotizolam each at 2 $\mu\text{g}/\text{ml}$; pentobarbital, lidocaine, morphine, hyoscyamine, codeine, scopolamine, warfarin, clopamide, metolazone, pipamperone, mefloquine,

flupentixol each at 10 $\mu\text{g}/\text{ml}$. Dilutions were performed with pure water for RPLC studies and pure ACN for HILIC analysis because of the influence of the dilution solvent on peak shape in HILIC, as previously demonstrated elsewhere [15]. Finally, because of the reasonable employed concentrations, no problem of solubility occurred.

2.1.2. First example: drug cocktail

Tramadol (TMD), O-desmethyltramadol (O-TMD), N-desmethyltramadol (N-TMD) and N,N-didesmethyltramadol (N,N-TMD) were a gift from Prof. P. Dayer (Clinical Pharmacology Division, Geneva University Hospital, Geneva, Switzerland). Venlafaxine (VLX), O-desmethylvenlafaxine (O-VLX), N-desmethylvenlafaxine (N-VLX) and N,O-didesmethylvenlafaxine (N,O-VLX) were a gift from Dr A. E. Balant–Gorgia (Department of Psychiatry, Geneva University Hospital, Geneva, Switzerland). A stock solution at 1 mg/ml of each compound was prepared in pure MeOH, then a solution at 10 $\mu\text{g}/\text{ml}$ was injected in RPLC and HILIC conditions using the appropriated sample diluents, as previously specified.

2.1.3. Second example: impurity profiling

An antihistaminic drug and 14 related substances (synthesis products, synthetic impurities and denaturation products) were kindly provided by a company that cannot be named due to a confidentiality agreement. The chemical structure of the antihistaminic drug (API: Active Pharmaceutical Ingredient) and the 14 compounds (A to N) can also not be specified. Stock solutions were prepared at 1 mg/ml by dissolving appropriate amount of substances in a mixture of sulfuric acid 0.01% in water–acetonitrile (75:25, v/v). A dilution solution containing all compounds was prepared at 25 $\mu\text{g}/\text{ml}$ in water for RPLC analysis and at 12.5 $\mu\text{g}/\text{ml}$ in ACN for HILIC analysis.

2.2. Instrumentation

Chromatographic experiments were performed using a Waters Acquity ultra performance liquid chromatography (UPLC) system (Waters, Milford, MA, USA) that can deliver mobile phases at pressures up to 1000 bar. This instrument was equipped with a binary solvent manager with a maximum delivery flow rate of 2 ml/min, an autosampler with a 2 μl loop operating in the full loop injection mode, a UV–vis programmable detector with a 500 nl flow cell set at 220 or 230 nm. The column manager composed of a column oven was replaced by a column coupler prototype developed by Cabooter et al. [23,24]. Data acquisition, data handling, and instrument control were performed by the Empower software v2.0. The acquisition rate and time constant of the UV detector were fixed at 20 Hz and 50 ms, respectively. For this system, the extra column volume (V_{ext}), and dwell volume (V_{d}) were experimentally measured at 13 and 100 μl , respectively. The columns employed in this study were listed in Table 1.

The column coupler prototype consists of two high-pressure multiposition switching valves, TitanHT, HT715-000 from Rheodyne (Rhonert Park, CA) that can withstand pressures of 1000 bar. The stator consisted of six peripheral ports with one central port and had a port-to-port volume of only 300 nl. The rotor was custom-made to allow the valves to be used in six different positions. The valves were operated with the Empower software. The connection tubes between injector and column coupler, and column coupler to detector (Nanoviper fingertight fitting, 75 μm I.D., Dionex, Sunnyvale, USA), were kept as short as possible to reduce band broadening. PEEKsil tubing (75 μm I.D., resistant to pressures up to 1000 bar, Infochroma, Zug, Switzerland) was used to connect the columns to the switching valves. Each piece of tubing between valve and column had a maximum length of 10 cm. The return

Table 1
Column properties.

Column name	Suppliers	Particles diameter	Pore size	Surface area	Carbon load	pH range	Temperature limits
Acquity BEH C18	Waters	1.7 μm	130 Å	185 m^2/g	18%	1–12	Low pH = 80 °C High pH = 60 °C
Acquity BEH Shield RP18	Waters	1.7 μm	130 Å	185 m^2/g	17%	2–11	Low pH = 50 °C High pH = 45 °C
Acquity BEH Phenyl	Waters	1.7 μm	130 Å	185 m^2/g	15%	1–12	Low pH = 80 °C High pH = 60 °C
Acquity CSH C18	Waters	1.7 μm	130 Å	185 m^2/g	15%	1–11	Low pH = 80 °C High pH = 45 °C
Acquity BEH HILIC	Waters	1.7 μm	130 Å	185 m^2/g	Unbounded	1–9	Low pH = 45 °C High pH = 45 °C
Acquity BEH Amide	Waters	1.7 μm	130 Å	185 m^2/g	12%	2–11	Low pH = 90 °C High pH = 90 °C

capillary has a length of 20 cm. A mobile phase preheater (diameter 125 μm , Dionex, Sunnyvale, USA) was directly connected to the column coupler. For the two applications in RPLC mode, the column coupler was configured with the Acquity BEH C18 of 5 and 10 cm lengths in positions 1 and 3, respectively and Acquity CSH C18 of 5 and 10 cm lengths in positions 2 and 4, respectively. For HILIC analysis, Acquity BEH C18 and Acquity CSH C18 were replaced by Acquity BEH HILIC and Acquity BEH amide columns of the same lengths. For a schematic representation of the column coupler, the column positioning and some possible configurations of the valves, see Fig. 1 of [23].

The analysis of the 45 compounds was performed on a Waters Acquity UPLC system hyphenated with a Waters TQD triple quadrupole mass spectrometer fitted with a Z-spray electrospray ionization source. The ESCi[®] ionization source was used in the ESI positive and negative modes and Selected Ion Recording (SIR) performed. Nitrogen was used as drying gas. The capillary voltage and the source extractor voltage were set at +2.5 kV and +3 V, respectively. The source temperature was maintained at 120 °C, the desolvation gas temperature and flow rate at 350 °C and 600 L/h, respectively, and the cone gas flow at 20 L/h. Cone voltage was set at 30 V for all compounds. Finally, dwell time and inter-channel delay were set to 5 ms to obtain a sufficient number of data points acquisition. Data acquisition, data handling and instrument control were performed with the Masslynx v4.1 Software.

2.3. Data analysis

Data were analyzed by PCA with the SIMCA-P software (version 12, Umetrics, Umeå, Sweden). Autoscaling, i.e. mean centering and unit variance normalization, was applied as preprocessing to assign an equal weight to the variability of each analytical column.

3. Results and discussion

3.1. Complementarity between RPLC and HILIC

A dataset of 45 drugs covering a wide range of physico-chemical properties was initially selected to evaluate the potential of both RPLC and HILIC in the pharmaceutical field. Around 75% of these compounds possess basic properties while the remaining 25% were either acidic, neutral or zwitterionic, providing a representative picture of marketed drugs. Log *D* values at pH 3 and 9, respectively, are displayed as a function of *pK_a* values for the 45 model compounds in Fig. 1A and B. As shown, *pK_a* values ranged between 0 and 11 and log *D* between –3 and +5. In the presence of an acidic mobile phase, pH 3 (Fig. 1A), charged analytes (i.e. zwitterionic and basic compounds) are more hydrophilic than in basic conditions, pH 9 (Fig. 1B) and thus less retained in RPLC and more retained in HILIC. As expected, the opposite situation is observed for acidic

compounds. This observation underlined the well-known influence of pH on retention in liquid chromatography.

Various chromatographic conditions consisting of different combinations of mobile phase pH, organic modifier and stationary phase were tested in RPLC and HILIC. A dataset resulting from the analysis of 45 compounds in 28 experimental conditions (24 in RPLC and 4 in HILIC) was obtained. Apparent retention factors were used to characterize each analyte with respect to each setup. A first PCA model was built on the overall data table and the first principal plane (PC1 \times PC2) expressed about 90% of the initial variance. Results are presented in Fig. 2. RPLC and HILIC conditions were clearly separated on the score plot (Fig. 2A) based on the investigated analytes. Four stationary phases, a C18 (Acquity UPLC BEH C18), a polar-embedded C18 (Acquity UPLC BEH Shield RP18), a phenyl (Acquity UPLC BEH Phenyl), and the new charge surface hybrid (CSH) C18 (Acquity UPLC CSH C18) columns were considered. Regarding the mobile phase, two organic mixtures containing MeOH and ACN at three different mobile phase pH values (i.e. 3, 6, and 9) were investigated. Thus, 24 different combinations were evaluated and the corresponding PCA score plot (PC1 \times PC2) obtained for the 45 drugs is reported in Fig. 2B. More than 94% of explained variance of the data set was obtained. Based on this model, it appears that selectivity was strongly influenced by the mobile phase organic modifiers and pH (see the two directions of variation represented by dashed lines in Fig. 2B). Concerning the stationary phase, although the chromatographic behaviour seems to be similar at pH 6 and 9 with either MeOH or ACN, some significant differences were observed at pH 3. Indeed, at low pH values in ACN or MeOH, the four stationary phases can be clustered into two groups of selectivity: (i) polar-embedded C18 and CSH C18; (ii) C18 and phenyl. This observation can be easily related to the nature of the investigated compounds and the structure of the stationary phases. Indeed, most of the compounds at pH 3 are ionized and thus less retained in RPLC (75% of basic drugs). The C18 and phenyl phases possess a purely hydrophobic retention mechanism, while the CSH and polar-embedded C18 columns present a simultaneous hydrophobic and electrostatic retention mechanism. Therefore, in the case of method development, one column from each group should be selected to present sufficient difference in selectivity and to limit the injection number.

In HILIC, two different stationary phases, namely bare hybrid silica and silica derivatized with amide functional groups, were tested in combination with two mobile phase pH (i.e. 3 and 6) using ACN as organic modifier. Due to the lower pH stability of the unbounded hybrid silica stationary phase, higher pH values were not investigated in HILIC. Furthermore, only ACN was evaluated as organic modifier since MeOH decreases both ion exchange interaction as well as hydrophilic interaction with the mobile phase due to its ability to form hydrogen bonding with the analytes and silanol groups, leading to a lack of retention [25,26]. First, it is important to notice

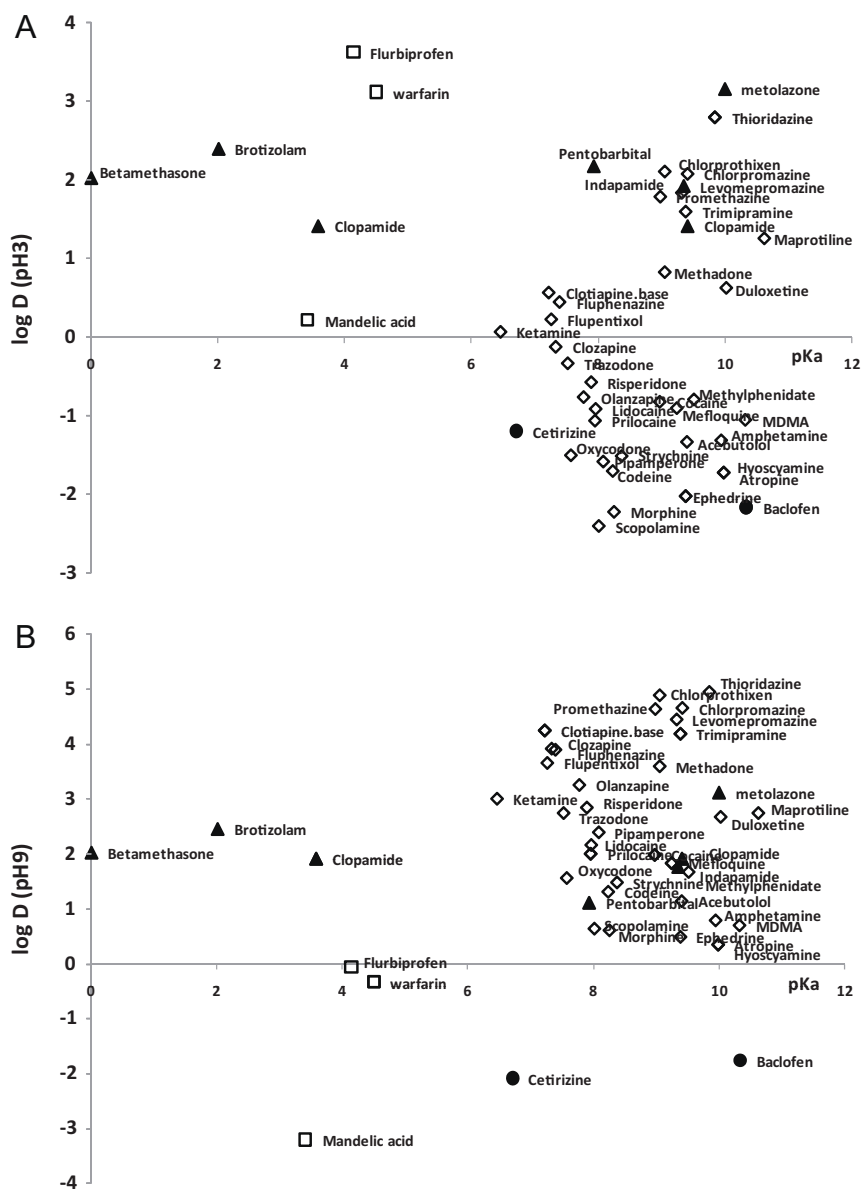


Fig. 1. Representation of pK_a vs. $\log D$ at pH 3 (A) and pH 9 (B) for the 45 model pharmaceutical compounds. Acidic, neutral, basic and zwitterionic compounds are represented by empty squares (\square), full triangles (\blacktriangle), empty diamond-shapes (\diamond) and full circles (\bullet), respectively.

that all the investigated compounds were sufficiently retained at pH 3 and pH 6 on both HILIC columns, confirming the previous findings of McCalley, that HILIC can be a valuable alternative to RPLC for the separation of ionisable compounds of diverse polarity [21,22]. Fig. 2A shows the PCA representation of the HILIC conditions. Accordingly, the pH remains the most important parameter for tuning selectivity in HILIC but, compared to RPLC, the nature of the stationary phase is also of utmost importance. The interpretation of the results is however limited by the fact that only 4 different experimental conditions were investigated in HILIC, particularly because of the restricted number of commercially available HILIC columns packed with sub- $2\ \mu\text{m}$ particles.

In conclusion, both HILIC and RPLC allow a sufficient retention of our 45 model compounds, since most of them were positively charged in acidic conditions. Second, the selectivity offered by HILIC and RPLC was very different for this set of analytes. This is illustrated in Fig. 2A, where the variability in selectivity is less important when mobile phase pH, organic modifier and stationary phase are modified in RPLC than when changing from RPLC to HILIC. Therefore, these two orthogonal chromatographic retention mechanisms

were evaluated for the analysis of a drug cocktail and the impurity profiling example. To limit the number of injections, only a reasonable number of RPLC and HILIC conditions were selected.

3.2. Analysis of a drug cocktail

One of the most important steps of drug discovery is the *in vitro* drug metabolism study, to evaluate the metabolic properties of a new chemical entity (NCE) [27–29], including metabolic stability, inhibition/induction of isozymes and metabolite identification assays. Cytochrome P450 (CYP450s) isozymes have been widely studied because of their involvement in the functionalization reactions including oxidation, reduction and hydrolysis (phase I metabolism). LC coupled with UV or MS detection appears as the gold standard technology for the analysis of samples resulting from various *in vitro* drug metabolism assays.

Two pharmaceutical compounds (venlafaxine, VLX and tramadol, TMD) and their desmethylated metabolites (O-VLX, N-VLX, N,O-VLX, O-TMD, N-TMD, and N,N-TMD) were selected because of their close characteristics [30,31]. Indeed,

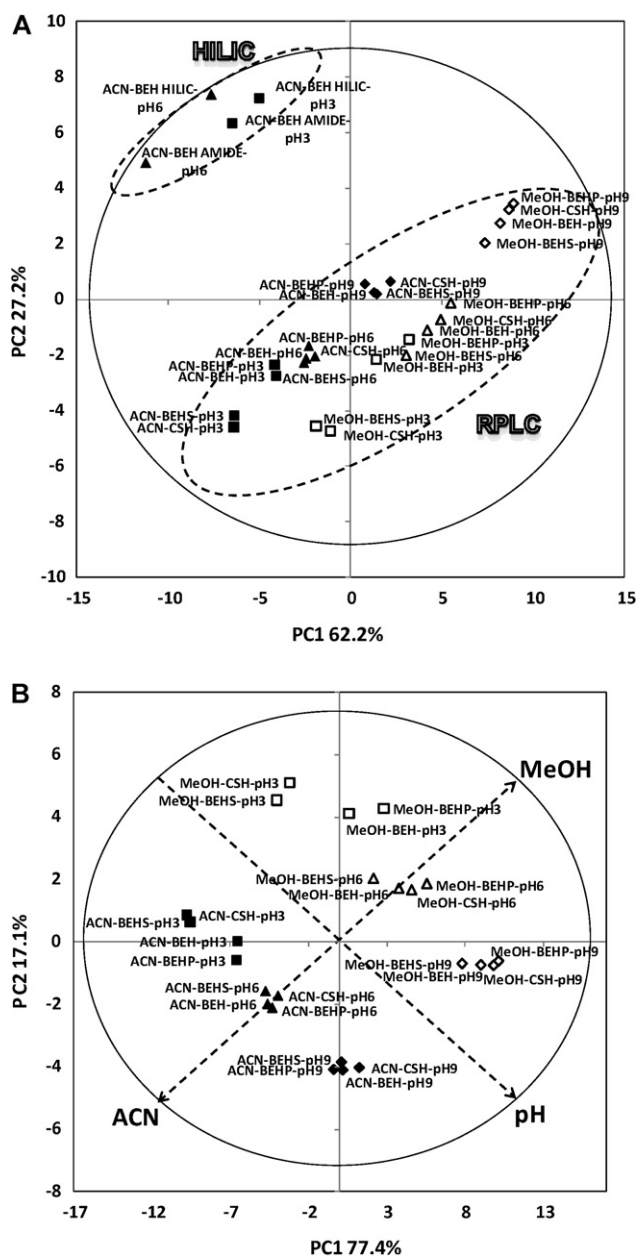


Fig. 2. Principal component analysis (PCA) score plot (PC1 × PC2) of 45 pharmaceutical compounds analyzed in (A) RPLC and HILIC conditions and (B) RPLC mode only. RPLC analyses were conducted with 2 different organic modifiers in the mobile phase (MeOH and ACN represented by empty and filled symbols, respectively), on 4 different stationary phases (2.1 mm × 50 mm, 1.7 μm): Acquity BEH C18 (BEH), Acquity BEH Shield RP18 (BEHS), Acquity BEH Phenyl (BEHP) and Acquity CSH C18 (CSH), and 3 mobile phase pH (3, 6, and 9 represented by squares, triangles and diamond-shape, respectively). HILIC analyses were carried out with 2 different stationary phases: Acquity BEH amide and Acquity BEH HILIC (2.1 mm × 100 mm, 1.7 μm) and 2 pH (3 and 6). Conditions in RPLC: mobile phase consisting of ammonium formate (10 mM, pH 3), ammonium acetate (20 mM, pH 6), or ammonium formate (10 mM, pH 9), gradient profile: 5–95% organic modifier in 4 min, flow rate of 500 μl/min, injected volume = 2 μl, $T = 30^\circ\text{C}$. Conditions in HILIC: mobile phase consisting of ammonium formate (20 mM, pH 3) or ammonium acetate (20 mM, pH 6), gradient profile: 95% ACN for 2 min then 95–65% ACN in 4 min, flow rate of 500 μl/min, injected volume = 2 μl, $T = 30^\circ\text{C}$.

these two drugs are chemically similar and undergo a metabolic pathway by CYP450. VLX (1[–2-(dimethylamino)-1-(4-methoxyphenyl)ethyl]cyclohexanol hydrochloride) is an effective antidepressant drug, while TMD (2-[(dimethylamino)methyl]-1-(3-methoxyphenyl)cyclohexanol hydrochloride) is a centrally acting opioid analgesic used to treat moderate to severe pain. Due

Table 2

Tramadol (TMD), venlafaxine (VLX) and their metabolites properties.

Compounds name	MS <i>m/z</i>	MS/MS <i>m/z</i>	<i>pKa</i> (amine)	Log <i>D</i> (pH3)	Log <i>D</i> (pH9)
VLX	278	58	9.26	–0.77	1.96
TMD	264	58	9.61	–0.78	1.73
O-VLX	264	58	9.24	–1.49	1.20
N-VLX	264	44	10.24	–0.7	1.23
O-TMD	250	58	9.61	–1.32	1.14
N-TMD	250	44	10.56	–1.42	0.21
N,O-VLX	250	44	10.38	–1.42	0.47
N,N-TMD	236	189	10.27	–1.36	0.57

pKa and log *D* values were calculated using Advanced Chemistry Development (ACD/Labs) Software V11.021.

to these similarities, VLX and TMD have demonstrated additive or reverse therapeutic actions [30–32]. As reported elsewhere, false positive results for TMD were observed in case of patients being treated with VLX [33] due to the similar MS transition shared by the metabolite O-desmethylvenlafaxine (O-VLX) and TMD. Table 2 shows the properties and MS transitions of TMD, VLX and their desmethylated metabolites. It can be seen that in MS analysis, various analytes cannot be distinguished (i.e. TMD, O-VLX, N-VLX with *m/z* equal to 264 and, O-TMD, N-TMD, N,O-VLX with *m/z* equal to 250). In MS/MS analysis, the selectivity is enhanced but still insufficient for TMD and O-VLX (264 → 58) and also for N-TMD and N,O-VLX (250 → 44). Because of the MS limitations for this application, it is thus mandatory to develop a LC method able to separate these different constituents.

3.2.1. RPLC conditions

In a first instance, BEH and CSH columns of 50 mm length were tested at pH 3 and 9 (Fig. 3). In acidic conditions (Fig. 3A and B), the CSH offers the best performance in terms of selectivity and peak width. The thinner peaks observed with the CSH material are in agreement with our expectations since the latter possesses a positively charged weak basic moiety at the surface, thus limiting the secondary ionic interactions between positively charged analytes and negatively charged residual silanols. The selectivity was very close between both columns and elution order remained identical. The separation between TMD and N-TMD was the only improvement observed with the CSH compared to BEH. In basic conditions (Fig. 3C and D), the separation was drastically enhanced regarding peak shape and resolution. This is a well-known statement in RPLC related to the ionization state of basic analytes which is emphasized by the use of ammonium salt that could mask residual silanols and minimize electrostatic interactions between basic analytes and deprotonated silanols, inducing better peak shapes [34,35]. However, such elevated pH conditions can only be applied with the last generations of silica-based stationary phases. As the mobile phase pH was close to the analytes *pKa*, and because the nature of the stationary phase surface was very different between the BEH and the CSH, the selectivity was significantly modified and the critical peak pairs were different on the two stationary phases. Indeed, N,N-TMD and O-VLX were baseline resolved on BEH while O-TMD, N,N-TMD and, O-VLX and N-TMD were better resolved on CSH column. To conclude, the RPLC separation of these substrates and metabolites was improved at pH 9.

The resolution was not sufficient in any of the chromatograms presented in Fig. 3 and since the analysis time was extremely short (less than 2 min), the column length was extended to 100 mm and gradient conditions transferred using the basic rules of LC method transfer [36,37]. Fig. 4A and B shows the separation obtained on the 100 mm BEH column and 100 mm CSH, respectively. As shown, the analysis time remained very short (<4 min) but the separation was enhanced (Fig. 3C and D). However, the separation of the critical

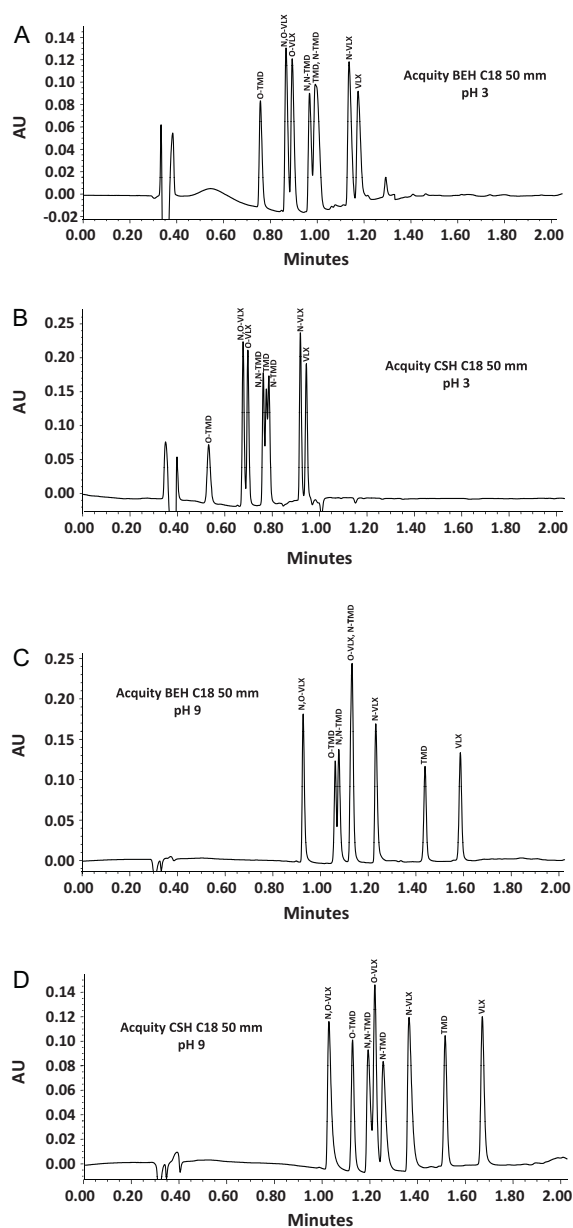


Fig. 3. Influence of the stationary phase type and the mobile phase pH on the separation of tramadol (TMD), venlafaxine (VLX) and their metabolites in RPLC. Conditions: mobile phase ammonium formate (10 mM, pH 3) or ammonium formate (10 mM, pH 9), gradient profile: 10–80% ACN in 2 min, flow rate of 400 μ l/min, injected volume = 2 μ l, $T = 45^\circ\text{C}$, $\lambda = 220$ nm. A mixture of the 8 compounds at 10 μ g/ml in water was injected. (A) Column Acquity BEH C18 (2.1 mm \times 50 mm, 1.7 μ m); pH 3, (B) Column Acquity CSH C18 (2.1 mm \times 50 mm, 1.7 μ m); pH 3, (C) Column Acquity BEH C18 (2.1 mm \times 50 mm, 1.7 μ m); pH 9, (D) Column Acquity CSH C18 (2.1 mm \times 50 mm, 1.7 μ m), pH 9.

pair remained difficult on the BEH column and the analytes were not baseline resolved with the CSH material. Since a complementarity between the BEH and CSH column was previously observed (i.e. critical pairs were not the same with the two columns), the 50 mm BEH and the 50 mm CSH were coupled in series using the column coupler prototype [23,24]. The resulting separation is presented in Fig. 4C and the minimal resolution between O-VLX and N-TMD was equal to 1.3, which is quite reasonable for an analysis time of about 3 min and a backpressure of 830 bar. Last, independent of the column order, BEH–CSH or CSH–BEH, the final chromatograms were identical although it has previously been reported that slight

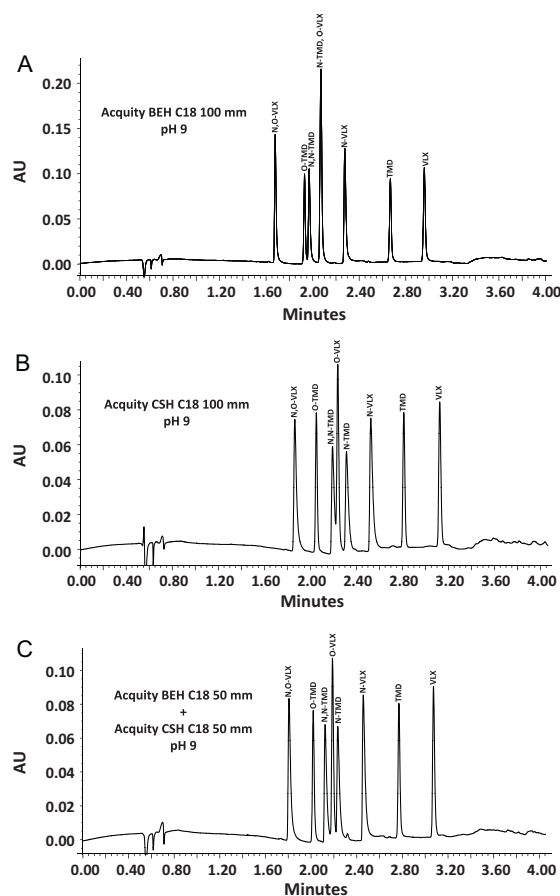


Fig. 4. Effect of the increase in column length for the separation of tramadol (TMD), venlafaxine (VLX) and their metabolites in RPLC. Conditions: ammonium formate (10 mM, pH 9), gradient profile: 10–80% ACN in 4 min, flow rate of 400 μ l/min, injected volume = 2 μ l, $T = 45^\circ\text{C}$, $\lambda = 220$ nm. A mixture of the 8 compounds at 10 μ g/ml in water was injected. (A) Column Acquity BEH C18 (2.1 mm \times 100 mm, 1.7 μ m), (B) Column Acquity CSH C18 (2.1 mm \times 100 mm, 1.7 μ m), (C) Column Acquity BEH C18 (2.1 mm \times 50 mm, 1.7 μ m) directly coupled to column Acquity CSH C18 (2.1 mm \times 50 mm, 1.7 μ m) using the column coupler prototype.

changes in selectivity can occur when changing the column order in the gradient mode [38]. The data presented in Fig. 2 showed that the nature of the stationary phase was not the main parameter for tuning selectivity in the case of a mixture of 45 very diverse analytes. In the case of structurally related compounds presented in Figs. 3 and 4, however, the chromatographic support was shown to play a key role for the fine tuning of critical peak pairs (Fig. 4C).

3.2.2. HILIC conditions

First it is important to mention that the sample solvent should be adapted to the elution mode. Therefore pure acetonitrile was employed for HILIC experiments, as discussed elsewhere [15].

In this case, two different stationary phases packed with sub-2 μ m particles, namely BEH HILIC and BEH amide were selected. Since the generated backpressure in HILIC was lower (in average 4 times lower than RPLC because of the weak viscosity of mobile phase containing a proportion of acetonitrile > 70%), columns of 100 mm were chosen to compensate for the broader peaks generally observed in HILIC vs. RPLC (dominance of ion exchange mechanism in HILIC, the latter possessing slow interaction kinetics). Regarding the selection of pH, values of 3 and 6 were initially evaluated (to have basic analytes under a positively charged form). Chromatograms obtained at pH 3 presented unacceptable peak shape which should be related to the nature of the investigated

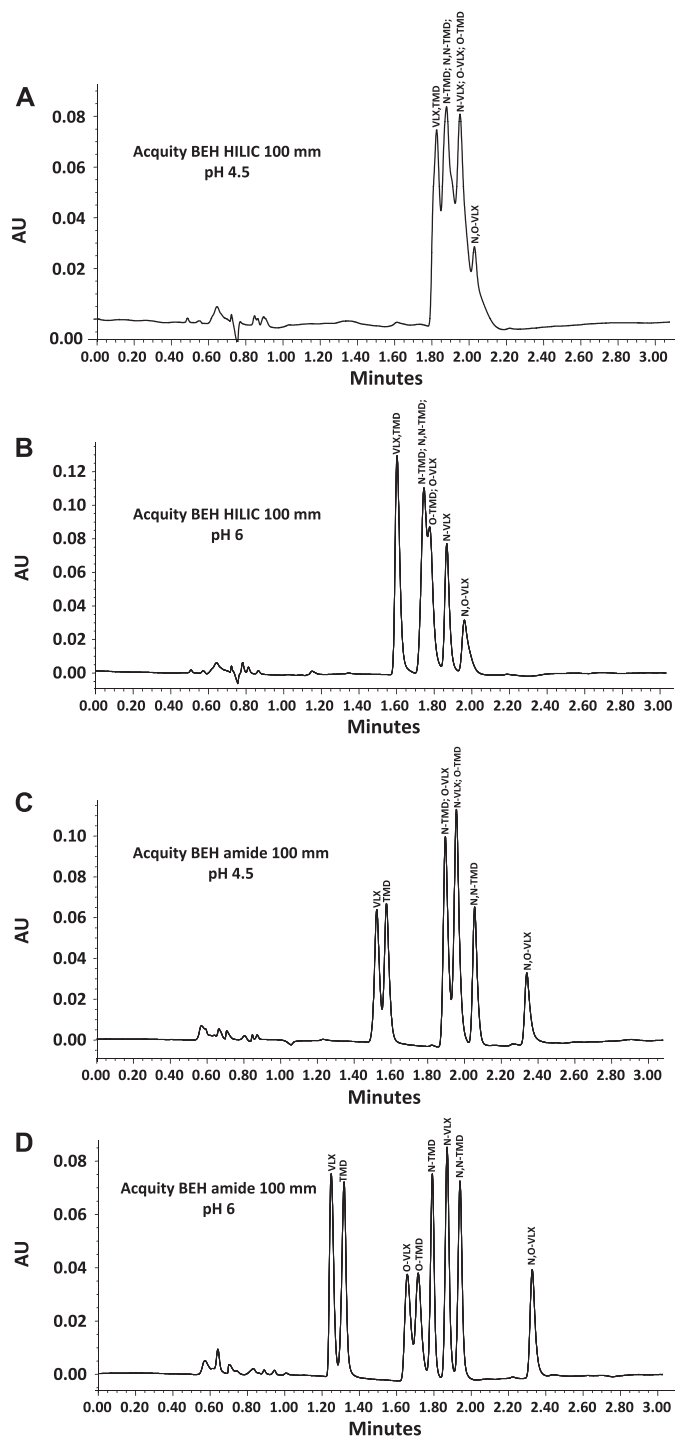


Fig. 5. Influence of the stationary phase type and the mobile phase pH on the separation of tramadol (TMD), venlafaxine (VLX) and their metabolites in HILIC. Conditions: ammonium acetate (20 mM, pH 4.5) or ammonium acetate (20 mM, pH 6), gradient profile: 85–75% ACN in 4 min on the Acquity BEH HILIC or 90–75% ACN in 4 min on the Acquity BEH amide, flow rate of 400 μ l/min, injected volume = 2 μ l, $T = 45^\circ\text{C}$, $\lambda = 220\text{ nm}$. A mixture of the 8 compounds at 10 $\mu\text{g/ml}$ in ACN was injected. (A) Column Acquity BEH HILIC (2.1 mm \times 100 mm, 1.7 μm); pH 4.5, (B) Column Acquity BEH HILIC (2.1 mm \times 100 mm, 1.7 μm); pH 6, (C) Column Acquity BEH amide (2.1 mm \times 100 mm, 1.7 μm); pH 4.5, (D) Column Acquity BEH amide (2.1 mm \times 100 mm, 1.7 μm); pH 6.

analytes. Thus, pH was set at 4.5 and 6 to assess its impact on the quality of the HILIC separation. Corresponding chromatograms for the four combinations of conditions (2 columns and 2 pH values) are reported in Fig. 5. From these results, it is obvious that the HILIC

BEH was not suitable, independent of the pH. Indeed, although the retention and peak width were acceptable on this stationary phase, the selectivity, particularly at pH 4.5, was very poor and all the compounds eluted at about 80 and 82% ACN at pH 4.5 and 6, respectively. On the other hand, the HILIC amide column displayed a significantly enhanced selectivity. Again, the selectivity was quite poor at pH 4.5 but satisfactory at pH 6. The difference in behaviour between pH 4.5 and 6 could be explained by: (i) a change in the compounds polarity between pH 4.5 and 6, modifying the retention governed by the hydrophilic interaction mechanism, (ii) an increase in the amount of ammonium hydroxide to attain pH 6 vs. pH 4.5, leading to an increased number of masked silanols, (iii) the pK_a of analytes and silanols as well as pH of mobile phase which could be very different in highly organic conditions vs. pure water thus altering the ionization state of the analytes and silanols.

Finally, the best separation was achieved in HILIC mode using the 100 mm BEH Amide stationary phase at pH 6. Compared to the RPLC method, the resolution was lower in HILIC (minimal resolution of 0.88 between O-VLX and O-TMD) but since the backpressure was only equal to 238 bar and the analysis time only 2.4 min, the possibility exists to further extend the column length of the BEH Amide column to 200 mm to achieve a baseline resolution of these compounds in HILIC within a reasonable timeframe. Second, it is also worth mentioning that the average peak widths at half height in RPLC and HILIC conditions were equal to 0.020 and 0.027 min; respectively, confirming that the kinetic performance in HILIC at pH 6 was slightly reduced compared to RPLC at pH 9. Last, the selectivity between the best RPLC (Fig. 4C) and HILIC (Fig. 5D) method was very different but interestingly, the elution order of the peaks in HILIC was not the inverse of the elution order in RPLC.

3.3. Analysis of an active pharmaceutical ingredient and related substances

Based on the recommendations of numerous regulatory authorities such as ICH [39,40], there is a need to evaluate the purity content and identify impurities of any active pharmaceutical ingredient (API), to avoid problems of biological safety related to an individual impurity. In the pharmaceutical field, an impurity is considered as any other organic material including by-products, starting materials or intermediates and degradation products.

HPLC has been widely employed in the field of impurity profiling and is considered as a reference method. An antihistaminic drug (API) that cannot be named due to confidentiality reasons was selected and fourteen related substances including by-products, starting materials or intermediates and degradation products were simultaneously analyzed. The physico-chemical properties of all the compounds contained within the mixture were very different since the $\log D$ values at pH 3 varied between -5.5 to $+4$ and between -4.9 and $+6.7$ at pH 9.

3.3.1. RPLC conditions

Similarly to the previous study on the drug cocktail, the same methodology was employed to attain a suitable separation for this complex mixture, in a limited number of experiments. Thus, the 50 mm BEH and CSH columns were initially selected and investigated at pH 3 and 9. The corresponding chromatograms are presented in Fig. 6. The selectivity at pH 3 was very poor and most of the compounds were eluted at around 40–50% ACN, except impurity A ($\log D$ pH 3 of -5.5) and L ($\log D$ pH 3 of $+4$) which were far more polar and apolar than the other ones, respectively. Impurity A was not retained in these conditions while compound L required 95% ACN to be eluted from the columns. The same separation was conducted at pH 9 and in this case, the peaks were

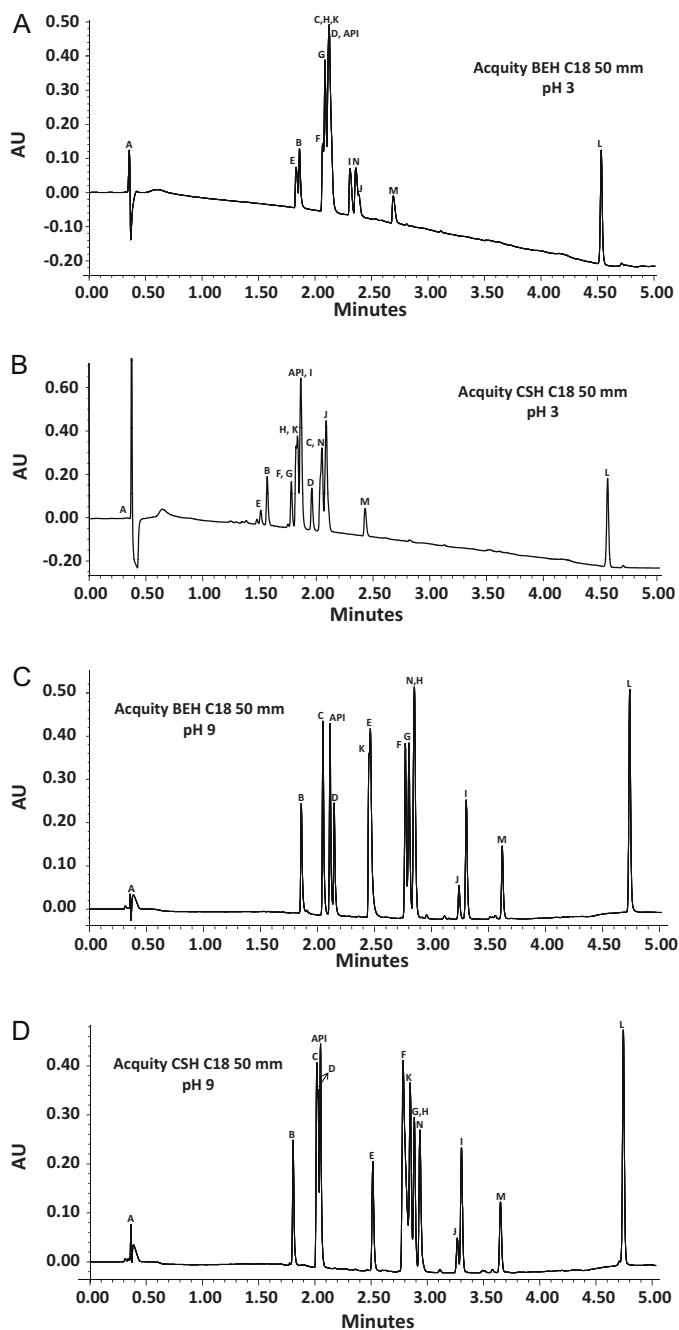


Fig. 6. Influence of the stationary phase type and the mobile phase pH on the separation of API and 14 related substances in RPLC. Conditions: mobile phase ammonium formate (10 mM, pH 3) or ammonium formate (10 mM, pH 9), gradient profile: 5–95% ACN in 4 min then 1.5 min at 95% ACN, flow rate of 400 μ l/min, injected volume = 2 μ l, $T = 45^\circ\text{C}$, $\lambda = 230$ nm. A mixture of the 15 compounds at 25 μ g/ml in water was injected. (A) Column Acquity BEH C18 (2.1 mm \times 50 mm, 1.7 μ m); pH 3, (B) Column Acquity CSH C18 (2.1 mm \times 50 mm, 1.7 μ m); pH 3, (C) Column Acquity BEH C18 (2.1 mm \times 50 mm, 1.7 μ m); pH 9, (D) Column Acquity CSH C18 (2.1 mm \times 50 mm, 1.7 μ m), pH 9.

correctly spread over the chromatogram with both the BEH and CSH stationary phases. This confirms that pH is certainly the most important parameter for adjusting retention and selectivity. With the BEH column (Fig. 6C), some peaks were not fully resolved (API and D; F and G) and resolution was close to zero between peaks N and H and between E and K. Interestingly, the critical peak pairs were not similar on the CSH column, confirming the complementarity of the two stationary phases for the separation of structurally related compounds. Indeed, on the CSH material, the peaks API, C

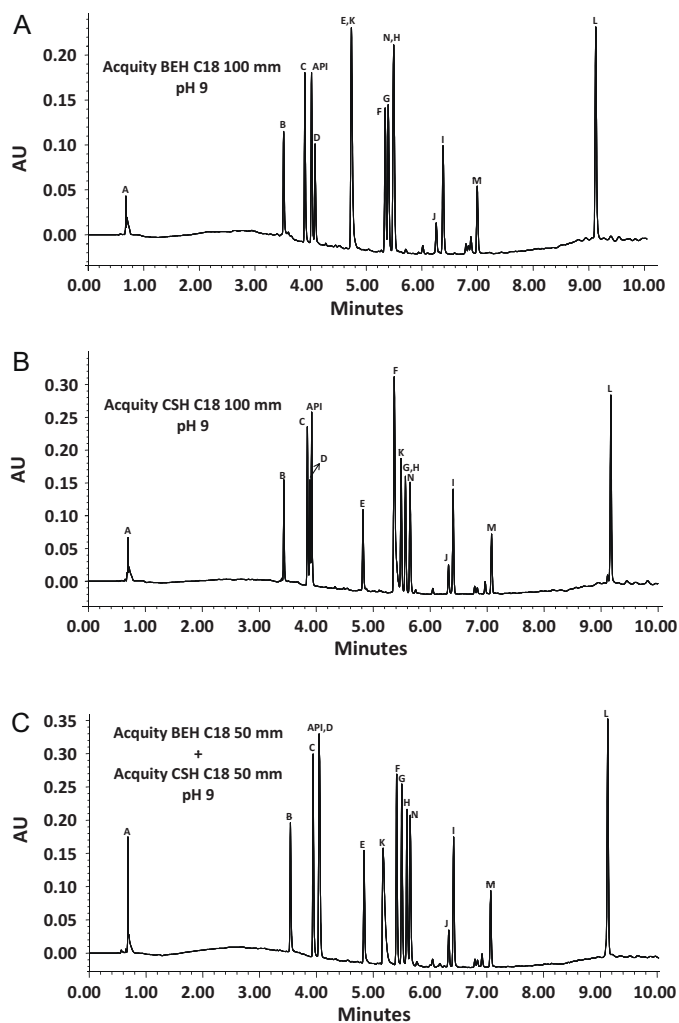


Fig. 7. Effect of the increase in column length for the separation of API and 14 related substances in RPLC. Conditions: ammonium formate (10 mM, pH 9), gradient profile: 5–95% ACN in 8 min then 3 min at 95% ACN, flow rate of 400 μ l/min, injected volume = 2 μ l, $T = 45^\circ\text{C}$, $\lambda = 230$ nm. A mixture of the 15 compounds at 25 μ g/ml in water was injected. (A) Column Acquity BEH C18 (2.1 mm \times 100 mm, 1.7 μ m), (B) Column Acquity CSH C18 (2.1 mm \times 100 mm, 1.7 μ m) directly coupled to column Acquity BEH C18 (2.1 mm \times 50 mm, 1.7 μ m) using the column coupler prototype.

and D were not fully resolved and there was also a critical separation for the peaks F, K, G and H. The resolution was close to zero for impurities G and H and for C and D. It is finally important to notice that the impurity K had a completely different retention on the two investigated RPLC columns.

Because of the complexity of the separation and the limited overall resolution, the column length was further extended to improve peak capacity. Similarly to Fig. 4, the BEH 100 mm, CSH 100 mm and BEH 50 mm + CSH 50 mm configurations were tested and corresponding chromatograms are reported in Fig. 7. In all these conditions, the gradient time was adjusted to 8 min instead of 4 min, to maintain a similar selectivity. With the 100 mm BEH column (Fig. 7A), the selectivity between peaks N and H and, E and K remained null and the resolution between peaks F and G was still too limited. For the 100 mm CSH column (Fig. 7B), a number of peak pairs were insufficiently separated. This is for example the case for peaks C, D and API and also for peaks G and H. Since the problematic peak pairs were not identical on the two columns, the BEH 50 mm and CSH 50 mm were coupled in series using the column coupler prototype (Fig. 7C). As expected, the resolution improved for all

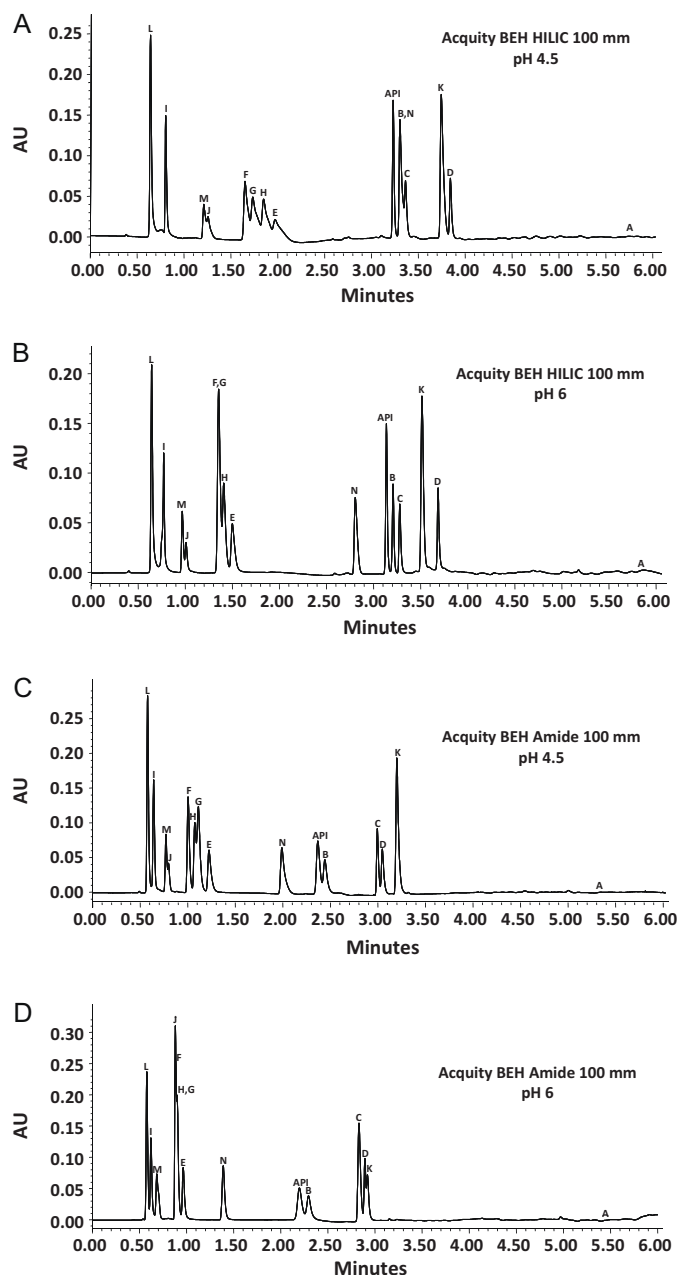


Fig. 8. Influence of the stationary phase type and the mobile phase pH on the separation of API and 14 related substances in HILIC. Conditions: mobile phase ammonium acetate (20 mM, pH 4.5) or ammonium acetate (20 mM, pH 6), gradient profile: 95% ACN for 1 min, then 95–65% ACN in 4 min, then 1 min at 65% ACN, flow rate of 400 μ l/min, injected volume = 2 μ l, $T = 45^\circ\text{C}$, $\lambda = 230\text{ nm}$. A mixture of the 15 compounds at 12.5 $\mu\text{g/ml}$ in ACN was injected. (A) Column Acquity BEH HILIC (2.1 mm \times 100 mm, 1.7 μm); pH 4.5, (B) Column Acquity BEH HILIC (2.1 mm \times 100 mm, 1.7 μm); pH 6, (C) Column Acquity BEH amide (2.1 mm \times 100 mm, 1.7 μm); pH 4.5, (D) Column Acquity BEH amide (2.1 mm \times 100 mm, 1.7 μm); pH 6.

the peaks except API and D impurity, for which resolution was not achieved. Indeed, on the CSH column, impurity D was eluted prior to API while it was eluted after API with on the BEH column. Since the retentions are, in a first approximation, additive when columns are combined in series, the overall resolution was not satisfactory [41].

To further improve this separation and find analytical conditions wherein API and impurity D could be separated, it would be interesting to evaluate a higher number of pH, organic modifier and columns in an automated way. In addition, because of the

complexity of the separation, UHPLC columns of 150–200 mm should be selected, the mobile phase flow rate adjusted and the gradient time extended to at least 30 min. Such experiments are out of the scope of the present paper but will be investigated in a forthcoming study, using automated method development software.

3.3.2. HILIC conditions

Even though the compounds are spread over a wide polarity range (log D values at pH 3 vary from -5.4 to $+4$), the HILIC mode was evaluated as all the investigated impurities were ionisable and could thus be sufficiently retained by an ion exchange mechanism. Again, the results obtained with a mobile phase pH of 3 were unacceptable. This condition was discarded and replaced by pH 4.5, while pH 6 was also tested. All the columns were 100 mm long because of the low backpressure in HILIC mode. A first remark is that impurity A, identified using MS detection (lack of chromophoric group), was eluted late on the chromatogram because of its high polarity (65% ACN were required). On the other hand, the peak corresponding to the very apolar impurity L eluted during the isocratic initial step at 95% ACN. The results obtained with the BEH HILIC stationary phase are presented in Fig. 8A and B. At pH 4.5, all peaks were sufficiently retained but peak shapes of F, G, H, E, M, J were not acceptable. In addition, the selectivity was poor for peaks M and J; F, G, H, E and B, N, C. The peak shapes were significantly improved with the BEH Amide stationary phase at pH 4.5 (Fig. 8C), but the selectivity remained low and retention was drastically reduced since 8 impurities were eluted during the initial isocratic step at 95% ACN. This decrease of retention was attributed to the reduction of ion exchange mechanism because of the lower silanol activity (amide bonding). For this separation, pH 6 allowed a significant improvement of the separation quality, both with the BEH HILIC and BEH Amide column. The separation remained also critical for the BEH Amide, particularly for impurities F, G, H, J and for C, D and K. The separation with BEH HILIC (Fig. 8B) was better, only the triplet F, G, H and the compounds M and J were insufficiently resolved.

In this example, there was no interest in coupling the two 100 mm HILIC columns in series since the peaks F, G and H were not resolved with both columns at pH 6. However, it could be interesting to increase the column length of the BEH HILIC at pH 6, up to 200 or 300 mm, to improve the separation shown in Fig. 8B, while maintaining a reasonable analysis time.

4. Conclusion

The development of a new HPLC method in the pharmaceutical field is a long and tedious process. In the present contribution, columns packed with sub-2 μm porous particles (UHPLC conditions) were systematically employed to increase the throughput during method development. However, it is possible to transfer the UHPLC method developed in R&D laboratories to HPLC conditions, when quality control laboratories do not have UHPLC systems at their disposal.

In a first instance, various RPLC and HILIC conditions (i.e. stationary phase nature, organic modifier, pH) were tested using a representative set of 45 pharmaceutical compounds covering a wide range of physico-chemical properties (i.e. log P , log D and pK_a). PCA was applied to highlight the complementarity and differences between chromatographic systems. First, PCA showed that a change of the chromatographic mode from any RPLC conditions to any HILIC conditions would generate very different chromatograms, an information of prime importance in method development. As expected, pH is the most important parameter for

tuning selectivity, while organic modifier and stationary phase are relevant but to a lesser extent. It would be interesting to include some unique stationary phases to this study such as a fluorophenyl and Cyano to better underline differences between columns, but the latter were not available in UHPLC dimensions at the time where the study was conducted. In the specific case of UHPLC, methanol is generally avoided because of its high viscosity inducing important backpressure. In the present work, only pH and various hybrid stationary phases compatible with alkaline pH were evaluated with ACN for method development purposes.

Since HILIC provides very different selectivities compared to RPLC, it is important to demonstrate that HILIC could be employed for most of the separations carried out in the pharmaceutical field. For this purpose, two representative examples were selected: the separation of a drug cocktail containing various substrates and metabolites and the impurity profiling of an anti-histaminic drug. All the analytes were sufficiently retained in both modes, provided that the correct combination of pH and stationary phase was selected even if in the anti-histaminic drug example the different analytes were not all resolved. In all cases, the elution order and selectivity were very different but it was always possible to find an “almost equivalent separation” in RPLC and HILIC. Finally, HILIC has the additional advantage to generate a very low backpressure, allowing the use of longer columns and also to improve the MS sensitivity significantly because of the better desolvation of highly organic mobile phase [42,43].

Acknowledgments

The authors wish to thank Prof. P. Dayer of Clinical Pharmacology Division and Dr A.E. Balant-Gorgia from the Department of Psychiatry of Geneva University Hospital for providing venlafaxine, tramadol and their metabolites. The authors also acknowledged E. Bachmann from the Department of Clinical Chemistry in Lausanne, Switzerland for the gift of several pharmaceutical compounds used in this study. Cedric Schelling from the University of Geneva is finally acknowledged for valuable comments and help.

References

- [1] R. Al Bakain, I. Rivals, P. Sassi, D. Thiébaud, M.-C. Hennion, G. Euvrard, J. Vial, Comparison of different statistical approaches to evaluate the orthogonality of chromatographic separations: application to reverse phase systems, *J. Chromatogr. A* 1218 (2011) 2963–2975.
- [2] U.D. Neue, C.H. Phoebe, K. Tran, Y.-F. Cheng, Z. Lu, Dependence of reversed-phase retention of ionizable analytes on pH, concentration of organic solvent and silanol activity, *J. Chromatogr. A* 925 (2001) 49–67.
- [3] S. Heinisch, J.L. Rocca, Effect of mobile phase composition, pH and buffer type on the retention of ionizable compounds in reversed-phase liquid chromatography: application to method development, *J. Chromatogr. A* 1048 (2004) 183–193.
- [4] N. Tanaka, H. Goodell, B.L. Karger, The role of organic modifiers on polar group selectivity in reversed-phase liquid chromatography, *J. Chromatogr. A* 158 (1978) 233–248.
- [5] K. Le Mapihan, J. Vial, A. Jardy, Organic solvent effects in reversed-phase liquid chromatography in relation to column testing, *Chromatographia* 57 (2003) S163–S170.
- [6] K. Le Mapihan, J. Vial, A. Jardy, Reversed-phase liquid chromatography column testing: robustness study of the test, *J. Chromatogr. A* 1061 (2004) 149–158.
- [7] K. Le Mapihan, J. Vial, A. Jardy, Reversed-phase liquid chromatography testing: role of organic solvent through an extended set of columns, *J. Chromatogr. A* 1088 (2005) 16–23.
- [8] K. Le Mapihan, J. Vial, A. Jardy, Reversed-phase liquid chromatography column testing and classification: Physicochemical interpretation based on a wide set of stationary phases, *J. Chromatogr. A* 1144 (2007) 183–196.
- [9] T.H. Dzido, T.E. Kossowski, D. Matosiuk, Comparison of retention of aromatic hydrocarbons with polar groups in binary reversed-phase high-performance liquid chromatography systems, *J. Chromatogr. A* 947 (2002) 167–183.
- [10] L.R. Snyder, Changing reversed-phase high performance liquid chromatography selectivity. Which variables should be tried first? *J. Chromatogr. B: Biomed. Sci. Appl.* 689 (1997) 105–115.
- [11] X. Li, P.W. Carr, Effects of first dimension eluent composition in two-dimensional liquid chromatography, *J. Chromatogr. A* 1218 (2011) 2214–2221.
- [12] M. Gilar, P. Olivova, A.E. Daly, J.C. Gebler, Orthogonality of separation in two-dimensional chromatography, *Anal. Chem.* 77 (2005) 6426.
- [13] A.J. Alpert, Hydrophilic-interaction chromatography for the separation of peptides, nucleic acids and other polar compounds, *J. Chromatogr. A* 499 (1990) 177–196.
- [14] P. Hemström, K. Irgum, Hydrophilic interaction chromatography, *J. Sep. Sci.* 29 (2006) 1784–1821.
- [15] J. Ruta, S. Rudaz, D.V. McCalley, J.-L. Veuthey, D. Guillaume, A systematic investigation of the effect of sample diluent on peak shape in hydrophilic interaction liquid chromatography, *J. Chromatogr. A* 1217 (2010) 8230–8240.
- [16] W. Jian, R.W. Edom, Y. Xu, N. Weng, Recent advances in application of hydrophilic interaction chromatography for quantitative bioanalysis, *J. Sep. Sci.* 33 (2010) 681–697.
- [17] Q. Yang, X. Shi, Y. Wang, W. Wang, H. He, X. Lu, G. Xu, Urinary metabolomic study of lung cancer by a fully automatic hyphenated hydrophilic interaction/RPLC-MS system, *J. Sep. Sci.* 33 (2010) 1495–1503.
- [18] Y. Liu, X. Xue, Z. Guo, Q. Xu, F. Zhang, X. Liang, Novel two-dimensional reversed-phase liquid chromatography/hydrophilic interaction chromatography, an excellent orthogonal system for practical analysis, *J. Chromatogr. A* 1208 (2008) 133–140.
- [19] K. Spagou, H. Tsoukali, N. Raikos, H. Gika, I.D. Wilson, G. Theodoridis, Hydrophilic interaction chromatography coupled to MS for metabolomic/metabolomic studies, *J. Sep. Sci.* 33 (2010) 716–727.
- [20] Y. Wang, R. Lehmann, X. Lu, X. Zhao, G. Xu, Novel, fully automatic hydrophilic interaction/reversed-phase column-switching high-performance liquid chromatographic system for the complementary analysis of polar and apolar compounds in complex samples, *J. Chromatogr. A* 1204 (2008) 28–34.
- [21] D.V. McCalley, Study of the selectivity, retention mechanisms and performance of alternative silica-based stationary phases for separation of ionised solutes in hydrophilic interaction chromatography, *J. Chromatogr. A* 1217 (2010) 3408–3417.
- [22] D.V. McCalley, Is hydrophilic interaction chromatography with silica columns a viable alternative to reversed-phase liquid chromatography for the analysis of ionisable compounds? *J. Chromatogr. A* 1171 (2007) 46–55.
- [23] D. Cabooter, W. Decrop, S. Eeltink, R. Swart, M. Ursem, F. Lestremou, G. Desmet, Automatic column coupling system to operate chromatographic supports closer to their kinetic performance limit and to enhance method development, *Anal. Chem.* 82 (2010) 1054–1065.
- [24] D. Cabooter, D. Clcq, F. De Boever, F. Lestremou, R. Szucs, G. Desmet, A variable column length strategy to expedite method development, *Anal. Chem.* 83 (2011) 966–975.
- [25] S. Vikingson, R. Kronstrand, M. Josefsson, Retention of opioids and their glucuronides on a combined zwitterion and hydrophilic interaction stationary phase, *J. Chromatogr. A* 1187 (2008) 46–52.
- [26] W.C. Chung, S.C. Tso, S.T. Sze, *J. Chromatogr. Sci.* 45 (2007) 104–111.
- [27] P. Baranczewski, A. Stanczak, K. Sundberg, R. Svensson, A. Wallin, J. Jansson, P. Garberg, H. Postlind, Introduction to in vitro estimation of metabolic stability and drug interactions of new chemical entities in drug discovery and development, *Pharmacol. Rep.* 58 (2006) 453–472.
- [28] M.Y. Lee, J.S. Dordick, High-throughput human metabolism and toxicity analysis, *Curr. Opin. Biotechnol.* 17 (2006) 619–627.
- [29] R. Nicoli, S. Martel, S. Rudaz, J.-L. Wolfender, J.-L. Veuthey, P.-A. Carrupt, D. Guillaume, Advances in LC platforms for drug discovery, *Expert Opin. Drug Discov.* 5 (2010) 475–489.
- [30] J.S. Markowitz, K.S. Patrick, Venlafaxine-tramadol similarities, *Med. Hypo.* 51 (1998) 167–168.
- [31] R.R. Reeves, S.K. Cox, Similar effects of tramadol and venlafaxine in major depressive disorder, *South. Med. J.* 101 (2008) 193–195.
- [32] A. Wrzosek, I. Obara, J. Wordliczek, B. Przewlocka, Efficacy of tramadol in combination with dexoprin or venlafaxine in inhibition of nociceptive process in the rat model of neuropathic pain: an isobolographic analysis, *J. Physiol. Pharmacol.* 60 (2009) 71–78.
- [33] K.R. Allen, Interference by venlafaxine ingestion in the detection of tramadol by liquid chromatography linked to tandem mass spectrometry for the screening of illicit drugs in human urine, *Clin. Toxicol.* 44 (2006) 147–153.
- [34] J. Schappler, R. Nicoli, D. Nguyen, S. Rudaz, J.-L. Veuthey, D. Guillaume, Coupling ultra high-pressure liquid chromatography with single quadrupole mass spectrometry for the analysis of a complex drug mixture, *Talanta* 78 (2009) 377–387.
- [35] L. Peng, T. Farkas, Analysis of basic compounds by reversed-phase liquid chromatography-electrospray mass spectrometry in high-pH mobile phases, *J. Chromatogr. A* 1179 (2008) 131–144.
- [36] D. Guillaume, D.T.T. Nguyen, S. Rudaz, J.L. Veuthey, Method transfer for fast liquid chromatography in pharmaceutical analysis: Application to short columns packed with small particle. Part I: Isocratic separation, *Eur. J. Pharm. Biopharm.* 66 (2007) 475–482.
- [37] D. Guillaume, D.T.T. Nguyen, S. Rudaz, J.-L. Veuthey, Method transfer for fast liquid chromatography in pharmaceutical analysis: Application to short columns packed with small particle. Part II: Gradient experiments, *Eur. J. Pharm. Biopharm.* 68 (2008) 430–440.

- [38] M. De Beer, F. Lynen, M. Hanna-Brown, P. Sandra, Multiple step gradient analysis in stationary phase optimised selectivity LC for the analysis of complex mixtures, *Chromatographia* 69 (2009) 609–614.
- [39] International Conference on Harmonization, Draft revised guidance on impurities in new drug products, Federal Register Q3B(R) 65 (2000) 44791–44797.
- [40] International Conference on Harmonization, Draft revised guidance on impurities in new drug substances, Federal Register Q3A(R) 65 (2000) 45085–45090.
- [41] S. Lamotte, R. Brindle, K.D. Bischoff, A new and effective tool for optimization in HPLC, *CLB Chem. Lab. Biotech.* 57 (2006) 349–351.
- [42] E.S. Grumbach, D.M. Diehl, U.D. Neue, The application of novel 1.7 μm ethylene bridged hybrid particles for hydrophilic interaction chromatography, *J. Sep. Sci.* 31 (2008) 1511–1518.
- [43] E.S. Grumbach, D.M. Wagrowski-Diehl, J.R. Mazzeo, B. Alden, P.C. Iraneta, Hydrophilic interaction chromatography using silica columns for the retention of polar analytes and Enhanced ESI-MS sensitivity, *LC-GC N.A.* 22 (2004) 1010–1023.



Water content determination of superdisintegrants by means of ATR-FTIR spectroscopy

G. Szakonyi^a, R. Zelkó^{b,*}

^a Gedeon Richter Plc., Formulation R&D, Gyömrői Str. 19–21., H-1103 Budapest, Hungary

^b University Pharmacy Department of Pharmacy Administration, Semmelweis University, Hógyes E. Street 7–9, 1092 Budapest, Hungary

ARTICLE INFO

Article history:

Received 18 November 2011

Received in revised form 18 January 2012

Accepted 19 January 2012

Available online 28 January 2012

Keywords:

ATR-FTIR spectroscopy

Water content determination

Superdisintegrants

Particle size

Quality control

ABSTRACT

Water contents of superdisintegrant pharmaceutical excipients were determined by attenuated total reflectance Fourier transform infrared (ATR-FTIR) spectroscopy using simple linear regression. Water contents of the investigated three common superdisintegrants (crospovidone, croscarmellose sodium, sodium starch glycolate) varied over a wide range (0–24%, w/w). In the case of crospovidone three different samples from two manufacturers were examined in order to study the effects of different grades on the calibration curves. Water content determinations were based on strong absorption of water between 3700 and 2800 cm^{-1} , other spectral changes associated with the different compaction of samples on the ATR crystal using the same pressure were followed by the infrared region between 1510 and 1050 cm^{-1} . The calibration curves were constructed using the ratio of absorbance intensities in the two investigated regions. Using appropriate baseline correction the linearity of the calibration curves was maintained over the entire investigated water content regions and the effect of particle size on the calibration was not significant in the case of crospovidones from the same manufacturer. The described method enables the water content determination of powdered hygroscopic materials containing homogeneously distributed water.

© 2012 Elsevier B.V. All rights reserved.

1. Introduction

Pharmaceutical superdisintegrants (crospovidone, croscarmellose sodium, sodium starch glycolate) are polymeric excipients with special physico-chemical features (polar groups, cross-linked porous structure, amorphous or partially amorphous state), which are responsible for their strong interaction with water molecules and for the rapid moisture absorption from the air under inappropriate storage conditions. Their major mechanism of action is the combination of swelling and water wicking and particle shape deformation as they come into contact with fluids [1]. Water content of hygroscopic pharmaceutical excipients can largely affect the manufacturing processes and the performance of the final product, too [2,3]. That is the reason why different pharmacopeias (European Pharmacopoeia 7.3 [4], USP 34-NF 29 [5]) specify their maximum acceptable water contents in the form of loss on drying (5%, w/w, in the case of crospovidone and 10%, w/w, in the case of sodium starch glycolate and croscarmellose sodium).

For the determination of water content of different materials several methods such as loss on drying, Karl-Fischer titration, NMR

spectroscopy, near infrared spectroscopy, etc. are applied. These methods greatly differ from each other in their accuracy, time-demand and applicability [6]. The loss on drying method requires relatively large amount of excipients and long measuring time. The most widely used spectroscopic method for water content determination is near infrared (NIR) spectroscopy. It is a non-invasive analytical tool which enables parallel measuring of different chemical and physical parameters. However the analytical signal strongly depends on many attributes of the sample, for example on particle size [7] that can be changed during water absorption in the case of superdisintegrants.

The advantage of attenuated total reflectance Fourier transform infrared (ATR-FTIR) spectroscopy is that it does not require special sample preparation, and the water content of sensitive samples is not altered in the course of the measurement, as it could occur in the case of the commonly applied KBr-disc method during mixing and grinding with the KBr crystals and the subsequent disc forming. In this study we investigated the quantity of the absorbed water of the three common superdisintegrants based on their ATR-FTIR spectra and as reference method weight measurement of samples was used since water absorption and desorption could be quantitatively tracked by weight changes. From crospovidone we obtained three samples from two manufacturers of different particle size distributions to study their effect on the calibration.

* Corresponding author. Tel.: +36 1 2170927; fax: +36 1 2170927.
E-mail address: zelrom@gytk.sote.hu (R. Zelkó).

2. Materials and methods

2.1. Materials

The selected powdered cospovidone (Polyplasdone XL, ISP; Polyplasdone XL-10, ISP; and Kollidon CL-SF, BASF), sodium starch glycolate (Explotab, JRS Pharma), and croscarmellose sodium (Vivasol, JRS Pharma) superdisintegrants were gift samples from the manufacturers. Cospovidone is the cross-linked homopolymer of N-vinyl-2-pyrrolidone; sodium starch glycolate is the sodium salt of a carboxymethyl ether of starch or of a cross-linked carboxymethyl ether of starch; croscarmellose sodium is the sodium salt of a cross-linked, partly O-(carboxymethylated) cellulose. The particle sizes of Polyplasdone XL, Polyplasdone XL-10 and Kollidon CL-SF were 100–130 μm , 30–50 μm , and 10–30 μm , respectively based on the manufacturers' data.

2.2. Sample preparation

The superdisintegrants were stored at different humidity conditions for different periods of time in small plastic open containers to absorb water. In the case of cospovidones dried samples (95 °C, 0.5 h) were also prepared. The maximum water content of cospovidones was attained with storage at 75% relative humidity (R.H.) for 48 h, and in the case of sodium starch glycolate and croscarmellose sodium at 100% R.H. for 48 h. In the case of all five excipients nine samples of different water contents were prepared for the calibrations, thus 45 samples were involved in the investigation. The amount of absorbed or desorbed water was calculated based on weight changes of the samples and measured with analytical balance (BP 110 S, Sartorius) with 0.1 mg accuracy. The initial water content of superdisintegrants was determined by loss on drying according to the pharmacopeias.

2.3. ATR-FTIR spectroscopic examinations

After the weighing, samples were immediately transferred from the small plastic containers to closed glass vials to avoid changes in water content and the spectral measurements were carried out. ATR-FTIR spectra were collected on Jasco FT/IR-4200 spectrophotometer between 4000 and 300 cm^{-1} with an ATR PRO470-H single reflection accessory (Jasco) equipped with flat pressure tip. The spectral measurements were performed at the maximum 1700 kg/cm^2 pressure on the diamond ATR crystal, in absorbance mode. To obtain homogenous and reproducible sample layer over the ATR crystal, we pressed each sample twice with the flat pressure tip at the maximum pressure (i.e. after the first press with the ATR accessory some materials were put on the formed compact layer and after this a second press was carried out). 16 Scans at a resolution of 4 cm^{-1} were co-added by the FT-IR software (Spectra Manager-II, Jasco). From each sample eight parallel spectral measurements were carried out.

2.4. Data treatment

The eight parallel ATR-FTIR spectra of the samples were averaged in the case of each sample with the data accumulation function of the FT-IR software to obtain a common spectra representative for a sample of given water content.

Along with the decrease of the water content of samples, the baselines of their spectra increased, which distort the calculation of the area under the curve values. Therefore, for each excipient, the baselines of their spectra were corrected to be equal at 4000 and 1900 cm^{-1} to the baseline of the sample of maximum water content, thus receiving overlapping spectra in the non-absorbing regions (between 4000 and 3700 cm^{-1} and 2700 and 1800 cm^{-1})

(Fig. 1). The absorption band intensities (areas of spectral bands) of the averaged spectra were calculated between 3700 and 2800 cm^{-1} and 1510 and 1050 cm^{-1} after the baseline correction and their ratios (denoted as A^*/B^*) were used for constructing the calibration lines. Water content of samples (g/100 g water-free excipient) was plotted against the A^*/B^* values since linear relationship was expected between these values.

2.5. Confidence and prediction intervals

The 95% confidence and prediction intervals of the regression lines were calculated using Eqs. (1) and (2) respectively.

$$\text{Confidence interval: } \left[y_c \pm t_{n-2}^{5\%} \cdot S_e \sqrt{\frac{1}{n} + \frac{(x_c - \bar{x})^2}{\sum (x_i - \bar{x})^2}} \right] \quad (1)$$

$$\text{Prediction interval: } \left[y_p \pm t_{n-2}^{5\%} \cdot S_e \sqrt{1 + \frac{1}{n} + \frac{(x_p - \bar{x})^2}{\sum (x_i - \bar{x})^2}} \right] \quad (2)$$

where $t_{n-2}^{5\%}$ is the two tail critical value of the t -distribution, n is the degree of freedom, $S_e = \sqrt{\sum e_i^2 / n - 2}$, $\sum e_i^2$ is the error sum of squares, x_c and x_p are the values of x_i for which the confidence interval and the prediction interval calculations are made, and y_c and y_p are calculated based on the regression equations at x_c and x_p , respectively.

2.6. Limit of detection (LOD) and limit of quantitation (LOQ)

The LOD and LOQ values were calculated based on "Standard Deviation of the Response and the Slope" entitled in an ICH guideline [13]. Standard deviations (SD) of the responses were estimated based on the standard deviations of the measured data at zero analyte content and the slopes (S) were estimated from the calibration lines. The measured spectral values of the water-free excipients were used as blank samples. Since eight parallel measurements were performed in the case of each sample and its average values were used for the calibrations the standard error of the means (SEM) of the averaged blank data ($\text{SEM} = \text{SD} / \sqrt{n}$, $n = 8$) were used to calculate the LOD and LOQ values ($3.3 \cdot \text{SEM} \cdot S$ and $10 \cdot \text{SEM} \cdot S$, respectively) and standard deviations of the blank samples were estimated from the values of the parallel measurements.

2.7. Theory of the ATR-FTIR spectroscopy

In the case of powdered materials the samples have to be compressed on the ATR crystal of the ATR-accessory with high pressure to obtain reproducible and good quality spectra. In contrary to the transmission technique at the ATR-FTIR spectroscopy the incident infrared (IR) beam is totally reflected at the ATR crystal/sample interface, only an evanescent wave penetrates into the sample [8]. This evanescent wave interacts with the absorbing material resulting in the spectrum. The penetration depth of the evanescent wave is only a few microns, therefore from this surface region quantitative information could be obtained to the bulk if the molecules are homogeneously distributed inside the material.

There is linear relationship between the penetration depth (d_p) of the evanescent wave and the wavelength (λ) of the IR beam according to Eq. (3), where n_1 and n_2 are the refractive indices of the ATR crystal and the sample, respectively, and θ_i is the incident angle of the IR beam (typically 45°).

$$d_p = \frac{\lambda}{2\pi n_1 \sqrt{(\sin\theta_i)^2 - \left(\frac{n_1}{n_2}\right)^2}} \quad (3)$$

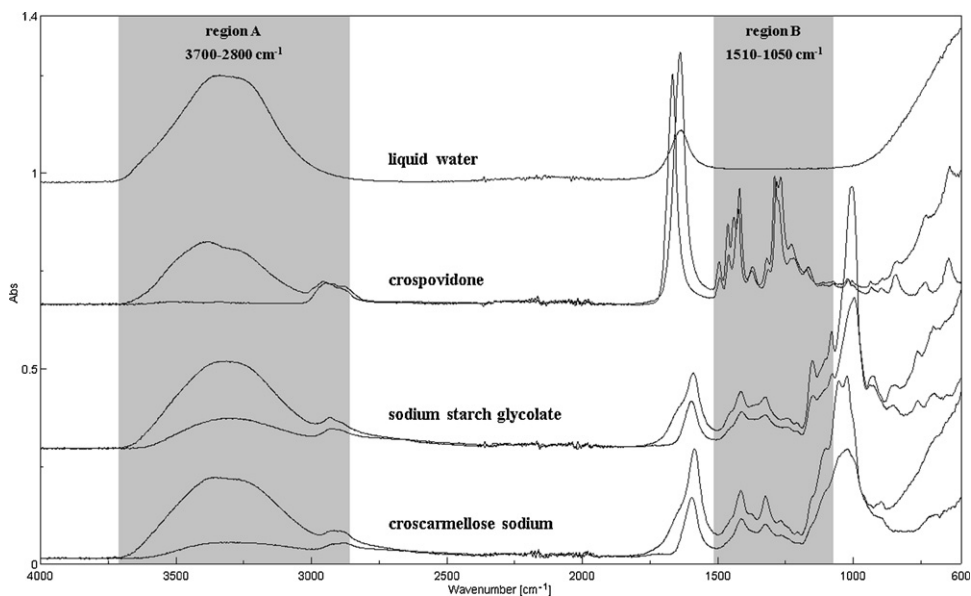


Fig. 1. Spectra of liquid water and the three types of excipients of maximum and minimum water contents using maximal ATR pressure.

The denominator of the equation can be combined into a coefficient k (function of n_1 , n_2 , and θ_i), that is constant if the refractive index of the sample is not altered using the same ATR-accessory. Due to the wavelength dependence of the penetration depth, the spectral intensities will be relatively more intense in the low wavenumber region compared to the high wavenumber region. Since the ratio of two absorbance intensities was used for calibration, this ratio is not or less sensitive to the changes of the parameters of the ATR accessory (n_1 , θ_i) and of the sample (n_2). Along with the changes of the coefficient k , integral absorbances in the two regions vary with the same extent, since $d_p = k^{-1}\lambda$, thus the calculated ratio remains unchanged. However it is important to note that the refractive index of an absorbing material is not constant and varies rapidly around a strong absorption band [9]. It falls below the average value at the lower wavelength (higher wavenumber) side of an absorption band, and rises above to the average value at the higher wavelength (lower wavenumber) side, the average being the value in the absence of any absorption. This phenomenon is called anomalous dispersion. Therefore the d_p will be lower at the higher wavenumber side around an absorption band and higher at the low wavenumber side and the shape and area of absorption bands will change [10]. These phenomena can be well demonstrated by the comparison of the ATR spectrum of water with their transmission spectrum [11]. Despite the anomalous dispersion of refractive index, the uncorrected absorption intensities of ATR-FTIR spectra can be used in quantitative analysis. The reason of it could be the counter-balanced effect of change of the penetration depth due to anomalous dispersion; since d_p is lower at the higher wavenumber side of an absorption and it is higher on the other side. Max et al. [12] also showed that the intensity of aqueous salt solutions follows the Beer–Lambert law in the case of ATR-FTIR spectroscopy. Disruption of the linearity of the calibration lines due to anomalous dispersion was not observed in our experiments.

3. Results and discussion

3.1. Spectra of the different samples

Liquid water has strong absorption around 1640 cm^{-1} due to its bending vibration and very strong absorption between 3700 and 2800 cm^{-1} (called region A) due to its stretching vibrations,

therefore the changes of water contents in materials can be easily followed by the changes of the absorbance intensities in this region (Fig. 1).

However in the case of amorphous or partially amorphous polymeric excipients the densities of the polymer chains on the ATR crystal should be considered because these materials have excess (free) volume between the polymer chains [14], therefore their density extensively changes with the compression. Since water molecules are inside the polymer domain, the polymer density also determines the amount of water which could interact with the evanescent wave. Along with the increase of water content of the excipients, the densities of the polymer chains will increase on the ATR crystal, due to the plasticizing effect of water. As a result of it more intense spectra could be observed in the entire infrared region with increasing water contents. Similar findings were found by Elkhider et al. [15] investigating hydroxypropylmethylcellulose tablets exposed to different relative humidity values. The absorbed water reduces the glass transition temperature, increases the free volume and consequently the molecular mobility of amorphous materials [14,16]. The higher free volume resulted in denser re-arrangement of the polymer chains in the course of the ATR compression, and assuming similar penetration depth, the evanescent wave will interact with more molecules. The two effects—increasing water content and increasing polymer density over the ATR crystal—changed together the absorbance intensities in the region A. In order to study the density of the polymer chains on the ATR crystal, the $1510\text{--}1050\text{ cm}^{-1}$ region (region B) was selected, because in this region water has only weak absorption due to combination bands [17], while the excipients and most organic molecules have intense absorption in this region.

Fig. 2a and b compares the spectra of croscarmellose sodium samples with different water contents at maximum pressure with the spectra of samples at maximum water content and different pressures. Similar nature of the spectra can be observed in region B ($1510\text{--}1050\text{ cm}^{-1}$), therefore it can be stated that the spectral changes in region B are due to the different compaction of the samples in both cases while water has relatively less effect on the absorption intensities in this region. By the calculation of the absorbance intensities in region A and B, and taking its ratio (A^*/B^*), linear relationship could be obtained between these values and the water content of the samples in the form of amount of water/100 g water-free excipient. The reason is if the absorbance intensity

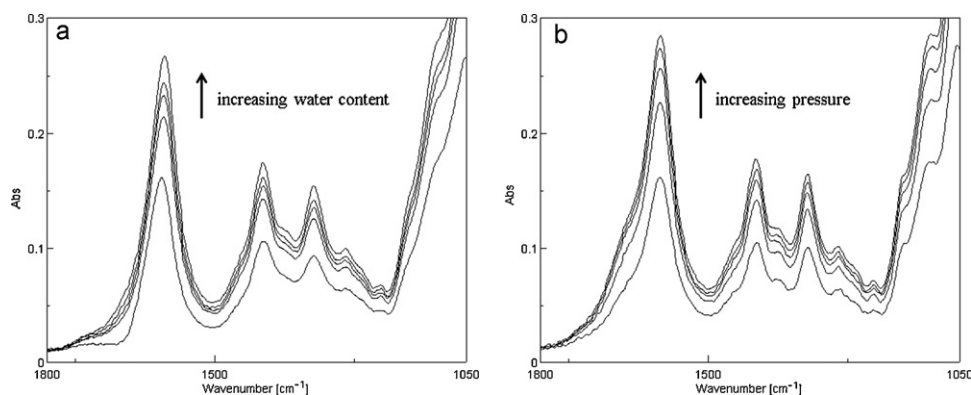


Fig. 2. Spectral region of croscarmellose sodium samples (a) of different water contents at the maximum pressure, (b) of maximum water content obtained by increasing pressure on the ATR-accessory.

values in region A (A^*) are normalized against the absorbance intensity values in region B (B^*), then A^* could be responsible solely to the water absorption of the samples and by taking B^* constant (unit) the amount of water-free polymer that interact with the evanescent wave is also constant mathematically.

3.2. Baseline shifts

Scattering of the infrared radiation on the excipient particles during the ATR-FTIR measurements should be considered in the quantitative analysis. If the particle size is commensurable to the wavelength, the electromagnetic radiation scatters thus considerably increasing the baseline. The latter can be seen in the case of Polyplasdone XL (crospovidone with highest particle size) samples (Fig. 3).

The increase of baselines with decreasing water content can be observed in the case of each excipient, but its extent is different depending on the type of the superdisintegrants. The baseline shifts can be also explained with the plasticizing effect of water. With increasing water content the high pressure ATR-accessory is able to form a more homogeneous smooth surface on the ATR crystal, consequently the scattering of the infrared radiation will be decreased. With the appropriate baseline correction it is possible to generate regression lines of the two Polyplasdone samples which do not significantly differ from each other according to their 95% confidence intervals (Fig. 4), therefore a common calibration line was constructed for Polyplasdone.

However in the case of Kollidon CL-SF the slope of the regression line was slightly greater. In order to clarify this tendency different Kollidon grades should be also examined. Since there was no significant difference between the regression lines of the two Polyplasdone, it can be supposed that the water content determination with ATR-FTIR measurement is not sensitive to the change of the

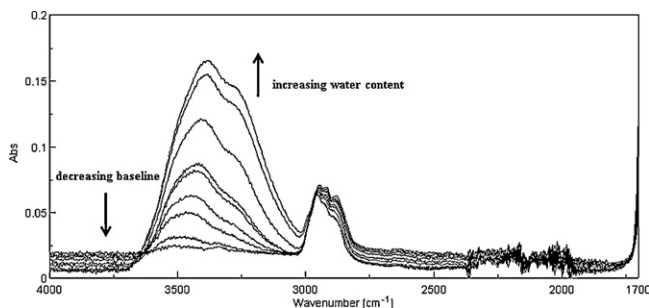


Fig. 3. Baseline shift of spectra of Polyplasdone XL as a function of the water content in the 4000–1700 cm^{-1} region.

particle size if appropriate baseline correction is used. In the case of Vivasol samples the baseline correction does not improved the regression line, maybe due to its irregular rod-like particle shape and special scattering property; therefore the uncorrected raw spectral data were used for the calculations (Fig. 5).

3.3. Quantitative results

Water content of superdisintegrants is an important parameter from the point of manufacturing. In the two pharmacopeias loss on drying test is specified instead of water content determination. However, in the course of drying, in the lack of volatile components and thermal decomposition mostly water leaves, therefore water content determination can be an alternative to the loss on drying method. Table 1 summarizes the pharmacopeial requirements of the loss on drying method and the quantitative parameters of the suggested ATR-FTIR method. In the case of crospovidone excipient the drying time is not determined in the pharmacopeias only the drying to constant weight is required, therefore 2 h were chosen as drying time. According to the spectra of dried crospovidone (Fig. 1) this period was enough for complete drying. Crospovidone being a tertiary amide has no absorption in the region of 3700–3050 cm^{-1} and the absence of water band of the dry spectrum in this region indicated that the drying was successful and also indicated that in the course of the ATR-FTIR measurement the hygroscopic material were unable to absorb significant amount of water.

Since the infrared wave interacts with a very small volume of samples on the ATR crystal the local inhomogeneities in water distribution could cause the relatively large standard deviation of the measured A^*/B^* values as it was observed during our measurements. To avoid the relatively large standard deviation (SD) of the measured values, each measurement was repeated eight times and their mean was used to generate one data value. The given LOD and LOQ values are valid assuming eight parallel measurements are performed. The increase of the number of parallel measurements will decrease the LOD and LOQ values of the method.

Each superdisintegrant met the pharmacopeial requirements. From the precision interval it can be seen that if the water content of the excipients is not around the limit of the acceptable value, the ATR-FTIR method is able to prove the compliance with requirements. However, the precision of water content determinations is lower than in the case of loss on drying and Karl-Fischer titration methods but this is derived partly from the methodology and not from the reproducibility of the A^*/B^* values. Several simplifications are necessary during quantitative evaluation of ATR spectra. Application of different correction methods (considering the anomalous dispersion of the refractive index, the baseline shift,

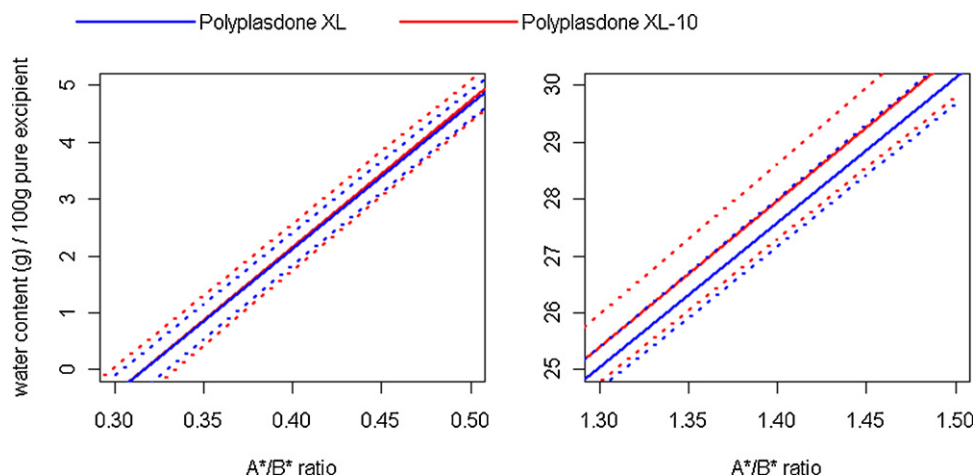


Fig. 4. The two end sections of the regression lines of the two Polyplasdone grades with 95% confidence intervals (dotted lines).

Table 1

Summary of the pharmacopeial requirements and the quantitative parameters of the described method.

	Kollidon CL-SF	Polyplasdone XL	Polyplasdone XL-10	Explotab	Vivasol
Loss on drying method ^a	105 °C/2 h	105 °C/2 h	105 °C/2 h	130 °C/1.5 h	105 °C/6 h
Max. acc. water ^b	5	5	5	10	10
Max. inv. water ^c	22	22	23	19	24
Water by drying ^d	3.68 (0.02)	3.50 (0.01)	3.02 (0.11)	7.56 (0.09)	5.92 (0.05)
Water by ATR ^e	4.11	3.54	2.95	7.65	6.39
PI at the max. acc. water ^f	±1.3	±0.7	±0.7	±0.5	±1.4
PI at zero water ^g	±1.3	±0.8	±0.8	±0.6	±1.5
PI at inv. max. water ^h	±1.5	±0.8	±0.8	±0.6	±1.6
LOD ⁱ	0.3	0.2	0.2	0.3	0.6
LOQ ^j	0.9	0.7	0.7	0.8	1.8

^a Drying temperature and time applied for the determination of the initial water content.

^b Maximum acceptable water content of excipients by pharmacopeias based on loss on drying method (% w/w).

^c Maximum investigated water content of excipients (% w/w).

^d Initial water content of excipients with standard deviation ($n = 3$) determined by the pharmacopeia loss on drying test (% w/w).

^e Calculated initial water content of excipients based on the calibration lines (% w/w).

^f 95% prediction interval of the calculated water content values in the case new measured samples near the maximum acceptable water contents (% w/w).

^g 95% prediction interval of the calculated water content values in the case new measured samples near zero water contents (% w/w).

^h 95% prediction interval of the calculated water content values in the case new measured samples near the maximum investigated water contents (% w/w).

ⁱ Limit of detection performing eight parallel measurements (% w/w).

^j Limit of quantitation performing eight parallel measurements (% w/w).

and the absorption of water in region B) could result in more accurate water content determination. It has to be also mentioned that the absorbance bands of hydrophilic groups of polymers are affected by hydrogen-bonds during water absorption and their

wavenumber position and intensity alter as it can be observed on the spectra of crospovidone between 1510 and 1050 cm^{-1} (Fig. 1). In addition, superdisintegrants of high water contents lose moisture very rapidly; therefore controlled humidity environment or

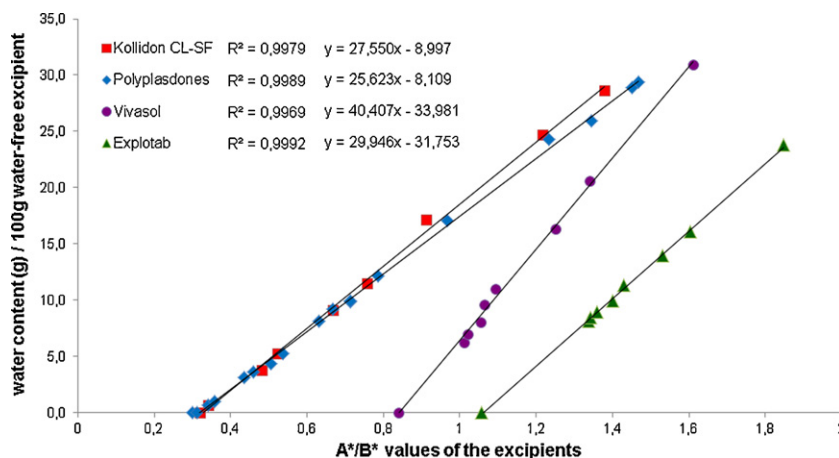


Fig. 5. Equations and correlation coefficients of regression lines of examined excipients using a common calibration line to the two Polyplasdone grades of different particle sizes.

special ATR sample holder developed for hygroscopic materials [18] would be advantageous for more accurate ATR-FTIR measurements.

4. Conclusion

A fast screening method was developed for the water content determination of polymer superdisintegrants containing homogeneously distributed water. The two main advantages of the method are that it could be used for thermosensitive materials and also for materials that cannot be dissolved in the medium of the Karl-Fischer titration.

ATR-FTIR method enabled water content determination over the entire investigated range of the water content by using appropriate spectral regions after baseline correction. Further development of the method could offer an alternative solution for the existing time- and reagent demanding techniques.

Since the method was independent of the chemical nature of the investigated materials it could assume that it works in the case of other powdered polymer excipients, too.

References

- [1] R. Thibert, B.C. Hancock, Direct visualization of superdisintegrant hydration using environmental scanning electron microscopy, *J. Pharm. Sci.* 85 (1996) 1255–1258.
- [2] R. Steendam, H.W. Frijlink, C.F. Lerk, Plasticisation of amylopectin by moisture. Consequences for compaction behaviour and tablet properties, *Eur. J. Pharm. Sci.* 14 (2001) 245–254.
- [3] K.C. Waterman, B.C. Macdonald, Package selection for moisture protection for solid, oral drug products, *J. Pharm. Sci.* 99 (2010) 4437–4452.
- [4] European Pharmacopoeia 7.3, Council of Europe, Strasbourg, 2012.
- [5] United States Pharmacopoeia 34-National Formulary 29, The United States Pharmacopoeial Convention, Rockville, MD, 2012.
- [6] H.D. Isengard, Rapid water determination in foodstuffs, *Trends Food Sci. Technol.* 6 (1995) 155–162.
- [7] G. Reich, Near-infrared spectroscopy and imaging: basic principles and pharmaceutical applications, *Adv. Drug Deliv. Rev.* 57 (2005) 1109–1143.
- [8] T. Buffeteau, B. Desbat, D. Eyquem, Attenuated total reflection Fourier transform infrared microspectroscopy: theory and application to polymer samples, *Vib. Spectrosc.* 11 (1996) 29–36.
- [9] S. Luthra, D.S. Kalonia, M.J. Pikal, Effect of hydration on the secondary structure of lyophilized proteins as measured by Fourier transform infrared (FTIR) spectroscopy, *J. Pharm. Sci.* 96 (2007) 2910–2921.
- [10] J.M. Chalmers, G. Dent, *Industrial Analysis with Vibrational Spectroscopy*, Royal Society of Chemistry, Information Services, Cambridge, UK, 1997.
- [11] J. Grdadolnik, *Int. J. Vib. Spectrosc.* 6 (2002) 6, <http://www.ijvs.com/volume6/edition2/section3.html>.
- [12] J.-J. Max, S. de Blois, A. Veilleux, C. Chapados, IR spectroscopy of aqueous alkali halides. Factor analysis, *Can. J. Chem.* 79 (2001) 13–21.
- [13] European Medicines Agency, ICH Topic Q2 (R1) Validation of Analytical Procedures: Text and Methodology, European Medicines Agency, London, 1995.
- [14] M.G. Abiad, M.T. Carvajal, O.H. Campanella, A review on methods and theories to describe the glass transition phenomenon: applications in food and pharmaceutical products, *Food Eng. Rev.* 1 (2009) 105–132.
- [15] N. Elkhider, K.L.A. Chan, S.G. Kazarian, Effect of moisture and pressure on tablet compaction studied with FTIR spectroscopic imaging, *J. Pharm. Sci.* 96 (2007) 351–360.
- [16] B.C. Hancock, G. Zografi, Characteristics significance of the amorphous state in pharmaceutical systems, *J. Pharm. Sci.* 86 (1997) 1–12.
- [17] J.-J. Max, C. Chapados, IR spectroscopy of aqueous alkali halide solutions: pure salt-solvated water spectra and hydration numbers, *J. Chem. Phys.* 115 (2001) 2664–2675.
- [18] M.D.S. Lekgoathi, J.P. le Roux, Attenuated total reflectance powder cell for infrared analysis of hygroscopic samples, *Spectrochim. Acta A* 82 (2011) 529–531.



Identification, characterization and quantification of a new impurity in deferasirox active pharmaceutical ingredient by LC–ESI–QT/MS/MS

Saji Thomas^{a,*}, Subhash Chandra Joshi^a, Dharam Vir^b, Ashutosh Agarwal^b, Raghavendra Desai Rao^c, I. Sridhar^c, Cijo M. Xavier^c, Chandra S. Mathela^d

^a Jubilant Life Sciences Ltd., Analytical Research Department, R&D Centre, C-26, Sector-59, Noida, Uttar Pradesh 201 301, India

^b Jubilant Life Sciences Ltd., Chemical Research Department, R&D Centre, C-26, Sector-59, Noida, Uttar Pradesh 201 301, India

^c Jubilant Life Sciences Ltd., Analytical Research Department, 56-59, KIADB Industrial Area, Nanjangud, Mysore, Karnataka 571 302, India

^d Department of Chemistry, Kumaun University, D.S.B. Campus, Nainital, Uttarakhand 263 001, India

ARTICLE INFO

Article history:

Received 2 September 2011

Received in revised form 18 January 2012

Accepted 19 January 2012

Available online 28 January 2012

Keywords:

Deferasirox

Impurity

LC–MS/MS

NMR

Validation

ABSTRACT

An unknown impurity was detected in deferasirox drug substance by a newly developed high performance liquid chromatography (HPLC) method. The unknown impurity was identified by liquid chromatography–tandem mass spectrometry using electrospray ionization source and Q-trap mass analyzer (LC–ESI–QT/MS/MS). Based on LC–MS/MS data and knowledge of the synthetic scheme of deferasirox, this impurity was proposed as the regio-isomer of deferasirox. Structural confirmation of this impurity was unambiguously carried out by synthesis followed by characterization using nuclear magnetic resonance (NMR), infrared spectroscopy (IR), mass spectrometry, elemental analysis (EA) and the impurity was confirmed as 2-[3,5-bis(2-hydroxy-phenyl)-[1,2,4]-triazol-1-yl]-benzoic acid (Imp-1). The newly developed method was validated according to ICH guidelines. The resolution between Imp-1 and deferasirox was found to be more than 6.0 and the detection limit of impurities was in the range of 0.0005–0.01%, indicating high selectivity and sensitivity of the newly developed method.

© 2012 Elsevier B.V. All rights reserved.

1. Introduction

Deferasirox (Fig. 1) is an orally active iron chelator that is used in the management of chronic iron overload due to blood transfusion. Deferasirox is a tridentate ligand that binds iron with high affinity in a 2:1 ratio from the soluble iron pool in the plasma. It is indicated for the treatment of transfusional iron overload due to blood transfusions such as β -thalassemia or sickle cell disease and other chronic anemias (transfusional hemosiderosis). Deferasirox has been developed to reduce iron-related morbidity and mortality. Deferasirox is the first oral medication approved in USA for this purpose [1–4].

Several methods have been reported in literature for deferasirox. Long term efficacy and safety of deferasirox has been reported [5]. A LC–MS method for the analysis of deferasirox in biological samples [6], pharmacokinetics, distribution, metabolism and excretion of deferasirox and its iron complex in rats have also been reported [7,8]. A stability indicating LC method for deferasirox in bulk drugs and pharmaceutical dosage forms, LC determination of deferasirox in pharmaceutical formulations and preparation of highly pure deferasirox have been reported recently

[9–11]. Deferasirox is not listed in any pharmacopoeias such as USP, EP and BP, etc.; and no reports available on the impurity profile study of deferasirox using LC–MS/MS techniques.

During HPLC analysis of deferasirox samples by the reported method [9] it was found that one unknown impurity was co-eluting with the main peak. Therefore it was felt necessary to develop a new method to resolve this impurity from the main peak. Upon analysis of deferasirox samples by the newly developed method, two impurities were detected in several batches. One of the impurities was found to be known [11], the unknown impurity which was co-eluting with the main peak in the previously reported method was found to be well resolved from deferasirox peak and was in the range of 0.1–0.15%. ICH guidelines indicate that unknown impurities at or above 0.05% in the drug substance require identification [12] depending on the maximum daily dosage. Characterization of unknown impurity is also essential to ascertain that an impurity does not have genotoxic concern, hence characterization of unknown impurities is critical to establish the quality, safety and efficacy of drug substances. As a common practice, efforts should be made to identify and characterise all unknown impurities in the drug substance due to the ever increasing demand from regulatory agencies to manufacture high purity drug substances. Impurity profiling of drugs is one of the most important issues in the modern pharmaceutical analysis [13–19] for developing process technology to manufacture high purity drug substance. Objective of the current

* Corresponding author. Tel.: +91 120 4362210; fax: +91 120 2580033.

E-mail address: saji.thomas@jubil.com (S. Thomas).

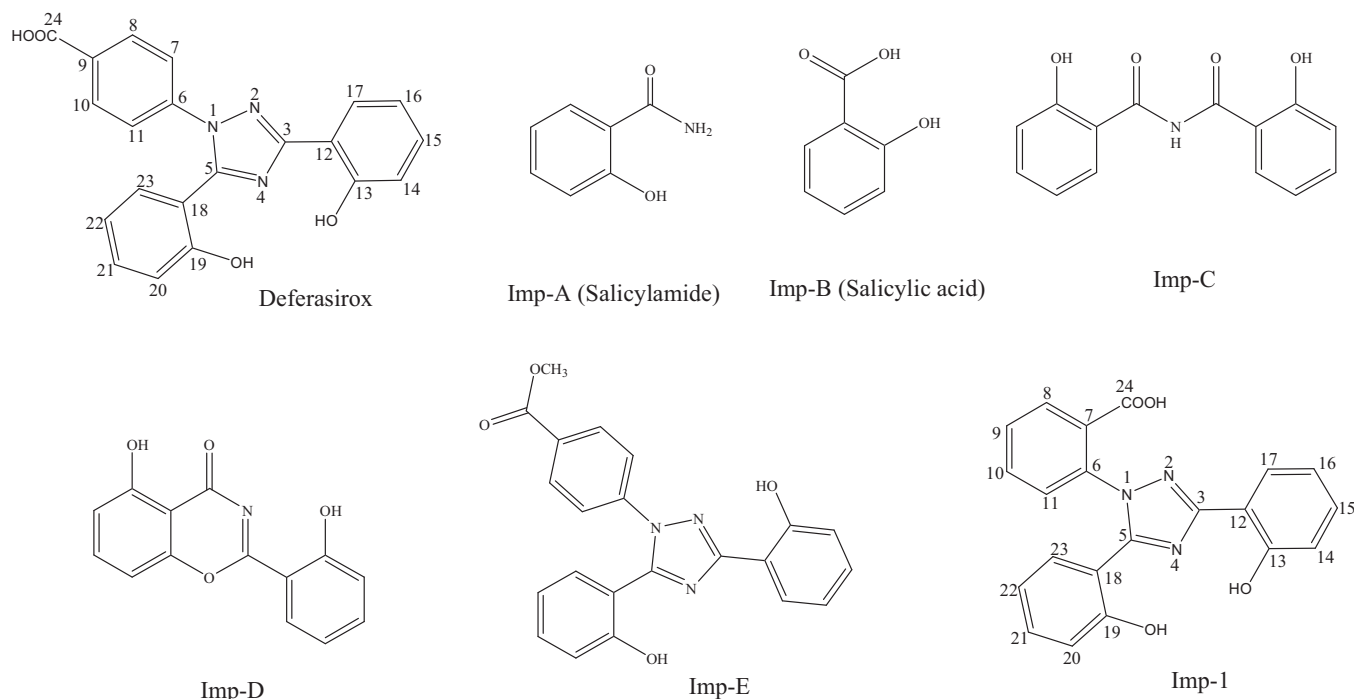


Fig. 1. Chemical structures of deferasirox and impurities, numbering has been assigned for NMR characterization.

study was to characterise the unknown impurity detected consistently in several batches of deferasirox. Structure of impurity was proposed based on LC–MS/MS data and evaluating the synthetic scheme of deferasirox. The proposed structure was further unambiguously confirmed by synthesis followed by characterization using NMR, IR and elemental analysis. A plausible mechanism for the formation and control of new impurity in deferasirox has also been proposed. Newly developed method was validated according to ICH guidelines [20].

2. Experimental

2.1. Materials and reagents

Sample of deferasirox API (batch no. DFX/RD-crude), Imp-A (salicylamide), Imp-B (salicylic acid), Imp-C (2-hydroxy-*N*-(2-hydroxyphenyl)carbonyl)benzamide, Imp-D(2-(2-hydroxyphenyl)-4*H*-1,3-benzoxazin-4-one) and Imp-E (4-[3,5-bis(2-hydroxyphenyl)-1-*H*-1,2,4-triazol-1-yl]methyl benzoate) (Fig. 1) were obtained from Jubilant Life Sciences Limited (Mysore, India). Deionised water was prepared using a Milli-Q plus water purification system from Millipore (Bedford, MA, USA). HPLC grade methanol and acetonitrile were purchased from Merck India Limited (Maharashtra, India). Dimethyl sulfoxide- d_6 (for NMR) was purchased from Sigma–Aldrich Corporation (St. Louis, MO, USA). Analytical reagent grade trifluoroacetic acid and formic acid were purchased from Qualigens India Limited (Mumbai, India). Potassium bromide FT-IR grade was purchased from Merck KGaA (Hesse, Germany). Laboratory reagent grade 2-hydrazinobenzoic acid, 4-hydrazinobenzoic acid, pyridine, triethylamine, ethanol, ethyl acetate, *n*-hexane, thionyl chloride, *o*-xylene, potassium dihydrogen phosphate and sodium sulfate were purchased from Spectrochem (Mumbai, India).

2.2. High performance liquid chromatography

Samples were analysed on a Waters alliance 2690 separation module equipped with 2487 UV detector (Waters corporation, MA,

USA) using an Inertsil ODS-3V column (GL Sciences Inc., Tokyo, Japan), (250 mm × 4.6 mm, 5 μ m). Mobile phase A consisted of water–trifluoroacetic acid (100:0.05, v/v) and mobile phase B consisted of acetonitrile–methanol–trifluoroacetic acid (50:50:0.05, v/v/v) in gradient mode (T_{\min} A:B) T_0 50:50, T_{20} 20:80, T_{35} 20:80, T_{40} 50:50, T_{45} 50:50 with a flow rate of 1.0 mL/min, detector wavelength at 245 nm and the column temperature maintained at 25 °C throughout the analysis. Injection volume was 10 μ L for a sample concentration of 400 μ g/mL prepared in mobile phase-B.

2.3. Liquid chromatography–tandem mass spectrometry (LC–MS/MS)

The MS and MS/MS studies were performed on 3200 Q-trap mass spectrometer (AB Sciex, CA, USA) using electrospray ionization source (–ive mode). The instrument was operated in enhanced product ion mode with the following settings: collision energy of –40V, collision energy spread –10V declustering potential –10V and the capillary ion spray voltage was –4500 V. Nitrogen was used as curtain gas and CAD gas at a pressure of 15 psi. Zero air at a pressure of 45 psi was used as nebuliser gas and heater gas.

The HPLC consisted of LC-20AD binary gradient pump, SPD-10AVP UV detector, SIL-10HTC auto sampler and a column oven CTO-10ASVP (Shimadzu Corporation, Kyoto, Japan). A Symmetry shield RP18 column (Waters Corporation, MA, USA, 250 mm × 4.6 mm, 5 μ m) was used for chromatographic separation. Mobile phase A consisted of 0.1% (v/v)formic acid and mobile phase B consisted of 0.1% formic acid in acetonitrile–methanol mixture (50:50:0.1, v/v/v) in gradient mode (T_{\min} A:B) T_0 50:50, T_{20} 20:80, T_{35} 20:80, T_{40} 50:50, T_{45} 50:50 and a flow rate of 1.0 mL/min was used. Injection volume was 10 μ L for a sample concentration of 400 μ g/mL prepared in mobile phase-B. The column was maintained at 25 °C throughout the analysis.

2.4. NMR spectroscopy

^1H and ^{13}C NMR spectra were recorded at 399.957 MHz and 100.432 MHz respectively, using a Bruker AVANCE 400 MHz

spectrometer (Bruker, Fallanden, Switzerland) equipped with a 5 mm BBO probe and a z-gradient shim system. The ^1H NMR spectra were recorded with 1 s pulse repetition time using 30° flip angle, whilst ^{13}C NMR spectra were recorded with power gated decoupling using 30° flip angle with repetition time of 2 s. Samples were dissolved in dimethyl sulfoxide- d_6 . The ^1H and ^{13}C chemical shift values were reported on the δ scale in ppm relative to DMSO- d_6 (2.50 ppm for ^1H NMR and 39.5 ppm for ^{13}C NMR). All spectra were recorded with sample spinning.

2.5. FT-IR spectroscopy

The IR spectrum was recorded in the solid state as KBr powder dispersion using Nicolet FT-IR model AVTAR 370 (Thermo Electron Scientific Instruments, Madison, WI, USA) with a DTGBS KBr detector. Data were collected between 400 and 4000 cm^{-1} , with a resolution of 4.0 cm^{-1} . A total of 16 scans were obtained and processed using the OMNIC software version 6.0.

2.6. Elemental analysis

Elemental analysis (C, H, N) was carried out using an elemental analyzer model Vario EL III with TCD detector (Elementar Analysensysteme GmbH, Hanau, Germany). Samples were weighed in a tin boat, to which tungsten oxide was added and neatly packed. The sample in tin boat was loaded in an auto sampler tray and was dropped into the combustion tube automatically at a temperature of 1200°C . Complete combustion of sample was ensured with a special oxygen jet injection.

2.7. Preparation of solutions for method validation

A test preparation of $400\text{ }\mu\text{g/mL}$ of deferasirox sample was prepared by dissolving appropriate amount in methanol. A stock solution of impurities were prepared by dissolving 10 mg each of Imp-A, Imp-B, Imp-C, Imp-D, Imp-E and Imp-1 in 100 mL of methanol. From this stock solution a solution containing $0.6\text{ }\mu\text{g/mL}$ each of Imp-A, Imp-B, Imp-C, Imp-D, Imp-E, Imp-1 and $400\text{ }\mu\text{g/mL}$ of deferasirox was prepared in mobile phase-B.

3. Results and discussion

3.1. Method development

Initially deferasirox samples were analysed by reported method [9]. A critical evaluation of chromatographic data revealed that one of the impurities was co-eluting with the main peak (Fig. 2a and b). Peak broadening was also a major concern about the specificity and efficiency of the reported method. Therefore it was felt necessary to develop a new HPLC method with higher selectivity in order to resolve all the impurities from the main peak. Several trials using potassium dihydrogen phosphate and acetonitrile combination on an Inertsil ODS-3V ($250\text{ mm} \times 4.6\text{ mm}$, $5\text{ }\mu\text{m}$) were not given satisfactory improvements in resolution of impurities. Several method development experiments were performed to optimise gradient profile, chromatographic conditions before finalizing the conditions as described under Section 2.2. In the new method, resolution between deferasirox and Imp-1 was found to be more than 6.0 indicating high selectivity of the newly developed method (Fig. 2c).

3.2. Detection of impurities by HPLC

Deferasirox drug substance sample was analysed using the newly developed HPLC method as described in Section 2.2. The analysis revealed the presence of two impurities at retention time 17.91 min (RRT 0.88) and 24.87 min (RRT 1.23) (Fig. 2c). All known

impurities were spiked with deferasirox sample and relative retention times (RRTs) were compared. Based on elution order, known impurities in the spiked preparation were marked as Imp-A (RT 5.01 min; RRT 0.24), Imp-B (RT 8.45 min; RRT 0.41), Imp-C (RT 10.57 min; RRT 0.51), Imp-D (RT 16.17 min; RRT 0.78) and Imp-E (RT 25.68 min; RRT 1.23). Impurity at retention time 17.91 min (RRT 0.88) was found to be unknown and marked as Imp-1 (Fig. 2d).

3.3. Identification and characterization of Imp-1 by LC-MS/MS

A LC-MS method, as described in Section 2.3 was used to identify the unknown impurity. Mass spectral data of deferasirox showed deprotonated molecular ion peak m/z 372 (Fig. 3a). The mass spectral data obtained for Imp-1 did not match with any of the known impurities; therefore, a comprehensive investigation was carried out for identification and characterization of Imp-1. Prior to characterization work on Imp-1, it is logical to understand the LC-MS/MS data for deferasirox, the parent drug molecule. The MS^2 spectra obtained for deferasirox showed prominent product ion peaks at m/z 328 and m/z 252 (Fig. 3b). Formation of these product ions can be attributed to the neutral loss of CO_2 (44 Da) and the subsequent cleavage of aromatic ring resulting in the loss of benzyne (76 Da) as depicted in Fig. 4a. The proposed mass fragmentation pattern was further supported by previously reported values [8].

The mass spectrum of Imp-1 showed a deprotonated molecular ion at m/z 372 (Fig. 3c) equal to that of molecular ion of deferasirox. The MS^2 spectra obtained for Imp-1 also showed prominent product ion peaks at m/z 328 and m/z 252 (Fig. 3d). The fragment at m/z 328 presumed to be identical with the product ion peak of deferasirox showing a difference of 44 amu from the mass of parent ion peak $[\text{M}-\text{H}]^-$ and can be attributed to the neutral loss of CO_2 (44 Da). Formation of other product ions can be rationalised considering the plausible fragmentation pathway for Imp-1. Loss of similar moieties, both from deferasirox and Imp-1 indicated that Imp-1 could be regio-isomer of deferasirox (Fig. 4a and b). The knowledge of the route of synthesis of deferasirox led to proposing the molecular structure of the unknown impurity based on LC-MS/MS data. During the synthesis of deferasirox, salicylic acid and salicylamide were treated in presence of thionyl chloride to get DFX-I intermediate, which on further reaction with 4-hydrazinobenzoic acid, using ethanol as a solvent leads to the formation of deferasirox. The presence of 2-hydrazinobenzoic acid (positional isomeric impurity) in 4-hydrazinobenzoic acid was suspected to contribute the formation of Imp-1. The synthetic scheme for the plausible formation of Imp-1 is depicted in Fig. 5. Based on LC-MS/MS data and synthetic chemistry knowledge, the structure of Imp-1 was proposed as 2-[3,5-bis(2-hydroxy-phenyl)-[1,2,4]-triazol-1-yl]-benzoic acid. Imp-1 was independently synthesised [21] and used for further structural confirmation by NMR, FT-IR and EA techniques.

3.4. Synthesis of Imp-1

Salicylic acid was treated with thionyl chloride to get salicyloyl chloride followed by condensation with salicylamide resulted in formation of 2-(2-hydroxyphenyl)benzo[e][1,3]oxazin-4-one (DFX-I). DFX-I was further treated with 2-hydrazinobenzoic acid under reflux using ethanol as solvent. The mixture was cooled, poured into water and extracted with ethyl acetate. Ethyl acetate layer was concentrated under vacuum and the residue was crystallised from ethyl acetate and *n*-hexane mixture to get 2-[3,5-bis(2-hydroxyphenyl)-[1,2,4]triazol-1-yl]benzoic acid. HPLC purity of Imp-1 was found to be 97.6%. The synthesised Imp-1 was co-spiked with deferasirox sample, retention time of Imp-1 in deferasirox sample and co-spiked sample was found to be exactly same. The MS and MS^2 spectra obtained for synthesised Imp-1

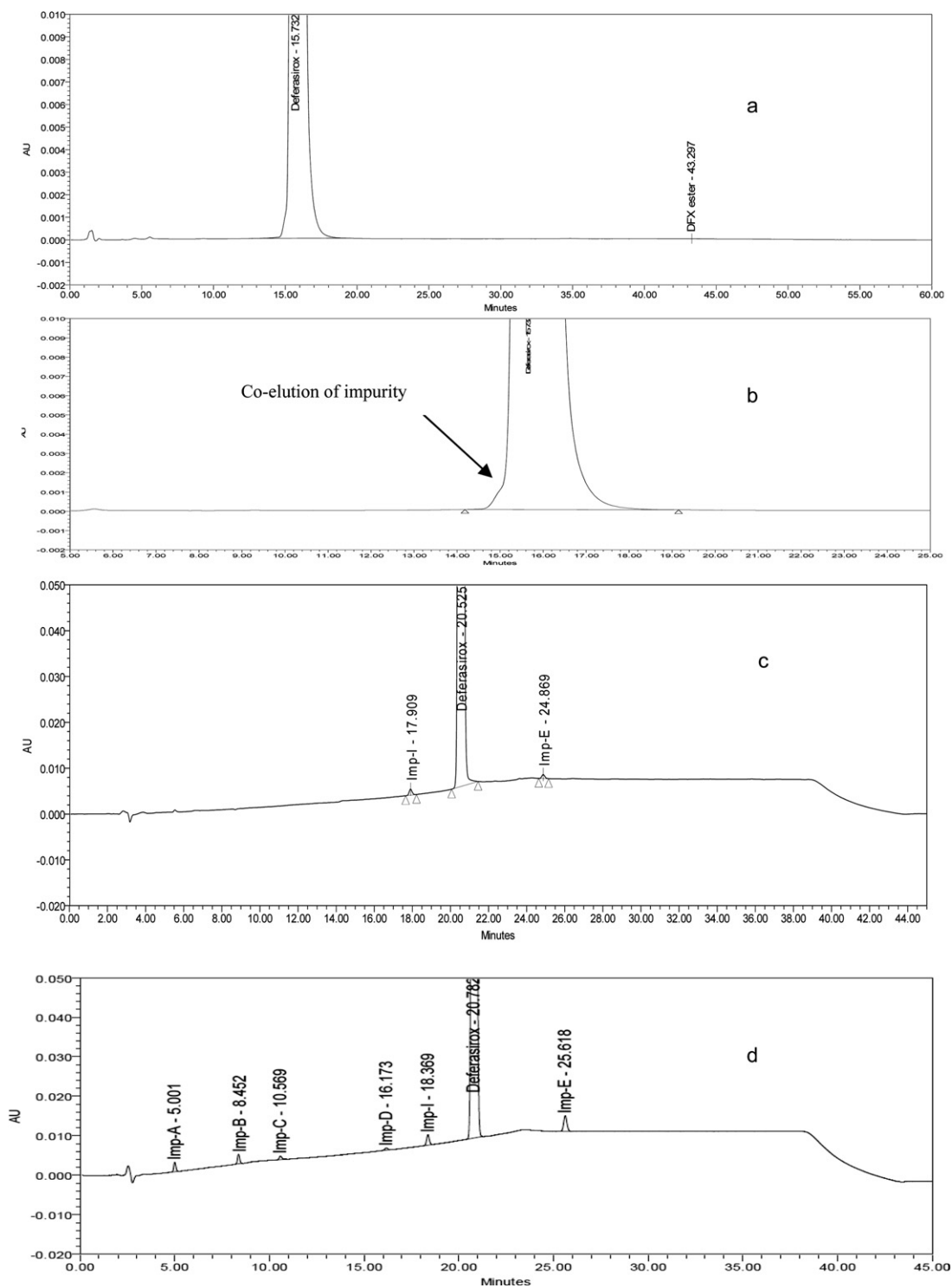


Fig. 2. (a) Chromatogram of deferasirox sample in previously reported method, (b) expanded chromatogram of deferasirox sample showing co-elution of unknown impurity in previously reported method, (c) chromatogram of deferasirox sample showing resolution of unknown impurity in new method, (d) chromatogram of deferasirox sample spiked with impurities in new method.

using direct infusion mode was also found to be exactly same as that of on-line LC–MS/MS analysis.

3.5. Structural confirmation by NMR, FT-IR and CHN analysis

The NMR spectral data of deferasirox and Imp-1 were compared (Table 1). The ^1H NMR spectrum of deferasirox and Imp-1 showed three singlets at δ 10.05, 10.95, 13.20 and 10.25, 10.92,

13.25 ppm assigned to exchangeable hydroxyl and carboxylic protons respectively. It is apparent from the comparison of the NMR spectral data of deferasirox and Imp-1 that both have almost similar chemical shifts for more than half a molecule except the phenyl ring containing carboxylic acid functional group. The symmetrical para disubstituted pattern of deferasirox (positions 8/10 and 7/11; δ 7.99 and δ 7.55 respectively) was lacking in Imp-1, where the four protons (positions 8, 9, 10, 11) having different chemical

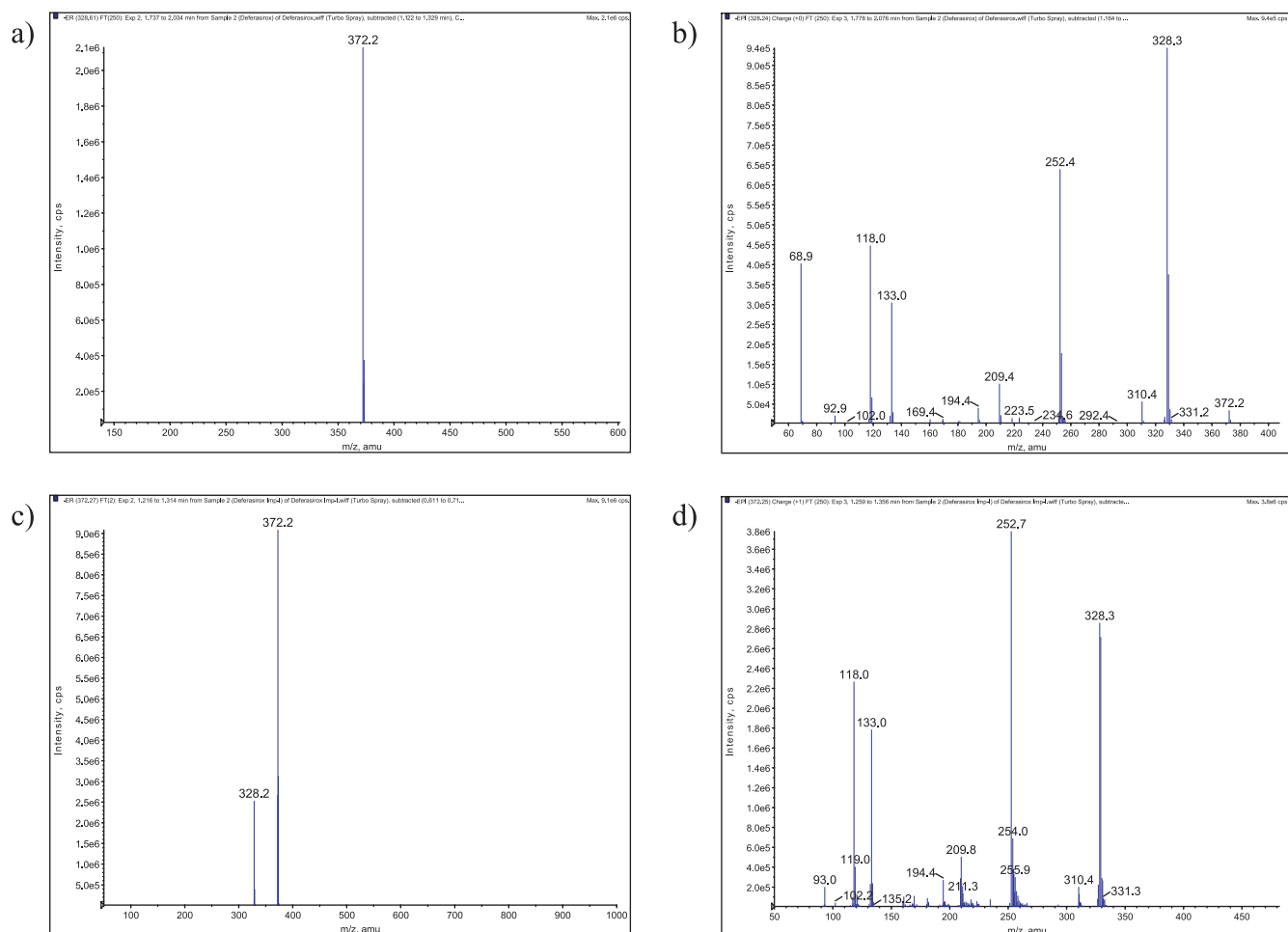


Fig. 3. (a) Mass spectrum of deferasirox (b) MS/MS spectrum of deferasirox (c) mass spectrum of Imp-1 (d) MS/MS spectrum of Imp-1.

Table 1
Comparative NMR assignments for deferasirox and Imp-1.

Position	Deferasirox			Imp-1		
	¹ H	¹³ C	DEPT	¹ H	¹³ C	DEPT
1	–	–	–	–	–	–
2	–	–	–	–	–	–
3	–	160.3	Cq	–	159.6	Cq
4	–	–	–	–	–	–
5	–	152.5	Cq	–	153.3	Cq
6	–	141.7	Cq	–	135.0	Cq
7	7.55/m	123.8	CH	–	136.9	Cq
8	7.99/m	130.8	CH	7.98/dd (8.0, 1.6 Hz)	130.5	CH
9	–	131.0	Cq	7.27/m	127.0	CH
10	7.99/m	130.8	CH	7.70/m	131.5	CH
11	7.55/m	123.8	CH	7.62/m	128.8	CH
12	–	114.1	Cq	–	113.9	Cq
13	10.95/br s (OH)	156.8	Cq	10.92/br s (OH)	156.7	Cq
14	6.99/m	117.5	CH	6.83/d (8.0 Hz)	117.4	CH
15	7.38/m	131.9	CH	7.28/m	132.6	CH
16	6.99/m	120.1	CH	6.99/m	120.0	CH
17	8.04/dd (8.0, 1.6 Hz)	127.2	CH	7.86/dd (8.0, 1.6 Hz)	127.0	CH
18	–	114.8	Cq	–	114.3	Cq
19	10.05/br s (OH)	155.6	Cq	10.25/br s (OH)	156.1	Cq
20	6.86/d (8.0 Hz)	116.6	CH	6.81/d (8.0 Hz)	116.7	CH
21	7.38/m	133.0	CH	7.28/m	133.1	CH
22	6.99/m	119.9	CH	6.99/m	119.4	CH
23	7.55/m	131.5	CH	7.62/m	131.7	CH
24	13.20/br s (COOH)	166.9	Cq	13.25/br s (COOH)	166.3	Cq

s; Singlet, d; doublet, m; multiplet, br s; broad singlet, Cq; quaternary carbon, coupling constant are given in bracket. For numbering of deferasirox and Imp-1 refer Fig. 1.

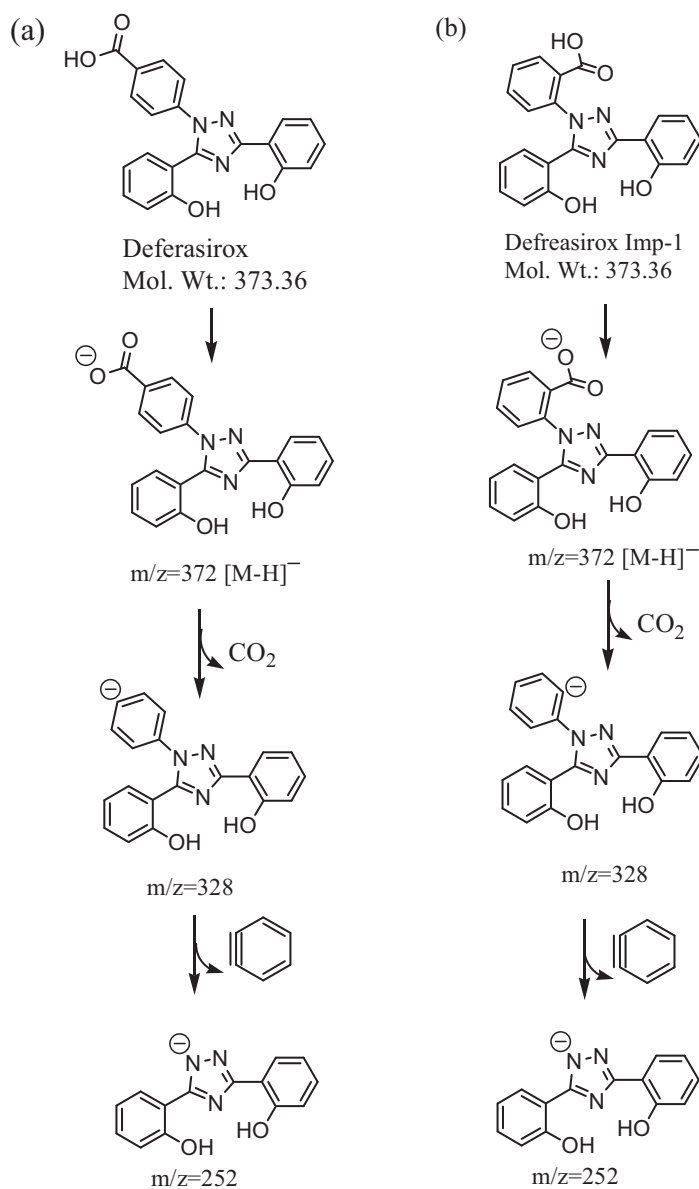


Fig. 4. (a) Plausible fragmentation pathway for deferasirox. (b) Plausible fragmentation pathway for Imp-1.

shifts appeared as a characteristic ortho disubstituted benzenoid pattern. ¹³C and DEPT spectral data also supported these observations. The upfield chemical shift at meta position to the carboxylic acid (δ 7.27 and δ 127.0 in the ¹H and ¹³C spectrum respectively) of Imp-1 favours the regioisomeric nature of Imp-1. The characteristic carboxylic carbon at δ 166.9 ppm in deferasirox and at 166.3 in Imp-1 confirmed the presence of C=O group in both structures. The proposed NMR assignments were further supported by previously reported values [8].

FT-IR spectrum of deferasirox displayed characteristic absorptions at 3435 cm⁻¹ (OH, stretching), 1687 cm⁻¹ (acid, conjugated C=O stretching), 1587 cm⁻¹ (aromatic, C=C stretching). The IR spectrum of Imp-1 displayed characteristic absorptions at 3440 cm⁻¹, (OH, stretching), 1690 cm⁻¹ (acid, conjugated C=O stretching), 1605 cm⁻¹, 1589 cm⁻¹ (aromatic, C=C stretching). ¹H NMR, ¹³C NMR and FT-IR spectral data confirms the proposed structure for Imp-1. CHN data obtained for Imp-1 showed carbon 67.46%, nitrogen 11.18% and hydrogen 4.03% against theoretical values of

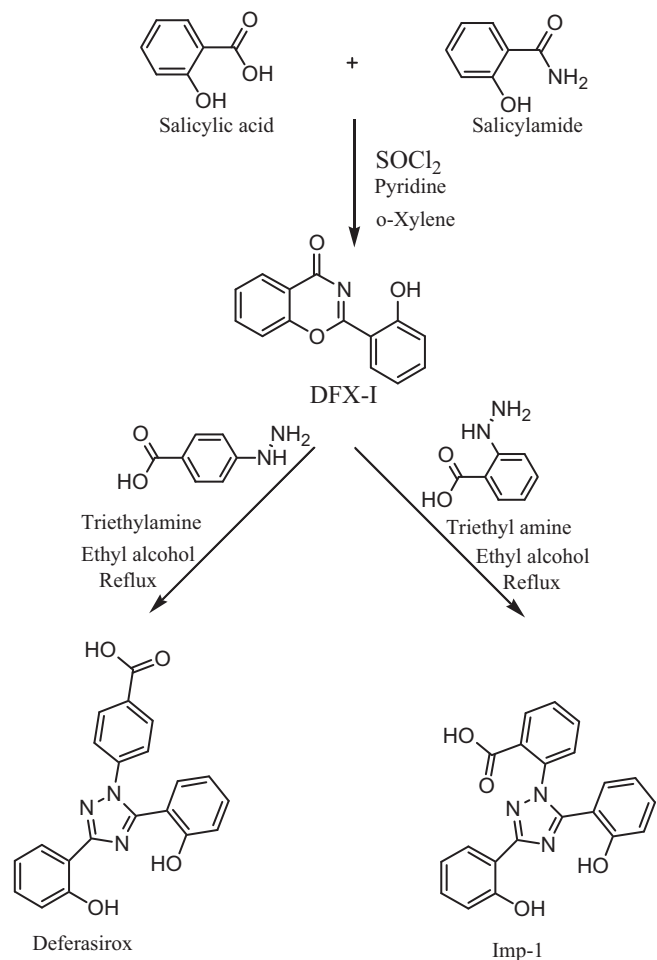


Fig. 5. Synthetic scheme of deferasirox and plausible pathway for the formation of Imp-1.

carbon 67.56%, nitrogen 11.25% and hydrogen 4.05%. CHN data confirms the proposed structure based on LC-MS/MS data.

4. Method validation

The newly developed method was validated for precision, linearity, accuracy, sensitivity, robustness and system suitability according to ICH guidelines [20]. Validation study was carried out for the analysis of Imp-A, Imp-B, Imp-C, Imp-D, Imp-E and Imp-1. The system suitability and selectivity were checked by injecting 400 μ g/mL of deferasirox solution containing 0.15% of all impurities and diluted standard solution of 0.4 μ g/mL of deferasirox and monitored throughout the validation, method validation results are showed in Table 2.

4.1. Specificity

Specificity is the ability of the method to unequivocally assess the analyte response in the presence of its potential impurities. Specificity was established by injecting deferasirox co-spiked with potential impurities. Forced degradation studies were also performed on deferasirox to provide an indication of the stability indicating property and specificity of the proposed method. The stress conditions employed for degradation study included acid hydrolysis (1.0N and 5.0N HCl), base hydrolysis (1.0N and 5.0N NaOH) and oxidation (1.0% and 10% H₂O₂). Solid state stability of the drug substance was carried out by (a) thermal degradation at

Table 2
Method validation summary report.

Parameter	Imp-A	Imp-B	Imp-C	Imp-D	Imp-1	Deferasirox	Imp-E
System suitability							
RT (min)	5.001	8.452	10.569	16.173	18.369	20.782	25.618
RRT	0.24	0.41	0.51	0.78	0.88	1.00	1.23
R_s	–	13.06	10.96	28.77	7.56	9.06	15.36
N	9766	12,566	136,790	63,174	71,514	86,289	107,852
T	1.01	1.09	1.02	0.90	0.96	1.05	1.01
Linearity							
r	0.9996	0.9997	0.9997	0.9995	0.9997	0.9996	0.9996
Slope	95,181	105,427	8434	63,913	149,584	161,150	177,265
Intercept	–131	342	71	–360	–515	–702	–773
Detection limit (%w/w)	0.0009	0.0005	0.01	0.002	0.0007	0.0005	0.0005
Quantitation limit (%w/w)	0.002	0.002	0.03	0.007	0.003	0.002	0.002
Precision %RSD ($n=6$)	4.99	6.64	4.49	4.61	6.26	6.10	5.10
Repeatability (intra day) %RSD ($n=6$)	1.28	1.36	1.42	1.01	1.10	1.21	1.11
Intermediate precision (inter day) %RSD ($n=12$)	1.31	0.82	2.21	2.03	1.41	1.31	0.27
Accuracy at QL level ($n=3$)							
Amount added ($\mu\text{g/mL}$)	0.0080	0.0080	0.1200	0.0280	0.0120	0.0088	0.0088
Amount recovered ($\mu\text{g/mL}$)	0.0079	0.0076	0.1206	0.0285	0.0124	0.0088	0.0088
% Recovery	98.75	95.00	100.50	101.79	103.33	100.00	100.00
Accuracy at 100% level ($n=3$)							
Amount added ($\mu\text{g/mL}$)	0.6000	0.6000	0.6000	0.6000	0.6000	0.6000	0.6000
Amount recovered ($\mu\text{g/mL}$)	0.6216	0.6040	0.5960	0.5996	0.6088	0.6060	0.6076
% Recovery	103.60	100.67	99.33	99.93	101.13	101.00	101.27
Accuracy at 150% level ($n=3$)							
Amount added ($\mu\text{g/mL}$)	0.9000	0.9000	0.9000	0.9000	0.9000	0.9000	0.9000
Amount recovered ($\mu\text{g/mL}$)	0.8924	0.9076	0.9460	0.8992	0.9036	0.8948	0.9016
% Recovery	99.16	100.84	105.11	99.91	100.40	99.42	100.18
Accuracy at 200% level ($n=3$)							
Amount added ($\mu\text{g/mL}$)	1.2000	1.2000	1.2000	1.2000	1.2000	1.2000	1.2000
Amount recovered ($\mu\text{g/mL}$)	1.1900	1.2100	1.2612	1.1988	1.2044	1.2008	1.2020
% Recovery	99.17	100.83	105.10	99.90	100.37	100.07	100.17

n : Number of determinations, RT: retention time, RRT: relative retention time, R_s : USP resolution, N : number of theoretical plates, T : USP tailing factor, r : correlation coefficient.

105°C for 48 h; (b) photolytic degradation was performed by keeping 500 mg of each solid sample in two separate loss on drying bottles (dark control and photolytic exposure) in photo stability chamber model TP 0000090G (Thermo Lab equipments Pvt. Ltd., Mumbai, India). Samples were exposed to get a minimum exposure of 1.2 million lx h for light and 200 Wh/m² for ultraviolet region as per ICH guidelines [22]. Samples were withdrawn at appropriate times and subjected to HPLC analysis using 400 $\mu\text{g/mL}$ sample concentration. Peak purity of stressed samples of deferasirox was checked using a 2996 photo diode array detector (Waters Corporation, MA, USA). From the degradation studies and peak purity test results derived from PDA detector it was confirmed that the spectral purity of deferasirox was homogenous thus confirmed the stability indicating power of the newly developed method.

4.2. Precision

The precision of the related substances method was checked by injecting six individual preparations of 400 $\mu\text{g/mL}$ deferasirox spiked with 0.15% Imp-A, Imp-B, Imp-C, Imp-D, Imp-E and Imp-1. Percentage relative standard deviation for area of each impurity was calculated. Precision study was also determined by performing the same procedures on a different day (inter-day precision). The intermediate precision (ruggedness) of the method was also evaluated by a different analyst on different column (from the same manufacturer) and different instrument in the same laboratory. %RSD of area for each impurity were within 5.0 confirming the good precision of the developed analytical method.

4.3. Sensitivity

Sensitivity was determined by establishing the detection limit (DL) and quantitation limit (QL) for all impurities estimated at a signal-to-noise ratio of 3:1 and 10:1 respectively, by injecting a

series of dilute solutions with known concentrations. The precision study was also carried out at QL level by injecting six individual preparations of all impurities. Percentage RSD for the areas of each impurity was calculated. The DL of Imp-A, Imp-B, Imp-C, Imp-D, Imp-1 and Imp-E was 0.0009%, 0.0005%, 0.01%, 0.002%, 0.0007% and 0.0005% (of analyte concentration, *i.e.* 400 $\mu\text{g/mL}$) respectively for 20 μL injection volume. Quantitation limit was 0.002%, 0.002%, 0.03%, 0.007%, 0.003% and 0.002% for Imp-A, Imp-B, Imp-C, Imp-D, Imp-1 and Imp-E respectively.

4.4. Linearity and range

A linearity test solution for related substance method was prepared by diluting the impurity stock solution to the required concentrations. The solutions were prepared at seven concentration levels. From QL to 200% of the permitted maximum level to the impurities and was subjected to linear regression analysis with the least squares method. Calibration equation obtained from regression analysis was used to calculate the corresponding predicted responses. Linear calibration plot for the related substance method was obtained over the calibration range tested, *i.e.* QL to 0.225% for each impurity. The correlation coefficients obtained were greater than 0.999 for all six impurities. The result showed an excellent linear response for all the impurities and the diluted standard.

4.5. Accuracy

The accuracy of the method was evaluated in triplicate at three concentration levels, *i.e.* QL, 0.6 $\mu\text{g/mL}$, 0.9 $\mu\text{g/mL}$ and 1.2 $\mu\text{g/mL}$ of the analyte concentration (400 $\mu\text{g/mL}$). The percentage recovery of impurities was found in the range of 95.0–105.1% (Table 2) indicating the high accuracy of the newly developed method. Chromatogram of deferasirox spiked with impurities is showed in Fig. 2d.

4.6. Robustness

To determine the robustness of the method, experimental conditions were deliberately altered. Close observation of analysis results of deliberately changed chromatographic conditions *viz.*: flow rate (1.0 ± 0.1 mL/min), mobile phase composition (mobile phase B; $\pm 5\%$ methanol) and column temperature (25 ± 2 °C) revealed that resolution between deferasirox and Imp-1 was greater than 6.0 and there was no significant change in relative retention time for impurities in spiked sample illustrating the robustness of the method.

4.7. Solution stability

The solution stability of deferasirox sample and its related impurities was carried out by leaving both spiked and unspiked sample solutions in tightly capped HPLC vials at 25 °C for 25 h in an auto sampler. Content of each impurity was determined against freshly prepared standard solution. Significant changes were not observed in the content of any impurities during solution stability and mobile phase stability experiments when performed using the related substance method. The solution stability and mobile phase stability experiment data confirms that the sample solutions and mobile phase used during related substance determination were stable for at least 24 h and 72 h respectively.

5. Conclusion

In this study, a new impurity in deferasirox was detected using a newly developed HPLC method. A plausible structure was proposed based on LC–MS/MS data and knowledge of synthetic scheme of deferasirox. Proposed structure was further confirmed by independent synthesis followed by structural elucidation using NMR, FT-IR and EA techniques. Based on the spectroscopic, spectrometric and elemental analysis data, the molecular formula of unknown impurity was deduced as $C_{21}H_{15}N_3O_4$ and the corresponding structure was characterised as 2-[3,5-bis(2-hydroxy-phenyl)-[1,2,4]-triazol-1-yl]-benzoic acid. The newly developed method has been validated as per ICH guidelines. The method was found to be specific, precise, stability indicating, accurate and can be used for routine and stability studies. Formation of newly characterised impurity can be eliminated in the drug substance by appropriately controlling the level of 2-hydrazino-benzoic acid in 4-hydrazino-benzoic acid.

Acknowledgements

The authors are thankful to the management of Jubilant Life Sciences Limited for providing necessary facilities. Authors would like

to thank Dr. Anil Holkar, Dr. Chetan Patel, Mr. Saroj Kumar Paul, Mr. Anil Kumar and Mr. Sanjeev Shandilya for their co-operation in carrying out this work.

References

- [1] J.E.F. Reynolds (Ed.), Martindale – The complete drug reference, thirty sixth ed., Royal Pharmaceutical Society of Great Britain, 2009, pp. 471–477.
- [2] M. Valencic, xPharm: The comprehensive pharmacology reference, 2008, 1–4.
- [3] R.C. Hider, Charge states of deferasirox–ferric iron complexes, *Am. J. Kidney Dis.* 55 (2010) 614–615.
- [4] H. Nick, Deferasirox preclinical overview, *Semin. Hematol.* 44 (2007) 12–15.
- [5] M.D. Cappellini, Long-term efficacy and safety of deferasirox, *Blood Rev.* 22 (2008) 35–41.
- [6] E. Chauzit, S. Bouchet, F.X. Mahon, N. Moore, K. Titi, M. Molimard, A method to measure deferasirox in plasma using HPLC coupled with MS/MS detection and its potential application, *Ther. Drug Monit.* 32 (2010) 476–481.
- [7] A. Skerjanc, J. Wang, K. Maren, L. Rojkaj, Investigation of the pharmacokinetic interactions of deferasirox, once daily oral iron chelator, with midazolam, rifampin and repaglinide in healthy volunteers, *J. Clin. Pharmacol.* 50 (2010) 205–213.
- [8] G.J.M. Bruin, T. Faller, H. Wiegand, A. Schweitzer, H.N.J. Schneider, K.O. Boernsen, F. Waldmeier, Pharmacokinetics, distribution, metabolism, and excretion of deferasirox and its iron complex in rat, *Drug Metab. Dispos.* 36 (2008) 2523–2538.
- [9] R.K. Raja, K.V. Surendranath, P. Radhakrishnan, J. Satish, P.V.V. Satyanarayana, A stability indicating LC method for deferasirox in bulk drugs and pharmaceutical dosage forms, *Chromatographia* 72 (2010) 441–446.
- [10] V.K. Chakravarthy, D.G. Sankar, LC determination of deferasirox in pharmaceutical formulation, *J. Global Treat. Pharm. Sci.* 1 (2010) 42–52.
- [11] S.N. Reddy, E. Sajja, V. Reddy, S. Govindan, MSN Laboratories Limited, process for the preparation of 4-[3,5-bis(2-hydroxyphenyl)-1H-1,2,4-triazol-1-yl]-benzoic acid and its amine salts, World intellectual property organization, WO 2011/021218 A2, 2011.
- [12] ICH Guidelines, Q3A (R2), Impurities in new drug substances, October 25, 2006.
- [13] E.M. Sheldon, J.B. Downar, Development and validation of a single robust HPLC method for the characterization of a pharmaceutical starting material and impurities from three suppliers using three separate synthetic routes, *J. Pharm. Biomed. Anal.* 23 (2000) 561–572.
- [14] E.M. Sheldon, Development of a LC–MS complete heart-cut approach for the characterization of a pharmaceutical compounds using standard instrumentation, *J. Pharm. Biomed. Anal.* 31 (2003) 1153–1166.
- [15] D. Bartos, S. Gorog, Recent advances in the impurity profiling of drugs, *Curr. Pharm. Anal.* 4 (2008) 215–230.
- [16] R.N. Rao, V. Nagaraju, An overview of the recent trends in development of HPLC methods for the determination of impurities in drugs, *J. Pharm. Biomed. Anal.* 33 (2003) 335–377.
- [17] S. Gorog (Ed.), *Determination of Impurities in Drugs*, Elsevier Sciences, Amsterdam, 1999.
- [18] S. Ahuja, *Impurities Evaluation in Pharmaceuticals*, Marcel Dekker, New York, 1998.
- [19] S. Husain, R.N. Rao, Monitoring of process impurities in drugs, in: Z. Dev1, I. Miksik, F. Taglirao, E. Tesarova (Eds.), *Advanced Chromatographic and Electromigration Methods in Biosciences*, Elsevier Sciences, Amsterdam, 1998, pp. 834–888.
- [20] International Conference on Harmonization (ICH) Guidelines Q2 (R1), validation of analytical procedures: test and methodology, November, 2005.
- [21] R. Lattmann, P. Acklin, A.G. Novartis, Substituted 3,5-diphenyl-1,2,4-triazoles and their use as pharmaceutical metal chelators, World intellectual property organization, WO 97/49395, 1997.
- [22] International Conference on Harmonization (ICH) Guidelines, Q1B, photo stability testing of new drug substances and products.



Identification of phenolic compounds from *Scutellaria lateriflora* by liquid chromatography with ultraviolet photodiode array and electrospray ionization tandem mass spectrometry

Jing Li^a, Yan-Hong Wang^b, Troy J. Smillie^b, Ikhlas A. Khan^{a,b,c,*}

^a Department of Pharmacognosy, School of Pharmacy, The University of Mississippi, University, MS 38677, USA

^b National Center for Natural Products Research, School of Pharmacy, The University of Mississippi, University, MS 38677, USA

^c Department of Pharmacognosy, College of Pharmacy, King Saud University, Riyadh, Saudi Arabia

ARTICLE INFO

Article history:

Received 7 November 2011

Received in revised form 17 January 2012

Accepted 21 January 2012

Available online 30 January 2012

Keywords:

HPLC-ESI/MSⁿ

Scutellaria lateriflora

Flavonoids

Fragmentation pathways

ABSTRACT

Scutellaria lateriflora has been used more than 200 years as a mild relaxant and as a therapy for anxiety, nervous tension, and convulsions. Currently, it is one of the most popular botanicals with many products on the USA market. Flavonoids with anxiolytic property have been reported from the aerial parts of this plant. From the HPLC chromatogram of the methanolic extract of this plant, it can be concluded that some flavonoids have not been identified yet. In the present study a simple high-performance liquid chromatography with UV and electrospray ionization mass spectrometric detection (HPLC-DAD/ESI-MSⁿ) method has been developed for the identification of major phenolic compounds from it. The ESI-MSⁿ fragmentation pathways of four types of flavonoid references have been interpreted which provide very useful guidance for the characterization of different types of flavonoids from this plant. Further analysis of the methanolic extract of *S. latellaria* based on the combination of their fragmentation patterns with the UV spectra led to characterize thirteen flavonoids and one stilbene derivative, seven of which are described for the first time from this species.

© 2012 Elsevier B.V. All rights reserved.

1. Introduction

Scutellaria lateriflora L., a native North America plant belonging to Labiatae (Lamiaceae) family, was utilized for its reputed tonic, tranquilizing, and antispasmodic remedies for more than 200 years [1]. To date, it is regulated as a dietary supplement in America and there are many products claiming to contain *S. lateriflora* on the market. Results from *in vivo* animal behavior trials suggested that the aqueous extract of plant material of *S. lateriflora* has anxiolytic property and the flavonoids may be responsible for this activity [2]. Significant anxiolytic effects have been demonstrated in a double blind, placebo-controlled study of healthy volunteers, results indicated that commercial *S. lateriflora* products have clinical benefits as a relaxing nervine [3].

The flavonoids far outnumber other components found in the aerial parts of *S. lateriflora*. Eleven flavonoids and five diterpenoids have been reported from this plant [4,6,7]. Recently, six more

flavonoids, three minor coumarins, and four triterpenes were isolated and identified by authors [5]. In addition to significant antioxidant activity observed, the extract of this species as well as its characteristic flavonoids, including baicalein, baicalin, wogonin, chrysin, etc. significantly stimulated the PPAR α/γ activities in a dose-dependent manner (Data not shown here). The results of our study provide useful information on potential new application of *S. lateriflora* for the treatment of diabetic-related diseases and the flavonoids may be contributed to these activities. From the HPLC chromatogram of this plant, it can be concluded that some flavonoids have not been identified yet. Therefore, detailed identification of the indigenous flavonoid components is necessary for better understanding of its potential uses as a source of natural antioxidants and PPARs agonists. Meanwhile, it will be very helpful for the authentication of *S. lateriflora* as well as its products. HPLC methods have been described to quantitative determination of its several major flavonoids recently [8,9]. However, no efforts have been attributed to systematically identify flavonoids in it.

In this context, the paper aims to characterize the major flavonoids present in the methanolic extract of the aerial parts of *S. lateriflora* by liquid chromatography with photodiode array and tandem mass spectrometric detection (LC-DAD/ESI-MSⁿ). In present study, thirteen flavonoids and one stilbene derivative were identified

* Corresponding author at: National Center for Natural Products Research, School of Pharmacy, The University of Mississippi, University, MS 38677, USA.
Tel.: +1 6629157821; fax: +1 6629157989.

E-mail address: ikh@olemiss.edu (I.A. Khan).

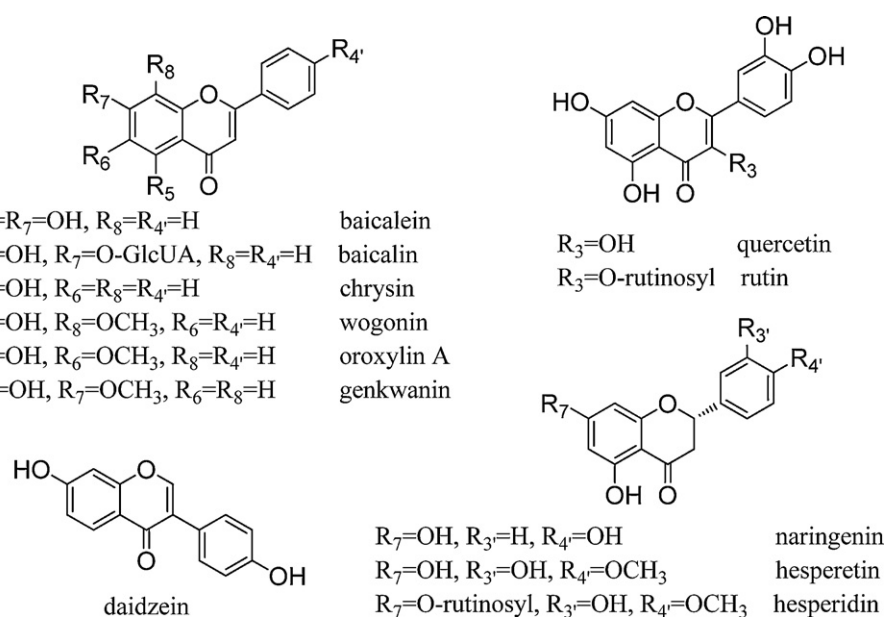


Fig. 1. Chemical structures of twelve reference flavonoids investigated.

in *S. lateriflora*, seven of which, including 5-(β -D-glucosyloxy)-3-hydroxy-*trans*-stilbene-2-carboxylic acid, norwogonin-7-*O*-glucuronide, galangin-7-*O*-glucuronide, 5,6,7-trihydroxy-flavanone-7-*O*-glucuronide, wogonin-7-*O*-glucuronide, dihydrooroxylin A-7-*O*-glucuronide, and 5,7-dihydroxy-6,8-dimethoxy flavone-7-*O*-glucuronide, are described for the first time in this species.

2. Experimental

2.1. Solvents and chemicals

Acetonitrile, water and acetic acid, were HPLC grade and purchased from Fisher Scientific (Fair Lawn, NJ, USA) and Sigma (St. Louis, MO, USA).

Twelve reference flavonoids used in this study (see Fig. 1), namely baicalein, baicalin, chrysin, oroxylin A, wogonin, gankwanin, quercetin, rutin, naringenin, hesperetin, hesperidin, and daidzein, were isolated from *Scutellaria* species by authors. Their structures were elucidated based on the 1D and 2D NMR spectra, HRMS data as well as comparison with reported data. The purity of these standards was above 95% confirmed by chromatographic methods (TLC and HPLC).

Reference flavonoid solutions were prepared at a concentration of 1 mg/mL in methanol. Working solutions were obtained by twenty folds dilutions of concentrations from 1 mg/mL to 50 μ g/mL. All these solutions were stored in refrigerator.

2.2. Sample preparation

The aerial parts of *S. lateriflora* investigated were purchased from Starwest botanicals (<http://www.starwest-botanicals.com>) and authenticated by Dr. Vaishali Joshi at the National Center for Natural Products Research, University of Mississippi, where a retention sample (no. 2120) has been deposited.

The dried powder of the aerial parts (1.0520 g) of *S. lateriflora* was extracted with 20 mL MeOH under ultrasonication for 30 min followed by centrifugation for 5 min at 1550 rpm. The supernatant was transferred to 100 mL flask. This process was repeated twice and respective supernatants were combined and evaporated to dryness. The residue was dissolved in 2 mL of HPLC grade methanol and transferred to 5 mL volumetric flask. The flask was rinsed with

about 1.5 mL methanol twice and the final volume was adjusted to 5 mL with methanol.

Prior to injection, this solution was mixed thoroughly and 2 mL of it was filtered through 0.45 μ m membrane. The first 0.5 mL was discarded and the remaining volume was collected into LC vial for analysis.

2.3. HPLC conditions

The HPLC system employed in the LCQ ion trap instrument consists of a model TSP P4000 quaternary pump coupled with a mode TSP AS3000 autosampler and a model TSP UV6000 diode-array detector. The chromatographic analysis was conducted at 25 °C and the chromatographic separations were carried out on a Luna C₁₈ column (5 μ m, 250 mm \times 4.6 mm i.d., Phenomenex) equipped with a 2 cm LC-18 guard column (Phenomenex Inc.). The mobile phase consisted of acetonitrile (A) and water (B), all containing 0.2% acetic acid, which were applied in the following gradient: 0–5 min, 15–20% A; 5–30 min, 20–25% A; 30–60 min, 25–55% A; 60–65 min, 55% A; 65–70 min, 55–100% A, then hold 5 min. Each run was followed by a 5 minutes washing procedure with 100% acetonitrile. The flow rate was adjusted to 1 mL/min, and the injection volume was 10 μ L. Re-equilibration was done with 15% A for 12 min. Total run time was 75 min.

2.4. Mass spectrometric conditions

Mass spectrometry experiment was performed on a LCQ ion trap instrument (Finnigan MAT. Thermo Scientific, Waltham, MA, USA) with an electrospray source. Ultrahigh pure helium (He) was used as the collision gas and high purity nitrogen (N₂) as the nebulizing gas. The optimized MS conditions were as follows: electrospray voltage of the ion source at 3.5 kV with the sheath gas at 45 arbitrary units (AU), capillary voltage at 28 V, auxiliary gas at 15 AU, capillary temperature at 300 °C, and tube lens offset voltage at –10 V. For full scan MS analysis, negative ions spectra of the column elute were recorded in the range of *m/z* 100–1000. The collision energy for collision induced dissociation (CID) was between 30% and 45%, and the isolation width of precursor ions was 1.0 U. The data were analyzed using the XCalibur software.

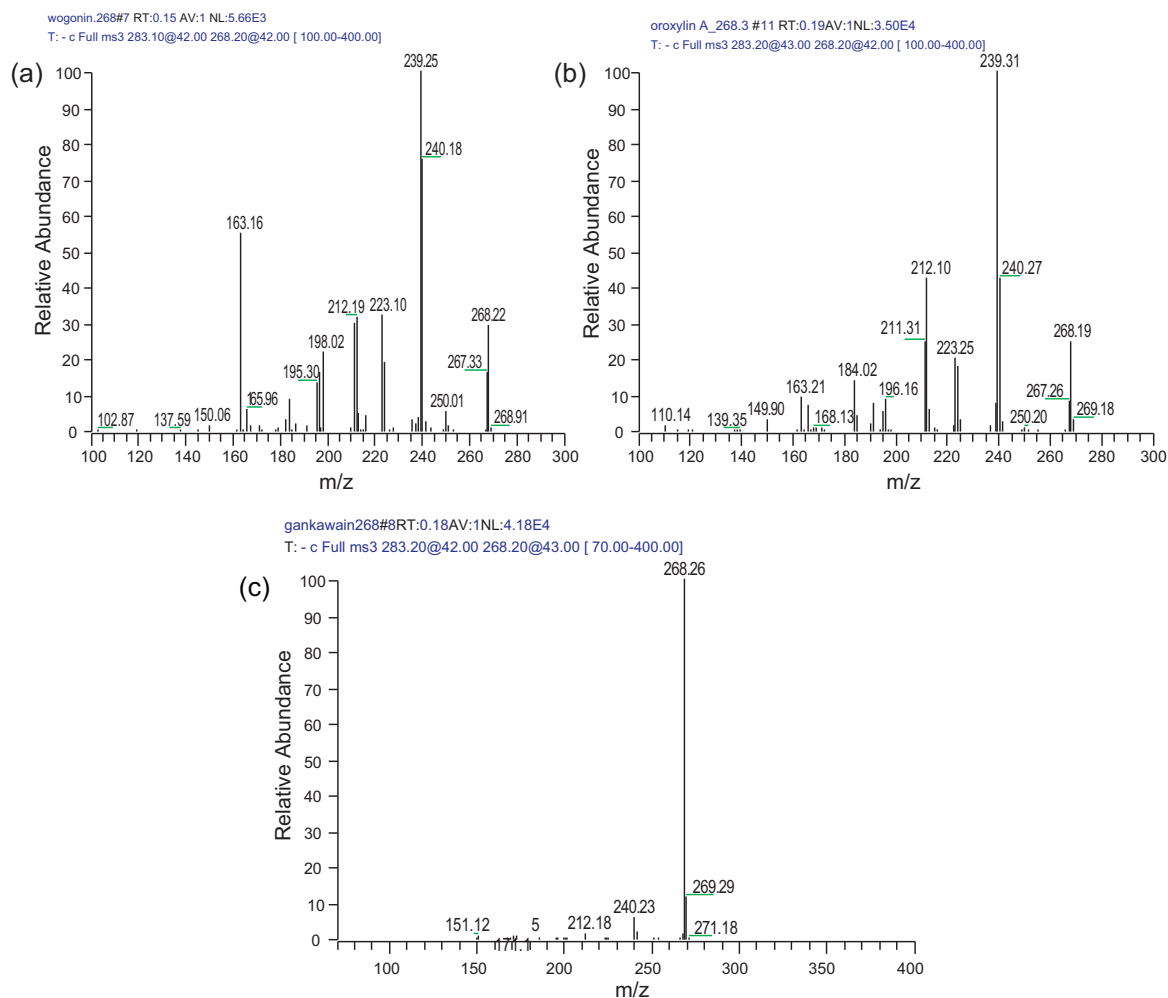


Fig. 2. ESI-MS³ spectra of three methoxylated flavone isomers: (a) wogonin; (b) oroxylin A; (c) gankwanin.

3. Results and discussion

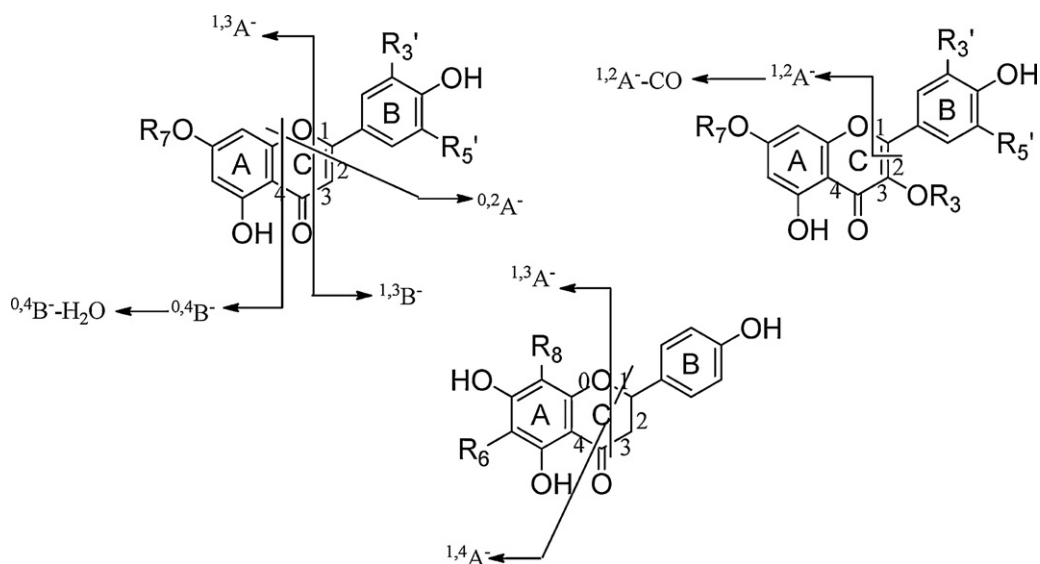
In this paper, mass fragmentation behaviors of twelve reference flavonoids present in *Scutellaria* species were examined in the negative ion mode, and fragmentation patterns for each compound were discussed. Thereafter the phenolic compounds from the methanolic extract of *S. lateriflora* were characterized. For the identification of the different compounds from the extract, sample was injected in full scan mode in order to choose the compounds of interest. Then, the MS–MS scan mode was selected based on the predominant ions obtained in the mass spectrum in full scan mode. The structure of each compound was identified by the elucidation of its fragmentation pathways as well as by the comparison of its fragmentation information with that of reference compounds or reported data.

For the convenience of discussion the CID-MS–MS spectra, the fragments recorded for the two bonds cleavages of C ring have been annotated according to the nomenclature proposed by Ma et al. [10]. Scheme 1 shows the various retrocyclization fragments observed in this study. The ⁱjA⁻ and ⁱjB⁻ represent product ions containing intact A and B rings, the superscript i and j indicate the C-ring bonds that have been broken.

3.1. Fragmentation pathways of twelve reference flavonoids

In the present study, the ESI-MSⁿ fragmentation behaviors as well as their corresponding UV characteristics of twelve reference flavonoids, shown in Fig. 1 which included flavones (baicalein,

baicalin, chrysin, wogonin, oroxylin A, gankwanin), flavonols (quercetin and rutin), flavanones (hesperetin, hesperidin and naringenin), and isoflavone (daidzein), have been investigated in detail and summarized in Table 1. Negative ion mode was chosen for ESI-MSⁿ analysis because background noise and interfering peaks derived from mobile phase in negative mode were found to be much less than that in the positive one. The diagnostic fragment ions resulted from the cleavage of two bonds at positions 1/3, 0/2 and 0/4 of the C-ring are very helpful for the structural determination of the A- and B-ring substitution patterns. Furthermore, the neutral loss of glucuronic acid (176 Da) or glucose residue (162 Da) can be easily observed since the O-glycosylic bond was easily cleaved to generate its aglycone. It is very useful for the identification of different O-glycoside. In addition, losses of H₂O and •CH₃, etc. are valuable in the determination of the presence of some functional groups. For example, in the ESI-MS² experiment of baicalein, the product ion at m/z 251 as base peak was observed, which was resulted from the loss of H₂O from [M–H]⁻ at m/z 269. Same product ion could not be observed for chrysin in this study as well as for luteolin reported [11] in which two hydroxyl groups are located on C-5 and C-7 position, respectively. Therefore, the ion involved in the loss of H₂O can be observed only when the flavone has vicinal hydroxyl groups. It is worth noticing that the fragmentation pathways of different types of flavonoids with the same MW are similar, such as isoflavonoid daidzein and flavone chrysin, and same type of flavonoids including wogonin, oroxylin A, and genkwanin. However, the ratio of relative abundance of their product ions for each compound is different.



Scheme 1. Nomenclature adopted for the different retrocyclization cleavage fragments of deprotonated flavones, flavonols and flavanones observed in this study. Adapted from Ma.

Table 1
LC-UV/MSⁿ characteristics of twelve reference flavonoids.

Compound	UV λ_{\max} (nm)	[M-H] ⁻ <i>m/z</i>	MS ⁿ ions <i>m/z</i> (relative abundance)
Baicalein	216, 274, 322	269	MS full scan: 269 (100); MS ² [269]: 251 (100), 241 (30), 223 (32), 197 (20), 169 (7); MS ³ [251]: 223 (100), 213 (7)
Baicalin	216, 275, 316	445	MS full scan: 891 (100), 445 (83), 269 (62); MS ² [445]: 269 (100), 175 (16)
Wogonin	216, 274	283	MS full scan: 283 (100); MS ² [283]: 268; MS ³ [268]: 240 (56), 239 (100), 224 (14), 223 (34), 212 (22), 211 (34), 163 (44); MS ⁴ [239]: 211 (100)
Oroxylin A	215, 271, 317	283	MS full scan: 283 (100); MS ² [283]: 268; MS ³ [268]: 240 (36), 239 (100), 224 (12), 223 (20), 212 (38), 211 (25), 163 (7); MS ⁴ [239]: 211 (100)
Gankwanin	215, 266, 336	283	MS full scan: 283 (100); MS ² [283]: 268; MS ³ [268]: 240 (9), 239 (3)
Hesperetin	286	301	MS full scan: 301 (100); MS ² [301]: 286 (100), 283 (48), 257 (59), 242 (99), 233 (4), 215 (9), 199 (12), 125 (9); MS ³ [286]: 258 (97), 242 (100), 201 (36), 174 (22), 164 (16)
Hesperidin	283	609	MS full scan: 609 (100); MS ² [609]: 301 (100)
Quercetin	205, 255, 370	301	MS full scan: 301 (31); 603 (100), 905 (31); MS ² [301]: 273 (13), 257 (11), 193 (5), 179 (100), 151 (45); MS ³ [273]: 245 (17), 229 (100), 163 (16); MS ³ [257]: 239 (79), 229 (100), 211 (67); MS ³ [179]: 169 (30), 151 (100)
Rutin	206, 255, 355	609	MS full scan: 609 (100); 1219 (69); MS ² [609]: 301 (100), 300 (91), 271 (13); MS ³ [301]: 273 (15), 271 (97), 257 (12), 255 (57), 179 (100)
Narigenin	216, 287	271	MS full scan: 271 (100); MS ² [271]: 177 (17), 151 (100); MS ³ [177]: 133 (12), 109 (100); MS ³ [151]: 107 (100);
Chrysin	212, 267, 311 (sh)	253	MS full scan: 253 (100); MS ² [253]: 225 (2), 209 (20), 181 (2), 151 (4)
Daidzein	247, 302 (sh)	253	MS full scan: 253 (100); 507 (54); MS ² [253]: 225 (16), 209 (7);

Based on the differences in the relative abundances of some specific ions these isomeric flavonoids mentioned above can be discriminated. For instance, wogonin (8-OCH₃), oroxylin A (6-OCH₃), and genkwanin (7-OCH₃) are three methoxylated flavone isomers with the same MW of 284. They exhibited a significant [M-H-CH₃]⁻ radical anion at *m/z* 268 as base peak and no other fragmentation was observed in their MS² spectra. The loss of a CH₃ radical (15 Da) from the [M-H]⁻ ion explained the presence of a methoxy group.

The MS³ product ion spectra of these three compounds, obtained under the same conditions, are shown in Fig. 2. In MS³ experiment of the [M-H-CH₃]⁻ ion of genkwanin, no any other fragmentation, except for low signal intensity ions at *m/z* 240 (9, -CO) and 239 (3, -COH[•]), were observed. This suggested that this radical anion is probably rearranged to a stable 7-keto-diconjugated-3,4-enol derivative avoiding any further fragmentation for this 7-methoxy-4-hydroxyflavone aglycone [11]. Six ions were observed in MS³

Table 2
ESI-MSⁿ product ions of three methoxylated flavonoids.

Scan mode	Product ion(s)	Wogonin	Oroxylin A	Gankwanin
MS full scan	[M-H] ⁻	283	283	283
	[M-H-CH ₃] ⁻	268	268	268
MS ² [283]	[M-H-CH ₃ -CO] ⁻	240 (56)	240 (36)	240 (9)
	[M-H-CH ₃ -COH] ⁻	239 (100)	239 (100)	239 (3)
MS ³ [268]	[M-H-CH ₃ -CO ₂] ⁻	224 (14)	224 (12)	
	[M-H-CH ₃ -CO ₂ H] ⁻	223 (34)	223 (20)	
	[M-H-CH ₃ -2CO] ⁻	212 (22)	212 (38)	
	^{0,2} A ⁻	163 (44)	163 (7)	

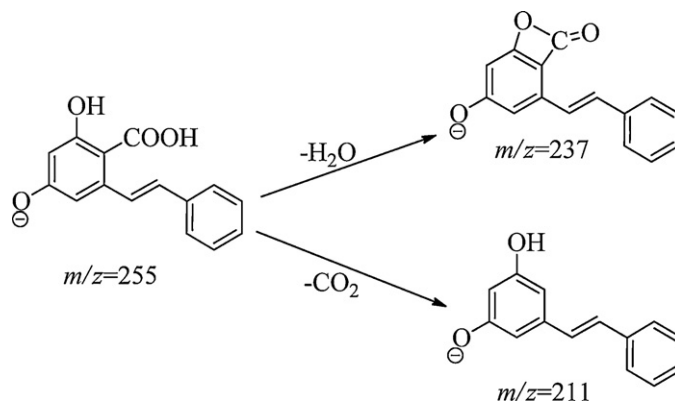
spectra for both wogonin and oroxylin A. Although the fragments of wogonin were almost identical to those of oroxylin A in MS³ experiment, interesting differences between these two isomers could be observed from MS³ spectra and are listed in Table 2. The relative abundance of ion ^{0,2}A⁻ at *m/z* 163 is higher than that of the ion at *m/z* 212 for wogonin. On the contrary, the relative abundance of ion ^{0,2}A⁻ at *m/z* 163 is lower than that of the ion at *m/z* 212 for oroxylin A. Based on the different fragmentation behaviors of their MS³ spectra these three isomers can be differentiated.

3.2. Characterization of phenolic compounds from *S. lateriflora* using HPLC-DAD/ESI-MSⁿ

The LC-MS chromatogram (TIC) of the methanolic extract of *S. lateriflora* in negative ion mode is shown in Fig. 3. Fourteen phenolic compounds were identified by the elucidation of their fragmentation pathways and by comparison of their MS fragmentation patterns as well as UV spectra (see Fig. 4 and Table 3) with standard flavonoids or reported data.

Compound **1** exhibited a UV spectrum with characteristic bands at 251 nm and 301 nm, which are not consistent with the typical UV spectral pattern of flavonoids, suggesting a nonflavonoid type of compound. The characteristics of the UV spectrum of this compound are identical with those of trans-stilbene [12,13]. The ESI-MS in full scan mode gave an ion [M-H]⁻ at *m/z* 417 and an ion [M-H-162]⁻ at *m/z* 255 produced by the loss of a glucose residue. In the MS² experiment, the ion at *m/z* 237 represented the base peak resulted from the loss of H₂O of [M-H-162]⁻, suggesting vicinal hydroxyl groups or a hydroxyl and one free carboxylic group present in the molecule. The ion at *m/z* 211 was attributed to the neutral loss of CO₂, supporting the presence of carbonyl group. The proposed fragmentation pathway of **1** was shown in Scheme 2. Based on these results compound **1** was tentatively identified as 5-(β-D-glucosyloxy)-3-hydroxy-trans-stilbene-2-carboxylic acid, which has been isolated from *S. scandens* [14].

Compound **2**, **3** and **5** are isomers with the same ion [M-H]⁻ at *m/z* 445 in full scan mode. The product ion [M-H-176]⁻ at *m/z* 269 corresponded to neutral loss of a glucuronic acid residue from [M-H]⁻ ion in MS² experiment for these three isomers. In the MS² experiment of compounds **2** and **3**, ion at *m/z* 269 of both compounds produced the identically diagnostic neutral losses of H₂O (18 Da), CO (28 Da), and the losses of both H₂O and CO



Scheme 2. Proposed fragmentation pathways of compound **1** aglycone.

(46 Da), resulting in the ion at *m/z* 251, 241 and 223, respectively, whose fragmentation mechanism was consistent with the standard baicalein. Since the *t_R* value as well as the UV spectrum of compound **3** were identical to those of reference baicalin, it was identified as baicalin. Compound **2** exhibited the same UV behavior as norwogonin 7-O-glucuronide [15], indicating **2** is norwogonin-7-O-glucuronide. In the MS² experiment of compound **5**, no product ion attributed to the neutral loss of H₂O from its precursor ion at *m/z* 269, indicating absence of vicinal hydroxyl groups in A ring, whereas product ions at *m/z* 241 and 225 corresponding to neutral losses of CO and CO₂, respectively, suggested that **5** is galangin-7-O-glucuronide. This compound was confirmed by the comparison of its MS² fragmentation behaviors as well as UV spectrum to those of reported data [16].

The peak **4** showed [M-H]⁻ ion at *m/z* 447 and aglycone signal [M-H-176]⁻ at *m/z* 271 in full scan mode, which are indicative of the presence of a glucuronic acid residue. Further MS² spectra of *m/z* 271 yielded the ions at *m/z* 253, 243, 227, and 167. The ion at *m/z* 253 resulted from the loss of H₂O, revealing the presence of two OH groups in *ortho* position. The ions at *m/z* 243 and 227 resulted from the neutral losses of CO and CO₂ from the corresponding [M-H-176]⁻ ion. The ion at *m/z* 167 was attributed to the ^{1,3}A and suggested the occurrence of three OH groups in A ring. The molecular mass of this compound was 2 Da greater than that of baicalin. In addition, band I associated with the absorption ascribed to the B-ring cinnamoy system, was weak in its UV

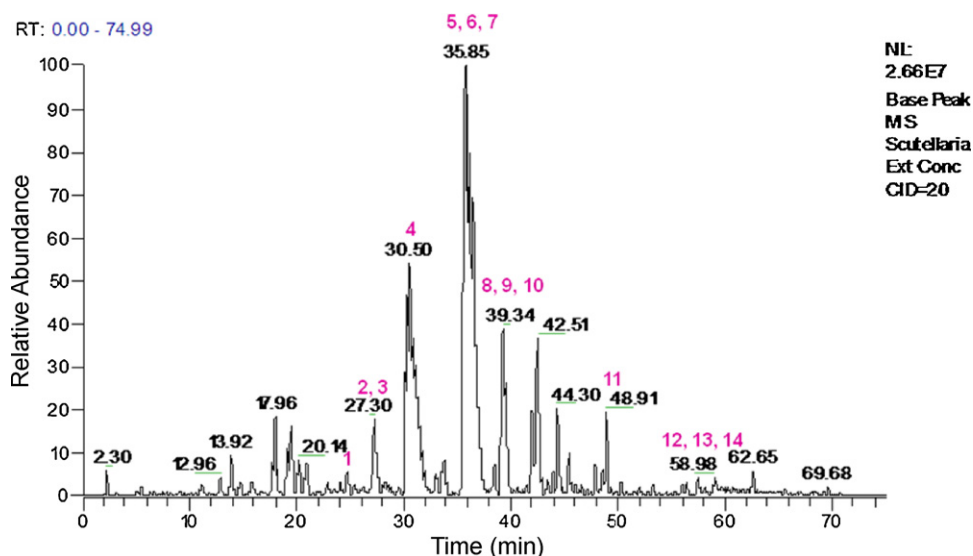
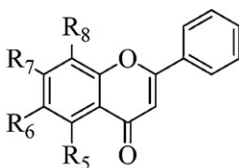
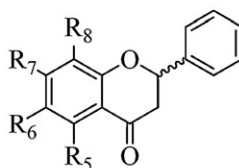


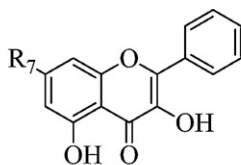
Fig. 3. LC-negative ion ESI-MS total ion current (TIC) chromatogram.



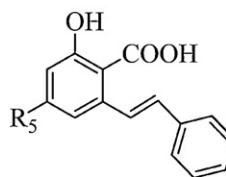
$R_5=R_8=OH, R_6=H, R_7=O-GlcUA$	norwogonin-7- <i>O</i> -glucuronide (2)
$R_5=R_6=OH, R_7=O-GlcUA, R_8=H$	baicalin (3)
$R_5=OH, R_6=OCH_3, R_7=O-GlcUA, R_8=H$	oroxylin A-7- <i>O</i> -glucuronide (7)
$R_5=OH, R_6=H, R_7=O-GlcUA, R_8=OCH_3$	wogonin-7- <i>O</i> -glucouronide (8)
$R_5=OH, R_6=R_8=OCH_3, R_7=O-GlcUA$	5,7-dihydroxy-6,8-dimethoxy flavone-7- <i>O</i> -glucuronide (9)
$R_5=R_6=R_7=OH, R_8=H$	baicalein (11)
$R_5=R_7=OH, R_6=H, R_8=OCH_3$	wogonin (12)
$R_5=R_7=OH, R_6=OCH_3, R_8=H$	oroxylin A (13)
$R_5=R_7=OH, R_6=R_8=H$	chrysin (14)



$R_5=R_6=OH, R_7=O-GlcUA, R_8=H$	dihydrobaicalin (4)
$R_5=OH, R_6=OCH_3, R_7=O-GlcUA, R_8=H$	dihydrooroxylin A-7- <i>O</i> -glucuronide (6)
$R_5=OH, R_6=H, R_7=O-GlcUA, R_8=OCH_3$	dihydrowogonin-7- <i>O</i> -glucuronide (10)



$R_7=O-GlcUA$ galangin-7-*O*- glucuronide (**5**)



$R_5=O-GlcUA$

5-(β -D-glucosyloxy)-3-hydroxy-trans-stilbene-2-carboxylic acid (**1**)

Fig. 4. Chemical structures of thirteen flavonoids and one stilbene derivative identified from American skullcap.

spectrum, while band II associated with absorption involving the A-ring benzoy system showed bathochromic shift with respect to the value of baicalin, indicating a flavanone-type compound. Based on the evidence that all 7-*O*-glucuronides showed essentially identical UV spectra with their corresponding aglycones [17], 7-*O*-OH glycosylation was proposed for **4**. Comparing the UV spectrum of **4** with reported data [17], this compound was characterized as 5,6,7-trihydroxy-flavanone-7-*O*-glucuronide.

Peaks **7** and **8** are isomers with the molecular weight of 460 Da. They showed the same product ion $[M-H-176]^-$ at m/z 283, which indicated the loss of a glucuronic acid moiety as discussed above. For the aglycone part of these two compounds, a significant $[M-H-CH_3]^\bullet$ radical anion at m/z 268 presented as base and sole peak in their MS^2 spectra and suggested the presence of a methoxy group for both compounds. To further investigate the structures of

these two isomers, tandem mass experiments were employed on the two $[M-H-176-15]^\bullet$ ions at m/z 269. Although the products ions of m/z 269 for these two compounds were identical, the relative intensities of ion at m/z 212 and m/z 163 were different. Comparison with the results obtained for reference wogonin and oroxylin A suggested that peaks **7** and **8** are oroxylin A-7-*O*-glucuronide and wogonin-7-*O*-glucuronide, respectively.

Compounds **6** and **10** both gave an $[M-H]^-$ ion at m/z 461 and their aglycone ion $[M-H-176]^-$ at m/z 285 corresponding to presence of a glucuronic acid moiety. The UV spectra of these two compounds only exhibited band II, indicating a flavanone skeleton. The MS^2 spectra of the ion at m/z 285 yielded an ion at m/z 270, which resulted from the loss of a CH_3 radical (15 Da) from the ion $[M-H-176]^-$ at m/z 285. In addition, the ion $^{1,3}A^-$ at m/z 166, which are the characteristic of flavanone, suggested that these

Table 3
LC–UV/MSⁿ Identification of phenolic compounds in *S. lateriflora*.

Peak no.	t _R (min)	UV λ _{max} (nm)	[M–H] [–] m/z	ESI-MS (MS ⁿ) m/z (relative abundance)	Identification
1	24.50	251, 301	417	ESI-MS: 417, 255; MS ² [417]: 255 (7), 237 (100), 211 (18)	5-(β-D-Glucosyloxy)-3-hydroxy-trans-stilbene-2-carboxylic acid ^b
2	27.72	275, 350 (sh)	445	ESI-MS: 445, 269; MS ² [445]: 269 (100), 251 (83), 241 (15), 223 (30), 197 (18), 171 (9), 151 (5), 137 (5)	Norwogonin-7-O-glucuronide ^b
3	28.44	268, 315	445	ESI-MS: 445, 269; MS ² [445]: 269 (100), 251 (72), 241 (37), 223 (37), 197 (22), 171 (9), 145 (5)	Baicalin ^a
4	30.36	242, 282, 348 (sh)	447	ESI-MS: 447, 271; MS ² [447]: 271 (100); MS ³ [271]: 253 (49), 243 (100), 227 (24), 199 (13), 167 (8)	5,6,7-Trihydroxy flavanone-7-O-glucuronide ^b (dihydrobaicalin)
5	36.22	232, 282	445	ESI-MS: 445, 269; MS ² [445]: 269 (76), 241 (65), 225 (100), 197 (45), 183 (7), 181 (9), 171 (8)	Galangin-7-O-glucuronide ^b
6	36.62	237, 282	461	ESI-MS: 461, 285; MS ² [461]: 285 (100), 270 (22); MS ³ [285]: 270 (31), 269 (100), 243 (6), 166 (11)	Dihydrooroxylin A-7-O-glucuronide ^b
7	37.59	268, 308	459	ESI-MS: 459, 283; MS ² [459]: 283 (100), 268 (51), 175 (5), 113 (11) MS ³ [283]: 268 (100), 239 (8)	Oroxylin A-7-O-glucuronide ^b
8	39.67	236, 268	459	ESI-MS: 459, 283; MS ² [459]: 283 (100), 268 (70), 175 (4); MS ³ [283]: 268 (100), 137 (4)	wogonin-7-O-glucouronide ^b
9	39.80	237, 280, 329	489	ESI-MS: 489, 313; MS ² [489]: 313 (100), 298 (83), 283 (26); MS ³ [313]: 298 (100), 283 (3), 269 (5), 254 (5), 214 (3), 193 (3), 167 (3)	5,7-Dihydroxy-6,8-dimethoxy flavone-7-O-glucuronide ^b
10	40.34	239, 291	461	ESI-MS: 461, 285; MS ² [461]: 285 (100), 270 (32); MS ³ [285]: 270 (100), 243 (6), 223 (5), 166 (8)	Dihydrowogonin-7-O-glucuronide ^b
11	47.50	270, 320	269	ESI-MS: 269, 251; MS ² [269]: 251 (100), 241 (33), 223 (30), 197 (18), 169 (7)	Baicalein ^a
12	56.22	280	283	ESI-MS: 283.18, 268.36; MS ² [283]: 268 (100); MS ³ [268]: 240 (53), 239 (100), 224 (14), 223 (36), 212 (20), 211 (34), 163 (44)	Wogonin ^a
13	58.06	272, 316	283	ESI-MS: 283.18, 268.36; MS ² [283]: 268 (100); MS ³ [268]: 240 (32), 239 (100), 224 (14), 223 (20), 212 (39), 211 (27), 163 (8)	Oroxylin A ^a
14	56.62	271, 320 (sh)	253	ESI-MS: 253, 209; MS ² [253]: 225 (4), 209 (26), 181 (2), 151 (6)	Chrysin ^a

^a Identified by comparing the retention time, UV spectra and MSⁿ data with reference flavonoids.

^b Identified by UV and MSⁿ data in comparison with literature data.

two compounds are either dihydrowogonin or dihydrooroxylin A. Compound **6** was identified as dihydrooroxylin A-7-O-glucuronide since its UV spectrum was consistent with the literature [18], and was characterized **10** as dihydrowogonin-7-O-glucuronide.

Compounds **9** exhibited an [M–H][–] ion at *m/z* 489. CID of this compound produced ion [M–H–176][–] at *m/z* 313 related to the neutral loss of a glucuronic acid residue. Fragments of *m/z* 298 and 283, due to the sequential losses of CH₃ radicals, indicated the presence of two methoxy groups. In the MS³ experiment of *m/z* 313, the product ion at *m/z* 298 was base peak. The product ion at *m/z* 269 was produced by the loss of COH[•], and ion at *m/z* 254 was produced by loss of CO₂ from *m/z* 298. The ion ^{0,2}A[–] at *m/z* 193 along with above mentioned two ions at *m/z* 269 and 254 were indicative for the second methoxy group on A ring. The UV spectrum of **9** was same as 5,7-dihydroxy-6,8-dimethoxy flavone-7-O-glucuronide reported in the literature [17]. Thus, compound **9** was identified as 5,7-dihydroxy-6,8-dimethoxy flavone-7-O-glucuronide.

Compounds **11**, **12**, **13**, and **14** were positively characterized as baicalein, wogonin, oroxylin A, and chrysin, respectively, by the comparison of their UV spectrum and MSⁿ fragmentation patterns with corresponding references.

4. Conclusion

As has been demonstrated, the MS–MS spectra of the deprotonated molecules [M–H][–] for four types of flavonoids yielded different fragmentation profiles. These fragmentation patterns have been used as guidance for the determination of the flavonoids presented in the crude extracts of *S. lateriflora*.

LC/ESI-MSⁿ is a very promising complementary tool for the characterization of flavonoids. The LC/MS–MS method developed in this study was successfully employed to separate and identify the major flavonoids from *S. lateriflora*, which provides knowledge of both its chemical composition and its potential diverse uses. In this study, we have demonstrated how the combination of UV spectra and ESI-MSⁿ spectra allows a fast characterization of thirteen flavonoids and one stilbene derivative without time-consuming isolation of compounds. It is worthy noted that the choice of appropriate conditions for collision induced fragmentation is very important to assure acquisition of enough fragmentation information for structural characterization of these types of compounds. Also special care should be taken during the interpretation of MS data since there are many isomers co-existed in the extract of *S. lateriflora*.

Acknowledgments

This work was funded in part by the Food and Drug Administration (FDA) under grant number 2U01 FD 002071-07 and the United States Department of Agriculture, Agriculture Research Service Specific Cooperative Agreement under No. 58-6408-06-067.

References

- [1] E.P. Claus, Pharmacognosy, third edition, Lea and Febiger, Philadelphia, PA, 1956, pp. 219–220.
- [2] R. Awad, J.T. Arnason, V. Trudeau, C. Bergeron, J.W. Budzinski, B.C. Foster, Z. Meralli, Phytochemical and biological analysis of skullcap (*Scutellaria lateriflora* L.): a medicinal plant with anxiolytic properties, *Phytomedicine* 10 (2003) 640–649.
- [3] J.-L. Wolfender, M. Maillard, K. Hostettmann, Thermospray liquid chromatography–mass spectrometry in phytochemical analysis, *Phytochem. Anal.* 5 (1994) 153–159.

- [4] S. Gafner, C. Bergeron, L.L. Batcha, J. Reich, J.T. Arnason, J.E. Burdette, J.M. Pezuto, C.K. Angerhofer, Inhibition of [^3H]-LSD binding to 5-HT $_7$ receptors by flavonoids from *Scutellaria lateriflora*, J. Nat. Prod. 66 (2003) 535–537.
- [5] J. Li, Y.Q. Ding, X.C. Li, D. Ferreira, S. Khan, T. Smillie, I.A. Khan, Scuteflorins A and B, dihydropyranocoumarins from *Scutellaria lateriflora* L, J. Nat. Prod. 72 (2009) 983–987.
- [6] B. Maurizio, C. Maria, L.B. Maria, P. Franco, C. de la, T. María, R. Benjamín, S. Orietta, Neo-clerodane diterpenoids from *Scutellaria lateriflora*, Phytochemistry 48 (1998) 687–691.
- [7] Z.Z. Zhang, X.Y. Lian, S.Y. Li, J.L. Stringer, Characterization of chemical ingredients and anticonvulsant activity of American skullcap (*Scutellaria lateriflora*), Phytomedicine 16 (2009) 485–493.
- [8] J.Y. Gao, A. Sanchez-Medina, B.A. Pendry, M.J. Hughes, G. Webb, P.O. Corcoran, Validation of a HPLC method for flavonoid biomarkers in skullcap (*Scutellaria*) and its use to illustrate wide variability in the quality of commercial tinctures, J. Pharm. Pharm. Sci. 11 (2008) 77–87.
- [9] L.-Z. Lin, J.M. Harnly, R. Upton, Comparison of the phenolic component profiles of skullcap (*Scutellaria lateriflora*) and germander (*Teucrium canadense* and *T. chamaedrys*), a potentially hepatotoxic adulterant, Phytochem. Anal. 2 (2009) 298–306.
- [10] Y.L. Ma, Q.M. Li, V.D.H. Heuvel, M. Claeys, Characterization of flavone and flavonol aglycones by collision-induced dissociation tandem mass spectrometry, Rapid Commun. Mass Spectrom. 11 (1997) 1357–1364.
- [11] N. Fabre, I. Rustan, E. de Hoffmann, J. Quetin-Leclercq, Determination of flavone, flavonol, and flavanone aglycones by negative ion liquid chromatography electrospray ion trap mass spectrometry, J. Am. Soc. Mass Spectrom. 12 (2001) 707–715.
- [12] R.N. Beale, E.M.F. Roe, Ultraviolet absorption spectra of trans- and cis-stilbenes and their derivatives. I. Trans- and cis-stilbenes, J. Chem. Soc. (1953) 2755–2763.
- [13] H. Suzuki, The ultraviolet absorption spectra of stilbene and some related compounds in the solid state measured by the pressed KCl disk technique, Bull. Chem. Soc. Jpn. 33 (1960) 944–952.
- [14] Y. Miyaichi, Y. Imoto, T. Tomimori, T. Namba, Studies on the nepalese crude drugs. IX: on the flavonoid constituents of the root of *Scutellaria scandens* BUCH.-HAM. ex D. DON, Chem. Pharm. Bull. 36 (1988) 2371–2376.
- [15] Y. Oi, K. Matsuzaki, K. Takanashi, T. Okuyama, S. Shibata, Studies of the constituents of scutellaria species. I. The flavonoid glucuronides of Bo Ye Huang Qin *Scutellaria ikonnikovii* Juz, Chem. Pharm. Bull. 36 (1988) 3206–3209.
- [16] J. Han, M. Ye, M. Xu, J.H. Sun, B.R. Wang, D.A. Guo, Characterization of flavonoids in the traditional Chinese herbal medicine-huangqin by liquid chromatography coupled with electrospray ionization mass spectrometry, J. Chromatogr. B 848 (2007) 355–362.
- [17] G.Z. Liu, J.Y. Ma, Y.Z. Chen, Q.Q. Tian, Y. Shen, X.S. Wang, B. Chen, S.Z. Yao, Investigation of flavonoid profile of *Scutellaria baicalensis* Georgi by high performance liquid chromatography with diode array detection and electrospray ion trap mass spectrometry, J. Chromatogr. A 1216 (2009) 4809–4814.
- [18] Y. Miyaichi, T. Tomimori, Studies on the constituents of scutellaria species XVII. Phenol glycosides of the root of *Scutellaria baicalensis* Georgi (2), Nat. Med. 49 (1995) 350–353.



Application of nanoLC-ESI-TOF-MS for the metabolomic analysis of phenolic compounds from extra-virgin olive oil in treated colon-cancer cells

S. Fernández-Arroyo^{a,b,1}, A. Gómez-Martínez^{c,1}, L. Rocamora-Reverte^c, R. Quirantes-Piné^{a,b},
A. Segura-Carretero^{a,b,*}, A. Fernández-Gutiérrez^{a,b}, J.A. Ferragut^{c,**}

^a Department of Analytical Chemistry, Faculty of Sciences, University of Granada, C/Fuentenueva S/N, 18071 Granada, Spain

^b Functional Food Research and Development Center, Health Science Technological Park, Avenida del Conocimiento S/N, 18100 Armilla, Granada, Spain

^c Instituto de Biología Molecular y Celular, Miguel Hernández University, Avenida de la Universidad S/N, 03202 Elche, Alicante, Spain

ARTICLE INFO

Article history:

Received 25 October 2011

Received in revised form 23 January 2012

Accepted 24 January 2012

Available online 1 February 2012

Keywords:

NanoLC-TOF-MS

Olive oil

Phenolic compounds

Colon adenocarcinoma

Metabolomic

ABSTRACT

Crude phenolic extracts (PE) have been obtained from naturally bearing Spanish extra-virgin olive oil (EVOO) showing different polyphenol families such as secoiridoids, phenolic alcohols, lignans, and flavones. EVOO-derived complex phenols (especially from the Arbequina variety olive) have been shown to suppress cell growth of SW480 and HT29 human colon adenocarcinoma cell lines. Inhibition of proliferation by EVOO-PE Arbequina variety extract was accompanied by apoptosis in both colon-cancer-cell lines and a limited G₂M cell-cycle arrest in the case of SW480 cells. The metabolized compounds from EVOO-PE in culture medium and cytoplasm of both cell lines were analyzed using nano-liquid chromatography (nanoLC) coupled with electrospray ionization-time-of-flight-mass spectrometry (ESI-TOF-MS). The results showed many phenolic compounds and their metabolites both in the culture medium as well as in the cytoplasm. The main compounds identified from EVOO-PE were hydroxylated luteolin and decarboxymethyl oleuropein aglycone.

© 2012 Elsevier B.V. All rights reserved.

1. Introduction

Several studies have reported that olive-oil consumption has potential protective effects against several pathologies, especially those related to cancer [1]. For years, the healthy properties of EVOO were attributed exclusively to its high monounsaturated fatty acid (MUFA) content, mostly in the form of oleic acid, and also the long-chain n-3 polyunsaturated fatty acids, such as conjugated linoleic acid and gamma-linolenic acid have shown tumor-inhibitory effects [2]. In addition to fatty acids, evidence has mounted concerning the bioactivity of minor components of EVOO, particularly phenolic compounds [3]. The main families of phenolic compounds in olive oil are: simple phenols, lignans, flavonoids, and secoiridoids [4]. These compounds are also present in by-products generated during olive-oil production, such as olive

leaves, although they appear mainly as glycosides [5]. A large body of evidence indicates that polyphenols can exert chemopreventive effects against different cancers, and several studies have explored the anticarcinogenic activity of olive-oil polyphenols, mainly in *in vitro* studies where individual compounds or olive-oil extracts were incubated in different types of human cancer-cell lines (prostate, leukemic, breast) [6]. These studies suggest that the olive-oil polyphenols analyzed are able to affect the overall process of carcinogenesis, because they have the abilities to inhibit the cell cycle, cell proliferation or oxidative stress, improve the efficacy of detoxification enzymes, induce apoptosis, and stimulate the immune system. Recently, Menendez et al. [7] have also studied the effect of olive-oil polyphenols, supplemented individually or in the oil matrix, in different human breast-cancer lines and their findings revealed that the presence of these polyphenols, especially those fractions rich in lignans and secoiridoids had a significantly stronger ability to decrease cell viability [8] and the expression status of HER2, one of the most commonly analyzed protooncogenes in human-cancer studies.

However, although there is evidence suggesting that olive-oil polyphenols show anticarcinogenic activity, the molecular mechanism of the uptake and metabolism of these compounds in the cancer cells has not yet been investigated, and only *in vitro* studies with cells of the gastrointestinal tract, CaCo-2 cells [9], and a human hepatoma cell line (HepG2) [10] have been undertaken.

Abbreviations: EVOO, extra-virgin olive oil; PE, phenolic extract; CRC, colorectal cancer; nanoLC, nano-liquid chromatography; MeOH, methanol; DOA, decarboxymethyl oleuropein aglycone; FCM, flow cytometry.

* Corresponding author at: Functional Food Research and Development Center, Health Science Technological Park, Avenida del Conocimiento S/N, E-18100 Granada, Spain. Tel.: +34 958 243296; fax: +34 958 249510.

** Corresponding author. Tel.: +34 966658431; fax: +34 966658758.

E-mail addresses: ansegura@ugr.es (A. Segura-Carretero), ja.ferragut@umh.es (J.A. Ferragut).

¹ These authors have equally contributed to this research.

Colorectal cancer (CRC) represents one of the most frequent malignancies worldwide with distant recurrence primarily affecting the liver as the predominant cause of CRC-related mortality. The 5-year survival rate of 90% in patients with tumor restricted to the colon decreases to 10% in the presence of distant metastasis [11]. Risk factors suggested in CRC etiology include genetic predisposition and dietary intake, such as high consumption of fat and low intake of fibers and flavonoids [12]. It is demonstrated that the phenolic compounds from EVOO prevent the carcinogenesis and invasion of colon-cancer cells and metastasis [13], including hydroxytyrosol and oleuropein aglycone [14].

Nano-liquid chromatography coupled to electrospray ionization-time-of-flight mass spectrometry (nanoLC-ESI-TOF MS) is a new powerful analytical tool, providing a wide number of important applications, especially in proteomics and also in fields such as pharmaceutical, environmental and enantiomeric analysis. The application of nanoLC in the field of food analysis is very limited, but we have recently demonstrated the potential of this technique in the determination and quantification of polyphenols from olive-oil samples [8]. The first attempts to use packed capillary columns with very small inside diameters, ranging from 20 to 70 μm , and flow rates on the order of 50–200 nL/min were reported by Novotny [15]. From a theoretical standpoint, it has been demonstrated that sensitivity can increase on decreasing the column inside diameter. This effect can be ascribed to both a reduction of analyte chromatographic dilution and greater efficiency [16]. A complementary approach to increase the sensitivity in nanoLC involves the coupling of separation system with mass spectrometry. Hyphenation is easy to achieve because of the relatively low flow rate involved in the separation process. Indeed, when the electrospray ionization (ESI) is used as the continuous-flow ionization technique, a lower flow rate raises the number ions in the gas phase and, consequently, augments sensitivity [17].

In this context, the present paper uses nanoLC-ESI-TOF-MS to elucidate for the first time the uptake, antiproliferative activity, and metabolism of the main families of olive-oil polyphenols in relation to human colon adenocarcinoma cells (SW480 and HT29) with an exogenous supplementation of olive-oil extracts.

2. Materials and methods

2.1. Chemicals

All chemicals were of analytical reagent grade. For the optimization of the extraction procedure, methanol and hexane were purchased from Panreac (Barcelona, Spain), hydrochloric acid from Scharlau (Barcelona, Spain), and ethyl acetate from Lab-Scan (Dublin, Ireland). Methanol from Lab-Scan (Dublin, Ireland) and acetic acid from Fluka (Buchs, Switzerland) were used for preparing mobile phases and also for the extraction procedures. Water was deionized by using a Milli-Q-system (Millipore, Bedford, MA, USA).

The EVOOs used corresponded to five different olive varieties from different geographic zones in Spain: two Hojiblanca variety olive oils produced in Málaga (EVOO 01) and Seville (EVOO 09), seven Picual variety oils produced in Málaga (EVOO 02), Jaén (EVOOs 04, 10 and 11), and Granada (EVOOs 05, 06 and 07); one Cornezuelo variety oil produced in Granada (EVOO 03); one Manzanilla variety oil produced in Seville (EVOO 08); and three Arbequina variety oils produced in Tarragona (EVOO 12) and Seville (EVOOs 13 and 14).

2.2. Extraction and characterization of phenolic compounds from extra-virgin olive oil

As indicated in the literature [18], after conditioning a Diol-cartridge with 10 mL of methanol and 10 mL of hexane, 60 g of EVOO

dissolved in 60 mL of hexane were passed through the cartridge. The non-polar fraction was eluted with 15 mL of hexane, and then 40 mL of methanol was passed to recover the phenolic compounds. The eluted solutions were dried in a vacuum system at 35 °C, and the residues were dissolved in 2 mL of methanol. For the supplementation to the cells, and to avoid the toxic effect of methanol, 1 mL of the methanol extract was evaporated and reconstituted in 125 μL of ethanol, since this solvent has a lower toxic effect on the cells.

These phenolic extracts were completely characterized using HPLC-ESI-TOF-MS by Lozano-Sánchez et al. [4].

2.3. Cell culture and cell-extract preparation

Colon adenocarcinoma HT29 and SW480 cells from IMIM (Institut Municipal d'Investigació Mèdica, Barcelona, Spain) and ATCC (American Type Culture Collection, LGC Promochem, UK), respectively, were grown in DMEM supplemented with heat-inactivated fetal bovine serum (5%), L-glutamine (2 mM), penicillin G (50 U/mL), and streptomycin (50 $\mu\text{g}/\text{mL}$), at 37 °C in a humidified atmosphere and 5% CO_2 . Cells were plated at a density of 10,000 cells/ cm^2 in 60 mm-diameter culture plates and permitted to adhere overnight at 37 °C. When cells reached 80% confluence, they were trypsinized (1 mL/25 cm^2), neutralized with culture medium at a 1:5 ratio (trypsin:medium) and pelleted for further analysis.

The cytosolic fraction of control (untreated HT-29 and SW480 cells) and HT29 or SW480 cells treated with olive-oil extracts, was obtained upon cell disruption with a Polytron homogenizer at 4 °C. First, cells were washed with phosphate-buffered saline (PBS) solution (Sigma-Aldrich Madrid, Spain) and sedimented. The pellet was resuspended with homogenization buffer Tris-HCl (10 mM, pH 7.4) containing EDTA (5 mM), NaCl (120 mM) and a protease inhibitor cocktail (Sigma-Aldrich Madrid, Spain), containing 4-(2-aminoethyl)benzenesulfonyl fluoride (AEBSF), pepstatin A, E-64, bestatin, leupeptin, and aprotinin. Upon centrifugation at 14,000 $\times g$ for 14 min at 4 °C, the pellet was discarded and supernatant was centrifuged for 1 h at 100,000 $\times g$ and 4 °C. The supernatant (cytosolic fraction) was stored at -80 °C until the metabolite-extraction procedure was performed. At this temperature, enzyme activity is stopped and samples can safely be stored without continuing metabolic activity.

2.4. Cell proliferation, apoptosis, and cell-cycle analysis

Cell proliferation was determined by the crystal-violet-staining assay. Cells were analyzed in 96-well plates at a density in the range of 4–6 $\times 10^6$ cells per well and treated with different rates of olive extracts (0.01% or 0.1%) in ethanol using six wells per treatment for 24 h. Then, cells were fixed and stained with a crystal-violet paraformaldehyde solution. Excess crystal-violet dye was removed by washing with deionized water, and culture plates were dried overnight. The crystal-violet dye was released from cells by brief incubation with HCl (0.1 M) and shaking. The optical density of each well was measured by a microplate reader at 620 nm (Anthos 2001 Labtec Instruments GmbH, Wals, Austria).

The cell cycle was analyzed essentially as described in [19]. Briefly, for cell-cycle distribution of DNA content, control and cells treated with the different olive-oil extracts were trypsinized, washed with PBS, and fixed with 75% cold ethanol at -20 °C for at least 1 h. Then, cells were incubated with Triton X-100 (0.5%) and RNase A (25 $\mu\text{g}/\text{mL}$) in PBS, stained with propidium iodide (25 $\times 10^{-3}$ $\mu\text{g}/\text{mL}$), incubated for 30 min in the dark and analyzed using an Epics XL flow cytometer equipped with a 0.75 W argon laser set at 488 nm (Beckman Coulter Co., Miami, FL, USA).

The apoptosis induced by treatment of the cells with 0.1% EVOO-PE14 for 24 h, was measured by flow cytometry by determining

the amount of apoptotic cells in the sub-G1 peak, as previously described [19].

Flow-cytometry data were analyzed upon gating the cells to eliminate dead cells and debris. A total of 10^5 cells were measured during each sample analysis.

2.5. Treatment of biological samples for the identification of metabolites

The treatment of biological samples was based on a previous study described in the literature [8]. The optimal extraction procedure was basically a liquid–liquid extraction with ethyl acetate including certain slight differences according to the type of sample. For the culture media, the best extraction procedure was as follows: 1 mL of the culture medium was mixed with 1 mL of ethyl acetate, extracted for 10 min using a vortex, centrifuged at $18,800 \times g$ at 4°C for 10 min and the supernatant was evaporated to dryness. The dried sample was reconstituted in 200 μL of water/acetic acid/MeOH (79.5/0.5/20, v/v/v).

For the cytoplasm samples the extraction procedure consisted of stirring 100 μL of cytoplasm with 100 μL of MeOH–HCl (0.5 M) 200 μL of ethyl acetate for 10 min using a vortex. The mixture was maintained in the freezer for 1 h at -20°C . After the samples reached room temperature, they were centrifuged at $18,800 \times g$ for 10 min at 4°C and the supernatant was evaporated to dryness. The dried sample was reconstituted in 100 μL of water/acetic acid/MeOH (79.5/0.5/20, v/v/v).

2.6. NanoLC-ESI-TOF-MS analysis

2.6.1. NanoLC

The chromatographic conditions were optimized following García-Villalba et al. [8]. A commercially available instrumentation EASY-nLC™ (Bruker Daltonik GmbH, Bremen, Germany) was used, composed of one module equipped with three pumps, three pressure sensors, four valves, two flow sensors, an autosampler, and a touchscreen.

A short capillary trapping column (100 μm inside diameter, effective length 20 mm, 5 μm particle size) and a fused silica capillary column (75 μm inside diameter, effective length 10 cm, 3 μm particle size), both packed with C18 stationary phase, were used for the chromatographic separation. The mobile phases were composed of water with acetic acid (0.25%) (phase A) and methanol (phase B) with the following gradient: 0 min, 5% B; 7 min, 35% B; 12 min, 45% B; 17 min, 50% B; 22 min, 60% B; 25 min, 95% B; 27 min, 5% B, and finally a conditioning cycle of 5 min with the same conditions for the next analysis. Before the following analysis was started, the pre-column and column were re-equilibrated with phase A at 6 $\mu\text{L}/\text{min}$ for 2 min and 0.6 $\mu\text{L}/\text{min}$ for 8 min, respectively. The flow rate used to elute the compounds in the analytical column was 300 nL/min at 25°C and 5 μL of the sample was injected into the loop.

2.6.2. Mass spectrometry

The nanoLC system was coupled to a Bruker Daltonik microTOF mass spectrometer (Bruker Daltonik, Bremen, Germany) using electrospray ionization (ESI).

The nanoLC system was interfaced to the mass spectrometry using a commercial sheathless nano-spray interface with a tapered fused silica sprayer tip. The key parameters of the nano-ESI were adjusted for the flow rate used (300 nL/min) to achieve stable spray across the entire gradient range: pressure 0.4 bar, dry gas flow 4 L/min and a dry gas temperature of 150°C .

The mass spectrometer was run in the negative mode and was operated to acquire spectra in the range of 50–1000 m/z . The accurate mass data of the molecular ions, provided by the TOF analyzer,

were processed by DataAnalysis 4.0 software (Bruker Daltonik GmbH), which lists possible molecular formulas consistent with the accurate mass measurement and the true isotopic pattern. High mass accuracy requires mass calibration. For this, we used a mixture of well-known phenols present in the olive-oil extracts as an internal calibration, giving mass peaks throughout the desired range of 100–400 m/z , according to García-Villalba et al. [8].

3. Results and discussion

3.1. Screening of antiproliferative activity of EVOO-PE

Growth inhibition of colon-cancer HT29 and SW480 cells by treatments with each of the 14 olive-oil extracts at concentrations 0.01% and 0.1% for 24 h, was measured by the crystal-violet assay. Depending on the extract and on the concentration used, the effect on cell proliferation was very different (Tables 1A and 1B). Thus, while concentrations of 0.1% reduced cell growth by up to 20% with respect to control of untreated cells in both cell lines (Table 1B), inhibition of cell proliferation at 0.01% was much less drastic (Table 1A).

Also, the antiproliferative activity of the olive-oil extracts preferentially affected the SW480 cells, with significant differences in growth inhibition induced by some of the 14 olive-oil samples. All of

Table 1A

Cell proliferation of human colon cells upon incubation with 0.01% of 14 olive-oil crude extracts for 24 h.

	SW480	HT29
Control	100	100
EVOO-PE01	83.1 \pm 2.6*	101.6 \pm 6.4
EVOO-PE02	79.0 \pm 2.9*	108.6 \pm 3.8*
EVOO-PE03	75.1 \pm 2.5*	101.5 \pm 6.5
EVOO-PE04	82.5 \pm 2.1*	96.9 \pm 4.6
EVOO-PE05	85.7 \pm 3.5*	93.7 \pm 3.6
EVOO-PE06	79.0 \pm 4.1*	94.4 \pm 5.6
EVOO-PE07	89.5*	93.3 \pm 2.2
EVOO-PE08	79.5 \pm 4.0*	82.8 \pm 4.3*
EVOO-PE09	77.0 \pm 4.6*	84.5 \pm 1.8*
EVOO-PE10	80.0 \pm 6.4*	90.0 \pm 3.8*
EVOO-PE11	86.1 \pm 4.3*	93.1 \pm 3.1
EVOO-PE12	80.0 \pm 3.1*	95.3 \pm 2.3
EVOO-PE13	79.2 \pm 4.1*	96.9 \pm 3.2
EVOO-PE14	76.9 \pm 4.9*	87.9 \pm 2.0*

Data are expressed as percentages of cell growth with respect to control of untreated cells \pm SEM ($n = 3$).

* Significance value ($p < 0.01$) by a one-way ANOVA with respect to control.

Table 1B

Cell proliferation of human colon cells upon incubation with 0.1% of 14 olive-oil crude extracts for 24 h.

	SW480	HT29
Control	100	100
EVOO-PE01	37.4 \pm 1.3*	51.1 \pm 5.0*
EVOO-PE02	38.3 \pm 1.1*	50.4 \pm 6.8*
EVOO-PE03	36.8 \pm 1.7*	45.8 \pm 3.9*
EVOO-PE04	41.2 \pm 2.1*	51.9 \pm 6.6*
EVOO-PE05	21.7 \pm 1.2*	34.9 \pm 3.1*
EVOO-PE06	22.7 \pm 0.8*	37.8 \pm 3.9*
EVOO-PE07	26.8 \pm 5.7*	39.6 \pm 1.8*
EVOO-PE08	23.5 \pm 1.5*	39.0 \pm 2.6*
EVOO-PE09	23.1 \pm 0.8*	24.2 \pm 0.8*
EVOO-PE10	20.7 \pm 1.6*	23.9 \pm 0.8*
EVOO-PE11	22.6 \pm 1.5*	24.8 \pm 0.9*
EVOO-PE12	56.8 \pm 2.8*	24.3 \pm 2.0*
EVOO-PE13	40.6 \pm 5.4*	21.9 \pm 0.8*
EVOO-PE14	33.3 \pm 4.2*	22.9 \pm 1.5*

Data are expressed as percentages of cell growth with respect to control of untreated cells \pm SEM ($n = 3$).

* Significance value ($p < 0.01$) by a one-way ANOVA with respect to control.

Table 2

Retention time, [M–H][–] measured, error (in ppm) between the theoretical calculated and measured masses, and the molecular formula of phenolic compounds from EVOO-PE14 and their metabolites found in culture medium and cytoplasm of HT29 and SW480 cell lines.

Compound	Retention time (min)	[M–H] [–]	Error (ppm)	Molecular formula	Culture medium		Cytoplasm	
					HT29	SW480	HT29	SW480
Phenolic compounds								
DOA	11.65	319.1165	4.1	C ₁₇ H ₂₀ O ₆				X
Vanillin	11.7	151.0401	0.3	C ₈ H ₈ O ₃	X	X		
Oleuropein aglycone	11.95	377.1247	1.7	C ₁₉ H ₂₂ O ₈				X
4-OH-benzoic acid	12.35	137.0244	0.1	C ₇ H ₆ O ₃	X	X		
Vanillic acid	12.6	167.0348	0.7	C ₈ H ₈ O ₄	X			
Hydroxytyrosol acetate	20.05	195.0661	0.6	C ₁₀ H ₁₂ O ₄	X			
10-H-oleuropein aglycone	20.1	393.1205	4.8	C ₁₉ H ₂₂ O ₉	X			
Syringaresinol	21	417.153	5.3	C ₂₂ H ₂₆ O ₈		X		
Acetoxy-pinoresinol	21.55	415.1378	4.5	C ₂₂ H ₂₄ O ₈	X	X	X	X
Pinoresinol	21.8	357.1339	1.3	C ₂₀ H ₂₂ O ₆		X		
Hydroxytyrosol	23.1	153.0555	0.7	C ₈ H ₁₀ O ₃	X	X		
Elenolic acid	25.8	241.0714	1.0	C ₁₁ H ₁₄ O ₆		X	X	
Luteolin	27.3	285.0399	1.9	C ₁₅ H ₁₀ O ₆	X	X		
Methyl-DOA	30.5	333.1152	3.0	C ₁₈ H ₂₂ O ₆	X		X	
Apigenin	31.1	269.0468	4.3	C ₁₅ H ₁₀ O ₅		X		
Metabolites								
Quercetin	38	301.0352	0.5	C ₁₅ H ₁₀ O ₇				X
Methyl-hydroxy-DOA	38.1	349.1278	5.0	C ₁₈ H ₂₂ O ₇			X	X
Methyl-luteolin	38.2	299.0574	4.3	C ₁₆ H ₁₂ O ₆				X

DOA, decarboxymethyl oleuropein aglycone.

these have been completely characterized by Lozano-Sánchez et al. [4]. While other EVOO-PEs present high antiproliferative activity, EVOO-PE14 displays a notable and quite different antiproliferative activity both in HT29 and in SW480 cells, and therefore it was selected for further analysis. This extract, belonging to the Arbequina variety from Seville (Spain), is characterized by a high content in lignans (especially in decarboxymethyl oleuropein aglycone, DOA). Furthermore, its traceability is well documented.

3.2. Metabolomic analysis using nanoLC-ESI-TOF-MS

The optimum nanoLC-ESI-TOF-MS method was applied to analyze EVOO-PE14 phenolic compounds derived from the treatment of HT29 and SW480 cells with this extract in either culture medium or in the cytosolic fraction of the cells.

The method proved the specificity for these compounds, since no interfering endogenous compounds were detected at the elution times of the polyphenols in the extracted ion chromatograms, when blank samples were analyzed. To identify the phenolic compounds in their free form and their possible metabolites formed after incubation, we used the information available in literature, the polarity of the compounds in the reverse phase, and the valuable information provided by the TOF analyzer. This provided a list of possible molecular formulas using the information on mass accuracy and the isotopic pattern of the compounds.

Table 2 shows the compounds from EVOO-PE14 and their metabolites found in the culture medium and the cytoplasm of HT29 and SW480 cell lines. Three metabolites deriving from EVOO-PE14 were found in the cytoplasm due to the metabolism of the cells, namely, methyl-hydroxy-DOA, methyl-luteolin, and quercetin (by hydroxylation of luteolin). Fig. 1 shows the extracted ion chromatograms (EIC) of some of the compounds found in both the culture medium as well as the cytoplasm. It should be highlighted that quercetin was the main compound found in cytoplasm, with much higher intensity than other compounds. Decarboxymethyl oleuropein aglycone (DOA) also presented high intensity, although lower than quercetin.

The complexity of crude olive-oil extracts makes hard to assign the above antiproliferative activity to individual components of the extracts. However, it is noteworthy that, according to Table 2

and Fig. 1, oleuropein (or its metabolic derivatives) and quercetin, were the two main phenolic compounds found in the cytoplasm of the EVOO-PE14-treated colon-cancer cells. Both compounds have demonstrated to possess antiproliferative activity in colon-cancer-cell lines [20], acting through diverse mechanisms including protein inhibition [21], apoptosis [22], or inhibition of enzyme activities [14,23]. In our case, we found that apoptosis (see below) accompanies the inhibition of proliferation upon treatment of the cells with the EVOO-PE14 olive-oil extract, regardless of the presence of other mechanisms that could also be present.

3.3. Cell-cycle analysis

Fig. 2 shows the distribution of DNA from control and EVOO-PE14-treated HT29 and SW480 cells determined by flow cytometry (FCM).

Tables 3A and 3B display the DNA content of the different phases of cell cycle corresponding to control and HT29 or SW480 cells treated with olive-oil-extract EVOO-PE14 according to Fig. 2. It can be seen that EVOO-PE14 induced apoptosis in HT29 and SW480 cells (10% and 14%, respectively, Table 3A), indicated by an arrow signaling the SubG1 phase in Fig. 2. However, the DNA-distribution profile was found to be quite different between the two cell lines when the relative DNA content of each phase was estimated assuming that 100% refers to the sum of the G1, S, and G₂M phases, i.e. without taking into account the contribution of the apoptotic cell population SubG1 (Table 3B). Thus, no significant changes were

Table 3A

Distribution of DNA from control and HT29 or SW480 cells treated with 0.1% of EVOO-PE14 for 24 h.

Phase	HT29		SW480	
	Control	EVOO-PE14	Control	EVOO-PE14
G1	40.7 ± 1.1	35.7 ± 6.3	64.5 ± 5	41.2 ± 4.9**
S	28.3 ± 7.4	25.1 ± 1.3	18.0 ± 1.5	15.3 ± 7.4
G ₂ M	28.5 ± 8.1	28.2 ± 11.7	15.3 ± 2.5	18.4 ± 2.5
SubG1	1.9 ± 0.3	10.3 ± 3.4*	1.3 ± 0.7	14.2 ± 8.9

Data are expressed as percentages of the cells ± SD estimated by FCM (n = 3).

* p < 0.05 between control and EVOO-PE14-treated cells (paired t-test).

** p < 0.01 between control and EVOO-PE14-treated cells (paired t-test).

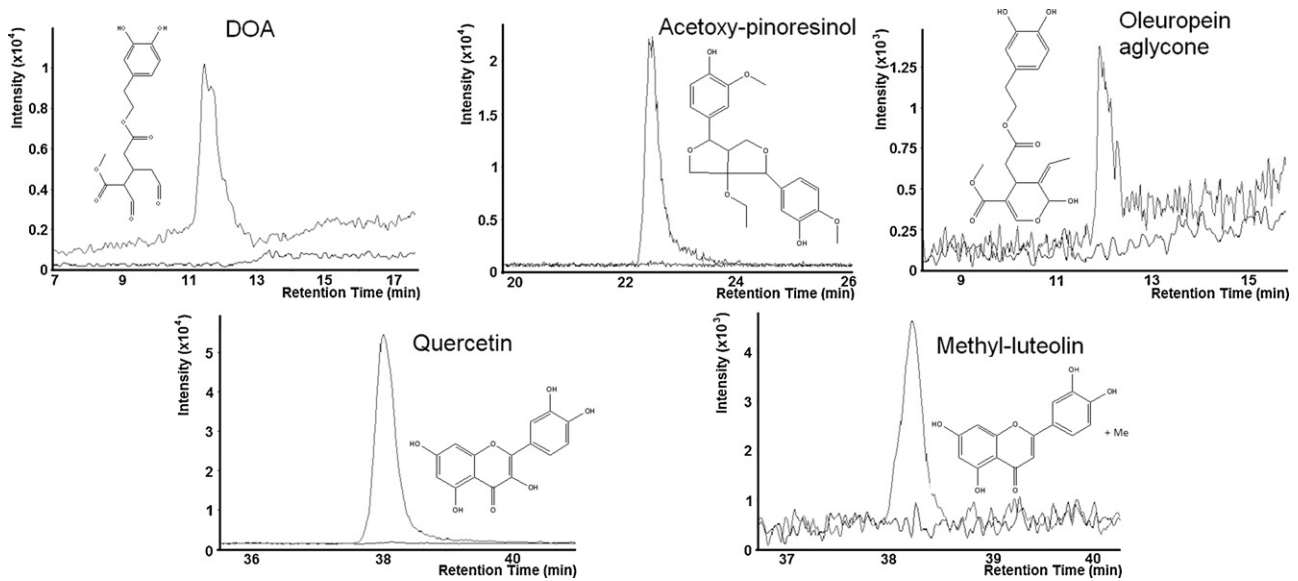


Fig. 1. Extracted ion chromatogram (EIC) of the main compounds and their metabolites found in culture medium and cytoplasm of HT29 and SW480 cell lines. For each identified compound, two signals of EIC corresponding to untreated and EVOO-PE14-treated cell lines are represented. DOA, decarboxymethyl oleuropein aglycone.

found in the cell cycle between control and HT29 EVOO-PE14-treated cells, despite a decrease in G₁ concomitant to an increase in G₂M in SW480 EVOO-PE14-treated cells with respect to control SW480 cells. This observation indicates that EVOO-PE14: (a) induces a cytotoxic effect in HT29 and SW480 cells, promoting

apoptosis; and (b) also exerts a cytostatic effect in SW480 cells indicated by cell arrest in G₂M, probably as a step prior to apoptosis.

Several works have demonstrated that olive-oil polyphenols act as inhibitors of cell proliferation in human tumor-cell lines from lung [24], liver [25], leukemia [26], and colon [22], involving

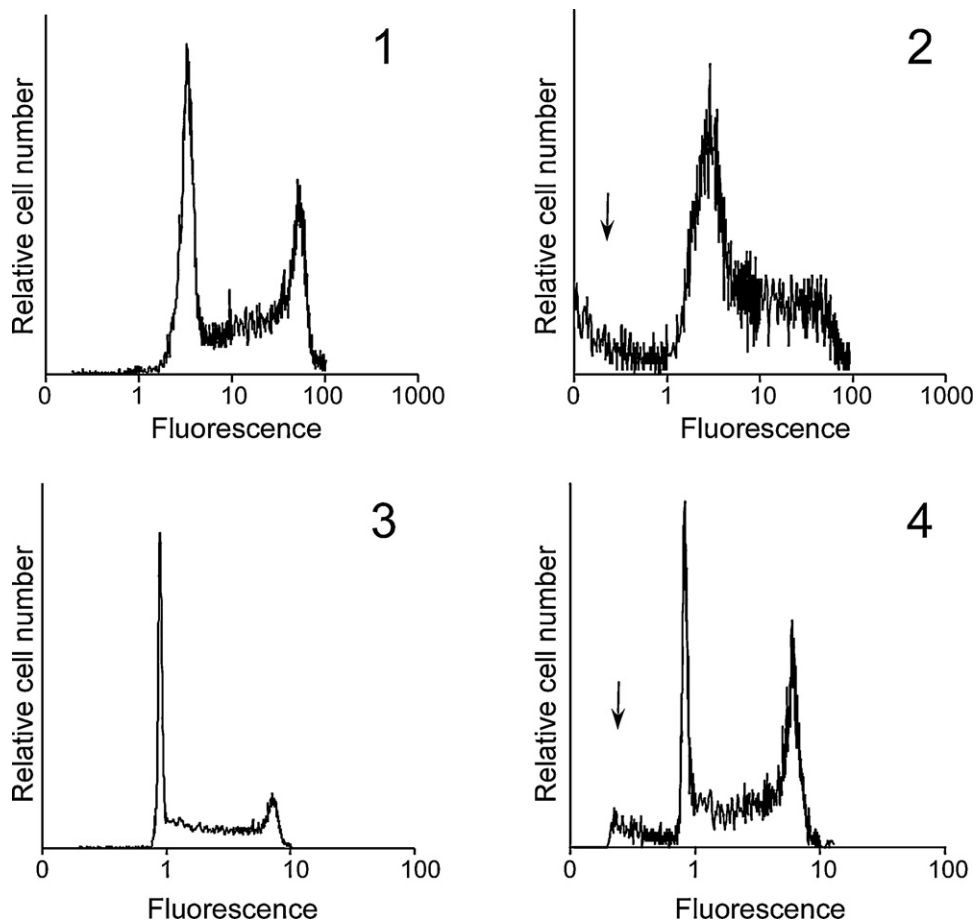


Fig. 2. Distribution of cellular DNA in control HT29 or SW480 cells (panels 1 and 3, respectively) and 0.1% EVOO-PE14-treated HT-29 (panel 2) or SW-480 (panel 4) cells for 24 h, determined by FCM. Arrows on panels 2 and 4 indicate the apoptotic cell population (sub-G₁ phase).

Table 3B

Distribution of DNA from control and HT29 or SW480 cells treated with 0.1% of EVOOPE14 for 24 h after subtracting the content of the subG1 phase (apoptosis) included in Table 3A.

Phase	HT29		SW480	
	Control	EVOO-PE14	Control	EVOO-PE14
G1	41.5 ± 1.1	40.5 ± 5.6	65.3 ± 4.9	55 ± 4.2
S	27.6 ± 7.2	28.3 ± 1.1	18.2 ± 1.5	20.5 ± 6.3
G ₂ M	27.7 ± 7.9	32 ± 10.5	15.5 ± 2.5	24.5 ± 2.1**

Data are expressed as percentages of the cells ± SD estimated by FCM ($n=3$).

** $p < 0.01$ between control and EVOO-PE14-treated cells (paired t -test).

many different action mechanisms. Thus, oleuropein inhibits cell growth in SW620 human colon-cancer cells [14], while quercetin down-regulates Erb2/Erb3 signaling [21], activates AMPK signaling pathway [27], depresses cyclooxygenase-2 expression [23] in HT29 cells, and inhibits β -catenin/Tcf signaling in SW480 cells [28].

The relative high abundance of quercetin or oleuropein aglycone (and its derivatives) in the cytoplasm of the EVOO-PE14-treated cells (Table 2), points to these two components as apoptosis inducers in HT29 and SW480 cells. It seems reasonable to assume that the absence of quercetin, the flavonoid most commonly related to apoptosis, in the cytoplasm of HT29 EVOO-PE14-treated cells (Table 2), could be responsible for the lower degree of apoptosis found in these cells (10%) with respect to that observed in the SW480 cells (14%). Metabolic derivatives of quercetin and oleuropein aglycone, such as those listed in Table 2, might also be involved in the induction of apoptosis. In addition to the antiproliferative activity shown by individual phenolic compounds against colon-cancer-cell lines, synergic effects leading to apoptosis between the compounds listed in Table 2 cannot be ruled out.

Although the present work demonstrates the antiproliferative and pro-apoptotic activities of olive-oil extracts on colon-cancer cells, new experimental studies are needed to clarify the molecular and cellular mechanisms underlying the dietary benefits of olive-oil consumption with respects to human cancer.

4. Concluding remarks

New and powerful analytical tools able to characterize the cellular metabolites are needed to elucidate the action mechanism of phenolic compounds in cancer cells. In the present work, the cellular uptake and metabolism of olive-oil polyphenols in human colon adenocarcinoma cells are evaluated, taking advantage of the sensitivity of the nanoLC-ESI-TOF-MS. This analytical platform has demonstrated its potential in the analysis of small molecules in biological fluids. The analysis of culture medium and cytoplasm suggests that some compounds, mainly quercetin and oleuropein aglycone (and its derivatives), are the main compounds exerting an antiproliferative effect in SW480 and HT29 cell lines. These metabolites could affect some signaling pathways and cause apoptosis, promoting the entry into subG1 phase.

Conflict of interest

The authors have declared no conflict of interest.

Acknowledgements

The authors are grateful to the Spanish Ministry of Education and Science for the projects AGL2008-05108-C03-03 and AGL2011-29857-C03-02 and to Andalusian Regional Government Council of Innovation and Science for the projects P07-AGR-02619, P09-CTS-4564 and P10-FQM-6563.

References

- [1] C. Pelucchi, C. Bosetti, E. Negri, L. Lipworth, C. La Vecchia, Olive oil and cancer risk: an update of epidemiological findings through 2010, *Curr. Pharm. Des.* 17 (2011) 805–812.
- [2] E. Escrich, M. Solanas, R. Moral, I. Costa, L. Grau, Are the olive oil and other dietary lipids related to cancer? Experimental evidence, *Clin. Transl. Oncol.* 8 (2006) 868–883.
- [3] R.W. Owen, A. Giacosa, W.E. Hull, R. Haubner, B. Spiegelhalter, H. Bartsch, The antioxidant/anticancer potential of phenolic compounds isolated from olive oil, *Eur. J. Cancer.* 36 (2000) 1235–1247.
- [4] J. Lozano-Sanchez, A. Segura-Carretero, J.A. Menendez, C. Oliveras-Ferraro, L. Cerretani, A. Fernandez-Gutierrez, Prediction of extra virgin olive oil varieties through their phenolic profile. Potential cytotoxic activity against human breast cancer cells, *J. Agric. Food Chem.* 58 (2010) 9942–9955.
- [5] D. Arraez-Roman, S. Sawalha, A. Segura-Carretero, J. Menendez, A. Fernandez-Gutierrez, Identification of phenolic compounds in olive leaves using CE-ESI-TOF-MS, *Agro Food Ind. Hi-Tech.* 19 (2008) 18–22.
- [6] T.G. Sotiropoulos, S.A. Kyrtopoulos, A. Xenakis, G.T. Sotiropoulos, Chemopreventive potential of minor components of olive oil against cancer, *Ital. J. Food Sci.* 15 (2003) 169–185.
- [7] J.A. Menéndez, A. Vazquez-Martin, C. Oliveras-Ferraro, R. Garcia-Villalba, A. Carrasco-Pancorbo, A. Fernandez-Gutierrez, A. Segura-Carretero, Extra-virgin olive oil polyphenols inhibit HER2 (erbB-2)-induced malignant transformation in human breast epithelial cells: relationship between the chemical structures of extra-virgin olive oil secoiridoids and lignans and their inhibitory activities on the tyrosine kinase activity of HER2, *Int. J. Oncol.* 34 (2009) 43–51.
- [8] R. García-Villalba, A. Carrasco-Pancorbo, G. Zurek, M. Behrens, C. Baessmann, A. Segura-Carretero, A. Fernández-Gutiérrez, Nano and rapid resolution liquid chromatography-electrospray ionization-time of flight mass spectrometry to identify and quantify phenolic compounds in olive oil, *J. Sep. Sci.* 33 (2010) 2069–2078.
- [9] C. Manna, P. Galletti, G. Maisto, V. Cucciolla, S. D'Angelo, V. Zappia, Transport mechanism and metabolism of olive oil hydroxytyrosol in CaCo-2 cells, *FEBS Lett.* 470 (2000) 341–344.
- [10] L. Goya, R. Mateos, L. Bravo, Effect of the olive oil phenol hydroxytyrosol on human hepatoma HepG2 cells – protection against oxidative stress induced by tert-butylhydroperoxide, *Eur. J. Nutr.* 46 (2007) 70–78.
- [11] A. Jemal, T. Murray, E. Ward, A. Samuels, R.C. Tiwari, A. Ghafoor, E.J. Feuer, M.J. Thun, Cancer statistics, 2005, *CA-Cancer J. Clin.* 55 (2005) 10–30.
- [12] S.A. Bingham, N.E. Day, R. Luben, P. Ferrari, N. Slimani, T. Norat, F. Clavel-Chapelon, E. Kesse, A. Nieters, H. Boeing, A. Tjønneland, K. Overvad, C. Martinez, M. Dorronsoro, C.A. Gonzalez, T.J. Key, A. Trichopoulou, A. Naska, P. Vineis, R. Tumino, V. Krogh, H.B. Bueno-de-Mesquita, P.H.M. Peeters, G. Berglund, G. Hallmans, E. Lund, G. Skeie, R. Kaaks, E. Riboli, Dietary fibre in food and protection against colorectal cancer in the European Prospective Investigation into Cancer and Nutrition (EPIC): an observational study, *Lancet* 361 (2003) 1496–1501.
- [13] Y.Z.H. Hashim, I.R. Rowland, H. McGlynn, M. Servili, R. Selvaggini, A. Taticchi, S. Esposto, G. Montedoro, L. Kaisalo, K. Wahala, C.I.R. Gill, Inhibitory effects of olive oil phenolics on invasion in human colon adenocarcinoma cells in vitro, *Int. J. Cancer* 122 (2008) 495–500.
- [14] M. Notarnicola, S. Pisanti, V. Tutino, D. Bocale, M.T. Rotelli, A. Gentile, V. Memeo, M. Bifulco, E. Perri, M.G. Caruso, Effects of olive oil polyphenols on fatty acid synthase gene expression and activity in human colorectal cancer cells, *Genes Nutr.* 6 (2011) 63–69.
- [15] K.E. Karlsson, M. Novotny, Separation efficiency of slurry-packed liquid-chromatography microcolumns with very small inner diameters, *Anal. Chem.* 60 (1988) 1662–1665.
- [16] J.P.C. Vissers, Recent developments in microcolumn liquid chromatography, *J. Chromatogr. A* 856 (1999) 117–143.
- [17] C. Legido-Quigley, N.W. Smith, D. Mallet, Quantification of the sensitivity increase of a micro-high-performance liquid chromatography-electrospray ionization mass spectrometry system with decreasing column diameter, *J. Chromatogr. A* 976 (2002) 11–18.
- [18] A.M. Gómez Caravaca, A. Carrasco Pancorbo, B. Cañabate Díaz, A. Segura Carretero, A. Fernández Gutiérrez, Electrophoretic identification and quantitation of compounds in the polyphenolic fraction of extra-virgin olive oil, *Electrophoresis* 26 (2005) 3538–3551.
- [19] E. Carrasco-García, M. Saceda, S. Grasso, L. Rocamora-Reverte, M. Conde, Á. Gómez-Martínez, P. García-Morales, J.A. Ferragut, I. Martínez-Lacaci, Small tyrosine kinase inhibitors interrupt EGFR signaling by interacting with erbB3 and erbB4 in glioblastoma cell lines, *Exp. Cell Res.* 317 (2011) 1476–1489.
- [20] S. Kuo, Antiproliferative potency of structurally distinct dietary flavonoids on human colon cancer cells, *Cancer Lett.* 110 (1996) 41–48.
- [21] W.K. Kim, M.H. Bang, E.S. Kim, N.E. Kang, K.C. Jung, H.J. Cho, J.H.Y. Park, Quercetin decreases the expression of ErbB2 and ErbB3 proteins in HT-29 human colon cancer cells, *J. Nutr. Biochem.* 16 (2005) 155–162.
- [22] C.P.R. Xavier, C.F. Lima, A. Preto, R. Seruca, M. Fernandes-Ferreira, C. Pereira-Wilson, Luteolin, quercetin and ursolic acid are potent inhibitors of proliferation and inducers of apoptosis in both KRAS and BRAF mutated human colorectal cancer cells, *Cancer Lett.* 281 (2009) 162–170.

- [23] R. Narayansingh, R.A.R. Hurta, Cranberry extract and quercetin modulate the expression of cyclooxygenase-2 (COX-2) and I kappa B alpha in human colon cancer cells, *J. Sci. Food Agric.* 89 (2009) 542–547.
- [24] T. Nguyen, E. Tran, T. Nguyen, P. Do, T. Huynh, H. Huynh, The role of activated MEK-ERK pathway in quercetin-induced growth inhibition and apoptosis in A549 lung cancer cells, *Carcinogenesis* 25 (2004) 647–659.
- [25] A. Belen Granado-Serrano, M. Angeles Martin, L. Bravo, L. Goya, S. Ramos, Quercetin induces apoptosis via caspase activation, regulation of Bcl-2, and inhibition of PI-3-kinase/Akt and ERK pathways in a human hepatoma cell line (HepG2), *J. Nutr.* 136 (2006) 2715–2721.
- [26] J. Duraj, K. Zazrivcova, J. Bodo, M. Sulikova, J. Sedlak, Flavonoid quercetin, but not apigenin or luteolin, induced apoptosis in human myeloid leukemia cells and their resistant variants, *Neoplasma* 52 (2005) 273–279.
- [27] H. Kim, S. Kim, B. Kim, S. Lee, Y. Park, B. Park, S. Kim, J. Kim, C. Choi, J. Kim, S. Cho, J. Jung, K. Roh, K. Kang, J. Jung, Apoptotic effect of quercetin on HT-29 colon cancer cells via the AMPK signaling pathway, *J. Agric. Food Chem.* 58 (2010) 8643–8650.
- [28] C.H. Park, J.Y. Chang, E.R. Hahm, S. Park, H.K. Kim, C.H. Yang, Quercetin, a potent inhibitor against beta-catenin/Tcf signaling in SW480 colon cancer cells, *Biochem. Biophys. Res. Commun.* 328 (2005) 227–234.



Analysis of herbal dietary supplements for sexual performance enhancement: First characterization of propoxyphenyl-thiohydroxyhomosildenafil and identification of sildenafil, thiosildenafil, phentolamine and tetrahydropalmatine as adulterants

Stéphane Balayssac, Véronique Gilard, Chantal Zedde, Robert Martino, Myriam Malet-Martino*

Groupe de RMN Biomédicale, Laboratoire SPCMIB (UMR CNRS 5068), Université Paul Sabatier, 118 route de Narbonne, 31062 Toulouse cedex, France

ARTICLE INFO

Article history:

Received 8 December 2011
Received in revised form 24 January 2012
Accepted 26 January 2012
Available online 4 February 2012

Keywords:

Dietary supplements
Adulterants
Propoxyphenyl-thiohydroxyhomosildenafil
NMR
MS

ABSTRACT

Nine herbal dietary supplements intended to be beverages for enhancing sexual performance were analyzed before their possible launch on the market. Four of them contained a sildenafil analog reported for the first time as an adulterant. After isolation and characterization using NMR, MS, IR and UV, this analog was named propoxyphenyl-thiohydroxyhomosildenafil as the ethoxy chain on the phenyl ring of the already known analog thiohydroxyhomosildenafil was replaced by a propoxy moiety. One formulation was tainted with thiosildenafil, another unapproved PDE-5 inhibitor. Sildenafil along with the natural alkaloid tetrahydropalmatine that has no documented effect for enhancing erectile dysfunction were identified in two formulations. Another formulation was adulterated with phentolamine, a drug that is not approved for boosting male sexual performance when taken orally. The last formulation containing osthole, a bioactive natural coumarine improving sexual dysfunction, is most probably truly natural.

© 2012 Elsevier B.V. All rights reserved.

1. Introduction

Dietary supplements are products between medicines and conventional foods whose consumption is rising steeply. The control of their quality is therefore of paramount importance in order to ensure their safety and to protect consumers. There is a growing trend in the intentional adulteration of dietary supplements with drugs, which represents an alarming emerging risk to public health. Some recent articles have highlighted this problem and demonstrated the complexity to combat it (see for example [1]).

Adulterants are frequently detected in dietary supplements or herbal medicines aimed at increasing sexual function. In addition to the approved phosphodiesterase-5 (PDE-5) inhibitors, sildenafil (Viagra®), tadalafil (Cialis®) and vardenafil (Levitra®) in Europe and USA, udenafil (Zydena®) in South Korea and Malaysia, mirodenafil (Mvix®) in South Korea, and lodenafil carbonate (Helleva®) in Brazil, it has been reported that “natural” herbal products were also adulterated with unapproved analogs in which most often minor modifications were brought to the parent structure and for which no toxicological data are available. To our knowledge, 33 analogs have been described so far in the literature as illegal additives in

herbal drugs and dietary supplements [2,3]. Besides PDE-5 inhibitor analogs, the most common adulterants, many other pharmacologically active substances have been used to taint dietary supplements and herbal products consumed for enhancing sexual performance [4].

In this study, nine dietary supplements intended to be introduced into the South European market were submitted for analysis. Their exact composition was unknown but they were claimed to contain only a mixture of various herbs and sugars. They were presented in unlabeled plastic bags as brown powders (10 g per bag) to be dissolved in water for beverages and to be taken once a day. Four were adulterated with a new sildenafil analog called propoxyphenyl-thiohydroxyhomosildenafil (PP-THHS), one with thiosildenafil (THIO), two with sildenafil (SILD) along with tetrahydropalmatine (THP), one with phentolamine (PHE) and the last contained osthole (OST). The chemical structures of these compounds were elucidated using NMR and MS.

2. Experimental

2.1. Chemicals

Authentic standards of SILD citrate, OST and PHE mesylate (methanesulfonate) were purchased from Sigma–Aldrich (St. Louis,

* Corresponding author. Tel.: +33 5 61 55 68 90; fax: +33 5 61 55 76 25.
E-mail address: martino@chimie.ups-tlse.fr (M. Malet-Martino).

MO, USA). THIO was previously purified from a formulation adulterated with this analog [2].

2.2. NMR analysis

2.2.1. Preparation of samples for NMR analysis

Around 500 mg of each powder was mixed with 2 mL of CD₃CN:D₂O (80:20 v/v) under vortex agitation during 10 min and then sonicated for 10 min. The suspension was then centrifuged (10 min, 4000 rpm) and 550 µL of the supernatant was analyzed. One of the referee of this article underlined that tadalafil which is active at low doses (2 mg/day) could have not been extracted in the solvent system used owing to its poor solubility in most organic solvents and water. To demonstrate that the method was valid for detecting low-dosed tadalafil, 500 mg of powder 9 was spiked with 2 or 5 mg of pure tadalafil and treated as described above. In both cases, the ¹H NMR signals of tadalafil were easily detected in the CD₃CN:D₂O extracts, thus showing that the method of extraction is appropriate even for low quantities of this PDE-5 inhibitor.

For the quantitative analysis, around 40 mg of each powder was mixed with 10 mL of methanol under magnetic stirring during 15 min, then sonicated for 10 min. After centrifugation (5 min, 4000 rpm), an aliquot of 1 mL was evaporated to dryness and the residue dissolved in 1 mL of methanol-d₄. The experiments were done in triplicate. The quantification was performed on the ¹H NMR signals of the aromatic protons H15 and H18 (doublets) for SILD, THIO and PP-THHS, H1 and H4 (singlets) for THP, H9/H13 and H10/H12 (respectively XX' and AA' parts of an AA'XX' system) for PHEN and H4 and H5 (doublets) for OST (see Fig. 1 for numbering). The solid residue from the first extraction was re-extracted with the same protocol. The mixture obtained was centrifuged (5 min, 4000 rpm) and the supernatant evaporated to dryness. The residue was dissolved in 1 mL of methanol-d₄ for ¹H NMR analysis. The proton signals used for quantification could not be detected.

2.2.2. NMR recording conditions

The NMR experiments were performed on a Bruker Avance 500 spectrometer (Bruker BioSpin AG, Fällanden, Switzerland) equipped with a 5 mm dual ¹H-¹³C TCI cryoprobe. Sodium 2,2,3,3-tetradeutero-3-trimethylsilylpropionate (TSP; Sigma–Aldrich) was used as an internal reference for chemical shift (δ) measurement and quantification. A solution of TSP (10 µL) was added before the NMR analysis at a final concentration of 0.2 mM in all the samples analyzed. The recording and processing conditions for ¹H NMR, quantitative ¹H NMR and 2D DOSY ¹H NMR spectra have already been described [5,6].

The identification of SILD and THIO was achieved by spiking the formulation extracts with authentic standards and comparing the peak heights in the ¹H NMR spectra recorded before and after addition. The structural elucidation of PP-THHS, THP and OST was performed on isolated purified compounds, and that of PHEN on crude extract, using 1D (¹H and ¹³C) and 2D (gCOSY, gHSQC and gHMBC) experiments. To confirm the structures determined, standard OST and PHE were also added to solutions of purified OST or to crude extracts containing PHE.

2.3. Isolation of the new SILD analog, THP and OST

For the purification of the new SILD analog, 3 × 1 g of powder was extracted with 3 × 10 mL of methanol. The liquid phases were pooled, evaporated to dryness and then redissolved in 4 mL of a mixture of acetonitrile:water (80:20). The purification was performed on a XBridge™ Prep C18 column (150 mm × 19 mm; 5 µm particle size; Waters Corporation, Milford, MA, USA), using a Waters Delta Prep 4000 system equipped with a 486 tunable absorbance detector set at 270 nm. The elution was carried out using a linear

gradient of 20 to 50% acetonitrile from 0 to 20 min with 0.1% trifluoroacetic acid in both aqueous and organic phases. The flow rate was 15 mL min⁻¹. The eluted fractions were collected and analyzed with a Waters Acquity UPLC–DAD system controlled by Waters Empower 2 software. The analysis conditions were: Acquity UPLC BEH C18 column (50 mm × 2.1 mm i.d.; 1.7 µm particle size); mobile phase: (A) demineralized water and (B) acetonitrile (HPLC grade) both containing 0.1% (v/v) trifluoroacetic acid; flow rate: 0.3 mL min⁻¹; detection wavelength: 270 nm. The gradient condition was as follows: 0–1 min, isocratic elution with a 90:10 A:B mixture; 1–6 min, linear increase to 10:90 A:B ratio; isocratic elution during 1 min; re-equilibration for 1 min with a 90:10 A:B mixture before the start of the next run. The unknown compound eluted at 4.5 min.

For the purification of THP and OST, 500 mg of each formulation 6 and 9 was dissolved in 20 mL of water and the solutions left overnight at 4 °C. The precipitates were filtered, washed three times with water and evaporated to complete dryness.

2.4. MS, MS/MS and high resolution MS analyses

The methanolic extracts of powders and the purified compounds dissolved in methanol were directly infused in an Applied Biosystems API 365 triple-quadrupole mass spectrometer (Applied Biosystems Inc., Foster City, CA, USA), equipped with a TIS interface and controlled by the Analyst software (version 1.4). The mass spectrometer was operated in positive ionization mode. Nitrogen served both as auxiliary and collision gas and oxygen served as nebulizer gas. The operating conditions for TIS interface were as follows: (1) in MS mode: scan range m/z 100–1000, step size 0.1. Q1 TIS MS spectra were recorded in profile mode, IS 4700 V, DP 65 V, FP 330 V for the new analog and IS 5000 V, DP 25 V, FP 200 V for PHE and OST; and (2) in MS–MS mode: precursor ions at m/z 535 for the unknown analog, 282 for PHE and 245 for OST; scan range m/z 30–600 for the unknown analog and 50–300 for PHE and OST, step size 0.1; MS–MS spectra were recorded in profile mode, IS 5000 V, DP 65 V, FP 330 V, CE 50 V, CAD 3 for the new analog, and IS 5000 V, DP 25 V, FP 200 V, CE 25 V, CAD 3 for PHE and OST.

The accurate masses of the new analog, PHE and OST were determined on a Waters GCT Premier time-of-flight (TOF) mass spectrometer equipped with a Desorption Chemical Ionization (DCI) probe employing methane as the reagent gas and controlled by the MassLynx 4.1 software. The TOF-MS was operated between m/z 150 and 850 in positive ionization mode. The accurate mass measurements of THP and its product ions were acquired using a Waters XEVO G2 QTOF mass spectrometer. The instrument parameters were as follows: positive ionization mode; for MS analysis: cone voltage 30 V, scan range m/z 100–1200; for MS/MS analysis: coil energy 35 V, cone voltage 40 V, scan range m/z 100–440. The samples were dissolved in methanol and analyzed after direct infusion.

2.5. IR spectroscopy

The FT-IR spectrum of the new SILD analog was recorded on a Nicolet 6700 total reflectance device (Thermo Nicolet Corporation, Madison, WI, USA) using a diamond crystal at an incidence angle of 45° over the spectral range 4000–500 cm⁻¹.

3. Results and discussion

3.1. Overview of the ¹H NMR spectra of the nine formulations analyzed

The ¹H NMR spectra of CD₃CN:D₂O (80:20 v/v) extracts of formulations 1–4 on one hand and 6–7 on the other hand were

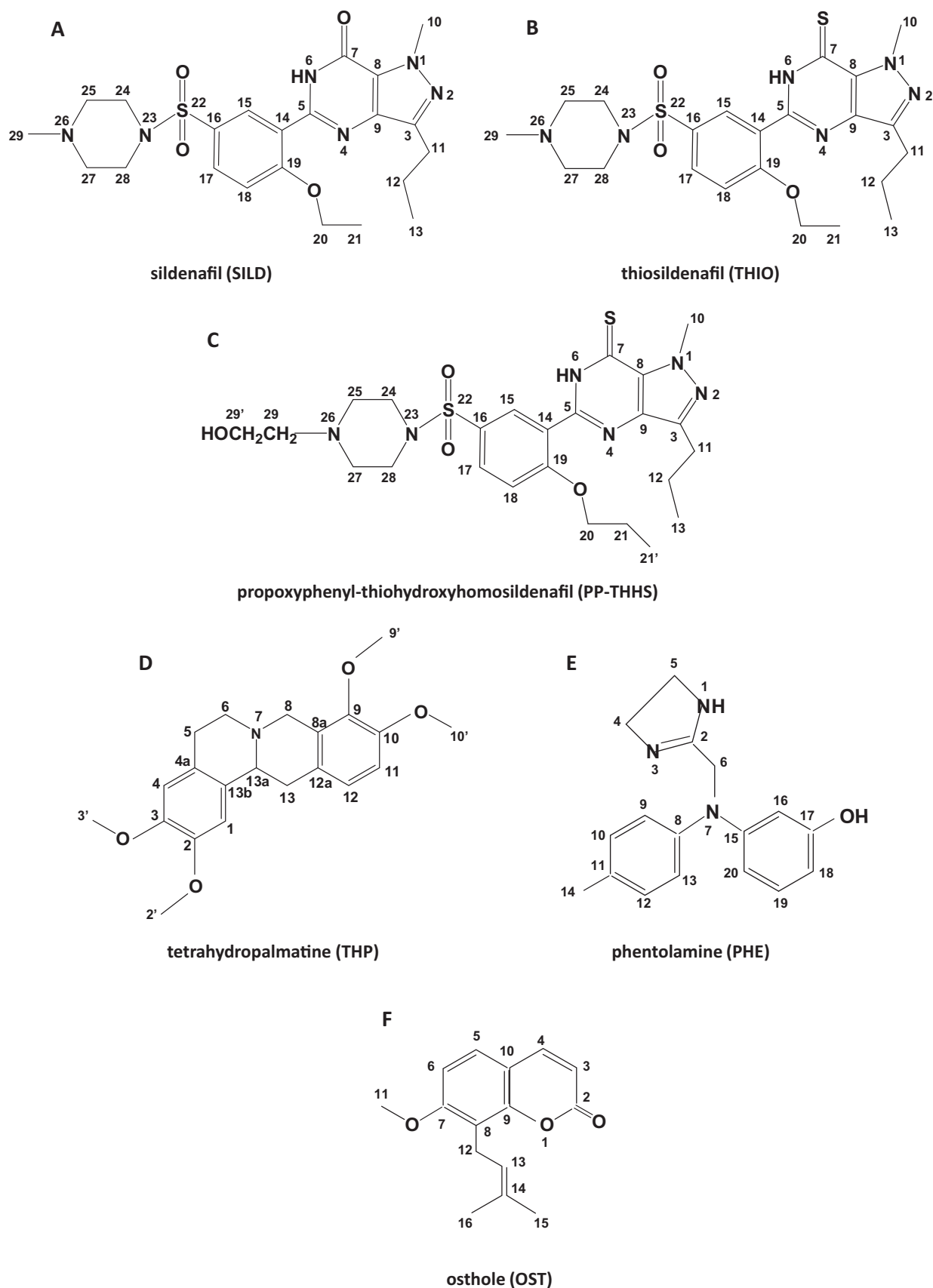


Fig. 1. Chemical structures of the actives identified in the dietary supplements analyzed: (A) sildenafil (SILD), (B) thiosildenafil (THIO), (C) propoxyphenyl-thiohomosildenafil (PP-THHS), (D) tetrahydropalmatine (THP), (E) phentolamine (PHE), (F) osthole (OST).

identical, whereas those of all the other formulations displayed different fingerprints. As an illustration, we present in Figs. 2 and 3 the characteristic ^1H NMR spectra of formulations 4, 5, 6, 8 and 9. All the spectra revealed the presence of sugar(s) (S) with anomeric signal(s) at ≈ 5.3 ppm and highly overlapped peaks between ≈ 3.4 and 3.8 ppm, and fatty acids (FA) with characteristic signals at ≈ 0.9 (terminal CH_3 protons), ≈ 1.3 ppm ($-(\text{CH}_2)_n-$ protons), ≈ 1.5 ppm (CH_2 protons β to the carboxyl group) and ≈ 2.2 ppm (CH_2 protons α to the carboxyl group). S (Fig. 3) and FA resonances were respectively lined up in the 2D DOSY ^1H NMR spectra. Ethanol (EtOH; triplet at 1.13 ppm) was detected in formulations 2, 6, 7 and 9, and citrate (AB system with δ_A 2.68 ppm and δ_B at 2.62 ppm, $J = 15.4$ Hz) in formulations 6 and 7. Mesylate (singlet at 2.61 ppm), a non-toxic acid often used to form salts of active pharmaceutical ingredients containing basic centers, was observed in formulation 8. Other major resonances were present in all formulations. They could correspond to PDE-5 inhibitors in formulations 1–7.

3.2. Characterization of the new SILD analog in formulations 1–4

2D DOSY ^1H NMR spectra of formulations 1–4 presented a pattern of identical lined up resonances which strongly looked like that of a PDE-5 inhibitor (data not shown). Moreover, the profile

of the aromatic protons of this compound called compound 1 (**1**) resembled the coupling pattern of a 1,2,4-substituted phenyl ring system and suggested that its chemical structure could be related to that of a PDE-5 inhibitor derived from SILD or vardenafil.

The LC-DAD analysis of extracts of these formulations showed the presence of a major peak at RT 4.5 min whose UV spectrum with absorption bands at λ_{max} 227, 295 and 353 nm (Fig. 4) was similar to that of THIO (λ_{max} 224, 295 and 354 nm), and different from that of SILD (λ_{max} 211, 224 and 291 nm). All the pyrazolopyrimidinethiones (THIO and analogs) and PDE-5 inhibitors with imidazoquinazolinethione-type chemical structure present a band at 350–370 nm, which was ascribed to the conjugated heterocyclic thiones ([7–10] for some examples), whereas the UV absorption bands of pyrazolopyrimidinones (SILD and analogs) as well as PDE-5 inhibitors with imidazotriazenone core (vardenafil and analogs) and piperazinedione ring (tadalafil and analogs) appear at $\lambda \leq 300$ nm ([7,8,11] for some examples). It can be thus inferred that **1** was a THIO analog.

^1H and ^{13}C NMR data of THIO and isolated **1** are summarized in Table 1. The 1D ^1H and ^{13}C NMR spectra of isolated **1** are presented in Fig. 5, while the ^1H NMR spectrum of THIO in a commercial formulation was reported in a previous paper [2]. The strong resemblance of ^1H and ^{13}C NMR spectra of the two compounds also indicated that **1** is a THIO derivative. Indeed,

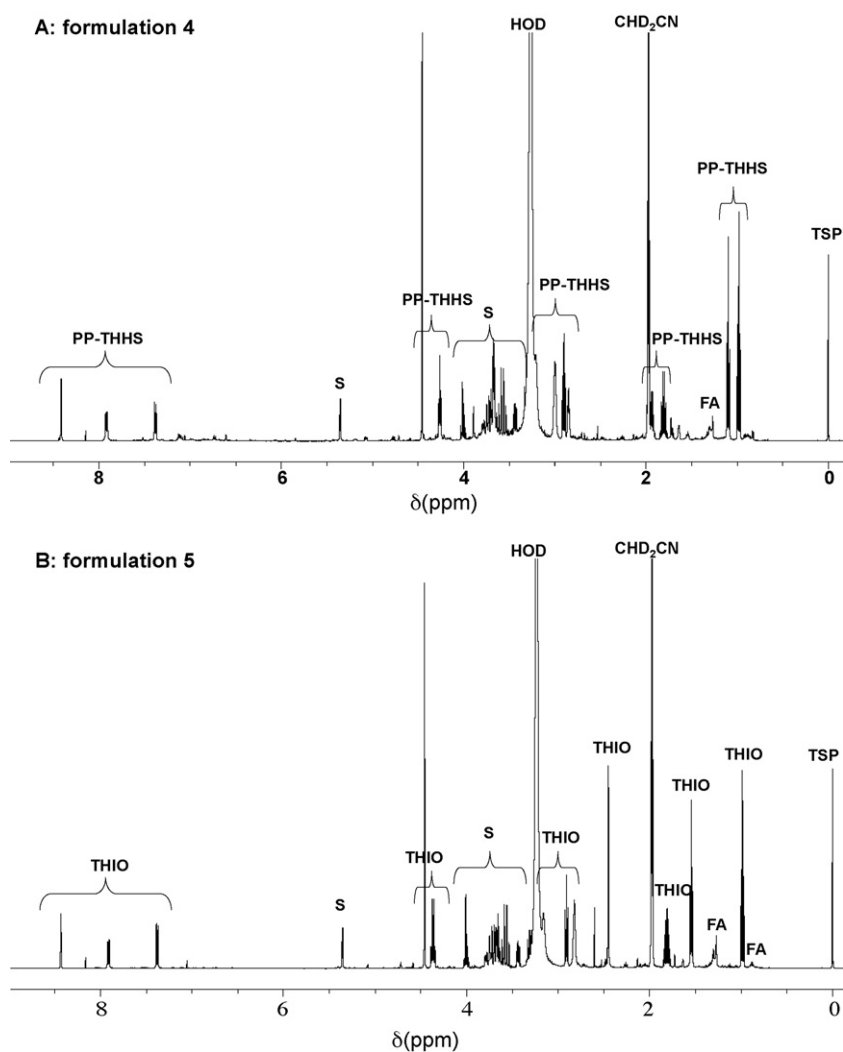


Fig. 2. ^1H NMR spectra of $\text{CD}_3\text{OD}:\text{D}_2\text{O}$ (80:20) extracts of (A) formulation 4, (B) formulation 5, (C) formulation 6 and (D) formulation 9.

PP-THHS: propoxyphenyl-thiohydroxyhomosildenafil, THIO: thiosildenafil, SILD: sildenafil, THP: tetrahydropalmatine, OST: osthole, ●: imperatorine; S: sugars, FA: fatty acids, EtOH: ethanol, TSP: sodium 2,2,3,3-tetradeutero-3-trimethylsilylpropionate (internal reference).

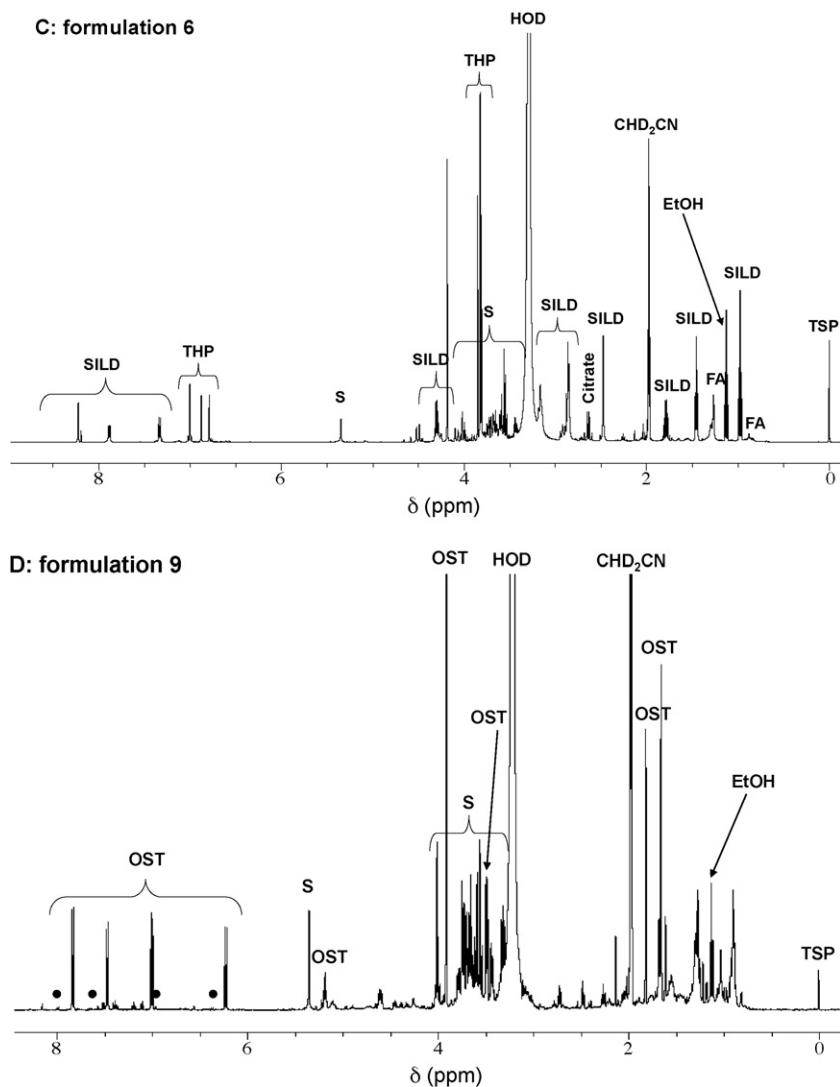


Fig. 2. (Continued).

the ^{13}C signal at 175.7 ppm and the ^1H singlet at 4.46 ppm are respectively characteristic of the $\text{N}-\text{C}=\text{S}$ and $\text{N}-\text{CH}_3$ moieties of a THIO pyrazolopyrimidine ring as the corresponding resonances in a SILD pyrazolopyrimidine ring would appear in the range 148–154 ppm (for the $\text{N}-\text{C}=\text{O}$ group) and 4.15–4.3 ppm [11–13]. Moreover, the NMR characteristics of protons (δ and J) and protonated carbons (δ) of pyrazolopyrimidine (and its N -methyl and C -propyl lateral chains) and phenyl rings are very similar for **1** and THIO (within 0.03 ppm for ^1H and with a systematic mean deshielding of 1.25 ppm (range 0.8–1.55 ppm) for ^{13}C). However, the ^1H (s, 2.38 ppm) and ^{13}C (44.9 ppm) methyl resonances of the N -methylpiperazine (NMP) entity of THIO are missing in the spectra of **1**. On the other hand, two triplets at 2.49 and 3.57 ppm, with a $\text{H}-\text{H}$ COSY correlation between them, each integrating for two protons, are present in the ^1H spectrum of **1**. Their ^{13}C resonances were assigned at 61.9 and 60.9 ppm, respectively from HSQC correlations. These data indicated the presence of a hydroxyethyl moiety. HMBC correlations between the ^1H triplet at 2.49 ppm and the ^{13}C resonance at 54.8 ppm (C-25/27) of the piperazine ring as well as those between the protons 25/27 at 2.58 ppm and the ^{13}C signal at 61.9 ppm demonstrated that the NMP moiety of THIO was replaced by an N -hydroxyethylpiperazine (NHEP) in **1**. Moreover, a ^1H signal at 1.93 ppm (tq) which is not present in THIO was observed in **1**. The $\text{H}-\text{H}$ COSY correlations

between this signal and those at 4.26 ppm (t) and 1.10 ppm (t) suggested the presence of a propoxy moiety instead of an ethoxy group. The correlations observed in HSQC and HMBC experiments supported this assignment and established that the substitution occurred at the C19 position of the phenyl ring. **1** was thus identified as 5-{5-[4-(2-hydroxyethyl)piperazine-1-sulfonyl]-2-propoxyphenyl}-1-methyl-3-propyl-1,6-dihydropyrazolo[4,3-d]pyrimidine-7-thione hereinafter referred to as propoxyphenyl-thiohydroxyhomosildenafil (PP-THHS) (Fig. 1C) since the THIO analog with an ethoxyphenyl group is named as thiohydroxyhomosildenafil (THHS).

To confirm the structure of **1**, a MS study was conducted. The full scan mass spectrum exhibited the presence of a very major pseudo-molecular ion $[\text{M}+\text{H}]^+$ at m/z 535. The accurate mass of this ion was found at m/z 535.2162 in agreement with the calculated mass 535.2161 of $\text{C}_{24}\text{H}_{35}\text{N}_6\text{O}_4\text{S}_2$ within 0.2 ppm, which corresponds to the atomic composition of PP-THHS $\text{C}_{24}\text{H}_{34}\text{N}_6\text{O}_4\text{S}_2$. The parent ion was selected to be fragmented in the MS/MS system. It produced two prominent ions at m/z 299 and 99 and other representative fragment ions at m/z 517, 359, 341, 315, 271, 129, 112, 84 and 58 (Fig. 6). A summary of proposed structures for these ions is depicted in Fig. 7. The product ion at m/z 517 (loss of H_2O from the hydroxyethyl group) was very probably formed by an initial migration of the hydroxyethyl group to the sulfur atom of the

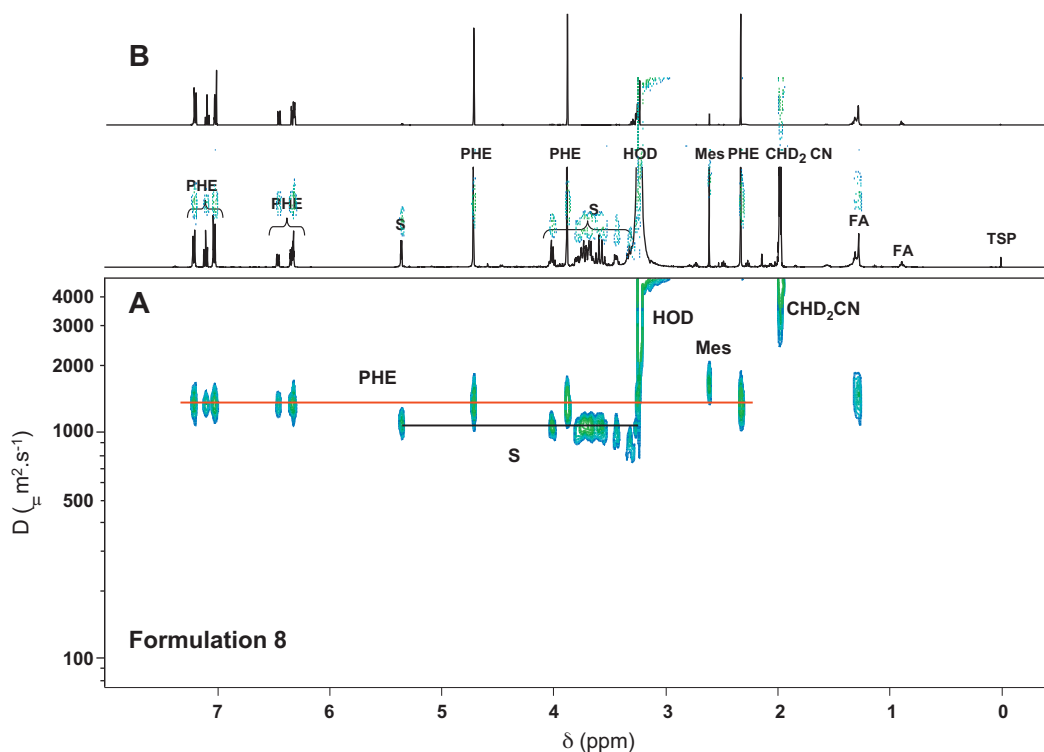


Fig. 3. (A) 2D DOSY ^1H NMR spectrum of a $\text{CD}_3\text{CN}:\text{D}_2\text{O}$ (80:20) extract of formulation 8. (B) 1D ^1H NMR spectrum of phentolamine (PHE) extracted from the 2D DOSY ^1H NMR spectrum at $D = 1356 \mu\text{m}^2 \text{s}^{-1}$.

S: sugars, Mes: mesylate, FA: fatty acids, TSP: sodium 2,2,3,3-tetradeutero-3-trimethylsilylpropionate (internal reference).

thiocarbonyl function, followed by elimination of water (Fig. 7(a)), as recently demonstrated for THHS [14]. The heterolytic cleavage of the S–N sulfonamide bond generated peaks corresponding to NHEP ion at m/z 129 and fragment ions at m/z 112 (loss of hydroxyl radical) and 99 (loss of methanal) which respectively give other ions at m/z 84 (loss of methyleneamino radical) and 58 (loss of neutral azirine entity). The structures of all these ions (Fig. 7(b)) were proposed by Ahn et al. [15]. The product ions at m/z 341 and 299 arise respectively from successive losses of a neutral molecule of 194 Da corresponding to the sulfinic acid $\text{NHEP-SO}_2\text{H}$ ($\text{C}_6\text{H}_{14}\text{N}_2\text{O}_3\text{S}$) (Fig. 7(c)) and neutral propene (C_3H_6) entity from the propoxy substituent of the phenyl ring (Fig. 7(d)). The first fragmentation was previously described for SILD and THIO with formation of analogous ions at m/z 311 and 327 which have an expected mass shift of 30 and 14 Da respectively compared to that

of the corresponding PP-THHS ion [16]. The second fragmentation is identical to that reported in the literature for the ethyl group of an ethoxy substituent leading to the same ion at m/z 299 for THIO, thiohomosildenafil and THHS and to an ion at m/z 283 for SILD, homosildenafil and hydroxyhomosildenafil with a mass shift of 16 Da as the C=S group is replaced by a C=O [8,10,14]. The ion at m/z 271 was observed not only in the MS/MS spectrum of PP-THHS but also in those of THIO, thiohomosildenafil and THHS. It could be generated from the ion at m/z 299 by loss of a neutral ethene (C_2H_4) moiety from the propyl chain of the pyrazolopyrimidine ring [8,10,14] (Fig. 7(e)). Indeed, this fragmentation pathway from the propyl chain of vardenafil, an isomer of SILD, was reported by Gratz et al. [17]. Moreover, SILD, homosildenafil and hydroxyhomosildenafil also exhibit a similar fragmentation as an ion at m/z 255 most probably formed by the loss of a neutral C_2H_4 molecule from the

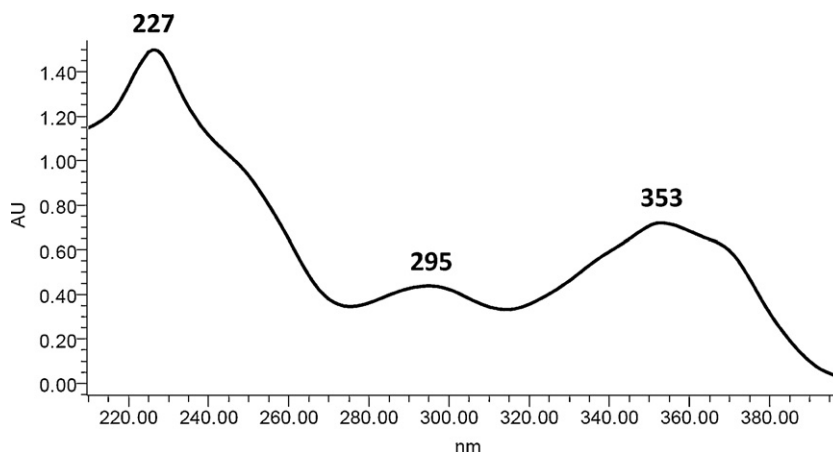


Fig. 4. UV spectrum of the new sildenafil analog, propoxyphenyl-thiohydroxyhomosildenafil, obtained using the chromatographic conditions indicated in the Section 2.

Table 1
NMR data of thiosildenafil (THIO) and propoxyphenyl-thiohydroxyhomosildenafil (PP-THHS, **1**) in CD₃CN/D₂O 80/20.

THIO				PP-THHS (1)								
Pos ^a	Group	δ ¹ H (ppm)	Multiplicity ^b (J (Hz))	δ ¹³ C (ppm)	δ ¹ H (ppm)	Multiplicity ^b (J (Hz))	H,H-COSY		δ ¹³ C (ppm)	HMBC		
							³ J	⁴ J		² J	³ J	⁴ J
3	Cq aromatic			147.3					148.4	H-11	H-12	
5	Cq aromatic			148.5					152.0		H-15	H-18
7	Cq C=S			173.6					175.7			H-10
8	Cq aromatic			133.7					135.6		H-10	
9	Cq aromatic			135.0					137.2		H-11	
10	N—CH ₃	4.45	s	40.3	4.46	s			41.6			
11	CH ₂	2.91	t (7.4)	28.4	2.90	t (7.4)		H-12	29.9	H-12	H-13	
12	CH ₂	1.81	sext (7.4)	23.3	1.80	sext (7.4)		H-11, H-13	24.8 ₅	H-11, H-13		
13	CH ₃	0.98	t (7.4)	14.6	0.99	t (7.4)		H-12	16.0	H-12	H-11	
14	Cq aromatic			122.2					125.8	H-15	H-18	H-17
15	CH aromatic	8.41	d (2.5)	131.6	8.40	d (2.5)			133.0		H-17	
16	Cq aromatic			128.8					130.1	H-15, H-17	H-18	
17	CH aromatic	7.91	dd (2.5, 8.9)	133.8	7.94	dd (2.5, 8.9)		H-18	134.6		H-15	
18	CH aromatic	7.38	d (8.9)	115.7	7.40	d (8.9)		H-17	116.5	H-17		H-15
19	Cq aromatic			162.0					163.3	H-18	H-15, H-17, H-20	
20	O—CH ₂	4.36	q (7.0)	67.7	4.26	t (6.3)		H-21	74.4	H-21	H-21'	
21	CH ₃ or CH ₂	1.54	t (7.0)	15.4	1.93	tq (7.4, 6.3)		H-20, H-21'	24.9	H-20, H-21'		
21'	CH ₃				1.10	t (7.4)		H-21	12.9	H-21	H-20	
24/28	N—CH ₂ piperazine	3.13	broad signal	45.6	3.06	broad signal		H-25/27	48.6	H-25/27		
25/27	N—CH ₂ piperazine	2.72 ^c	t (4.3)	54.3	2.58 ^c	t (4.8)		H-24/28	54.8	H-24/28	H-29	
29	N—CH ₃ or N—CH ₂	2.38	s	44.9	2.49	t (5.9)		H-29'	61.9	H-29'	H-25/27	
29'	CH ₂ OH				3.57	t (5.9)		H-29	60.9	H-29		

^a Position (Pos) number (see Fig. 1B and C for the numbering) indicates either hydrogen (H,H-COSY) or carbon (HMBC) signal.

^b s: singlet; d: doublet; dd: doublet of doublet; t: triplet; q: quadruplet; tq: triplet of quadruplet; sext: sextuplet.

^c Strongly broadened signals.

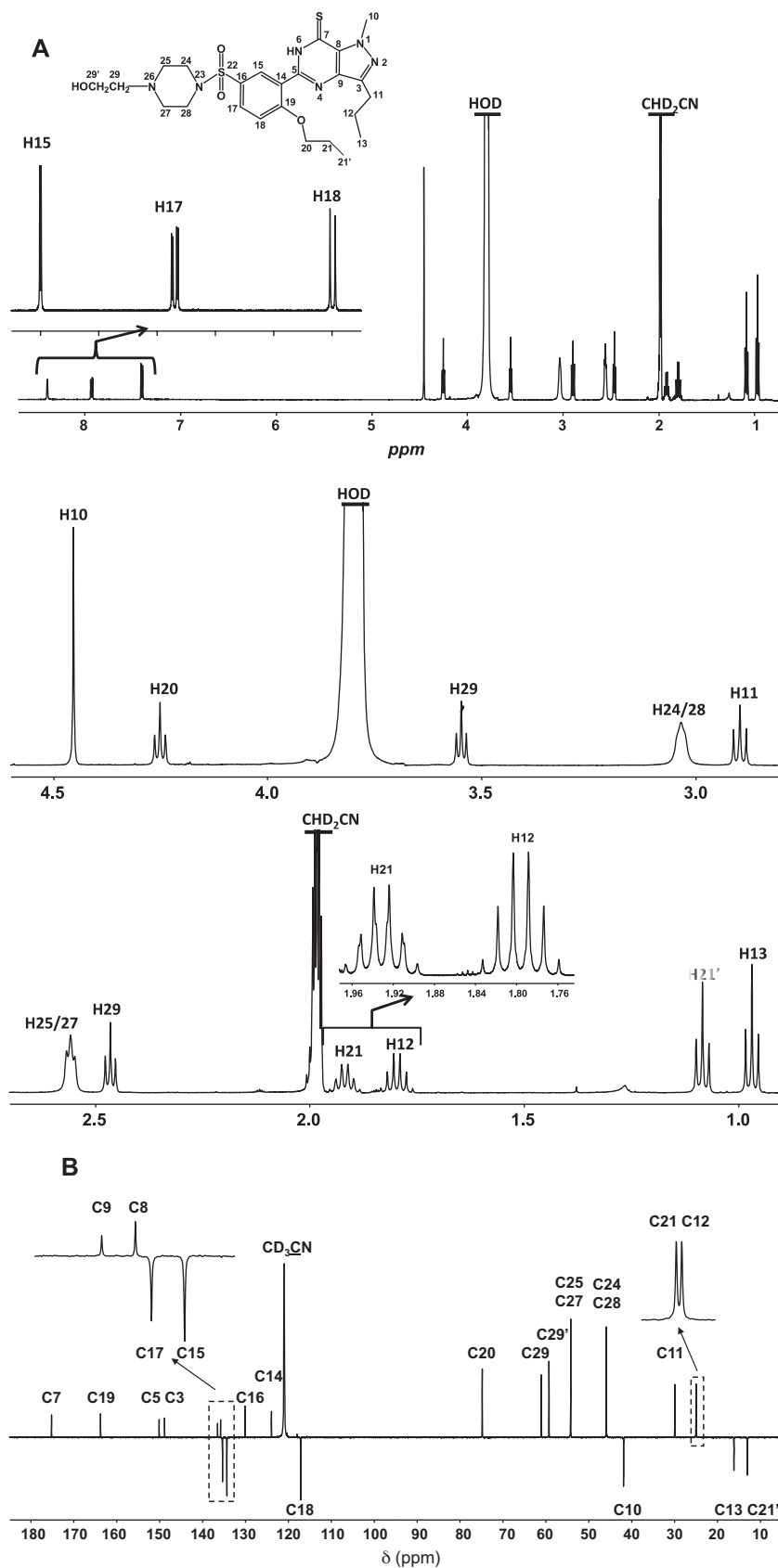


Fig. 5. ^1H (A) and ^{13}C (B) NMR spectra of the new sildenafil analog, propoxyxyphenyl-thiohydroxyhomosildenafil, after isolation and purification, recorded in $\text{CD}_3\text{CN}:\text{D}_2\text{O}$ (80:20).

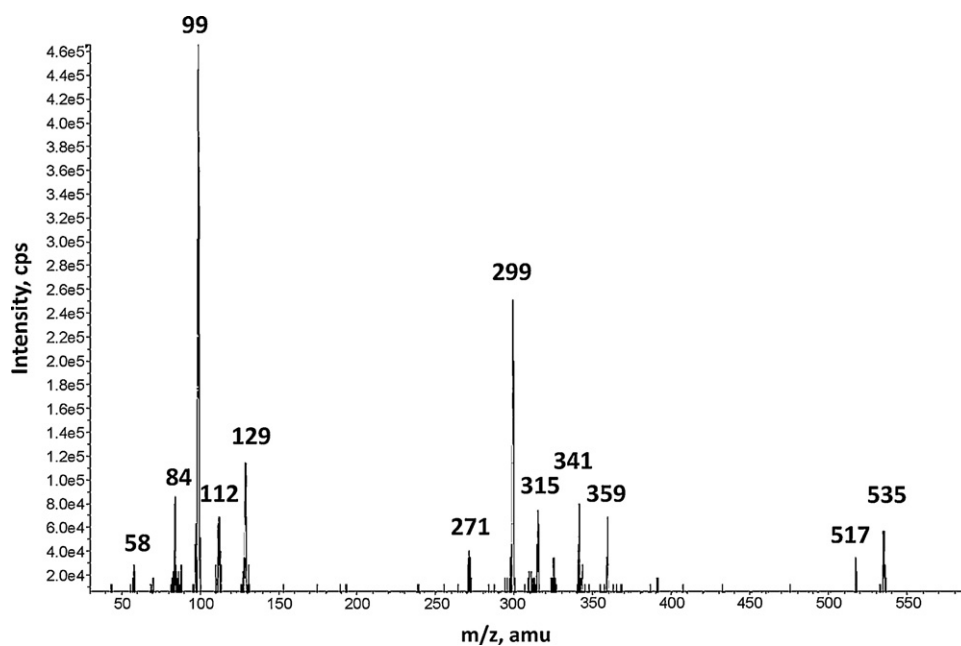


Fig. 6. MS–MS spectrum of pure propoxyphenyl-thiohydroxyhomosildenafil (product ion spectrum of the molecular peak at m/z 535).

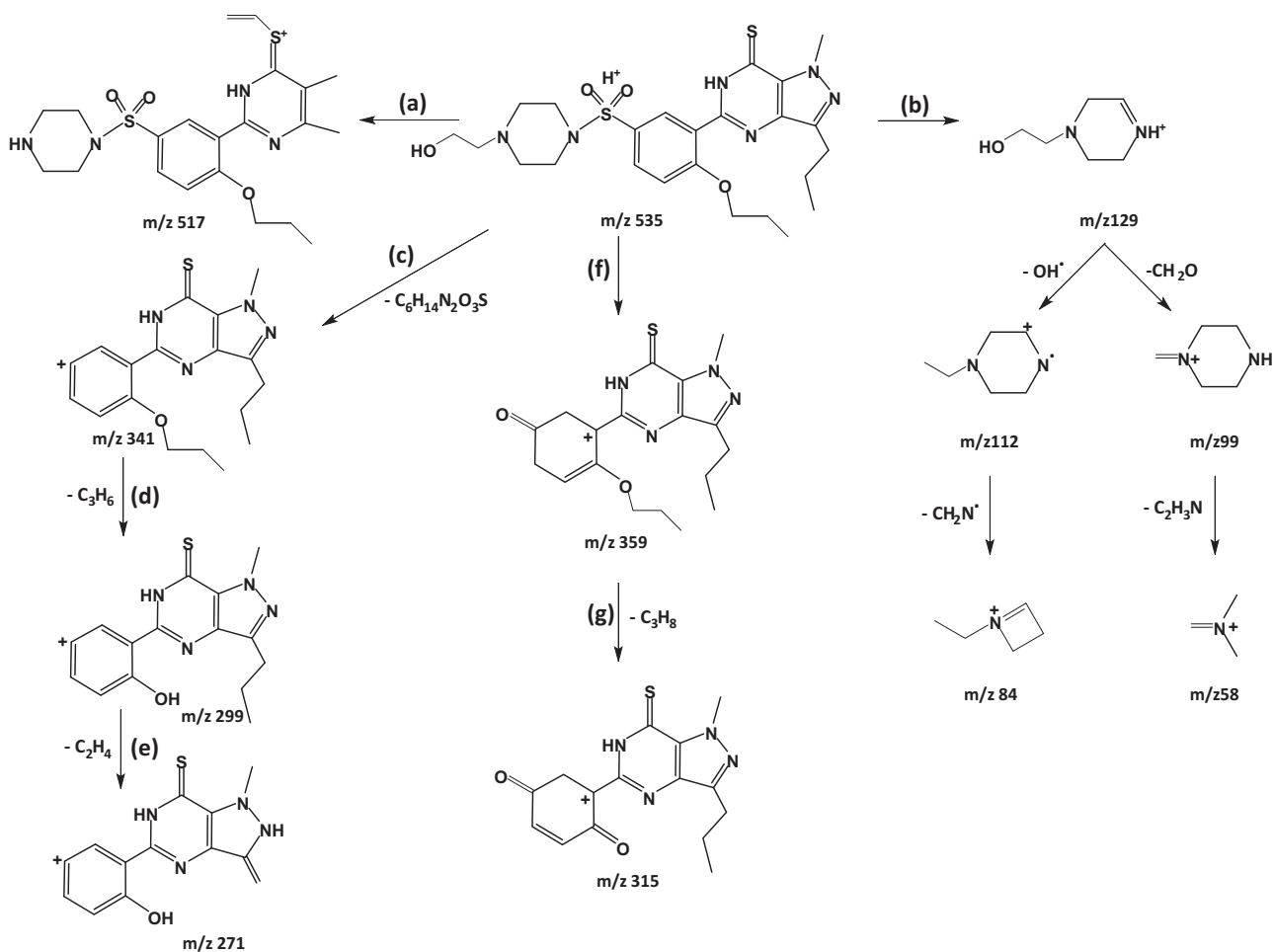


Fig. 7. Summary of proposed fragmentation pathways for the new analog propoxyphenyl-thiohydroxyhomosildenafil.

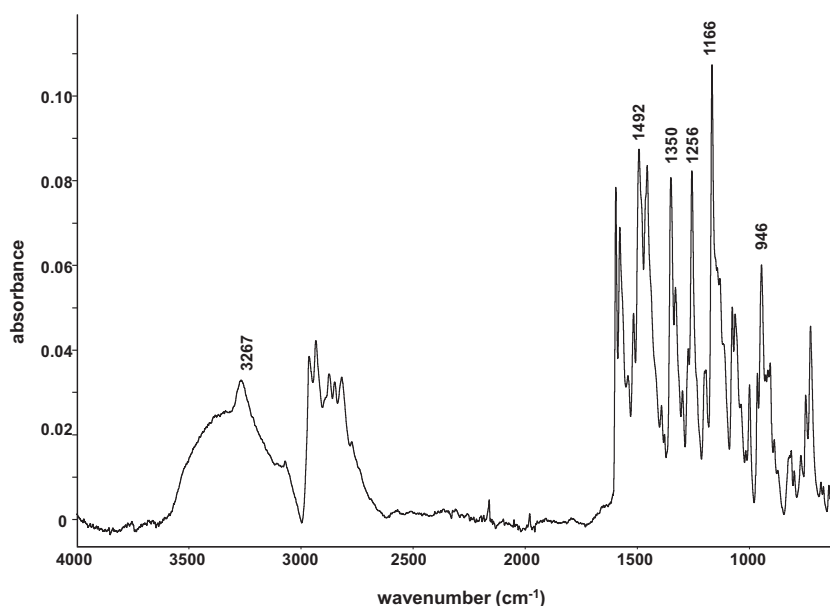


Fig. 8. Infrared spectrum of the new sildenafil analog, propoxyphenyl-thiohydroxyhomosildenafil.

prominent ion at m/z 283 is observed [8]. The structure of the ion at m/z 359 was tentatively proposed to be the same than that reported for SILD ion at m/z 329 [17]. Indeed, it exhibits a mass shift of 30 Da as expected due to replacements of the C=O and ethoxy groups of SILD with C=S and propoxy groups, respectively (Fig. 7(f)). The ion at m/z 315 could be generated from the ion at m/z 359 by the cleavage of the O–C bond of the propoxy moiety followed by the formation of a cationic 1,4-benzoquinone moiety resulting in the loss of the neutral propane (C_3H_8) molecule (Fig. 7(g)). The structure of this ion is similar to that reported for the vardenafil fragment ion at m/z 299 with a mass shift of 16 Da as the carbonyl group is replaced by a thiocarbonyl group [17].

The IR spectrum of isolated **1** is reported in Fig. 8. It displayed an absorption band at 3267 cm^{-1} , characteristic of the N–H stretching vibration of an amine moiety. The three bands at 1492 , 1256 and 946 cm^{-1} suggested the presence of a thioamide (N–C=S) group. Indeed, in such a group, the C=S stretching vibration is strongly coupled to that of the C–N part leading to three signals in the regions 1570 – 1395 cm^{-1} , 1420 – 1260 cm^{-1} and 1140 – 940 cm^{-1} that are partly due to the $\nu_{C=S}$ vibration [18]. The strong absorption bands at 1350 and 1166 cm^{-1} correspond to the asymmetric and symmetric stretching vibrations of SO_2 in a sulfonamide group that occur respectively at 1360 – 1315 cm^{-1} and 1180 – 1140 cm^{-1} in the solid phase [18]. These characteristic group frequencies are very similar to those observed in THIO (ν_{NH} at 3271 cm^{-1} , $\nu_{C=S}$ at 1498 , 1253 and 939 cm^{-1} and ν_{SO_2} at 1352 and 1171 cm^{-1} , confirming that **1** is a THIO analog.

To our knowledge, PP-THHS already patented by Kim et al. [19] in 2004 was never detected as an adulterant in a dietary supplement.

3.3. Characterization of THIO in formulation 5

In the 2D DOSY 1H NMR spectrum of formulation 5, the resonances pattern of the major compound was very similar to that observed in formulations 1–4. This compound was identified as THIO (Fig. 1B) by spiking with an authentic standard and comparing the 1H NMR spectra recorded before and after its addition.

3.4. Characterization of SILD and THP in formulations 6 and 7

In addition to the lined up resonances of S (translational diffusion coefficient (D) = $865\text{ }\mu\text{m}^2\text{ s}^{-1}$) and FA ($D = 1118\text{ }\mu\text{m}^2\text{ s}^{-1}$), the 2D DOSY 1H NMR spectra displayed those of ethanol and two other major compounds with close D values. The pattern of resonances of the first one ($D = 947\text{ }\mu\text{m}^2\text{ s}^{-1}$) was consistent with a PDE-5 inhibitor of the SILD class. It was definitely identified as the citrate salt of SILD (Fig. 1A) by comparison of the 1H NMR spectra of the crude formulation extracts before and after addition of authentic SILD citrate. The 1H NMR characteristics of the second main compound ($D = 1069\text{ }\mu\text{m}^2\text{ s}^{-1}$), called compound **2** (**2**), did not match with a usual PDE-5 inhibitor structure. **2** was isolated with a purity of 80% with residual presence of less than 15% of SILD.

The 1H and ^{13}C NMR spectra of **2** indicated the presence of two aromatic rings with eight quaternary carbons (Cq), four methoxy groups and five other aliphatic carbon signals. The 1D and 2D COSY 1H NMR spectra exhibited resonances of CH_2 – CH_2 and CH – CH_2 spin systems as well as a pair of doublets each integrating for one proton at δ 3.62 and 4.22 ppm with a large J_{H-H} (16.1 Hz) characteristic of geminal protons. The corresponding ^{13}C signal of these two protons at 55.6 ppm as determined from the HSQC experiment indicated that this isolated methylene group was probably a N– CH_2 moiety. The aromatic region displayed two singlets each integrating for one proton consistent with two para related hydrogens in one of the aromatic rings and an AB pattern integrating for two protons with $J = 9.1\text{ Hz}$ which suggested the presence of two ortho hydrogens in the second aromatic ring. Unambiguous assignments of Cq were achieved considering that the cross-peaks in the HMBC experiment were more intense for $^3J_{C-H}$ correlations than for 2J or $^4J_{C-H}$ across the aromatic systems. The H–H, direct C–H and long-range C–H bond correlations observed in the COSY, HSQC and HMBC experiments supported the assignment of all 1H and ^{13}C signals summarized in Table 2 and allowed identifying **2** as THP (5,8,13,13a-tetrahydro-2,3,9,10-tetramethoxy-6H-dibenzo[a,g]quinolizine) (Fig. 1D). The 1H and ^{13}C NMR assignments were slightly different from those previously reported data [20].

High-resolution MS (HR-MS) and MS/MS studies of **2** corroborated its identification as THP. Indeed, the accurate mass of

Table 2
NMR data of tetrahydropalmatine (THP; **2**) in CD₃CN/D₂O 80/20.

Pos ^a	Group	δ ¹ H (ppm)	Multiplicity ^b (J (Hz))	H,H-COSY		δ ¹³ C (ppm)	HMBC		
				² J	³ J		² J	³ J	⁴ J
1	CH aromatic	6.87	s			111.7			
2	Cq aromatic					150.3			H-4, H-2'
3	Cq aromatic					150.2			H-1, H-3'
4	CH aromatic	6.76	s			114.4			H-5 _{p-ax}
4a	Cq aromatic					129.0	H-5 _{p-ax} , H5 _{p-eq}		H-1
5 ^c	CH ₂	H _{p-ax} 2.74 ^d H _{p-eq} 3.07 ^e	d (16.9) m	H-5 _{p-eq} H-5 _{p-ax}	H-6 _{eq} H-6 _{eq} , H-6 _{ax}	30.4			H-4
6 ^c	N—CH ₂	H _{ax} 2.71 ^d H _{eq} 3.27 ^e	dd (11.9, 8.8) d (9.3)	H-6 _{eq} H-6 _{ax}	H-5 _{p-eq} H-5 _{p-eq} , H-5 _{p-ax}	53.6	H-5 _{p-eq}		H-8 _{p-ax} , H-8 _{p-eq} , H-13a
8 ^c	N—CH ₂	H _{p-ax} 3.62 H _{p-eq} 4.22	d (16.1) d (16.1)	H-8 _{p-eq} H-8 _{p-ax}		55.6			H-6 _{ax} , H-13a
8a	Cq aromatic					129.8 ₅	H8 _{p-ax} , H8 _{p-eq}		H-12, H-13 _{p-ax} , H-13 _{p-eq}
9	Cq aromatic					147.4			H11, H-8 _{p-eq} , H-9'
10	Cq aromatic					153.1			H-12, H-10'
11	CH aromatic	6.94 ₅	AB system (B) (9.1)			114.4	H-12		
12	CH aromatic	6.95	AB system (A) (9.1)			127.0	H-11		
12a	Cq aromatic					129.9	H13 _{p-ax} , H-13 _{p-eq}		H-13 _{p-eq}
13 ^c	CH ₂	H _{p-ax} 2.73 ^d H _{p-eq} 3.46	dd (15.8, 12.4) dd (16.1, 3.3)	H-13 _{p-eq} H-13 _{p-ax}	H-13a H-13a	37.5			H-12
13a ^c	N—CH (H _{ax})	3.69 ^e	d (10.1)		H-13 _{p-ax} , H-13 _{p-eq}	61.8	H-13 _{p-ax} , H-13 _{p-eq}		H-6 _{ax} , H-6 _{eq} , H-8 _{p-ax} , H-8 _{p-eq}
13b	Cq aromatic					131.3	H-13a		H-4, H-5 _{p-ax} , H-13 _{p-ax}
2'	O—CH ₃	3.80	s			58.1			
3'	O—CH ₃	3.81 ₅	s			58.3			
9'	O—CH ₃	3.79 ₅	s			62.6			
10'	O—CH ₃	3.84	s			58.3			

^a Position (Pos) number (see Fig. 1D for the numbering) indicates either hydrogen (H,H-COSY) or carbon (HMBC) signal.

^b s: singlet; d: doublet; dd: doublet of doublet; m: multiplet.

^c As the two benzene moieties in the tetrahydroprotoberberine skeleton force the carbons of the non-planar quinolizidine core to adopt a conformation similar to cyclohexene, the protons on carbons adjacent to the unsaturated bonds (C-5, C-8, C-13 and C-13a) are tilted from the usual axial/equatorial (ax/eq) orientation to a pseudo-axial/pseudo-equatorial (p-ax/p-eq) orientation, except the proton on C-13a because the trans-fused quinolizidine system requires an axially oriented substituent. The ax/eq or p-ax/p-eq protons were assigned considering that, for each methylene group, the axial proton is more shielded than the equatorial.

^d The signals of H-5_{p-ax}, H-6_{ax} and H-13_{p-ax} are overlapped. Their respective δ and J were determined from the fine structure of the cross-peaks in the HSQC spectrum.

^e Strongly broadened signals.

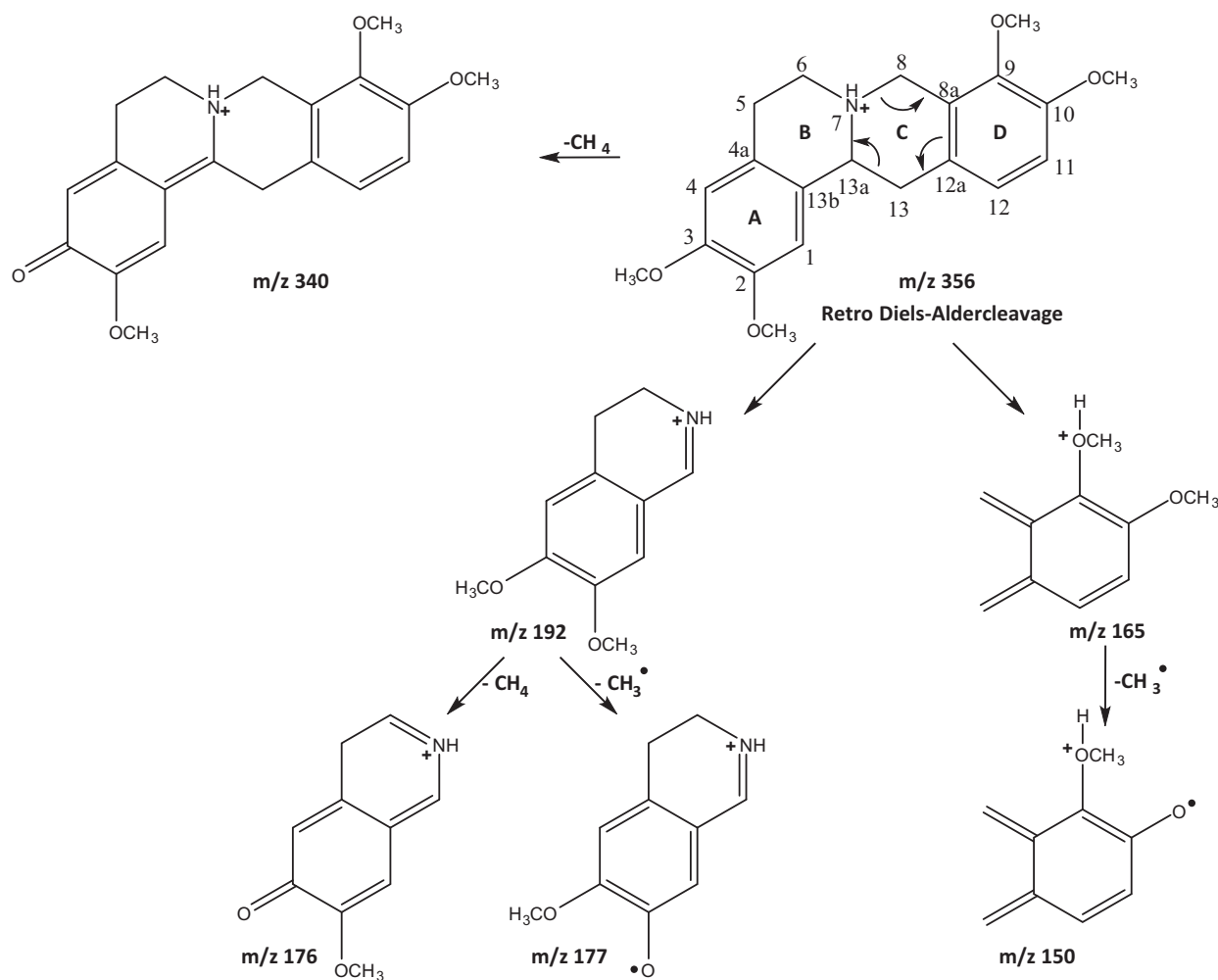


Fig. 9. Tentatively proposed structures of representative product ions of protonated tetrahydropalmatine (THP).

the protonated molecular ion was measured at m/z 356.1859 in agreement with the calculated mass 356.1862 of $\text{C}_{21}\text{H}_{26}\text{NO}_4$ within an error of -0.8 ppm, which corresponds to the elemental composition of THP, $\text{C}_{21}\text{H}_{25}\text{NO}_4$. Moreover, the HR MS/MS spectrum revealed representative product ions at various m/z within 1.2 ppm relative to calculated masses, except for ion at m/z 192 for which the error reached 3.1 ppm (Table 3). The elemental formulae of these protonated ions correspond to characteristic fragments due to a retro Diels–Alder cleavage of ring C of a tetrahydroberberine skeleton into two pieces that can be protonated (see for example [21]) (Fig. 9). Moreover, these two product ions and the parent ion can release a neutral methyl radical and/or a neutral methane molecule from a methoxy group.

3.5. Characterization of PHE in formulation 8

The ^1H NMR spectrum of formulation 8 showed unknown resonances along with those of S, FA, and mesylate (Fig. 3). The fact that all the major unknown resonances were lined up in the 2D DOSY ^1H NMR spectrum at $D = 1356 \mu\text{m}^2 \text{s}^{-1}$ supports the presence of a sole major product, called compound 3 (**3**) (Fig. 3A). The corresponding ^1H slice DOSY spectrum enables the attribution of the resonances of **3** even if two signals of FA are detected due to the closeness of their D values ($1492 \mu\text{m}^2 \text{s}^{-1}$ for FA) (Fig. 3B).

The ^1H and ^{13}C NMR characteristics of **3** were determined on the crude extract of formulation 8 and are listed in Table 4. The aliphatic region of the ^1H NMR spectrum exhibited three aliphatic singlet signals at δ 2.32, 3.87 and 4.71 ppm integrating respectively

Table 3
Accurate masses of protonated THP (**2**) and of its major product ions.

Mass found	Mass calculated	Error (ppm)	Elemental formula
356.1859	356.1862	-0.8	$\text{C}_{21}\text{H}_{26}\text{NO}_4$
340.1550	340.1549	0.3	$\text{C}_{20}\text{H}_{22}\text{NO}_4$
192.1031	192.1025	3.1	$\text{C}_{11}\text{H}_{14}\text{NO}_2$
177.0791	177.0790	0.6	$\text{C}_{10}\text{H}_{11}\text{NO}_2$
176.0714	176.0712	1.1	$\text{C}_{10}\text{H}_{10}\text{NO}_2$
165.0918	165.0916	1.2	$\text{C}_{10}\text{H}_{13}\text{O}_2$
150.0681	150.0681	0	$\text{C}_9\text{H}_{10}\text{O}_2$

Table 4
NMR data of phentolamine (PHE; **3**) mesylate in CD₃CN/D₂O 80/20.

Pos ^a	Group	δ ¹ H (ppm)	Multiplicity ^b (J (Hz))	H,H-COSY		δ ¹³ C (ppm)		HMBC			
				³ J	⁴ J	³ J	⁴ J	² J	³ J	⁴ J	
2	Cq aromatic										
4/5	CH ₂ -N (imidazoline)	3.87	s			171.6		H-6	H-4/5		
6	CH ₂ -N (phenyl)	4.71	s			45.8		H-4 (C5), H-5 (C4)			
8	Cq aromatic					50.2					
9/13	CH aromatic	7.03	AA'XX' system (XX')			145.5		H-9/13	H-10/12, H-6		
10/12	CH aromatic	7.21	AA'XX' system (AA')	H-10/12		124.4		H-10/12	H-9 (C13), H-13 (C9)		
11	Cq aromatic			H-9/13		131.3 _s		H-9/13	H-10 (C12), H-12 (C10)		
14	CH ₃	2.32	s		H-10/12	135.3		H-14	H-9/13		
15	Cq aromatic					21.0			H-10/12		
16	CH aromatic	6.31	t (2.2)		H-18, H-20	150.0		H-16, H-20	H-19, H-6		H-18
17	Cq aromatic					106.6			H-18, H-20		H-19
18 ^c	CH aromatic	6.45	ddd (8.8, 2.2, 0.8)		H-16	159.0		H-16, H-18	H-19		H-20
19	CH aromatic	7.10	t (8.1)			109.9					
20 ^c	CH aromatic	6.34	ddd (8.1, 2.3, 0.8)		H-16	131.4			H-16, H-20		
CH ₃ (mesylate)	2.61	s				111.1		H-19			
						39.7					

^a Position (Pos) number (see Fig. 1E for the numbering) indicates either hydrogen (H,H-COSY) or carbon (HMBC) signal.

^b s: singlet; t: triplet; ddd: doublet of doublet of doublet.

^c The ¹H and ¹³C assignments of CH-18 and CH-20 could be inverted.

for 3, 4 and 2 protons with corresponding HSQC direct carbon correlations at 21.0, 45.8 and 50.2 ppm. The aromatic region of the ¹³C spectrum displayed six protonated carbon signals corresponding to eight carbon atoms from comparison of their relative intensities, and five Cq signals indicating the presence of two aromatic rings. The ¹H spectrum showed resonances of eight aromatic protons. The AA'XX' system at δ 7.03 and 7.21 ppm had long-range H,H COSY correlations with the singlet signal of the methyl group (2.32 ppm) providing firm evidence of a para-methyl substituted aromatic ring. The multiplicity, coupling constants and H,H COSY correlations suggested that the second aromatic ring was 1,3-disubstituted. The long-range H,H COSY correlations between the N-CH₂ singlets at 3.87 and 4.71 ppm and their HMBC correlations with the Cq at 171.6 ppm which does not belong to the two aromatic rings suggested the presence of an imidazoline moiety with a CH₂-N substituent located at C2. Moreover, the other HMBC correlations between the N-CH₂ protons at 4.71 ppm and Cq at 145.5 (part of one aromatic ring) and 150.0 ppm (part of the second aromatic ring) implied that the N atom was connected to these two moieties. The meta substituent on the second aromatic ring could be assigned to an hydroxyl group based on the high δ value of the connected Cq (159.0 ppm). **3** was thus identified as PHE (3-[(4,5-dihydro-1H-imidazol-2-ylmethyl)(4-methylphenyl)amino]phenol) (Fig. 1E), whose structure was confirmed by comparison of the ¹H NMR spectra before and after addition of authentic PHE mesylate.

MS, MS/MS and HR-MS were carried out in positive ionization mode on the crude extract of formulation 8. The full scan mass spectrum showed the presence of a pseudo-molecular ion [M+H]⁺ at m/z 282. Based on the accurate mass determination, **3** has a chemical formula of C₁₇H₂₀N₃O for the [M+H]⁺ ion (measured mass m/z 282.1648, calculated mass m/z 282.1606, error 14.9 ppm) which corresponds to the atomic composition of PHE C₁₇H₁₉N₃O. The MS/MS fragmentation of the parent ion at m/z 282 produced a characteristic, dominant base peak at m/z 212 which is achieved with the loss of neutral imidazoline molecule.

3.6. Characterization of OST in formulation 9

The ¹H NMR spectrum of formulation 9 exhibited resonances of S, FA, EtOH and unknown compounds among which the major one was isolated for identification.

The ¹H and ¹³C NMR data of the purified compound, called compound 4 (**4**), are summarized in Table 5. In the aromatic region of the ¹H spectrum, two H,H COSY correlated pairs of doublets with a large coupling constant (\approx 9 Hz) were observed indicating the presence of two ortho protons located on two different aromatic rings. The methyl proton singlet at 3.94 ppm with a HSQC direct carbon correlation at 59.0 ppm was consistent with a methoxy group on an aromatic ring. H,H COSY correlations between the proton at 5.21 ppm and methylene (3.51 ppm) and methyl (1.68 and 1.84 ppm) signals indicated the presence of a (CH₂)HC=C(CH₃)₂ moiety. The ¹³C spectrum exhibited fifteen carbon signals: five aromatic and ethylenic CH, one CH₂ and three CH₃ in accordance with proton observations, and six Cq, one of them being ethylenic. Therefore, the two aromatic systems contained nine carbon atoms, four CH and five Cq. Based on the Cq chemical shift values, one corresponded to an O=C=O carbon suggesting the presence of a coumarine entity, and a second bore a methoxy group. HSQC and HMBC spectroscopic data provided firm evidence that **4** was OST (7-methoxy-8-(3'-methyl-2'-butenyl)-2H-1-benzopyrane-2-one) (Fig. 1F), whose structure was authenticated by spiking with standard OST and comparing the ¹H spectra before and after addition. Moreover, an unequivocal assignment of all ¹H and ¹³C resonances of OST was accomplished by a careful inspection of the correlations observed in the H,H COSY

Table 5
NMR data of osthole (OST; **4**) in CD₃CN/D₂O 80/20.

Pos ^a	Group	$\delta^1\text{H}$ (ppm)	Multiplicity ^b (J (Hz))	H,H-COSY		$\delta^{13}\text{C}$ (ppm)	HMBC	
				³ J	⁴ J		² J	⁴ J
2	Cq (C=O)					165.0	H-3	
3	CH aromatic	6.26	d (9.5)	H-4		115.2	H-4	H-4
4	CH aromatic	7.88	d (9.5)	H-3		148.0	H-3	H-5
5	CH aromatic	7.51	d (8.7)	H-6		130.1	H-6	H-4
6	CH aromatic	7.04	d (8.7)	H-5		111.0	H-5	H-5, H-11, H-12
7	Cq aromatic					163.2	H-6	H-6
8	Cq aromatic					119.9	H-12	H-4, H-5, H12
9	Cq aromatic					155.5	H-4, H-5	H-3, H-6
10	Cq aromatic					116.0	H-4, H-5	
11	O—CH ₃	3.94	s			59.0	H-13	
12	CH ₂	3.51	d ^c (7.2)	H-13		24.5	H-12	H-15, H-16
13	CH ethylenic	5.21	t hept (7.2, 1.4)	H-12		124.1	H-15, H-16	
14	Cq ethylenic					135.7	H-12	
15	CH ₃	1.68	d ^c (1.1)	H-13		27.8	H-13, H-16	
16	CH ₃	1.84	s ^c	H-13		20.0	H-13, H-15	

^a Position (Pos) number (see Fig. 1F for the numbering) indicates either hydrogen (H,H-COSY) or carbon (HMBC) signal.

^b s: singlet; d: doublet; t: hept; triplet of heptuplet.

^c Strongly broadened signals.

Table 6

Contents of adulterants identified in the formulations analyzed.

Formulation	Actives identified	Content ^a
1	PP-THHS ^b	80 ± 3
2	PP-THHS ^b	65 ± 5
3	PP-THHS ^b	103 ± 5
4	PP-THHS ^b	81 ± 5
5	thiosildenafil	89 ± 2
6	sildenafil	117 ± 6 ^c
	tetrahydropalmatine	96 ± 5
7	sildenafil	66 ± 2 ^c
	tetrahydropalmatine	44 ± 5
8	phenolamine	64 ± 3 ^d
9	osthole ^e	41 ± 3

^a Contents are expressed in mg per 10 g of powder.

^b PP-THHS: propoxyphenyl-thiohydroxyhomosildenafil.

^c The formulation contains sildenafil citrate but the amount is that of the free base (molecular weight 474.6 g mol⁻¹).

^d The formulation contains phenolamine mesylate but the amount is that of the free base (molecular weight 281.35 g mol⁻¹).

^e Osthole was not considered as an adulterant in formulation 9 (cf. text).

and H,C HSQC and HMBC spectra, considering that the ¹³C resonance of the “Z methyl group” was more shielded (usually 4–6 ppm, 7.8 ppm for OST) than the “E one” due to the γ effect.

MS and HR-MS data confirmed the structure determined from NMR. The full scan mass spectrum of isolated **4** generated protonated monomeric and dimeric peaks at m/z 245 [M+H]⁺ and 489 [M₂+H]⁺. The accurate masses of these ions were m/z 245.1082 and 489.2294 giving estimated elemental compositions of C₁₅H₁₇O₃ (calculated mass 245.1178, error –39.2 ppm, –9.6 mDa) and C₃₀H₃₃O₆ (calculated mass 489.2277, error 3.7 ppm, 1.7 mDa) as the most approximate results. Both compositions corresponded to the atomic composition of OST C₁₅H₁₆O₃. The MS/MS fragmentation of the parent ion at m/z 245 produced prominent ion at m/z 189 generated by the elimination of the neutral dimethyl-1,1-ethene (H₂C=C(CH₃)₂) molecule. This ion was further fragmented to yield another ion at m/z 161 (loss of CO) with rearrangement of the 2-oxopyrane ring into a furane one. A subsequent loss of CH₂O occurred with a peak observed at m/z 131. This fragmentation pattern was characteristic of OST as described by Chen et al. [22]. The loss of CH₂O from the ion at m/z 189 produced an ion at m/z 159.

3.7. Quantification of adulterants in the formulations analyzed

The contents of the different adulterants detected are listed in Table 6. Even if the amounts of the approved PDE-5 inhibitor SILD in formulations 6 and 7 (117 and 66 mg per 10 g bag) are slightly higher than or below the maximum recommended daily dose (100 mg/day), the consumers are not aware of taking a prescription drug that has severe contraindications. In addition to SILD, these formulations enclosed THP (96 and 44 mg per 10 g bag, respectively), an alkaloid of the benzyloquinoline class that is one of the more bioactive constituent of plants from the botanical genera *Corydalis* and *Stephania*. The molar ratio SILD/THP, determined as the ratio of the mean integrated areas of H15 and H18 SILD signals in one hand and of H1 and H4 THP signals on the other hand in ¹H NMR spectra of formulations 6 and 7, is very close to 1 (range 0.97–0.995), indicating that the same SILD-THP mixture was added in the two formulations. Formulation 6 was adulterated by a two-fold SILD-THP dose than formulation 7, as the absolute amount of the two compounds is roughly two-fold higher in the former one. Moreover in our opinion, added THP did not come from a crude extract of plants known to contain great quantities of this bioactive such as *Stephania* and *Corydalis* species.

Indeed, the aromatic region in the ^1H NMR spectra of formulations 6 and 7 showed the same pattern of minor intensity resonances whose δ and J characteristics are consistent with those of alkaloids identified in these plants in addition to THP such as corydaline, corydalmine, stylopine... (see for example [20,23,24]). The integrated area of THP aromatic resonances represented more than 85% of that of all alkaloids detected with the reasonable assumption that, on average, these compounds have four aromatic protons as THP. THP represents $\approx 70\%$ of the alkaloid content extracted from *S. bancroftii* or *yunnanensis* [20,24] and less than 25% of the tertiary alkaloids extracted from *C. yanhusuo* [23]. Therefore THP found in formulations 6 and 7 probably arises from THP-enriched extracts commercially available under the form of powders prepared from natural rhizome *Corydalis yanhusuo* which can contain up to 98% of THP. THP is used in traditional Chinese herbal preparations for the treatment of chronic pain and anxious insomnia as it possesses remarkable analgesic, sedative and hypnotic activities. It also exhibits anticonvulsant, hypotensive, bradycardial, neuroprotective and antioxidant properties but was not reported as effective for enhancing erectile dysfunction and sexual performance in man [20,21]. However, its possible interactions with SILD are not known.

The quantities of the two unapproved analogs, THIO and the newly identified compound PP-THHS, in formulations 1–5, ranged between 65 and 103 mg/10 g bag, which could place consumers at risk for potentially serious side-effects. Indeed, THIO and PP-THHS have an inhibitory activity against the isolated enzyme PDE-5 (IC_{50}) of 0.59 and 0.46 nM, respectively, i.e. more than ten-fold higher than that of SILD ($\text{IC}_{50} = 6.86$ nM) [19]. As drug safety is dependent on both activity and pharmacokinetics, the fact that the pharmacokinetic profiles of these two unlicensed compounds are unknown could increase the risks for consumers who unwittingly consume these substances.

Formulation 8 contains 64 mg of the synthetic drug PHE per 10 g bag. This compound is a reversible, non-selective α -1 and α -2 adrenergic receptor antagonist that induces vasodilatation of the smooth muscle cells. It was firstly used to manage hypertensive crisis. It is currently used to quickly restore tactile sensation after local dental anesthesia by injection into soft tissues. It is primarily employed for treating erectile dysfunction either as an oral solo drug formulation not approved by the FDA but sold on line under the name of Vasomax or in combination with papaverine (Bimix[®]) which is one of the three main agents for intracavernosal injection approved by the FDA [25,26].

Formulation 9 is most probably a natural dietary supplement. Indeed, *Cnidium monnieri* extracts that have long been used in China as an herbal medicine to improve male sexual dysfunction contain numerous bioactive coumarins such as xanthotoxin, isopimpinellin, bergapten, imperatorin (IMP) and OST. OST exerts a non-specific relaxant effect on vascular smooth muscles, including cavernosal, attributable to the release of nitric oxide which raises cGMP and cAMP levels by inhibiting the corresponding phosphodiesterases [27]. In ethanolic extracts of *C. monnieri* fruits, OST and IMP are the main compounds with IMP molar amount accounting for $\approx 45\%$ of that of OST [28]. However, when a supercritical fluid extraction is performed, IMP only represents 4% of OST [29]. IMP resonances attributed according to Liu et al. [30] were observed in the aromatic region of the ^1H NMR spectrum of formulation 9 (Fig. 2D) and accounted for $\approx 3\%$ of those of OST. It can thus be assumed that OST found in formulation 9 resulted from such an extraction of *C. monnieri* fruits. Moreover, the amount of OST measured in formulation 9 (41 mg/10 g bag) is comparable to that contained (50–60 mg) in a capsule of *C. monnieri* extracts marketed worldwide via the internet, suggesting that its amount in formulation 9 was standardized to the efficient dose enhancing male sexual activity.

4. Conclusion

Among the nine herbal formulations analyzed, eight were adulterated with a synthetic drug. Four of them contained PP-THHS, an unapproved SILD analog detected for the first time as an adulterant. Two were tainted with SILD and THP that has no reported effect for enhancing erectile dysfunction, and one with THIO, another unapproved PDE-5 inhibitor. Another formulation was adulterated with PHE that is unapproved for boosting male sexual performance as oral formulation. The last formulation contains the bioactive coumarin derivative, OST, a major compound present in *Cnidium monnieri* fruits, and is most probably truly natural.

Acknowledgements

The authors wish to thank Dr. J.C. Garrigues for helpful discussions, Dr. C. Routaboul from IR and Raman Department and researchers from the Mass Spectrometry Department for technical assistance.

References

- [1] A. Petroczi, G. Taylor, D.P. Naughton, Mission impossible? Regulatory and enforcement issues to ensure safety of dietary supplements, *Food Chem. Toxicol.* 49 (2011) 393–402.
- [2] J. Vaysse, V. Gilard, S. Balayssac, C. Zedde, R. Martino, M. Malet-Martino, Identification of a novel sildenafil analogue in an adulterated herbal supplement, *J. Pharm. Biomed. Anal.* 59 (2012) 58–66, and references quoted in.
- [3] V.M. Toomey, J.J. Litzau, C.L. Flurer, Isolation and structural characterization of two tadalafil analogs found in dietary supplements, *J. Pharm. Biomed. Anal.* 59 (2012) 50–57.
- [4] B.J. Venhuis, M.E. Zwaagstra, J.D.J. van den Berg, A.J.H.P. van Riel, H.W.G. Wagenaar, K. van Grootheest, D.M. Barends, D. de Kaste, Illicit erectile dysfunction products in the Netherlands – a decade of trends and a 2007–2010 product update, RIVM Report 370030003/2010, National Institute for Public Health and the Environment (2010).
- [5] S. Balayssac, S. Trefi, V. Gilard, M. Malet-Martino, R. Martino, M.A. Delsuc, 2D and 3D DOSY ^1H NMR, a useful tool for analysis of complex mixtures: application to herbal drugs or dietary supplements for erectile dysfunction, *J. Pharm. Biomed. Anal.* 50 (2009) 602–612.
- [6] S. Trefi, C. Routaboul, S. Hamieh, V. Gilard, M. Malet-Martino, R. Martino, Analysis of illegally manufactured formulations of tadalafil (Cialis[®]) by ^1H NMR, 2D DOSY ^1H NMR and Raman spectroscopy, *J. Pharm. Biomed. Anal.* 47 (2008) 103–113.
- [7] B.J. Venhuis, G. Zomer, D. de Kaste, Structure elucidation of a novel synthetic thiono analogue of sildenafil detected in an alleged herbal aphrodisiac, *J. Pharm. Biomed. Anal.* 46 (2008) 814–817.
- [8] P. Zou, P. Hou, S.S.Y. Oh, Y.M. Chong, B.C. Bloodworth, M.Y. Low, H.L. Koh, Isolation and identification of thiohomosildenafil and thiosildenafil in health supplements, *J. Pharm. Biomed. Anal.* 47 (2008) 279–284.
- [9] N. Uchiyama, K. Saisho, R. Kikura-Hanajiri, Y. Haishima, Y. Goda, Determination of a new type of phosphodiesterase-5 inhibitor, thioquinapiperil, in a dietary supplement promoted for sexual enhancement, *Chem. Pharm. Bull.* 56 (2008) 1331–1334.
- [10] L. Li, M.Y. Low, F. Aliwarga, J. Teo, X.W. Ge, Y. Zeng, B.C. Bloodworth, H.L. Koh, Isolation and identification of hydroxythiohomosildenafil in herbal dietary supplements sold as sexual performance enhancement products, *Food Addit. Contam.* 26 (2009) 145–151.
- [11] T. Hasegawa, K. Takahashi, M. Saijo, T. Ishii, T. Nagata, M. Kurihara, Y. Haishima, Y. Goda, N. Kawahara, Isolation and structural elucidation of cyclopentynafil and N-octylnortadalafil found in a dietary supplement, *Chem. Pharm. Bull.* 57 (2009) 185–189.
- [12] I. Wawer, M. Pisklak, Z. Chilmonczyk, ^1H , ^{13}C , ^{15}N NMR analysis of sildenafil base and citrate (Viagra) in solution, solid state and pharmaceutical dosage forms, *J. Pharm. Biomed. Anal.* 38 (2005) 865–870, and references quoted in.
- [13] S. Trefi, V. Gilard, S. Balayssac, M. Malet-Martino, R. Martino, The usefulness of 2D DOSY and 3D DOSY-COSY ^1H NMR for mixture analysis: application to genuine and fake formulations of sildenafil (Viagra), *Magn. Reson. Chem.* 47 (2009) S163–S173, and references quoted in.
- [14] J.C. Reepmeyer, Direct intramolecular gas-phase transfer reactions during fragmentation of sildenafil and thiosildenafil analogs in electrospray ionization mass spectrometry, *Rapid Commun. Mass Spectrom.* 23 (2009) 927–936.
- [15] S. Ahn, J.Y. Hong, M.K. Hong, Y.P. Jang, M.S. Oh, J.H. Jung, J. Hong, Structural determination of sildenafil and its analogues in dietary supplements by fast-atom bombardment collision-induced dissociation tandem mass spectrometry, *Rapid Commun. Mass Spectrom.* 23 (2009) 3158–3166.

- [16] J. Lee, H.H. Yoo, M.Y. Kang, D.H. Kim, Low-energy collision-induced dissociation of sildenafil thiono analogues: gas-phase intramolecular nucleophilic substitution through ion-neutral complexes between a cationic substrate and a thione-containing neutral nucleophile, *Rapid Commun. Mass Spectrom.* 19 (2005) 1767–1770, and references quoted in.
- [17] S.R. Gratz, B.M. Gamble, R.A. Flurer, Accurate mass measurement using Fourier transform ion cyclotron resonance mass spectrometry for structure elucidation of designer drug analogs of tadalafil, vardenafil and sildenafil in herbal and pharmaceutical matrices, *Rapid Commun. Mass Spectrom.* 20 (2006) 2317–2327.
- [18] G. Socrates, *Infrared and Raman Characteristic Group Frequencies*, third ed., John Wiley & Sons, Chichester, 2001.
- [19] J.H. Kim, Y. Kim, K.I. Choi, D.H. Kim, G. Nam, J.H. Seo, Novel pyrazolopyrimidinethione derivatives, preparation methods thereof and their use as therapeutics for erectile dysfunction, US Patent 0176371 A1 (2004).
- [20] J.T. Blanchfield, D.P.A. Sands, C.H.L. Kennard, K.A. Byriel, W. Kitching, Characterisation of alkaloids from some Australian *Stephania* (Menispermaceae) species, *Phytochemistry* 63 (2003) 711–720, and references quoted in.
- [21] J.M. Gao, P. Kamnaing, T. Kiyota, J. Watchueng, T. Kubo, S. Jarusophon, Y. Konishi, One-step purification of palmatine and its derivative *dl*-tetrahydropalmatine from *Enantia chlorantha* using high-performance displacement chromatography, *J. Chromatogr. A* 1208 (2008) 47–53, and references quoted in.
- [22] Y. Chen, G. Fan, Q. Zhang, H. Wu, Y. Wu, Fingerprint analysis of the fruits of *Cnidium monnieri* extract by high-performance liquid chromatography-diode array detection-electrospray ionization tandem mass spectrometry, *J. Pharm. Biomed. Anal.* 43 (2007) 926–936.
- [23] Z.Z. Ma, W. Xu, N.H. Jensen, B.L. Roth, L.Y. Liu-Chen, D.Y.W. Lee, Isoquinoline alkaloids isolated from *Corydalis yanhusuo* and their binding affinities at the dopamine D₁ receptor, *Molecules* 13 (2008) 2303–2312.
- [24] R. Hu, X. Dai, Y. Lu, Y. Pan, Preparative separation of isoquinoline alkaloids from *Stephania yunnanensis* by pH-zone-refining counter-current chromatography, *J. Chromatogr. B* 878 (2010) 1881–1884.
- [25] H.J. Wiser, T.S. Köhler, Self-injection transurethral and topical therapy in erectile dysfunction, in: K.T. McVary (Ed.), *Contemporary Treatment of Erectile Dysfunction. A Clinical Study*, Springer, 2011, pp. 107–125.
- [26] E.R. McNamara, C.F. Donatucci, Oral therapy for erectile dysfunction, in: K.T. McVary (Ed.), *Contemporary Treatment of Erectile Dysfunction. A Clinical Study*, Springer, 2011, pp. 93–106.
- [27] J. Chen, W.F. Chiou, C.C. Chen, C.F. Chen, Effect of the plant-extract osthole on the relaxation of rabbit corpus cavernosum tissue in vitro, *J. Urol.* 163 (2000) 1975–1980.
- [28] D. Chen, J. Wang, Y. Jiang, T. Zhou, G. Fan, Y. Wu, Separation and determination of coumarins in *Fructus cnidii* extracts by pressurized capillary electrochromatography using a packed column with a monolithic outlet frit, *J. Pharm. Biomed. Anal.* 50 (2009) 695–702.
- [29] Q. Chen, P. Li, F. Yuan, F. Cheng, J. He, J. Liu, Z. Zhang, Identification and quantification of the volatile constituents in *Cnidium monnieri* using supercritical fluid extraction followed by GC–MS, *J. Sep. Sci.* 32 (2009) 252–257.
- [30] R. Liu, L. Feng, A. Sun, L. Kong, Preparative isolation and purification of coumarins from *Cnidium monnieri* (L.) *Cusson* by high-speed counter-current chromatography, *J. Chromatogr. A* 1055 (2004) 71–76.



Applicability of total reflection X-ray fluorescence (TXRF) as a screening platform for pharmaceutical inorganic impurity analysis

Bradley J. Shaw^{a,*}, David J. Semin^a, Michael E. Rider^b, Meredith R. Beebe^{c,1}

^a Analytical Research and Development, Amgen Inc., One Amgen Center Drive, Thousand Oaks, CA 91320, United States

^b X-ray Fluorescence, Bruker AXS, Inc., 2700 North Crescent Ridge Drive, The Woodlands, TX 77381, United States

^c Technos International, Inc., 60 E. Rio Salado Parkway, Tempe, AZ 85281, United States

ARTICLE INFO

Article history:

Received 22 September 2011

Received in revised form 27 January 2012

Accepted 28 January 2012

Available online 7 February 2012

Keywords:

Total reflection X-ray fluorescence (TXRF)

Inductively coupled plasma-mass

spectrometry (ICP-MS)

Trace metal analysis

Heavy metals

ABSTRACT

Palladium (Pd) is extensively used in pharmaceutical small molecule drug substance processes, however it must be removed prior to release of the active pharmaceutical ingredient (API). Evaluation of four TXRF instruments and configurations were compared to ICP-MS instrumentation for trace metal analysis, most importantly for Pd. Standards and six pharmaceutical drug substances, triprolidine HCl, diphenhydramine HCl, chlorpheniramine maleate, pseudoephedrine HCl, ephedrine sulfate, and scopolamine HBr, were analyzed to determine linearity, sensitivity, accuracy, and precision for Pd plus Cr, Fe, Cu, Rh, and Pt versus interferences, particularly from Cl, S, and Ar, on the various X-ray fluorescence lines. Irrespective of instrument platform, in general X-ray sources capable of accessing Pd-K lines were found to be most effective in determination of Pd in APIs.

© 2012 Elsevier B.V. All rights reserved.

1. Introduction

In order to understand and control the safety profile of a pharmaceutical it is critical to reliably, accurately, and rapidly assess heavy metals during process development and manufacturing of drug substances and products. Heavy metal testing is used throughout preclinical, clinical, and commercial phases. Unintended human consumption of residual levels of heavy metals can cause serious health concerns based upon the particular metal, dose and duration [1]. Residual heavy metals can come from a variety of sources during the manufacturing process, for example, those arising from reagents, starting materials, reaction equipment, solvents, and catalysts. Thus, strict regulatory obligations exist to ensure controls are in place to guarantee clinical and commercial subject safety [2,3].

In order to ensure product quality is within regulatory guidelines, metal analysis needs to be applied at numerous points in the development process. Metal analysis becomes important starting with late discovery and early development when material is prepared for preclinical and clinical studies. For example, during the chemistry route scouting and optimization, or process development phase, catalyst screening and loading study evaluations

may take place. During this phase it is probably most important to have a metal analysis workflow to support process understanding at the gram scale that is rapid (< hr), sensitive (ppm), and semi-quantitative when only milligram quantities of sample are available for testing. During the manufacturing processing phase in early development metal analysis may be part of the in process control measures. It is important during in-process testing that process control is demonstrated through ensuring the levels or the clearance of metal species in a process. Lastly, during the release testing phase metal analysis is performed to determine whether the material is within established specifications.

In this work we considered which metals are typically used as catalysts in the pharmaceutical industry [4]. Catalysis is important in the pharmaceutical chemistry industry as it can be used to reduce the energy activation during carbon-carbon and carbon-heteroatom bond formation. Thus the efficiency of the synthetic transformation is improved, decreasing overall cost and time. Palladium is generally considered the most versatile metal for forming carbon-carbon and carbon-heteroatom bonds and is extensively used in the pharmaceutical industry for catalytic reactions [5–7].

There are a number of techniques for metal analysis such as wet chemical, inductively-coupled plasma (ICP) techniques [8], X-ray fluorescence including total reflection X-ray fluorescence [7,9,10], and adsorptive stripping voltammetry [11]. The current wet chemical compendial method, USP Chapter (231), is based on the principle of ashing a sample to form a sulfate species of

* Corresponding author. Tel.: +1 805 313 6448; fax: +1 805 447 8673.

E-mail address: bshaw@amgen.com (B.J. Shaw).

¹ Present address: Beebe Consulting, 7515 W 91st Street, Los Angeles, CA 90045, United States.

heavy metals which may be present [12,13]. The technique can be easily transferred from lab-to-lab and does not require high-end analytical instrumentation or highly trained personnel. However, the limitation of the method is the subjective nature of analysis and the large sample quantity (grams) required to obtain parts per million detection sensitivity. Other limitations include non-uniform ashing process per element, potential loss of volatile elements, and the visual inspection or subjectivity by the analyst conducting the assay.

Numerous articles have highlighted the advantages of using ICP-MS for metal speciation and detection [14–20]. In short, the advantages include its specificity, sensitivity (ppt), wide quantitative dynamic range (9 orders), robustness and multi-element analysis capabilities. However, one disadvantage is the time-to-result per experiment is on the order of hours when extensive sample preparation techniques are required, such as microwave digestion. Direct dilution of pharmaceutical samples has been shown for some many samples using 80% nitric acid [16], 2-butoxyethanol:water (25:75) [18], and recently using N,N-dimethylformamide (DMF) [20], although limitations on sample type have been reported by Tu et al. for each diluent with DMF affording at least 95% of samples [20]. Generally, ICP platforms are the predominant platform for most applications of inorganic impurity analysis.

The multi-element technique of total reflection X-ray fluorescence (TXRF) developed during the early 1970s [21] has been demonstrated to be successful for low level detection of metals on bare silicon or other polished substrates [22,23]. TXRF, with an X-ray incident beam below the critical angle to the sample, minimizes the high background of traditional X-ray fluorescence (XRF) through total reflection of the primary radiation and offers surface sensitive, ultra-trace elemental analysis with much lower detection limits than traditional XRF, and recently for the analysis of active pharmaceutical ingredients [24–26]. The principles of TXRF are based upon targeting X-rays on a planar surface at less than the critical angle to the sample and measuring the emitted fluorescence radiation. In short, the advantages of TXRF versus ICP-MS are ease of use, and versus XRF is sensitivity with lower material demand.

The use of ICP-MS as a screening tool has been explored in the pharmaceutical process development environment [27]. By using ICP-MS as the gold standard, the study of this work was to compare two commercially available TXRF platforms against ICP-MS for the detection of pharmaceutically relevant elements and to demonstrate applicability of TXRF as a screening platform for pharmaceutical material. Based on developing a screening platform we chose the following test specifications: (1) limit of detection of <5 ppm, (2) precision of <30% RSD, (3) accuracy of 60–140% recovery, and (5) linearity of $R^2 > 0.99$. These specifications were chosen to be appropriate for the intended purpose of providing a fit-for-purpose screening system while limiting the sample amount per assay. Subsequently in this study and in order to evaluate multiple instruments simultaneously, samples were sent to the vendors without disclosure of contents and concentrations, thus minimizing vendor biases on the results. To demonstrate the goal of achieving the above specifications we studied standards and 20 pharmaceutically relevant metals in six drug substances with a material demand of about 10 mg or less per sample assay.

2. Experimental

2.1. ICP-MS

A general methodology has been developed to analyze for all elements of interest. This general platform was established in our laboratory incorporating ICP-MS, has been utilized on

Table 1
ICP-MS parameters.

ICP-MS	Parameter
RF power	1175 W
Plasma gas flow rate	15.0 l/min
Auxiliary gas flow rate	1.20 l/min
Nebulizer gas flow rate	0.96 l/min
Lens voltage	6.25 V
Instrument mode	Standard
Sweeps/reading	20
Readings/replicate	1
Replicates	6
Scan mode	Peak Hopping
Dwell time	50.0 ms
Integration time	1000 ms

thousands of pharmaceutical process development samples, and defines our control platform for this study. The ICP-MS used was a PerkinElmer Elan DRC II (PerkinElmer, Waltham, MA, USA) with a quartz concentric nebulizer (Meinhard® A3, Part No. WE024371, PerkinElmer) and quartz cyclonic spray chamber (Part No. WE025221, PerkinElmer). The parameters for this method are found in Table 1. Estimated ICP-MS LOD was determined using 3.3 times the standard deviation of multiple blank measurements divided by the calibration slope, estimated $LOD = 3.3 \times \sigma_{\text{blank}} / \text{calibration slope}$.

Internal standardization of standards and samples was carried out using certified reference material internal standards consisting of beryllium, gallium, gold, lutetium, scandium, tellurium, thallium, thorium, and yttrium and custom prepared by Inorganic Ventures (Christiansburg, Virginia, USA). Calibration of the ICP-MS was performed using diluted certified reference material standards that were custom prepared by Inorganic Ventures containing sulfur, phosphorus silicon, boron, titanium, antimony, molybdenum, tin, iridium, mercury, palladium, platinum, rhodium, ruthenium calcium, iron, potassium, sodium, aluminum, arsenic, barium, bismuth, cadmium, cesium, chromium +3, cobalt, copper, indium, lead, lithium, magnesium, manganese, nickel, rubidium, selenium, silver, strontium, vanadium, and zinc.

Concentrated nitric and hydrochloric acids were purchased from Fisher Scientific (Optima grade, Fair Lawn, NJ, USA), water was purchased from EMD Chemicals (OmniTrace Ultra™, Gibbstown, NJ, USA), and methanol was purchased from Honeywell Burdick and Jackson® (LC-MS grade, Morristown, NJ, USA).

2.2. TXRF: Bruker AXS

All standard and sample solutions were prepared by Amgen. All standard or sample analyses were performed by Bruker AXS (The Woodlands, TX, USA); subsequent internal standard was added, where 10 μl standard and sample aliquots were spotted into the center of a 30 mm round quartz disc and dried on a heating plate. The TXRF instrument used was the Bruker S2 Picofox TXRF (Bruker GmbH, Germany) with either a Mo-K or W-K source X-ray tube and a 30 mm² Silicon Drift Detector in a benchtop model. The parameters for the Mo or W instruments include 50 kV at 750 μA or 50 kV at 1000 μA tube settings, respectively, and 1000 s or 2000 s measurement times, respectively. Estimated Bruker AXS LOD was determined by the software using 3 times the concentration of the element divided by the measured area of the element peak times the square root of the background area of the subjacent to the peak, estimated $LOD = 3 \times C_i / N_i \times \sqrt{N_{\text{bkgd}}}$.

2.3. TXRF: Technos

All standard and sample solutions were prepared, spotted, and dried onto sample substrates by Amgen; aliquots of 5 μl of each

internally standardized standard and sample solution were spotted and dried onto silicon wafers in an oven at 50 °C for about 5 min prior to delivery of the silicon wafers to Technos for analysis. All standard or sample analyses were performed by Technos (Osaka, Japan) or under the direction of Technos. The TXRF instrument used was the TREX 6000 (Osaka, Japan) which is not a benchtop system with either a Cr-K, Ag-K or W-L source X-ray tube and a Si(Li) detector. The parameters for the Cr-K α , Ag-K α , Ag-K β_1 , or W-L β_1 sources include 0.02°, 35 kV at 35 mA; 0.03°, 40 kV at 35 mA; 0.03°, 50 kV at 30 mA; or 0.05°, 40 kV at 40 mA angle and tube settings, respectively, and 500 s measurement times. The Technos TXRF was developed specifically for location inside a semiconductor fab to measure trace metal contamination on bare silicon wafers and was not geared for the pharmaceutical industry. Estimated Technos LOD was determined by the software using 3 times the concentration of the element divided by the measured intensity of the element peak times the square root of the background intensity divided by the measurement time, estimated $LOD = 3 \times C_i / I_i \times \sqrt{(I_{bkgd} / T)}$.

Silicon wafers were purchased from Silicon Valley Microelectronics, Inc. (Santa Clara, CA, USA). The wafers were 200 mm in diameter, P/Boron type/dopant, 0–100 Ω cm resistivity, 725 μ m thick, and polished on the front side. The wafers were siliconized on the front surface using Surfasil™ (Product #42855, Pierce, Rockford, IL, USA).

2.4. Evaluation 1: standard sample analysis

Standards were prepared using certified reference material standards from Inorganic Ventures containing 10,000 μ g/ml each of aluminum, calcium, chromium + 3, copper, iron, manganese, magnesium, molybdenum, nickel, palladium, phosphorus, platinum, potassium, rhodium, ruthenium, silicon, sodium, sulfur, tungsten, or zinc. Three standard solutions were prepared in diluent consisting of 2% (w/v) nitric acid and 0.5% (w/v) hydrochloric acid and three standard solutions in dimethyl sulfoxide.

For ICP-MS, standard samples were diluted to the appropriate level with diluent consisting of 2% (w/v) nitric acid and 0.5% (w/v) hydrochloric acid, and referenced to the appropriate internal standard element.

For TXRF, all standard samples analyses were performed by Bruker AXS or Technos, and referenced to Ca, Cu, or Mn to ensure adequate signal for internal standardization.

2.5. Evaluation 2: drug substance sample analysis

Evaluation 2 samples were prepared using USP reference standard material from U.S. Pharmacopeia consisting of triprolidine HCl, diphenhydramine HCl, chlorpheniramine maleate, pseudoephedrine HCl, ephedrine sulfate, and scopolamine HBr.

For ICP-MS, drug substance samples were prepared at 1 mg/ml in diluent consisting of 2% (w/v) nitric acid and 0.5% (w/v) hydrochloric acid with added internal standards; spiked samples were prepared with added standards, as well. Drug substance samples and spikes were prepared in triplicate, except for ephedrine sulfate spike.

For TXRF, drug substance samples and spikes sent to Bruker AXS, triprolidine HCl, diphenhydramine HCl, and pseudoephedrine HCl, were prepared with about 10 mg in 1 ml for 10 mg/ml; chlorpheniramine maleate, ephedrine sulfate, and scopolamine HBr were prepared with about 5 mg in 1 ml for 5 mg/ml in diluent consisting of 50% (v/v) methanol in 2% (w/v) nitric acid and 0.5% (w/v) hydrochloric acid; Bruker AXS added 2.0 μ g/ml Sr as internal standard. Drug substance samples and spikes sent to Technos were prepared with about 10 mg in 10 ml for 1 mg/ml in diluent consisting of 50% (v/v) methanol in 2% (w/v) nitric acid and 0.5% (w/v)

hydrochloric acid with 0.1 μ g/ml V internal standard. Drug substance samples and spikes were prepared in triplicate.

All drug substance samples for TXRF analyses were performed by Bruker AXS or Technos.

3. Results

The evaluation of the TXRF instruments was structured to answer three objectives based on a general understanding of TXRF:

- (1) Can TXRF be used to accurately, precisely and sensitively measure palladium in pharmaceutical drug substances?
- (2) Can TXRF be used to screen other pharmaceutically relevant metals used in drug development processing?
- (3) What are the advantages of TXRF versus ICP-MS for such analyses; i.e. sample flow, time, etc.?

To answer these three objectives, an evaluation of two vendors' TXRF systems was performed; given different targeted industries for each system, comparison of the generalized approach of TXRF to answer the objectives shall be discussed. Each vendor had two distinct instruments or configurations, one allowing access of only the Pd-L shell (binding energy 3.61 keV) with fluorescent emission lines (primarily 2.84 keV Pd-L α , 2.99 keV Pd-L β_1) for analysis, and the other to access the Pd-K shell (binding energy 24.35 keV) with fluorescent emission lines (primarily 21.13 keV K α , 23.82 keV K β_1). As the measurement of palladium is the primary objective of the study, access of both Pd-K and Pd-L shells in separate instruments or configurations is necessary because each instrument or configuration uses different incident X-rays. These different incident X-ray sources generally have different optimum fluorescent sensitivities based upon fluorescent energy. An ideal configuration would be an accurate and sensitive instrument that would be capable of measuring both Pd-K and Pd-L emission lines. The Bruker AXS Picofox platform only has an option for one X-ray source. The Mo source system utilizes a Mo-K α (17.4 keV) incident line, and is capable of effectively measuring Pd-L lines. The W source system utilizes a W-K α (58.9 keV) incident line, and is capable of effectively measuring Pd-K lines. The original instrument configuration of the Technos system contained a Cr source, a W source, and a Ag source, utilizing a Cr-K α (5.4 keV) incident line, a W-L β_1 (9.7 keV) incident line, and a Ag-K α (22.1 keV) incident line, respectively, where Ag-K α and W-L β_1 are capable of effectively measuring Pd-L lines. During this evaluation, Technos reconfigured the instrument hardware to allow the use of a Ag-K β_1 (24.9 keV) incident line which has a higher energy than the binding energy of the Pd-K shell and is, thus, capable of measuring Pd-K lines, but was not optimized for accuracy and sensitivity.

3.1. Evaluation 1—standards: details linearity, sensitivity, accuracy and precision

Multi-level standards were used to assess the instrumentation alone for linearity, sensitivity, accuracy and precision. The use of standards will help distinguish differences in instrumentation and help to standardize the results from the pharmaceutical samples.

Standards were sent to two vendors, Bruker AXS and Technos for evaluation, with two instrument configurations for the Bruker AXS using either Mo or W X-ray source for all elements and one instrument configuration for Technos using Ag-K α X-ray source for all elements including for Pd-L. Standards were also analyzed using ICP-MS to compare the results with the TXRF results. Standards contain elements at three different levels: 1, 10, and 100 μ g/ml each elements. These concentrations were varied per standard and were not disclosed to the vendors in order to minimize vendor bias. It is

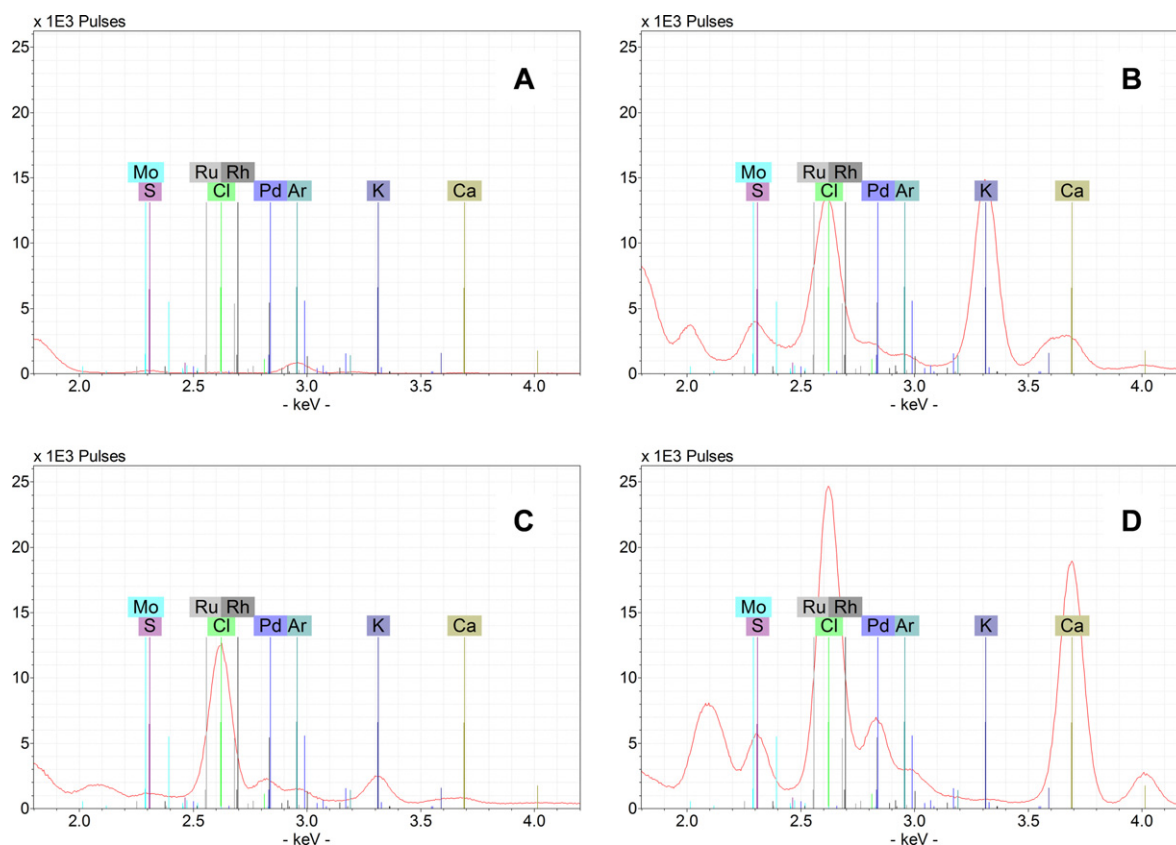


Fig. 1. Standard samples in dilute acid from Bruker AXS Mo source TXRF: blank (A); standard 1 (B) with Mo and Ru at 100 µg/ml, Rh at 10 µg/ml, Pd at 1 µg/ml; standard 2 (C) with Mo, Ru and Pd at 10 µg/ml, Rh at 1 µg/ml; and standard 3 (D) with Rh and Pd at 100 µg/ml, Mo and Ru at 10 µg/ml. Note: S, K and Ca spiked for reference only in (B), (C), and (D); Mo-L, Ru-L, Rh-L, and Pd-L lines shown.

also important to note that internal standardization was essential in these analyses to remove method bias, such as spotting and drying of samples that would influence the results.

Fig. 1 shows representative spectra of the standard solutions from the Bruker AXS Mo source instrument with a focus around the Pd-L line energies. In order to determine the element line interferences and assess line widths the concentrations of the elements were varied. In Fig. 1B, Pd concentration is at 1 µg/ml, and is not well resolved and thus provides a complication for accurate quantitation determination. As you increase Pd concentration from 10 µg/ml in Fig. 1C to 100 µg/ml in Fig. 1D Pd is more dominant in the spectra relative to Cl and therefore should be able to be deconvoluted unless an even greater amount of Cl is present. For low concentrations of S there is no interference found. Whereas, for Ru and Rh there is significant interference from Cl regardless of the concentration.

Tabulated results for linearity, sensitivity, accuracy, and precision for Cr, Mn, Fe, Ni, Cu, Zn, Mo, Ru, Rh, Pd, W, and Pt in both dilute

acid and DMSO diluents are provided in the [Supplemental Material Table S1](#).

Of particular note the Bruker AXS Mo and Technos Ag-K α instruments used Pd-L lines and Bruker AXS W instrument Pd-K lines.

Linearity was evaluated over three levels and measured using the correlation coefficient, R^2 , with a target $R^2 > 0.99$. Most elements passed the target criteria, where R^2 for Pd is found in [Table 2](#).

Sensitivity was evaluated over three levels and measured by estimating the limit of detection (LOD) for each standard solution, with a target LOD < 0.050 µg/ml, which corresponds to an LOD of 5 µg/g when a 10 mg/ml sample solution is used. The Bruker AXS Mo instrument has the lowest estimated LOD for most of the elements (Cr, Mn, Fe, Ni, Cu, Zn, W, and Pt), especially when no interference is observed. The Bruker AXS W instrument has the lowest estimated LOD for Mo, Ru, Rh, and Pd with estimated LOD for Pd found in [Table 2](#). Due to interferences on Pd-L lines as previously described, estimated LOD values using Bruker AXS Mo (9X) and

Table 2
Evaluation 1, results for palladium standards in two diluents for ICP-MS and TXRF platforms.

Instrument platform		Diluent ^a	Accuracy, % Recovery	Precision, % RSD	Linearity, R^2	Sensitivity, LOD, µg/ml
ICP-MS	PE ELAN DRC II	S1	105	0.6	1.00	0.001
		S2	113	0.6	1.00	0.001
TXRF	Bruker AXS S2 Picofox (Mo-K source) ^b	S1	332	27	1.00	0.453
		S2	737	36	1.00	0.635
TXRF	Bruker AXS S2 Picofox (W-K source) ^c	S1	101	3	1.00	0.053
		S2	100	12	1.00	0.070
TXRF	Technos TREX 6000 (Ag-K α source) ^b	S1	955	14	0.93	1.743
		S2	876	34	0.88	2.873

^a S1: dilute acid; S2: dimethyl sulfoxide.

^b Pd-L lines.

^c Pd-K lines.

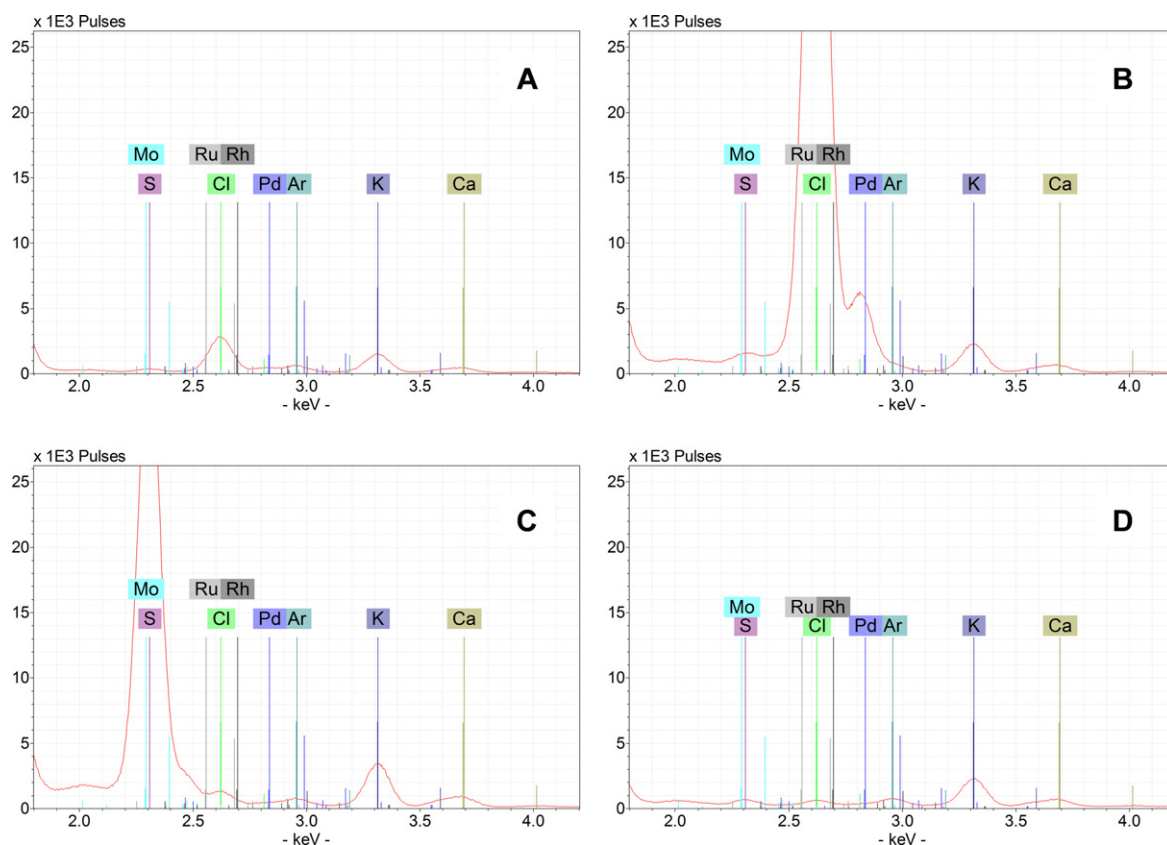


Fig. 2. Drug substance samples from Bruker AXS Mo source TXRF: diphenhydramine HCl (A); chlorpheniramine maleate (B) with Mo, Ru, Rh, and Pd spiked at 100 $\mu\text{g/g}$; ephedrine sulfate (C) with Mo, Ru, Rh, and Pd spiked at 200 $\mu\text{g/g}$; and scopolamine HBr (D) with Mo, Ru, Rh, and Pd spiked at 200 $\mu\text{g/g}$. Note: S, K and Ca spiked for reference only all; Mo-L, Ru-L, Rh-L, and Pd-L lines shown.

Technos Ag-K α (33X) instruments were considerably higher than for the Bruker AXS W instrument. Accuracy was evaluated over three levels and measured by calculation of the percent recovery for the spiked concentration, with a target of 60–140% recovery. Most instruments and elements pass the target criteria for accuracy, except of particular note is Pd where % recovery for Pd is found in Table 2. The Bruker AXS Mo instrument and the Technos Ag-K α instrument do not recover Pd well in the standards, only the Bruker AXS W instrument does. The difference between the instruments is the detection of Pd-L lines versus Pd-K lines, respectively.

Precision was evaluated over three levels and measured by calculation of the relative standard deviation, with a target of $<\pm 30\%$ RSD. Most elements passed the target criteria in most of the instruments, with a few exceptions (e.g. Fe) that are mostly indicative of contamination (where the same sample was used across all platforms) during the analysis where % RSD for Pd is found in Table 2.

3.2. Evaluation 2—samples: details accuracy, precision and sensitivity

A diverse array of six different generic pharmaceutical drug substances was sent to each of the vendors for analysis of accuracy, precision and sensitivity. Pd-L lines are potentially overlapped by S-K, Cl-K, and Ar-K lines. So, the generic pharmaceutical drug substances were chosen based upon the potential overlap of Pd. One drug substance, chlorpheniramine maleate, contains a covalently bound chlorine, three drug substances are HCl salts, one drug substance is a sulfate salt, and the sixth drug substance is an HBr salt without any chlorine or sulfur.

Samples were sent to Bruker AXS and Technos for evaluation, with two instrument configurations for the Bruker AXS using either

Mo or W X-ray sources for analysis of all elements, and two instrument configurations for Technos using either W-L β_1 plus Ag-K α or Ag-K β_1 X-ray sources for analysis of all elements where Pd was determined using W-L β_1 for Pd-L or Ag-K β_1 for Pd-K. Samples were analyzed using ICP-MS to compare the results with TXRF. Samples were prepared in triplicate, where available; spiked samples were prepared in triplicate and contain element concentrations at 100, 200, 1000, or 2000 $\mu\text{g/g}$ for samples sent to Bruker AXS and at 100 or 1000 $\mu\text{g/g}$ for samples sent to Technos. High spiking concentrations were driven by estimated LOD values determined in evaluation 1 where due to small sample sizes, solution concentrations are limiting sensitivity when interferences are found. Tabulated results for sensitivity, accuracy, and precision for Cr, Mn, Fe, Ni, Cu, Zn, Mo, Ru, Rh, Pd, W, and Pt in each drug substance is provided as supplemental material. Again, it is important to note that the contents and concentrations of each sample supplied to the vendors were not disclosed in order to minimize vendor bias.

Fig. 2 shows representative spectra of the sample solutions from the Bruker AXS Mo source instrument with a focus around the Pd-L line energies. From Fig. 2B, the interference from Cl-K lines are significant as chlorpheniramine maleate, with a covalently bound Cl, has the largest interference on Pd-L lines. From Fig. 2C, it is observed that the interference from S-K lines as measured with ephedrine sulfate, with a counter ion containing S, on Pd-L lines is not significant. Throughout all spectra in Fig. 2, it is noted that the Ar-K signal does slightly interfere with the Pd-L signal and is most evident with the Bruker AXS Mo instrument such that Pd recovery is 41% in scopolamine HBr samples where no Cl or S are added as observed in Fig. 2D.

Fig. 3 shows representative spectra of the sample solutions from the Bruker AXS W source instrument and highlight the Pd-K line

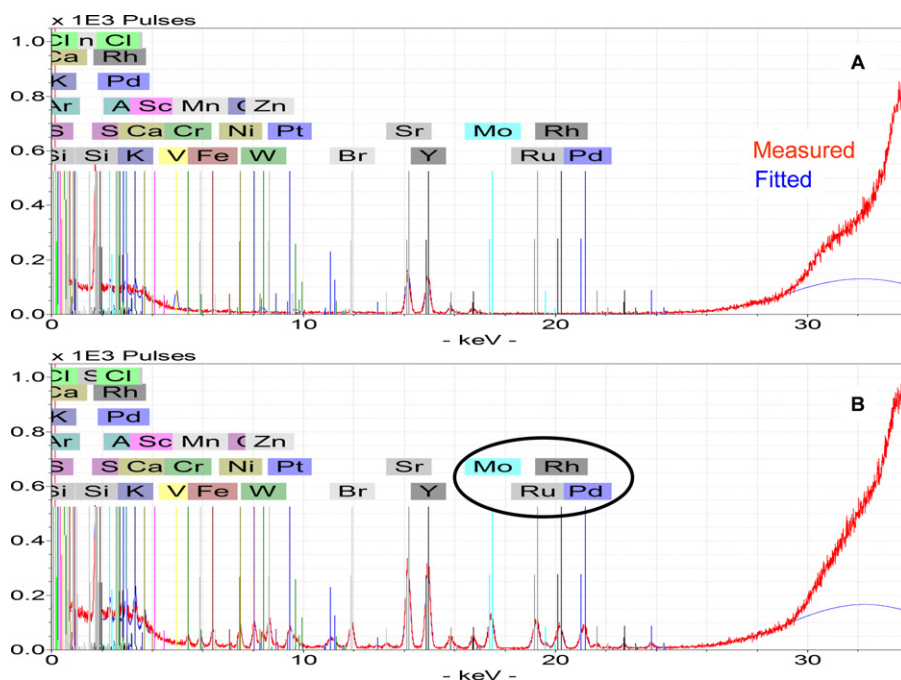


Fig. 3. Drug substance sample spectra from Bruker AXS W source TXRF of pseudoephedrine HCl: sample (A) and spike (B). Pd-K lines well resolved from Cl, Br, S, and Ar; no significant interference from W source. Optimization of internal standard required for quantization; Mo-K, Ru-K, Rh-K, and Pd-K lines shown.

region. No other element lines are found to interfere at the line energies of the Pd-K lines as well as the Mo-K, Ru-K and Rh-K lines.

Results are shown in Fig. 4 for accuracy, precision, and sensitivity for Cr, Fe, Cu, Rh, Pd, and Pt in all six drug substances. Tabulated results for accuracy, precision, and sensitivity for Cr, Mn, Fe, Ni, Cu, Zn, Mo, Ru, Rh, Pd, W, and Pt in all six drug substances are provided in the Supplemental Material Table S2.

Accuracy was evaluated for three spiked samples and measured by calculation of the percent recovery for the spiked concentrations, with a target of 60–140% recovery. From Fig. 4A ICP-MS recoveries are well within the range as expected. Of note is the chlorpheniramine maleate sample, where a covalently bound Cl highlights the instrument differences for Pd analysis. The two TXRF instruments measuring Pd-L and Rh-L lines deviate significantly from the target range for recovery (Bruker AXS Mo gives 0% recovery for Pd and Technos W- β_1 gives 0% recovery for Pd as in Table 3) when covalently-bound Cl is present within the chlorpheniramine maleate sample, while the TXRF instruments measuring Pd-K and Rh-K lines provide recoveries within the target range (Bruker AXS W gives 92% recovery for Pd and Technos Ag-K β_1 gives 73% recovery for Pd as in Table 3) even when covalently-bound Cl is present.

Precision was measured for all three levels and evaluated by calculation of the relative standard deviation, with a target of $< \pm 30\%$ RSD. From Fig. 4B precision is found within the range for most of the instruments, except where interferences on Pd-L and Rh-L lines are found as discussed above where % RSD for Pd is found in Table 3.

Sensitivity was measured for all three levels and evaluated by estimating the limit of detection for each standard solution, with a target LOD $< 5.0 \mu\text{g/g}$. From Fig. 4C sensitivity is found within the range for all elements measured by ICP-MS. The TXRF instruments measuring Pd-L and Rh-L lines are generally within the range, except where interferences are present as discussed above where estimated LOD for Pd is found in Table 3. The TXRF instruments measuring Pd-K and Rh-K lines are out of the range for low atomic number elements such as Cr, Fe, and Cu.

3.3. Discussion of Pd

As reported in Fig. 4, the data from the Bruker AXS Mo-source and Technos Ag-K α source TXRF instruments suggest an interference from Cl-K lines and Ar-K lines on Pd-L lines as observed in the chlorpheniramine maleate sample; Ru-L and Rh-L lines are also interfered with in this sample. However, interference of S-K lines on Pd-L lines are less evident as observed in the ephedrine sulfate sample. Naturally, as the energy of Pd-K lines are much higher than Pd-L lines, when the same sample is analyzed for by Pd-K lines using the Bruker AXS W-source, as observed in Fig. 3, and Technos Ag-K β_1 source TXRF instruments, the interference from Cl-K lines and Ar-K lines are not observed. For Pd analysis, usage of instruments capable of Pd-K line analysis for the quantitative determination of Pd is recommended especially since many pharmaceutical drug substances contain covalently bound chlorine.

3.4. Discussion of secondary elements: tungsten (W-K) X-ray source performs well for secondary elements

The secondary elements Cr, Fe, Cu, Rh, and Pt all show poorer sensitivity (by estimated detection limit) with an instrument targeting Pd-K lines, than the comparable instrument targeting Pd-L lines as found in Fig. 4C. Sensitivity is better for the secondary elements with the X-ray sources that are used to target Pd-L lines, when there are no interferences that limit the measurement. So there is a trade-off when targeting Pd-K lines as the primary determinate for the TXRF platform. However, given the lack of Pd analysis capability and the necessity of Pd analysis for pharmaceutical drug substances, targeting the Pd-K line instruments is more important. It is interesting to note that the Technos instrument handles multiple X-ray sources within one instrument; this configuration is theoretically ideal as to maximize the detection of all elements of interest, but may not be practical due to an increased cost of such an instrument that is geared specifically for the semiconductor industry.

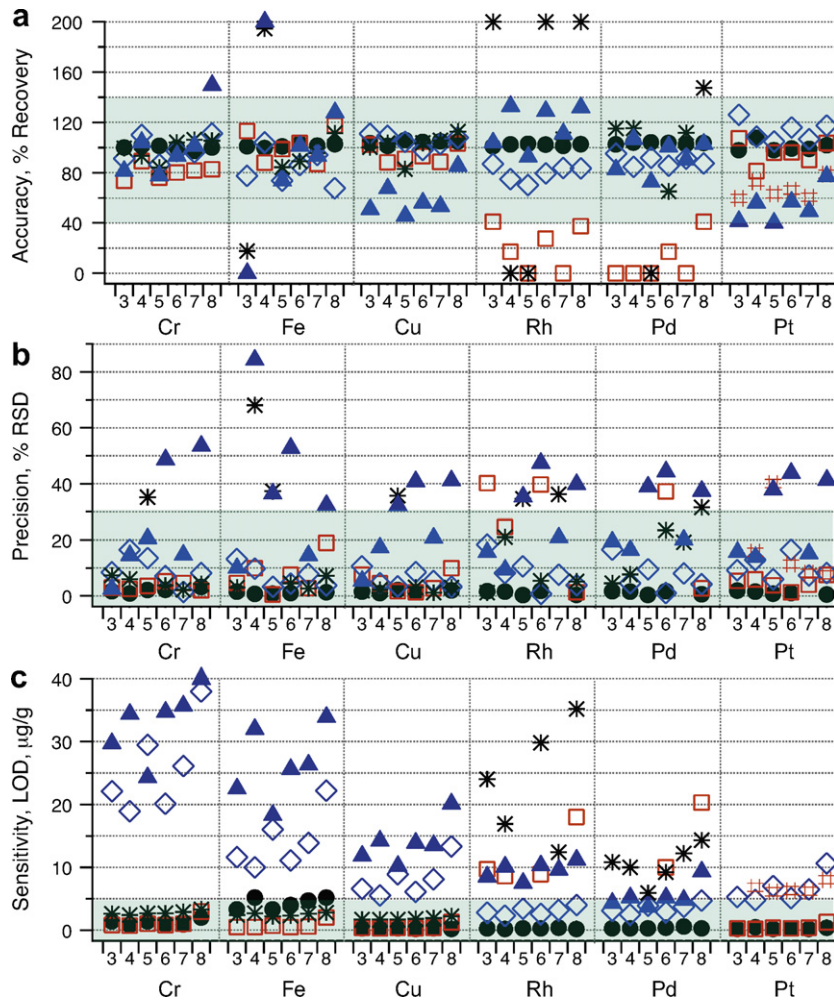


Fig. 4. Evaluation 2 – samples [sample identifier shown on x-axis representing: triprolidine HCl (3), diphenhydramine HCl (4), chlorpheniramine maleate (5), pseudoephedrine HCl (6), ephedrine sulfate (7), and scopolamine HBr (8)] representing ICP-MS (●), Bruker AXS Mo (□), Bruker AXS W (◇), Technos W-Lβ (*), Technos Ag-Kα (#), and Technos Ag-Kβ (▲).

3.5. Discussion sample flow: sample flow for ICP-MS and TXRF; generalization of the sample flow stream for ICP-MS and TXRF for universal sample processing

Introducing TXRF as a platform depends upon the sample flow and the instrumentation. TXRF sample flow in comparison to ICP-MS is relatively quicker and easier than when microwave processing is needed for ICP-MS. The primary advantages of TXRF

are its ability to accept organic solvent-based diluents, its ease of use, and the low operational cost of TXRF as compared to argon-based ICP platforms while still achieving good results. A significant challenge for development of pharmaceutical drug substances is aqueous solubility [28]. Therefore, pharmaceutical drug substances in development may not have great water solubility, but generally are soluble in organic solvents. Thus, dilute-and-shoot sample processing as a core to the sample flow for TXRF

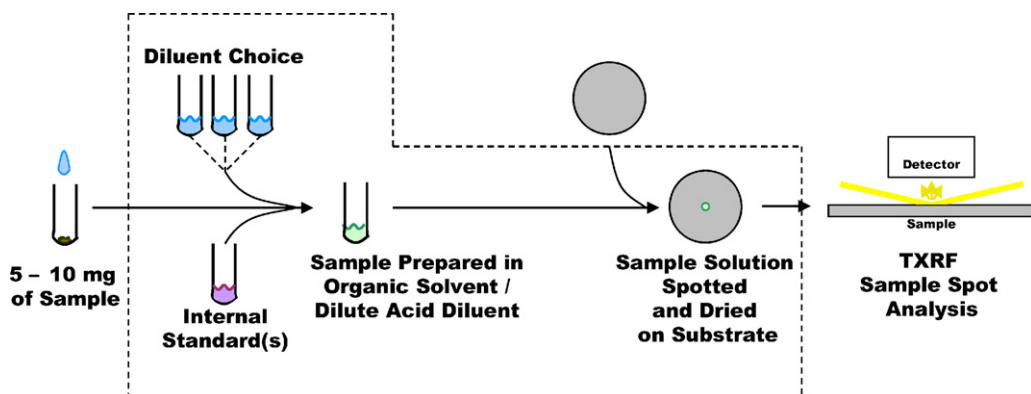


Fig. 5. TXRF sample flow diagram.

Table 3
Evaluation 2, results for palladium in six pharmaceutical drug substance samples for ICP-MS and TXRF platforms.

Instrument platform		Pharmaceutical drug substance ^a	Accuracy, % recovery	Precision, % RSD	Sensitivity, LOD, µg/g
ICP-MS	PE ELAN DRC II	S3	103	1.7	0.3
		S4	104	1.5	0.3
		S5	104	0.4	0.3
		S6	104	1.7	0.4
		S7	103	N/A	0.6
		S8	104	0.6	0.3
		S3	0		
		S4	0		
TXRF	Bruker AXS S2 Picofox (Mo-K source) ^b	S5	0		
		S6	17	37	10.0
		S7	0		
		S8	41	3	20.3
		S3	95	17	3.1
		S4	85	4	2.5
		S5	92	9	3.9
		S6	86	1	2.9
TXRF	Bruker AXS S2 Picofox (W-K source) ^c	S7	91	8	3.7
		S8	87	4	4.7
		S3	115	4	10.8
		S4	115	8	10.0
		S5	0		5.9
		S6	65	23	9.2
		S7	112	19	12.2
		S8	147	32	14.3
TXRF	Technos TREX 6000 (W-Lβ ₁ source) ^b	S3	83	19	4.3
		S4	107	16	5.2
		S5	73	39	3.7
		S6	101	44	5.2
		S7	90	20	4.8
		S8	103	37	9.3

^a S3: triprolidine HCl; S4: diphenhydramine HCl; S5: chlorpheniramine maleate; S6: pseudoephedrine HCl; S7: ephedrine sulfate; S8: scopolamine HBr.

^b Pd-L lines.

^c Pd-K lines.

is very possible where TXRF sample preparation is not limited to fully-soluble samples as with ICP-MS, but handles fully-soluble samples through homogeneous suspensions with proper mixing of samples. Tu et al. has demonstrated a novel ICP-OES method utilizing *N,N*-dimethylformamide (DMF) as a “universal” solvent for dilute-and-shoot sample analysis, however, with less than 100% applicability for samples [20]. The utilization of TXRF for solutions and suspensions indicates a 100% applicability of samples in the process development space. One scheme is represented in Fig. 5 where dilute-and-shoot processing is utilized for fast and efficient sample preparation, and is the subject of ongoing research, where we are currently demonstrating this screening platform in the process development space in order to determine its full utility. The use of TXRF would give obvious advantages as an easy and quick screening platform versus ICP-MS for elemental impurity or heavy metal analysis for pharmaceutically relevant elements while requiring relatively small sample sizes which is suitable for pharmaceutical development environments.

4. Conclusions

It is clear that the most important factor for the usage of TXRF as a screening platform for analysis of pharmaceutical drug substances is the instrument configuration and the X-ray source in particular. Analysis of Pd in pharmaceutical drug substances has interference limitations when Pd-L lines are used for this analysis, but are alleviated when Pd-K lines are used. A TXRF screening platform for the analysis of pharmaceutical drug substances is possible with current TXRF instrumentation, however there is a clear trade-off that must be weighed between Pd (and Rh) analysis versus sensitivity for most other elements of interest. This trade-off is not found with ICP-MS, and as a result, TXRF can compliment ICP-MS in a pharmaceutical development setting. It is our conclusion

that a screening platform based upon detection of Pd should be the primary driver for the adoption of a TXRF platform. Ideally, an instrument with multiple sources would alleviate this trade-off, but only at the expense of another trade-off: cost.

Acknowledgements

The authors wish to thank the editor and reviewers of this manuscript for very thoughtful critique of this work. The authors wish to acknowledge Drs. Gary Guo and Tiffany Thiel, Messrs. Chris Scardino, Mike Ronk, and David Yeung from Amgen Inc., and Mr. Addison Arlow, a summer intern at Amgen. The authors wish to acknowledge Alexander Seyfarth, Arkady Buman, Hagen Stosnach, and Edward P. (JR) Doris from Bruker AXS, Inc., and Françoise Queromes from Technos International, Inc. Additionally the authors wish to acknowledge H. Murakami and Hikari Takahara from Technos Company, Ltd. and Chris Sparks from SVTC Technologies, Inc.

Appendix A. Supplementary data

Supplementary data associated with this article can be found, in the online version, at [doi:10.1016/j.jpba.2012.01.037](https://doi.org/10.1016/j.jpba.2012.01.037).

References

- [1] D.R. Abernethy, A.J. DeStefano, T.L. Cecil, K. Zaidi, R.L. Williams, USP Metal Impurities Advisory Panel, Metal impurities in food and drugs, *Pharm. Res.* 27 (2010) 750–755.
- [2] International Conference on Harmonization, Q3 quality guidelines, 2006, www.ich.org.
- [3] European Medicines Agency, Doc. Ref. EMEA/CHMP/SWP/4446/2000, London, 21 February 2008.
- [4] C.E. Garrett, K. Prasad, The art of meeting palladium specifications in active pharmaceutical ingredients produced by Pd-catalyzed reactions, *Adv. Synth. Catal.* 346 (2004) 889–900.

- [5] M. Lamblin, L. Nassar-Hardy, J. Hierso, E. Fouquet, F. Felpinb, Recyclable heterogeneous palladium catalysts in pure water: sustainable developments in Suzuki, Heck, Sonogashira and Tsuji–Trost reactions, *Adv. Synth. Catal.* 352 (2010) 33–79.
- [6] D.M. D'Souza, T.J.J. Müller, Multi-component syntheses of heterocycles by transition-metal catalysis, *Chem. Soc. Rev.* 36 (2007) 1095–1108.
- [7] E. Marguá, K. Van Meel, R. Van Grieken, A. Buendía, C. Fontàs, M. Hidalgo, I. Queralt, Method for the determination of Pd-catalyst residues in active pharmaceutical ingredients by means of high-energy polarized-beam energy dispersive X-ray fluorescence, *Anal. Chem.* 81 (2009) 1404–1410.
- [8] N. Lewen, The use of atomic spectroscopy in the pharmaceutical industry for the determination of trace elements in pharmaceuticals, *J. Pharm. Biomed. Anal.* 55 (2011) 653–661.
- [9] I. Savage, S.J. Haswell, The development of analytical methodology for simultaneous trace elemental analysis of blood plasma samples using total reflection X-ray fluorescence spectrometry, *J. Anal. At. Spectrom.* 13 (1998) 1119–1122.
- [10] L. Borgese, A. Zacco, E. Bontempi, M. Pellegatta, L. Vigna, L. Patrini, L. Riboldi, F.M. Rubino, L.E. Depero, Use of total reflection X-ray fluorescence (TXRF) for the evaluation of heavy metal poisoning due to the improper use of a traditional ayurvedic drug, *J. Pharm. Biomed. Anal.* 52 (2010) 787–790.
- [11] A.Z. Abu Zuhri, W. Voelter, Applications of adsorptive stripping voltammetry for the trace analysis of metals, pharmaceuticals and biomolecules, *Fresenius J. Anal. Chem.* 360 (1998) 1–9.
- [12] Pharmacopoeia of the United States of America, Procedure 121, Time-limit test for heavy metals, 8th revision, Lippincott, Philadelphia, PA, 1905.
- [13] The United States Pharmacopoeia/The National Formulary, USP 32/NF 29, The United States Pharmacopoeia Convention, Rockville, MD, 2011, Chapter 231, Heavy Elements, pp. 135–136.
- [14] D. Beauchemin, Inductively coupled plasma mass spectrometry, *Anal. Chem.* 78 (2006) 4111.
- [15] C.A. Ponce de Leon, M. Montes-Bayon, J.A. Caruso, Elemental speciation by chromatographic separation with inductively coupled plasma mass spectrometry detection, *J. Chromatogr. A* 974 (2002) 1–21.
- [16] T. Wang, J. Wu, R. Hartman, X. Jia, R. Egan, A multi-element ICP-MS survey method as an alternative to the heavy metals limit test for pharmaceutical materials, *J. Pharm. Biomed. Anal.* 23 (2000) 867–890.
- [17] J. Huang, X. Hu, J. Zhang, K. Li, Y. Yan, X. Xu, The application of inductively coupled plasma mass spectrometry in pharmaceutical and biomedical analysis, *J. Pharm. Biomed. Anal.* 40 (2006) 227–234.
- [18] N. Lewen, S. Mathew, M. Schenkenberger, T. Raglione, A rapid ICP-MS screen for heavy metals in pharmaceutical compounds, *J. Pharm. Biomed. Anal.* 35 (2004) 739–752.
- [19] R.N. Rao, M.V.N. Kumar Talluri, An overview of recent applications of inductively coupled plasma-mass spectrometry (ICP-MS) in determination of inorganic impurities in drugs and pharmaceuticals, *J. Pharm. Biomed. Anal.* 43 (2007) 1–13.
- [20] Q. Tu, T. Wang, V. Antonucci, High-efficiency sample preparation with dimethylformamide for multi-element determination in pharmaceutical materials by ICP-AES, *J. Pharm. Biomed. Anal.* 52 (2010) 311–315.
- [21] Y. Yoneda, T. Horiuchi, Optical flats for use in X-ray spectrochemical microanalysis, *Rev. Sci. Instrum.* 42 (1971) 1069–1070.
- [22] S. Pahlke, Quo Vadis total reflection X-ray fluorescence? *Spectrochim. Acta Part B* 58 (2003) 2025–2038.
- [23] H. Aiginger, Historical development and principles of total reflection X-ray fluorescence analysis (TXRF), *Spectrochim. Acta* 46B (1991) 1313–1321.
- [24] M. Wagner, P. Rostam-Khani, A. Wittershagen, C. Rittmeyer, B.O. Kolbesen, H. Hoffman, Trace element determination in drugs by total-reflection X-ray fluorescence spectrometry, *Spectrochim. Acta Part B* 52 (1997) 961–965.
- [25] S. Nomura, T. Ninomiya, K. Taniguchi, S. Ikeda, Application of total reflection X-ray fluorescence spectrometry to drug analysis, in: C.S. Barrett, J.V. Gilfrich, T.C. Huang, R. Jenkins, G.J. McCarthy, P.K. Predecki, R. Ryon, D.K. Smith (Eds.), *Advances in X-Ray Analysis*, vol. 35B, Plenum Press, New York, 1992, pp. 969–974.
- [26] M. Wagner, P. Rostam-Khani, A. Wittershagen, C. Rittmeyer, H. Hoffmann, B.O. Kolbesen, Application of total reflection X-ray fluorescence (TXRF) to trace element determination in pharmaceutical substances, *Pharmazie* 51 (1996) 865–868.
- [27] Q. Tu, T. Wang, C.J. Welch, High-throughput metal screening in pharmaceutical samples by ICP-MS with automated flow injection using a modified HPLC configuration, *J. Pharm. Biomed. Anal.* 51 (2010) 90–95.
- [28] M. Ishikawa, Y. Hashimoto, Improvement in aqueous solubility in small molecule drug discovery programs by disruption of molecular planarity and symmetry, *J. Med. Chem.* 54 (2011) 1539–1554.



Qualitative and quantitative reversed-phase high performance liquid chromatographic analysis of glycoprotein hormones in the presence of a large excess of human serum albumin

B.E. Almeida^a, J.E. Oliveira^a, R. Damiani^a, S.L. Dalmora^b, P. Bartolini^a, M.T.C.P. Ribela^{a,*}

^a Biotechnology Department, IPEN-CNEN, Av. Prof. Lineu Prestes 2242, Cidade Universitária, 05508-900 São Paulo, Brazil

^b Department of Industrial Pharmacy, Federal University of Santa Maria, Santa Maria, RS, Brazil

ARTICLE INFO

Article history:

Received 30 November 2011

Received in revised form 27 January 2012

Accepted 29 January 2012

Available online 6 February 2012

Keywords:

RP-HPLC

HSA

Glycoprotein hormones

Excipient

WHO standards

ABSTRACT

The present work describes reversed-phase high performance liquid chromatographic methodologies (RP-HPLC) for the qualitative and quantitative analysis of the human glycoprotein hormones thyrotropin (hTSH), follitropin (hFSH), choriogonadotropin (hCG) and lutropin (hLH) in the presence of a large excess (up to 250:1) of human serum albumin (HSA). Chromatographic profiles with a good separation between the hormone and HSA were obtained by using a C4 column and specific gradient elution conditions for each hormone. Parameters such as resolution factor, tailing factor and relative retention time, were determined, and are useful for the evaluation of the quality of the separation obtained between the active pharmaceutical ingredient and the excipient present in the final formulation. The potential of each method for quantification of both HSA and the hormone was also demonstrated. Besides furnishing chromatographic quantifications that can substitute for in vivo bioassays and animal use, the chromatograms also provide a direct panorama of the quality and heterogeneity of the protein of interest.

© 2012 Elsevier B.V. All rights reserved.

1. Introduction

Long-term stability is a quality requirement for both pharmaceutical proteins and reference standards, and addition of stabilizers is crucial for attaining this goal [1]. In the final preparations, the active pharmaceutical substance is, in general, present in extremely limited amounts as compared to the large amounts of excipients. These are added to prevent adsorption of proteins to the vial, increase their stability, and protect them during storage. Common excipients include sugars (e.g., saccharose, lactose, trehalose), amino acids (e.g., methionine, arginine, glycine), polyols (e.g., mannitol), polymers (e.g., poloxamer P188), detergents (e.g., polysorbate 20), salts (e.g., sodium chloride, sodium phosphate) and proteins [2].

Human serum albumin (HSA), in particular, has been quite successfully employed as a protein excipient. The stabilizing, antioxidant and cryoprotective properties of HSA prevent losses due to adsorption and degradation, which correlate with reduced bioactivity and enhanced immunogenic reactions [3]. A major drawback of the presence of this excipient is its interference with many analytical techniques. Suitable analytical methods that permit an adequate discrimination between excipients and protein

thus need to be developed. For this reason, several chromatographic and electrophoretic methods that attempt to circumvent this limitation have been reported in the literature. Bietlot and Girard [4], utilizing high-performance capillary electrophoresis (HPCE), analyzed recombinant human erythropoietin (r-hEPO) in the presence of HSA by adding 1 mM nickel chloride to the electrophoretic buffer, obtaining a complete separation of the two proteins. In this case, the added metal ions interacted selectively with HSA, decreasing its electrophoretic mobility. Wilczynska et al. [5] described a reversed-phase high performance liquid chromatographic (RP-HPLC) procedure for the quantitative estimation of r-hEPO in biopharmaceutical products formulated with HSA. A suitable resolution between albumin, r-hEPO and related proteins was established utilizing a C18 column and a gradient profile developed specifically for this purpose. Qian et al. [6] developed a high performance size exclusion chromatographic (HPSEC) method to evaluate HSA stability over the three year shelf-life of a pharmaceutical preparation of interferon alfa-2b (IFN). For this purpose, several key factors that affect HPSEC selectivity and chromatographic performance were optimized, such as column type, mobile phase, sample preparation (concentration, diluents, method of mixing), injection volume and flow rate. Eertmans et al. [7] developed and validated a RP-HPLC method that allows a quick and reliable determination of the HSA content in assisted reproductive techniques-related media, without the interference of other matrix ingredients. They utilized a C4 column at 40 °C and gradient elution over 20 min, with HSA

* Corresponding author. Tel.: +55 11 31339694; fax: +55 11 31339694.

E-mail address: mtribela@ipen.br (M.T.C.P. Ribela).

eluting within the first 10 min. Another approach for eliminating the interference of excipients in biopharmaceuticals analysis is to remove them from the pharmaceutical formulations or to extract the active protein. Lara-Quintanar et al. [8] proposed the removal of HSA from r-hEPO formulations by immunochromatography in their capillary electrophoretic method. Liu et al. [9] isolated recombinant follitropin (r-hFSH) with high purity and yield from a pharmaceutical preparation formulated with multiple excipients. The authors adopted a purification strategy involving anion exchange chromatography followed by desalting, utilizing a centrifuge device with a 10 kDa cut off ultrafiltration membrane.

Besides pharmaceutical preparations, International Standards and Reference Reagents, including those prepared by the National Institute for Biological Standards and Control (NIBSC) on behalf of World Health Organization (WHO), are also frequently lyophilized in the presence of a large excess of a protecting/stabilizing protein such as HSA [10–12]. This is mostly due to the fact that these precious purified, controlled and calibrated reagents are used to prepare thousands of ampoules in which they are present in very small amounts. These preparations are intended for use as standards for in vivo and in vitro bioassays in which the extraneous protein is practically inert. Nonetheless, this hampers the utilization of such standards for chromatographic testing, a type of assay that is progressively substituting bioassays because of higher precision and lower cost. In addition, physical chemical tests provide an alternative to the use of animals, avoiding the associated ethical considerations [13]. In this context, the use of the same reference standard for monitoring the content/potency of therapeutic products in both types of assays is extremely important.

The focus of this work was, therefore, the development of high resolution RP-HPLC techniques for the analysis of reference preparations of human glycoprotein hormones, specifically hFSH, hLH, hTSH and hCG, in the presence of up to 250-fold larger amounts of human serum albumin. For this purpose, three new chromatographic conditions were developed by introducing modifications to the five conditions already set up by our research group for glycoprotein hormone analysis by RP-HPLC [12,14–16]. Besides allowing the quantitative chromatographic determination of these specific hormones, these methodologies also provide a real-time panorama of the quality and heterogeneity of the protein of interest.

2. Materials and methods

2.1. Chemicals and reagents

Water was obtained from a Milli-Q Plus water-purification system (Millipore, Bedford, MA, USA). Acetonitrile (HPLC-grade, Mallinckrodt Baker) was purchased from Hexis (São Paulo, Brazil). All other chemicals were analytical reagent grade, purchased from Merck (São Paulo, Brazil) and Sigma (St. Louis, MO, USA).

2.2. Hormone preparations

The WHO International Standards for glycoprotein hormones utilized in this work were from the National Institute for Biological Standards and Control (NIBSC, South Mimms, UK): International Reference Preparation of Thyroid Stimulating Hormone (TSH) Pituitary, Human, for Immunoassay (WHO 80/558); International Standard of Follicle-Stimulating Hormone (FSH) Recombinant, Human, for Bioassay (WHO 92/642); International Standard of Luteinizing hormone (LH) Recombinant, Human, for Bioassay (WHO 96/602); International Standard of human Chorionic Gonadotropin (CG) Urinary (WHO 07/364). Commercial recombinant preparations from Genzyme Corporation (Framingham, MA, USA) and from Laboratoires Serono S.A. (Aubonne, Switzerland)

Table 1
Bioactivities of all recombinant and native preparations.

Preparation	Hormone mass (µg/ampoule)	Unitage (IU/ampoule)	Specific activity (IU/mg)
p-hTSH (WHO 80/558)	7.5 ^a	0.037 ^a	4.9
r-hFSH (WHO 92/642)	10 ^a	138 ^a	13,800
u-hCG (WHO 07/364)	13.7 ^b	162 ^a	11,825
r-hLH (WHO 96/602)	8.8 ^a	189 ^a	21,477
r-hTSH (Thyrogen)	1100 ^a	–	4–12 ^a
r-hFSH (Gonal-f)	5.5 ^a	75 ^a	13,636
r-hCG (Ovidrel)	250 ^a	6500 ^a	26,000
r-hLH (Luveris)	3.0 ^c	75 ^a	25,000

^a Declared by the manufacturer.

^b Calculated with basis on a MW of 35.1 kDa [17] from the declared content of 0.39 nmol.

^c Calculated from BCA determinations [12].

were also utilized: Thyrogen (r-hTSH), Gonal-f (r-hFSH), Luveris (r-hLH) and Ovidrel (r-hCG). In Table 1, the declared units and/or mass contents are reported, together with the calculated specific bioactivities.

2.3. Reversed-phase high performance liquid chromatography (RP-HPLC)

RP-HPLC analyses of the WHO glycoprotein hormones (hFSH, hLH, hTSH and hCG), formulated with HSA were carried out with a Shimadzu Model SCL-10A HPLC apparatus with a SPD-10AV UV detector using a C4-Grace Vydac (Separations Group, Hesperia, CA, USA) 214 TP 54 column (25 cm × 4.6 mm I.D., pore diameter of 300 Å and particle diameter of 5 µm) coupled to a guard column Grace Vydac 214 FSK 54 (1 cm × 4.6 mm I.D.). A silica pre-column (packed with LiChrosorb Si 60, 7.9–12.4 µm, Merck, Darmstadt, Germany) was inserted between the pump and the injector. The column temperature was maintained at 25 °C and detection was by UV absorbance at 220 nm. Gradient solutions A and B were utilized, solution A being sodium phosphate buffer (pH 7.0; 0.05 M) and solution B acetonitrile. For hFSH and hTSH elution, linear gradients from A:B (87.5:12.5, v/v) to A:B (50:50, v/v) over 40 min and from A:B (50:50, v/v) to A:B (35:65, v/v) over 20 min were utilized. For hLH elution, linear gradients from A:B (73:27, v/v) to A:B (58:42, v/v) over 60 min and from A:B (58:42, v/v) to A:B (35:65, v/v) over 20 min were utilized. For hCG, linear gradients from A:B (75:25, v/v) to A:B (50:50, v/v) over 50 min and from A:B (50:50, v/v) to A:B (35:65, v/v) over 20 min were used. Aliquots of 20–125 µl of these preparations were processed, at a flow-rate of 0.5 ml/min. To evaluate the quality of the separation between HSA and the hormones, the resolution factor (Rf) was determined, according to definition that considers the peak asymmetry [18]. In general, Rf > 1.5 is indicative of complete resolution, allowing an accurate integration of the individual peaks and their quantification.

$$Rf = \frac{2(t_2 + w_2/2(1 - 1/Tf_2)) - t_1 - w_1/2(1 - 1/Tf_1)}{w_1 + w_2}$$

where t_2 and t_1 are the retention times of HSA and the hormone, respectively, w_2 and w_1 are the peak width at baseline of the eluted HSA and hormone peaks, respectively, and Tf_2 and Tf_1 are the tailing factors of HSA and hormone, respectively.

The degree of peak asymmetry was estimated via the tailing factor, determined according to the definition:

$$Tf = \frac{a + b}{2a}$$

where a and b are the peak widths of the left and right sides, respectively, measured at the baseline, with $w = a + b$. The peak is symmetrical when Tf is 1.00.

Table 2
System suitability parameters determined for RP-HPLC analysis of WHO glycoprotein hormones: retention time (t_R), peak width (w), tailing factor (Tf), relative retention time (T_{RR}) and resolution factor between each hormone and HSA (Rf).

Preparation	Hormone			HSA			T_{RR}	Rf
	t_{R1}^a (min)	w_1 (min)	Tf ₁	t_{R2}^a (min)	w_2 (min)	Tf ₂		
p-hTSH (WHO 80/558)	33.61 ± 0.12	1.98	1.0	46.42 ± 0.05	3.24	1.2	0.72	5.02
r-hFSH (WHO 92//642) α	32.32 ± 0.29	2.72	1.2	46.62 ± 0.35	4.71	1.3	0.69	3.95
r-hFSH (WHO 92//642) β	23.29 ± 0.19	2.43	1.3				0.50	6.01
u-hCG (WHO 07/364)	24.87 ± 0.11	4.10	1.1	51.37 ± 0.25	8.29	1.2	0.48	4.36
r-hLH (WHO 96/602)	30.00 ± 0.16	11.40	1.6	72.12 ± 0.12	18.28	1.1	0.42	2.72

^a Mean ± standard deviation ($n=3$).

An index of relative retention of the hormones (T_{RR}) was determined according to the definition:

$$T_{RR} = \frac{t_R \text{ hormone}}{t_R \text{ HSA}}$$

For the determination of the HSA content, a calibration curve was constructed by plotting the HSA peak area (in arbitrary units) as a function of the amount of added HSA (μg), over the range of 5–200 μg . For hormone quantification, highly purified commercial recombinant preparations, already characterized in previous work in our laboratory [12,14,15], were utilized as internal reference preparations, since the WHO standards containing hormone + HSA were considered to be the unknown preparations in this study. In the case of r-hFSH quantitation, the determination was done by considering peak areas of the two subunits. The results were then compared with those obtained via a previously set up RP-HPLC condition that is able to determine the undissociated heterodimeric peak [13,15]. Both HSA and the hormones were determined in three independent assays.

3. Results

Specific RP-HPLC conditions were set up that provided useful separations between the huge peak of HSA, present in the WHO standard preparations, and the peaks of hTSH, hFSH, hLH or hCG (see Section 2). Under optimal chromatographic conditions for each hormone, the heterogeneous formulations, analyzed in three RP-HPLC assays, showed good separation between the two peaks (Fig. 1). All peaks presented retention times with a relative standard deviation (RSD) < 1%, tailing factors (Tf) $1 < \text{Tf} < 1.6$ and resolution factor (Rf) > 2 (Table 2). These system suitability parameters are in agreement with the Food and Drug Administration (FDA) validation requirements [19]. The lowest resolution of the hormone relative to HSA was found for hLH, probably because it presents the highest degree of asymmetry (Tf = 1.6). Conversely, the peak corresponding to hTSH was symmetrical, with Tf = 1, while the resolution relative to HSA was the second highest (Rf = 5.02), even though the two peaks eluted quite close to each other ($T_{RR} = 0.72$).

The HSA present in the WHO ampoules of p-hTSH, r-hFSH, u-hCG and r-hLH (Table 3) was determined by utilizing the constructed calibration curve:

$$Y_{u.a.} = 223.34X_{\mu\text{g}} - 124.69, \quad r = 0.9994 (n = 6)$$

Table 3
Quantitative analysis of glycoprotein hormones and HSA in WHO ampoules.

Preparation	Hormone			HSA		
	Nominal amount (μg)	Found amount ^a (μg)	RSD (%)	Nominal amount (mg)	Found amount ^a (mg)	RSD (%)
p-hTSH (WHO 80/558)	7.5	4.22 ± 0.04	0.95	1.0	1.06 ± 0.02	1.89
r-hFSH (WHO 92//642)	10.0	10.72 ± 0.21	1.96	2.0	2.10 ± 0.06	2.86
u-hCG (WHO 07/364)	13.7	7.20 ± 0.25	3.47	2.0	1.79 ± 0.08	4.47
r-hLH (WHO 96/602)	8.8	8.76 ± 0.23	2.63	2.0	1.80 ± 0.05	2.78

^a Mean ± standard deviation ($n=3$).

The hormone contents in the WHO ampoules, also shown in Table 3, were determined relative to the previously characterized reference preparations, which served as secondary standards. The inter-day quantitative determinations indicated a relative standard deviation (RSD) of 0.95–4.5%. The minimal detectable amount, determined according to the Rodbard definition of sensitivity [20], was in the order of 6–20 ng for the four hormones. The mean percent recoveries of HSA were 97.6 ± 9.1 relative to the stated nominal HSA contents. Concerning the hormone contents in the ampoules, the mean percent recovery was 103.4 ± 5.5 for recombinant preparations of hFSH and hLH; however, a significant discrepancy was found for p-hTSH and u-hCG, a recovery of only 56% and 53% being observed, respectively.

4. Discussion

An important issue in biopharmaceutical drug quality control is the availability of chromatographic tools that permit the accurate analysis of the active principle without interference from other components of the final drug formulation with similar hydrophobic, ionic and/or spectrophotometric characteristics. In this context, the three RP-HPLC methodologies developed here for the qualitative and quantitative analysis of hTSH, hFSH, hCG and hLH in the presence of substantial excesses of HSA successfully permit the quantitative and qualitative analysis of all of the proteins present in each formulation. For the first time, these hormones could be analyzed merely by altering and optimizing the chromatographic conditions, without the need for salt addition, extraction or protein removal typical of other approaches in the literature [4,8,9], thus providing a powerful instrument for identification and quality control of these precious preparations. Albumin is not used as an excipient in the recombinant human glycoprotein hormones preparations currently on the pharmaceutical market, but we believe that improved separations between hormone and albumin are useful as a model for qualitative and quantitative analysis of glycoprotein hormone in the presence of excipients. They can also provide an initial characterization of recombinant hormone before final separation of a major albumin-like contaminant, which is very common in the CHO cell serum-free media.

Reproducible chromatographic profiles, with a good separation between the hormone and HSA (Rf > 2), were achieved using a C4 column and gradient elution conditions optimized for each

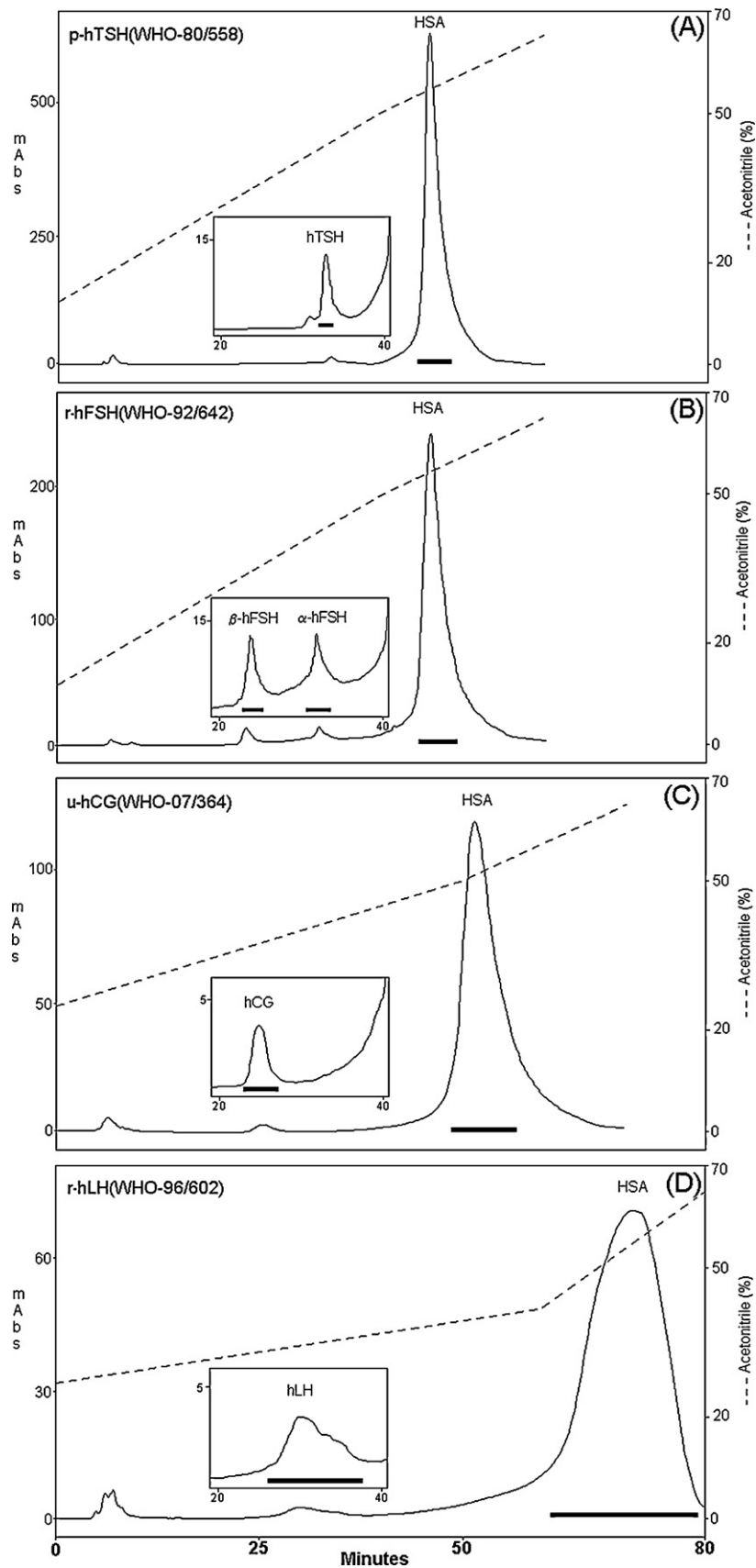


Fig. 1. RP-HPLC profile of different WHO International Standard preparations with HSA/hormone ratio of 200–250: (A) p-hTSH (WHO-80/558); (B) r-hFSH (WHO-92/642); (C) u-hCG (WHO-07/364); and (D) r-hLH (WHO-96/602).

hormone. In the methods previously developed for hLH and hCG in our laboratory [12], lower T_{RR} and poorer resolutions between the hormone and HSA had been obtained. An approximately 2-fold improvement in both of these parameters was achieved thanks to the current methodologies. Parameters such as the resolution factor, tailing factor and relative retention time were found to be suitable in general for evaluating the chromatographic resolution and selectivity between the active protein and the excipient. The sensitivities, determined for the methodologies described, were excellent for all four hormone preparations.

Quantitative estimation of the hormones in the International Standard formulations showed very good agreement with the declared content for the recombinant hormones (r-hFSH and r-hLH). However, for urinary-hCG and pituitary-hTSH, a significant bias (~50%) was found, probably due to the much lower specific activity of these native pituitary and urinary preparations compared to the recombinant ones. We emphasize, for example, that a recent recombinant hTSH Standard (WHO 03/192) has a bioactivity of 10.9 IU/mg against the 4.9 IU/mg of p-hTSH (WHO 80/558). The less pure native preparations were quantified against highly purified recombinant preparations and therefore a correspondent lower mass was found, per unit. Thus, the RP-HPLC strategy described herein is able to reveal the correct relationship between biological activity and real amount of hormone present. It is worth mentioning that hFSH quantitation was possible considering both subunits area combined, since well-defined peaks were obtained for each subunit. However, when these areas are not as easy to define, as for example for pituitary hFSH subunits, the hormone quantitation could utilize the RP-HPLC condition previously developed in our laboratory for the determination of intact heterodimeric hFSH [15]. Our RP-HPLC strategy was also successfully employed for HSA quantification and allowed accurate determination of the amount of HSA present in the drug formulations. In addition, the complete chromatographic separation of the hormone from the protein excipient also provided a qualitative estimate of the hormone under analysis and of its possible heterogeneity.

In conclusion, this work demonstrates the enormous potential of RP-HPLC for the separation and the quantitative and qualitative evaluation of protein excipients and hormones, underlining its importance as a chromatographic method for the rapid analysis of standards, reference preparations and biopharmaceutical in general.

Acknowledgements

This work was supported by FAPESP, São Paulo, Brazil (11/07289-0) and by the Brazilian National Research Council (CNPq), Brasilia, Brazil (PQ 303839/2008-2 and PQ 300473/2009-5).

References

[1] M.C. Manning, D.K. Chou, B.M. Murphy, R.W. Payne, D.S. Katayama, Stability of protein pharmaceuticals: an update, *Pharm. Res.* 27 (2010) 544–575.

- [2] D. Wong, J. Parasrampur, *Pharmaceutical excipients for the stabilization of proteins*, *Biopharm* 10 (1997) 52–61.
- [3] A. Hawe, W. Friess, *Formulation development for hydrophobic therapeutic proteins*, *Pharm. Dev. Technol.* 12 (2007) 223–237.
- [4] H.P. Bietlot, M. Girard, *Analysis of recombinant human erythropoietin in drug formulations by high-performance capillary electrophoresis*, *J. Chromatogr. A* 759 (1997) 177–184.
- [5] J.D. Wilczynska, I. Roman, E. Anuszevska, *The separation of EPO from other proteins in medical products formulated with different stabilizers*, *Acta Pol. Pharm.* 62 (2005) 177–182.
- [6] J. Qian, Q. Tang, B. Cronin, R. Markovich, A. Rustum, *Development of a high performance size exclusion chromatography method to determine the stability of human serum albumin in a lyophilized formulation of interferon alfa-2b*, *J. Chromatogr. A* 1194 (2008) 48–56.
- [7] F. Eertmans, V. Bogaert, P. Barbara, *Development and validation of a high-performance liquid chromatography (HPLC) method for the determination of human serum albumin (HSA) in medical devices*, *Anal. Methods* 3 (2011) 1296–1302.
- [8] P. Lara-Quintana, I. Lacunza, J. Sanz, J.C. Díez-Masa, M. Frutos, *Immuno-chromatographic removal of albumin in erythropoietin biopharmaceutical formulations for its analysis by capillary electrophoresis*, *J. Chromatogr. A* 1153 (2007) 227–234.
- [9] C. Liu, S. Dong, X. Xu, Y. Yin, Z. Shriver, I. Capila, J. Myette, G. Venkataraman, *Assessment of the quality and structural integrity of a complex glycoprotein mixture following extraction from the formulated biopharmaceutical drug product*, *J. Pharm. Biomed. Anal.* 54 (2011) 27–36.
- [10] M.T.C.P. Ribela, A.C. Bianco, P. Bartolini, *The use of recombinant human thyrotropin produced by Chinese hamster ovary cells for the preparation of immunoassay reagents*, *J. Clin. Endocrinol. Metab.* 81 (1996) 249–256.
- [11] E. Tarelli, A. Mire-Sluis, H.A. Tivnann, B. Bolgiano, D.T. Crane, C. Gee, X. Lemerainier, M.L. Athayde, N. Sutcliffe, P.H. Corran, B. Rafferty, *Recombinant human albumin as a stabilizer for biological materials and for the preparation of international reference reagents*, *Biologicals* 26 (1998) 331–346.
- [12] B.E. Almeida, J.E. Oliveira, C.M. Carvalho, S.L. Dalmora, P. Bartolini, M.T.C.P. Ribela, *Analysis of human luteinizing hormone and human chorionic gonadotropin preparations of different origins by reversed-phase high-performance liquid chromatography*, *J. Pharm. Biomed. Anal.* 53 (2010) 90–97.
- [13] B.E. Almeida, J.E. Oliveira, R. Damiani, S.L. Dalmora, P. Bartolini, M.T.C.P. Ribela, *A pilot study on potency determination of human follicle-stimulating hormone: a comparison between reversed-phase high-performance liquid chromatography method and the in vivo bioassay*, *J. Pharm. Biomed. Anal.* 54 (2011) 681–686.
- [14] J.E. Oliveira, F. Mendonça, C.N. Peroni, P. Bartolini, M.T.C.P. Ribela, *Determination of Chinese hamster ovary cell-derived recombinant thyrotropin by reversed-phase liquid chromatography*, *J. Chromatogr. B* 787 (2003) 345–355.
- [15] R.F. Loureiro, J.E. Oliveira, P.A. Torjesen, P. Bartolini, M.T.C.P. Ribela, *Analysis of intact human follicle-stimulating hormone preparations by reversed-phase high-performance liquid chromatography*, *J. Chromatogr. A* 1136 (2006) 10–18.
- [16] C.M. Carvalho, J.E. Oliveira, B.E. Almeida, E.K.M. Ueda, P.A. Torjesen, P. Bartolini, M.T.C.P. Ribela, *Efficient isolation of the subunits of recombinant and pituitary glycoprotein hormones*, *J. Chromatogr. A* 1216 (2009) 1431–1438.
- [17] P. Laidler, D.A. Cowan, R.C. Hider, A. Keane, A.T. Kicman, *Tryptic mapping of human chorionic-gonadotropin by matrix-assisted laser-desorption ionization mass-spectrometry*, *Rapid Commun. Mass Spectrom.* 9 (1995) 1021–1026.
- [18] D. Song, J. Wang, *Modified resolution factor for asymmetrical peaks in chromatographic separation*, *J. Pharm. Biomed. Anal.* 32 (2003) 1105–1112.
- [19] G.A. Shabir, *Validation of high-performance liquid chromatography methods for pharmaceutical analysis: understanding the differences and similarities between validation requirements of the US Food and Drug Administration, the US Pharmacopeia and the International Conference on Harmonization*, *J. Chromatogr. A* 987 (2003) 57–66.
- [20] D. Rodbard, *Statistical estimation of minimal detectable concentration (sensitivity) for radioligand assays*, *Anal. Biochem.* 90 (1978) 1–12.



Short communication

A homogeneous fluorescent sensor for human serum albumin

Rongsheng E. Wang¹, Ling Tian¹, Yie-Hwa Chang*

Mediomics, LLC, 5445 Highland Park Drive, St. Louis, MO 63110, USA

ARTICLE INFO

Article history:

Received 20 October 2011

Received in revised form

14 December 2011

Accepted 30 December 2011

Available online 28 January 2012

Keywords:

Human serum albumin (HSA)

Enzyme-linked immunosorbent assay

(ELISA)

Time-resolved fluorescence energy transfer

(TR-FRET)

Sensor

ABSTRACT

Human serum albumin is the most abundant protein in the body and is an important biomarker used for disease-related diagnosis. Although the traditional enzyme-linked immunosorbent assay (ELISA) approach can precisely measure the concentration of human serum albumin, the multi-step procedure and time-consuming preparations of ELISA limit its diagnostic applications, preventing accurate point-of-care testing, for example. Herein, we report the recent development of an antibody-based albumin sensor that allows for a homogeneous measurement of albumin concentrations in saliva, urine and serum, in which this type of sensor is validated for the first time. The assay only requires simple mixing, and relies on time-resolved (TR) fluorescence resonance energy transfer (FRET) to produce robust, sensitive signals. The whole process, from sample preparation to final read-out, is expected to take less than 1 h and requires only a standard plate-reader, thus making the sensor a convenient and cost-effective tool for albumin analysis.

© 2012 Elsevier B.V. All rights reserved.

1. Introduction

Human serum albumin (HSA) is a negatively charged, non-glycosylated globular protein with a molecular weight of 67 kDa [1]. Reported to be the most abundant protein in the body, HSA accounts for 60% of the total proteins in plasma [2], and is synthesized exclusively in the liver, primarily in the polysomes of hepatocytes [1]. Possessing several low- and high-affinity ligand binding sites, HSA is able to bind ligands such as metal ions, pharmaceutical compounds, fatty acids, as well as metabolites [1,3]. Besides serving as a carrier, HSA displays a variety of properties such as antioxidation, reactive oxygen/nitrogen species (ROS/RNS) scavenging and anti-inflammation [1].

Clinically, albumin was used in past decades to maintain vascular volume in patients with cirrhosis due to its regulation of oncotic pressure [1,4]. Today, combined with other therapeutic approaches, the volume-expanding properties of albumin are still believed to be beneficial for patients with cirrhosis [1]. Further, administration of albumin has been shown in small studies to help resuscitate patients from hemorrhagic shock [5], treat intradialytic hypotensions [6], and prevent ovarian hyperstimulation syndrome [7].

Besides its applications in therapy, HSA is regarded as a standard biomarker, with its levels in serum, urine and saliva serving as

diagnostic and prognostic criteria [2]. The normal concentration of HSA in blood serum is 35–50 g/L [2,8]. In diseased conditions, however, low levels of albumin in serum (hypoalbuminemia < 30 g/L) may reveal malnutrition, liver disease, nephrosis, gastrointestinal protein loss, shock, edema and cardiovascular disease [2]. On the other hand, high serum levels of albumin (hyperalbuminemia > 55 g/L) are accompanied by dehydration and increasing body weight or body fat [2]. The reference range of albumin in urine is 2.2–25 mg/L [2,9]. Albumin higher than 25 mg/L in urine is normally filtered through the glomerulus, and reabsorbed or catabolized by the proximal tubules. However, albumin loss increases once the renal glomeruli become more permeable due to diabetes or renal damage [2]. The severe leakage of the glomerular filtration mechanism can lead to either micro-albuminuria or macro-albuminuria, depending on the amount of albumin lost (detectable by a simple urine test) [10]. While the normal concentration of HSA in saliva is less than 0.5 g/L [2], a higher concentration of saliva albumin usually indicates type-2 diabetes mellitus [11], or, for some cancer therapy patients, the potential for stomatitis [12].

Currently the most common method used to determine albumin levels is the enzyme-linked immunosorbent assay (ELISA), which is accurate but time-consuming. Heyduk et al. previously reported a novel antibody-based sensor technology that allows homogeneous detection of target proteins based on simple fluorescence [13,14]. With this platform, a series of homogenous sensors have been developed. They include sensors for cardiac troponin I [15], C-reactive protein [15], insulin [16], C-peptide [16], and pathogenic bacteria [17]. Herein, we describe a similar sensor design that can be adapted to rapidly determine albumin concentrations in biological

* Corresponding author. Tel.: +1 314 802 7454; fax: +1 314 997 2422.

E-mail addresses: wangr@mediomics.com (R.E. Wang),yiechang@mediomics.com (Y.-H. Chang).¹ Equal contribution.

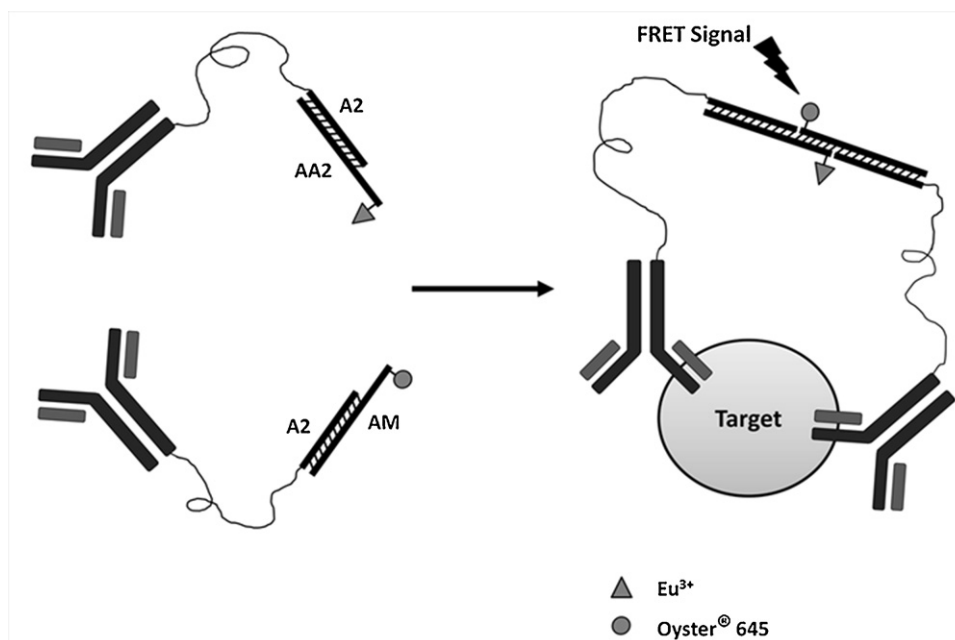


Fig. 1. Mechanism of the sensor. A pair of antibodies that recognize the target antigen is labeled with oligos that have complementary oligonucleotides at the ends. Both oligonucleotides are labeled with fluorophores that can be paired as donor and receptor. The presence of the target is expected to drive the annealing of the probe-labeled DNA, bringing the donor and receptor in close enough proximity to generate FRET signals.

samples. Using simple time-resolved fluorescence (TRF), the *in vitro* detection of human serum albumin can reach 3.9–1000 ng/mL. Most importantly, we demonstrate here for the first time the validation of this type of sensor in saliva, urine and serum, with the measured concentrations matching the results obtained with the traditional ELISA method. This validation confirms the sensor as a sensitive, reliable and convenient tool for albumin analysis.

2. Materials and methods

2.1. Sensor design

This assay consists of two human albumin-specific antibodies which recognize different epitopes of human albumin (Fig. 1). Each antibody is conjugated with short duplex DNA with overhangs complementary to each other. In the presence of human albumin, the two overhangs associate to form a duplex. Time-resolved fluorescence resonance energy transfer (TR-FRET) is initiated between the two fluorophores (labeled at the end of the two oligonucleotides) once they are brought into close proximity. The intensity of the FRET signal is proportional to the concentration of human albumin in the samples.

2.2. Materials

The Traut's reagent, NHS-(PEG)₁₂-maleimide, protein biconinonic acid (BCA) test kit, and human IgG (catalog number: 31154) were from Pierce, Thermo Scientific (Rockford, IL). Ethanol, glycogen, Tris (hydroxymethyl) aminomethane, sodium chloride, pH 7.4 PBS pouch, as well as human insulin (catalog number: I0908) and bovine serum albumin (catalog number: B6917), were all purchased from Sigma–Aldrich (St. Louis, MO). The human albumin standard (catalog number: J80310072), albumin antibodies (monoclonals, catalog numbers: 6501-100063, 6502-100064), and human C-reactive protein (catalog number: J81610) were obtained from Biospecific (Emeryville, CA). The 384-well low-volume black microplates were from Corning (Lowell, MA). The Synergy plate reader (Synergy 4, BioTek Instruments, Winooski,

VT), was equipped with a TR-FRET function and a 330 nm excitation filter (40 nm band pass), as well as a 620 nm (20 nm band pass) and a 665 nm (8 nm band pass) emission filters. The albumin sandwich ELISA kit was purchased from Assaypro (St. Louis, MO) and the ELISA was conducted exactly according to the instructions.

All oligonucleotides were synthesized and purified by Integrated DNA Technologies (Coralville, IA). The following oligonucleotides were used in the sensor experiments:

A2: 5'-amino-GCAGCCGATTCGACTTGC-3'

AA2: 5'-GTCAT-GCAAGXCGAATCGGCTGC-3' (X=T modified with Europium at the C6 position)

AM: 5'-AYGAGCG-GCAAGTCGAATCGGCTGC-3' (Y=T modified with Oyster645 dye at the C6 position)

AA2 and AM contain the 5'-overhang sequences (italicized) that are expected to anneal to each other and generate TR-FRET signals in the presence of the antigen (human albumin).

2.3. Antibody modifications

The antibody modification and purifications were based on previously published procedures [15,16]. For a detailed description of experimental procedures, please see Section S1.1 in Supplementary Material.

2.4. Human sample collections

Urine and saliva samples were randomly collected from apparently healthy personnel (including males and females) and stored at -20°C , which were later on thawed only once before the immediate measurements. The human serum samples were collected by Innovative Research (Novi, MI), from people between the ages of 18 and 65 under FDA regulations. Due to the limited number of serum samples, they were randomly processed after purchasing, by either concentrating or diluting to make their albumin concentrations in a diverse range. The processed serum samples were then stored at -20°C , and thawed only once before the immediate

measurements. Since it is not for the clinical applications, the collection of these human samples was not under the IRB approval.

2.5. The assay and validation procedures

The assay of albumin concentration with the standard curve as well as data analysis was similar to the previously published procedures [15,16]. A detailed description of experimental procedures is available at Sections S1.2 and S1.5 of Supplementary Material.

2.6. Time course study, cross-reactivity assay, intra- and inter-assay

The methods to characterize sensor kinetics, specificity, and accuracy were summarized in Sections S1.3, S1.4, and S1.6 of Supplementary Material.

3. Results and discussion

3.1. Development of the albumin sensor

Earlier, the most dominant methods for albumin detection used chromogenic dyes such as bromocresol green (BCG) and bromocresol purple (BCP) that colorimetrically detected albumin concentrations of 10 g/L or higher in plasma and pleural or peritoneal fluids [2]. Later, however, false high backgrounds were found for both dyes [2]. BCG reacted with heparins and some globulins, especially lipoproteins. Though BCP was not reactive with BCG-targeted proteins, it could still be bound by δ -bilirubin [2]. In the quest for a more specific assay, immunochemical procedures utilizing antibodies were gradually accepted [8,18] and replaced the dye-binding method when high sensitivity was required to detect the albumin on a mg/L scale. The initial strategy made use of a competition reaction, where albumin in the sample displaced the added antibody-bound albumin derivative. The released albumin derivative was then detected by fluorescence, radiation, scintillation or colorimetrics [8,9,18–22]. The most sensitive detection, however, was achieved with the sandwich ELISA technique, in which a pair of antibodies are used in combination with a peroxidase conjugate to detect urinary albumin in concentrations of 3–1000 μ g/L [23]. Even the simplified ELISA, with only one antibody, can still detect urinary albumin at concentrations as low as 15 μ g/L [24]. Despite its high sensitivity, the ELISA technique requires a considerable length of time and multiple operational steps from sample preparation to data acquisition. Even the modern commercially available ELISA kit, which uses a plate pre-coated with antibodies, still needs at least 3 h to produce results.

Compared to regular FRET, TR-FRET using lanthanides, especially europium (III), can significantly reduce the endogenous background fluorescence and thus achieve improved sensitivity [25]. Since the binding affinity of antibodies is key to the performance of biosensors [16], we chose a pair of antibodies that, to the best of our knowledge, have the highest affinity for albumin, with a K_a of 10^9 M⁻¹(L/mol). To prepare the human serum albumin sensor, we first modified the pair of albumin antibodies with the donor (Europium, excitation at 330 nm, emission around 620 nm) labeled oligonucleotide and the acceptor (Oyster645, excitation around 645 nm, emission at 665 nm) labeled oligonucleotide, respectively. When the pair of modified antibodies was mixed with buffer only, the background TR-FRET intensity was around 2000 (excitation at 330 nm, emission monitored at 665 nm). In the presence of increasing amounts of human albumin, we observed a stable and reproducible TR-FRET signal that was proportional to the concentration of albumin in the samples. The maximum intensity of TR-FRET can reach around 20000, when sensor was incubated with 1000 ng/mL albumin. The TR-FRET signal change relative to

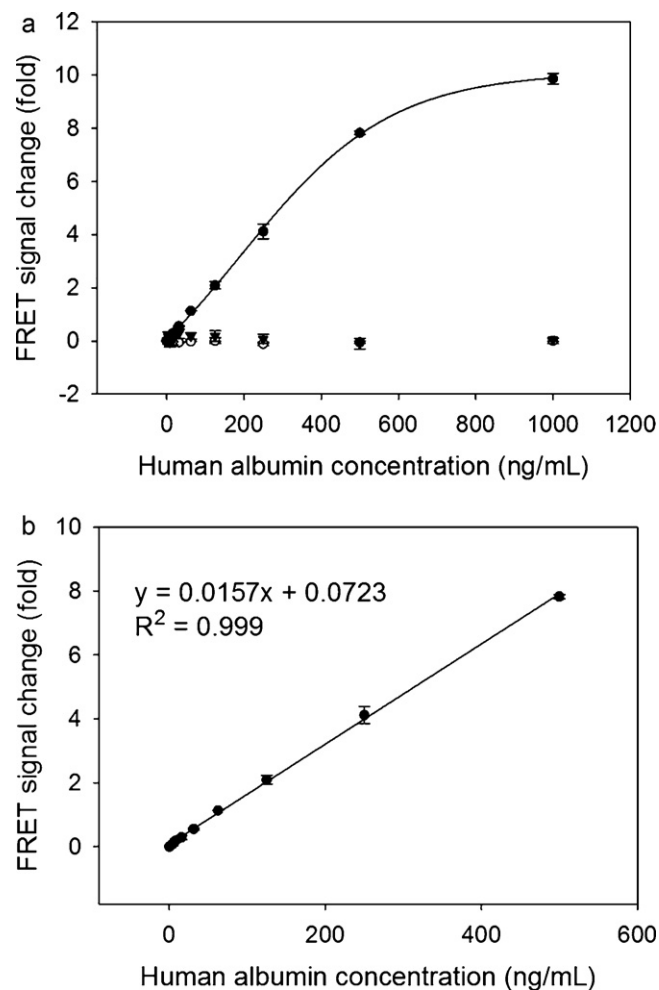


Fig. 2. The standard curves of human albumin measured by sensor. The signal change in fold (sensor's response) is plotted against the albumin concentrations. (a) The detectable range of albumin by sensor (●) is from 3.9 to 1000 ng/mL. As negative controls, the A2 modified antibody 6502 labeled by Europium is mixed with the A2 modified antibody 6501 (○), and the A2 modified antibody 6502 is mixed with the A2 modified antibody 6501 labeled by Oyster (▼). Both mixtures are not able to generate proportional signal changes upon their incubation with increasing concentrations of albumins. (b) The linear detection range of albumin by sensor (●) is from 3.9 to 500 ng/mL.

the background level was then used to plot against the concentrations of human serum albumin, with the generated standard curves shown in Fig. 2a. As expected for the negative controls, mixtures of both antibodies functionalized with the DNA A2, but only one antibody labeled with either the donor (Europium) or the acceptor (Oyster645), failed to generate TR-FRET signals proportional to the increasing concentration of albumin samples (Fig. 2a). In fact, when excited at 330 nm, the mixture with only one antibody labeled by the donor dye had a TRF reading around 2000 at 665 nm, whose intensity is similar to the background of the sensor. On the other hand, the mixture of antibodies with only one of them labeled by the acceptor dye emitted the TRF only at an intensity around 200–300 at 665 nm. This observation indicates that the background TR-FRET of the biosensor is mainly caused by the TRF of the donor dye – Europium. Taken together, in the regular TBS containing buffer, this biosensor can detect standard human serum albumin in concentrations from 3.9 ng/mL to 1000 ng/mL, with a coefficient of variation (CV) less than 3% (Fig. 2a). Within this broad detectable scope, the linear range is from 3.9 ng/mL to 500 ng/mL (Fig. 2b). The sensitivity of the sensor is comparable to most ELISA kits that are currently on the market. Although antibody 6501 was

labeled by the acceptor dye and antibody 6502 was labeled with the donor dye here, as illustrated in Fig. 2 and all through this paper, it is noteworthy that a switched modification (antibody 6501 labeled by the donor dye and antibody 6502 modified with the acceptor dye) would also result in the same sensor performance.

3.2. Kinetic studies of the albumin sensor

To demonstrate this homogenous biosensor's capability for rapid and convenient measurements, we next measured the kinetic characteristics by showing the time-dependence of signal changes in response to the amount of human albumin added (Fig. S1 in Supplementary Material). An increased incubation time was required to achieve either half or full signal responses when increasing amounts of antigens were added, presumably to allow the sensor mix to fully recognize the antigens present in the system and to reach an equilibrium. Full signal responses were usually achieved 40 min after addition of the antigens, with the only exception that when the maximum detectable amount of albumin was added, the system took around 50 min to reach full signal response. The repeated FRET measurements at different time-points may cause the photo-bleaching of probes, which, in our case, resulted in a slight decrease in signal response compared to the results of one-time measurement after 40 min. In all cases, a time length within 20 min after adding the albumin samples was needed to reach 50% of the maximum signal response. The full signal responses remained stable for 100 min (Fig. S1 in Supplementary Material) and even up to several hours after addition of the sample. In general, this assay is simple and fast, needing only one step of mixing and an incubation time of 40 min to produce results.

3.3. Specificity of the albumin sensor

To determine whether this sensor is specific to human serum albumin, we tested its cross-reactivities with human insulin, human CRP, and human IgG, which are proteins commonly existing in serum (Table S1 in Supplementary Material). While increasing TR-FRET was observed for human albumin at increasing concentrations from 0.06 nM to 15 nM (equaling 3.9 ng/mL to 1 μ g/mL), no positive signals were detected for any other proteins at concentrations up to 1 μ M. Normal insulin levels in plasma are 20–350 pM, and could be up to 100 nM in inflamed or other abnormal status. The level of human CRP in serum is usually less than 10 mg/L, but can be up to 200 mg/L (8 μ M) in diseased samples. Human IgG has a concentration in blood of 4–16 mg/mL (around 0.1 mM in maximum). Since the normal albumin level in human plasma is 35–50 g/L, a serum sample would need to be diluted at least 18000 fold for albumin determination by our sensor. Likewise, the concentrations of insulin, hCRP and IgG should be much lower than 100 nM in the samples diluted for albumin analysis, thereby presenting no interference with the performance of the albumin sensor. To see whether this sensor is reactive to albumin from different species, we tested its response to BSA, to find no positive readings for BSA at concentrations up to 1 μ M (Table S1 in Supplementary Data). In fact, no cross-reactivity was observed even when the concentration of BSA was increased to 10 mg/mL (142.8 μ M) (data not shown). Taking these results together, this simple, homogeneous assay exhibits high specificity towards human serum albumin.

3.4. Validation of the albumin sensor with the traditional ELISA method

To validate this albumin sensor's quantitative determination of albumin levels in saliva, urine and serum, we compared the results of the sensor with the results from a commercial ELISA kit performed under standard procedures. Twelve randomly

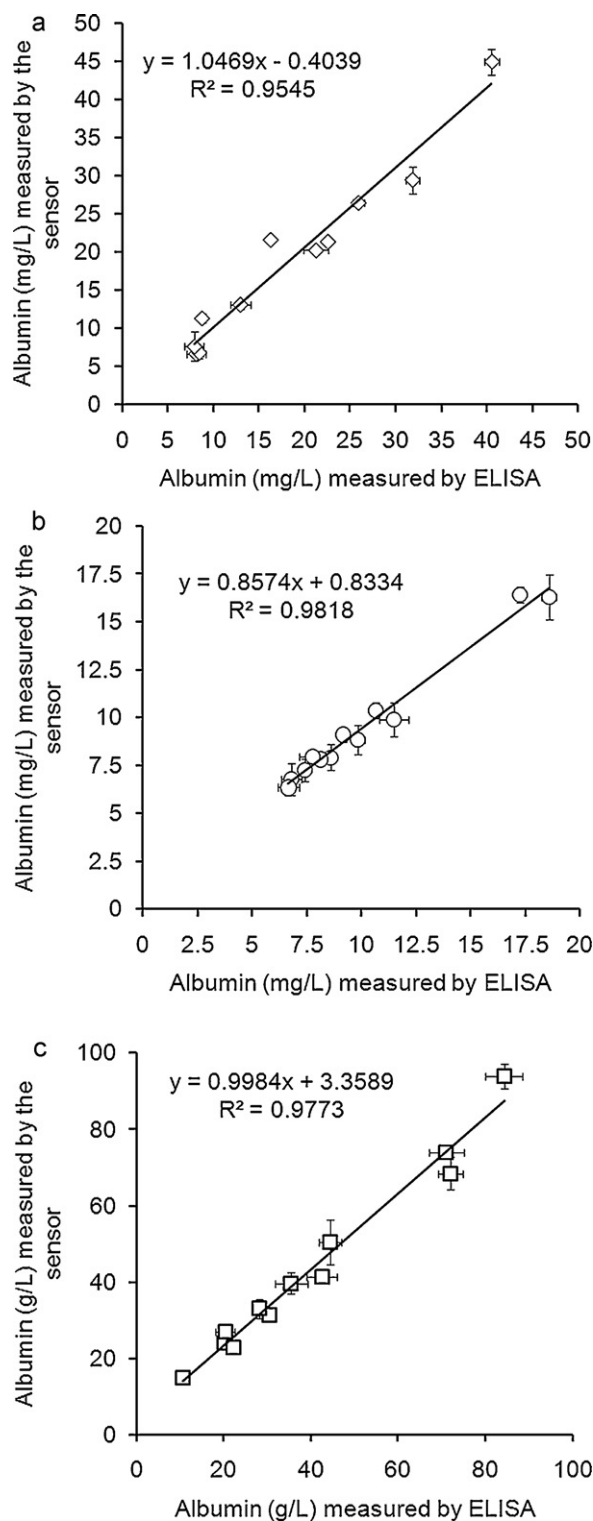


Fig. 3. The validation of sensor with ELISA. Albumin concentrations were measured in (a) saliva (\diamond), (b) urine (\circ), and (c) serum (\square).

collected saliva and urine samples and twelve randomly processed serum samples were assayed using both the sensor and the ELISA method. The results obtained from both methodologies are plotted in Fig. 3. There are high correlations between ELISA and the albumin sensor ($R^2 = 0.9545$ for saliva, $R^2 = 0.9818$ for urine, $R^2 = 0.9773$ for serum), demonstrating that the sensor technology is feasible for quantitative determination of human albumin levels in biofluids such as saliva, urine and serum. Based on the measured values,

human albumin exists in a wide range of concentrations in the saliva (5–45 mg/L) and urine (6–20 mg/L) of healthy people. Both results are within the range reported in the literature [2,9].

3.5. Intra- and inter-CV of the albumin sensor

To examine the accuracy and consistency of albumin measurements in specimens, samples randomly chosen from saliva, urine and serum were subjected to between-assay precision and inter-assay precision studies (Tables S2 and S3 in Supplementary Material). For an assay to be useful, the intra-assay CVs should be less than 10% and the inter-assay CVs should be less than 15% [26–28]. The intra-assay CVs of our albumin sensor were all less than 10%, with most less than 5% (Table S2 in Supplementary Material). Inter-assay CVs were also mostly less than 10% (Table S3 in Supplementary Material). Both the intra- and inter-assay CVs for most measurement of saliva were lower than those for urine and serum, while the CVs appear to be the highest for inter-assay measurements of serum. Overall, the albumin sensor is highly accurate with the precisions required for diagnostic and research applications.

4. Conclusion

We have developed a homogenous sensor that can rapidly detect human albumin in serum, saliva and urine with high specificity and sensitivity. The assay only requires simple operations, needing only one step of mixing and 30–40 min of waiting for the result. The signal generated is robust and stable, and does not require any sophisticated or expensive instruments. The homogenous sensor has a similar sensitivity and accuracy to the traditional ELISA method, but requires fewer operational steps and less assay time. It is therefore conceivable that this sensor can be a promising tool for future diagnostic and prognostic applications. For future work, it would be of interest to apply this sensor to real measurements in a diverse group of patient samples, and to confirm the clinical results with ELISA validation.

Acknowledgements

This work was partially supported by STTR grants from National Institutes of Health (GM079891, GM079891-02S1).

Appendix A. Supplementary data

Supplementary data associated with this article can be found, in the online version, at doi:10.1016/j.jpba.2011.12.035.

References

- [1] G.J. Quinlan, G.S. Martin, T.W. Evans, Albumin: biochemical properties and therapeutic potential, *Hepatology* 41 (2005) 1211–1219.
- [2] T. Peters, *All About Albumin: Biochemistry, Genetics, and Medical Applications*, Academic Press, San Diego, CA, 1996.
- [3] T.A. Strand, R.K. Adhikari, R.K. Chandyo, P.R. Sharma, H. Sommerfelt, Predictors of plasma zinc concentrations in children with acute diarrhea, *Am. J. Clin. Nutr.* 79 (2004) 451–456.
- [4] C. Schindler, G. Ramadori, Albumin substitution improves urinary sodium excretion and diuresis in patients with liver cirrhosis and refractory ascites, *J. Hepatol.* 31 (1999) 1132.
- [5] R. Wettstein, P. Cabrales, D. Erni, A.G. Tsai, R.M. Winslow, M. Intaglietta, Resuscitation from hemorrhagic shock with MalPEG-albumin: comparison with MalPEG-hemoglobin, *Shock* 22 (2004) 351–357.
- [6] P.M. Fortin, K. Bassett, V.M. Musini, Human albumin for intradialytic hypotension in haemodialysis patients, *Cochrane Database Syst. Rev.* (2010), CD006758.
- [7] B.M. Cohen, Role of human albumin in ovarian hyperstimulation syndrome, *Fertil. Steril.* 89 (2008) 1845–1846.
- [8] S. Choi, E.Y. Choi, D.J. Kim, J.H. Kim, T.S. Kim, S.W. Oh, A rapid, simple measurement of human albumin in whole blood using a fluorescence immunoassay (I), *Clin. Chim. Acta* 339 (2004) 147–156.
- [9] S. Akman, I. Kurt, M. Gultepe, I. Dibirdik, C. Kilinc, T. Kutluay, L. Karaca, N.K. Bingol, The development and validation of a competitive, microtiter plate enzymeimmunoassay for human albumin in urine, *J. Immunoassay* 16 (1995) 279–296.
- [10] M.H. Hemmeler, D. de Zeeuw, P.E. de Jong, Measurement of glomerular charge selectivity in non-diabetic renal disease, *Nephrol. Dial. Transplant* 12 (1997) 57–62.
- [11] P.B. Vaziri, M. Vahedi, S.H. Abdollahzadeh, H.R. Abdolsamadi, M. Hajilooi, S.H. Kasraee, Evaluation of salivary albumin in diabetic patients, *Iran. J. Public Health* 38 (2009) 54–59.
- [12] K.T. Izutsu, E.L. Truelove, W.A. Bleyer, W.M. Anderson, M.M. Schubert, J.C. Rice, Whole saliva albumin as an indicator of stomatitis in cancer-therapy patients, *Cancer* 48 (1981) 1450–1454.
- [13] E. Heyduk, E. Knoll, T. Heyduk, Molecular beacons for detecting DNA binding proteins: mechanism of action, *Anal. Biochem.* 316 (2003) 1–10.
- [14] T. Heyduk, E. Heyduk, Molecular beacons for detecting DNA binding proteins, *Nat. Biotechnol.* 20 (2002) 171–176.
- [15] E. Heyduk, B. Dummit, Y.H. Chang, T. Heyduk, Molecular pincers: antibody-based homogeneous protein sensors, *Anal. Chem.* 80 (2008) 5152–5159.
- [16] E. Heyduk, M.M. Moxley, A. Salvatori, J.A. Corbett, T. Heyduk, Homogeneous insulin and C-peptide sensors for rapid assessment of insulin and C-peptide secretion by the islets, *Diabetes* 59 (2010) 2360–2365.
- [17] E. Heyduk, T. Heyduk, Fluorescent homogeneous immunosensors for detecting pathogenic bacteria, *Anal. Biochem.* 396 (2010) 298–303.
- [18] R.D. Nargessi, J. Landon, M. Pourfarzaneh, D.S. Smith, Solid-phase fluoroimmunoassay of human albumin in biological fluids, *Clin. Chim. Acta* 89 (1978) 455–460.
- [19] H.E. Hart, E.B. Greenwald, Scintillation proximity assay (SPA)—a new method of immunoassay. Direct and inhibition mode detection with human albumin and rabbit antihuman albumin, *Mol. Immunol.* 16 (1979) 265–267.
- [20] D.W. Miles, C.E. Mogensen, H.J. Gundersen, Radioimmunoassay for urinary albumin using a single antibody, *Scand. J. Clin. Lab. Invest.* 26 (1970) 5–11.
- [21] A. Silver, A. Dawnay, J. Landon, W.R. Cattell, Immunoassays for low concentrations of albumin in urine, *Clin. Chem.* 32 (1986) 1303–1306.
- [22] J. Woo, M. Floyd, D.C. Cannon, B. Kahan, Radioimmunoassay for urinary albumin, *Clin. Chem.* 24 (1978) 1464–1467.
- [23] B.A. Fielding, D.A. Price, C.A. Houlton, Enzyme immunoassay for urinary albumin, *Clin. Chem.* 29 (1983) 355–357.
- [24] O. Torffvit, J. Wieslander, A simplified enzyme-linked immunosorbent assay for urinary albumin, *Scand. J. Clin. Lab. Invest.* 46 (1986) 545–548.
- [25] I. Hemmila, S. Dakubu, V.M. Mukkala, H. Siitari, T. Lovgren, Europium as a label in time-resolved immunofluorometric assays, *Anal. Biochem.* 137 (1984) 335–343.
- [26] S. Bansal, A. DeStefano, Key elements of bioanalytical method validation for small molecules, *AAPS J.* 9 (2007) E109–E114.
- [27] T. Mori, M. Sakatani, F. Yamagishi, T. Takashima, Y. Kawabe, K. Nagao, E. Shigeto, N. Harada, S. Mitarai, M. Okada, K. Suzuki, Y. Inoue, K. Tsuyuguchi, Y. Sasaki, G.H. Mazurek, I. Tsuyuguchi, Specific detection of tuberculosis infection: an interferon-gamma-based assay using new antigens, *Am. J. Respir. Crit. Care Med.* 170 (2004) 59–64.
- [28] C.W. Damen, H. Rosing, J.H. Schellens, J.H. Beijnen, Application of dried blood spots combined with high-performance liquid chromatography coupled with electrospray ionisation tandem mass spectrometry for simultaneous quantification of vincristine and actinomycin-D, *Anal. Bioanal. Chem.* 394 (2009) 1171–1182.



Short communication

Salsolinol and isosalsolinol: Condensation products of acetaldehyde and dopamine. Separation of their enantiomers in the presence of a large excess of dopamine

María de los Ángeles Juricic^a, Pablo A. Berríos-Cárcamo^a, Mónica L. Acevedo^a, Yedy Israel^{a,b}, Iriux Almodóvar^c, Bruce K. Cassels^{b,c,*}

^a Department of Toxicological and Pharmacological Chemistry, Faculty of Chemical and Pharmaceutical Sciences, Santiago, Chile

^b Millennium Institute for Cell Dynamics and Biotechnology, University of Chile, Casilla 653, Santiago 7800024, Chile

^c Department of Chemistry, Faculty of Sciences, University of Chile, Casilla 653, Santiago 7800024, Chile

ARTICLE INFO

Article history:

Received 25 September 2011

Received in revised form 2 February 2012

Accepted 3 February 2012

Available online 10 February 2012

Keywords:

Dopamine
Salsolinol
Isosalsolinol
Chiral separation
HPLC-ECD

ABSTRACT

Dopamine (DA) condenses, at least *in vitro*, with acetaldehyde, the primary metabolite of ethanol, to form the regioisomers salsolinol (SAL) and isosalsolinol (isoSAL). An alternative *in vivo* route to SAL, requiring a decarboxylation step, has been suggested *via* condensation of DA with pyruvic acid. SAL has been proposed as a mediator of the rewarding effects of ethanol in the brain. We have now shown by HPLC, nuclear magnetic resonance (NMR) and mass spectrometry (MS) that the commercially available SAL contains about 10% of isoSAL, whose biological activity is unknown. If SAL is indeed the biologically active metabolite, rather than isoSAL, it is also unknown whether the rewarding molecule is (*S*)- or (*R*)-SAL. We have developed methodologies for the quantitative determination of DA, SAL and isoSAL using ion-pair reversed-phase HPLC, and for the separation of DA from (*S*)- and (*R*)-SAL and an isoSAL enantiomer on a β -cyclodextrin-modified column, in both cases with electrochemical detection. A significant advance over earlier methods was achieved for the analysis of (*S*)- and (*R*)-SAL in the presence of a large excess of DA (100:1 DA-SAL ratio), as expected to occur *in vivo*, by suppressing the DA peak by selective derivatization with 2,3-naphthalenedicarboxaldehyde into a molecule that is electrochemically silent at the electrode potential used. The methodologies developed will allow the separation and determination of the pharmacological activity of these two products of condensation of acetaldehyde with DA. Further, the techniques for (*S*)- and (*R*)-SAL separation at a high DA:SA ratio will allow the existence of a putative (*R*)-SAL synthase to be determined and, if it exists, its role in alcoholism.

© 2012 Elsevier B.V. All rights reserved.

1. Introduction

Studies over the past decade and most recently in the last year suggest that the reinforcing effects of ethanol are mediated by acetaldehyde generated in the brain [1–3], and possibly by salsolinol (Fig. 1, inset, SAL, 1-methyl-6,7-dihydroxy-1,2,3,4-tetrahydroisoquinoline), a non-enzymatic condensation product of acetaldehyde with dopamine (DA) [4,5]. The existence of an (*R*)-SAL synthase has also been postulated, but not yet demonstrated [6]. The spontaneous condensation of DA with acetaldehyde gives not only SAL but also isosalsolinol (Fig. 1, inset, isoSAL,

1-methyl-7,8-dihydroxy-1,2,3,4-tetrahydroisoquinoline) [7], and at pH 7 both isomers are formed in approximately equal amounts [8]. In view of this fact, the presence in the brain of isoSAL concentrations comparable to those of SAL after ethanol ingestion seems likely.

Commercial (\pm)-SAL hydrochloride (Sigma–Aldrich) is sold as “~85% powder”. As several biological studies have been carried out with this material [4,5,9,10] we deemed it appropriate to determine if isoSAL might be a significant contaminant of SAL. Publications on SAL analysis have concentrated on the separation of its enantiomers and do not mention the regioisomeric (*R*)- and (*S*)-isoSAL [11–15]. In order to ascertain the putative existence of (*R*)-salsolinol synthase and the possible role of the SAL enantiomers in alcoholism, as well as to examine the effects of isoSAL on brain function, we have developed methodologies to separate (*R*)- and (*S*)-SAL and isoSAL from DA even when the latter is present in large excess, as expected in brain samples.

* Corresponding author at: Department of Chemistry, Faculty of Sciences, University of Chile, Casilla 653, Santiago 7800024, Chile. Tel.: +56 2271 3881; fax: +56 2271 3888.

E-mail address: bcassels@uchile.cl (B.K. Cassels).

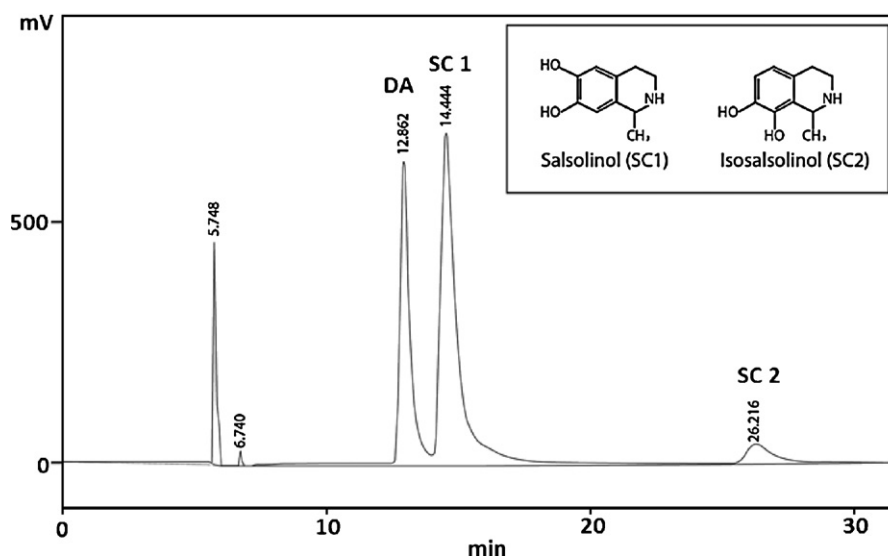


Fig. 1. Ion-pairing reversed-phase chromatograms of DA (1.37×10^{-6} M) and commercial (*R,S*)-SAL (2.88×10^{-6} M SAL and 2.50×10^{-7} M isoSAL). All samples were dissolved in 0.1 M perchloric acid, which gives a peak eluting at 5.76 min. Insets show the molecular structures of salsolinol and isosalsolinol.

2. Experimental

2.1. General

HPLC grade MeOH, analytical grade 85% H_3PO_4 , glacial AcOH, $\text{Na}_2\text{HPO}_4 \cdot 7\text{H}_2\text{O}$, and ammonium acetate were from Merck (Darmstadt, Germany). HPLC grade 2-propanol was from J.T. Baker (Ecatepec, Mexico). (\pm)-SAL-HCl, DA-HCl, EDTA disodium salt, 1-octanesulfonic acid sodium salt, triethylamine (TEA), and NaOH were from Sigma Life Science (St. Louis, MO). Analytical grade 70% HClO_4 and $\text{NaH}_2\text{PO}_4 \cdot \text{H}_2\text{O}$ were from Winkler (Santiago, Chile). ^1H NMR spectra were recorded on a Bruker AMX 400 spectrometer at 300 K, in D_2O solution. Chemical shifts are reported as δ (ppm) downfield from TMS, using the HDO resonance (4.75 ppm) as the secondary internal standard. MS were recorded in the electron impact mode (70 eV) on a Finnigan MAT95 XP (Thermo Scientific, San Jose, CA), and using an ESI-IT Esquire 4000 electrospray-ion trap Bruker Daltonik (Bremen, GFR) instrument in which N_2 was injected at 300 °C and 10 psi, at 5 l/min. The latter spectra were acquired in the positive mode, using esquireControl Version 5.2 software.

2.2. Sample preparation and calibration curves

Stock solutions of DA-HCl (1.37×10^{-2} M) and commercial (\pm)-SAL-HCl (27 mg in 10 ml) were prepared in 0.1 M HClO_4 to minimize oxidation. Assuming a 92:8 ratio of (\pm)-SAL to (\pm)-isoSAL (see below) the concentrations of these compounds in the latter solution should be approximately 1.15×10^{-2} M and 1.00×10^{-3} M, respectively. Dilutions of the stock solutions were prepared in 0.1 M HClO_4 or 0.1 M phosphate buffer (pH 7.4), using distilled and deionized water. Calibration curves were built for DA, SAL and isoSAL. For DA, six concentrations of DA-HCl in the range 1.37×10^{-7} M to 2.74×10^{-6} M were used. For (*R*)- and (*S*)-SAL, six concentrations of commercial (\pm)-SAL-HCl were used, in the range from 1.44×10^{-7} M to 2.88×10^{-6} M considering an estimated isoSAL content of 8% based on the ^1H NMR spectrum of commercial SAL (Supplementary Material, Fig. 1S). Thus, the concentrations of each isoSAL enantiomer were about 1.25×10^{-8} M to 2.50×10^{-7} M.

2.3. HPLC condition

DA, (\pm)-SAL and (\pm)-isoSAL were separated using a Shimadzu LC-10AD (Kyoto, Japan) isocratic pump coupled to a BASi LC-4C (West Lafayette, IN) amperometric detector. 50 μl samples were injected onto a silica gel- C_{18} SUPELCOSIL LC-18 column, 250 mm \times 4.6 mm, 5 μm particle size (Sigma-Aldrich, St. Louis, MO) kept at 30 °C by means of a Shimadzu CTO-10A (Kyoto, Japan) oven. The mobile phase was 20:80 (v/v) MeOH- NaH_2PO_4 (0.1 M, pH 3.4) containing 0.03% EDTA and 141 mg/l 1-octanesulfonic acid sodium salt at a flow rate of 0.4 ml/min. The electrode potential was 700 mV, and the detector sensitivity was 20 nA. The results were analyzed using CLASS CR10 Version 1.2 (Shimadzu Corporation). The SAL enantiomers were separated by injecting 50 μl samples onto a β -cyclodextrin-modified NUCLEODEX β -OH column, 200 mm \times 4 mm, 5 μm particle size (Macherey-Nagel, Düren, GFR) kept at room temperature. To achieve a complete separation of the purified isoSAL enantiomers the column was kept at approximately 2 °C with a Nexcare (3 M, St. Paul, MN) cold pack that had been cooled to this temperature. The mobile phase was aqueous ammonium acetate (100 mM, pH 4.0) containing 0.03% EDTA and 0.10% TEA, at a flow rate of 0.2 ml/min. The electrode potential was 700 mV, and the detector sensitivity was 10 nA.

2.4. Suppression of the dopamine peak

In the above studies, DA and SAL concentrations were approximately 1 μM . In order to evaluate the suppression of the DA peak, DA was injected together with (\pm)-SAL in a 100:1 molar ratio (DA 500 μM and SAL 5.00 μM), either without or with prior derivatization, adapting a published procedure involving reaction of primary, but not secondary amines with 2,3-naphthalenedicarboxaldehyde (NDA) [16]. 100 mM NDA (Fluka) was prepared in methanol by vigorous shaking for 10 min, and 100 mM 2-mercaptoethanol (β -ME) and 100 mM sodium borate buffer, pH 9.5, were also prepared. The derivatization reaction was carried out adding sodium borate buffer (26 μl), β -ME (3 μl), and NDA (12 μl) in that order to a solution of 100 μl of 500 μM DA-HCl and 5 μM (\pm)-SAL-HCl (Sigma), and sufficient nanopure water to reach 150 μl . The solution was left at room temperature for 20 min, and 150 μl of 0.1 M HClO_4 were added to stop the reaction. Finally, 15 μl of this solution was diluted to 200 μl

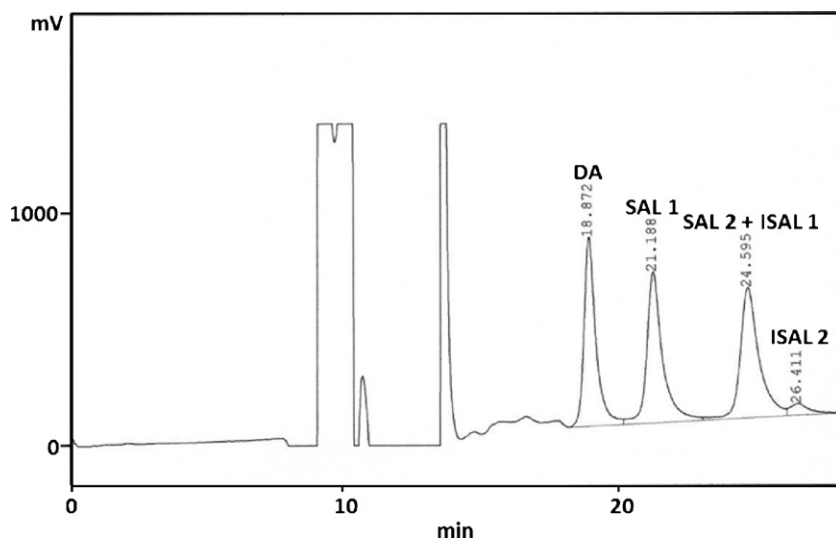


Fig. 2. Chiral HPLC chromatogram of dopamine (DA, 2×10^{-7} M) and commercial salsolinol (4.6×10^{-7} M SAL and 4×10^{-8} M isoSAL, ISAL) in 0.1 M perchloric acid. The two SAL enantiomers were completely resolved with a resolution coefficient of 3.3.

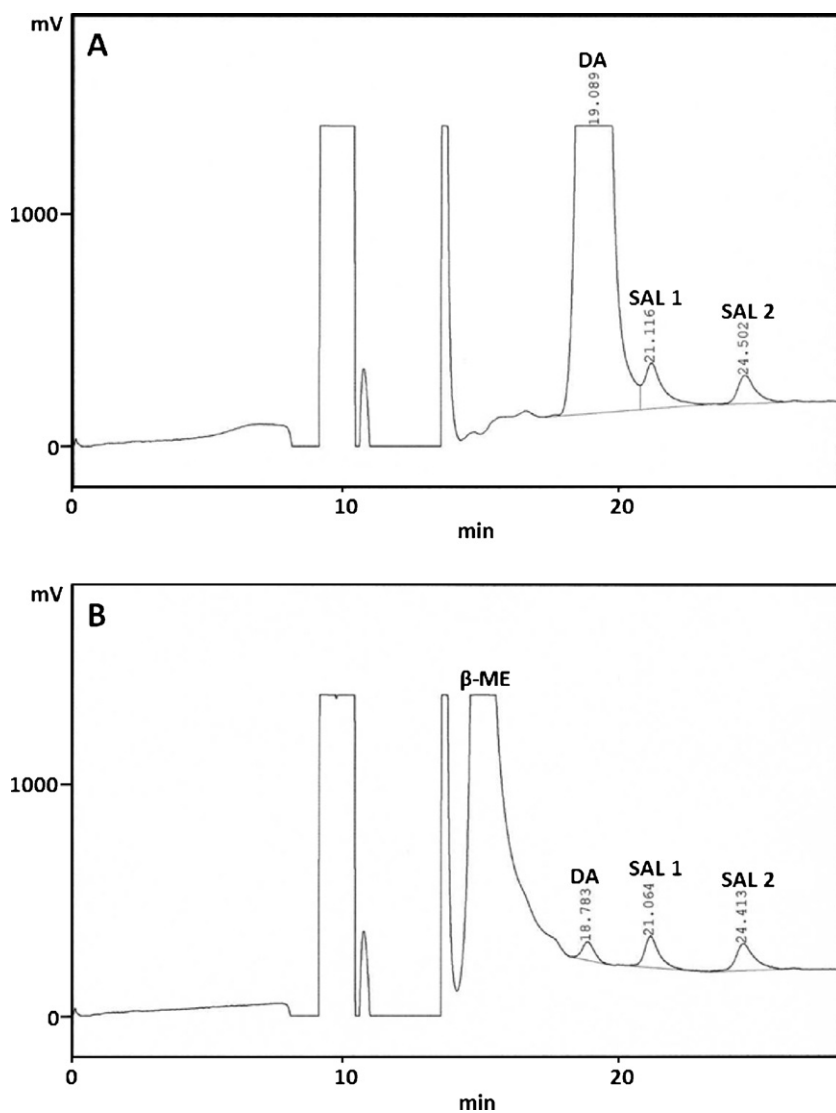


Fig. 3. Chiral HPLC chromatograms of dopamine (5.00×10^{-4} M) and commercial salsolinol (5.00×10^{-6} M) in 0.1 M perchloric acid: (A) no derivatization; (B) following dopamine derivatization with NDA. For the HPLC injection, samples were equally diluted to attain concentrations of 1.25×10^{-5} M for DA and 1.25×10^{-7} M for SAL.

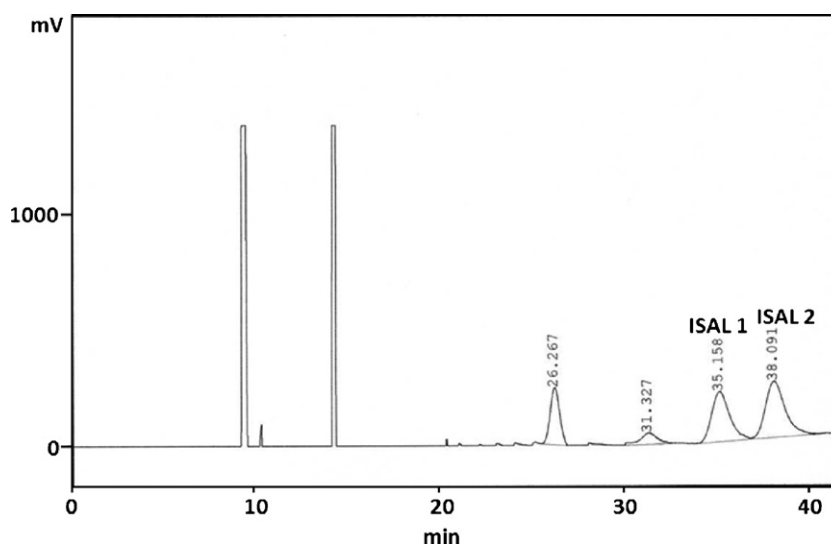


Fig. 4. Chiral HPLC chromatogram of synthetic (\pm)-isoSAL (ISAL) previously purified in the achiral HPLC system. The two IsoSAL enantiomers were completely resolved with a resolution coefficient of 1.7.

with 0.1 M HClO₄, and 50 μ l of the final solution was injected on the NUCLEODEX β -OH column. The mobile phase, flow rate, electrode potential, and detector sensitivity were the same as those described above for the chiral separation.

2.5. Mass spectral analysis

For the identification of the HPLC fractions presumed to contain SAL or isoSAL, the amperometric detector was disconnected and 0.6 ml fractions were collected. Each of these fractions was then analyzed by HPLC to determine homogeneity, and only those containing a single substance were subjected to MS analysis (Supplementary Material, Fig. 2S).

3. Results and discussion

3.1. Achiral HPLC

Preliminary HPLC runs showed that DA eluted at 13.01 ± 0.17 min ($n = 18$). Commercial SAL (SC) – in the presence of a similar concentration of dopamine – gave two chromatographic peaks, with retention times of 14.39 ± 0.01 min (SC1, $n = 18$) and 26.14 ± 0.02 min (SC2, $n = 18$) (Fig. 1), reflecting the presence of two oxidizable substances. The ratio of the peak areas of SC1 and SC2 was 11.5 ± 1.6 ($n = 18$). Thus, SC1 represents $91.91 \pm 1.01\%$ of the oxidizable compounds in this sample, while SC2 represents $8.09 \pm 1.01\%$. These percentages are in close agreement with the 92:8 ratio estimated by ¹H NMR, and SC1 and SC2 were identified as SAL and isoSAL respectively (Supplementary Material, Fig. 1S and 1S bis). To confirm this structural assignment, SC1 and SC2 were collected separately and subjected to MS analysis. Both fractions exhibited an m/z ratio of 180 ($M+H^+$), which agrees with the molecular weight of both regioisomers (179 Da). Both gave the same characteristic fragment ions, but with different relative abundances. In both cases the base peak (100%) occurred at $m/z = 163$, while the fragments at m/z 145, 137 and 117 showed relative abundances of 55%, 44% and 7% (SC1) and 20%, 4% and 9% (SC2), respectively (Supplementary Material, Fig. 2S).

3.2. Chiral HPLC

DA eluted from the β -cyclodextrin-modified column at 18.88 ± 0.05 min ($n = 7$). Commercial SAL gave three peaks (Fig. 2),

two large ones at 21.20 ± 0.09 min ($n = 9$) and 24.62 ± 0.16 min ($n = 8$), and a much smaller one at 26.44 ± 0.16 min ($n = 8$). When SC1 from the achiral column was injected onto the β -cyclodextrin-modified column, two peaks of similar area appeared at 21.2 and 24.6 min. On the other hand, injection of SC2 afforded two similar peaks at 24.8 and 26.4 min which also appeared when the purified synthetic (\pm)-isoSAL was injected, showing that SC2 and the first isoSAL peak (isoSC1) elute at very similar retention times. The identification of the third commercial SAL peak as isoSC2 was achieved by spiking the sample with purified synthetic isoSAL (data not shown). The asymmetry factors of the DA, SC1 and SC2 peaks were 1.4, 1.7, and 2.0, respectively. Given the greater stability of the (*R*)-SAL- β -cyclodextrin complex [17], the substance eluting first is presumed to be (*S*)-SAL, as found by other authors using a similar HPLC system [12–15,18,19]. Interestingly, a published HPLC of commercial SAL, using a similar column, clearly shows two small, poorly resolved peaks that can now be attributed to isoSAL [11].

Previous analyses of (*R*)- and (*S*)-SAL have either failed to separate DA from (*S*)-SAL [14], required mass-spectral detection with or without chemical derivatization and the use of deuterated standards to distinguish both compounds [15,18,20], or did not address this problem at all [6,12]. In our HPLC system, the (*S*)-SAL peak only appeared as a shoulder on the large DA peak (Fig. 3A) when a mixture containing 500 μ M DA and 5 μ M (\pm)-SAL (containing isoSAL) was injected. To suppress the DA peak we added NDA and β -ME [16]. Under these conditions the (*S*)- and (*R*)-SAL peaks, at concentrations of approximately 2.5 μ M each, were again clearly visible and quantifiable (Fig. 3B). Although SC2 and isoSC1 present in commercial (\pm)-SAL-HCl could not be resolved by our system, when (\pm)-isoSAL was injected alone both enantiomers were separated with a resolution coefficient of 1.7 (Fig. 4).

Acknowledgements

This work was funded by grants from FONDECYT (1095021 and 3100059) and ICM (P05-001-F).

Appendix A. Supplementary data

Supplementary data associated with this article can be found, in the online version, at doi:10.1016/j.jpba.2012.02.002.

References

- [1] M. Correa, J.D. Salamone, K.N. Segovia, M. Pardo, R. Longoni, L. Spina, A.T. Peana, S. Vinci, E. Acquas, Piecing together the puzzle of acetaldehyde as a neuroactive agent, *Neurosci. Biobehav. Rev.* 36 (2011) 404–430.
- [2] E. Karahanian, M.E. Quintanilla, L. Tampier, M. Rivera-Meza, D. Bustamante, V. Gonzalez-Lira, P. Morales, M. Herrera-Marschitz, Y. Israel, Ethanol as a prodrug: brain metabolism of ethanol mediates its reinforcing effects, *Alcohol. Clin. Exp. Res.* 35 (2011) 606–612.
- [3] R. Deitrich, Ethanol as a prodrug: brain metabolism of ethanol mediates its reinforcing effects—a commentary, *Alcohol. Clin. Exp. Res.* 35 (2011) 581–583.
- [4] Z.A. Rodd, R.L. Bell, Y. Zhang, A. Goldstein, A. Zaffaroni, W.J. McBride, T.K. Li, Salsolinol produces reinforcing effects in the nucleus accumbens shell of alcohol preferring (P) rats, *Alcohol. Clin. Exp. Res.* 27 (2003) 440–449.
- [5] Z.A. Rodd, S.M. Oster, Z.M. Ding, J.E. Toalston, G. Deehan, R.L. Bell, T.K. Li, W.J. McBride, The reinforcing properties of salsolinol in the ventral tegmental area: evidence for regional heterogeneity and the involvement of serotonin and dopamine, *Alcohol. Clin. Exp. Res.* 32 (2008) 230–239.
- [6] M. Naoi, W. Maruyama, P. Dostert, K. Kohda, T. Kaiya, A novel enzyme enantioselectively synthesizes (R)salsolinol, a precursor of a dopaminergic neurotoxin, N-methyl(R)salsolinol, *Neurosci. Lett.* 212 (1996) 183–186.
- [7] G.S. King, B.L. Goodwin, M. Sandler, Isosalsolinol formation: a secondary reaction in the Pictet-Spengler condensation, *J. Pharm. Pharmacol.* 26 (1974) 476–478.
- [8] H.A. Bates, K. Bagheri, P.M. Vertino, Effect of pH on the regioselectivity of Pictet-Spengler reactions of 3-hydroxyphenethylamines with formaldehyde and acetaldehyde, *J. Org. Chem.* 51 (1986) 3061–3063.
- [9] L. Hipólito, M.J. Sánchez-Catalán, L. Granero, A. Polache, Local salsolinol modulates dopamine extracellular levels from rat nucleus accumbens: shell/core differences, *Neurochem. Int.* 55 (2009) 187–192.
- [10] S. Matsuzawa, T. Suzuki, M. Misawa, Involvement of mu-opioid receptor in the salsolinol-associated place preference in rats exposed to conditioned fear stress, *Alcohol. Clin. Exp. Res.* 24 (2000) 366–372.
- [11] S.S. Baum, H. Rommelspacher, Determination of total dopamine, R- and S-salsolinol in human plasma by cyclodextrin bonded-phase liquid chromatography with electrochemical detection, *J. Chromatogr. B* 660 (1994) 235–241.
- [12] M. Cai, Y.M. Liu, Quantification of salsolinol enantiomers by stable isotope dilution liquid chromatography with tandem mass spectrometric detection, *Rapid Commun. Mass Spectrom.* 22 (2008) 4171–4177.
- [13] Y. Deng, W. Maruyama, P. Dostert, T. Takahashi, M. Kawai, M. Naoi, Determination of the (R)- and (S)-enantiomers of salsolinol and N-methyl salsolinol by use of a chiral high-performance liquid chromatographic column, *J. Chromatogr. B* 670 (1995) 47–54.
- [14] Y. Deng, W. Maruyama, M. Kawai, P. Dostert, K. Yamamura, T. Takahashi, M. Naoi, Assay for the (R)- and (S)-enantiomers of salsolinols in biological samples and foods with ion-pair high-performance liquid chromatography using beta-cyclodextrin as a chiral mobile phase additive, *J. Chromatogr. B* 689 (1997) 313–320.
- [15] J. Lee, B.X. Huang, Z. Yuan, H.Y. Kim, Simultaneous determination of salsolinol enantiomers and dopamine in human plasma and cerebrospinal fluid by chemical derivatization coupled to chiral liquid chromatography/electrospray ionization-tandem mass spectrometry, *Anal. Chem.* 79 (2007) 9166–9173.
- [16] G. Rammouz, M. Lacroix, J.C. Garrigues, V. Poinso, F. Couderc, The use of naphthalene-2,3-dicarboxaldehyde for the analysis of primary amines using high performance liquid chromatography and capillary electrophoresis, *Biomed. Chromatogr.* 21 (2007) 1223–1239.
- [17] M.J. Huang, Z. Qua, Y.M. Liu, Computational modelling of inclusion complexes of beta-cyclodextrin with enantiomers of salsolinol, N-methyl-salsolinol, and 1-benzyl-tetrahydroisoquinoline, *Int. J. Quantum Chem.* 109 (2009) 81–90.
- [18] T. Rojkovicová, Y. Mechref, J.A. Starkey, G. Wu, R.L. Bell, W.J. McBride, M.V. Novotny, Quantitative chiral analysis of salsolinol in different brain regions of rats genetically predisposed to alcoholism, *J. Chromatogr. B* 863 (2008) 206–214.
- [19] Y.M. Liu, P. Gordon, S. Green, J.V. Sweedler, Determination of salsolinol enantiomers by gas chromatography–mass spectrometry with cyclodextrin chiral columns, *Anal. Chim. Acta* 420 (2000) 81–88.
- [20] J. Lee, V.A. Ramchandani, K. Hamazaki, E.A. Engleman, W.J. McBride, T.K. Li, H.Y. Kim, A critical evaluation of influence of ethanol and diet on salsolinol enantiomers in humans and rats, *Alcohol. Clin. Exp. Res.* 34 (2010) 242–250.

Editors

B. Chankvetadze, Department of Chemistry, School of Exact and Natural Sciences, Tbilisi State University, 0179 Tbilisi, Georgia. E-mail: jpba_bezhan@yahoo.com

S. Görög, Chemical Works of Gedeon Richter Ltd., P.O. Box 27, H-1475 Budapest 10, Hungary. E-mail: s.gorog@richter.hu

J. Haginaka, Faculty of Pharmaceutical Sciences, Mukogawa Women's University, 11-68 Koshien Kyuban-cho, Nishinomiya 663-8179, Japan. E-mail: jpba@mukogawa-u.ac.jp

R. Moaddel, Baltimore, MD. 21224. USA. Tel: - +1-301-792-6579.

S. Pinzauti, Department of Pharmaceutical Sciences, University of Florence, Polo Scientifico, Via U. Schiff 6, 50019 Sesto Fiorentino, Italy. E-mail: pinz@unifi.it

Editorial Advisory Board

S.W. Baertschi (Indianapolis, IN, USA)

C. Barbas (Madrid, Spain)

C. Bertucci (Bologna, Italy)

F. Bressolle (Montpellier, France)

P.S. Callery (Morgantown, WV, USA)

A. Cifuentes (Madrid, Spain)

S. Fanali (Monterotondo Scalo, Italy)

S. Furlanetto (Florence, Italy)

M. Ganzer (Innsbruck, Austria)

R. Gotti (Bologna, Italy)

P. Hubert (Sart-Tilman Liège, Belgium)

U. Holzgrabe (Würzburg, Germany)

K. Jozwiak (Lublin, Poland)

K. Kakehi (Higashi-Osaka, Japan)

R. Kaliszan (Gdansk, Poland)

S.P. Li (Macau, China)

B.K. Matuszewski (West Point, PA, USA)

N. Medlicott (Dunedin, New Zealand)

R.H.H. Neubert (Halle/Saale, Germany)

B.A. Olsen (Indianapolis, IN, USA)

K.W. Phinney (Gaithersburg, MD, USA)

S. Pichini (Rome, Italy)

M.A. Raggi (Bologna, Italy)

K.E. Scriba (Jena, Germany)

K. Shimada (Sendai, Japan)

S. Singh (S.A.S. Nagar, India)

E. Szökő (Budapest, Hungary)

T-H. Tsai (Taipei, Taiwan)

Y. Vander Heyden (Brussels, Belgium)

J.-L. Veuthey (Geneva, Switzerland)

I.D. Wilson (Macclesfield, UK)

G. Xu (Dalian, China)

Author enquiries

For enquiries relating to the submission of articles (including electronic submission) please visit this journals homepage at <http://www.elsevier.com/locate/jpba>. Contact details for questions arising after acceptance of an article, especially those relating to proofs, will be provided by the publisher. You can track accepted articles at <http://www.elsevier.com/trackarticle>. You can also check our Author FAQs at <http://www.elsevier.com/authorFAQ> and/or contact Customer Support via <http://support.elsevier.com>.

Funding body agreements and policies

Elsevier has established agreements and developed policies to allow authors whose articles appear in journals published by Elsevier, to comply with potential manuscript archiving requirements as specified as conditions of their grant awards. To learn more about existing agreements and policies please visit <http://www.elsevier.com/fundingbodies>

Orders, claims, and journal enquiries: please contact the Elsevier Customer Service Department nearest you:

St. Louis: Elsevier Customer Service Department, 3251 Riverport Lane, Maryland Heights, MO 63043, USA; phone: (877) 8397126 [toll free within the USA]; (+1) (314) 4478878 [outside the USA]; fax: (+1) (314) 4478077; e-mail: JournalCustomerService-usa@elsevier.com

Oxford: Elsevier Customer Service Department, The Boulevard, Langford Lane, Kidlington, Oxford OX5 1GB, UK; phone: (+44) (1865) 843434; fax: (+44) (1865) 843970; e-mail: JournalsCustomerServiceEMEA@elsevier.com

Tokyo: Elsevier Customer Service Department, 4F Higashi-Azabu, 1-Chome Bldg, 1-9-15 Higashi-Azabu, Minato-ku, Tokyo 106-0044, Japan; phone: (+81) (3) 5561 5037; fax: (+81) (3) 5561 5047; e-mail: JournalsCustomerServiceJapan@elsevier.com

Singapore: Elsevier Customer Service Department, 3 Killiney Road, #08-01 Winsland House I, Singapore 239519; phone: (+65) 63490222; fax: (+65) 67331510; e-mail: JournalsCustomerServiceAPAC@elsevier.com
